ASME
SETTING THE STANDARD

Transactions of the ASME, Journal of Turbomachinery (ISSN 0889-504X) is published quarterly (Jan., Apr., July, Oct.) by The American Society of Mechanical Engineers, Three Park Avenue, New York, NY 10016. Periodicals postage paid at New York, NY and additional mailing offices.
POSTMASTER: Send address changes to Transactions of the ASME, Journal of Turbomachinery, c/o THE AMERICAN SOCIETY OF MECHANICAL ENGINEERS, 22 Law Drive, Box 2300, Fairfield, NJ 07007-2300.
CHANGES OF ADDRESS must be received at Society headquarters seven weeks before they are to be effective. Please send old label and new address.

Journal of Turbomachinery

Published Quarterly by ASME

VOLUME 129 • NUMBER 2 • APRIL 2007

TECHNOLOGY REVIEW

TECHNICAL PAPERS

(Contents continued on inside back cover)

This journal is printed on acid-free paper, which exceeds the ANSI Z39.48-1992 specification for permanence of paper and library materials. ♾™
♻ 85% recycled content, including 10% post-consumer fibers.

Journal of Turbomachinery Volume 129, Number 2 APRIL 2007

The ASME Journal of Turbomachinery is abstracted and indexed in the following:

Aluminum Industry Abstracts, Aquatic Science and Fisheries Abstracts, Ceramics Abstracts, Chemical Abstracts, Civil Engineering Abstracts, Compendex (The electronic equivalent of Engineering Index), Corrosion Abstracts, Current Contents, Ei EncompassLit, Electronics & Communications Abstracts, Energy Information Abstracts, Engineered Materials Abstracts, Engineering Index, Environmental Science and Pollution Management, Excerpta Medica, Fluidex, Fuel and Energy Abstracts, INSPEC, Index to Scientific Reviews, Materials Science Citation Index, Mechanical & Transportation Engineering Abstracts, Mechanical Engineering Abstracts, METADEX (The electronic equivalent of Metals Abstracts and Alloys Index), Metals Abstracts, Oceanic Abstracts, Pollution Abstracts, Referativnyi Zhurnal, Shock & Vibration Digest, Steels Alert

Journal of Turbomachinery

Technology Review

Gas Turbine Heat Transfer: Ten Remaining Hot Gas Path Challenges

Ronald S. Bunker
GE Global Research Center,
Niskayuna, NY 12309

The advancement of turbine cooling has allowed engine design to exceed normal material temperature limits, but it has introduced complexities that have accentuated the thermal issues greatly. Cooled component design has consistently trended in the direction of higher heat loads, higher through-wall thermal gradients, and higher in-plane thermal gradients. The present discussion seeks to identify ten major thermal issues, or opportunities, that remain for the turbine hot gas path (HGP) today. These thermal challenges are commonly known in their broadest forms, but some tend to be little discussed in a direct manner relevant to gas turbines. These include uniformity of internal cooling, ultimate film cooling, microcooling, reduced incident heat flux, secondary flows as prime cooling, contoured gas paths, thermal stress reduction, controlled cooling, low emission combustor-turbine systems, and regenerative cooling. Evolutionary or revolutionary advancements concerning these issues will ultimately be required in realizable engineering forms for gas turbines to breakthrough to new levels of performance. Herein lies the challenge to researchers and designers. It is the intention of this summary to provide a concise review of these issues, and some of the recent solution directions, as an initial guide and stimulation to further research.
[DOI: 10.1115/1.2464142]

Introduction

The technology of cooling gas turbine components has developed over the years from simple smooth cooling passages to very complex geometries involving many differing surfaces, architectures, and fluid-surface interactions. The fundamental aim of this technology area is to obtain the highest overall cooling effectiveness with the lowest possible penalty on the thermodynamic cycle performance. Figure 1 provides a generic view of the gross cooling effectiveness for turbine airfoils with the cooling technologies developed over the years.

Actively or passively cooled regions in both aircraft engine and power-generating gas turbines include the stationary vanes or nozzles and the rotating blades or buckets of the high pressure turbine (HPT) stages, the shrouds bounding the rotating blades, and the combustor liners and flame-holding segments. Collectively, these components are referred to as the hot gas path. All such engines additionally cool the interfaces around the immediate hot gas path, thereby bringing into consideration the secondary flow circuits of the turbine wheelspaces and the outer casings that serve as both cooling and positive purge flows. The ever present constraints common to all components and systems include but are not limited to pressure losses, material temperatures, component stresses, geometry and volume, aerodynamics, fouling, and coolant conditions. Conventional cooling technology, as applied to gas turbine engine components is composed of five main elements: (i) internal convective cooling, (ii) external surface film cooling, (iii) materials selection, (iv) thermal-mechanical design at both the component and system levels, and (v) selection and/or pre-treatment of the coolant fluid. Together these technologies define the thermal management capabilities and limitations in today's gas turbines.

The enhancement of internal convective flow surfaces for the augmentation of heat transfer was initiated through the introduction of turbulators and pinbanks within investment cast airfoils. These surface enhancement methods continue to play a large role in today's turbine cooling designs. With the advancements in materials and manufacturing technologies of the last decade, a drastically larger realm of surface enhancement techniques has become cost effective for use in the cooling of turbine airfoils.

The art and science of film cooling concerns the bleeding of internal component cooling air through the external walls to form a protective layer of cooling between the hot gases and the component external surfaces. The application of effective film-cooling techniques provides the first and best line of defense for hot gas path surfaces against the onslaught of extreme heat fluxes, serving to directly reduce the incident convective heat flux on the surface.

Materials most commonly employed in cooled parts include high-temperature, high-strength nickel-or cobalt-based superalloys coated with yttria-stabilized zirconia oxide ceramics (thermal barrier coatings (TBC)). The protective ceramic coatings are today actively used to enhance the cooling capability of the internal convection mechanisms and to dampen thermal gradients during transient events.

The thermomechanical design of the components must marry these first three elements into a package that has acceptable thermal stresses, coating strains, oxidation limits, creep-rupture properties, and aeromechanical response. Under the majority of practical system constraints, this means the highest achievable internal convective heat transfer coefficients with the lowest achievable friction coefficient or pressure loss. More often than not, however, the challenge lies in the manufacturing limitations for such thermomechanical designs to be cost effective for the life of the components.

The last cooling design element concerns the correct selection of the cooling fluid to perform the required function with the least impact on the cycle efficiency. This usually is achieved through the use of compressor air bled from the most advantageous stage of the compressor, but can also be done using off-board cooling sources, such as closed-circuit steam or air, as well as intracycle and intercycle heat exchangers.

Contributed by the Turbomachinery Division of ASME for publication in the JOURNAL OF TURBOMACHINERY. Manuscript received July 12, 2006; final manuscript received July 16, 2006. Review conducted by David Wisler.

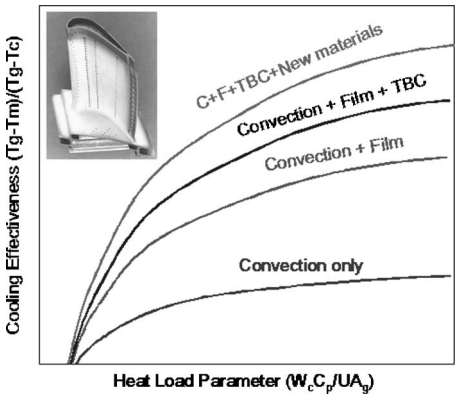

Fig. 1 Generic cooling technology curves and example cooled hpt blade

Conflicts and Crossroads

Gas turbine heat transfer and thermal management technology meets very advanced requirements today, but it is also true that it has reached a plateau, for the most part, with further increases in efficiency and life, coming as small incremental improvements rather than revolutionary changes. The present status was actually reached five to ten years ago with the widespread use of shaped film cooling and TBC. In the interim period, advancements in cooling technology have primarily been in the more detailed understanding of boundary conditions and the higher sophistication of analysis tools. Having reached this plateau, there are several questions to be considered in pushing thermal technology further:

1. Can we, or should we, seek to cool a component better in specific locations (i.e., chasing hotspots), rather than globally improving cooling performance?
2. Can we do a better job of shielding the component from the incident heat load?
3. Should we make the component, or portions thereof, hotter instead of cooler, and perhaps do this as a function of engine operating point?
4. Can we move the thermal energy (heat) to somewhere else and deal with it there (i.e., use it or reject it)?

Note that these questions do not also ask if the manufacturing technology exists to support solutions nor if the solutions are cost effective. These issues will be left off the table for the present discussion. Focus is placed only on the identification of major thermal aspects here, trusting that means for solutions will be developed in parallel with the solutions themselves.

The questions that have been posed may seem to lack definition, but the nature of the thermal issues is, in fact, the same today as they were decades ago. Progress in heat transfer and cooling for turbines has simply brought more definition to the magnitude and detail of the issues. The ultimate goals in gas turbine thermal management are consistent with the thermodynamics of isentropic energy transfer. By this it is meant that (i) the component or some portion of it is desired to be isothermal to eliminate all internal thermal stresses, (ii) the component is desired to be at or close to the hot gas temperature to minimize heat loads and inefficient energy transfers, and (iii) thermal gradients from the component to the support and containment structure are desired to be minimized for these same reasons. To the latter point, if the component and support structure can be thermally disconnected, then the desired spatial thermal gradient will be large while the separate material thermal gradients are small (i.e., insulated for reduced heat loss). This is essentially where gas turbine design began, and it is still the objective, only at a far higher operating temperature today. The advancement of turbine cooling has allowed engine design to exceed normal material temperature limits, but it has introduced complexities that have accentuated the thermal issues greatly. Cooled component design has consistently trended in the direction of higher heat loads, higher through-wall thermal gradients, and higher in-plane thermal gradients.

Ten Remaining Thermal Challenges

The present discussion seeks to identify ten major thermal issues, or opportunities, that remain today. It is not the intention here to imply that these are all-inclusive issues. The issues are very roughly categorized to follow similar lines of thinking as the four questions posed above. Solutions to these issues will ultimately be required to address these questions in realizable engineering, wherein lies the challenge to researchers and designers:

1. Active Cooling Technology
   - uniformity of internal cooling
   - ultimate discrete hole film cooling
   - microcooling
2. Hot Gas Flow Paths
   - reducing incident heat flux
   - secondary flows as prime HGP cooling
   - micro-3D HGP surfaces
3. Component Design
   - thermal stress reduction
   - controlled and adaptable cooling
4. Systems Design
   - low-emission combustor-turbine systems
   - regenerative cooling

Uniformity of Internal Cooling. As noted in the Introduction, the majority of internal cooling augmentation improvement has dealt with the use of various forms of turbulators and pin fins, or similar repeated surface features, to generate fluid turbulence, vortices, and bulk mixing for greater heat transfer coefficients. In so doing, some methods have obtained augmentation factors relative to smooth surface heat transfer coefficients of as much as 4, with even higher magnitudes possible under certain rotational conditions. Such levels match the other well-known cooling method of jet impingement, which is most commonly used in stationary components. In all of these methods, further increases in heat transfer coefficient magnitudes may be desirable, but these increases typically also come with undesirable increased material thermal gradients. For open-loop cooling, in which the heat flux is processed through the component wall to the coolant and then combined again in the hot gases as the coolant is injected as film, the peak magnitude of heat transfer coefficient is no longer so important as the gradients in coefficient and material temperature. Higher gradients lead to stress and strain barriers, either steady or cyclic, as well as greater levels of thermodynamic unmixedness or inefficiencies.

A greater degree of uniformity in internal cooling is key to many current thermal stress-strain limitations. As implied earlier, this uniformity may also take the form of less cooling in some locations to gain a more isothermal material condition. Turbine airfoils can generally withstand higher bulk temperatures as the local thermal gradients are reduced. Recent research into internal cooling has begun to investigate more distributed forms of cooling enhancement that may be formed as part of the airfoil walls, in essence creating a cooling flow network within the wall rather than a bulk flow effect within the hollow airfoil. Zhang et al. [1] addressed this type of cooling network for different open flow areas, or alternately different solidity of channel meshes, using straight channels that intersect with included angle of 60 deg, showing 2 to 2.5 times local heat transfer enhancement compared to a smooth channel. Heat transfer in small prefilm impingement

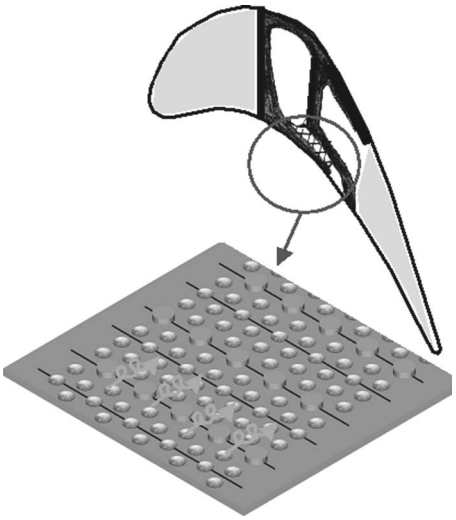

Fig. 2 Example of internal airfoil wall network cooling

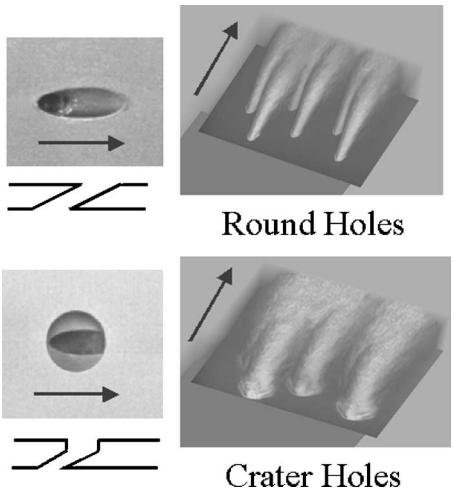

Fig. 3 Alternate film hole shaping for greater effectiveness

chambers within airfoil wall sections was studied by Gillespie et al. [2] showing the contributions to cooling of both chamber interior surfaces. Bunker et al. [3] examined various configurations of in-wall mesh, or network cooling, using combined flow augmentation techniques of pins, turbulators, and concavities. Figure 2 shows an example of the interior of one such cooling mesh. This research showed the potential of increased synergistic cooling by the interaction of augmentation features with more than three times the heat transfer of smooth channels.

Ultimate Discrete Hole Film Cooling. Over the past 30+ years, investigations have been performed by a broad spectrum of researchers to understand the fundamental physics of film cooling, and to improve the state of the art. The primary focus of most research has been on the use of discrete film holes, or rows of film holes, on the hot gas path surfaces of the turbine. Virtually all aspects of film cooling have been explored, some in great depth and others to a lesser extent, both experimentally and computationally. One of the goals of film cooling in gas turbines has been the achievement of ideal cooling films, such as those from two-dimensional (2D) continuous slots with uniformly distributed cooling supply. Because of the many competing constraints of turbine design (e.g., aerodynamics, thermal and mechanical stress, fabrication), it is generally impractical to place such slots into the high-temperature surfaces of the turbine components. As a consequence, film cooling is performed almost exclusively through the use of discrete holes and rows of evenly spaced holes. In practical applications, both commercial and military, all film-cooling holes are either round or shaped.

Considering the extent and diversity of research into film cooling, it is somewhat surprising to realize that only one primary advancement in this technology has been put into widespread practice over these many years. That single improvement has been the change from round film holes to fan-shaped, or diffuser, film holes. Furthermore, the use of the term "shaped," while allowing a potentially vast number of geometries, is actually limited again to a single class of geometry. Shaped holes are composed of round metering or throat sections with a uniform and symmetric expanded exit region on the hot gas surface. Most commonly, all shaped holes applied in practice have fan diffuser exits with divergence angles between 10 deg and 15 deg on each lateral side as well as on the side into the surface. It is as simple as that.

A recent review of shaped film cooling and its effects may be found in Bunker [4]. In this review, several concepts for alternative and improved discrete film cooling of the hot gas path are also presented. Moser et al. [5] analyzed a transonic wall jet geometry in which the film hole transitions from some interior cross section, perhaps circular, to a surface slit. This transition is such that the hole converges in both the axial and lateral directions. The basic principle of this design is the creation of a choked flow and underexpanded jet that will conform to the exterior curved surface via the Prandtl-Meyer effect for expansion waves. Sargison et al. [6] demonstrated a convergent slot-hole geometry. In this geometry, the hole transitions from circular to slot with convergence in the axial direction and divergence laterally. The hole area does diminish to cause the flow to accelerate, though not necessarily to a choked condition. The exit is the metering section. This accelerated flow is speculated to have lower jet turbulence and more stability. Flat-plate tests show the effectiveness and heat transfer coefficient enhancement to be on par with fan-shaped holes, while the aerodynamic loss is less. Fric and Campbell [7] investigated a so-called cratered film hole in which the circular hole exits into a shallow right circular surface cup or depression. The flow actually impinges on the edge of this depression causing it to deflect and fill the depression prior to issuing onto the external surface. Flat-plate tests show about a 50% improved effectiveness over round holes at $M=1$, and a greater increase as blowing ratio increases. Effectiveness improvement of 100% and more was observed at $M=5$. Figure 3 shows a comparison of round and cratered film cooling using planar laser induced fluorescence. Bunker [8] extended the work of [7] to a two-dimensional version, or trench film geometry. The intention of this geometry is the same, to cause the film-cooling flow to spread into the trench prior to issuing on the surface. The particular advantage of this geometry is that it can be formed using the protective coatings applied to the surface, such as TBC, without machining the trench into the substrate. Film-effectiveness improvements of 50–75% over round holes were measured in flat plate tests, putting this on par with shaped holes. Finally, Nasir et al. [9] tested round film holes with the addition of triangular tabs covering the upstream edge of the holes, either turned upward, downward, or flat. The flat and downward tabs modified the exit flow and vortex structure in a manner that kept the coolant from lifting off. Their data showed effectiveness consistent with shaped holes.

Microcooling. All cooled turbine airfoils in commercial operation today utilize cooling channels and film holes that are considered to be macroscopic in physical magnitude. The generally accepted delimiters between macro- and microcooling are (i) whether the feature (internal passage) can be repeatedly manufactured via investment casting methods and (ii) whether the flow passage (film hole) may become plugged by particles in the cooling fluid. The acceptable sizes are relative to the turbine size and the operating environment. Aircraft engine turbine airfoils are small and require smaller flow passages and film holes, while

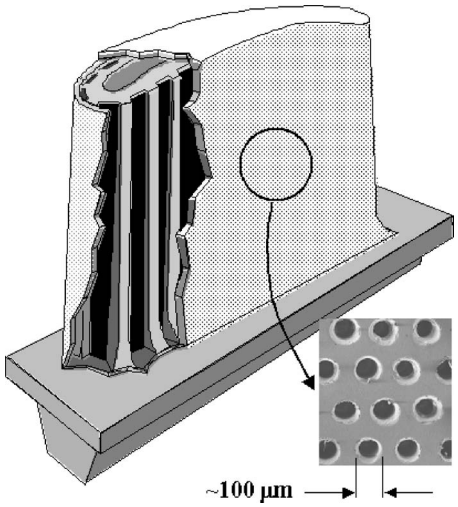

Fig. 4 Schematic of microcooled airfoil

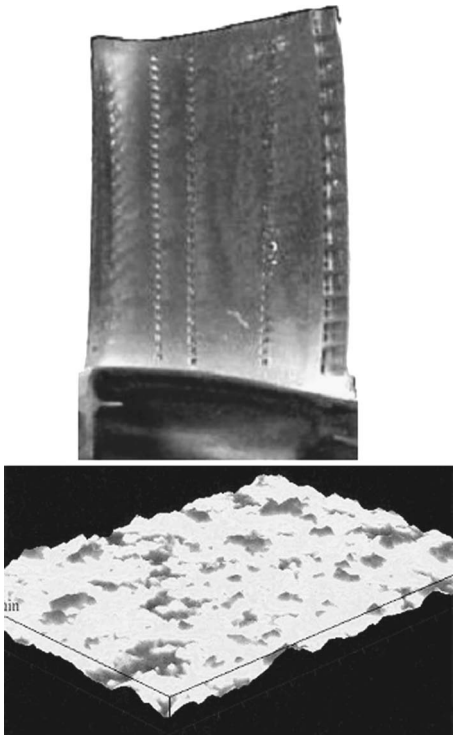

Fig. 5 Example of roughened turbine airfoil

large power turbine castings cannot support equivalent small passages and would more easily be plugged if the same size film holes were employed. As an example, an average aircraft engine may allow film hole diameters as small as 0.457 mm (0.018 in.), while an average heavy frame power turbine may be limited to a minimum diameter of only 1.02 mm (0.040 in.).

The concept of microcooling for airfoils is the natural application of thermodynamics and heat transfer to accomplish two main goals. First, to spread out the cooling network in a series of smaller and highly distributed channels, or subchannels, providing better uniformity of cooling and lesser in-plane thermal gradients. This is analogous to the distribution of blood vessels in the human body. Second, to bring the cooling fluid closer to the outer surface of the airfoil, thereby creating a more efficient transfer of heat. Microcooling may be thought of as a complete airfoil cooling solution, or as a regional cooling device (e.g., leading edges). Figure 4 provides a schematic version of generic microcooling for an airfoil using a transpiration surface.

The most notable developments of microcooling are those of the Allison Advanced Development Corporation, known by the tradenames of Lamilloy® and CastCool® [10]. The airfoil walls in Lamilloy are formed as two or more sheets of metal bonded together with distributed pins, while those of CastCool are investment cast and limited to a double-wall type. The cooling flow is introduced via impingement jets that are staggered with respect to the exiting film holes. Full cooling distribution is obtained, and a form of transpiration-like film cooling results from the normal holes in the outer layer. Examples of the overall cooling effectiveness and the film cooling are shown by Nakamata et al. [11] and Hale et al. [12], respectively. The challenges of this microcooling include hole plugging, wall strength, film cooling, manufacturing, and cost. No commercial use of these microcooled solutions has yet appeared.

Other forms of proposed microcooling include fabricated diffusion surfaces formed by electrogalvanic metal deposition, such as that described by Battisti [13]. An early attempt at transpiration described by Wolf and Moskowitz [14] used a wire wound external blade mesh over an airfoil spar with feed cooling channels. Russian and Ukrainian turbine airfoil research [15] developed a shell-and-spar approach to manufacturing. In this method, the interior portion of the airfoil is cast in a simple format, and cooling channels machined in the exposed surface. The channels are then filled with a leachable material, a thin outer airfoil skin is bonded to the nonchannel metal regions, and the filler is leached out. The result is a distribution of small cooling channels close to the outer surface. Again, these microcooling forms face significant material and processing challenges, as well as unexplored thermal and fluid design domains.

Reducing Incident Heat Flux. Certainly the most effective means for managing the heat transfer of the hot gas path components is to shield the surfaces from the incident heat flux. Before the introduction of ceramic coatings, film cooling was the primary method used to reduce the effective gas temperature driving heat flux to the surfaces. As long as a heat flux still exists, TBC can be effectively used to raise the external surface temperature, thereby also reducing heat flux to the surfaces. The usual design practice is to apply TBC while also decreasing the amount of coolant, which serves to improve efficiency, but tends to lead back to the original thermal gradients and heat flux levels. Aside from further increases in film-cooling effectiveness for a given cooling flow rate, or the application of thicker TBC coatings, new methods are required to fundamentally reduce incident heat flux.

The incident heat flux on the external surfaces can be described after a manner in terms of three components: that due to basic aerodynamics, that due to surface condition, and that due to thermal radiation. The first of these concerns design requirements that drive the pressure ratio and severity of convective heat transfer. Radiation is generally 5–10 % of the heat flux, except in regions viewing the flame zone, and while important is not a major factor. Surface condition may be primarily associated with roughness due to deposits, coating erosion, coating spallation, hot corrosion, and oxidation. Surface roughness can serve to raise convective heat transfer coefficients by up to 100% [16] and, thus, is a major factor requiring alleviation. The recent research of Bons et al. [17] surveyed the various types and magnitudes of roughness and investigated the effects on heat transfer and friction on modeled rough surfaces. Bunker [18] measured heat transfer coefficient enhancements on applied and polished air-plasma-sprayed (APS) TBC surfaces. Figure 5 shows a typical rough turbine blade from aircraft engine service, as well as a surface topology scan of an applied TBC (unpolished).

One potential method for the reduction of heat flux is to main-

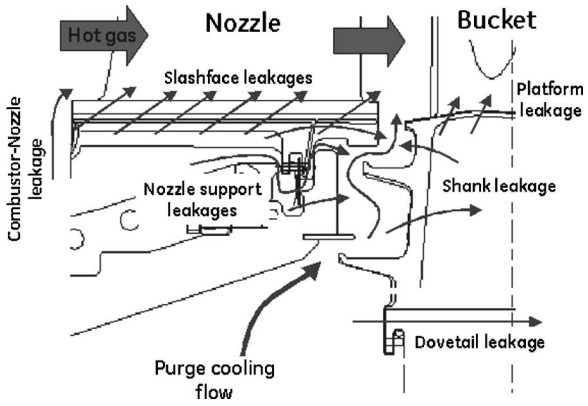

Fig. 6 Schematic of secondary purge and leakage flows

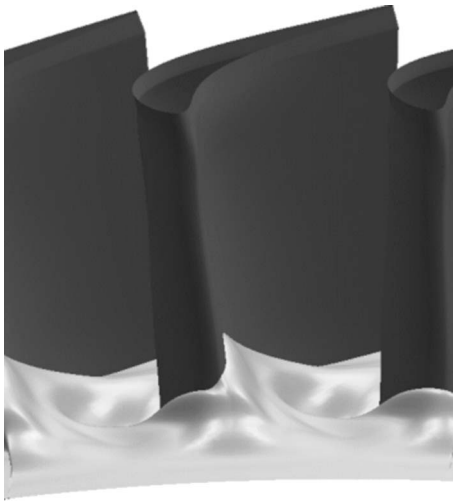

Fig. 7 Turbine blade end-wall contour example

tain a smooth surface condition throughout the service interval of the turbine. The lower temperature blade rows of compressors currently use classes of Teflon®-like coatings to produce an "antistick" surface that rejects deposits [19]. Can analogous coatings be developed for the more aggressive high-temperature environments of turbines? If so, the coatings must be durable and also compatible with the TBC, without the possibility of infiltrating the TBC and causing early failure. It may be possible that alternate forms of TBC coatings could provide this anti-stick function while still serving as an insulating layer. Air-plasma-sprayed TBC is applied as particles of TBC quenched on the surface leading to a randomly distributed, somewhat layered microstructure. Physical vapor-deposited (PVD) TBC is a vacuum vapor process at the molecular level that results in a typical columnar microstructure. Both APS and PVD TBC have porosity that is desirable for low thermal conductivity. If at least the exposed surface could be sealed and made smooth, then the airfoil would be less likely to collect deposits. An example of such an anti-stick turbine coating is described in Stowell et al. [20] for the prevention of buildup of corrosion products and other products of combustion from the hot gases.

Current research into advanced materials is heavily focused on the development of structurally capable high-temperature monolithic ceramics and ceramic-matrix composites. In some applications, such materials can replace the use of metal with TBC, while in many HPT applications the ceramics still require cooling and a form of TBC coating. Reduced incident heat flux is obtained through the increased allowable bulk material temperatures, but the limiting factor is still the coating temperature limit and strain.

Secondary Flows As Prime Hot Gas Path Cooling. Though most of the attention on cooling of the gas turbine focuses on the main body of the airfoils and end walls, there is also the entire secondary flow system that surrounds and contains the hot gas path. The secondary system flows are a required element of the turbine serving to keep the hot working gases within the primary turbine path, allowing component interfaces for accommodation of differential growths and assembly, and also sealing rotational boundaries under all operating conditions. Where the secondary flow system meets the hot gas path there are necessary leakages and purge flows that can be minimized but not eliminated. An example of secondary flows is depicted in Fig. 6 for one section of the turbine only.

The majority of these leakage flows are introduced into the hot gas path through an interface defined by the requirements of the bounding hardware. Put another way, these leakages are not first designed using the most effective flow interface (best cooling and lowest mixing loss), and the hardware then forced to fit this interface. Such leakage flows can amount to about 1–2 % of total core flow for each stage of the turbine. It is therefore a key challenge to find a middle ground that introduces these leakages in a manner serving as reliable and effective hot gas path cooling, while also maintaining functional interfaces. Research in this area has grown in the last several years, beginning with the study of interface leakage and flow path steps on film cooling and heat transfer performed by Hsing et al. [21]. More detailed cascade and turbine rig research is ongoing, including the work of Piggush and Simon [22], Cardwell et al. [23], and also Zhang and Jaiswal [24]. Innovations are required particularly in the wheelspace purge regions to transform these flows into effective cooling.

Micro-3D Hot Gas Path Surfaces. The aerodynamic design of the hot gas path emphasizes smoothly varying surfaces, preferably with small airfoil leading-edge diameters and razor thin trailing edges. Airfoil lean, bow, and twist are now more commonplace to improve efficiency and reduce hot gas secondary flow losses. Bounding end walls at the hub and casing are generally circular sections at any particular axial location through the turbine. The locations at the hub and casing where the airfoils meet the end walls usually only have a small manufacturing fillet as the surface transition. These locations are the sites of the remaining major secondary flow losses generated in the turbine, in addition to trailing-edge wakes, mixing losses, and shock interactions.

Recent research has begun to investigate the use of contoured flow-path end walls, or nonaxisymmetric end walls, as well as alternate shaping of airfoil–end-wall fillet regions. An example of end-wall contouring is shown in Fig. 7. As demonstrated by Lethander et al. [25], the use of a large leading-edge fillet can reduce the near wall gas temperatures by diminishing the horseshoe vortex strength that otherwise tends to draw core gases toward the wall. The turbine rig test of Rose et al. [26] showed that contoured end walls could lead to significant aerodynamic efficiency gains, though this depends on the initial design of the turbine. These are macrolevel examples of three dimensional surface contouring intended to benefit not only the aerodynamic performance, but also cooling effectiveness.

Microlevel surface contouring has the potential to influence local aerodynamic and cooling phenomena in the hot gas path. As shown by Maciejewski and Rivir [27], surface riblets aligned in the streamwise direction can reduce both drag and heat transfer coefficients by 5–10 %; this is more significant for heat transfer. Surface depressions or dimples, per Bunker [28], placed at certain locations on the airfoils may alter the boundary layer and decrease downstream heat transfer. Relating decreases in aerodynamic loss with lower heat transfer coefficients, LaFleur et al. [29] demonstrated complex contoured end wall surfaces that contained elements of both large-scale and microscale features.

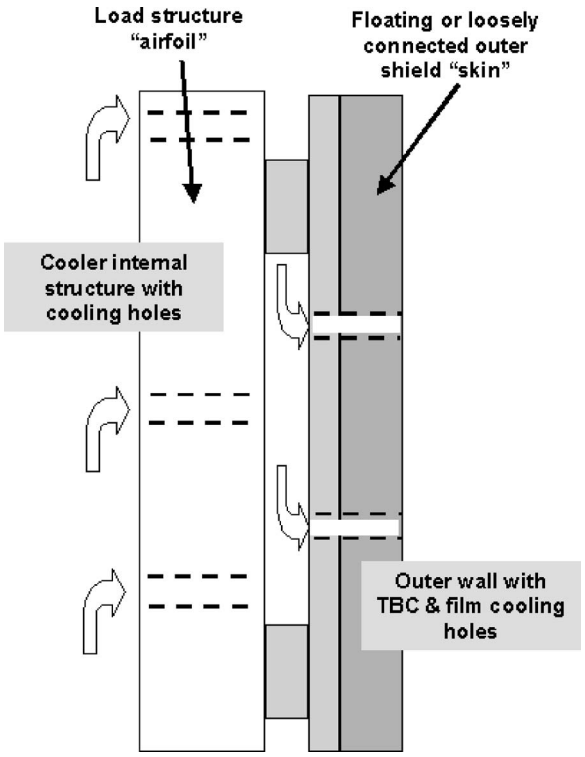

Fig. 8 Shell and spar airfoil design

The heat transfer and film-cooling aspects of both the macro- and microlevel flow-path surfaces have yet to be fully investigated and remain a fruitful research area.

Thermal Stress Reduction. Hot gas path component thermomechanical design is a constantly evolving field that seeks to satisfy all the required strength and durability aspects of turbine service while also accommodating the desired aerodynamics and cooling. Though improved cooling technologies can allow greater flexibility in design, it is also true that designs producing lower thermal stresses will reduce the cooling flow burden, i.e., are optimized. This assumes that the design still meets an upper temperature material limit, or is not simply cooled to extreme levels. The impact of thermal stresses is lessened as the material temperature levels decrease, both in specific locations and in bulk, due to better material properties at lower temperatures. Therefore, the conventional approach to reducing thermal stress is simply to cool the region or component better. In most designs, this higher degree of local cooling leads to overall inefficiency and waste of cooling fluid. Higher strength materials can alleviate this situation, but new superalloys are very expensive and require many years to develop. New classes of materials with higher temperature capabilities, such as ceramic matrix composites like Si-SiC, may some day replace certain metal components in the turbine. These new materials, however, tend also to have much lower strength than metals.

In addition to pure materials solutions, thermomechanical design can use cooling methods to reduce thermal stresses. As previously noted, greater degrees of cooling uniformity, or greater local control over specific cooling magnitudes, can be utilized to alter local thermal gradients. Such cooling methods may be combined with novel airfoil wall structures to isolate the external hot wall from the interior cooler portion of the airfoil, as shown schematically in Fig. 8. CastCool is one example in which the outer wall is very thin, thereby reducing hot structure stress. Other types of double-wall structures, such as those of Sellers et al. [30] and Dailey et al. [31], seek to attain similar goals. The only way to further reduce thermal stress in the outer airfoil wall is to thermally disconnect this wall from the rest of the airfoil, i.e., a floating wall concept similar to that employed today in some gas turbine combustor liners [32]. Even so, such a floating wall would need to be sectionalized to avoid chordal gradients. Local thermal stresses due to film holes and through-wall gradients will remain however.

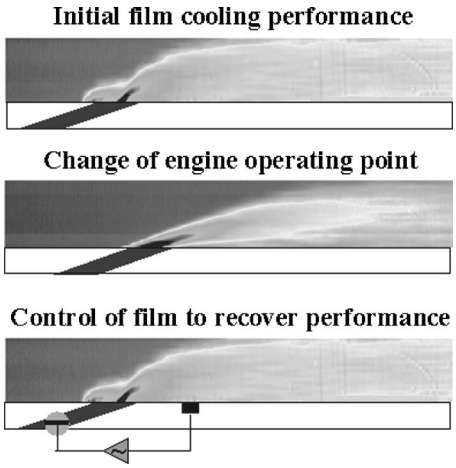

Fig. 9 Controlled film cooling (hypothesized)

Controlled and Adaptable Cooling. One of the most restrictive requirements in turbine design is that the hot gas path components must survive at all operational cycle points. With respect to the cooled components, this means that thermal designs must be based on the maximum conditions (takeoff for aircraft engines and full-speed full load for power turbines). For all passively cooled turbines, by which is meant uncontrolled cooling, this design requirement generally leads to overuse of valuable cooling fluid at operating conditions less than the maximum. It is highly desirable then to actively control the cooling magnitude to best match the operating point. Cooling control can be hypothesized at many levels of design, including overall blade row control, individual component control, and even local passage or film hole control.

Cooling control may also be visualized in terms of various responses to control parameters at the system or local level. Such responses could then also have the ability to change as the service condition of the engine is modified, making cooling adaptable for performance or life. The simplest example of cooling control is the use of a modulation valve feeding an entire blade row, where the valve may be a variable orifice. An appropriate gas temperature, such as the exhaust gas, or a surface temperature derived from a pyrometer sensor, might be used to control the valve. At the component or individual feature level, microelectromechanical systems (MEMS) have been suggested to actively control the cooling flows using local feedback sensors imbedded in the walls. As depicted in Fig. 9, the shift in film-cooling effectiveness that accompanies an off-design operating point might be modified back to higher performance by a MEMS device located in the film hole. Ample evidence exists in film-cooling literature to show the benefits that might be obtained if film injection blowing ratios could be actively controlled.

Other research suggests that under some circumstances convective cooling can be improved by imposing a forced driving frequency and amplitude on the mean cooling flow rate. Impingement heat transfer driven by a pulsed square wave forcing function was shown in the study of Sheriff and Zumbrunnen [33] to increase average heat transfer coefficients by ~30%. Internal flow control or modulation must however also account for potential effects on film cooling. The study of Bons et al. [34] showed that an acoustically driven pulsed coolant supply could severely degrade film-cooling performance at lower blowing ratios. In the

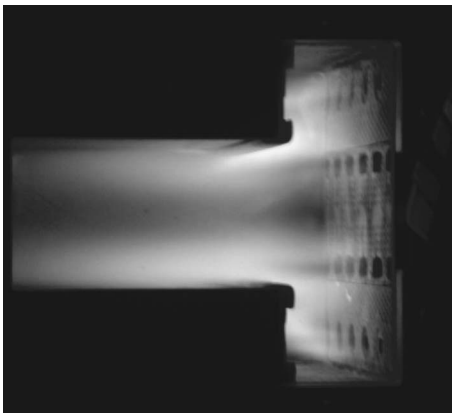

Fig. 10 Trapped vortex combustor

absence of film cooling, closed-circuit cooling can be adjusted to provide more or less cooling magnitude on an overall level, using component temperature sensors as feedback control.

Low-Emission Combustor-Turbine Systems. All conventional gas turbine engines employ separate combustion systems and turbines that must live in close proximity with the combustors. The design and operability of the combustor, whether of diffusion, premixed, or combined modes, gas or liquid fuels, has great influence on the thermal management of the turbine. In addition, the thermal management of the combustor system itself can significantly contribute to the resulting gas temperature profile and pattern factors, combustion instabilities, and emissions. With the required technology shift to low-emissions and zero-emissions engines, new combustion strategies will demand greater innovations in cooling. Many alternate combustion systems are being developed for this requirement.

Some of the new combustion systems under development seek the merging of the combustor and the turbine inlet guide vane into a single system. Advanced aircraft engine combustor-turbine systems may already experience a certain level of burning around the nozzle guide vanes. As demonstrated in the study of Kirk et al. [35], airfoil film cooling can react with unburned fuel to create film heating near the surfaces of the hot gas path. New types of combustion systems can more directly join the combustion zone to the guide vanes. For example, staged combustors may introduce a primary combustion zone upstream and a secondary combustion zone just ahead of, or into, the turbine inlet vanes. Although staging can be advantageous for reduced emissions, additional heat load burden is placed on the combustor, and more severe gas conditions are presented to the turbine airfoils.

Trapped vortex combustion (TVC), as described by Roquemore et al. [36] is a form of staged combustion that employs a recirculation wall cavity as the pilot burner. Figure 10 shows the flow and combustion flame in a natural gas fired TVC [37]. Fuel and air are injected into the cavity through the aft face in a manner that reinforces the primary vortex direction of the recirculating flow. As with conventional combustion systems, which utilize bluff bodies, swirl vanes, or rearward facing steps, the TVC device creates a flame stabilization zone providing continuous sources of ignition by mixing hot products and burning gases with the incoming fuel. The resulting TVC system has shown combustion efficiencies as high as 99%, with low lean blowout limits and low system pressure drop. The impact of TVC on the turbine and the cooling of the combustor have yet to be evaluated.

Industrial low-emissions combustors that operate on natural gas, or natural gas plus hydrogen, rely on little or no injection of air into the combustor for cooling purposes. This practice greatly aids the reduction of NO_x by allowing lower flame temperatures, but puts a large burden on backside cooling of the hardware. As discussed by Bailey et al. [38], the cooling of such combustors still presents challenges in both overall temperature reduction and thermal gradient elimination. Further improvements can be obtained by reducing the overall combustor system pressure drop, which requires increased cooling performance (higher heat transfer with lower pressure losses). Additionally, it is desired to further reduce cooling flows to the turbine, especially the inlet nozzle, for even greater benefit to emissions.

Regenerative Cooling. Thermal management of the hot gas path is necessary to obtain higher cycle efficiencies; however, it is preferred to waste as little of the removed thermal energy as possible in the process. In the traditional open-circuit cooling, the cooling fluid absorbs energy as it travels through the component and then is mixed into the hot gas flow as film-cooling injection. This preserves the removed energy in the cycle, but at the cost of bypassing valuable working fluid around the combustor. Other methods are needed that perform the function of cooling, or energy transfer, without the use and loss (partial or total) of compressor fluid. A process that minimizes or eliminates the impact of such cooling on the cycle efficiency is broadly referred to here as regenerative cooling.

Several designs for regenerative cooling have been proposed, and some are in commercial use. The most notable of these is the H-System® combined cycle gas and steam turbine power plant of GE Energy [39]. In this system, the superheated steam from an intermediate point in the steam turbine system is directed through the gas turbine airfoils as closed-circuit cooling and then returned to the steam turbine. In this fashion, the gas turbine acts as a reheat device for the steam turbine. There is no use of film cooling in these gas turbine airfoils. The energy extracted is contained within the combined cycle without using compressor air for cooling. In a similar manner, the 501G turbine of Siemens-Westinghouse utilizes closed-circuit air cooling of the rotating blades that is ported off board of the engine for heat exchange and compression [40]. This system may be used on land-based simple cycle turbine engines.

In aircraft engines, several schemes exist that utilize onboard turbocompressors and compact heat exchangers with available heat sinks to achieve lower cooling air temperatures in the turbine, which then reduces the amount of cooling air required. For example, the system of Coffinberry and Leonard [41] takes compressor discharge air and further cools the air by exchange with fan bypass air, then increases pressure using a small turbocompressor, and returns this air for cooling the turbine. In a similar method, Coffinberry [42] uses the fuel as the heat sink for cooling the air. In a further extension of this type of system, Bunker [43] describes a closed-circuit method that extracts cooler stage compressor air for turbine cooling, exchanges heat with an available sink, and then returns the air for reinjection to the compressor. This version is shown in Fig. 11.

Other methods have been suggested for heat removal or transport from the hot gas path components that do not involve system working fluids. Heat pipes have been studied for cooling of turbine nozzles. Zuo et al. [44] studied the use of heat pipes to cool turbine nozzle airfoils, where the heat pipes are embedded vertically in the walls of the airfoils and projected radially outward to a cooler heat sink. Ling et al. [45] studied the placement and heat transfer of heat pipes embedded inside turbine rotor disks. In this application, the heat pipes serve to move energy from the blade attachment region into the bulk portion of the disk, thereby allowing less active cooling of the rim. In a novel concept, Kerrebrock and Stickler [46] proposes the use of a self-contained internal blade and dovetail cooling in which a fluid is centrifugally thrown outward from the base into hollow blades, evaporated on the interior walls of the hot airfoils, and returned by the developed core pressure gradient to the dovetail for condensation.

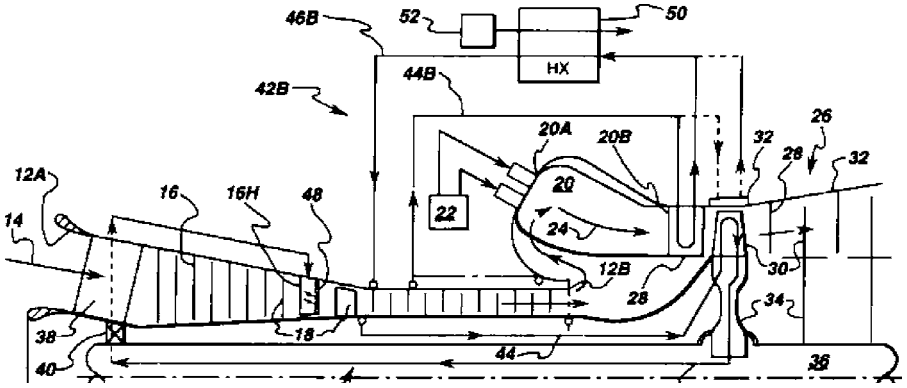

Fig. 11 One version of regenerative cooling for a turbine cycle

Conclusions

The ultimate goals in gas turbine thermal management include (i) isothermal components to eliminate all internal thermal stresses, (ii) hot components to minimize heat loads and inefficient energy transfers in the engine, and (iii) minimization of thermal gradients between components and their support/containment structures. The advancement of turbine cooling has allowed engine design to exceed normal material temperature limits, but has introduced complexities that have accentuated the thermal issues greatly. Cooled component design has consistently trended in the direction of higher heat loads, higher through-wall thermal gradients, and higher in-plane thermal gradients. Gas turbine heat transfer and thermal management technology advancements over the most recent 10–15 years have primarily come in the more detailed understanding of boundary conditions and the higher sophistication of analysis tools. Having reached this plateau, there are several issues/directions to be considered in pushing thermal technology further.

The present discussion has identified ten major thermal challenges, or opportunities, that remain for the turbine hot gas path today. These challenges address active cooling technologies, hot gas flow paths, component design, and systems design. No attempt has been made here to recommend specific solutions or to prioritize the issues identified. However, to provide the reader with some means of comparison, Fig. 12 depicts an approximate ranking of the issues on the basis of technology impact versus technology risk. Such risk-benefit rankings are commonly used to determine a balanced portfolio of funded technology projects within businesses, including research and development. Technology impact includes engine performance metrics and range of product applications, while technology risk refers to the probability of successful development and deployment. The shaded regions account for the low hanging fruit that make sense for immediate development (upper left) and the very low benefit-to-risk ratio items that should be avoided (lower right). The ten challenges discussed in this summary are seen to cover a broad spectrum of impact and risk, though individual opinions on rankings may differ. Those items on the left half of the chart mainly represent the issues most strongly being addressed by research today. Those higher risk items on the right side of the chart represent potentially fruitful directions requiring significant innovations and research. Singling out the highest risk-benefit technology identified in Fig. 12, regenerative cooling may cover extensive applications and formats from fairly simple concepts on components to very complex system/plant designs. Although some versions of regenerative cooling may not entail this high risk, such as those in practice today, this ranking is used to indicate the higher degree of total cycle complexity and risk for most broadly based concepts.

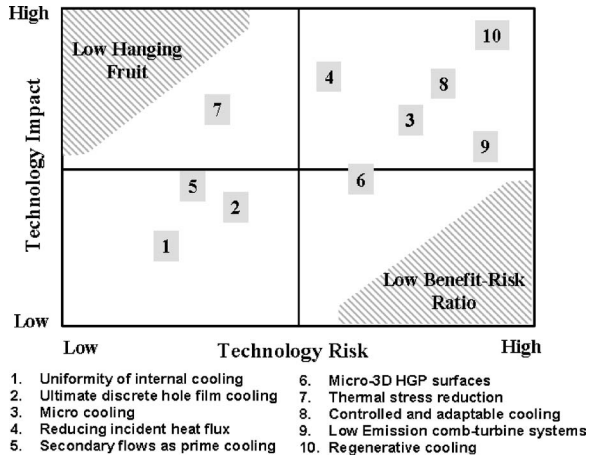

Fig. 12 Technology impact-risk ranking of the challenges

Research trends and potential solutions to these thermal issues have been briefly outlined in an attempt to stimulate thought and further ideas. There are no simple yes or no answers to the questions initially posed. It is hoped that this summary will aid in focusing attention in the critical areas of heat transfer and thermal management for gas turbine hot sections required to make significant new gains in overall efficiency, operability, and durability.

Nomenclature

A_g = exposed hot gas surface area of turbine airfoil
C_p = specific heat
T_c = cooling fluid supply temperature to airfoil
T_g = mean hot gas temperature
T_m = bulk airfoil metal temperature
U = overall hot gas heat transfer coefficient
W_c = cooling fluid flow rate

References

[1] Zhang, N., Yang, W. J., and Lee, C. P., 1993, "Heat Transfer and Friction Loss Performance in Flow Networks With Multiple Intersections," Exp. Heat Transfer, **6**, pp. 243–257.
[2] Gillespie, D., Wang, Z., Ireland, P., and Kohler, S. T., 1996, "Full Surface Local Heat Transfer Coefficient Measurements in a Model of an Integrally Cast Impingement Cooling Geometry," ASME J. Turbomach., **120**, pp. 92–99.
[3] Bunker, R. S., Bailey, J. C., Lee, C. P., and Stevens, C. W., 2004, "In-Wall Network (Mesh) Cooling Augmentation for Turbine Airfoils," IGTI Turbo Expo, Vienna, ASME Paper No. GT2004-54260.
[4] Bunker, R. S., 2005, "A Review of Turbine Shaped Film Cooling Technology," ASME J. Heat Transfer, **127**, pp. 441–453.
[5] Moser, S., Ivanisin, M., Woisetschlaeger, J., and Jericha, H., 2000, "Novel Blade Cooling Engineering Solution," IGTI Turbo Expo, Munich, ASME Paper No. 2000-GT-242.
[6] Sargison, J. E., Guo, S. M., Oldfield, M. L. G., Lock, G. D., and Rawlinson, A. J., 2001, "A Converging Slot-Hole Film Cooling Geometry—Part 1: Low-

Speed Flat Plate Heat Transfer and Loss," IGTI Turbo Expo, New Orleans, Paper No. 2001-GT-0126.
[7] Fric, T. F., and Campbell, R. P., 2002, "Method for Improving the Cooling Effectiveness of a Gaseous Coolant Stream Which Flows Through a Substrate, and Related Articles of Manufacture," U.S. Patent No. 6,383,602.
[8] Bunker, R. S., 2002, "Film Cooling Effectiveness Due to Discrete Holes Within a Transverse Surface Slot," IGTI Turbo Expo, Amsterdam, ASME Paper No. GT-2002-30178.
[9] Nasir, H., Acharya, S., and Ekkad, S., 2001, "Film Cooling From a Single Row of Cylindrical Angled Holes With Triangular Tabs Having Different Orientations," IGTI Turbo Expo, New Orleans, ASME Paper No. 2001-GT-0124.
[10] Sweeney, P. C., and Rhodes, J. P., 1999, "An Infrared Technique for Evaluating Turbine Airfoil Cooling Designs," ASME J. Turbomach., **122**, pp. 170–177.
[11] Nakamata, C., Okita, Y., Matsuno, S., Mimura, F., Matsushita, M., Yamana, T., and Yoshida, T., 2005, "Spatial Arrangement Dependence of Cooling Performance of an Integrated Impipngement and Pin Fin Cooling Configuration," IGTI Turbo Expo, Reno-Tahoe, ASME Paper No. GT2005-68348.
[12] Hale, C. A., Plesniak, M. W., and Ramadhyani, S., 1999, "Film Cooling Effectiveness for Short Film Cooling Holes Fed by a Narrow Plenum," ASME J. Turbomach., **122**, pp. 553–557.
[13] Battisti, L., 2002, "Boundary Layer Control of Aerodynamic Airfoils," U.S. Patent No. 6,488,238.
[14] Wolf, J., and Moskowitz, S., 1983, "Development of the Transpiration Air-Cooled Turbine for High-Temperature Dirty Gas Streams," ASME J. Eng. Power, **105**, pp. 821–825.
[15] Novikov, A. S., Meshkov, S. A., and Sabaev, G. V., 1988, "Creation of High Efficiency Turbine Cooled Blades With Structural Electron Beam Coatings," *Electron Beam and Gas-Thermal Coatings*, Paton IEW, Kiev, pp. 87–96.
[16] Bunker, R. S., 1997, "Separate and Combined Effects of Surface Roughness and Turbulence Intensity on Vane Heat Transfer," 1997 International Gas Turbine Conference, Orlando, ASME Paper No. 97-GT-135.
[17] Bons, J. P., 2002, "St and Cf Augmentation for Real Turbine Roughness With Elevated Freestream Turbulence," ASME J. Turbomach., **124**, pp. 632–644.
[18] Bunker, R. S., 2003, "The Effect of Thermal Barrier Coating Roughness Magnitude on Heat Transfer With and Without Flowpath Surface Steps," International Mechanical Engineering Conference, Washington DC, ASME Paper No. IMECE2003-41073.
[19] Morant GmbH, Ceral 3450sc product brochure, Grassau, Germany.
[20] Stowell, W. R., Nagaraj, B. A., Lee, C. P., Ackerman, J. F., and Israel, R. S., 2002, "Enhanced Coating System for Turbine Airfoil Applications," U.S. Patent No. 6,394,755.
[21] Hsing, Y. C., Chyu, M. K., and Bunker, R. S., 1998, "Measurements of the Cooling Performance of Gap Leakage on a Misaligned Component Interface Using a Thermographic Phosphor Fluorescence Imaging System," IGTI Conference, Stockholm, ASME Paper No. 98-GT-132.
[22] Piggush, J. D., and Simon, T. W., 2005, "Flow Measurements in a First Stage Nozzle Cascade Having Endwall Contouring, Leakage and Assembly Features," IGTI Turbo Expo, Reno-Tahoe, ASME Paper No. GT2005-68340.
[23] Cardwell, N. D., Sundaram, N., and Thole, K. A., 2005, "Effects of Roughness and a Mid-Passage Gap on Endwall Film Cooling," IGTI Turbo Expo, Reno-Tahoe, ASME Paper No. GT2005-68900.
[24] Zhang, L. J., and Jaiswal, R. S., 2001, "Turbine Nozzle Endwall Film Cooling Study Using Pressure Sensitive Paint," ASME J. Turbomach., **123**, pp. 730–738.
[25] Lethander, A. T., Thole, K. A., Zess, G., and Wagner, J., 2003, "Optimizing the Vane-Endwall Junction to Reduce Adiabatic Wall Temperatures in a Turbine Vane Passage," IGTI Turbo Expo, Atlanta, ASME Paper No. GT2003–38939.
[26] Rose, M. G., Harvey, N. W., Seaman, P., Newman, D. A., and McManus, D., 2001, "Improving the Efficiency of the Trent 500 HP Turbine Using Non-Axisymmetric Endwalls—Part II: Experimental Validation," IGTI Turbo Expo, New Orleans, ASME Paper No. 2001-GT-0505.
[27] Maciejewski, P. K., and Rivir, R. B., 1994, "Effects of Surface Riblets and Free-Stream Turbulence on Heat Transfer in a Linear Turbine Cascade," IGTI Turbo Expo, The Hague, ASME Paper No. 94-GT-245.
[28] Bunker, R. S., 2001, "Airfoil With Reduced Heat Load," U.S. Patent No. 6,183,197.
[29] LaFleur, R. S., Whitten, T. S., and Araujo, J. A., 1999, "Second Vane Endwall Heat Transfer Reduction by Iceform Contouring," IGTI Turbo Expo, Indianapolis, ASME Paper No. 99-GT-422.
[30] Sellers, R. R., Soechting, F. O., Huber, F. W., and Auxier, T. A., 1998, "Cooled Blades for a Gas Turbine Engine," U.S. Patent No. 5,720,431.
[31] Dailey, G. M., McCall, R. A., and Evans, P. A., 2000, "Cooled Aerofoil for a Gas Turbine Engine," European Patent Application EP-1-022-432-A2.
[32] Pidcock, A., Cooper, S. M., and Fry, P., 1995, "Removable Combustor Liner for Gas Turbine Engine Combustor," U.S. Patent No. 5,435,139.
[33] Sheriff, H. S., and Zumbrunnen, D. A., 1994, "Effect of Flow Pulsations on the Cooling Effectiveness of an Impinging Jet," ASME J. Heat Transfer, **116**, pp. 886–895.
[34] Bons, J. P., Rivir, R. B., MacArthur, C. D., and Pestian, D. J., 1995, "The Effect of Unsteadiness on Film Cooling Effectiveness," 33rd Aerospace Sciences Meeting, Reno, AIAA Paper No. 95-0306.
[35] Kirk, D. R., Guenette, G. R., Lukachko, S. P., and Waitz, I. A., 2002, "Gas Turbine Engine Durability Impacts of High Fuel-Air Ratio Combustors Part 2: Near Wall Reaction Effects on Film-Cooling Heat Transfer," ASME J. Eng. Gas Turbines Power, **125**, pp. 751–759.
[36] Roquemore, W. M., Shouse, D., Burrus, D., Johnson, A., Cooper, C., Duncan, B., Hsu, K. Y., Katta, V. R., Sturgess, G. J., and Vihinen, I., 2001, "Trapped Vortex Combustor Concept for Gas Turbine Engines," 39th AIAA Aerospace Sciences Meeting, Reno, ASME Paper No. 2001-0483.
[37] Public reports for U.S. Dept. of Energy Contract No. DE-FC26-01NT41020.
[38] Bailey, J. C., Intile, J., Tolpadi, A., Fric, T., Nirmalan, N. V., and Bunker, R. S., 2002, "Experimental and Numerical Study of Heat Transfer in a Gas Turbine Combustor Liner," ASME J. Eng. Gas Turbines Power, **125**, pp. 994–1002.
[39] Farmer, R., and Fulton, K., 1995, "Design 60% Net Efficiency in Frame 7/9H Steam-Cooled CCGT," Gas Turbine World, **25**(3), pp. 12–20.
[40] McQuiggan, G., and Southall, L. R., 1998, "An Evolutionary Approach to the Development of New Advanced Technology Gas Turbines," IGTI Turbo Expo, Stockholm, ASME Paper No. 98-GT-223.
[41] Coffinberry, G. A., and Leonard, G. L., 1999, "System and Method of Providing Clean Filtered Cooling Air to a Hot Portion of a Gas Turbine Engine," U.S. Patent No. US5918458.
[42] Coffinberry, G. A., 1995, "Gas Turbine Engine Cooling System," U.S. Patent No. US5392614.
[43] Bunker, R. S., 1997, "Closed-Circuit Air Cooled Turbine," U.S. Patent No. 5,611,197.
[44] Zuo, Z. J., Faghri, A., and Langston, L. S., 1997, "A Parametric Study of Heat Pipe Turbine Vane Cooling," IGTI Turbo Expo Congress, Orlando, ASME Paper No. 97-GT-443.
[45] Ling, J., Cao, Y., Rivir, R. B., and MacArthur, C. D., 2004, "Analytical Investigations of Rotating Disks With and Without Incorporating Rotating Heat Pipes," ASME J. Eng. Gas Turbines Power, **126**, pp. 680–683.
[46] Kerrebrock, J. L., and Stickler, D. B., 1998, "Vaporization Cooling for Gas Turbines, the Return-Flow Cascade," IGTI Turbo Expo, Stockholm, ASME Paper No. 98-GT-177.

High-Resolution Film Cooling Effectiveness Comparison of Axial and Compound Angle Holes on the Suction Side of a Turbine Vane

Scot K. Waye
e-mail: scotwaye@hotmail.com

David G. Bogard

Mechanical Engineering Department,
University of Texas at Austin,
Austin, TX 78712

Film cooling adiabatic effectiveness for axial and compound angle holes on the suction side of a simulated turbine vane was investigated to determine the relative performance of these configurations. The effect of the surface curvature was also evaluated by comparing to previous curvature studies and flat plate film cooling results. Experiments were conducted for varying coolant density ratio, mainstream turbulence levels, and hole spacing. Results from these measurements showed that for mild curvature, $2r/d \approx 160$*, flat plate results are sufficient to predict the cooling effectiveness. Furthermore, the compound angle injection improves adiabatic effectiveness for higher blowing ratios, similar to previous studies using flat plate facilities.* [DOI: 10.1115/1.2448016]

Keywords: film cooling, compound angle, curvature, turbine vane

Introduction

Increasing the inlet gas temperature into the turbine stage of a modern turbine engine increases the cycle efficiency. This gives greater power or increases fuel economy. The use of film cooling on the turbine airfoils helps keep the metal blade temperature within operable limits. Thermal barrier coatings and internal cooling are also implemented to protect the blades from failure. Keeping the airfoils protected from the hot mainstream gas extends the component lifetime and insures safety of the engine.

Extensive research has been conducted on film cooling during the past few decades. Many studies, in order to simplify the geometry, have modeled the airfoils as flat plates or cylinders with discrete cylindrical hole film cooling schemes. Only a few studies have shown the effects of curvature on film cooling performance, but these studies show that curvature can cause a substantial difference in cooling performance. Also, only a few investigations have been conducted on airfoil like geometry. Of those that actually use realistic airfoil models, most publications only have implemented axial cylindrical or shaped holes. There are only a few sources in the open literature that have discussed cylindrical, compound angle holes on a vane-like geometry. A description of the related film cooling investigations is given below.

Flat plate studies have yielded data for both axial and compound angle holes. Schmidt et al. [1] compared axial holes with 90 deg compound angle holes, and Schmidt et al. [2] investigated the effects of compound angles for 35 deg cylindrical and forward diffused holes at two different pitch to diameter ratios. These studies showed that by using compound angle holes, the film effectiveness improved at high-momentum flux ratios over round axial holes.

Ito et al. [3] and Schwarz et al. [4] both conducted studies of the effects of curvature on cooling performance. Cylindrical 35 deg holes spaced $3d$ apart were used on the suction and pressure sides of a blade in the work of Ito et al. [3]. Schwarz varied the hole diameters of a similar hole geometry on a curved channel in order to test three curvatures on the suction side ($2r/d=61$, 94, and 126) and two on the pressure side. Both studies showed that at low blowing ratios ($M=0.5$), the convex curvature performed better and the concave curvature performed worse than a flat plate. At a moderate blowing ratio of $M=1.0$, the convex surface increased film cooling performance and the concave surface was similar in performance compared to flat surfaces. At $M=2.0$, the concave surface increased cooling over convex and flat surfaces. The strength of curvature on the convex surfaces had a dramatic effect, increasing the cooling for smaller radii.

Experiments on airfoil geometries were conducted by Takeishi et al. [5], Ou and Han [6], and Ligrani et al. [7] using single row injection, and by Lander et al. [8], Goldstein et al. [9], Takeishi et al. [10], Ligrani et al. [11], and Dittmer et al. [12], using double or multiple rows of injection. Takeishi et al. [5] compared a stationary blade to a rotational one, and Ou and Han [6] studied the effect of an unsteady flow. The tests with multiple rows are not applicable for comparison to the current study. Most of the hole geometries for all of the studies were cylindrical and oriented in the streamwise direction, with a few exceptions. Both papers authored by Ligrani et al. [7,11] used compound angle holes, either in a single row or in two staggered rows. The compound angle holes showed an improvement in cooling performance. Dittmar et al. [12] used staggered cylindrical and discrete slots as well as a single row of axial and compound angle shaped holes.

Curved channels are often used to model curvature to provide a better understanding of the governing physics on curved surfaces, as opposed to a certain airfoil shape. Lutum et al. [13], Kruse [14], Schwarz and Goldstein [15], and Schwarz [4], provided investigations for discrete holes with such facilities. As previously mentioned, various ratios of surface curvature to film hole diameter were examined in each of the studies, which all showed that convex surfaces generally increased effectiveness (up to double the values of a flat plate) while concave surfaces generally decreased effectiveness (except at higher blowing ratios, where the opposite becomes true). The extent of the increase or decrease in values varied based on the degree of curvature. Small radii of curvature

Contributed by the International Gas Turbine Institute of ASME for publication in the JOURNAL OF TURBOMACHINERY. Manuscript received July 12, 2006; final manuscript received July 14, 2006. Review conducted by David Wisler. Paper presented at the ASME Turbo Expo 2006: Land, Sea and Air (GT2006), Barcelona, Spain, May 8–11, 2006. Paper No. GT2006-90225.

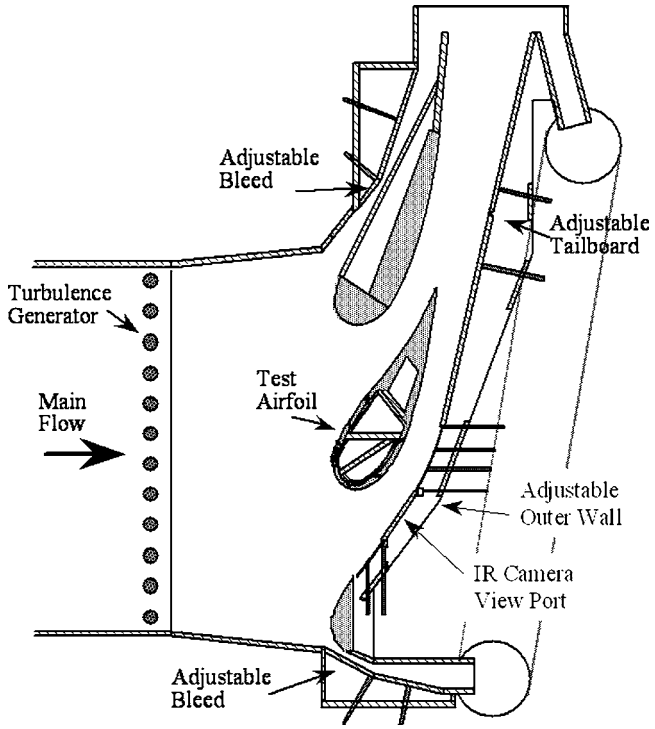

Fig. 1 Schematic of the simulated turbine vane test section

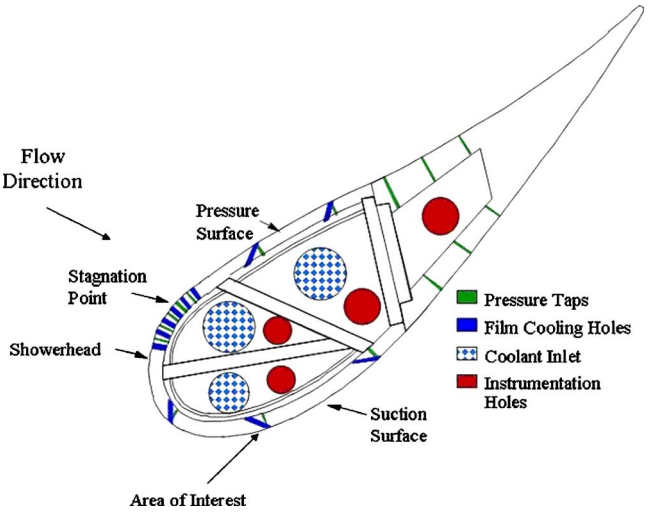

Fig. 2 Schematic of test vane details

increased the film effectiveness more than larger radii on the suction side. The curvature of the surface in Lutum et al. [13] was small ($2r/d=50$), and thorough analyses of the adiabatic effectiveness and heat transfer were conducted on two axial cylindrical hole geometries with different hole spacing, compound angle holes with the same hole spacing as one of the axial geometries, and two axial shaped hole geometries. The study was carried out for a zero pressure gradient and also for a favorable pressure gradient [16]. In general, the compound angle holes performed similarly to axial holes at $M=0.5$ and 1.0, but had almost double the adiabatic effectiveness at higher blowing, $M\geq 1.5$, for which coolant jets from the axial holes separated.

This study compares axial and compound angle holes, the effect of a moderately convex surface on the film cooling effectiveness, and the additive nature of film cooling due to hole spacing.

Experimental Facilities and Procedures

Experiments were conducted in a closed loop wind tunnel driven by a 50 hp adjustable speed fan. The test section shown, in Fig. 1, consisted of a simulated three-vane linear cascade. The vane geometry replicated an actual engine geometry scaled up nine times. The center vane was the test vane and is shown in Fig. 2. The outer wall was adjusted to achieve a nondimensional pressure distribution around the vane that matched an inviscid computational fluid dynamics (CFD) simulation of an infinite cascade. The approach velocity was 5.8 m/s and the exit velocity was 32 m/s, yielding an exit Reynolds number of $\mathrm{Re}=1.06\times 10^6$ (based on a true chord length of $C=594$ mm) to match realistic engine conditions. A removable passive turbulence generator 0.5 m upstream of the vane cascade consisted of 12 rods with outside diameter of 38 mm and pitched 85 mm apart. Previous measurements [17] determined that with the turbulence generator installed, the turbulence at $0.18C$ upstream of the test vane's leading edge was $\mathrm{Tu}_{\mathrm{app}}=21\%$ with an integral length scale of $\Lambda/d=10.0$. Without the turbulence generator installed, the turbulence was $\mathrm{Tu}_{\mathrm{app}}=3.5\%$ with $\Lambda/d=10.7$. The relatively high "low" mainstream turbulence condition was due to a simulated hot streak generator that was installed in the facility, but not used in this study. Horizontal bars that supported the hot streak impacted the integral length scale for the low turbulence tests. Therefore, the integral length scales were not predicted a priori, but instead, were measured directly. At the location of the holes tested the high mainstream turbulence intensity was measured to be $\mathrm{Tu}_\infty=3.9\%$ and the low mainstream turbulence level was $\mathrm{Tu}_\infty=1.0\%$ with similar length scales. This was due to flow acceleration around the vane. The local mainstream velocity accelerated while the fluctuating velocity remained nearly the same. At the current location, $U_\infty/U_{\mathrm{app}}=4.91$, causing a proportional decrease in the local turbulence level. The boundary layer parameters of the approaching boundary layer were $\delta/d=0.56$ and 0.44, $\delta_1/d=0.05$ and 0.07, and shape factors of $H=1.31$ and 1.67 for high and low mainstream turbulence, respectively. The shape factor for high mainstream turbulence indicated a turbulent boundary layer flow, while that for the low mainstream turbulence indicated a transitional boundary layer [18].

The vane was constructed of a low conductivity polyurethane foam, $k=0.048$ W/m K, to facilitate measurement of adiabatic wall temperature. The second row of coolant holes on the suction side, used for the current study, was located at $s/C=0.367$. At this location, the curvature was $2r/d=158$. Two different hole geometries were tested. Round holes oriented streamwise with an injection angle of $\alpha=30$ deg and $L/d=6.7$ were tested. Round compound angle holes with $\alpha=45$ deg, a compound angle of $\beta=45$ deg from the streamwise direction, and $L/d=4.5$ were also used. Note that the injection angle, α, is the angle between the hole axis and the plane tangent to the vane surface at the point of coolant injection, regardless of β. Two pitches, $p/d=5.55$ and 2.78, were used for the axial holes, while only $p/d=5.55$ was used for the compound angle holes. The origin $x/d=0$ was defined as the trailing edge of coolant hole. Experimental conditions are summarized in Table 1.

Adiabatic effectiveness was determined from the surface temperature distribution measured via infrared thermography (a FLIR ThermaCAM P20 infrared camera calibrated in situ using type E thermocouples). The thermocouple data were acquired using a National Instruments Data Acquisition system (NI DAQ). LabVIEW software was written to compute parameters in real time and write the data to disk. Adiabatic effectiveness, η, was determined using the following definition

$$\eta \equiv \frac{T_\infty - T_{\mathrm{aw}}}{T_\infty - T_c} \tag{1}$$

Density ratios of DR=1.3 and 1.5 for the coolant were achieved

Table 1 Test conditions

True chord length	59.4 cm
Vane span	54.9 cm
Vane pitch	45.7 cm
Inlet velocity	5.8 m/s
Exit Reynolds number	1.06×10^6
High-mainstream turbulence at inlet/ test location	$Tu_{app}=21\%$ $Tu_\infty=3.9\%$ $\Lambda=4.1$ cm
Low-mainstream turbulence at inlet/test location	$Tu_{app}=5.2\%$ $Tu_\infty=1.0\%$ $\Lambda=4.4$ cm
Film cooling hole diameter	4.11 mm
Hole length (axial)	27.5 mm ($L/d=6.7$)
Hole length (compound)	18.4 mm ($L/d=4.5$)
Axial hole angle	$\alpha=30$ deg, $\beta=0$ deg
Compound hole angles	$\alpha=45$ deg, $\beta=45$ deg
Hole pitch	22.8 mm ($p/d=5.55$), 11.4 mm ($p/d=2.78$)
Density ratio (ρ_c/ρ_∞)	1.3, 1.5

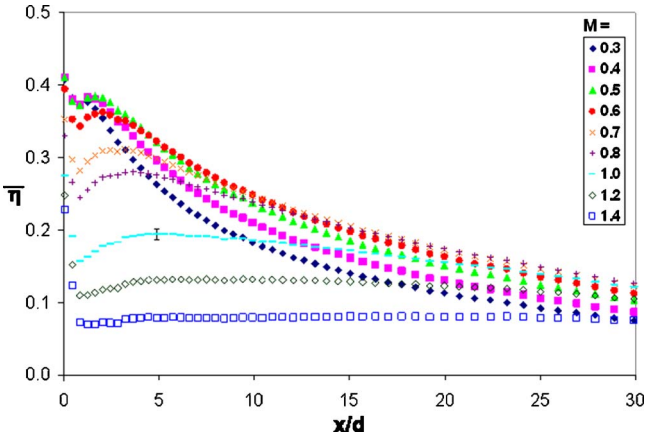

Fig. 3 Laterally averaged adiabatic effectiveness for axial holes for various *M*, *p*/*d*=2.78, $Tu_\infty=3.9\%$, DR=1.3

using liquid nitrogen to cool the air in a secondary loop that was then used as the coolant of the test vane. A range of suction side blowing ratios was tested from $M=0.2$ to 1.4.

Although the vane was constructed of low thermal conductivity foam, conduction through the wall of the vane caused the measured surface temperatures to be slightly lower than what they would have been for a truly adiabatic surface. Radiation effects were found to be negligible during adiabatic effectiveness tests. The effect of conduction was corrected with a one-dimensional (1D) conduction model as described by Ethridge et al. [19]. An in situ conduction correction was found during each experiment by blocking the flow of coolant to the film cooling holes in view of the infrared (IR) camera, and allowing the other holes to flow freely. The decrease in surface temperature due to conduction was measured directly. Near the holes, the conduction effect was slightly higher since there was 3D conduction near the holes. The conduction was nearly 1D when $x/d>3$. The wall temperature without film cooling, normalized like the adiabatic effectiveness, was designated η_0. The following equation was used to correct the other measurements for conduction

$$\eta=\frac{\eta_{\text{measured}}-\eta_0}{1-\eta_0} \tag{2}$$

A typical value for the conduction correction was $\eta_0=0.04$.

Uncertainties were calculated on a 95% confidence interval. Sources of uncertainty were the IR camera measurements, conduction correction, thermocouple measurements, and variation in the blowing ratio. Since comparisons of adiabatic performance done in separate tests of axial and compound angle holes was of primary importance, the precision of the experiments was the focus of the uncertainty analysis. The precision of the measurements was classified in two ways: test-to-test repeatability and within-test repeatability. Test-to-test uncertainties were used when comparisons were made for results obtained from separate experiments. Within-test uncertainties were used when evaluating the effects of parameters, such as blowing ratio and mainstream turbulence level, which were varied within a single experiment while holding other parameters constant. From multiple tests and through statistical analysis, the test-to-test uncertainties in the laterally averaged adiabatic effectiveness were $\delta\bar{\eta}=\pm0.04$ for $M=0.3$, $\delta\bar{\eta}=\pm0.02$ for $M=0.5$, and $\delta\bar{\eta}<\pm0.01$ for $M>1.0$. Similarly, the uncertainties for the spatially averaged adiabatic effectiveness were $\delta\bar{\bar{\eta}}=\pm0.03$ for $M=0.3$, $\delta\bar{\bar{\eta}}=\pm0.02$ for $M=0.5$, and $\delta\bar{\bar{\eta}}<\pm0.01$ for $M>0.7$. The uncertainty of the blowing ratio was found to range from $\delta M=\pm0.07$ for $M=0.3$ to $\delta M=\pm0.015$ for $M=1.4$ based on the uncertainty of the orifice meter reading, the mainstream velocity, and using the sequential perturbation method as suggested by Moffat [20]. During every experiment, various conditions were repeated in order to establish within-test repeatability. Statistical analysis showed the within-test uncertainty of $\bar{\eta}$ to be $\delta\bar{\eta}=\pm0.0075$ for moderate blowing ratios ranging from $M=0.6$ to 1.0.

Results

The values for the laterally averaged effectiveness for the axial holes with hole spacing of $p/d=2.78$ is given in Fig. 3. The blowing ratio that yielded the highest overall effectiveness was approximately $M=0.6$. The effectiveness levels were the highest in the range of $M=0.5-0.7$, giving values of $\bar{\bar{\eta}}>0.25$ for the surface area from $0<x/d<25$, as seen in Fig. 4. Further increases in blowing ratio presumably caused an increase in jet detachment, lowering the cooling on the surface.

Figure 4 also shows that when $\bar{\bar{\eta}}$ is plotted versus the momentum flux ratio, the peak effectiveness occurred at $I=0.23$. Goldstein and Stone [21] found that the peak effectiveness for flat plate cases occurs around $M=0.5$ for DR=0.95, and $M=0.75$ for DR=2.0 for axial holes. For both density ratios, this corresponded to $I=0.25$.

For low blowing ratios, $M=0.3$, 0.4, the effectiveness was high near the holes, then quickly degraded due to the lower mass flux exiting the holes. The peak values of $\bar{\eta}=0.4$ near the hole occurred at $M=0.3$ to 0.5, but the effectiveness quickly dropped to approximately 0.2 by $x/d=10$. Moderate blowing ratios, $M=0.5-0.7$, provided the best surface cooling. For these moderate blowing ratios, the surface cooling did not degrade to $\bar{\eta}=0.2$, or

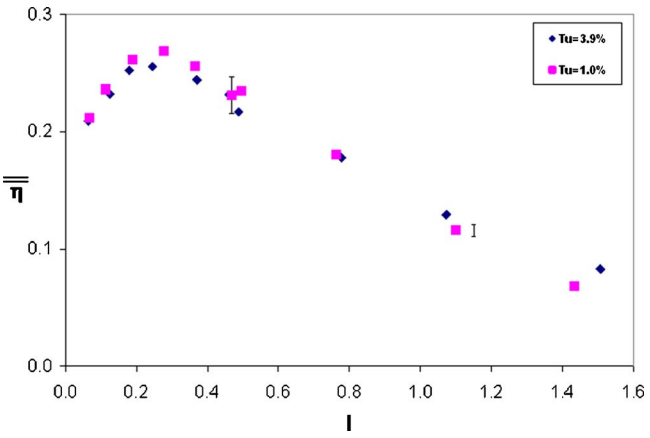

Fig. 4 Spatially averaged adiabatic effectiveness versus momentum flux ratio for axial holes, *p*/*d*=2.78, DR=1.3

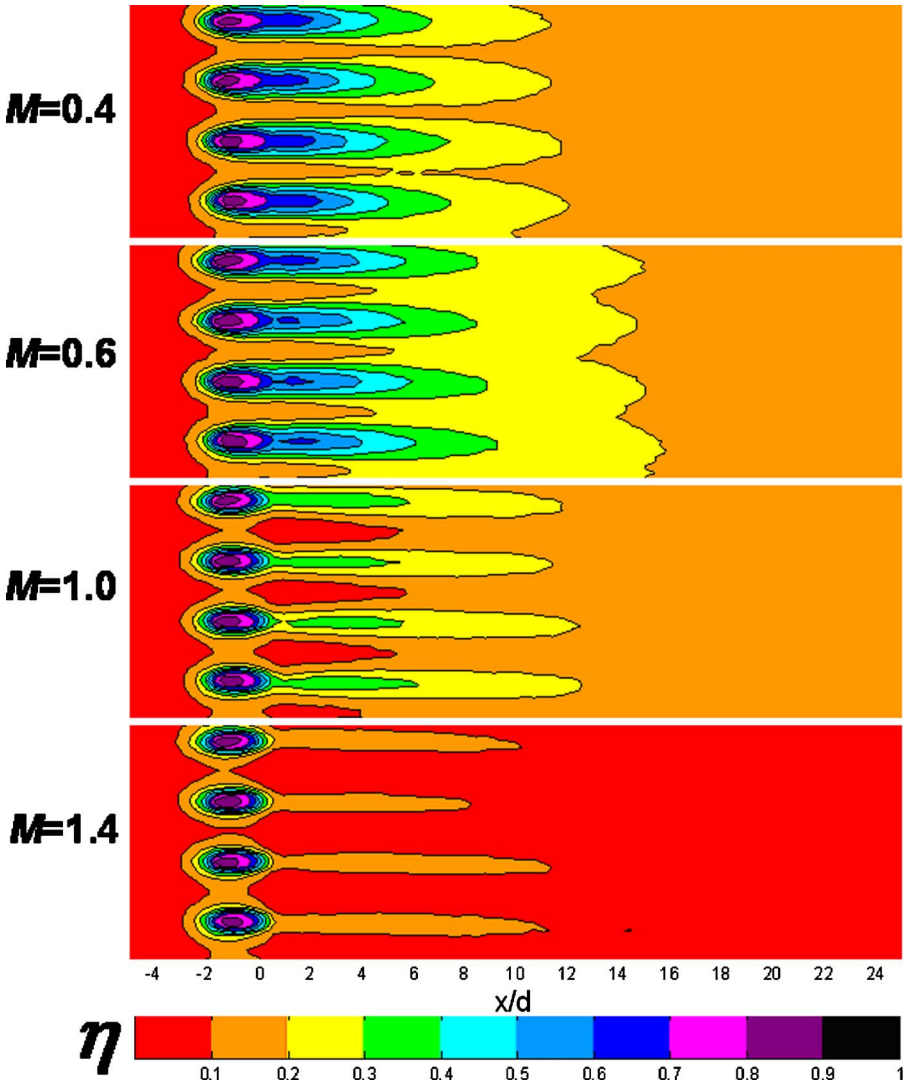

Fig. 5 Spatial plots of adiabatic effectiveness for axial holes at various *M*, *p*/*d*=2.78, Tu_∞=3.9%, DR=1.3

50% of the near hole value until $x/d \sim 15-20$. At these optimal levels, the jets appeared to interact with each other the most, as evidenced by little lateral variation downstream in Fig. 5, which shows the spatial distribution of the adiabatic effectiveness for low, moderate, and high M. At $M=0.7$, the effectiveness was approximately 15% lower near the hole than the optimal blowing ratio, but was about the same downstream ($x/d>10$) as $M=0.6$. With increasing blowing, more separation of the coolant jet occurred, resulting in lower cooling effectiveness. The effectiveness dropped about 30% from $M=0.8$ to $M=1.0$, and an additional 35% to $M=1.0$. The highest blowing ratio measured in the current study was $M=1.4$, and the film effectiveness was nearly constant for all x/d with a value less than $\bar{\eta}=0.1$. This low value suggests that the jet was almost completely detached at this blowing ratio. For all blowing ratios, a slight dip in the effectiveness noticed immediately after the holes was the result of sharp edged holes, causing a small separation region. This effect was more noticeable at low and moderate blowing ratios, as the jets at high blowing ratios were detached.

Figure 6 shows the effect of the density ratio on the adiabatic effectiveness for the high turbulence case. The effectiveness was nearly the same for low blowing ratios, slightly higher for moderate blowing ratios, and within the uncertainty for high blowing ratios. The two density ratios tested were close (DR=1.3, 1.5), which accounts for little to no change.

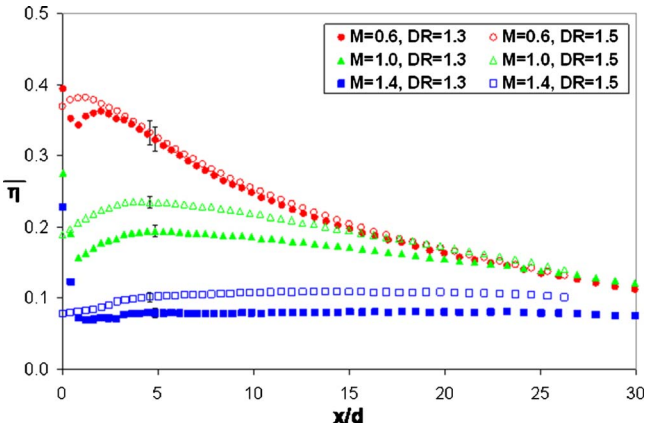

Fig. 6 Comparison of DR for axial holes, *p*/*d*=2.78

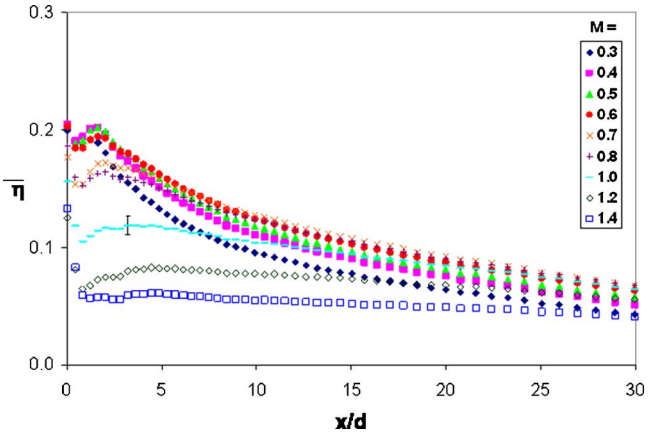

Fig. 7 Laterally averaged adiabatic effectiveness for axial holes for various M, $p/d=5.55$, $Tu_\infty=3.9\%$, DR=1.3

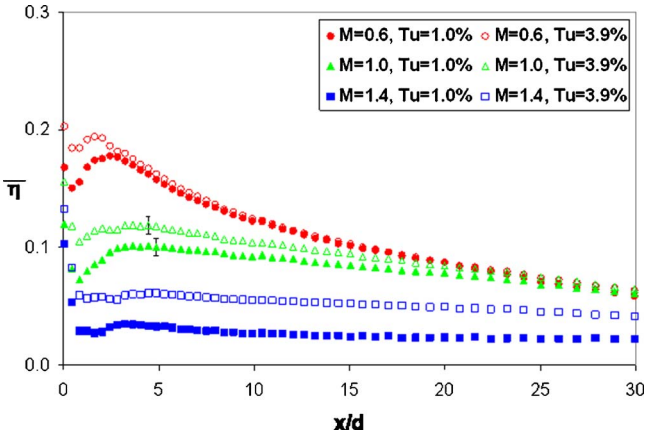

Fig. 9 Comparison of mainstream turbulence for axial holes, $p/d=5.55$, DR=1.3

Identical axial holes were used to test the effect of the hole spacing for the current airfoil geometry. Every other hole was blocked and covered, yielding a pitch of $p/d=5.55$, exactly double the other hole spacing. Figure 7 shows the laterally averaged adiabatic effectiveness for the high mainstream turbulence case for the range of blowing ratios tested. The effect of blowing ratio on adiabatic effectiveness was the same trend as the smaller hole spacing configuration. The highest overall effectiveness also occurred at $M=0.6$, with the range of blowing ratios from 0.5 to 0.7 giving similar values.

At low blowing ratios, the film effectiveness was $\bar{\eta}=0.2$ near the hole, then quickly decayed to around $\bar{\eta}=0.1$ by $x/d=10$. The rapid decay was due to low mass being ejected. Figure 8 shows the individualistic nature of the jets at $M=0.4$ and 0.6 and also shows that the coverage is sparse between the two holes. Moderate blowing ratios yielded the best cooling of the surface since there was more coolant mass ejected and it still remained attached. Near the hole, the effectiveness values were around 0.2 and dropped to around 0.1 by $x/d=15$. For higher blowing ratios, the jet detached from the surface, lowering η. The lower effectiveness levels suggest that the jet was mostly detached when $M=1.2$ and 1.4. The high blowing ratio cases had nearly constant effectiveness for all $x/d>3$. At $M=1.0$, $\bar{\eta}=0.12$ just after the hole and degraded to 0.09 by $x/d=30$. At $M=1.2$, $\bar{\eta}=0.08$, and $\bar{\eta}=0.06$ for $M=1.4$.

The adiabatic effectiveness levels were higher for the high mainstream turbulence case at moderate and high blowing ratios when compared to the low mainstream turbulence case, as seen in Fig. 9. For $M=1.0$, the values for the laterally averaged effectiveness for the high mainstream turbulence case were about $\Delta\bar{\eta}=0.02$ higher than the low mainstream turbulence. At $M=1.4$, the difference was about $\Delta\bar{\eta}=0.03$, resulting in nearly a 50% difference due to the lower absolute values of the effectiveness over the whole surface. The increase in the adiabatic effectiveness for the high mainstream turbulence case can be attributed to increased mixing with the mainstream, which brought some of the coolant back to the surface.

The two axial hole cases were compared to examine the effect of the pitch on the cooling effectiveness. The laterally averaged values for a few of the blowing ratios are compared in Fig. 10. It is quite obvious that the smaller pitch, $p/d=2.78$, had higher $\bar{\eta}$ values, as expected, since there was more coolant mass along

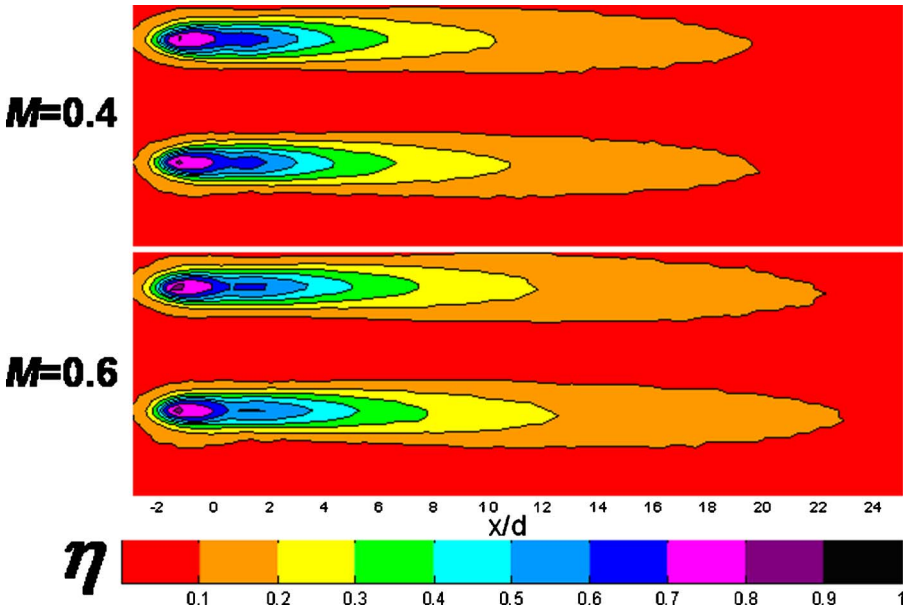

Fig. 8 Spatial plots of adiabatic effectiveness for axial holes at various M, $p/d=5.55$, $Tu_\infty=3.9\%$, DR=1.3

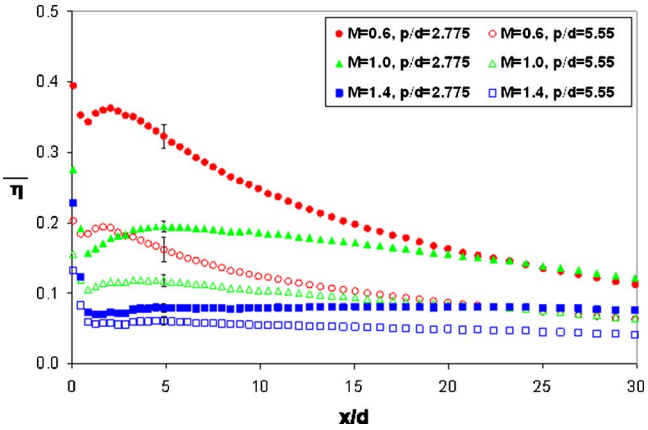

Fig. 10 Comparison of laterally averaged adiabatic effectiveness for two hole spacings, $Tu_\infty=3.9\%$, DR=1.3

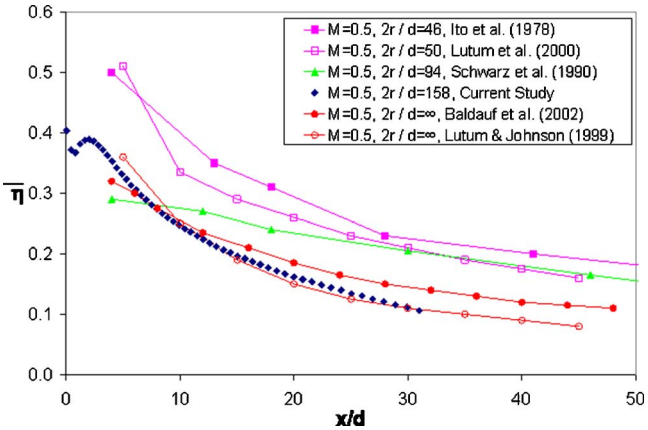

Fig. 12 Effect of curvature on laterally averaged adiabatic effectiveness for $M=0.5$

equal lateral distances. In fact, the values were about double the values of the larger pitch, $p/d=5.55$. Further evidence of the additive effect due to the pitch is given when looking at the spatially averaged effectiveness plots. Figure 11 shows that the spatially averaged adiabatic effectiveness for the smaller hole spacing was approximately twice that of the larger hole spacing. For convenience, the larger hole spacing values were multiplied by two to show the additive effect due to hole spacing. The blowing ratio that yielded the highest $\bar{\eta}$ and the trend for the spatially averaged effectiveness remained the same for both pitches.

As discussed in the introduction, the wall curvature can have a large effect on the adiabatic effectiveness. For convex surfaces, the adiabatic effectiveness increases dramatically when the radius of curvature is small. Figure 12 compares the laterally averaged adiabatic effectiveness for $2r/d=46$ [3], 50 [13], 94 [4], 158 (from the current study), and ∞ (flat plate) [1,22] for a blowing ratio of $M=0.5$, which is near the optimal blowing ratio. The results from the current study are consistent with the trends previously found in the literature, namely, that the adiabatic effectiveness would be expected to be lower than the other curvatures since the radius of curvature is larger. In fact, the comparison shows that at the location tested with a curvature of $2r/d=158$, the results compared with flat plate data better than any of the curved surfaces tested in literature.

Due to the mild curvature of the current location on the suction side ($2r/d=158$), the data were compared to flat plate results ($2r/d=\infty$) [1,22]. The $p/d=2.78$ configuration was compared to flat plate data with $p/d=3$. The injection angle was the same in Refs. [1,22] as the current study. Figure 13 shows the comparison of laterally averaged adiabatic effectiveness for the smaller pitches. The values compared well with the flat plate data.

Compound angle holes with the same pitch as one of the axial hole configurations was tested. The injection angle was steeper than the axial holes ($\alpha=45$ deg). As shown in Fig. 14, blowing ratios from $M=0.2$ to 0.6 yielded similar $\bar{\eta}$ distributions. For $M \geq 0.8$, $\bar{\eta}$ levels decrease suggesting the beginning of coolant jet separation.

The highest values for adiabatic effectiveness for all the blowing ratios were found at low blowing ratios: $M=0.2$ and 0.3. This peak was near the hole, yielding values of $\bar{\eta}=0.3$, but the effectiveness levels quickly declined. By $x/d=10$, the effectiveness had degraded to about $\bar{\eta}=0.15$. At low blowing ratios, the jet did not have much lateral momentum, so the mainstream flow quickly turned the jet into the streamline direction. At moderate blowing ratios, from $M=0.4$ to about $M=0.8$, the effectiveness was still above $\bar{\eta}=0.2$ near the holes, but did not degrade as fast as the lower blowing ratios. For higher blowing ratios, $M>0.6$, the effectiveness levels dropped due to increasing jet detachment. When the blowing ratio was $M=1.0$, the downstream value of the laterally averaged adiabatic effectiveness was approximately $\bar{\eta}=0.13$, while when $M=1.2$, it was $\bar{\eta}=0.1$, and for $M=1.4$, it was $\bar{\eta}=0.07$. Figure 15 shows the spatial distribution of η for low, moderate, and high blowing ratios. Lateral spreading of the coolant is

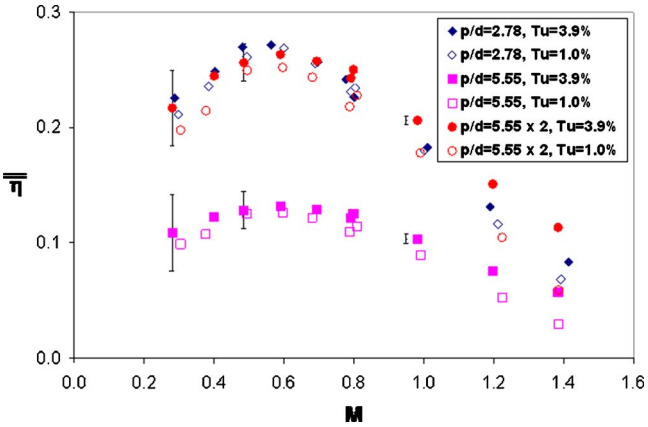

Fig. 11 Additive effect of hole spacing for axial holes (adiabatic effectiveness of larger pitch multiplied by two added for easier comparison), DR=1.3

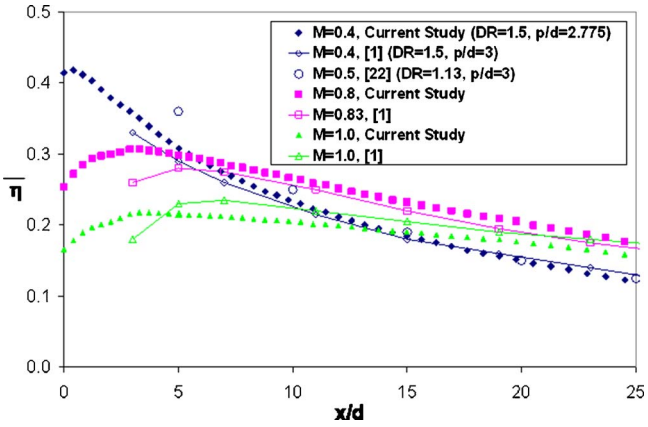

Fig. 13 Comparison of current study to flat plate data [1,22], $p/d\sim3$

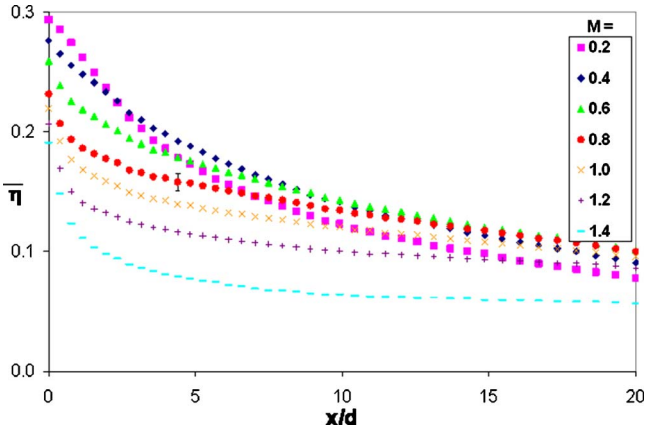

Fig. 14 Laterally averaged adiabatic effectiveness for compound angle holes for various M, $p/d=5.55$, $Tu_\infty=3.9\%$, DR =1.3

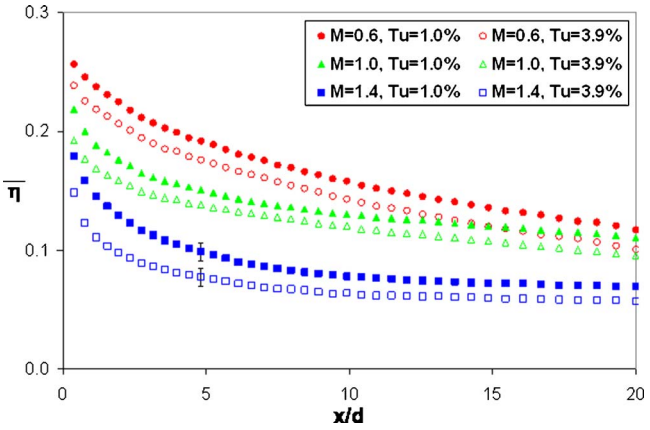

Fig. 16 Mainstream turbulence comparison for compound angle holes, DR=1.3

evident for $M>0.6$ since the highest effectiveness is not exactly downstream of the hole. Increased jet detachment is suggested in the contour plots at higher blowing.

The difference between the two turbulence levels for the compound angle holes is plotted in Fig. 16. In contrast to the result for the axial holes, the higher mainstream turbulence caused a 5–10%

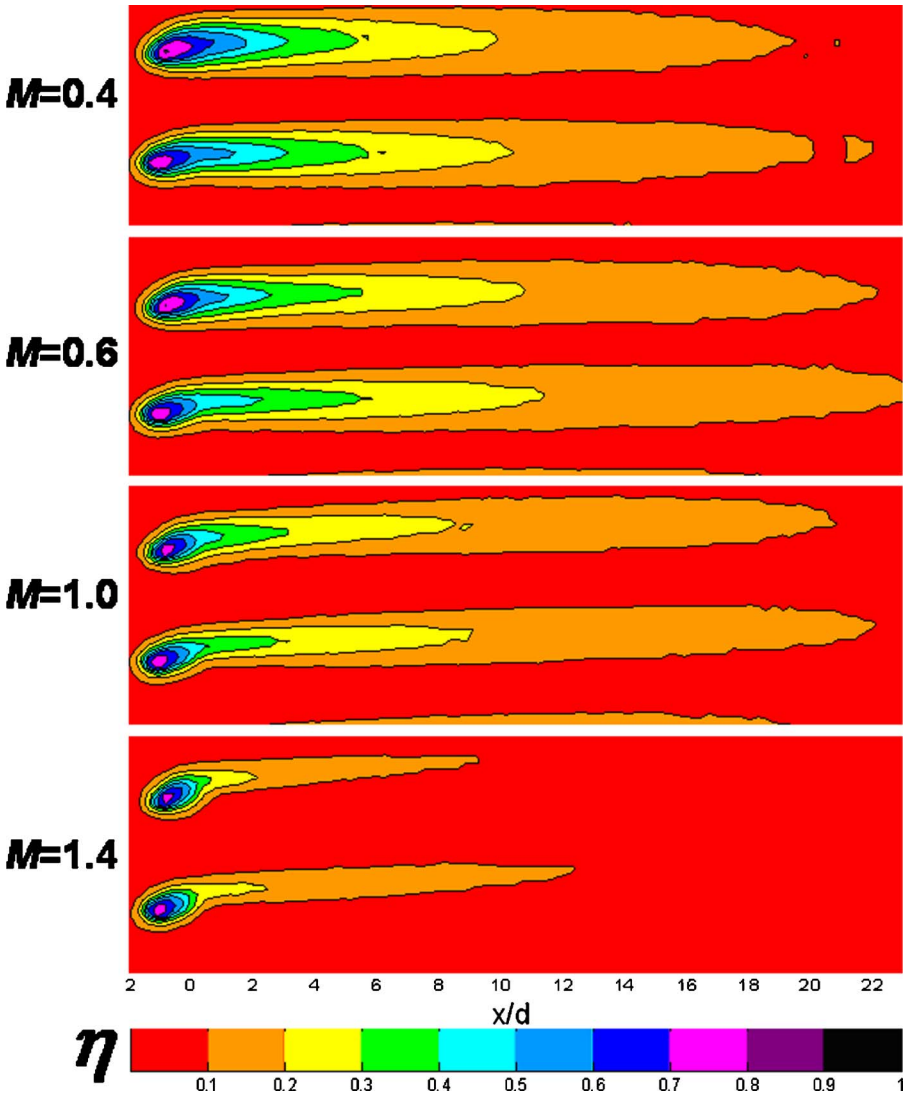

Fig. 15 Spatial adiabatic effectiveness for compound angle holes, $Tu_\infty=3.9\%$, DR=1.3

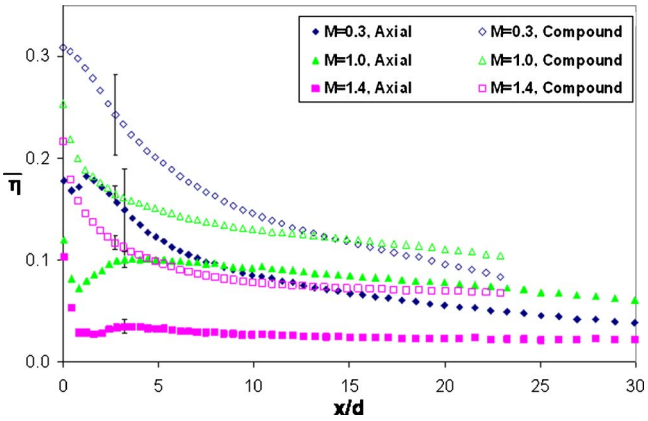

Fig. 17 Comparison of axial and compound angle holes, $p/d=5.55$, $Tu_\infty=1.0\%$, DR=1.3

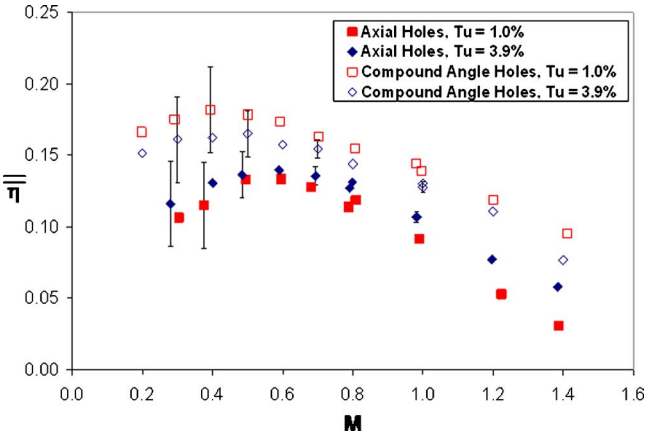

Fig. 18 Spatially averaged adiabatic effectiveness for axial and compound angle holes, $p/d=5.55$

decrease in $\bar{\eta}$. This reversal in the effect of high mainstream turbulence is speculated to be due to jets from the compound angle holes being less detached from the surface. Consequently the beneficial effect of high-mainstream turbulence of returning separated coolant to the wall is less significant for the compound angle holes, and the detrimental effect of greater coolant dispersion causes a net decrease in $\bar{\eta}$.

Comparing the effects of two different hole geometries allows a quantitative analysis on which of the configurations yields better cooling effectiveness. The baseline axial hole case and the compound angle hole case were compared. Both had the same pitch ($p/d=5.55$) and hole diameter and were located at the same position on the suction side of the vane, the injection angle was different. The axial holes had an injection angle of $\alpha=30$ deg and the compound angle holes had an injection angle of $\alpha=45$ deg oriented $\beta=45$ deg from the streamwise direction. It would be expected from literature that the injection angle of $\alpha=45$ deg for the compound angle holes would have a lower adiabatic effectiveness than similar holes with $\alpha=30$ deg. Therefore, if the injection angle of the compound holes used in the current study was the same as the axial holes ($\alpha=30$ deg), it would be expected that the adiabatic effectiveness values would be higher. It should also be noted that for both of the cases, the pitch is relatively large as to render the holes to act independently without jet to jet interaction.

Figure 17 shows a comparison of the two configurations for low mainstream turbulence. The compound angle hole geometry consistently had higher adiabatic effectiveness than the axial holes for all x/d locations. At low blowing ratios, the difference was greater than at moderate or high blowing ratios. Compound angle holes use the spanwise component of the coolant jet to laterally spread the coolant. For low mainstream turbulence, the adiabatic effectiveness of the compound angle holes was 25% to more than triple the levels seen for the axial holes for most x/d, depending on the blowing ratio. The increase of 300% at high blowing ratios was attributed more to the low levels of adiabatic effectiveness for the axial holes than the levels for the compound angle holes. For high-mainstream turbulence, the compound holes had higher adiabatic effectiveness than the axial holes near the holes (up to about 30%), but due to mixing with the mainstream, had nearly the same cooling downstream. Figure 18 confirms that the compound angle holes performed better than the axial holes when the spatially averaged adiabatic effectiveness is compared over the range of $0<x/d<20$. At low blowing ratios, the values are within the uncertainty, so no conclusion can be made as to which configuration is better for $M<0.6$.

The comparison of the both axial and compound angle holes for blowing ratios of $M=0.6$ and 1.2 with Ref. [2] shows that the current results agree well with the flat plate results of Ref. [2], as seen in Fig. 19. The geometry of the compound angle holes in Ref. [2] used for comparison was $p/d=6$, $\alpha=35$ deg, $\beta=60$ deg. The experiment was conducted on a flat plate with a density ratio of DR=1.6 with a similar approaching boundary layer as the current study.

The conclusion of Ref. [2] was that the compound angle holes performed only slightly better than axial holes at moderate blowing ratios, but did not experience the same drop in adiabatic effectiveness as the axial holes with increasing blowing. Therefore, the compound angle holes were found to be superior at higher blowing ratios. The lowest blowing ratio tested by Ref. [2] was $M=0.6$, while the current study measured M as low as $M=0.2$ for the compound angle holes and $M=0.3$ for the axial holes. Schmidt and Bogard [1] found that at low blowing ratios ($M=0.4$), radial holes ($\beta=90$ deg) had the same values of adiabatic effectiveness as the axial holes. In the current study, the same results were found: that the compound angle holes performed better at moderate and high blowing ratios.

Conclusions

The adiabatic effectiveness for cylindrical, 30 deg axial holes with a hole spacing of $p/d=5.55$ and 2.78 on the suction side of a vane increased with increasing blowing until reaching an optimal blowing ratio, where the adiabatic effectiveness was the highest for the whole surface, consistent with numerous studies found in the literature. The blowing ratio that yielded the highest overall effectiveness was $M=0.6$. With additional blowing, the effectiveness decreased, due to coolant jet detachment. The effects of the

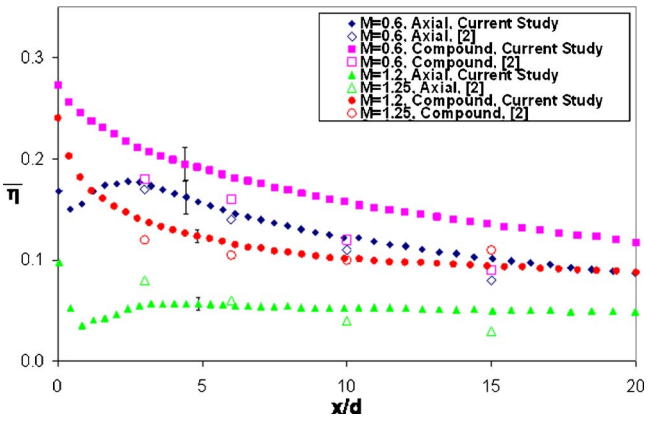

Fig. 19 Axial and compound angle hole results compared to similar flat plate results in the literature [2] at low Tu_∞

turbulence were relatively small, but this was somewhat expected since the local turbulence levels with and without the turbulence generator were $Tu_{app}=3.9\%$ and 1.0%, respectively. The difference of cooling performance due to the density ratio was in line with results found in the literature, namely, that the adiabatic effectiveness was slightly higher with a higher density ratio. Again, this was expected since the difference between the two density ratios tested was small: DR=1.3 and DR=1.5.

The difference in the hole spacing of the two axial hole cases was exactly a factor of two: $p/d=5.55$ and 2.78, respectively. When the effectiveness of the larger hole spacing was multiplied by two, the values were almost identical to those of the smaller hole spacing. Therefore, the principle of superposition or the additive nature of axial holes is reinforced, as previously presented in the literature.

For the current study, the surface was curved due to the location tested on the simulated turbine vane. The curvature at the location of the coolant holes was $2r/d=158$, which was between previously tested curvature found in the literature and flat plate literature. The laterally averaged adiabatic effectiveness values were in line with flat plate data. Schwarz et al. [4] showed an increase in adiabatic effectiveness of approximately 50% over flat plates for convex surfaces with $2r/d=126$ and almost a 100% increase for $2r/d=94$ and 61 for $I<1.0$ at $x/d=40$. For the current study, the data indicated that flat plate geometry closely approximates the values for such a mild curvature and therefore could be used to simplify testing to provide a broader application for locations on the vane with mild curvature.

The compound angle hole configuration, with $\alpha=45$ deg and compound angle $\beta=45$ deg and a hole spacing of $p/d=5.55$, had the same trend regarding the blowing ratio as did the axial holes. The blowing ratio that yielded the highest overall effectiveness was lower, at $M=0.4$. From the range of $M=0.2-0.7$, the spatially averaged effectiveness was nearly the same, showing less of an effect due to the blowing ratio when compared to axial holes. Compound angle holes provided higher laterally averaged adiabatic effectiveness than axial holes. Previous studies in the literature found similar adiabatic effectiveness for compound angles, and concluded that they performed better than axial holes, especially at high blowing ratios. The current study confirmed that this occurred, even when the compound angle hole configuration had a steeper injection angle than the axial hole configuration.

Acknowledgment

The authors gratefully acknowledge the support of the UTSR program (Contract No. 03-01-SR110) directed through the South Carolina Institute for Energy Studies (SCIES) and the Office of Naval Research (ONR) through the Electric Ship consortium.

Nomenclature

C = chord length
d = film cooling hole diameter
DR = density ratio, ρ_c/ρ_∞
H = shape factor, δ_1/δ_2
I = momentum flux ratio, $\rho_c U_c^2/\rho_\infty U_\infty^2$
k = thermal conductivity
L = hole length
M = blowing ratio, $\rho_c U_c/\rho_\infty U_\infty$
p = coolant hole pitch distance
r = radius of curvature
Re = Reynolds number, $U_{exit}C/\nu$
s = streamwise coordinate along vane
T = temperature
Tu = turbulence intensity, u_{rms}/U_{mean}
U = flow velocity
u = fluctuating velocity
x = streamwise distance from coolant holes

Greek

α = injection angle of hole relative to surface
β = injection angle of hole relative to mainstream flow
Δ = change or difference
δ = uncertainty or change in a parameter boundary layer thickness
δ_1 = displacement thickness
δ_2 = momentum thickness
η = adiabatic effectiveness, $(T_\infty-T_{aw})/(T_\infty-T_c)$
Λ = integral length scale
ν = kinematic viscosity
ρ = density

Subscripts and Superscripts

app = approach condition
aw = adiabatic wall
c = coolant
exit = exit condition
rms = root mean square
∞ = local mainstream
0 = without film cooling
– = laterally averaged
= = spatially averaged

References

[1] Schmidt, D. L., and Bogard, D. G., 1997, "Effects of Free-stream Turbulence and Surface Roughness on Laterally Injected Film Cooling," *Proceedings of National Heat Transfer Conference*, HTD-Vol. 350, Baltimore, MD, August 8–12.
[2] Schmidt, D. L., Sen, B., and Bogard, D. G., 1996, "Film Cooling with Compound Angle Holes: Adiabatic Effectiveness," ASME J. Turbomach., **118**, pp. 807–813.
[3] Ito, S., Goldstein, R. J., and Eckert, E. R. G., 1978, "Film Cooling of a Gas Turbine Blade," J. Eng. Power, **100**, pp. 476–481.
[4] Schwarz, S. G., Goldstein, R. J., and Eckert, E. R. G., 1990, "The Influence of Curvature on Film Cooling Performance," ASME J. Turbomach., **100**, pp. 472–478.
[5] Takeishi, K., Aoki, S., Sato, T., and Tsukagoshi, K., 1991, "Film Cooling on a Gas Turbine Rotor Blade," ASME J. Turbomach., **114**, pp. 828–834.
[6] Ou, S., and Han, J. C., 1994, "Unsteady Wake Effects on Film Effectiveness and Heat Transfer Coefficient from a Turbine Blade with One Row of Air and CO_2 Film Injection," J. Heat Transfer, **116**, pp. 921–928.
[7] Ligrani, P. M., Wigle, J. M., Ciriello, S., and Jackson, S. M., 1994, "Film Cooling from Holes with Compound Angle Orientations: Part 2—Results Downstream of a Single Row of Holes with 6D Spanwise Spacing," Int. J. Heat Mass Transfer, **116**, pp. 353–362.
[8] Lander, R. D., Fish, R. W., and Suo, M., 1972, "External Heat Transfer Distribution on Film Cooled Turbine Vase," J. Aircr., **9**, pp. 707–714.
[9] Goldstein, R. J., Kornblum, Y., and Eckert, E. R. G., 1982, "Film Cooling Effectiveness on a Turbine Blade," Isr. J. Technol., **20**, pp. 193–200.
[10] Takeishi, K., Matsuura, M., Aoki, S., and Sato, T., 1990, "An Experimental Study of Heat Transfer and Film Cooling on Low Aspect Ratio Turbine Nozzles," ASME J. Turbomach., **112**, pp. 488–496.
[11] Ligrani, P. M., Wigle, J. M., Ciriello, S., and Jackson, S. M., 1994, "Film Cooling from Holes with Compound Angle Orientations: Part 1—Results Downstream of a Two Staggered Rows of Holes with 3D Spanwise Spacing," Int. J. Heat Mass Transfer, **116**, pp. 341–352.
[12] Dittmar, J., Schulz, A., and Wittig, S., 2003, "Assessment of Various Film-Cooling Configurations Including Shaped and Compound Angle Holes Based on Large-Scale Experiments," ASME J. Turbomach., **125**, pp. 57–64.
[13] Lutum, E., von Wolfersdorf, J., Weigand, B., and Semmler, K., 2000, "Film Cooling on a Convex Surface with Zero Pressure Gradient Flow," Int. J. Heat Mass Transfer, **43**, pp. 2973–2987.
[14] Kruse, H., 1985, "Effects of Hole Geometry, Wall Curvature, and Pressure Gradient on Film Cooling Downstream of a Single Row," *AGARD Conference Proceedings*, Vol. 309, pp. 8.1–8.13.
[15] Schwarz, S. G., and Goldstein, R. J., 1988, "The Two-Dimensional Behaviour of Film Cooling Jets on Concave Surfaces," SME Paper No. 88-GT-161.
[16] Lutum, E., von Wolfersdorf, J., Semmler, K., Dittmar, J., and Weigand, B., 2001, "An Experimental Investigation of Film Cooling on a Convex Surface Subjected to Favourable Pressure Gradient Flow," Int. J. Heat Mass Transfer, **44**, pp. 939–951.
[17] Rutledge, J. L., Robertson, D. R., and Bogard, D. G., 2005, "Degradation of Film Cooling Performance on a Turbine Vane Suction Side due to Surface Roughness," ASME Paper No. GT2005-69045.
[18] Schlichting, H., 1968, *Boundary Layer Theory*, 6th ed., McGraw-Hill, New York, pp. 192–201, 470.
[19] Ethridge, M. I., Cutbirth, J. M., and Bogard, D. G., 2001, "Scaling of Perfor-

mance for Varying Density Ratio Coolants on an Airfoil with Strong Curvature and Pressure Gradient Effects," ASME J. Turbomach., **123**, pp. 231–237.
[20] Moffat, R. J., 1988, "Describing the Uncertainties in Experimental Results," Exp. Therm. Fluid Sci., **1**, pp. 3–17.
[21] Goldstein, R. J., and Stone, L. D., 1994, "Row-of-Holes Film Cooling of a Convex and a Concave Wall at Low Injection Angles," Clim. Change, **28**, pp. 15–29.
[22] Lutum, E., and Johnson, B. V., 1999, "Influence of the Hole Length-to-Diameter Ratio on Film Cooling with Cylindrical Holes," ASME J. Turbomach., **121**, pp. 209–216.

End-Wall Film Cooling Through Fan-Shaped Holes With Different Area Ratios

Giovanna Barigozzi
e-mail: giovanna.barigozzi@unibg.it

Giuseppe Franchini

Antonio Perdichizzi
e-mail: antonio.perdichizzi@unibg.it

Dipartimento di Ingegneria Industriale,
Università degli Studi di Bergamo,
Viale Marconi,
24044 Dalmine (BG) Italy

The present paper reports on the aerothermal performance of a nozzle vane cascade, with film-cooled end walls. The coolant is injected through four rows of cylindrical holes with conical expanded exits. Two end-wall geometries with different area ratios have been compared. Tests have been carried out at low speed ($M=0.2$)*, with coolant to mainstream mass flow ratio varied in the range 0.5–2.5%. Secondary flow assessment has been performed through three-dimensional (3D) aerodynamic measurements, by means of a miniaturized five-hole probe. Adiabatic effectiveness distributions have been determined by using the wide-band thermochromic liquid crystals technique. For both configurations and for all the blowing conditions, the coolant share among the four rows has been determined. The aerothermal performances of the cooled vane have been analyzed on the basis of secondary flow effects and laterally averaged effectiveness distributions; this analysis was carried out for different coolant mass flow ratios. It was found that the smaller area ratio provides better results in terms of 3D losses and secondary flow effects; the reason is that the higher momentum of the coolant flow is going to better reduce the secondary flow development. The increase of the fan-shaped hole area ratio gives rise to a better coolant lateral spreading, but appreciable improvements of the adiabatic effectiveness were detected only in some regions and for large injection rates.* [DOI: 10.1115/1.2464140]

Introduction

The demand for the continuous increase of gas turbine performance requires the enhancement of thermal protection all over the turbine surfaces, including the end-wall region. In fact, the increase in turbine inlet temperature, joined to combustor design improvements, give higher and flatter temperature distributions approaching the turbine first-stage nozzle vane. Moreover, inside the vane passage, secondary flows move high-temperature gas from the midspan region toward the end walls. All these aspects lead to the requirement of a quite effective end-wall cooling.

The first documented analysis of end-wall cooling is the one reported by Blair [1]. He showed that end-wall heat transfer is strongly influenced by the presence of the corner vortex, which was proved to be responsible for the large heat transfer coefficient variations inside the vane passage. A strong influence of secondary flows on the adiabatic effectiveness was also documented. The aerodynamic investigation of Sieverding and Wilputte [2] showed a relevant influence of end-wall coolant injection upon secondary flow losses and air exit angle distributions. These results were confirmed by the combined aerothermal investigation of Friedrichs et al. [3–5]. They found that end-wall coolant injection strongly alters the secondary flow structure. Concerning the coolant-to-mainstream mixing loss, a reduction was found for mass flow rates above 2%, when compared to the uncooled case. When coolant is injected at large mass flow rate, it reenergizes the boundary layer, thus weakening the secondary flows.

More recently Kost and Nicklas [6] and Nicklas [7] investigated the aerothermal behavior of a transonic cascade with end-wall film cooling. A strong interaction between the coolant and the main flow was detected. Again, coolant injection strengthens the end-wall boundary layer, thus reducing the end-wall cross-flow. A similar investigation, but on a different end-wall cooling scheme, was also performed by Knost and Thole [8]. They found that coolant behavior is strongly dependent on local blowing conditions for the cooling holes. The leading edge and the pressure side were found to be the most difficult regions to be efficiently cooled. Barigozzi et al. [9,10] tested an end-wall cooling scheme under variable injection mass flow rates. They found that the injection of a quite large coolant mass flow gives rise to a relevant reduction in the secondary vortex activity, leading to an almost two-dimensional (2D) flow-field configuration. The adiabatic effectiveness analysis confirmed that, to achieve a good end-wall protection, coolant has to be injected with a momentum large enough to resist to secondary cross-flow, but not too high to give rise to important jet liftoff.

The most common geometry used for end-wall cooling through hole is based on cylindrical holes inclined in the axial direction and with a compound angle. Goldstein et al. [11], and more recently Thole et al. [12] and Gritsch et al. [13–15], showed that, in a simple flat-plate configuration, the addition of an expanded exit provides better cooling performances in terms of larger adiabatic effectiveness, larger lateral spreading, and reduced heat transfer coefficient. Barigozzi et al. [10] compared a cylindrical with respect to a fan-shaped end-wall cooling configuration; the introduction of a conical expanded exit has been shown to increase the coolant protection capabilities at high injection rates. This was obtained by paying a "thermodynamic" loss increase; nevertheless, the passage vortex activity is significantly reduced.

The present paper compares the fan-shaped end-wall cooling scheme (CONF2) tested by Barigozzi et al. [10] to a second fan-shaped geometry (CONF3), presenting holes with a more extended diffusion section and, thus, a larger exit to inlet area ratio. The goal is to analyze the effects of a significant exit to inlet area ratio increase on the aerothermodynamic performance of a nozzle vane cascade, under different coolant injection rates.

Contributed by the International Gas Turbine Institute of ASME for publication in the JOURNAL OF TURBOMACHINERY. Manuscript received July 12, 2006; final manuscript received July 21, 2006. Review conducted by David Wisler. Paper presented at the ASME Turbo Expo 2006: Land, Sea and Air (GT2006), Barcelona, Spain, May 8–11, 2006. Paper No. GT2006-90684.

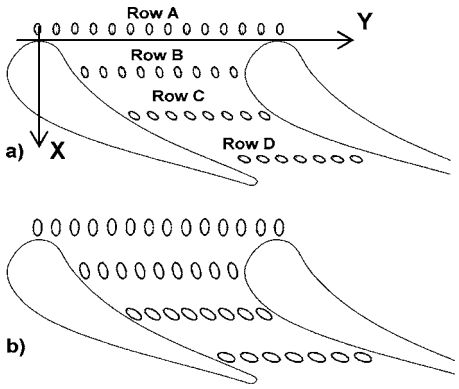

Fig. 1 Cascade and end-wall cooling geometry: (*a*) CONF2 and (*b*) CONF3

Experimental Details

Geometry and Test Conditions. Tests were performed in the subsonic wind tunnel for linear cascades at the Thermo-Fluid Dynamic Laboratory of Bergamo University. A description of the wind tunnel, including the cascade geometry and the secondary air supply system, is given in Ref. [9]. The test section presents a cascade with seven vanes, whose profile is typical of a first-stage nozzle guide vane. Figure 1 shows the tested vane together with the cooled end-wall geometries (CONF2 and CONF3). For both configurations, only one passage was cooled, with cooling assured by the presence of four rows of holes with a cylindrical section of 1.5 mm dia connected to a single plenum. The hole length over diameter ratio and the hole pitch are the same for both configurations ($L/D=10.7$ and $B/D=6$, respectively). Only the last row of CONF3 has a greater hole pitch ($7.3D$); this is in order to locate the external holes closer to the vane surfaces. Hole locations and geometrical characteristics are summarized in Table 1. The hole disposition inside of the vane passage is unchanged (see [10] for a deeper description). Hole injection angle has been set to 30 deg with respect to the end-wall surface. In the blade-to-blade plane, each row has a compound angle equal to the mean flow angle at midspan.

The conical final portion of each hole of both configurations has a divergence angle of 20 deg (Fig. 2). In the CONF3 case, the fan-shaped portion extends deeply inward ($4D$ against $2D$ of CONF2). Exit-to-inlet area ratio (defined where the hole axis intersects the end wall surface) is thus increased up to AR=5.8 for CONF3 (it was AR=3.1 in CONF2).

The cascade geometry and the operating conditions are summarized in Table 2; they are the same as in the previous investigation [10]. Tests were performed at low speed, i.e., at an isentropic Mach number $Ma_{2is}=0.2$, and low inlet turbulence intensity, namely, 1%. Air was blown as cooling flow (density ratio=1); during thermal tests, the secondary air was slightly heated, while the core flow was at ambient temperature. Small density differences (as large as 6%) between the two data sets do exist.

Table 1 Cooling system geometrical characteristics

	CONF3 (CONF2)			
Row	*A*	*B*	*C*	*D*
X/c_{ax}	−0.08	0.35	0.65	0.82
$N°$	14	9	8	7
γ	20 deg			
B/D	6			7.3 (6)
L/D	10.7			
α	30 deg			
AR	5.8 (3.1)			

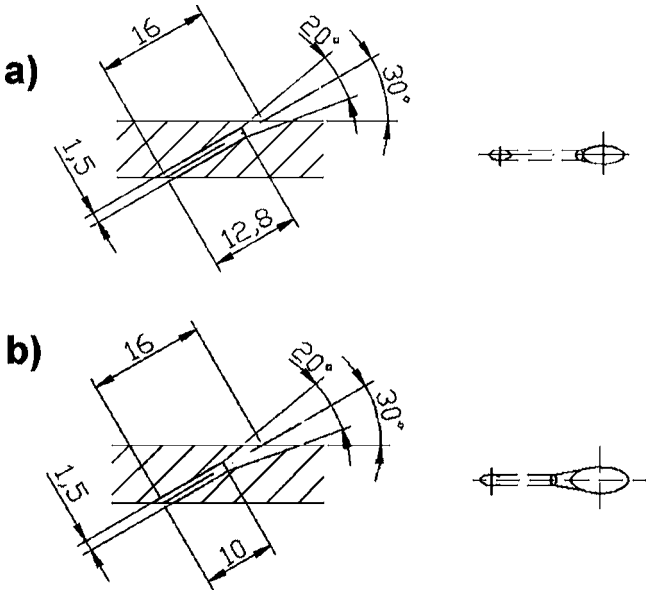

Fig. 2 Detail of hole geometry: (*a*) CONF2 and (*b*) CONF3

The coolant to mainstream mass flow rate (MFR) ratio was used to identify the injection conditions. Tests were performed for MFR values ranging between 0.5% and 2.5%.

Measurement Techniques. Aerodynamic measurements were performed by traversing a five-hole miniaturized aerodynamic pressure probe (1.6 mm head) downstream of the trailing-edge plane. Testing conditions were controlled through a continuous monitoring of the global coolant to mainstream mass flow rate MFR, by using an orifice device. Coolant total pressure and temperature were measured inside of the plenum by means of a pressure tap and a T-type thermocouple.

The traversing plane is located 50% of the axial chord downstream of the trailing edge ($X/c_{ax}=150\%$), and it covers three vane passages. The measurement grid consists of 30 points per pitch in tangential direction times 21 points along the nozzle guide vane height up to midspan. The grid spacing was reduced approaching the end-wall surface.

Sprayable wide-band thermochromic liquid crystals (TLC) (Hallcrest BM/R25C10WC17-10) have been used for the thermal measurements; the evaluation of film-cooling adiabatic effectiveness distributions was carried out by means of the transient technique. TLC images were acquired using a CCD camera, with a 767×573 pixels resolution. The primary lighting system consists of two 150 W white light sources, each one connected to two optical fibers. A proper in situ calibration of TLCs was performed. The Hue capturing technique proposed by Camci et al. [16] was applied to the recorded data. The relatively large thickness of the Plexiglas® end wall (externally insulated), assured the satisfaction of wall adiabatic condition during test duration. Nonadiabatic spurious effects due to heat conduction took place anyway just upstream and in-between the holes because the material thickness was too small. No conduction correction to the recorded data was applied. The film-cooling effectiveness measurement uncertainty

Table 2 Cascade geometry and operating conditions

$s/c=0.86$	$H/c=1.04$
$c=133.7$ mm	7 nozzle guide vanes
$\beta_1=90$ deg	$\beta_2'=21$ deg
$Ma_1=0.06$	$Ma_{2is}=0.2$
$Re_{2is}=0.66\ 10^6$	$Tu_1=1\%$

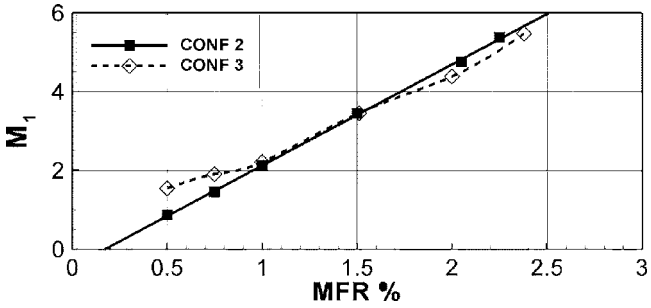

Fig. 3 M_1 **versus MFR**

ranges from ±4% with $\eta=0.3$, up to more than ±10% when $\eta=0.1$. These values surely increase where conduction phenomena take place (i.e., in the near hole exit region).

Discharge Coefficients and Local Blowing Ratios

Before discussing the results, the reader is reminded that local injection conditions are strongly influenced by the local values of parameters like blowing and momentum flux ratios. Since all the holes are fed by a single plenum such parameters experience large variations in both pitchwise and streamwise direction because of the large variation of static pressure on the end-wall surface. To identify each test condition, two overall parameters may be used: the coolant to mainstream mass flow ratio MFR and the inlet loss-free blowing ratio M_1. As previously stated, tests were run changing the MFR in the range of 0.5–2.5 %, corresponding to M_1 values between 1.5 and 5.5. Figure 3 reports the relationship between these two parameters for the two configurations.

The area ratio increase was expected to produce the injection of a larger mass flow rate, thanks to the pressure recovery in the hole diffusion section. From Fig. 3 it can be observed that, at small injection conditions (MFR$<1\%$), CONF3 needs a higher M_1 than CONF2 to reach the same MFR. At larger MFR ($>1\%$), CONF3 gives a small gain in the MFR value, at constant M_1.

In order to understand this unexpected behavior, the overall discharge coefficient C_d of the two cooling schemes was measured for all the considered injection conditions. The ideal coolant flow rate through each hole was estimated from coolant inlet total pressure and the local static pressure values at hole centerline exit locations $p_{\infty,i}$; the latter were evaluated from the blade-to-blade velocity distribution at midspan (measured by a 2D laser Doppler anemometer system). Of course, this implies that the static pressure distribution at the end wall is the same as at midspan, and that it is not affected by coolant injection. Regardless, it will give useful information on the share of the injected flow between the different holes. According to Gritsch et al. [15], the inlet cylindrical hole cross section was used as reference hole area. The overall actual coolant flow rate was measured directly from the orifice device. Tests were done with ($M_{2is}=0.2$) and without ($M_{2is}=0$) the external main flow. Figure 4 shows the C_d distributions as a function of the ratio between the plenum total pressure p_{tc} and the mean freestream static pressure p_∞, the latter computed by averaging all the hole exit static pressure values $p_{\infty,i}$. Of course, p_∞ becomes the atmospheric pressure when tests are run without the main flow. Figure 4 also shows, for comparison, the C_d distribution for the cylindrical hole configuration (CONF1) in the case with the external flow ($M_{2is}=0.2$).

If the two geometries with no external flow ($M_{2is}=0$, dotted lines) are compared, CONF3 always shows larger C_d values than CONF2, except for the very low injection rates; this is certainly due to the larger recovery in the diffusion section obtained by increasing the area ratio. Moving to the second test condition, i.e., with external cross-flow (solid lines), both CONF2 and CONF3 C_d values decrease. In agreement with Gritsch et al. [15] results, it

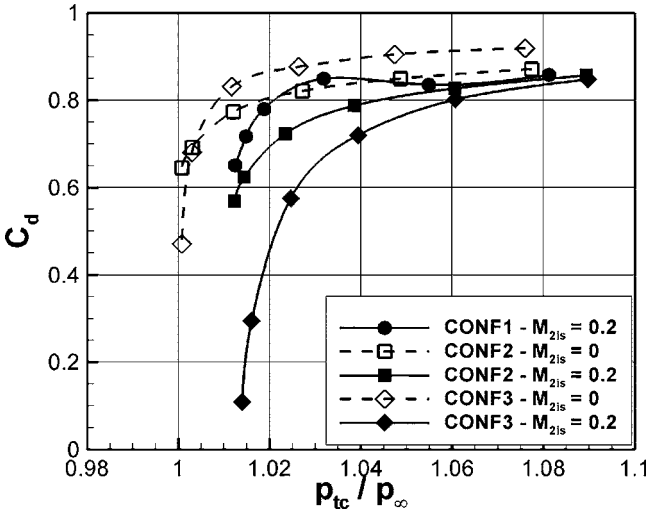

Fig. 4 C_d **values for the different cooling schemes**

can be noted that the external cross flow influence is more relevant at low-pressure ratios. The larger reduction found for the CONF3 case can be explained by the lower momentum of the flow injected through the high area ratio geometry. By comparing the two fan-shaped geometries to the cylindrical one (CONF1), it appears that the latter initially has lower losses and, thus, higher C_d values. This behavior disagrees with Gritsch et al. [15] results, but it can be explained by the higher area ratio of both CONF2 and CONF3 geometries, with respect to the one tested by Gritsch et al. When the pressure ratio, and thus the injected mass flow, is increased, all configurations tend to the same level.

It has to be pointed out that, even with no external flow, the C_d values for the two fan-shaped geometries are always lower than 1.0 and far from the values corresponding to the ideal diffusion. This means that only a quite limited recovery takes place in the diffusion section and that the coolant flow always undergoes a separation inside of the divergent section of cooling holes. Hence, it is clear that the advantage of a larger expanded exit is only in the possibility for the coolant to be better distributed on a wider area, just where the interaction with the main stream begins to take place.

An important factor to be considered in the analysis of the thermal results is the coolant share among the four rows. Therefore, a set of tests was performed by opening one single row with the three others closed, while the cascade was running at the test operating conditions (Table 2). Figure 5 shows, for both geometries, the mass flow share among the rows. Two different behaviors can be identified: for MFR below 1.5%, important variations in the mass flow share exist for both geometries. When the MFR becomes $>1.5\%$, the mass flow share becomes independent on the injected mass flow and on the hole geometry as well. This takes place for all rows but row D. Looking in more detail at the single row data, rows A to C (CONF3) are injecting larger coolant flows with respect to CONF2, whereas the opposite takes place for row D. This is consistent with the influence of the external flow evidenced by Gritsch et al. [15], that showed decreasing discharge coefficients when the external cross flow Mach number is increased. From these data, it can be concluded that the most relevant effect of the increased area ratio is to give rise to a larger mass coolant injection in the front part of the end-wall passage, especially at small MFR values.

Local injection parameters, such as blowing and momentum flux ratios, were also computed. The exit coolant velocity was evaluated from the ideal hole flow rate and the average discharge coefficient of each single row. The reference hole area was assumed equal to the one of the cylindrical hole. Figure 6 shows the

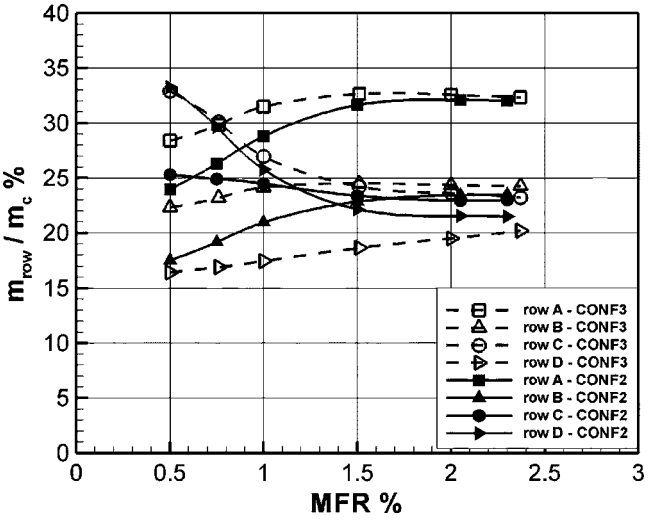

Fig. 5 Mass flow sharing among rows versus MFR

local BR values obtained for the CONF3 geometry, and the tested MFR. CONF2 data are not shown because they are very similar and were already presented and discussed in [10]. Nevertheless, the assumptions made in the used procedure, the reported BR values provide useful information on the share of the injected flow between the different holes of the same row.

All blowing rate values undergo a relevant increase when higher coolant flow rates are injected; in particular, quite high BR values are reached by holes belonging to row A and located close to the leading edge because of the very low mainstream velocity in the stagnation region. The following two rows, located inside of the vane passage, are characterized by progressively decreasing BR values. Because of the pressure gradient across the vane passage, there is also a BR reduction, proceeding from the pressure to the suction side. This happens of course for all MFR. On the opposite, the last row of holes, corresponding roughly to the throat section, show almost constant blowing ratios, with values of the same magnitude of those of the previous row located close to the suction side.

Aerodynamic Results

Because of the crucial role played by secondary flows in determining the end-wall cooling effectiveness, the first part of the investigation was devoted to establish how the secondary flows

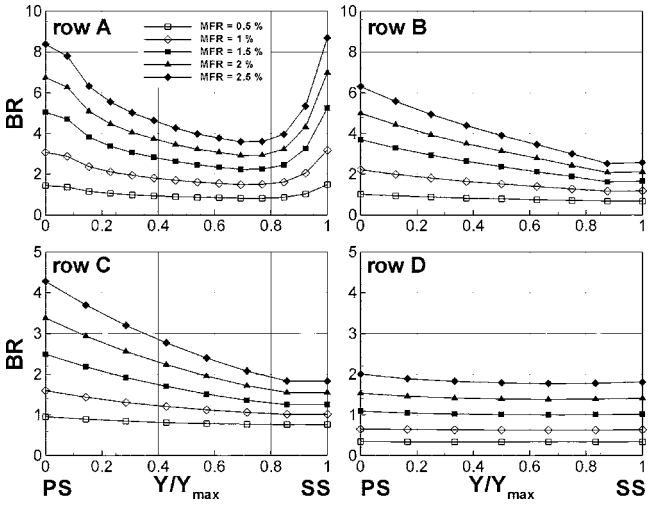

Fig. 6 CONF3 local BR values for variable MFR

are modified by the changes in the injection modes and to determine the loss production variation. To make the comparison between the two configurations easier, CONF2 results are also reported, even if they have been presented already and discussed in [10].

Figures 7–9 present contour plots of secondary energy loss coefficient and secondary velocity field; the vorticity distribution is superimposed. Each figure shows the results for CONF2 and CONF3 end walls at a constant MFR. Only data for the MFR =0.5%, 1.5%, and 2.5% conditions are shown. Each plot shows two wakes; the channel extending between $Y/s=0.5$ and 1.5 corresponds to the cooled channel. Actually, the second wake is the one that is affected by coolant injection, while the first one is not. The streamwise vorticity was computed for each measurement point, following the procedure suggested by Gregory-Smith et al. [17], based on Crocco relation. The vorticity values are normalized by using the inlet freestream velocity and the vane chord.

Looking at the loss distribution, it can be seen that the general behavior is similar for the two configurations. At small injection rates (MFR=0.5%, Fig. 7) the low-momentum fluid coming out from the holes is captured by the passage vortex and driven inside the loss core on the suction side of the wake, causing the increase in the loss peak value. This is accompanied by a relevant increase of the positive vorticity in the region corresponding to the passage vortex. When larger mass flow rate ratios are injected (MFR =1.5%, Fig. 8, and 2.5%, Fig. 9), the high-momentum fluid introduced at the end wall along the flow channel reenergizes the end-wall boundary layer, producing a stretching of the passage vortex and reducing the related cross-flow.

However, the comparison between the two geometries at MFR=0.5% shows a significant increase in the loss production in the case of CONF3 (compare Fig. 7(*a*) and 7(*b*)); the loss core associated with the passage vortex moves toward the midspan, extending in spanwise direction. The peak does not change its position (it is approximately centered at $Z/H=0.2$ for both configurations), but the secondary flows effects now affect almost 30% of the nozzle guide vane span. For CONF3, the crossflow at the end wall appears to be quite enforced and more extended away from the wall: as a result, the loss core related to the corner vortex is moved further in tangential direction, giving rise to a more twisted wake. Looking at the Ω and secondary velocity distributions, the positive vorticity region now extends over a larger portion of the wake.

Increasing the MFR up to 1.5% (Fig. 8), the peak value and pitchwise extension of the loss core related to the passage vortex reduce, together with the wake distortion in spanwise direction. The wake structure is much more similar to the CONF2 one, but the loss core is located farther from the end wall ($Z/H=0.2$ against 0.15 for CONF2). The CONF3 Ω distribution shows a still relevant positive vorticity region, occupying a large portion of the vane passage. At the same injection condition the CONF2 vorticity was instead strongly reduced.

Increasing the injected mass flow rate even more (MFR =2.5%, Fig. 9), the CONF3 loss distribution does not vary so much. The passage vortex loss core moves slightly toward the end wall ($Z/H=0.15$), and a relevant increase in the loss level can be noted all over the end wall. Anyway, some differences exist with respect to CONF2: the wake does not approach a 2D configuration and the corner vortex core remains aligned with the wake.

All these features, supported by the vorticity distributions, indicate that, in the CONF3 case, the secondary flow intensity (passage vortex and end-wall cross-flow) remains higher than for CONF2; this is caused by the lower momentum of the coolant flow, related to the larger expanded exit of the fan-shaped holes.

Deviation Angle. Local flow-field data were mass averaged over the pitch to obtain the spanwise distributions of deviation angle; Fig. 10 presents the results for two selected MFR (0.5%

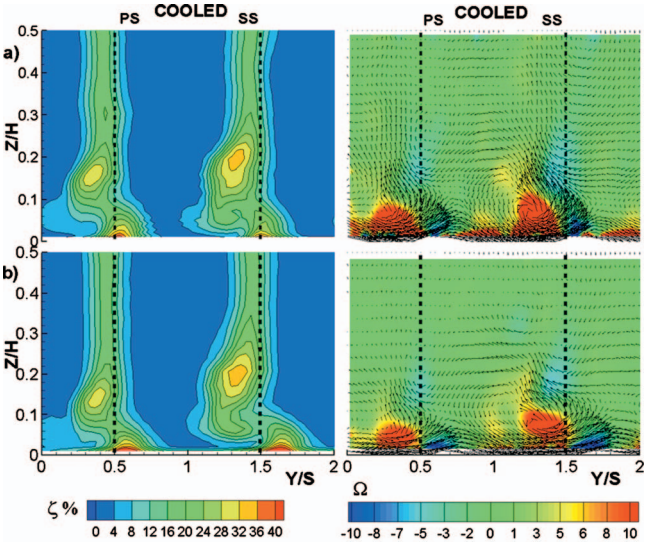

Fig. 7 Secondary kinetic energy loss coefficient (primary), vorticity and velocity vectors: MFR=0.5%: (*a*) CONF2, (*b*) CONF3

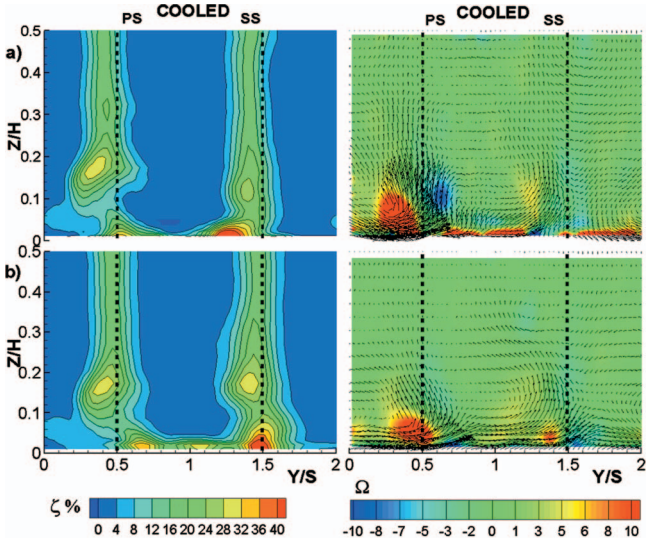

Fig. 9 Secondary kinetic energy loss coefficient (primary), vorticity, and velocity vectors: MFR=2.5%: (*a*) CONF2 and (*b*) CONF3

and 2.5%). The data obtained for the uncooled end wall and for CONF2 are also reported for comparison.

For low coolant injection rates, i.e., MFR=0.5% (Fig. 10(*a*)), the CONF3 deviation angle distribution shows larger values than the uncooled and CONF2 ones. The overturning angle rises to 8 deg at the wall (against 6 deg for the others), while the underturning angle reaches ~2 deg against ~1 deg of all the others. The spanwise extent of the region affected by secondary flows is also larger for CONF3, occupying ~36% of the span.

For MFR of 2.5%, the underturning disappears for CONF2, but not for CONF3, for which it is as large as 1 deg. The CONF3 overturning is only slightly reduced at the wall with respect to the uncooled case (5 deg against 6 deg), but the most distinguishing feature is that for CONF3 the deviation angle still varies over most of the span of the vane (36%). This means that, for all injection rates, the flow exiting the vane is less uniform along the span, with a detrimental effect on the incidence angle on the following blade. The beneficial effect on secondary flow deviation angle due to coolant injection found for CONF3 is smaller. This is likely to be due to the reduced coolant momentum caused by the larger losses at hole exists. Thus, CONF2 will be a better geometry from the downstream rotor point of view.

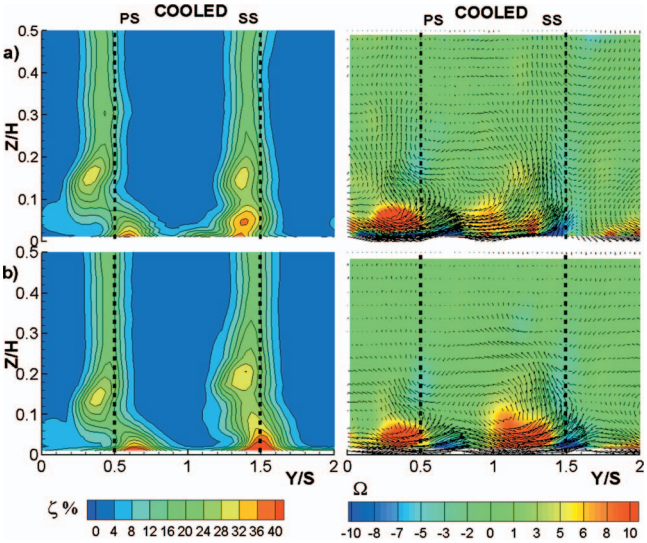

Fig. 8 Secondary kinetic energy loss coefficient (primary), vorticity and velocity vectors: MFR=1.5%: (*a*) CONF2, (*b*) CONF3

Mass-Averaged Results. In order to quantify the effect of coolant injection on the cascade aerodynamic performance, overall energy loss coefficients have been estimated by mass averaging the flow data all over the vane half passage. Following Kost and Holmes [18], two different energy loss coefficients were computed: the so-called primary and thermodynamic loss coefficients [10]. It is well known that the primary loss coefficient may give misleading results because it neglects the coolant flow energy. The thermodynamic loss coefficient takes into account the energy related to the injected flow, but it also includes losses inside the cooling holes.

The secondary loss is obtained by subtracting the pitchwise averaged loss at midspan from the total loss. Figure 11 presents both primary and thermodynamic secondary losses for the tested injection conditions and the two geometries, plotted against the overall coolant to mainstream mass flow ratio MFR.

CONF3 and CONF2 show similar trends; with the primary loss definition, the secondary loss progressively reduces, with increasing the injection conditions, as a result of the attenuation of secondary vortical structures. The thermodynamic loss strongly rises at high MFR values, due to the increased mass flow and the progressive augmentation of losses inside of the cooling holes. CONF3 secondary losses result to be always higher than the CONF2 ones, whatever loss coefficient definition is concerned. Moreover, while an almost constant minimum loss condition was found for CONF2 up to MFR=1%, CONF3 presents losses continuously increasing. The higher loss level for the larger area ratio case may be explained by the lower energy of the injected coolant flow and by a larger loss due to the mixing in the near hole exit region.

One additional test was run for both geometries with all holes externally closed, to quantify the disturbance induced by the discontinuity given by the hole exits on the end-wall surface. Secondary losses resulted to be larger than for the uncooled case (2.2% against 1.55%), but practically they are on the same level for both configurations.

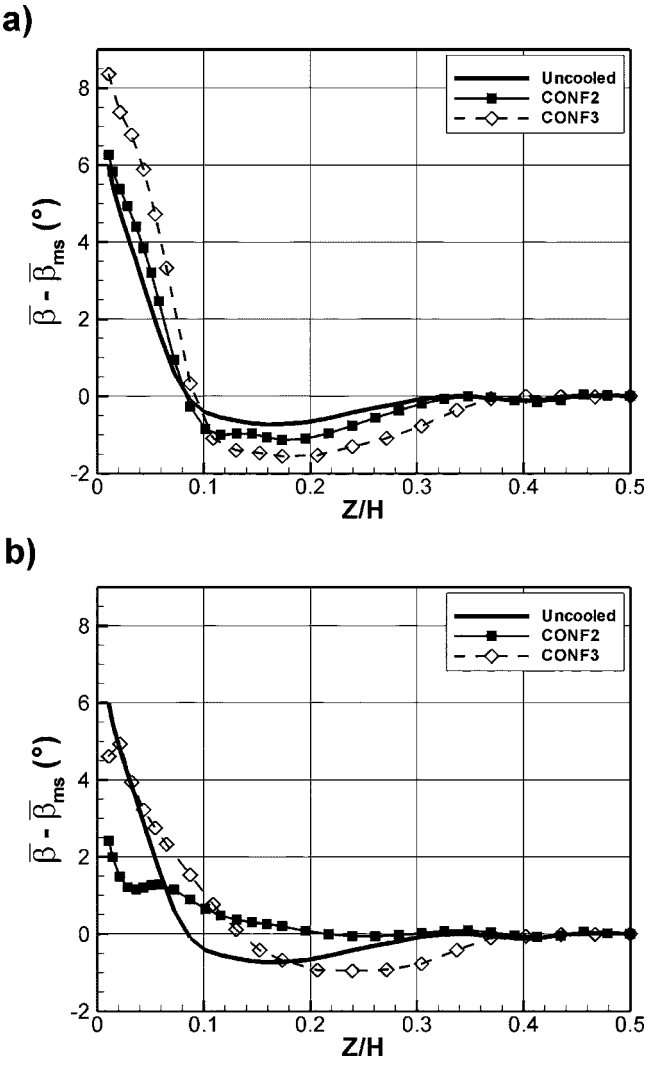

Fig. 10 Spanwise flow angle deviation: (*a*) MFR=0.5% and (*b*) MFR=2.5%

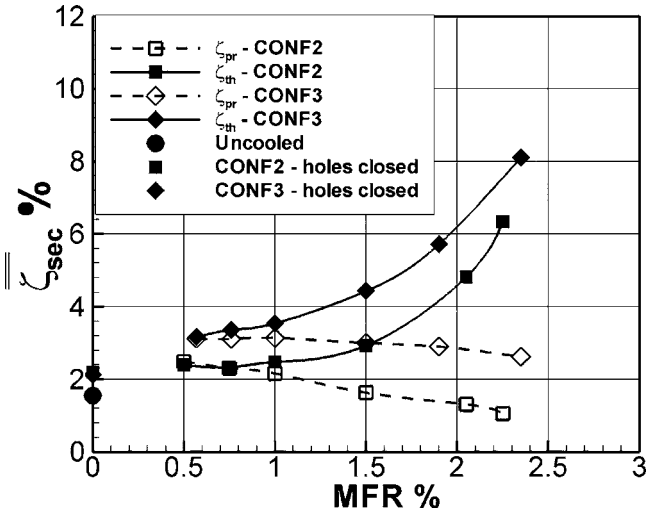

Fig. 11 Mass-averaged primary and thermodynamic secondary energy loss coefficients versus MFR

Adiabatic Effectiveness Results

In order to compare the thermal performance of different cooling geometries, the adiabatic effectiveness distributions have been determined for all the injection conditions. In general, good film-cooling performances can be reached if the jets remain attached to the wall, without penetrating the main flow. The jets should have a high enough mass flow rate to cover a large area, and a low turbulent mixing to avoid dilution by the mainstream. It has been shown that the use of expanded exits is a way to achieve these features [12–14]).

Figure 12 shows the adiabatic effectiveness η distributions for the two fan-shaped geometries and for five of the tested MFR values. Superimposed to the lower MFR value is the separation line determined for the uncooled case.

The adiabatic effectiveness distribution strongly depends on the coolant to mainstream relative momentum and, at the low injection rates, also on the secondary flow structure. Looking at the CONF2 plots for MFR=0.5% (Fig. 12(*a*)), the jets close to the leading edge are suddenly captured by the horseshoe vortex legs, leaving the leading-edge region practically uncooled. The coolant injected upstream of the separation line is moved by the passage cross-flow toward the suction side. Downstream of the separation line, two zones can be identified. Close to the pressure side, the jets follow the potential flow direction; moving toward the middle of the passage, the jets are entrained by the passage vortex and suddenly moved toward the suction side. Increasing the MFR up to 1.5%, the coolant jet momentum progressively grows, giving rise to jets that better resist to the secondary cross-flow. The jet traces persist further downstream, almost maintaining the potential flow direction all over the end wall. This confirms the suppression of the passage vortex, as found in the aerodynamic analysis. The optimum end-wall protection condition is obtained for MFR=1.5%. For larger injection rates, the jets momentum becomes too high, giving rise to jet liftoff phenomena downstream of the first two rows. This results in a worsening of the coolant thermal protection capabilities.

Comparing the two fan-shaped geometries at constant MFR, one can observe that, because of the increased hole exit area, the jet momentum is lower for CONF3 than for CONF2. The wider expanded exit of CONF3 end wall allows a better lateral spreading of the coolant flow; this takes place, in particular, for MFR up to 1.0%. But because of the increased turbulent mixing in the near-hole exit region, the jet decay in downstream direction becomes faster. This behavior is clearly shown in Fig. 13, where the η distributions measured at a fixed axial position just downstream of row A ($X/c_{ax}=2\%$), for the two cooling geometries are compared. The data refer to the MFR=1% case. Looking at the middle of the passage (between $Y/s=0.3$ and 0.6), where the influence of stagnation region disappears and the jet traces can be easily identified, CONF3 shows a smoother η distribution. Larger η can be found between the holes, resulting from the improved lateral spreading; lower η instead characterizes the mid jet traces, due to the increased mixing.

Generally speaking, the dependence of the CONF3 adiabatic effectiveness distribution on the injected mass flow rate is similar to the one shown by CONF2: at the small MFR, the jets are captured by the secondary flows, resulting in a poor η distribution. Raising the MFR, the jet momentum increases, allowing the jet to resist to the passage vortex cross-flow and resulting in an improved coolant performance. Increasing the MFR even more, the jet momentum becomes too high, worsening the end-wall thermal protection.

Looking in more detail at the low injection conditions (MFR =0.5–1.5 %), the CONF3 jet trajectories are more influenced by the secondary cross-flow. Significant jet deflection can still be found at MFR=1.5% all over the end wall. The jet traces are wider pitchwise, but they quickly decay in the axial direction. CONF3 allows a more uniform protection in tangential direction downstream of row A, even if on a lower η level. In a similar way

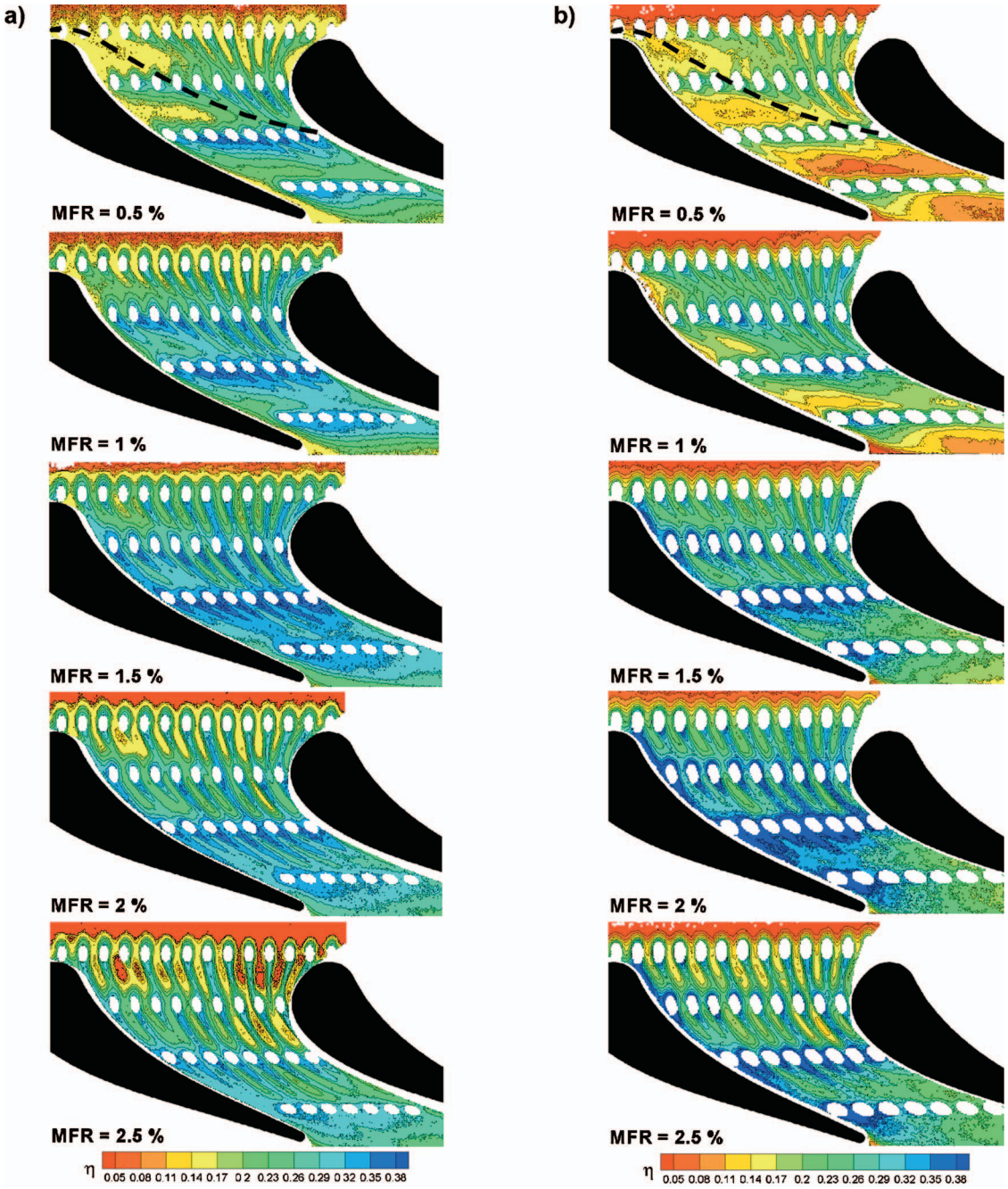

Fig. 12 η **distributions for selected MFR values: (*a*) CONF2 and (*b*) CONF3**

as for CONF2, raising the injection rate, row B jets appear to tend progressively toward the potential flow direction. Rows C and D coolant flow is instead much more influenced by the secondary cross-flow; the jets are suddenly moved toward the suction side.

The best end-wall protection is reached for an MFR of 2%. For this injection condition, the third row performs better than all the others, and also better than in the CONF2 best condition (MFR =1.5%), showing η values ~0.4 just downstream of the holes. The increased mixing again fasten the jet decay in the downstream direction. The traces of the jets coming out of the first two rows look like the potential flow streamlines at midspan. The same cannot be said for the last two rows: here a pitch wise variation of the η distribution is still evident. This means that the complete suppression of the passage vortex effects at the end wall (as found for the CONF2 case) is not achieved for CONF3, confirming the aerodynamic results. Moreover, downstream of row D the jets cannot be identified anymore. This is probably related to the large mixing taking place at the hole exit section.

Increasing the MFR value up to 2.5%, the thermal performance start to reduce: a jet liftoff takes place on the first two rows, row C also reduces its performance, while the last row (row D) still shows a good protection capability.

Averaged Results. Pitchwise-averaged values were computed for each axial position. The hole region and the zone extending approximately 4D upstream, where conduction effects are relevant, have been excluded. Figure 14 reports the pitch averaged η distributions for the two tested geometries. As a general feature, one can observe that there is a more pronounced influence of MFR for the high area ratio case.

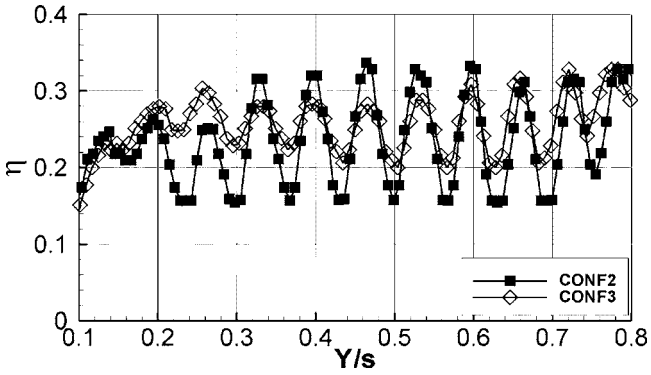

Fig. 13 Pitchwise η distribution downstream of row A: MFR =1%, X/c_{ax}=2%

Comparing the $\bar{\eta}$ distributions downstream of row A, it is evident that CONF3 leads to a good end-wall protection only for the high injection conditions (MFR$\geq$2%). The best performance is obtained at MFR=2%, with averaged values as large as 0.26; it is approximately the same level found in the best CONF2 case (MFR=1.5%). Downstream of the following row (row B) CONF3 shows slightly lower $\bar{\eta}$ values (as large as 0.28) for the optimum MFR of 2%. The passage vortex cross-flow and the increased mixing are responsible for the quick decay in axial direction downstream of rows B to D. Just downstream of row C, $\bar{\eta}$ has values as large as 0.39 for the best injection condition: it is larger than the one reached by CONF2 (0.37 at MFR=1.5%), but its decay is more evident. Downstream of the last injection row (row D), the surface protection for CONF3 progressively rises with increasing the MFR, without reaching an optimum condition.

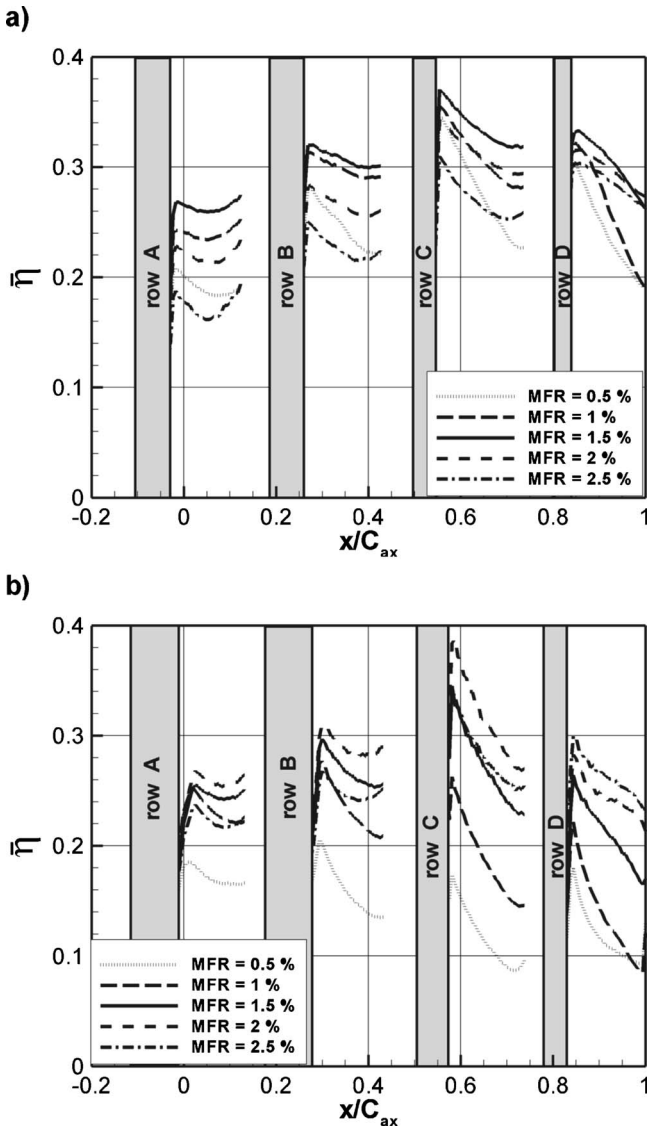

Fig. 14 Pitch-averaged adiabatic effectiveness distributions at different MFR: (*a*) CONF2 and (*b*) CONF3

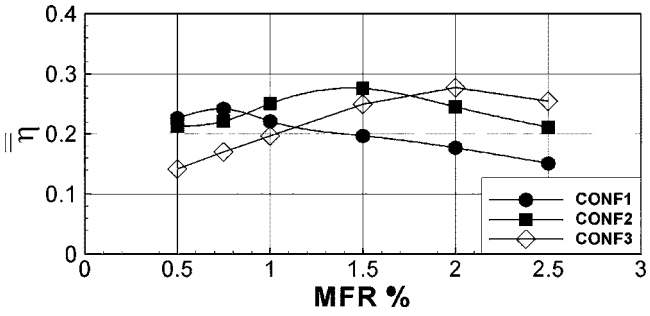

Fig. 15 Axial- and pitch-averaged adiabatic effectiveness distributions versus MFR

Averaging all the effectiveness values also in axial direction, a single global value for the adiabatic effectiveness $\bar{\bar{\eta}}$ was computed (Fig. 15). This value gives an idea of the global capability of the cooling scheme to protect the whole end-wall surface. CONF1 (cylindrical holes) results are also reported for comparison. It can be observed that CONF3 gives a better cooling protection only at high MFR, but also in such a condition the gain is limited. In particular, the maximum value for both fan shaped geometries is the same. For MFR values lower than 1.5%, the increase of area ratio is detrimental, as the cooling performance reduces with respect to the cylindrical hole case.

Conclusions

From the presented results, the following conclusions can be drawn:

- The increase of the area ratio caused a rise of thermodynamic secondary losses. This is related to a lower reduction of the secondary flow effects, also producing larger deviation angles along the span.
- The discharge coefficients analysis showed that no significant pressure recovery takes place in the fan-shaped sections; thus, the advantage of adopting a more expanded exit area resulted to be limited to a better coolant lateral spreading.
- The CONF2 end wall provides the optimum film-cooling coverage for MFR=1.5%, whereas the larger area ratio geometry presents the optimum for a greater MFR value of 2%. Comparing the two optimal overall film-cooling effectiveness conditions, both showed an average maximum effectiveness of 0.29.

Nomenclature

AR = exit to inlet hole area ratio
B = hole spacing
$\mathrm{BR}=(\rho_c U_c)/(\rho_\infty U_\infty)$ = local blowing rate
c = vane chord
C_d = discharge coefficient
D = hole diameter
H = vane height
L = hole length

m = mass flow rate
Ma = Mach number
$M_1 = \sqrt{p_{t,c} - p_1 / p_{t,1} - p_1}$ = Inlet loss-free blowing ratio
$\mathrm{MFR} = m_c / m_\infty$ = overall coolant to mainstream mass flow ratio
$\mathrm{Re}_{2is} = U_{2is} c / \nu$ = Isentropic outlet Reynolds number
s = vane pitch
T = temperature
$\mathrm{Tu} = \sqrt{0.5(\overline{u'^2} + \overline{v'^2})} / U_1$ = turbulence intensity,%
$U = \sqrt{u^2 + v^2 + w^2}$ = local mean velocity
u, v, w = streamwise, transverse and spanwise velocity components
X, Y, Z = cascade coordinate system
α = injection angle
β = flow angle (tangential direction)
γ = expansion angle
$\eta = (T_{aw} - T_\infty) / (T_c - T_\infty)$ = film-cooling adiabatic effectiveness
ν = kinetic viscosity
ρ = flow density
$\zeta = (U_{2is}^2 - U_2^2) / \bar{U}_{2is,ms}^2$ = local energy loss coefficient
Ω = vorticity

Subscripts

1 = inlet
2 = exit
a = adiabatic
c = cooling flow
is = isentropic condition
ms = at midspan
pr = primary
th = thermodynamic
∞ = freestream
w = local wall condition

Overbars

$\bar{}$ = time averaged, pitch averaged
$=$ = mass averaged
$'$ = rms

References

[1] Blair, M. F., 1974, "An Experimental Study of Heat Transfer and Film Cooling on Large-Scale Turbine Endwalls," ASME J. Heat Transfer, **96**, pp. 524–529.
[2] Sieverding, C. H., and Wilputte, Ph., 1981, "Influence of Mach Number and End Wall Cooling on Secondary Flows in a Straight Nozzle Cascade," ASME J. Eng. Power, **103**, pp. 257–264.
[3] Friedrichs, S., Hodson, H. P., and Dawes, W. N., 1996, "Distribution of Film-Cooling Effectiveness on a Turbine Endwall Measured With the Ammonia and Diazo Technique," ASME J. Turbomach., **118**, pp. 613–621.
[4] Friedrichs, S., Hodson, H. P., and Dawes, W. N., 1997, "Aerodynamic Aspects of Endwall Film-Cooling," ASME J. Turbomach., **119**, pp. 786–793.
[5] Friedrichs, S., Hodson, H. P., and Dawes, W. N., 1999, "The Design of an Improved Endwall Film-Cooling Configuration," ASME J. Turbomach., **121**, pp. 772–780.
[6] Kost, F., and Nicklas, M., 2001, "Film-Cooled Turbine Endwall in a Transonic Flow Field—Part I: Aero-dynamic Measurements," ASME Paper No. 2001-GT-0145.
[7] Nicklas, M., 2001, "Film-Cooled Turbine Endwall in a Transonic Flow Field—Part II: Heat Transfer and Film-Cooling Effectiveness," ASME Paper No. 2001-GT-0146.
[8] Knost, D. G., and Thole, K. A., 2004, "Adiabatic Effectiveness Measurements of Endwall Film-Cooling for a First Stage Vane," ASME Paper No. GT-2004-53326.
[9] Barigozzi, G., Benzoni, G., Franchini, G., and Perdichizzi, A., 2005, "Aerodynamic Measurement Over a Film Cooled Nozzle Vane Endwall," *Proc. of 6th European Conference on Turbomachinery Fluid Dynamics and Thermodynamics*, Vol. II, G. Bois, C. Sieverding, M. Manna, and T. Arts, eds., Lille, France, pp. 791–801.
[10] Barigozzi, G., Benzoni, G., Franchini, G., and Perdichizzi, A., 2005, "Fan-shaped Hole Effects on the Aero-Thermal Performance of a Film Cooled Endwall," ASME Paper No. GT2005–68544.
[11] Goldstein, R., Eckert, E., and Burggraf, F., 1974, "Effects of Hole Geometry and Density on Three-Dimensional Film Cooling," Int. J. Heat Mass Transfer, **17**, pp. 595–606.
[12] Thole, K., Gritsch, M., Schulz, A., and Wittig, S., 1996, "Flowfield Measurements for Film-Cooling Holes With Expanded Exits," ASME Paper No. 96-GT-174.
[13] Gritsch, M., Schulz, A., and Wittig, S., 1997, "Adiabatic Wall Effectiveness Measurements of Film-Cooling Holes With Expanded Exits," ASME Paper No. 97-GT-164.
[14] Gritsch, M., Schulz, A., and Wittig, S., 1998, "Heat Transfer Coefficient Measurements of Film-Cooling Holes With Expanded Exits," ASME Paper No. 98-GT-28.
[15] Gritsch, M., Schulz, A., and Wittig, S., 1997, "Discharge Coefficient Measurements of Film-Cooling Holes with Expanded Exits," ASME Paper No. 97-GT-165.
[16] Camci, C., Kim, K., and Hippensteele, S. A., 1992, "A New Hue Capturing Technique for the Quantitative Interpretation of Liquid Crystal Images Used in Convective Heat Transfer Studies," ASME J. Turbomach., **114**, pp. 765–775.
[17] Gregory-Smith, D. G., Graves, C. P., and Walsh, J. A., 1988, "Growth of Secondary Losses and Vorticity in an Axial Turbine Cascade," ASME J. Turbomach., **110**, pp. 1–8.
[18] Kost, F. H., and Holmes, A. T., 1985, "Aerodynamic Effect of Coolant Ejection in the Rear Part of Transonic Rotor Blades," *AGARD CP 390 "Heat Transfer and Cooling in Gas Turbines,"* Bergen (Norway), May 1985.

Modeling of Film Cooling—Part II: Model for Use in Three-Dimensional Computational Fluid Dynamics

André Burdet

Reza S. Abhari

Martin G. Rose

Turbomachinery Laboratory,
Department of Mechanical and Process Engineering,
Swiss Federal Institute of Technology – ETH Zürich,
CH-8092 Zürich, Switzerland

*Computational fluid dynamics (CFD) has recently been used for the simulation of the aerothermodynamics of film cooling. The direct calculation of a single cooling hole requires substantial computational resources. A parametric study, for the optimization of the cooling system in real engines, is much too time consuming due to the large number of grid nodes required to cover all injection holes and plenum chambers. For these reasons, a hybrid approach is proposed, based on the modeling of the near film-cooling hole flow, tuned using experimental data, while computing directly the flow field in the blade-to-blade passage. A new injection film-cooling model is established, which can be embedded in a CFD code, to lower the central processing unit (CPU) cost and to reduce the simulation turnover time. The goal is to be able to simulate film-cooled turbine blades without having to explicitly mesh inside the holes and the plenum chamber. The stability, low CPU overhead level (1%) and accuracy of the proposed CFD-embedded film-cooling model are demonstrated in the ETHZ steady film-cooled flat-plate experiment presented in Part I (Bernsdorf, Rose, and Abhari, 2006, ASME J. Turbomach., **128**, pp. 141–149) of this two-part paper. The prediction of film-cooling effectiveness using the CFD-embedded model is evaluated.* [DOI: 10.1115/1.2437219]

Introduction

Increasing the specific work and cycle efficiency of gas turbines is a major issue in modern energy conversion technology. This is dictated by economical and environmental considerations and can be achieved by increasing turbine inlet temperature. However, maintaining reasonable blade lives at high thermal loading requires an efficient cooling mechanism for the blades. One of the most frequently used techniques for external cooling is full-coverage film cooling, in which coolant air is injected through rows of shaped holes drilled on the turbine blade leading edge, pressure, and suction sides. In some situations, more than 300 cooling holes per blade can be used in order to ensure an efficient cooling. However, increasing cycle efficiency is counterbalanced by the losses induced by the cooling system, namely, the mass flow deficit at high enthalpy (fluid extracted from the compressor), and aerodynamic and mixing losses due to the jet-mainstream flow interaction. The designer therefore has to carefully balance the aerothermodynamics of the flow through the high-pressure turbine blade passages to maximize the turbine efficiency. This means that, to perform a good aerothermodynamic optimization, a parametric study has to be carried out. The designer needs, therefore, a design tool that is computationally efficient to shrink the turnover time so that design costs are accurate enough to ensure a useful final result. In this context, CFD becomes a powerful tool to help the design and optimization of film-cooled high-pressure turbine blades. However, the accurate prediction of such flows faces several severe drawbacks inherent to the complexity of flow structures that appear.

The jet-in-crossflow phenomenon is a multiscale problem, by nature, in time and space. The coolant jet gradually mixes with the freestream at a characteristic length scale of the hole diameter. In contrast to this, the aerodynamics of the passage, e.g., passage vortex, contains much larger length scales. These scales may differ by up to two orders of magnitude. Therefore, a relevant numerical simulation must be made with a mesh that allows at least the prediction of the important fluid structures of the smallest geometric scale, namely, the hole diameter. Many authors have shown that the accurate prediction of film-cooling effectiveness necessitates meshing inside the holes with a large number of grid nodes. The first numerical simulations of a coolant jet issuing from a hole drilled in a flat plate has been carried out by specifying the velocity at the hole exit location [1,2]. It was found that for a blowing ratio higher than 0.5, the result was strongly sensitive to the very complex velocity field that occurs at hole exit. To solve this issue, it has been suggested to explore alternative approaches, including extending the computational domain inside the hole and plenum chamber. In addition, the numerical simulations were performed with grid densities up to $N_x=15$, $N_y=7$ grid nodes per hole diameter. Based on results obtained, it has been recommended that the grid spacing should need to be more refined to accurately resolve the jet bending in the near-hole region. This is to ultimately ensure a good prediction of the downstream film-cooling effectiveness. The next numerical studies [3–5] presented full three-dimensional (3D) Reynolds-averaged Navier-Stokes (RANS) computations where the plenum chamber, coolant hole, and cross-flow region were modeled. In general, the mesh contained about 15 grid nodes per hole diameter near the hole exit plane, having in total from 2×10^5 to 7×10^5 grid nodes. It was systematically observed that the coolant flow inside the hole pipe is already complex and has a strong influence of the downstream evolution of the coolant fluid. In addition, the near hole flow structure is a function of many variables, such as the density and blowing ratio, the hole length and injection angle. The prediction of film-cooling effectiveness using a two-layer model did not show any gain of accuracy compared to wall function, except in the near hole region [4]. However, the introduction of an anisotropic term, to promote lateral turbulent diffusion, is found to bring a significant improvement for the prediction of film-cooling

Contributed by the International Gas Turbine Institute of ASME for publication in the JOURNAL OF TURBOMACHINERY. Manuscript received May 23, 2006; final manuscript received May 29, 2006. Review conducted by David Wisler. Paper presented at the ASME Turbo Expo 2005: Land, Sea and Air (GT2005), Reno, NV, June 6–9, 2005. Paper No. GT2006-68780.

effectiveness [5]. Surface heat transfer coefficient on film-cooled turbine blades has recently been numerically investigated using RANS code. These studies covered meshes starting at hole exit for the midspan region only [6] and for the full cascade [7] to a computational grid that includes the coolant plenum and hole in the midspan region only [8]. The grid size was of order 1.2×10^6 cells for the latter and 2.25×10^6 grid nodes for a transonic rotor blade fully modeled, with coolant velocity and temperature specified at wall. It was found that even with a proper imposition of hole exit coolant flow conditions, the discrepancy in predicting heat transfer can be as high as 60% on the suction side [6]. For useful prediction on the pressure surface, unsteady pressure fluctuation must be taken into account since it modulates the blowing ratio over a broad range [7]. The advantage of taking into account the plenum chamber and hole are still unclear.

The meshing of the film-cooling hole and plenum is a major strategic decision. A balance has to be struck between accuracy, on the one hand, and grid complexity and size and run time on the other. In particular, with hundreds of holes used in some turbine components, grids of hundreds of millions nodes may be required. To face this challenge, various authors proposed the application of film-cooling models within CFD.

Several jet-injection models were developed for two-dimensional viscous codes [9–14] using different strategies. They generally include an injection plane after hole exit, alleviating the problem to solve the jet bending. Coolant fluxes are either derived from a momentum and energy balance [9–11] or specified using a source term approach [14] or based on semi-empirical results and observations [12,13]. For moderate blowing ratio ($BR < 1.0$), prediction of centerline film-cooling effectiveness are, in general, fairly good. However, high blowing-ratio results were not entirely satisfactory. Few attempts were made to include a fully three-dimensional model within a RANS code. Dalhander et al. [15] proposed a 3D box source term approach, but the flow structures have not been revealed and the film-cooling effectiveness predictions show significant deviation from the measurements.

In this paper, a jet injection model is presented that deals with film cooling in a three-dimensional flow environment. The model is developed for a RANS-based CFD solver. The model, which reproduces the aerodynamic and associated temperature field after hole exit, is calibrated using PIV data obtained in the ETHZ film-cooled flat plate introduced by and described in Bernsdorf et al. [16], which is Part I of this paper. The numerical implementation issues are then discussed. The CFD-embedded film-cooling model performance, in terms of stability, CPU overhead, and grid independency, are quantified. A separate steady film-cooled flat-plate experiment [17] is eventually used to verify the capability of the CFD-embedded film-cooling model to predict film-cooling effectiveness, in an isotropic turbulence model context.

Film Cooling Model

Hypothesis and Main Variables. The near-hole region and its main geometrical parameters that drive the coolant jet behavior, is sketched in Fig. 1. The jet in cross-flow phenomenon can produce a broad range of flow structures downstream of the injection site, depending on the geometrical arrangement, as well as on the difference of flow properties between the incoming freestream and the coolant fluid (quantified by the density ratio (DR), blowing ratio, and momentum flux ratio (IR)). The validation of the proposed model covers cylindrical holes and a blowing ratio below 3.0. Long holes are assumed, i.e., the length of the hole is much higher than its diameter. Approaches will be added in future to relax this current restriction. The modeling approach is to experimentally anchor the near-hole mixing, which has been shown by many researchers to be very difficult to resolve. The model is simplified to a level that is resolved in RANS computation. The resultant flow field is injected into the CFD algorithm after the hole exit, in the so-called plane of injection, as shown in Fig. 1. Therefore, the model will only be applied in the near-hole downstream region, at a two-dimensional cross plane.

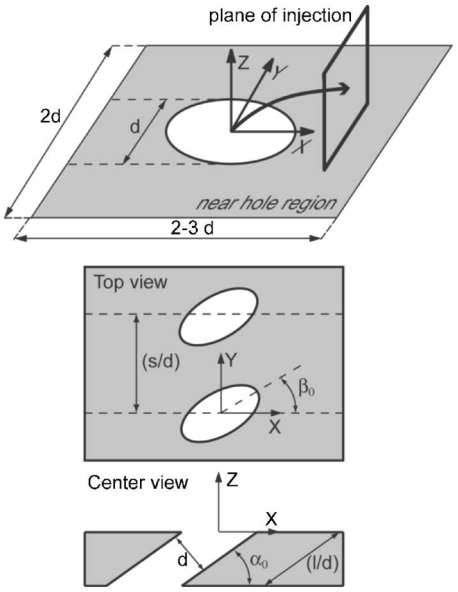

Fig. 1 Schematic of the near-hole region, with the jet intrinsic frame of reference (χ, ξ, η) on the plane of injection (top) and main geometrical parameters (bottom)

Structure of the Model. The jet flow behavior in the immediate vicinity of the hole exit is highly three-dimensional and contains flow features that are of primary importance for the downstream convection and diffusion of the coolant fluid with the freestream flow (see Ref. [18]). In Fig. 2, one can see the macroflow features near the hole that are relevant for a RANS-based film-cooling model. Between the hole exit and the plane of injection, the coolant jet bends due to the inertial force of the freestream. Furthermore, it starts to mix with the freestream, on a length scale that is much smaller than the hole diameter. The trajectory of the jet is the primary flow feature that affects the coolant fluid behavior. A high-momentum flux ratio can cause the coolant flow to penetrate through the boundary layer flow (i.e., "lift off"), dramatically lowering the cooling effectiveness. On the other hand, a low-momentum flux ratio allows the coolant fluid to

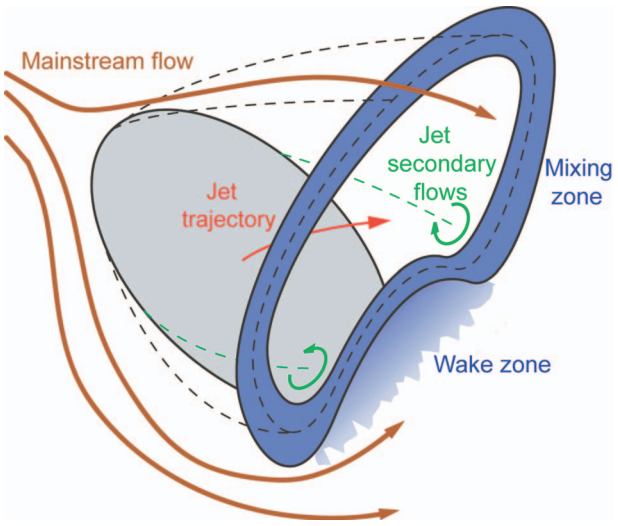

Fig. 2 Schematic of the near-hole macroflow features

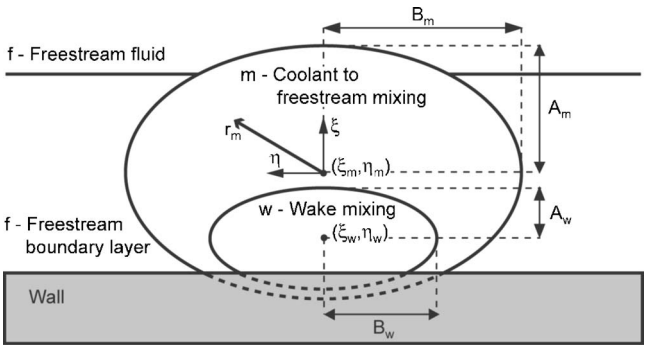

Fig. 3 Schematic of the jet mixing zones just after the injection site (cross section)

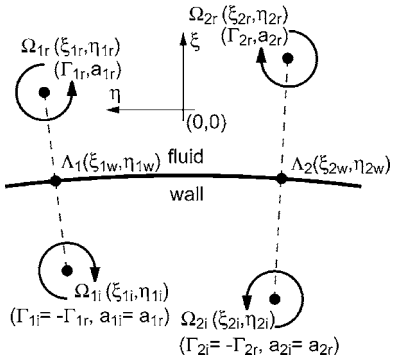

Fig. 4 Schematic of the image vortex procedure to determine the coolant jet secondary flow velocity vector

stick to the wall, but at a very low mass flow level. Even at a moderate momentum flux ratio, it is observed that a wake zone is forming very quickly downstream of the hole trailing edge, in the lower part of the jet. This lowers the penetration velocity of the coolant fluid located near the wall, allowing the freestream fluid to penetrate more easily underneath the core of the jet. Moreover, the vorticity ring coming out of the hole (from the jet boundary layer) bends and squeezes, forming the well-known counterrotating pair of vortices.

Jet Trajectory. The coolant jet penetration is computed using a trajectory model for circular jet developed by Abramovich [19] (see the Appendix). It is given by

$$\left(\frac{Z}{d}\right) = \sqrt{39k_1}\ln\left[\frac{10+\left(\frac{X}{d}\right)+\sqrt{\left(\frac{X}{d}\right)^2+20\left(\frac{X}{d}\right)+7k_1\cot^2\alpha_0}}{10+\sqrt{7k_1}\cot\alpha_0}\right] \tag{1}$$

where

$$k_1 = \frac{\pi \mathrm{IR}\sin\alpha_0}{4C_n} \tag{2}$$

C_n is the pressure force coefficient of the external flow. This coefficient can vary as a function of the distance between two holes (s/d), the streamwise angle of injection α_0, and the momentum flux ratio IR.

Jet Mixing. The coolant fluid mixing with the freestream can be divided in several zones as described in Fig. 3. There are two main mixing zones. The first one, denoted by m, is between the coolant c and the freestream f fluid. The second one, denoted by w, is located in the wake zone. When reconstructing the overall flow field on the plane of injection, one needs to know what the shape of the mixing is between these zones. The principle of superposition is used to link them together. For any flow quantity ϕ, we have

$$\phi = (\varepsilon^\phi + \Delta\varepsilon^\phi)\phi_c + (1-\varepsilon^\phi)\phi_f \tag{3}$$

where ε^ϕ is the mixing function between the coolant c and freestream f fluid and $\Delta\varepsilon^\phi$ is the wake deficit function on the lee side of the jet. The mixing function ε^ϕ varies from 0 to 1, whereas the wake deficit function is free, depending on the wake intensity. The shape of the coolant to freestream m and wake w mixing zones is modeled with an ellipse whose axes $(A_{m,w}, B_{m,w})$ are set as model coefficients. Therefore, for any local position (ξ, η) in the plane of modeling, the selected mixing zone (m or w) local radius $r_{m,w}$ is given by

$$r_{m,w} = \sqrt{\left[\frac{(\xi-\xi^0_{m,w})}{A_{m,w}}\right]^2+\left[\frac{(\eta-\eta^0_{m,w})}{B_{m,w}}\right]^2-1} \tag{4}$$

where $(\xi^0_{m,w}, \eta^0_{m,w})$ is the selected zone center, given by the jet trajectory model. For the thermodynamic quantities, namely, the total temperature and density, it has been shown by many researchers (see, for example, Ref. [19]) that the mixing zone can be well described using a hyperbolic function such as the following:

$$\varepsilon^T = 0.5\left[1+\left(\frac{\tanh[C^T(2r_m-1)]}{\tanh(C^T)}\right)\right] \tag{5}$$

where C^T is a model coefficient. For the jet-penetration velocity, the mixing function takes the form of a power law,

$$\varepsilon^U = [1-C^U(r_m)^{3/2}]^2 \tag{6}$$

where C^U is set so that when radius $r_m=1$, we have the highest rate of mixing. The wake-deficit function also takes the shape of a power law. The wake intensity I_w is changing as a function of the momentum flux ratio and the angle of injection,

$$\Delta\varepsilon^k = I_w[1-C_w(r_w)^{3/2}]^2 \tag{7}$$

Jet Secondary Flow. The jet secondary flow comes from the counterrotating vortex pair. It is modeled using an image vortex procedure as depicted in Fig. 4. The positions of the vortices $(\Omega_{jr}, j=1,2)$ are model coefficients. The position of the image vortices (Ω_{ji}) is computed as follows:

$$\Omega_{ji}(\xi_{ji},\eta_{ji}) = -\Omega_{jr}(\xi_{jr},\eta_{jr}) + 2\Lambda_j(\xi_{jw},\eta_{jw}) \tag{8}$$

where Λ_j is the location of the wall point that is nearest to vortex Ω_{jr}. The vortices are assumed to be of an Oseen-type [20]. That is the tangential velocity magnitude U^θ_l due to any vortex l ($l=1r$, $2r, 1i, 2i$):

$$U^\theta_l(\xi,\eta) = \frac{\Gamma_l}{2\pi r_l}\left[1-\exp\left(-\frac{r_l^2}{a_l^2}\right)\right] \tag{9}$$

where Γ_l and a_l are the circulation and core radius of vortex l, respectively. The vortex core radius a_l is equal to $2\sqrt{\nu t}$, ν being the kinematic viscosity and t the time existence of the vortex l. The radius r_l is given by

$$r_l = \sqrt{(\xi-\xi_l)^2+(\eta-\eta_l)^2} \tag{10}$$

The resulting two components of the velocity in the $\xi\eta$ plane are found by summing all the velocity components given for each vortex,

$$U_\xi(\xi,\eta) = \sum_{l=1r}^{2i} U^\theta_l(\xi,\eta)\left(\frac{\eta_l-\eta}{r_l}\right)$$

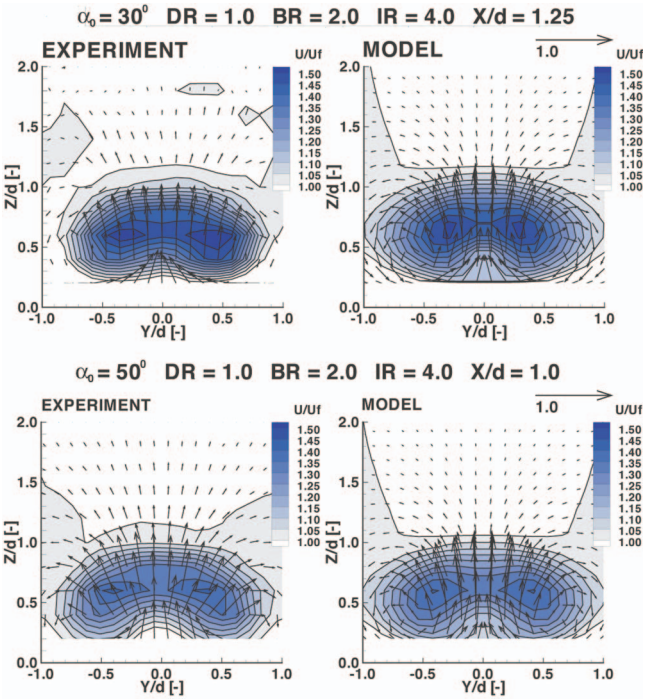

Fig. 5 Velocity field, comparison between experiment [16] and model for α_0=30 deg and 50 deg. The cross sections are located at X/d= +1.25 and +1.0 downstream of the hole center for α_0=30 deg and 50 deg respectively.

$$U_\eta(\xi,\eta) = \sum_{l=1r}^{2i} U_l^\theta(\xi,\eta)\left(\frac{\xi-\xi_l}{r_l}\right) \tag{11}$$

Derivation of Coolant and Freestream Flow. A power-law type of profile is assumed to reconstruct the freestream flow. The streamwise velocity, total temperature, and boundary layer thickness are known from the upstream flow conditions. The user gives the coolant total temperature and total pressure as input. The coolant mass flow has to be known to determine the density and blowing ratio, as well as the coolant velocity. To find it, the ideal coolant mass flow is first computed by assuming an isentropic expansion of the coolant through the hole. The near-hole static pressure is evaluated from the freestream static pressure level. Then, to get the real coolant mass flow, the ideal mass flow is scaled by the hole discharge coefficient inferred from empirical correlation from Gritsch et al. [21], for holes inclined at a streamwise angle of 30 deg. This correlation will be extended in our future activities.

Model Calibration and Evaluation

Three-Dimensional Velocity Field. The model coefficients describing the velocity field have been tuned using the film-cooled flat-plate PIV data of Bernsdorf et al. [16] (which gives more details). The model has been calibrated such as it reproduces accurately the three-dimensional velocity field at the plane of injection. Typically, the plane of injection is located in a cross section just after the hole trailing edge. All the density ratios ($1.0<\mathrm{DR}<1.6$), blowing ratios ($1.0<\mathrm{BR}<2.7$), and streamwise injection angles (α_0=30 deg and 50 deg) that have been experimentally investigated, have been studied. After an intensive tuning process, it has been found that the model coefficients are primarily a function of the momentum flux ratio. Thus, functional dependences of the model coefficients on the streamwise injection angle and momentum flux ratio have been derived. In Fig. 5, comparisons of the three-dimensional velocity field obtained with the PIV measurements and with the calibrated model are shown. This is displayed for two streamwise angles α_0, 30 deg and 50 deg, for the flow regime DR=1.0 and BR=2.0. Similar results have been obtained for the other flow regimes. It is first observed that the kidney shape of the jet is well reproduced by the calibrated model for these two streamwise injection angles. The calibration ensures that the streamwise velocity peaks are in close agreement in terms of spatial location ($\Delta Y/d<5.2\%, \Delta Z/d<3.1\%$) and magnitude ($\Delta U/U_f<1.3\%$) Furthermore, the lateral and vertical extent of the jet zone is well reproduced (e.g., for the contour U/U_f=1.25, $Y_{\max}/d=\pm0.71$ and ±0.69, $Z_{\max}/d=+0.96$ and $+0.88$ for α_0 =30 deg and 50 deg, respectively). Thus, an accurate specification of the jet penetration is ensured. In fact, this is an important result since the jet penetration adjusts the spatial location on the injection plane of all the other important flow features, such as the counterrotating pair of vortices and the thermal mixing region. It also determines the rate of the downstream convection that will occur. The PIV data have been used to assess the location and circulation of the vortices. A precise specification of the two counterrotating vortices strength and location is needed: they are the key factor that set the entrainment rate of the freestream flow underneath the jet, which adversely impacts on the film-cooling effectiveness.

Thermal Field Associated With the Velocity Field. The model coefficients are tuned to allow the reconstruction of the thermal field associated with the velocity field. In order to proceed, the film-cooled flat-plate experiment of Rydholm [22] is utilized, where the velocity and thermal fields are provided at different downstream cross sections. The test rig consists of a closed-loop, recirculating wind tunnel. From a secondary flow loop, cool air is injected into the hot mainstream through a row of five holes, each of them having a length of 8.0 hole diameters. A pitch distance of 3.0 hole diameters separates them. Each hole has a diameter of 5 mm, and a streamwise injection angle α_0 of 30 deg. Four measurement series were carried out for different density and blowing ratios. In each series, the test-rig pressure was at atmospheric level; with a freestream velocity of 47.4 m/s. Velocity measurements were made with a laser-doppler anemometer (LDA). The uncertainties can be estimated equal to 0.5 m/s for U and V and 1 m/s for W. The total temperature was measured by an iron/constantan thermocouple, whose global uncertainty is 0.5°C. A comparison of the velocity and thermal field obtained in the measurements and using the calibrated model is displayed in Fig. 6. This is shown for a density ratio of 1.17 and a blowing ratio of 1.35. The cross section is located at X/d=+1.0 downstream of the hole center. From a global point of view, the film-cooling model is shown to be capable of reproducing the main aerothermodynamics flow features happening just after the hole exit. The model coefficients that set the velocity field are known from the previous tuning resultobtained with the ETHZ film-cooled flat plate. The same conclusions apply here for the velocity field as the previous case. Model coefficients that set the thermal mixing are derived from the observation of the normalized total temperature field θ, plotted in the bottom of Fig. 6.

As shown, the calibrated film-cooling model is also capable of matching the thermal field found in the experimental measurements. In observing the contour θ=0.15, the jet core thermal zone, in the model, is only 7% too high vertically, but is 23% too narrow. However, in the lower zone (around Y/d=0.0, Z/d=+0.1) the normalized total temperature contour is about the same in the experiment than in the model ($0.25<\theta<0.30$). This result shows that the model offers a reasonably accurate specification of the total temperature at the plane of injection, near the wall. This is needed in order to ultimately get a good prediction of film-cooling effectiveness and/or wall heat transfer.

In summary, the model parameters have been anchored to detailed and accurate three-dimensional experimental data. The jet

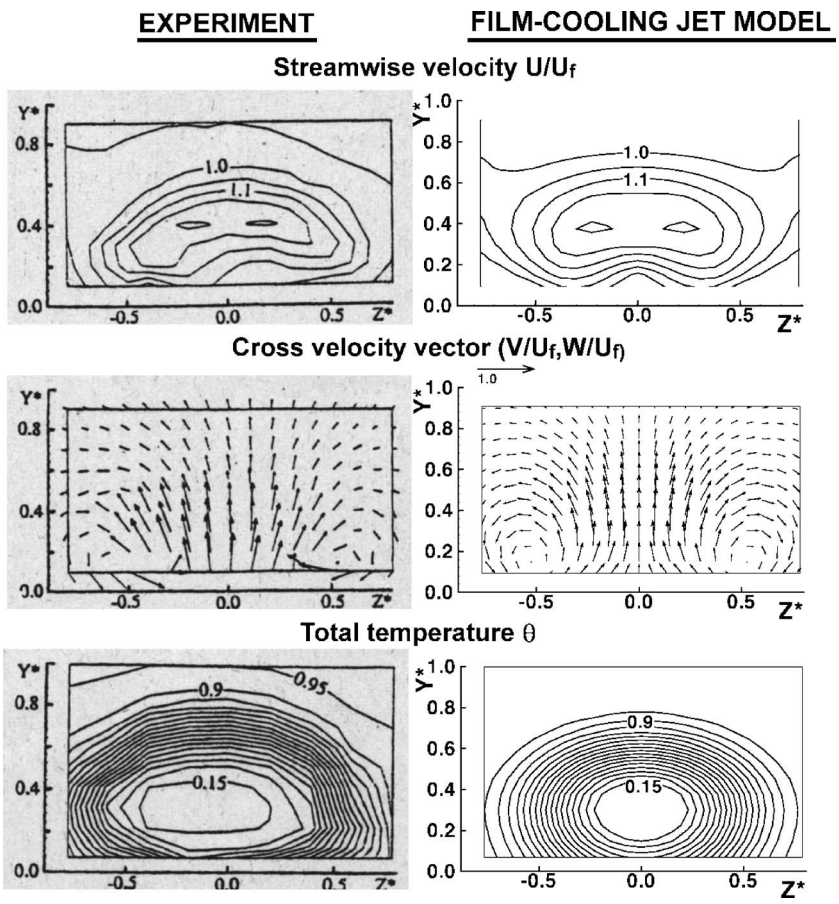

Fig. 6 Velocity and temperature field, comparison between the experiment [22] and model in the cross section located at $X/d=+1.0$ downstream of the hole center: DR=1.17 and BR=1.35. In this plot, Z^* is Y/d and Y^* is Z/d.

coolant flow model accurately reproduces the velocity and thermal field of a film-cooling jet just downstream of the hole exit.

Numerical Implementation of the Model and Computing Performance

Numerical Method. The CFD code used in this study, MULTI3, is based on solving the unsteady compressible RANS equations. The solution method is based on an explicit, finite-volume, node-based, Ni-Lax-Wendroff time-marching algorithm developed by Ni [23]. The technique was extended to 3D unstructured meshes and to viscous flows by Burdet and Lakehal [24]. The finite-volume formulation uses a central cell vertex variable location. To prevent high-frequency oscillations and capture shock waves, a combined second- and fourth-order numerical smoothing is added, which is consistent with the second-order accuracy in both space and time of the scheme. The eddy viscosity is determined with the help of the zero-equation Baldwin-Lomax turbulence model used in its low-Reynolds form. Several validation examples of the code used to predict flows in compressor and turbines can be found in Burdet and Lakehal [24] and Burdet et al. [25].

Jet Blockage Model. The model, as it stands, can only be used for the downstream evolution of the flow and does not give boundary conditions for the upstream region. The blockage effect in the incoming freestream boundary layer due to the presence of the coolant jet is of a primary importance because the potential field created adjusts the static pressure in the near-hole region. Furthermore, pressure waves (wakes, jets, etc.) incoming to the hole exit modulate the near-hole static pressure. As shown by Abhari and Epstein [26], this is a very important feature to determine the blowing-ratio level as well as the change in blade loading. In order to solve this issue, the numerical implementation of the model includes a three-dimensional boundary surface, which represents the jet core. The jet three-dimensional blockage is modeled between the hole exit and the plane of injection, as shown in Fig. 7. In fact, it has been hypothesized in the description of the structure of the model that the shear layer between the coolant and freestream in the near-hole exit region is thin. Therefore, in this region, the jet-to-freestream limit can be represented by a surface. This method should be independent of the mesh and CFD code used.

Immersed Boundary Condition. To implement this blockage model, the implicit immersed boundary method, based on the

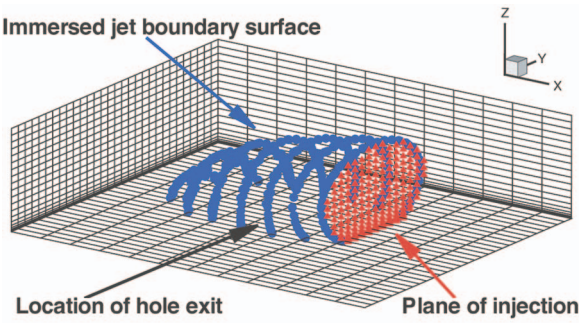

Fig. 7 Example of the near-hole coolant jet boundary surface immersed in the computational mesh

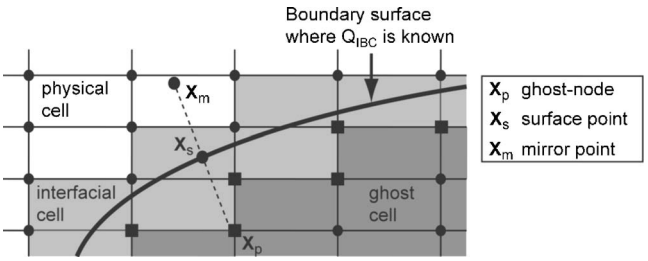

Fig. 8 Computational stencil used for the implicit immersed boundary method

work of Tseng and Ferziger [27], is used. The strategy is to locally immerse the jet boundary surface in the computational mesh. In detail, flow values are set at some particular grid nodes, so-called ghost-nodes $\boldsymbol{X}_p$, that are located at the vertices of cells crossed by the embedded jet surface (interfacial cells) (see Fig. 8). The state vector $\boldsymbol{Q}_p$ at ghostnode $\boldsymbol{X}_p$ is set such as the immersed boundary condition $\boldsymbol{Q}_{\mathrm{IBC}}$ at its corresponding surface point $\boldsymbol{X}_s$ is fulfilled. The immersed boundary condition $\boldsymbol{Q}_{\mathrm{IBC}}$ represents the effect of the jet surface on the surrounding flow. To extrapolate $\boldsymbol{Q}_p$, the knowledge of the near-jet surface flow field is needed, that is at the mirror point $\boldsymbol{X}_m$. The state vector $\boldsymbol{Q}_m$ at the mirror point $\boldsymbol{X}_m$ is found using an interpolation function based on an inverse distance weighting. For a Dirichlet boundary condition $\boldsymbol{Q}_{\mathrm{IBC}}$, $\boldsymbol{Q}_p$ is given by

$$\boldsymbol{Q}_p = (1+\lambda)\boldsymbol{Q}_{\mathrm{IBC}} - \lambda \boldsymbol{Q}_m \tag{12}$$

where λ is set equal to 2 by default. A von Neumann immersed boundary condition $\boldsymbol{Q}_{\mathrm{IBC}}$ gives

$$\boldsymbol{Q}_p = \lambda \boldsymbol{Q}_m - (1+\lambda)\boldsymbol{Q}_{\mathrm{IBC}}|X_s - X_p| \tag{13}$$

A good representative surface of the jet boundary to be included in the mesh needs to be specified. A toroidal surface has been chosen, since it gives a highly flexible and relevant representation of the jet shape in-between the hole exit and the plane of injection. A slip boundary condition is imposed at the jet boundary surface, allowing the freestream fluid to slide on it. Furthermore, an isothermal boundary condition is specified at the jet surface, the averaged temperature between the freestream and coolant ones being the specified temperature [28].

Benchmark Computational Domain. The ETHZ film-cooled flat-plate experiment of Bernsdorf et al. [16] has been selected as the benchmark test case to quantify the computing performance, in terms of stability, CPU overhead, and grid independency of the film-cooling model used in a CFD code. Twenty different grids were built up; the grid was refined more and more in the streamwise and lateral direction. The different grid densities used, per hole diameter, are $N_x=[1,3,5,9,13]$ and $N_y=[3,5,9,13]$. The computational domain, in terms of hole diameter, extended axially from −14.0 to +27.0, laterally from −2.0 to +2.0, and vertically from 0.0 to +5.0 hole diameter. A periodic boundary condition was specified at the lateral sides, no-slip boundary condition on the bottom wall, and slip boundary condition on the upper wall; to save CPU time, it was assumed that the flow at $Z/d=+5.0$ is almost unidirectional. A value of Y^+ between 1 and 2 has been ensured. There are 51 grid nodes in the vertical direction with about 15 grid nodes in the boundary layer. Inlet boundary layer characteristics were provided and can be found in Bernsdorf et al. [16]. All coolant flow regimes studied in [16] were tested.

Stability, CPU Overhead and Grid Independency. The computation of the flow with the CFD-embedded film-cooling model converged for every grid and coolant flow regime tested; residuals were $<10^{-5}$ and stable. The rate of convergence was almost identical when computing with and without the presence of a cooling jet. Therefore, the immersed boundary condition strategy chosen to represent the near-hole jet surface is shown to be very robust, for all the grid sizes tested. The CPU overhead for the case $\alpha_0=30$ deg and BR=2.0 has been investigated to verify that the CFD-embedded film-cooling model does not slow down dramatically the computing turnover time. The CPU overhead σ is defined as

$$\sigma = 100\left[\frac{\Delta t_{\mathrm{fcm}} - \Delta t_{\mathrm{ref}}}{\Delta t_{\mathrm{ref}}}\right] \tag{14}$$

where Δt_{ref} and Δt_{fcm} are the CPU time to iterate once the whole CFD solver algorithm computing the flow field in the channel with and without a coolant jet, respectively. The CPU time has been averaged over 100 iterations chosen randomly in the convergence history. For the coarsest grid levels, namely, N_x, $N_y \leq 3$, it has been found that $\sigma=8\%$. Beyond this grid density level, σ is dropping very quickly down to 2% for N_x, $N_y=5$ and then stabilize at 1% for N_x, $N_y \geq 9$. In order to evaluate the issue of grid independency, the evolution of the counterrotating vortex pair was observed for the different grid densities aforementioned. In all coolant flow regimes, it was observed that the trajectory of the vortices and their strength evolution downstream of the injection site were much too quickly diffused for grid densities of $N_x \leq 3$ and $N_y \leq 5$. Furthermore, beyond a grid density of $N_x=5$ and $N_y=9$, the aerodynamic flow pattern did not significantly change. In conclusion, a proper use of the CFD-embedded film-cooling model can be achieved at a grid level of $N_x \cong 5$, $N_y \cong 9$, without slowing down significantly the computational time, since the CPU overhead is 1% at this grid density. As discussed in the Introduction, this type of grid density is the minimum to perform a relevant computation of a coolant jet when meshing the plenum chamber and hole pipe. Thus, from a designer point of view, the use of the proposed CFD-embedded film-cooling model is affordable.

CFD-Embedded Film-Cooling Model Performance: 3D Aerothermal Flow Field

Three-Dimensional Jet Aerodynamics Prediction. The ETHZ film-cooled flat plate is used to evaluate and quantify the performance of the CFD-embedded film-cooling model to predict the three-dimensional jet aerodynamics. Four flow cases, with a streamwise injection angle of 30 deg and 50 deg, a density ratio of 1.0 and blowing ratio of 1.0 and 2.0 are selected here. The error in mass flow and energy conservation has first been checked for all the computed flow cases. The predicted (actual) coolant mass flow and energy injected at the plane of injection has been compared to the real one. This local mass flow and energy error was $<1\%$ for the refined grids ($N_x, N_y \geq 5$). Global error of the mass flow and energy was $<0.8\%$ for all computations. The presented CFD results are taken from computations carried out on a grid density level of $N_x=5$ and $N_y=9$. To give insight into the effect of the immersed jet surface on the near-hole flow field, the three-dimensional flow field is plotted in Fig. 9 for the case $\alpha_0=50$ deg, DR=1.0, and BR=2.0. The streamlines show the lateral and vertical deflection of the freestream fluid particles near the hole exit, demonstrating the right numerical treatment to immerse the jet surface. Just after the plane of injection, located at $X/d=+1.0$, it is clearly observed that the streamlines are joining back in the jet center revealing the three-dimensional entrainment of the freestream fluid due to the counterrotating vortex pair. Further downstream, the freestream fluid particles are convected inside the jet and start slowly to diverge. As it can be seen in three different cross planes ($X/d=+2.0$, +7.0, and +12.0), the streamwise vorticity ω_x^*, normalized by inlet freestream velocity and hole diameter, represents the downstream evolution and decay of the vortices. On the flat plate, the normalized static pressure change relative to freestream static pressure (ΔP_s) is depicted. The increase of static pressure just upstream of the hole exit is found by

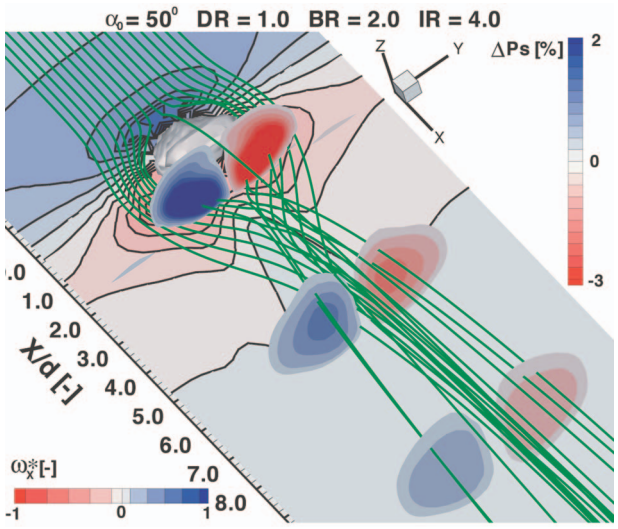

Fig. 9 Numerical prediction, using the film-cooling model, of the flow field near the hole exit. Contours of normalized static pressure ΔP_s are represented on the flat plate ($Z/d=0.0$). Normalized streamwise vorticity ω_x^* is shown at three different cross sections ($X/d=+2.0$, $+7.0$, and $+12.0$). The freestream streamlines are represented in dark green.

the numerical prediction, which confirms the blockage effect created by the locally embedded jet surface. Also, in a close inspection near the injection plane, one can see the low level of relative static pressure due to the flow deviation and the low momentum wake zone.

Near-Hole Static Pressure: Model Versus Full Computation. In order to validate the near-hole static pressure field, a companion numerical calculation has also been carried out for a single hole on a flat plate. The plenum chamber and hole were gridded, leading to about 5.5×10^5 grid nodes in total. This *full computation* has been made with the commercial software CFX 5.7 from ANSYS, Inc. The k-ω SST turbulence model has been selected to compute the eddy viscosity. The solution was processed on one CPU Intel Pentium 4, 2.8 GHz. Convergence was obtained (residuals $<10^{-4}$) in 13 hr CPU time. In comparison, convergence with the film-cooling model is obtained in ~2 hr CPU time to reach the same residuals level; the use of the proposed model is then about 6.5 times faster than a full computation. As is illustrated in Fig. 10, the near-hole static pressure field predicted in the full computation is found to be fairly similar with the model. The upstream high-pressure zone ($\Delta P_{s,\max}=+2.1\%$) is very similar in both results. In the downstream low-pressure zone, some discrepancies are observed. The minimum relative static pressure from using the model ($\Delta P_{s,\min}=-4.9\%$) is a bit higher than in the full computation ($\Delta P_s=-6.1\%$ at the same location). Note that between the hole trailing edge ($X/d=+0.65$) and plane of injection ($X/d=+1.0$), no conclusion is made since the immersed jet surface covers the region. This numerical back-to-back comparison implies that the shape chosen to simulate the near-hole jet boundary surface and the associated immersed boundary condition treatment seems to be able to create a near-hole static pressure field that is relevant. This is an important result because the near-hole static pressure modulates the blowing ratio [26].

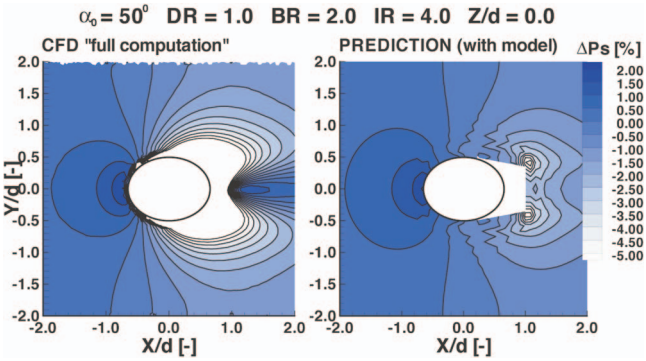

Fig. 10 Comparison of numerical predictions of the near-hole normalized static pressure ΔP_s

Jet Penetration and Spreading. In Fig. 11, contours of predicted normalized streamwise velocity, superimposed with freestream streamlines, are compared to experimental measurements in the center plane ($Y/d=0.0$). The streamlines exhibit the freestream flow deviation and also the rapid turning of the jet. As already noted by Bernsdorf et al. [16], the streamwise injection angle seems to play a minor role in the jet trajectory. In contrast, the blowing ratio is much more important in affecting the coolant jet path. It typically penetrates 50% more vertically in the BR $=2.0$ case, compared to the BR$=1.0$ case, at $X/d=+6.0$. This feature is well captured by the CFD prediction using the embedded film-cooling model. The windward side (velocity overshoot) is clearly seen in the high blowing-ratio case (BR$=2.0$). The computation predicts this phenomenon with high accuracy, but this is to be expected because the model has been carefully tuned to the experiment. Interestingly, the maximum streamwise velocity just after the plane of injection is higher in the $\alpha_0=30$ deg case ($U_{\max}/U_f=1.47$) than in the $\alpha_0=50$ deg case ($U_{\max}/U_f=1.36$); this might be because the jet has originally more streamwise momentum when emerging from the hole exit. As the coolant fluid flows downstream, it is moving away from the wall, forming a wake region of low streamwise velocity. In a close inspection of the streamwise velocity contours in this region, the velocity deficit is overpredicted, in the $\alpha_0=30$ deg case, by 30% on average for BR$=1.0$ and by 19% on average for BR$=2.0$. In the $\alpha_0=50$ deg case, this zone is better captured in the computation, although there is a small overprediction of 8% on average for the velocity deficit.

To better understand the formation of this wake zone, in Fig. 12 contours of normalized streamwise velocity are plotted, superimposed with the secondary flow vectors in the cross section $X/d=+4.0$. In the $\alpha_0=30$ deg case, although the spreading of the wake zone is well predicted, it is confirmed that the velocity deficit is too pronounced, for both blowing ratios. In observing the secondary flow vectors, the position of the vortices center are found to be insensitive of the streamwise injection angle but of the blowing ratio, in which the CFD prediction gives a satisfactory answer. However, numerical results end up constantly overpredicting the lateral spreading between center of the vortices by 15% to 30%.

Vorticity Field. It is clear that the counterrotating vortices help to lift the near-wall low-momentum fluid away from the wall. Although the position of the vortices is about the same in both angle cases for same blowing ratio, this vortical structure seems to play a much stronger role in the $\alpha_0=50$ deg case. Thus, the evolution of the strength of the vortices should impact on the formation of the wake zone. In order to focus on this issue, Fig. 13 shows the normalized streamwise ω_x^* and normal ω_z^* vorticity, at a plane $Z/d=+0.4$ for the two angles studied and BR$=2.0$. Agreement is also found between measured and predicted vorticity values, which verify the model. The two branches (of opposite sign) of the counterrotating vortex pair are seen in the streamwise vorticity plot (structure **A**). The four central legs in the vertical vorticity plot exhibit the downwash and upwash shearing sides of the two vortices (structure **E**). Furthermore, on the lateral sides of the

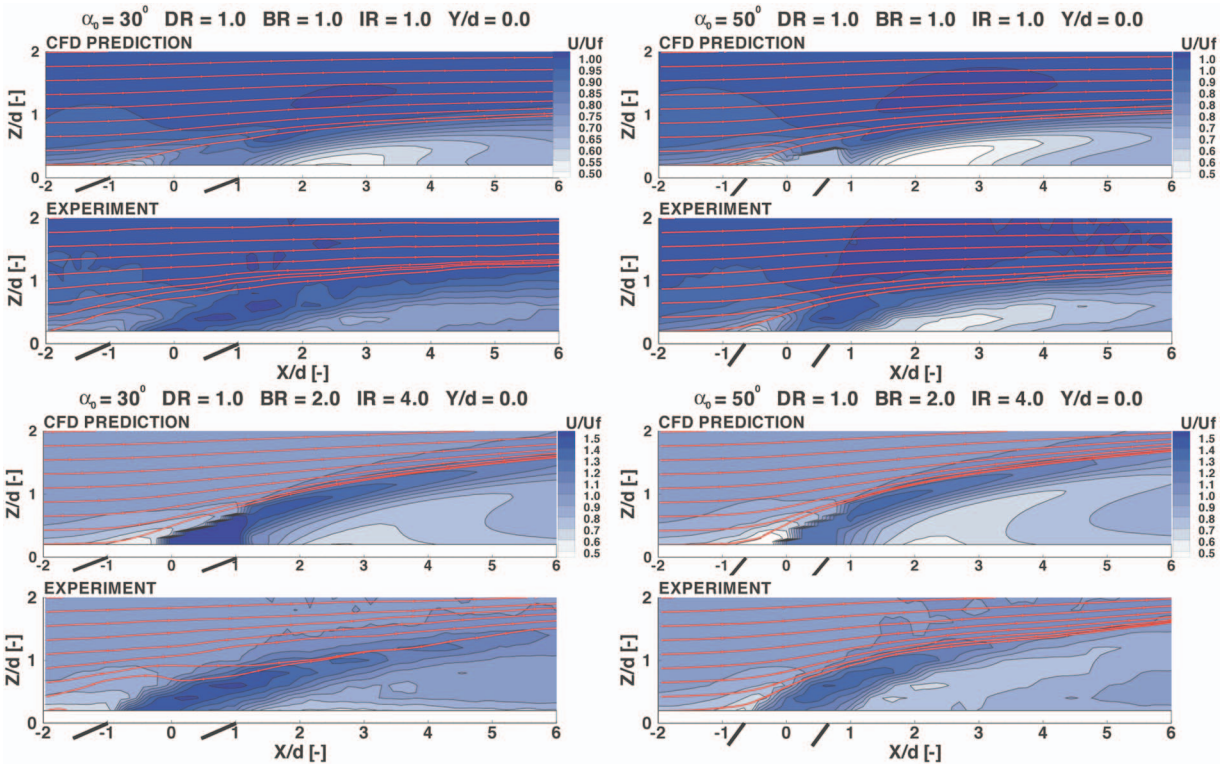

Fig. 11 Contours of normalized streamwise velocity (U/U_f), superimposed with freestream streamlines, in the center plane Y/d=0.0, found in the experimental measurements [16] and in the CFD prediction using the film-cooling model

counterrotating pair, a trace of vorticity of opposite sign can be distinguished in the experiment and is also reproduced in the computation (structure **C**). This might indicate a presence of a horseshoe vortex but no formal conclusion can be drawn from these plots.

In looking more closely at the strength evolution of the vortices, the streamwise vorticity is decaying more rapidly in the α_0 =30 deg case than what is found in the CFD prediction. In the α_0=50 deg case, the decay is shown to be of the same order. This

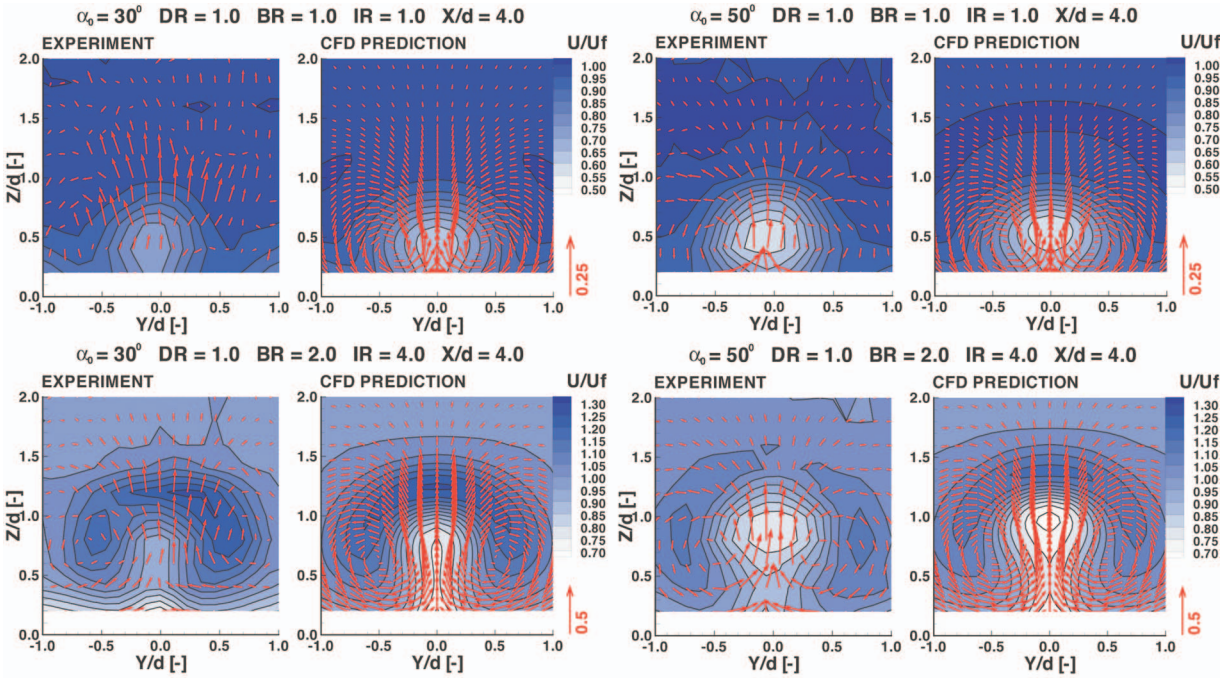

Fig. 12 Contours of normalized streamwise velocity (U/U_f), superimposed with secondary flow vectors (V/U_f, W/U_f), in the cross section X/d= +4.0, found in experimental measurements [16] and in CFD prediction using the film-cooling model

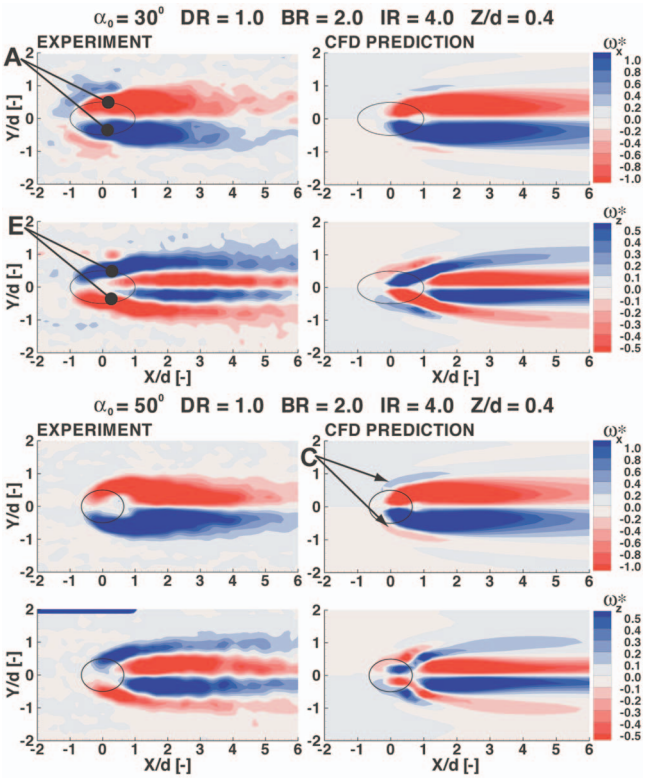

Fig. 13 Contours of normalized streamwise ω_x^* and normal ω_z^* vorticity in the cross section $Z/d=+0.4$; comparison between the experiment [16] (left) and CFD prediction using the film-cooling model (right)

feature is constantly observed in the other Z/d plane. To quantify this effect, in Fig. 14 the profile of the normalized absolute vorticity ω^* is plotted. Two streamwise location are represented, one just after the plane of injection and the second one at $X/d=+4.0$. The distribution of absolute vorticity exhibits a notable difference between the experiment and the CFD prediction just after the plane of injection. Indeed, the absolute vorticity profile is much more flattened in the experiment than what is found in the computation ($\Delta\omega^*$ from peak maxima to local central minima is ~140% overpredicted). This can be explained by the fact that the counterrotating vortex pair model does not account for any downward freestream momentum push and/or any particular lateral spreading. In observing the downstream evolution of the absolute vorticity profile, at $X/d=+4.0$, its distribution is well captured in the $\alpha_0=50$ deg case. In the $\alpha_0=30$ deg case, it is experimentally observed to have almost spread out completely. In this case, the

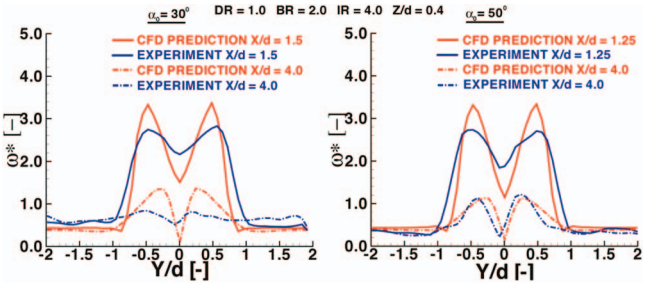

Fig. 14 Lateral profile of normalized absolute vorticity ω, comparison between experiment [16] and CFD prediction (using the film-cooling model) for $\alpha_0=30$ deg (left) and $\alpha_0=50$ deg (right), at $Z/d=+0.4$

discrepancy in predicted maximum ω^* is~60% too high (this fact is also observed in other Z/d plane, not shown here). It has been experimentally shown [29] that isotropic turbulence is not true anymore in this region. Although no definitive statement can be drawn from the present data, there is a presumption that the strength of the vortices is even more reduced by the enhanced turbulent stress in the lateral direction. This feature seems to be more pronounced in the low streamwise injection angle case. Furthermore, it has been observed [5] that isotropic turbulence models are not adequate to treat the near-wall region in this type of turbomachinery flows; the turbulent fluxes, which counteract against the entrainment effect of the vortices, are not promoted enough. This might explain the fact that the CFD predictions in this study are underestimating the decay of the near-wall absolute vorticity and also the spreading of the vortices. In return, the velocity deficit in the wake zone is overpredicted.

Film-Cooling Effectiveness Prediction. The ultimate goal of the model is to provide a numerical tool for the designer that allows predicting accurately film-cooling effectiveness in reasonable time scale. In order to demonstrate the capability of the CFD-embedded model to predict film-cooling effectiveness, the University of Karlsruhe film-cooled flat-plate experiment of Saumweber et al. [17] is used as a pure validation case. Briefly, the test rig consists of a continuous flow wind tunnel. From a secondary flow loop, cool air is injected into the hot mainstream through a row of three holes, each of them having a length of 6.0 hole diameters. A pitch distance of 4.0 hole diameters separates them. Each hole has a diameter of 5 mm and a streamwise injection angle α_0 of 30 deg. A turbulence grid is placed far upstream from the holes to control freestream turbulence intensity and length scale. As the turbulence model used in this study is a zero-equation model, the results with the lowest freestream turbulence, namely 3.5%, are utilized. An infrared camera allows mapping the temperature at the flat plate surface, carefully insulated to respect quasi-adiabatic condition. Film-cooling effectiveness is inferred from the temperature mapping, with an uncertainty of ±4%. Five measurements series are available, for a fixed density ratio of 1.7 and five different blowing ratios, namely, 0.5, 0.75, 1.0, 1.25, and 1.5. Uncertainty in fixing the blowing ratio is ±2%. Density ratio uncertainty is ±1.7%. The same computational domain as the preceding one is used, with a grid density of $N_x=5$, $N_y=9$.

The predicted local wall adiabatic film-cooling effectiveness η is first compared to the experimental measurements in Fig. 15 for the lowest (BR=0.5) and highest (BR=1.5) blowing ratio investigated. The centerline effectiveness is systematically overpredicted in the computational result for the BR=0.5 case, typical value 56%. However, the prediction of the centerline effectiveness is accurate to within the experimental contour resolution in the BR=1.5 case. Furthermore, the spreading of the coolant fluid is underpredicted in the BR=0.5 case; in the CFD prediction, $\eta=0$ at $Y/d=\pm2.0$, whereas there are still traces of cooling in the experiment. In the BR=1.5 case, η is slightly underpredicted, by 11% on average. This trend of oveprediction of centerline effectiveness and underprediction of lateral spreading of the coolant is in line with previous numerical studies on film cooling using an isotropic turbulence model [4,5]. The previous comments made on the inaccurate prediction of the evolution of the counterrotating vortex pair might help to shed light on these results. The near-wall central pinching of the coolant fluid might be predicted too pronounced. Also its lateral turbulent diffusion is not adequately promoted.

The comparison between experimental measurements and CFD prediction of the laterally averaged adiabatic film-cooling effectiveness $\overline{\eta}$ (η averaged over one pitch) is plotted in Fig. 16. For the lowest blowing ratio case (BR=0.5), the overestimated centerline effectiveness tends to compensate for the lack of lateral spreading, giving a reasonable prediction of $\overline{\eta}$. The numerical results for blowing ratios from 0.75 to 1.25 are also displayed but

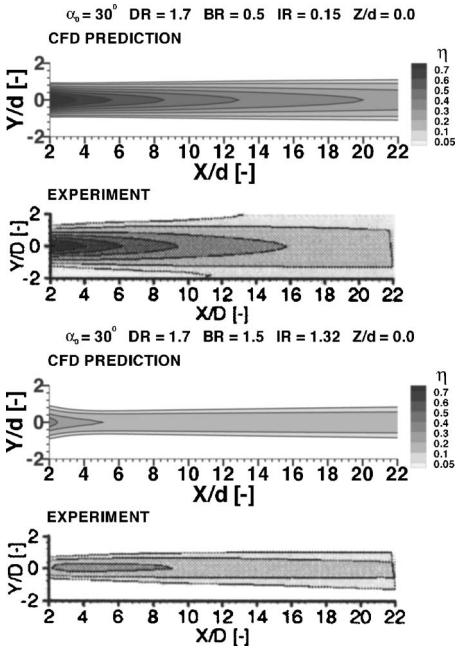

Fig. 15 Predicted and measured [17] local wall adiabatic film-cooling effectiveness η for BR=0.5 (top) and BR=1.5 (bottom)

not compared to the experiment (no data available). The predicted level of $\overline{\eta}$ decreases with increasing blowing ratio. It is remarkable to observe that the slope of the $\overline{\eta}$ curve in the far downstream region is still negative for BR=0.75 but start to be slightly positive from BR=1.0. The experiment confirms that the slope of the $\overline{\eta}$ curve flattens with BR increasing. Experimental results of Saumweber et al. [17], with higher freestream turbulence intensity (not shown here), show an increase of the slope of $\overline{\eta}$ for high BR. In conclusion, even if the model gives an accurate representation of the jet aerothermal flow field at the plane of injection, its downstream evolution and diffusion is subject to complex flow phenomena, as described earlier, that are out of the scope of the model itself.

Conclusion

The following comments are made to summarize this study:

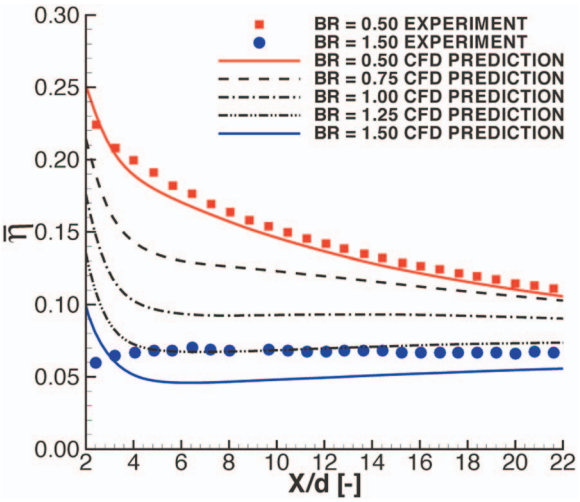

Fig. 16 Predicted and measured [17] laterally averaged wall adiabatic film-cooling effectiveness $\overline{\eta}$

- A macroflow feature-based film-cooling model is proposed, in which the jet trajectory, penetration, secondary flows, and mixing are accounted for. It is designed for use within a RANS-based CFD solver. It is only locally applied in the near-hole region. The model parameters are anchored to experimental data. The model is embedded in a CFD code using the implicit immersed boundary method.
- The CFD-embedded film-cooling model strategy has been shown to be very robust, whatever grid density of the computational mesh is. When using the model with a relevant grid density, with five or more grid nodes per hole diameter, the CPU overhead is 1%, making it affordable from a designer point of view.
- The local mass flow and energy error, at the plane of injection, is $<1\%$. Computational run time using the model is shown to be about 6.5 times faster than a full computation. For a turbine blade with holes, it is expected somewhere between one and two orders of magnitude faster computation.
- The near-hole static pressure and the three-dimensional flow structures downstream of the injection site are well captured by the numerical prediction, thanks to the accurate modeling of the near-hole coolant jet.
- Predictions of film-cooling effectiveness are in line with previous full computation numerical studies, using isotropic turbulence model.
- Improvements and testing of the film-cooling model are currently made for heat transfer and loss prediction in unsteady turbine flows.

Acknowledgment

The authors would like to acknowledge the support of this project by GE Aircraft Engines through their university strategic alliance program. Specifically, the technical interactions with Dr. Stefan Bernsdorf, Dr. Robert Bergholz, and Dr. Fred Buck have been very helpful in the formulation of this project. We also thank Claudio Christen for performing the full computation.

Nomenclature

X,Y,Z = axial (streamwise), lateral, vertical coordinate
U,V,W = mean velocity components
ρ = density
P = static pressure
T = total temperature
θ = normalized total temperature $=(T-T_c)/(T_f-T_c)$
d = hole diameter
s = pitch distance between two holes
l = length of the hole pipe
α_0 = streamwise injection angle
β_0 = lateral injection angle
ΔP = density ratio $=\rho_c/\rho_f$
BR = blowing ratio $=\rho_c U_c/\rho_f U_f$
IP = momentum flux ratio $=BR^2/DR$
A,B = ellipse axes
r = radius
ε = mixing function
$\Delta\varepsilon$ = wake deficit function
(χ,ξ,η) = jet intrinsic frame of reference
$\Omega(\xi,\eta)$ = vortex position, on the (ξ,η) plane
Γ = vortex circulation
a = vortex core radius
ω = vorticity
$\boldsymbol{Q}$ = state vector
N = grid density, per hole diameter
σ = CPU overhead
ΔP_s = normalized static pressure $=100(P-P_f)/P_f$

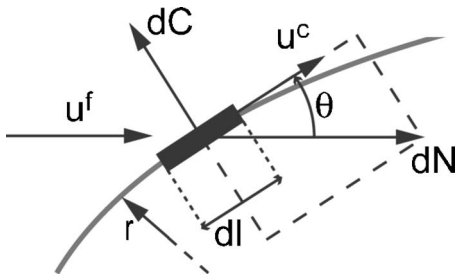

Fig. 17 Jet-solid curved cylinder analogy and forces applied to it

η = adiabatic wall film-cooling effectiveness = $(T_{\text{recovery}} - T_{\text{adiabatic wall}})/(T_{\text{recovery}} - T_c)$

Subscripts

c = coolant fluid
f = freestream fluid
m = coolant to freestream mixing zone
w = wake mixing zone

Appendix

The jet trajectory model is based on a two-dimensional analysis of the dynamical forces applying to a jet fluid element of length dl, as shown in Fig. 17. The jet is approximated as being a solid-curved cylinder. Two forces are balancing. The jet is first bent due to a force dN created by the incoming freestream flow pressure. This flow-pressure force is directed toward the freestream flow direction and is scaled by a flow-pressure resistance coefficient C_n.

$$dN = C_n \frac{\rho_f (U_f \sin \alpha)^2}{2} h dl \tag{A1}$$

where h is the width of the jet. Furthermore, as the jet is bending, a centrifugal force dC is applying. It tends pushing the jet curved axis outward of its direction of bending,

$$dC = \rho_c \frac{U_c^2}{r} S_n dl \tag{A2}$$

where r is the local radius of curvature of the jet axis. S_n represents the cross-sectional area of the jet

$$S_n \cong \frac{\pi h^2}{4} \tag{A3}$$

The forces are balancing as follows:

$$dN = -dC \tag{A4}$$

The jet cross-sectional area S_n, thus, also its width h, are in fact growing up when convecting downstream, due to the diffusion and lateral spreading of the jet. It is hypothesized that the spreading rate of the jet is constant. This means that

$$h = h_0 + c_h l \tag{A5}$$

According to its experiments, Abramovich [3] has suggested that $h_0 = 2.25d$ and $c_h = 0.22$. The streamwise trajectory Z/d can therefore by found by integrating Eq. (A4) over l.

$$\left(\frac{Z}{d}\right) = \sqrt{39k_1} \ln \left[\frac{10 + \left(\frac{X}{d}\right) + \sqrt{\left(\frac{X}{d}\right)^2 + 20\left(\frac{X}{d}\right) + 7k_1 \cot^2 \alpha_0}}{10 + \sqrt{7k_1} \cot \alpha_0} \right] \tag{A6}$$

References

[1] Bergeles, G., Gosman, A. D., and Launder, B. E., 1981, "The Prediction of Three-Dimensional Discrete-Hole Cooling Processes—Part 2," ASME J. Heat Transfer, **103**, pp. 141–145.
[2] Demuren, A. O., Rodi, W., and Schönung, B., 1986, "Systematic Study of Film Cooling With a Three-Dimensional Calculation Procedure," ASME J. Turbomach., **108**(3), pp. 124–130.
[3] Leylek, J. H., and Zerkle, R. D., 1994, "Discrete-Jet Film Cooling: A Comparison of Computational Results With Experiments," ASME J. Turbomach., **116**(3), pp. 358–368.
[4] Walters, D. K., and Leylek, J. H., 2000, "A Detailed Analysis of Film-Cooling Physics—Part I: Streamwise Injection With Cylindrical Holes," ASME J. Turbomach., **122**(1), pp. 102–112.
[5] Lakehal, D., 2002, "Near-Wall Modeling of Turbulent Convective Heat Transport in Film Cooling of Turbine Blades With the Aid of Direct Numerical Simulation Data," ASME J. Turbomach., **124**(3), pp. 485–498.
[6] Garg, V. K., and Gaugler, R. E., 1997, "Effect of Velocity and Temperature Distribution at the Hole Exit on Film Cooling of Turbine Blades," ASME J. Turbomach., **119**(2), pp. 343–445.
[7] Garg, V. K., and Abhari, R. S., 1997, "Comparison of Predicted and Experimental Nusselt Number for a Film-Cooled Rotating Blade," Int. J. Heat Fluid Flow, **18**, pp. 452–460.
[8] Heidmann, J. D., Rigby, D. L., and Ameri, A. A., 2000, "A Three-Dimensional Coupled Internal/External Simulation of a Film-Cooled Turbine Vane," ASME J. Turbomach., **122**(2), pp. 348–359.
[9] Crawford, M. E., Kays, W. M., and Moffat, R. J., 1976, "Heat Transfer to a Full Coverage Film-Cooled Surface With 30° Slant-Hole Injection," NASA Contractor Report No. CR-2786.
[10] Schönung, B., and Rodi, W., 1987, "Predictions of Film Cooling by a Row of Holes With a Two-Dimensional Boundary-Layer Procedure," ASME J. Turbomach., **109**(4), pp. 579–587.
[11] Haas, W., Rodi, W., and Schönung, B., 1992, "The Influence of Density Difference Between Hot and Coolant Gas on Film Cooling by a Row of Holes: Predictions and Experiments," ASME J. Turbomach., **114**(4), pp. 747–755.
[12] Tafti, D. K., and Yavuzkurt, S., 1990, "Prediction of Heat Transfer Characteristics for Discrete Hole Film Cooling for Turbine Blade Applications," ASME J. Turbomach., **112**(3), pp. 504–511.
[13] Abhari, R. S., 1996, "Impact of Rotor-Stator Interaction on Turbine Blade Film Cooling," ASME J. Turbomach., **118**(1), pp. 123–133.
[14] Kulisa, P., Leboeuf, F., and Perrin, G., 1992, "Computation of a Wall Boundary Layer With Discrete Jet Injections," ASME J. Turbomach., **114**(4), pp. 756–764.
[15] Dalhander, P., Abrahamsson, H., Martensson, H., and Hall, U., 1998, "Numerical Simulation of a Film Cooled Nozzle Guide Vane Using an Injection Model," ASME Paper No. 98-GT-439.
[16] Bernsdorf, S., Rose, M. G., and Abhari, R. S., 2006, "Modeling of Film Cooling—Part I: Experimental Study of Flow Structure," ASME J. Turbomach., **128**, pp. 141–149.
[17] Saumweber, C., Schulz, A., and Wittig, S., 2003, "Free-Stream Turbulence Effects on Film Cooling With Shaped Holes," ASME J. Turbomach., **125**(1), pp. 65–73.
[18] Morton, B. R., and Ibbetson, A., 1996, "Jets Deflected in a Crossflow," Exp. Therm. Fluid Sci., **12**, pp. 112–133.
[19] Abramovich, G. N., 1963, *The Theory of Turbulent Jets*, MIT Press, Cambridge, MS.
[20] Oseen, C. W., 1911, "Über die Stokes'sche Formel und über eine Verwandte Aufgabe in der Hydrodynamik," Ark. Mat., 6(29).
[21] Gritsch, M., Schulz, A., and Wittig, S., 1998, "Method for Correlating Discharge Coefficients of Film-Cooling Holes," AIAA J., **36**(6), pp. 976–980.
[22] Rydholm, H. A., 1998, "An Experimental Investigation of the Velocity and Temperature Fields of Cold Jets Injected Into a Hot Crossflow," ASME J. Turbomach., **120**(2), pp. 320–326.
[23] Ni, R. H., 1981, "A Multiple Grid Scheme for Solving the Euler Equations," AIAA J., **20**(11), pp. 1565–1571.
[24] Burdet, A., and Lakehal, D., 2002, "MULTI3—A Compressible Navier-Stokes Solver for 3D Turbomachinery Flow Simulation," Internal Report No. LSM-01-02, LSM, ETH-Zürich, Switzerland.
[25] Burdet, A., Mischo, B., Lakehal, D., Kalfas, A. I., and Abhari, R. S., 2003, "Predicting Vorticity Transport and Loss Generation Downstream of a Turbine Annular Cascade," *Proc., of 5th European Conference on Turbomachinery*, M. Stastny, C. H. Sieverding, and G. Bois, Prague, Czech Republic, pp. 995–1006.
[26] Abhari, R. S., and Epstein, A. H., 1994, "An Experimental Study of Film Cooling in a Rotating Transonic Turbine," ASME J. Turbomach., **116**(1), pp. 63–70.
[27] Tseng, Y.-H., and Ferziger, J. H., 2003, "A Ghost-Cell Immersed Boundary Method for Flow in Complex Geometry," J. Comput. Phys., **192**, pp. 593–623.
[28] Burdet, A., and Abhari, R. S., 2006, "A Computationally Efficient Film Cooling Jet Model Using the Implicit Immersed Boundary Method," Comput. Fluids, submitted.
[29] Kaszeta, R. W., and Simon, T. W., 2000, "Measurement of Eddy Diffusivity of Momentum in Film Cooling Flows With Streamwise Injection," ASME J. Turbomach., **122**(1), pp. 178–183.

Effect of Jet Pulsing on Film Cooling—Part I: Effectiveness and Flow-Field Temperature Results

Sarah M. Coulthard
Department of Mechanical Engineering,
Stanford University,
Stanford, CA 94305

Ralph J. Volino
e-mail: volino@usna.edu

Karen A. Flack

Department of Mechanical Engineering,
United States Naval Academy,
Annapolis, MD 21402

Pulsed film cooling was studied experimentally to determine its effect on film-cooling effectiveness. The film-cooling jets were pulsed using solenoid valves in the supply air line. Cases with a single row of cylindrical film-cooling holes inclined at 35 deg to the surface of a flat plate were considered at blowing ratios of 0.25, 0.5, 1.0, and 1.5 for a variety of pulsing frequencies and duty cycles. Temperature measurements were made using an infrared camera, thermocouples, and cold-wire anemometry. Hot-wire anemometry was used for velocity measurements. The local film-cooling effectiveness was calculated based on the measured temperatures, and the results were compared to baseline cases with continuous blowing. Phase-locked flow temperature fields were determined from cold-wire surveys. Pulsing at high frequencies helped to improve film-cooling effectiveness in some cases by reducing overall jet liftoff. At lower frequencies, pulsing tended to have the opposite effect. With the present geometry and a steady mainflow, pulsing did not provide an overall benefit. The highest overall effectiveness was achieved with continuous jets and a blowing ratio of 0.5. The present results may prove useful for understanding film-cooling behavior in engines, where mainflow unsteadiness causes film-cooling jet pulsation. [DOI: 10.1115/1.2437231]

Introduction

Film cooling has been studied extensively in order to provide improved cooling of the airfoils in gas turbine engines and thus increase the life of the airfoils and allow for higher turbine inlet temperatures. Approximately 20–25% of compressor air is used for cooling of high-performance turbine engines [1]. If the amount of required coolant air could be reduced, engine efficiency would increase. The present study investigates whether pulsing the film-cooling bleed air might allow for a reduction in coolant flow while still providing adequate protection to the turbine airfoils.

The interactions between a mainstream flow and a pulsed coolant jet are not well understood. Only a few studies have considered the effects of pulsed jets. Some discussed the effects of pulsations due to engine unsteadiness in which the jet flow was never turned off but was cyclically disturbed. Bons et al. [2] used a loudspeaker to induce pulsations in the jets and examined the effects of unsteadiness on film cooling of a flat plate. They found that pulsation resulted in reduced film-cooling effectiveness for low blowing ratios, and that the effectiveness increased slightly as the blowing ratio increased to 1.5. Ligrani et al. [3], Seo et al. [4], and Jung et al. [5] used static pressure pulsations of the mainstream flow generated by an array of rotating shutter blades downstream of the test section. They showed that pulsations cause the film-cooling jet to spread more uniformly across the test surface. The spreading was caused by the jet flow oscillating in both the normal and spanwise directions as it left the hole.

Ekkad et al. [1] were the first to consider direct control of the coolant jets to improve film cooling. They controlled the pulsing using solenoid valves. Their geometry was a single film-cooling hole angled at 20 deg to the spanwise direction and 90 deg to the streamwise direction, located on the leading section of a cylinder. Ekkad et al. [1] stated that pulsed jets increase the ability to effectively protect the surface and slightly lower heat transfer coefficients compared to continuous jets in some cases.

There are a few reasons to believe that pulsing may improve film cooling. Pulsing could presumably change the distribution of the jet velocity profile within the coolant holes. This could lead to more or less jet liftoff from the airfoil surface, particularly at high blowing ratios. Less liftoff would result in improved film cooling. Cycling a jet on and off would also result in a starting vortex each time the jet was turned on. Bons et al. [6] studied vortex generator jets (VGJs) for separation control on low-pressure turbine airfoils and noted that the starting vortex played a large role in keeping the boundary layer attached. Although the size and purpose of the VGJs were different from those of film-cooling jets, a similar effect could help keep film-cooling flow near a surface.

If coolant jets were cycled on and off, the cool fluid would presumably cool the airfoil surface as it passed over it and heat would flow back into the surface during the off portion of the cycle. If the jet disturbance caused more effective heat transfer out of the surface during the on portion of the cycle than during the off portion, then the net effect would be improved surface cooling for a given total coolant mass flow. A calm period following each jet pulse, similar to that observed following turbulent spots or wake-induced turbulent strips (e.g., [7]) might enhance this effect by reducing heat transfer during the off portion of the cycle. Volino [8] and Bons et al. [6] observed calm flow following disturbances caused by VGJs. It should be noted, however, that calming effects are typically observed in transitional boundary layers, while the boundary layer in most film-cooling applications is turbulent.

In the present study, film-cooling jets were pulsed using solenoid valves in the supply air line. The geometry consisted of a flat plate with a single row of five round holes inclined at 35 deg to the surface and parallel to the streamwise direction. The holes were spaced $3D$ apart, center to center, with a length to diameter ratio $L/D=4$. The geometry has been studied extensively with continuous jets. It matches that used by Bons et al. [2,9], Burd and

Contributed by the International Gas Turbine Institute of ASME for publication in the JOURNAL OF TURBOMACHINERY. Manuscript received May 25, 2006; final manuscript received May 31, 2006. Review conducted by David Wisler. Paper presented at the ASME Turbo Expo 2006: Land, Sea and Air (GT2006), Barcelona, Spain, May 8–11, 2006. Paper No. GT2006-91273.

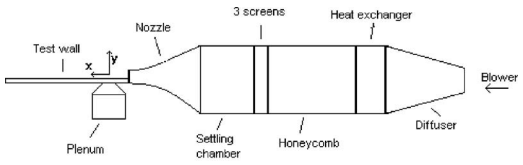

(*a*)

(*b*)

Fig. 1 Wind tunnel configuration: (*a*) schematic and (*b*) photograph of test wall with sidewalls

Simon [10], Schmidt et al. [11], Pedersen et al. [12], Kohli and Bogard [13], Sinha et al. [14], Pietrzyk et al. [15], and several others. Blowing ratios of 0.25, 0.5, 1.0, and 1.5 were investigated with varying frequencies and duty cycles. Phase-averaged jet velocity and flow temperature distributions, and film-cooling effectiveness results are presented below. Heat transfer results, including Stanton number and heat flux ratios, are presented in Part II of the present work [16].

Experimental Facilities and Techniques

Experiments were conducted with an open-loop subsonic wind tunnel with a test plate attached at the exit of the contraction, and a plenum to supply the film-cooling jets. The wind tunnel, shown in Fig. 1, was comprised of six sections: a blower, a diffuser with three screens, a heat exchanger to maintain air nominally at 20°C, a honeycomb, a settling chamber with three screens, and a nozzle with an 8.8 area reduction. The nozzle exit area was 0.38 m $\times$0.10 m. The exiting mainstream air was uniform in temperature and velocity to within 0.1°C and 1%, respectively. The freestream turbulence intensity at the nozzle exit was 1%. This value is lower than typical intensity levels in engines, which depend on the location in the turbine. Air exiting the nozzle forms a wall jet at U_∞=8 m/s along a flat plate, which serves as the test wall. The mainstream velocity remained at 8 m/s 18*D* downstream of the film-cooling holes. At this downstream location, the velocity outside the boundary layer was uniform up to the edge of the free shear layer, which was located 3*D* above the wall. The freestream unsteadiness level gradually increased in the streamwise direction to 6%. This increase is due to the growth of the shear layer at the edge of the wall jet. Spectral measurements indicate that the freestream fluctuations are nearly all at frequencies between 5 Hz and 50 Hz, with a peak at 22 Hz. These low frequencies are associated with large-scale structures formed in the shear layer, which will buffet the boundary layer but not promote significant turbulent mixing. The boundary layer is therefore expected to behave like a low-freestream turbulence boundary layer, and the heat transfer coefficient results in Part II [16] are typical of low-freestream turbulence conditions. The wall jet configuration is based on the facility of Burd and Simon [10].

The film-cooling supply plenum was a box with 0.38 m $\times$0.18 m $\times$0.36 m inside dimensions. It was supplied by a manifold connected to a high-pressure air source. The supply pressure was adjusted to vary the blowing ratio from B=0.25 to 1.5. The air passed through small-diameter, fast-response solenoid valves (General Valve Series 9 valves and Iota 1 controllers) between the manifold and the plenum. The valves could be set to cycle between fully open and fully closed positions. The duty cycle DC is defined as the fraction of the cycle that the valve is open. For example, a 10 Hz frequency with DC=0.25 means the valves are open for 0.025 s and then closed for 0.075 s each cycle. The flow through the valves was choked. For a given supply pressure, the film-cooling mass flow remains constant, independent of downstream conditions. Nine valves were operated in parallel to provide the desired coolant mass flow. The plenum contained a finned tube heat exchanger, midway between the valves and the film cooling holes. Warm water at 30°C circulated through the tubes, and the air from the valves passed over the tubes in a cross-flow manner, maintaining the temperature of the coolant jets at ~27°C. The distance from the valves to the film-cooling hole exits was ~0.46 m. Given this distance and the finite speed of sound, a lag of roughly 0.0013 s is expected between the opening or closing of the valves and the flow response at the film-cooling hole exits. The capacitance effect of the plenum volume along with the mechanical response time of the valves (~0.002 s)could increase this lag, and the results presented below indicate the valve-jet lag was ~0.004 s. As shown below, at the highest frequency considered (80 Hz), the pulsing period and valve-jet lag time were comparable, and the jets never fully turned on or off in response to the valve opening and closing. At lower pulsing frequencies, the period for a pulse was large compared to the valve-jet lag, so the effects of the lag were not as significant.

The test wall was constructed of polyurethane foam with a thermal conductivity of 0.03 W/mK. The dimensions were 0.38 m wide, 44 mm thick, and 1.17 m long, with a starting length of 13.3*D* upstream of the row of film cooling holes. A wall opposite the starting length and sidewalls along the length of the test wall, as shown in Fig. 1(*b*), helped limit interaction between the wind tunnel flow and the still air in the room. Foil heating elements were placed on the foam surface and are described in more detail in Part II [16] and in Coulthard et al. [17]. The heaters were covered with a 0.79 mm thick black sheet of Formica® laminate to provide a smooth test surface. The film-cooling geometry consisted of a single row of five round holes inclined at 35 deg to the surface and parallel to the streamwise direction. The sharp-edged holes had a diameter of D=19.05 mm spaced 3*D* apart, center to center, and with a length to diameter ratio L/D=4. A 1.6 mm thick trip was installed 11*D* upstream of the leading edge of the film cooling holes, and a velocity profile acquired 0.8*D* upstream of the holes confirmed that the boundary layer was fully turbulent. The test plate was instrumented with type E thermocouples of 76.2 μm dia wire, located between the heaters and Formica. Thermocouples were also placed in the film-cooling plenum, at the plenum-side end of the outermost film-cooling hole, at the wind tunnel exit, on the back of the test plate, in the ambient air, on the wall of the room to measure the surrounding temperature for radiation corrections, and in ice water as a reference. Constant current (cold-wire) and constant temperature (hot-wire) anemometry were used to measure flow temperature and velocity, respectively. Boundary layer probes with 1.27 μm dia platinum sensors (TSI model 1261A-P.5) were used for temperature measurements, and boundary layer probes with 3.81 μm dia tungsten sensors (TSI model 1218-T1.5) were used for the velocity. An infrared (IR) camera (FLIR Systems Merlin model) with a Stirling cooled detector was used to measure the surface temperature field of the test wall. The temperature resolution of the camera was 0.05°C. The camera had a 255$\times$318 pixel detector and was positioned such that each pixel corresponded to a 1 mm$\times$1 mm area on the test wall. The field of view on the test wall corresponded to 13.4*D*

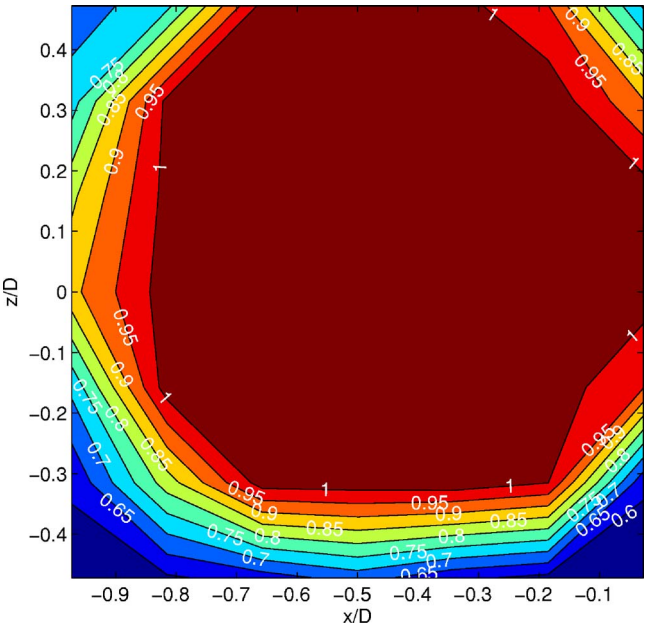

Fig. 2 Time-averaged dimensionless temperature profile θ at exit plane of center hole with $B=0.5$, steady flow

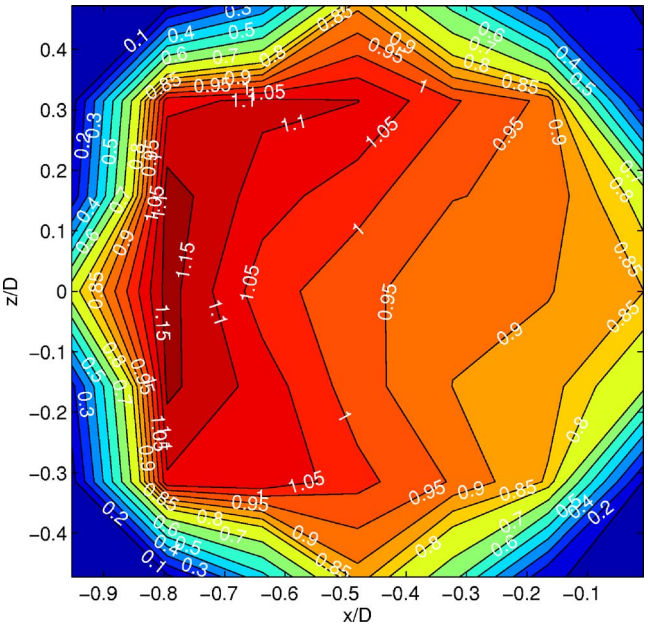

Fig. 3 Time-averaged velocity profile, U_{jet}/U_{∞}, at exit plane of center hole with $B=1.0$, steady flow

$\times 16.7D$. The emissivity of the test wall was determined to be 0.95 through comparison of IR images of the test wall and a surface of known emissivity (black electrical tape) at the same temperature.

The boundary layer $0.8D$ upstream of the film-cooling hole leading edge had a momentum thickness Reynolds number of 550 and a shape factor of 1.48. The skin friction coefficient at this location was 5.4×10^{-3}. The Reynolds number based on hole diameter and mainstream velocity was 10,000.

The film-cooling jet uniformity was measured by traversing the constant current and hot-wire probes over the hole exit with the main flow in the wind tunnel off. Figure 2 shows the temperature distribution for a jet flow corresponding to blowing ratio $B=0.5$. The origin of the coordinate system is the downstream edge of the center film-cooling hole. The intersection of the round hole with the plane of the test wall is an ellipse, and the measurements acquired for Figs. 2 and 3 were made in the plane of this ellipse. The data were plotted in Figs. 2 and 3 as projected onto a plane perpendicular to the hole axis; thus, the hole appears circular. The jet temperature was clearly very uniform and matched the plenum temperature to within 0.2°C. These results indicate very little cooling of the jet flow as it passed through the hole channel. The temperature distribution was checked for all blowing ratios and found to be uniform in all cases. Figure 3 shows the mean velocity for the jet flow in the $B=1.0$ case. The velocity distribution was similar at all blowing ratios. The higher-velocity region in the upstream section of the hole resulted from the flow of the jet from the plenum, through and out of the hole. Burd and Simon [10] discuss jet velocity distributions in similar configurations in more detail. The jet velocity and temperature distributions no doubt changed when the main flow was turned on, but the mean velocity remained the same since the flow rate was set by the choked mass flow through the upstream solenoid valves. Since the jets were only heated to ~7°C above the mainstream temperature, the density ratio of jets to mainstream was 0.98. Hence, the blowing and velocity ratios were essentially equal. The temperature and velocity measurements were compared between the five film-cooling holes. The hole-to-hole variation in temperature was 2% of the jet to mainstream temperature difference, and velocity variation was 8% of the mainstream velocity.

The film-cooling effectiveness and nondimensional frequency were defined, respectively, as follows:

$$\eta = \frac{T_{aw} - T_{\infty}}{T_{\text{jet}} - T_{\infty}} \tag{1}$$

$$F = \frac{fD}{U_{\infty}} \tag{2}$$

Measurements were made for each flow condition with the wall heaters on and off, to determine local T_{aw}, η and heat transfer coefficients based on measured temperatures. This is described in more detail in Part II [16].

The thermocouples and IR camera were calibrated against a precision blackbody source, and the cold-wire probe was calibrated against the thermocouples. The uncertainty in the measured temperature was 0.2°C, the uncertainty in the measured velocity

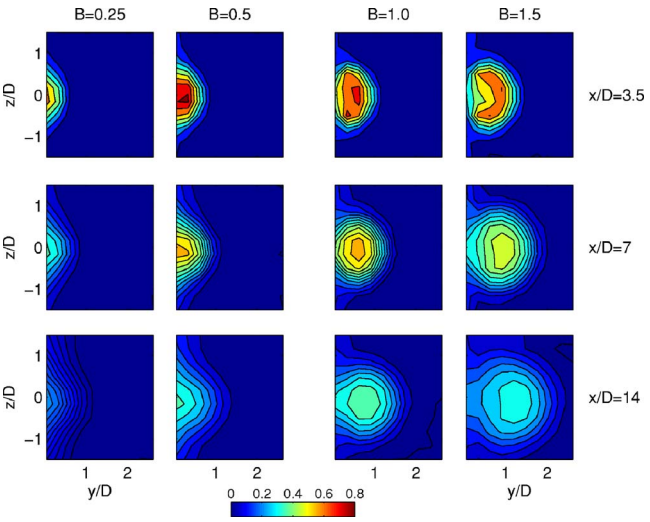

Fig. 4 Time-averaged dimensionless flow temperature contours θ, in *y-z* plane for steady-flow cases at four blowing ratios (columns) and three streamwise locations (rows)

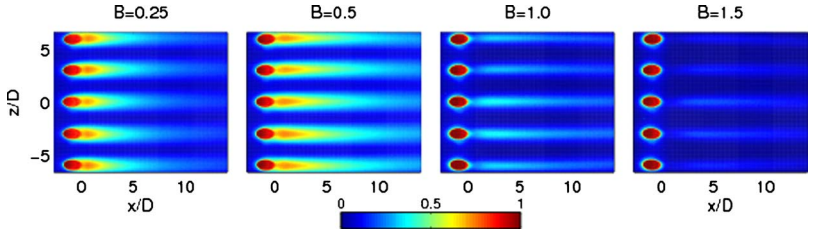

Fig. 5 Film-cooling effectiveness contours for steady blowing with B=0.25, 0.5, 1.0, and 1.5

was 3%, and the uncertainty in the atmospheric pressure was 1%. The uncertainty in the film-cooling effectiveness was determined to be 6% using standard propagation of error with a 95% confidence interval.

Baseline tests were conducted at blowing ratios of 0.25, 0.5, 1.0, and 1.5 with continuous cooling. For each case, the jet velocity distribution was measured by traversing the hot-wire probe through a 7×7 grid over the hole exit plane. The blowing ratio was determined by integrating the measured velocities over the exit plane. Since a single sensor hot-wire measures velocity magnitude perpendicular to the sensor, and not flow direction, it was assumed that the jet flow direction was along the axis of the hole. Given the length to diameter ratio of the holes (L/D=4), this assumption should be valid for the steady flow cases. With pulsing, some deviations in flow direction are possible, and the measured blowing ratios should be treated as approximate. Flow temperature was measured for each case in three planes, at x=3.5D, 7D, and 14D. In each plane, the cold-wire probe was traversed through a uniform 10×10 grid extending from z=−1.5D to 1.5D and from y=0.05D to 2.6D. Thermocouple data and the wall temperature distributions, as measured with the IR camera, were also documented for each case for heated and unheated wall conditions.

Pulsed cooling cases were documented at nominal blowing ratios of 0.5 and 1.0. The nominal blowing ratio is given as the expected blowing ratio during the valve-open portion of the jet pulsing cycle. The jet velocity was set with the solenoid valves fully open by measuring the jet velocity with a hot wire and adjusting the supply pressure to the valves. The time-averaged blowing ratio for the full jet pulsing cycle is approximately equal to the specified nominal blowing ratio times the jet duty cycle. Pulsed cooling cases at B=0.5 were documented with a jet duty cycle of DC=0.5 and dimensionless pulsing frequencies of F=0.0119, 0.0238, 0.0476, 0.0953, and 0.1905 (corresponding to dimensional frequencies of 5 Hz, 10 Hz, 20 Hz, 40 Hz, and 80 Hz). Cases with B=1.0 and DC=0.5 were documented with F=0.0238, 0.0476, 0.0953, and 0.1905. To investigate duty cycle effects, ad-

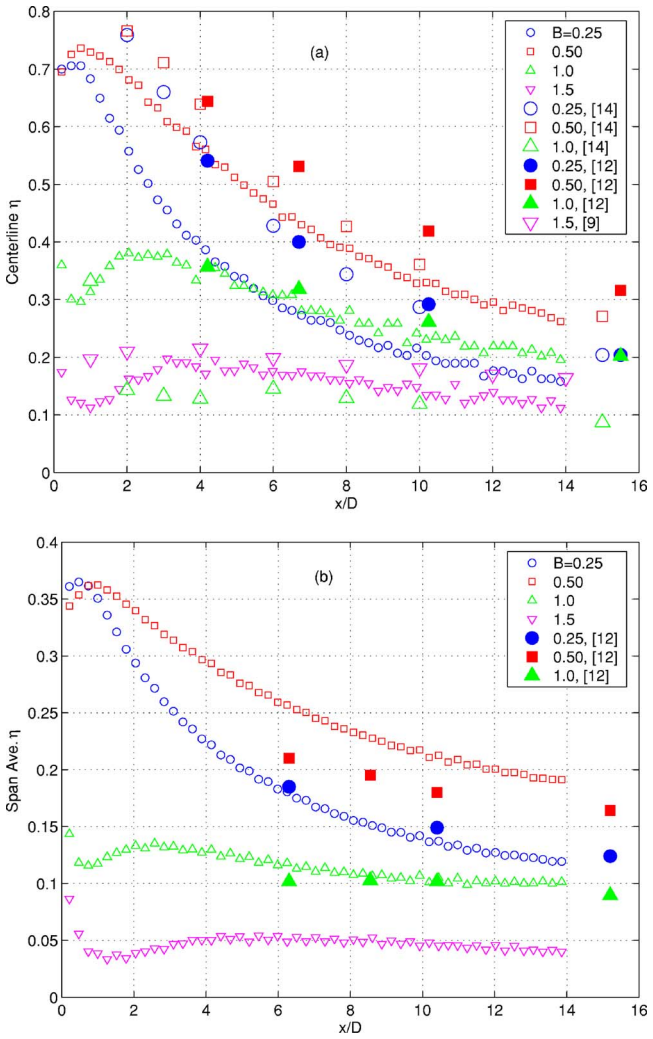

Fig. 6 Film-cooling effectiveness for steady blowing cases: (*a*) centerline and (*b*) spanwise averaged; small symbols for present study, large symbols for data from literature

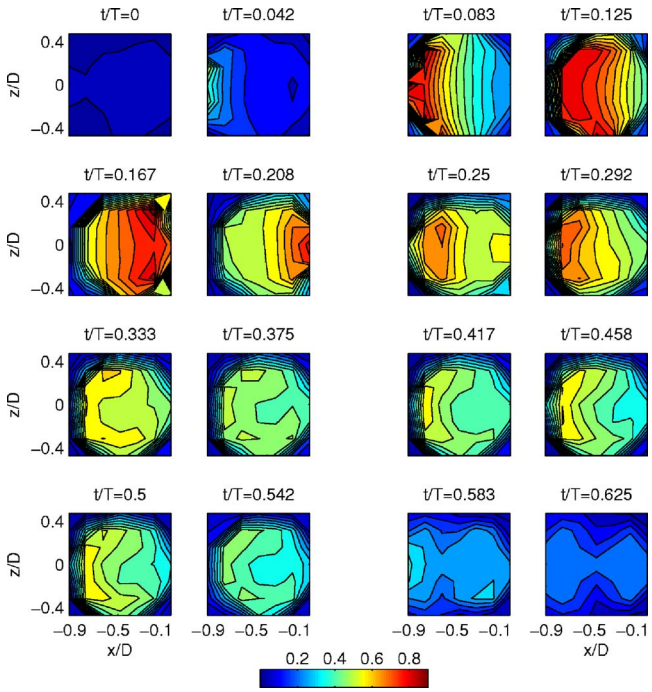

Fig. 7 Phase-averaged velocity profiles, U_{jet}/U_{∞}, at exit plane of center hole with B=0.5, F=0.0238, DC=0.5

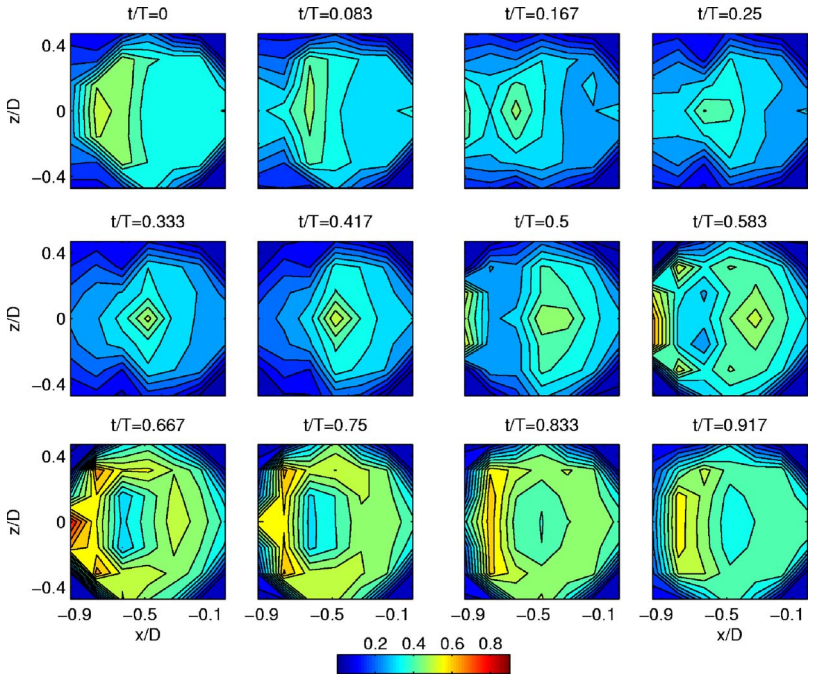

Fig. 8 Phase-averaged velocity profiles, U_{jet}/U_{∞}, at exit plane of center hole with B=0.5, F=0.1905, DC=0.5

ditional cases with B=0.5 and F=0.0238 were documented with DC=0.25 and 0.75. At B=1.0, four additional cases were studied with F=0.0238 and 0.1905, and DC=0.25 and 0.75. For each of the pulsed flow cases, the same measurements were made as in the steady flow cases described above. For the hot- and cold-wire surveys, the pulse train from the solenoid valve controllers was digitized along with the instantaneous anemometer voltages (13 s long traces) to allow phase averaging of the flow velocities and temperatures relative to the valve opening and closing. Phase-averaged results were computed at 24 increments during the jet pulsing cycle. The dimensionless frequencies selected for the study are in the range of representative dimensionless wake-passing frequencies in an engine, and wake-induced unsteadiness drives natural pulsations in film-cooling flow.

Results and Discussion

Steady Blowing Cases. Figure 4 shows the time-averaged dimensionless flow temperature θ contours in the $y-z$ plane for steady flow cases at four blowing ratios and three streamwise locations. These temperature contours show the core of the film-cooling jet with respect to the test surface. At B=0.25 and 0.5, the core remains close to the test surface as far as x=14D downstream of the holes. However, as the jet velocity increases, the core moves further away from the wall as it traverses downstream. This is evidence of jet liftoff, where the velocity of the jet is so great that it causes the jet to lift off from the wall on exiting the holes. In all cases, the size of the jet increases in the streamwise direction and θ drops as the jet mixes with the mainstream flow.

Figure 5 shows the film-cooling effectiveness contours for these steady blowing cases. The local η rises and falls in agreement with the near-wall θ shown in Fig. 4. This is further exemplified in Fig. 6, which shows the centerline (z=0) and spanwise-averaged film-cooling effectiveness for the steady blowing cases. The B=0.25 case has high film-cooling effectiveness directly downstream of the holes; however, it drops off significantly by x/D=2 due to the low coolant mass flow rate. The mainstream flow mixes with the coolant jet and reduces its effectiveness. By x/D=6, the film-cooling effectiveness has dropped to <50% of its peak value. The blowing ratio of B=0.5 has the best film-cooling effectiveness, which is high directly downstream of the holes and gradually declines further downstream. By x/D=14, the effectiveness has decreased by over 50%. The B=1.0 and 1.5 cases have significantly lower film-cooling effectiveness. The initial drop in η directly downstream of the holes is due to jet liftoff. As the jet core spreads, it has more of an influence on the test wall, and the effectiveness increases slightly. It then drops off again as the jet moves further downstream. The film-cooling effectiveness results agree with similar studies in the literature. Examples from a few cases are included in Fig. 6 for comparison. Data from Sinha et al. [14] and Pedersen et al. [12] are shown for B=0.25, 0.5, and 1.0.

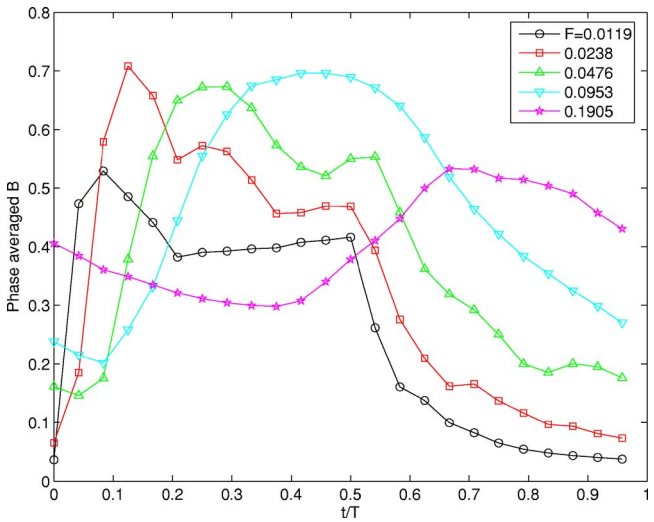

Fig. 9 Phase-averaged blowing ratio at various frequencies with nominal B=0.5, DC=0.5

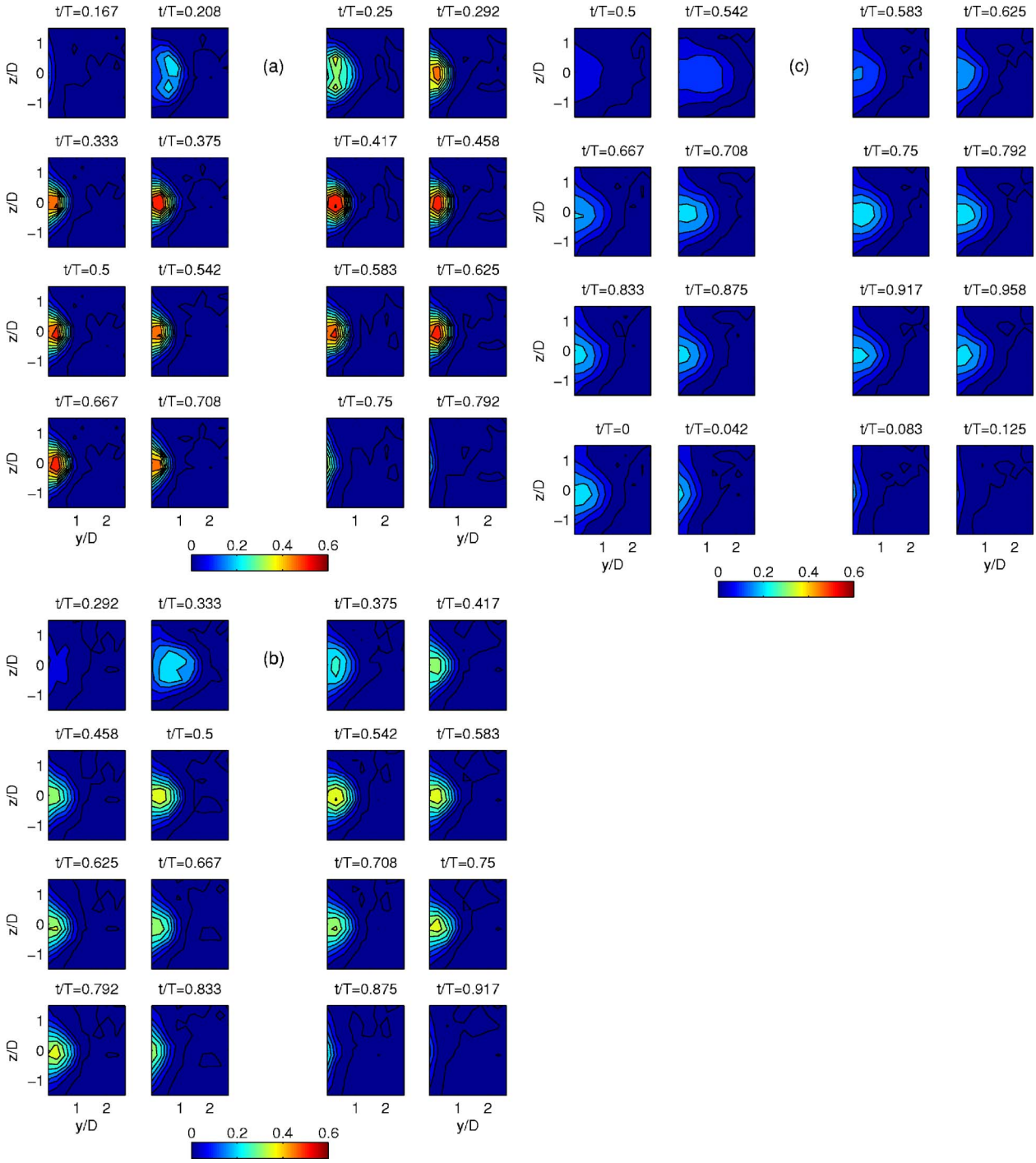

Fig. 10 Phase-averaged dimensionless flow temperature contours θ in *y-z* plane: $B=0.5$, $F=0.0238$, DC=0.5: (*a*) $x/D=3.5$, (*b*) $x/D=7$, and (*c*) $x/D=14$

Data from Bons et al. [9] are shown for $B=1.5$. The Sinha et al. [14] cases had a density ratio between coolant and mainstream of 1.2 (compared to 0.98 in the present study) and a Reynolds number of 16,000 (compared to 10,000 in the present study), but were otherwise similar to the present study. The Pedersen et al. [12] cases had a very large L/D for the holes (compared to $L/D=4$ in the present study) and Re between 5600 and 10,600, but were otherwise similar to the present study. The Bons et al. [9] case had Re=19,000, but was otherwise similar to the present study. Recognizing the experimental uncertainty in the data and the physical differences between the studies, the agreement is generally good. There is a large difference between the present data at $B=1.0$ and the Sinha et al. [14] case, but the present data agree well with the Pedersen et al. [12] data at this blowing ratio.

Pulsing Frequency Effects

$B=0.5$. Figure 7 shows the phase averaged velocity profiles of U_{jet}/U_{∞} at the exit plane of the center hole with $B=0.5$, $F=0.0238$ (10 Hz), and DC=0.5. The start of the cycle, $t/T=0$, is taken as the time when the solenoid valves open in all cases. There is a slight delay of 0.004 s before the jets appear at t/T

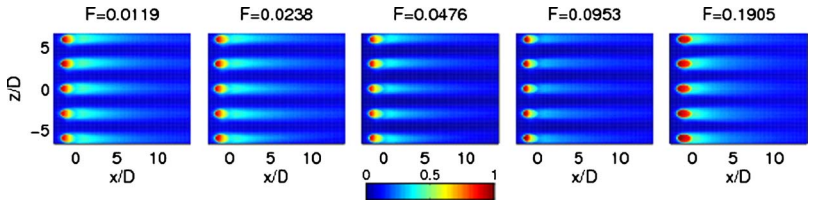

Fig. 11 Film-cooling effectiveness contours at various pulsing frequencies with nominal B=0.5 and DC=0.5

=0.042. The high velocity in the upstream region of the hole traverses across the face of the hole as the initial burst of air exits the jet plenum. This initial burst includes local high velocities nearly double those observed in the steady blowing case. By t/T=0.333, the jet has settled into a steady velocity profile. The upstream region of the hole has a somewhat higher velocity than the downstream region, and the profile agrees with the steady blowing velocity distribution of Fig. 3. The initial transient occupies ~30% of the cycle (0.03 s) and the steady-state period ~20% (0.02 s). At frequencies between F=0.0119 and 0.0953, the jet velocity distributions are similar to those of Fig. 7, but with some differences in timing. The initial transient continues to take ~0.03 s (regardless of the pulsing frequency), and this 0.03 s occupies a larger fraction of the cycle at high pulsing frequencies. This leaves less time and a smaller fraction of the cycle for the steadystate condition. In the F=0.0238 case of Fig. 7, the valve is shut off at t/T=0.5, and the jet velocity begins to drop toward zero at t/T=0.542.

Figure 8 shows the velocity profiles of U_{jet}/U_{∞} for B=0.5, F=0.1905 (80 Hz), and DC=0.5. In this case, the plenum is not able to respond rapidly enough to keep up with the valve opening and closing. The jet lags the valves, turning on at approximately t/T=0.5. The jet does not have time to settle to a steady condition, as it did at the lower frequencies. The jet velocity is dropping after t/T=0.917, but it never reaches a fully off condition before the next pulse. Figure 9 shows the phase-averaged blowing ratio at various frequencies with B=0.5 and DC=0.5. At the lower frequencies, there is an initial overshoot of the nominal blowing ratio when the valves open. This is due to a buildup of pressure in the manifold upstream of the valves when the valves are closed. When the valves first open there is an initial high mass flow until the upstream pressure can drop to its steady flow value. As the frequency increases to F=0.1905, the valve-off velocity increases significantly and the initial valve-on high velocity is not observed. The frequency at which the valve-off velocity becomes significant is believed to depend on the plenum dimensions.

Figure 10 shows the phase-averaged temperature contours for B=0.5, F=0.0238, and DC=0.5. The temperature contours are shown at three locations downstream of the film-cooling holes, and show the effect of jet liftoff even at low frequency. Note that only the jet on portion of the cycle is shown in each plane. At x=3.5D, the jet appears at approximately t/T=0.208 with the core of the jet slightly further from the wall than in the steady case, shown in Fig. 4. This initial liftoff is caused by a higher pressure when the jet first turns on and by the high local jet velocities, which were shown in Fig. 7. As the jet settles into a more uniform distribution, the core of the jet returns to the wall surface as

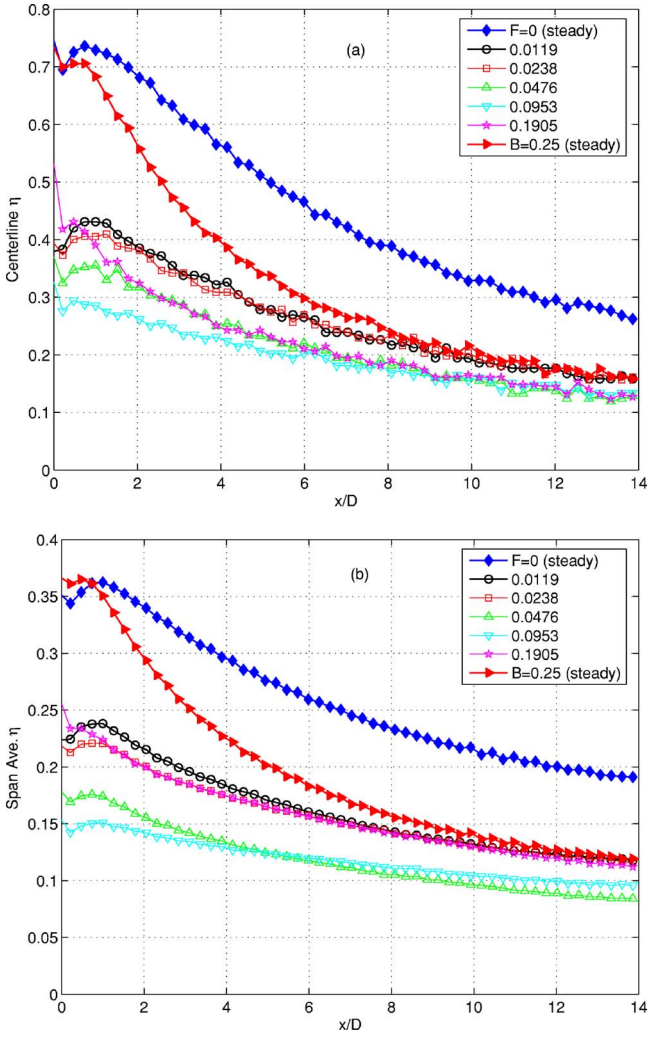

Fig. 12 Film-cooling effectiveness for nominal B=0.5, DC=0.5 cases, with steady B=0.25 and B=0.5 cases included for comparison: (*a*) centerline and (*b*) spanwise averaged

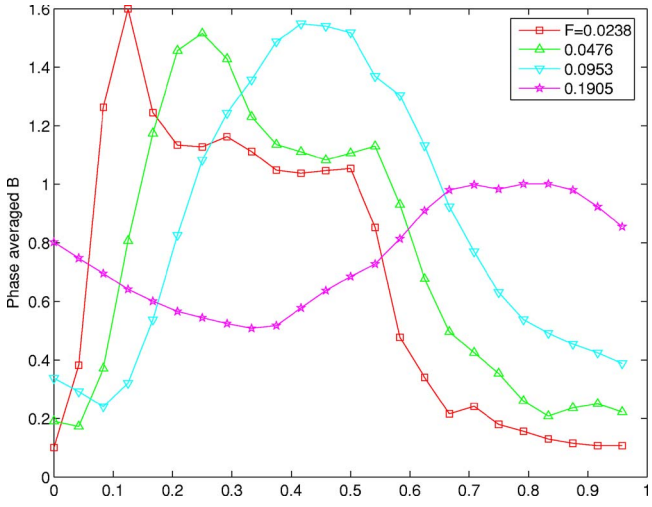

Fig. 13 Phase-averaged blowing ratio at various frequencies with nominal B=1.0 and DC=0.5

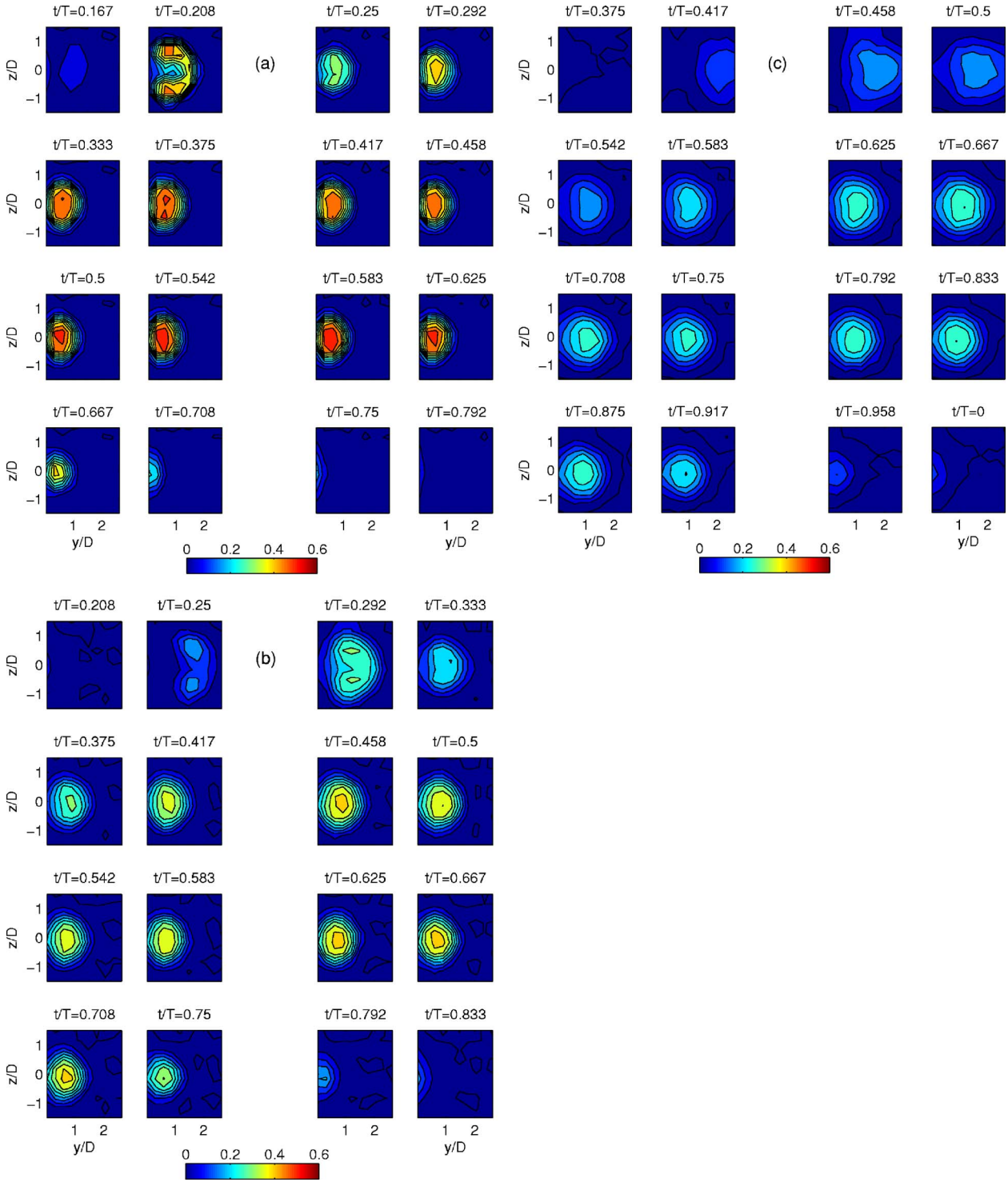

Fig. 14 Phase-averaged dimensionless flow temperature contours θ in *y-z* plane: $B=1.0$, $F=0.0238$, DC=0.5: (*a*) $x/D=3.5$, (*b*) $x/D=7$, and (*c*) $x/D=14$

shown at $t/T=0.333$ in Fig. 10. The core of the jet then remains close to the test wall until the jet turns off. The temperature contours also give insight into the flow structure of the film-cooling jet. Figure 10(*a*) suggests kidney-shaped starting vortices within the jet just after it exits the hole at $t/T=0.208$. At the downstream locations, the jet temperature decreases as it mixes with the mainstream, but the behavior observed at $x=3.5D$ is still apparent with the jet initially appearing relatively far from the wall and then moving toward the wall in the steady condition. The convective velocity of the jet fluid can be estimated from the time lag between the appearance of the jet in Fig. 7 and its appearance in the planes of Fig. 10. After the valve opens at $t/T=0$, the jet appears in the hole exit plane at $t/T=0.042$ in Fig. 7, and at $t/T=0.208$, 0.333, and 0.5 in Figs. 10(*a*)–10(*c*). The jet appears to move at about $0.5U_\infty$ between the hole and $x=3.5D$. This is reasonable since the initial jet velocity is half the mainstream velocity when

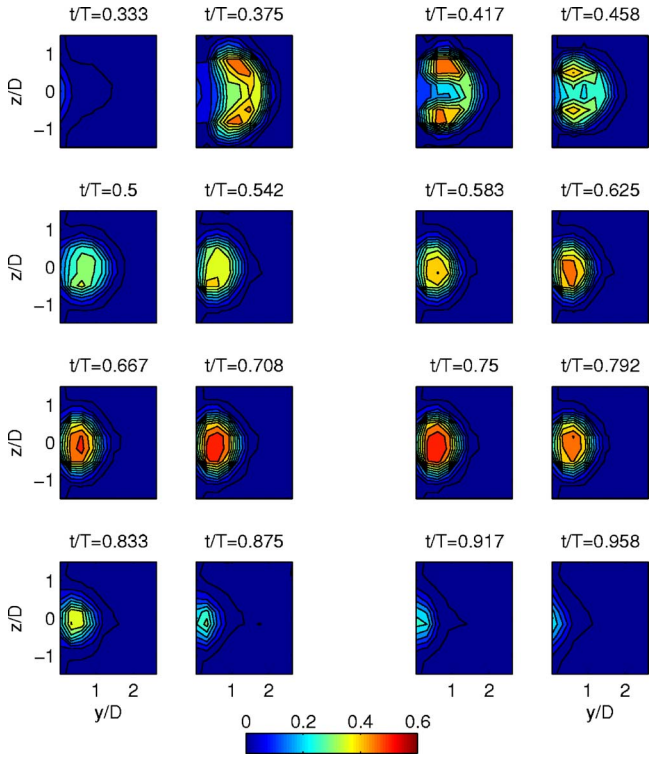

Fig. 15 Phase-averaged dimensionless flow temperature contours θ in *y-z* plane: $B=1.0$, $F=0.0476$, DC=0.5, $x/D=3.5$

$B=0.5$. Farther downstream, the jet fluid is entrained by the faster mainstream. The speed increases to about $0.7U_\infty$ between $x=3.5D$ and $7D$, and to about $1.0U_\infty$ between $x=7D$ and $14D$.

Figure 11 shows the film-cooling effectiveness contours at the various frequencies for the $B=0.5$, DC=0.5 cases. The best pulsed cases are $F=0.0119$ and 0.0238, with $F=0.0119$ having slightly higher effectiveness directly downstream of the film-cooling holes. Figure 12 shows the centerline and spanwise-averaged film-cooling effectiveness for the nominal $B=0.5$ DC=0.5 cases at varying frequencies, with the $B=0.25$ and 0.5 steady cases plotted for comparison. The $B=0.5$ steady case has the best film-cooling effectiveness. The pulsed cases have significantly lower film-cooling effectiveness due to the decrease in coolant mass flow caused by pulsing. The lower-frequency cases have the best film-cooling effectiveness because the effect of the initial liftoff is reduced compared to the higher-frequency cases. In the higher-frequency cases, the initial liftoff takes approximately the same time as in the lower-frequency cases, ~0.01 s. This 0.01 s transient occupies a larger fraction of the total cycle time at the higher frequencies, thus the time remaining at the steady condition is reduced. Since the instantaneous film-cooling effectiveness is reduced during the initial startup, and the startup occupies a larger fraction of the cycle at higher frequencies, there is a lower overall film-cooling effectiveness at the higher frequencies. The contours of Fig. 11 also show that the time-averaged temperature distributions within the holes themselves change as the frequency increases. At the higher frequencies, it appears the jet fluid is concentrated more toward the upstream part of the holes, again suggesting a greater importance of the initial transient at the higher frequencies. The $F=0.1905$ case is the exception to the above discussion. As shown in Figs. 8 and 9, the jet never fully turns off at $F=0.1905$, so low-momentum fluid is supplied during the valve off period. This raises η above the levels in all but the $F=0.0119$ pulsed case. It should be noted that in the upstream region, η in the pulsed cases is well below the level of the steady $B=0.25$ case, which has nominally the same coolant mass flow rate. Further downstream, η for the steady $B=0.25$ case is about equal to the level of the better pulsed cases.

$B=1.0$. Figure 13 shows the phase-averaged blowing ratio at various frequencies with $B=1.0$ and DC=0.5. This figure agrees with Fig. 9, but with B approximately doubled in all cases.

Figure 14 shows the phase-averaged temperature contours for $B=1.0$ pulsed at $F=0.0238$ and DC=0.5. The core of the jet is at approximately $y/D=1$ during the initial startup. As the jet settles to a steady condition, the core of the jet remains relatively far from the wall at approximately $y/D=0.5$, which results in a lower film-cooling effectiveness than in the $B=0.5$ case. This agrees with the steady cases of Fig. 4 and shows the effect increasing velocity has on jet liftoff. Figures 14(*a*) and 14(*b*) also suggest the appearance of the starting vortex. It can be seen even at $x/D=7$ for the higher blowing ratio. The time lag between the start of the jet in Fig. 13 and its appearance in the planes of Fig. 14 can again be used to estimate the jet convection speed. It is approximately $0.67U_\infty$ up to $x/D=3.5$ and $1.0U_\infty$ further downstream. These speeds are higher than in the $B=0.5$ case, as expected since the jet starts with a higher velocity and is located farther from the wall, increasing the entrainment by the mainstream. Figures 15 and 16 show the effect of increasing frequency on jet liftoff. Figure 15 shows flow temperature contours for $B=1.0$ with $F=0.0476$ and DC=0.5 at $x/D=3.5$. The behavior is very similar to that at $F=0.0238$ (Fig. 14(*a*)), but the initial transient takes twice as long a fraction of the cycle, since the dimensional period for the transient is about the same in both cases. This reduces the length of the steady part of the cycle at $F=0.0476$. Figure 16 shows the contours for $F=0.1905$ with the same blowing ratio and duty cycle. The core of the jet is even further from the wall than in the $F=0.0238$ case of Fig. 14, particularly at $x/D=7$ and 14. Compared to the lower-frequency cases, the initial transient takes an even longer fraction of the cycle period at $F=0.1905$. The jet never achieves the steady state observed at the lower frequencies. Although jet liftoff with a starting vortex is still clear when the jets turn on, there is significant jet fluid near the wall during the "off" portion of the cycle. This results from the continuous flow from the holes at this frequency, shown in Fig. 13 and explained above.

Figure 17 shows the film cooling effectiveness contour plots for $B=1.0$ and DC=0.5 at various frequencies. The best pulsing case is with $F=0.1905$. Figure 18 shows the centerline and spanwise-averaged film-cooling effectiveness for these cases with the $B=0.5$ and 1.0 steady cases included for comparison. In general, in agreement with the $B=0.5$ cases discussed above, higher-frequency results in lower effectiveness and the pulsing cases are not as good as the steady blowing case with the same coolant mass flow rate. The variation between the $F=0.0238$ to 0.0953 cases is small. Significant liftoff is observed in all of these cases regardless of the initial transient in the pulsing cycle, so changing the frequency has only a small effect. The steady $B=0.5$ case still has the best film-cooling effectiveness; however, the pulsed case with $F=0.1905$ has an improved upstream film-cooling effectiveness over the $B=1.0$ steady case. The higher-frequency results in a higher off-state velocity as shown in Figs. 9 and 13, which results in more coolant near the surface to increase the film-cooling effectiveness. This is supported by Fig. 16, which shows that the jet is near the wall for a larger fraction of the cycle. Since the $F=0.1905$ case has more liftoff than the steady or lower-frequency cases during the valve-on time, it must be the off-state flow that makes the effectiveness higher.

In the present study, pulsing did not provide a benefit over the best steady blowing case. It is, however, possible that pulsing may have overall beneficial effects with other geometries or when combined with an unsteady mainflow. It is notable that if pulsing occurs naturally, particularly at high frequencies, that trends with

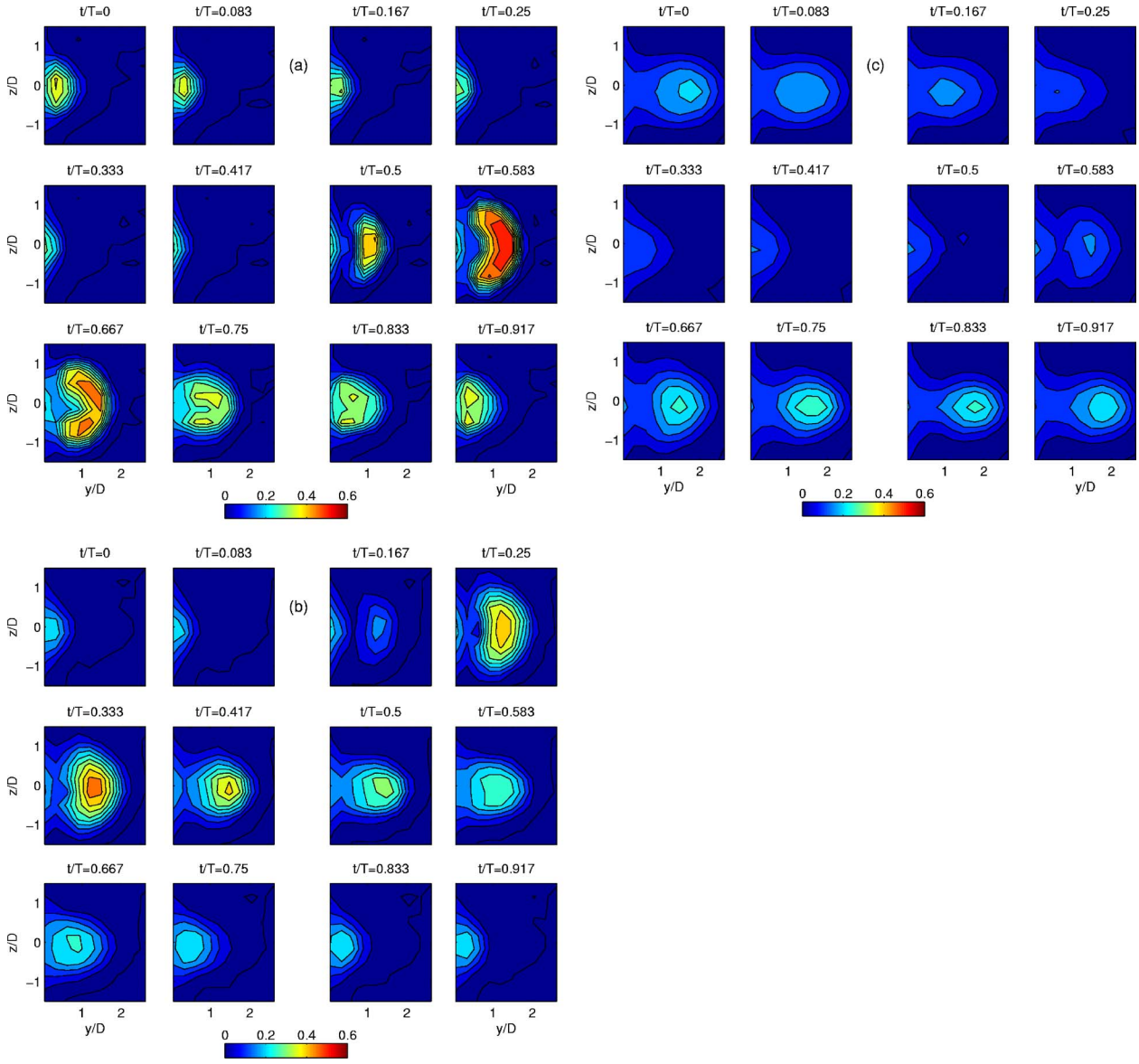

Fig. 16 Phase-averaged dimensionless flow temperature contours θ in *y-z* plane: $B=1.0$, $F=0.1905$, DC=0.5: (*a*) $x/D=3.5$, (*b*) $x/D=7$, and (*c*) $x/D=14$

blowing ratio may be different than in steady cases. Comparison of the $B=0.5$ and 1.0 steady cases of Fig. 6 show that η is higher with $B=0.5$ due to the jet liftoff that occurs when $B=1.0$. In contrast, comparison of the $F=0.1905$, DC=0.5 cases with $B=0.5$ in Fig. 12 and $B=1.0$ in Fig. 18 shows that the effectiveness is higher for the $B=1.0$ case. High-frequency pulsing helps mitigate jet liftoff effects, and the higher mass flow with $B=1.0$ results in higher effectiveness.

Duty-Cycle Effects. The frequency was held constant, and the

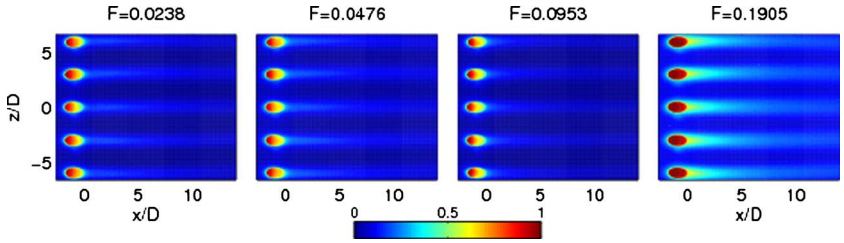

Fig. 17 Film-cooling effectiveness contours at various pulsing frequencies with nominal $B=1.0$ and DC=0.5

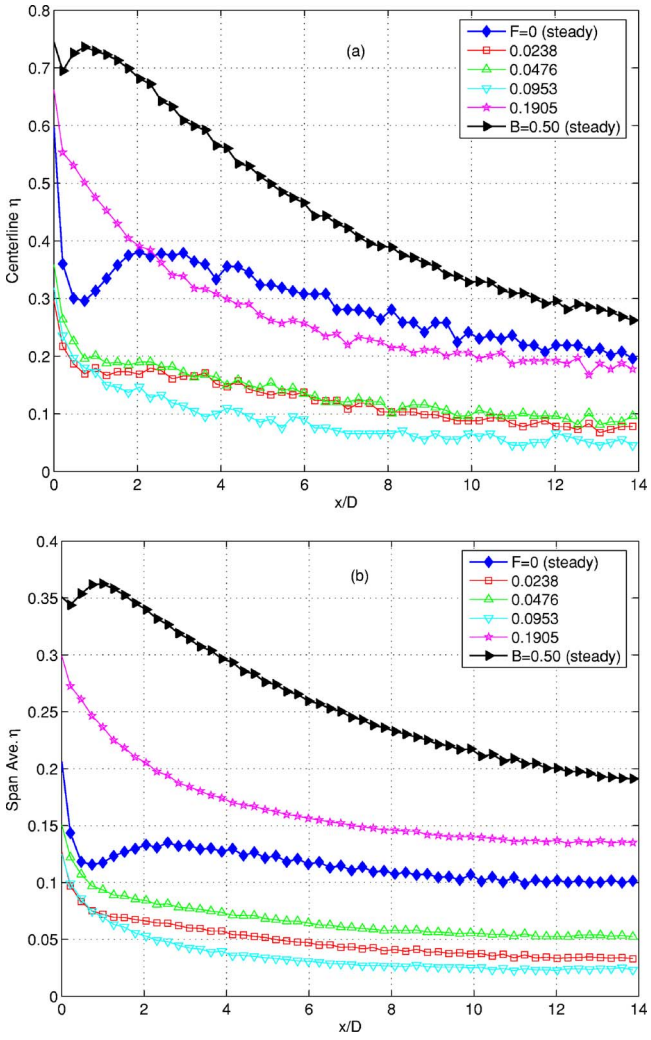

Fig. 18 Film-cooling effectiveness for nominal $B=1.0$ and DC $=0.5$ cases, with steady $B=0.5$ and $B=1.0$ cases included for comparison: (*a*) centerline and (*b*) spanwise averaged

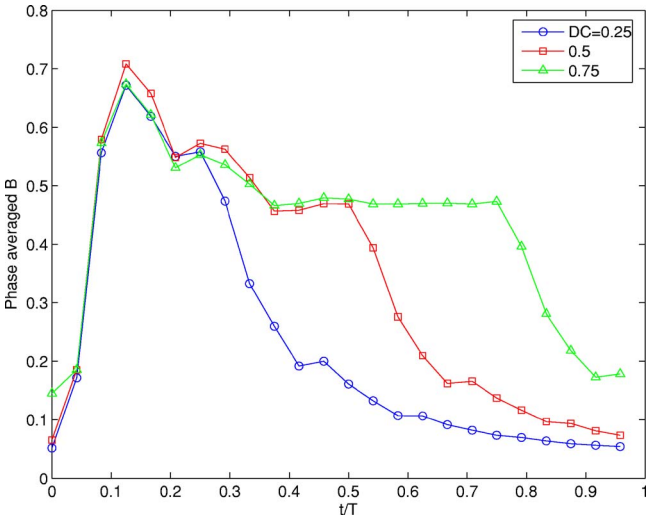

Fig. 19 Phase-averaged blowing ratio at various duty cycles with nominal $B=0.5$ and $F=0.0238$

duty cycle was varied in order to determine the reaction of the jet flow. Figure 19 shows the phase averaged blowing ratio at three duty cycles for $B=0.5$ and $F=0.0238$. It shows that as the duty cycles increases, more coolant mass is being used to protect the test surface. This idea is reinforced in Fig. 20, the film-cooling effectiveness contour plots for the same cases, where the effectiveness increases proportionally to the duty cycle. Figure 21 shows the centerline and spanwise-averaged film-cooling effectiveness for this case. The plots follow a logical trend where as the duty cycle increases, more coolant mass over a larger fraction of the cycle is being used to protect the test surface, and thus the film-cooling effectiveness increases. At DC=0.5, the effectiveness is approximately half that of the steady case, which is to be expected. The other duty cycles follow, respectively.

Figure 22 is of the phase-averaged blowing ratio at various duty cycles for $B=1.0$ and $F=0.0238$. It is consistent with the trends observed in Fig. 19. As the duty cycle increases, the coolant mass flow increases proportionally. Figure 23 shows the film-cooling effectiveness contour plot for $B=1.0$ and $F=0.0238$. As in Figs. 20 and 21, the effectiveness increases proportionally with the duty cycle. Figure 24 shows the centerline and spanwise-averaged film-cooling effectiveness for the same cases. The effectiveness at DC=0.5 is ~50% of that at DC=1.0 (steady state), and the other duty cycles follow the same trend. Thus, at low frequencies, the film-cooling effectiveness increases with an increasing duty cycle, independent of the velocity of the pulsing jet.

Figures 25 and 26 show the phased-averaged velocity profiles for $B=1.0$ and $F=0.1905$ with DC=0.25 and 0.75, respectively. The DC=0.5 case is not shown, but it is very similar to the $F=0.1905$, $B=0.5$, DC=0.5 case of Fig. 8, but with proportionally higher velocities. Figure 27 shows the phase averaged blowing ratios for the $B=1.0$, $F=0.1905$ cases. In the DC=0.25 case, the jet turns on and off at approximately $t/T=0.417$ and 0.75, respectively. The higher velocities remain in the upstream region of the hole with phase averaged B varying between 0.4 and 0.7. With DC=0.75 the jet turns on at approximately $t/T=0.583$ and off at $t/T=0.25$. The on-state B reaches 1.0, but the off-state value remains as high as 0.7. The average jet velocity increases as the duty cycle increases. The on-state B reaches the steady blowing value of 1.0 for DC of 0.5 or higher. High frequencies raise the off-state jet velocity, as shown above in Figs. 9 and 13. Higher duty cycles increase the off-state velocity by reducing the valve-closed time available for the velocity to drop.

Figure 28 shows the film-cooling effectiveness contour plots for $B=1.0$ and $F=0.1905$ with varying duty cycle. Figure 29 shows the centerline and spanwise averaged film cooling effectiveness for these cases. At this higher frequency, the best case is with DC=0.5, where the effectiveness is 40% higher than the steady case directly downstream of the holes at the centerline and 40% higher at all x/D locations in the spanwise-averaged data. This case was already discussed above. The DC=0.25 and 0.75 cases show some improvement over the steady case, and with lower coolant mass flow, but the effectiveness is not as high as in the DC=0.5 case. In the DC=0.25 case, this is likely due to the lower

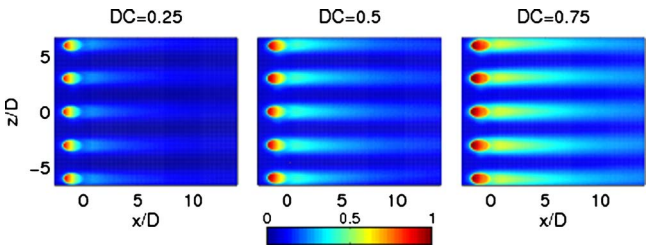

Fig. 20 Film-cooling effectiveness contours at various duty cycles with nominal $B=0.5$ and $F=0.0238$

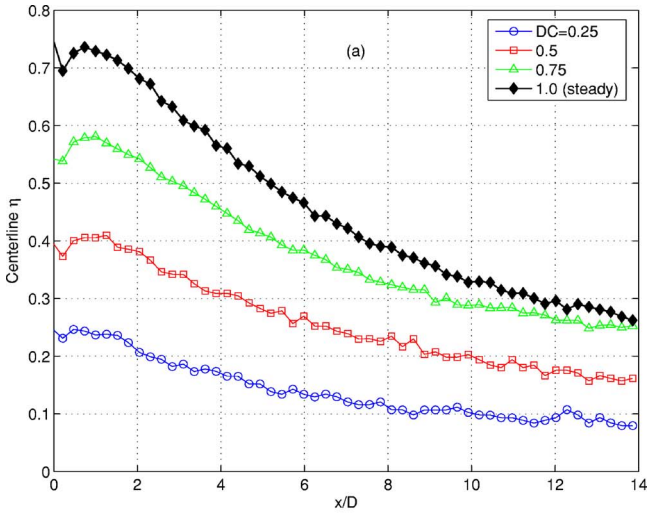

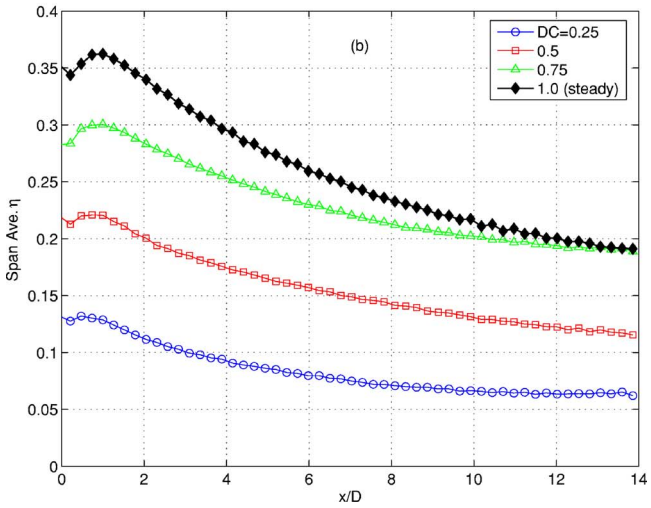

Fig. 21 Film-cooling effectiveness for nominal $B=0.5$ and $F=0.0238$ cases: (*a*) centerline and (*b*) spanwise averaged

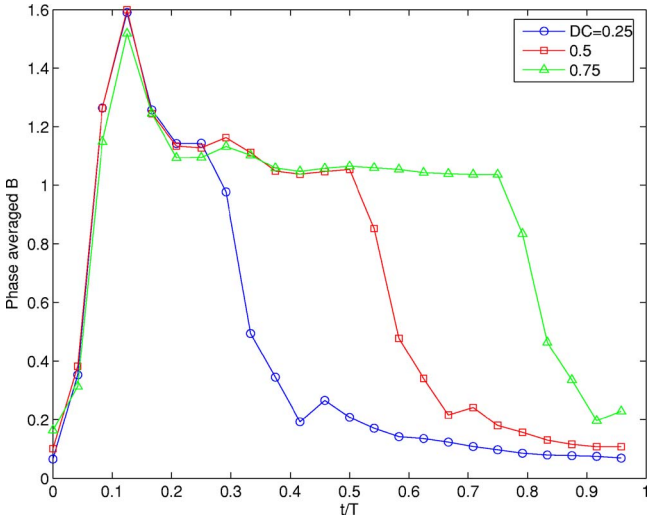

Fig. 22 Phase-averaged blowing ratio at various duty cycles with nominal $B=1.0$ and $F=0.0238$

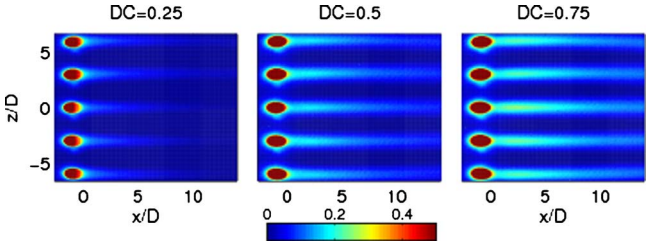

Fig. 23 Film-cooling effectiveness contours at various duty cycles with nominal $B=1.0$ and $F=0.0238$

coolant mass flow. In the DC=0.75 case, the jets are on for such a large fraction of the cycle that conditions start to approach those of the steady blowing case and the effects of pulsing seen at DC =0.5 are diminished.

Conclusions

For the geometry considered, steady injection with a blowing ratio of $B=0.5$ resulted in the highest film-cooling effectiveness. Higher blowing ratios resulted in lower effectiveness due to jet liftoff. Pulsing the coolant jet induced a high startup velocity until the jet reached a steady state. The startup effect momentarily increased jet liftoff. Higher frequencies result in more startups per

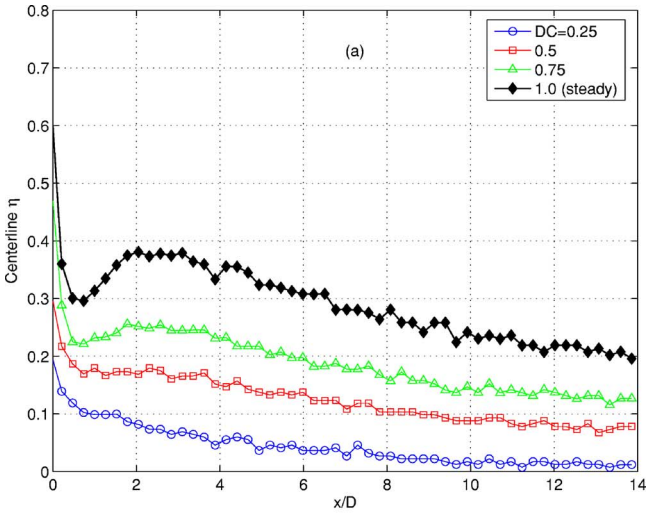

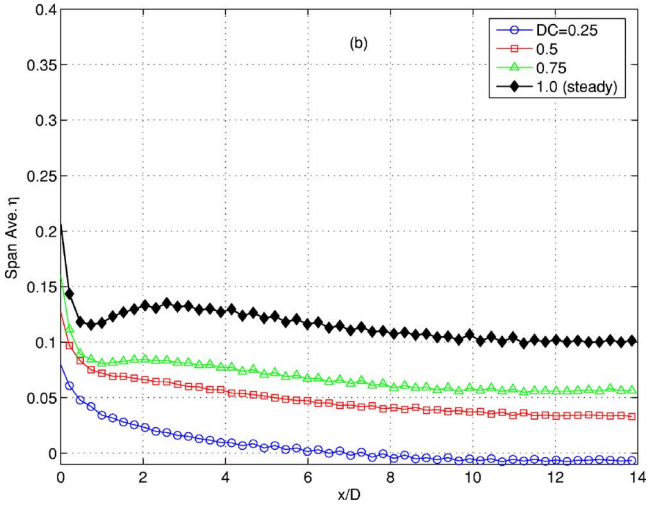

Fig. 24 Film-cooling effectiveness for nominal $B=1.0$ and $F=0.0238$ cases: (*a*) centerline and (*b*) spanwise averaged

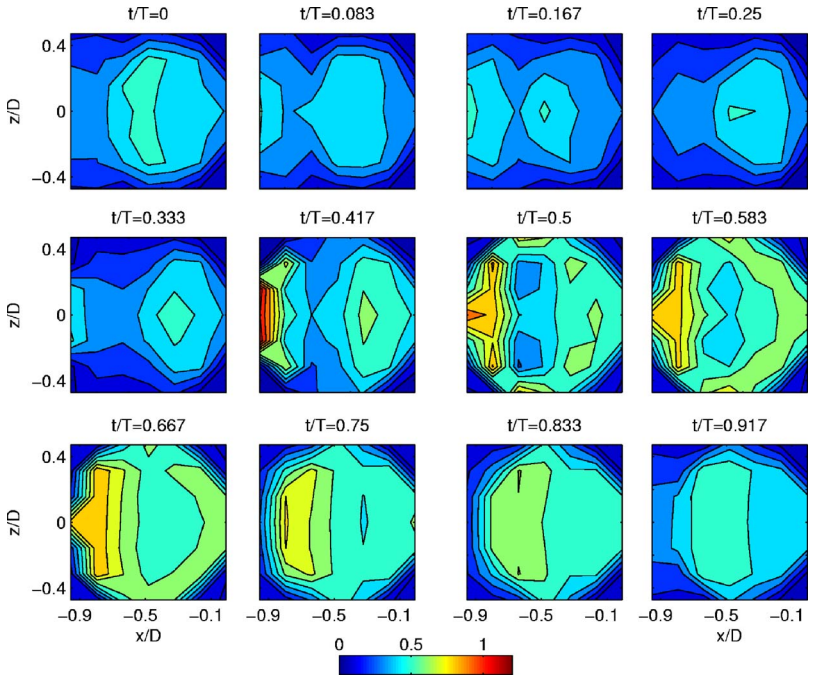

Fig. 25 Phase-averaged velocity profiles, U_{jet}/U_{∞}, at exit plane of center hole with $B=1.0$, $F=0.1905$, and DC=0.25

unit time, such that the starting period occupies a larger fraction of the total pulsing cycle. Thus higher frequencies tend to result in lower effectiveness. At the highest frequencies tested, however, this trend was reversed. There is insufficient time for the jets to reach a steady on or off condition at the highest frequencies. This results in some low-momentum flow from the hole during the "off" portion of the cycle. The low-momentum fluid does not lift off, and therefore increases film-cooling effectiveness. With $B=1.0$, there was jet liftoff in the steady case, and high-frequency pulsing helped to increase film cooling effectiveness with lower

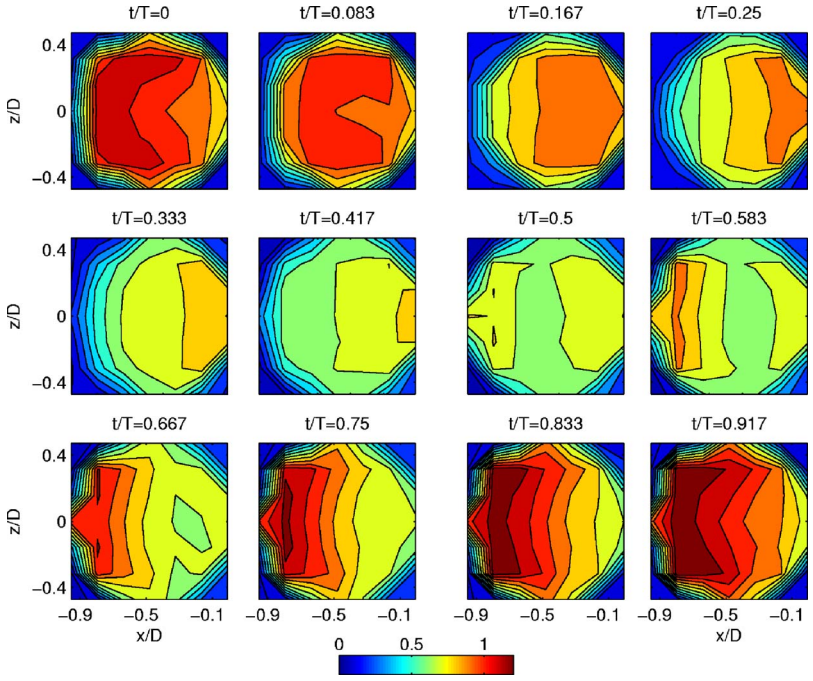

Fig. 26 Phase-averaged velocity profiles, U_{jet}/U_{∞}, at exit plane of center hole with $B=1.0$, $F=0.1905$, and DC=0.75

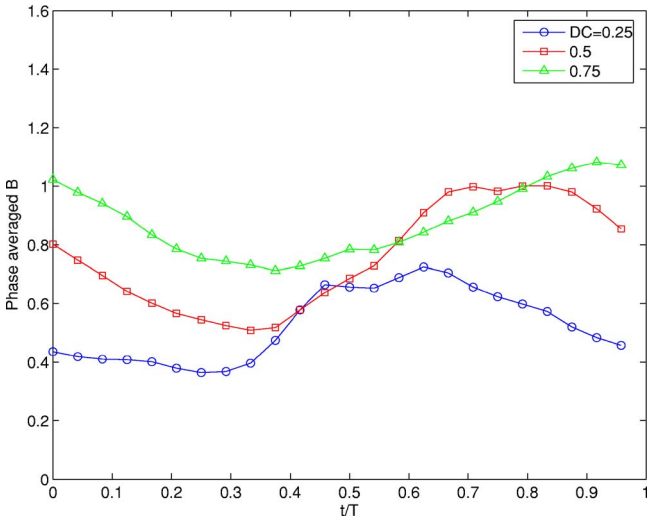

Fig. 27 Phase-averaged blowing ratio at various duty cycles with nominal B=1.0 and F=0.1905

total coolant mass flow. Results, as expected, showed that as the duty cycle increased, more coolant mass flow over a larger fraction of the cycle increased the film-cooling effectiveness.

Acknowledgment

This work was done under the Trident Scholar Program at the U.S. Naval Academy.

Nomenclature

B = $\rho_{\text{jet}}U_{\text{jet}}/\rho_\infty U_\infty$, blowing ratio
D = film-cooling hole diameter
DC = duty cycle, fraction of time valves are open
F = dimensionless frequency, fD/U_∞
f = frequency, Hz
L = length of film-cooling hole channel
T = temperature or pulsing period
t = time
U = velocity
x = streamwise coordinate, distance from the trailing edge of film-cooling holes
y = normal coordinate, distance from the wall
z = spanwise coordinate, distance from centerline of center hole
η = film-cooling effectiveness, $(T_{aw}-T_\infty)/(T_{\text{jet}}-T_\infty)$
ρ = density
θ = dimensionless temperature, $(T-T_\infty)/(T_{\text{jet}}-T_\infty)$

Subscripts

aw = adiabatic wall
jet = film-cooling jet velocity or plenum temperature
∞ = mainstream

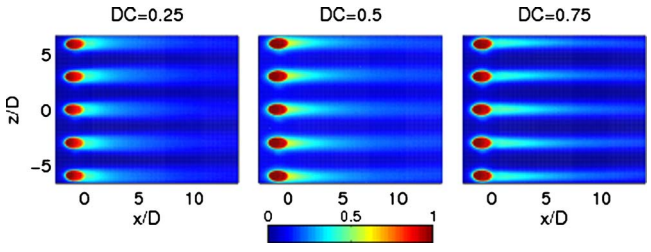

Fig. 28 Film-cooling effectiveness contours at various duty cycles with nominal B=1.0 and F=0.1905

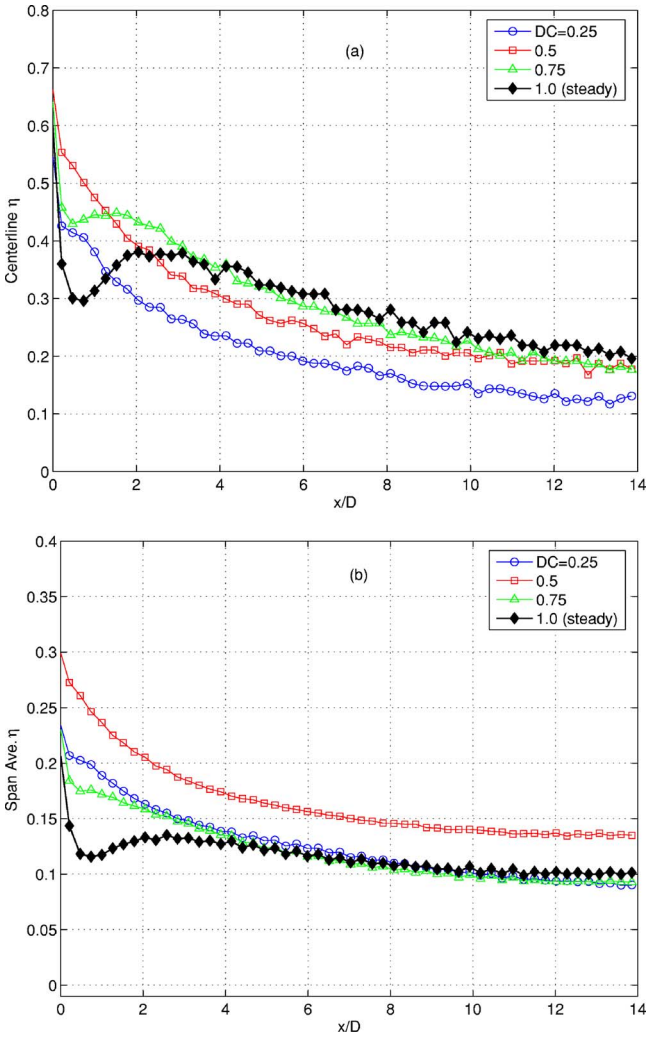

Fig. 29 Film-cooling effectiveness for nominal B=1.0 and F=0.1905 cases: (*a*) centerline and (*b*) spanwise averaged

References

[1] Ekkad, S. V., Ou, S., and Rivir, R. B., 2006, "Effect of Jet Pulsation and Duty Cycle on Film Cooling From a Single Jet on a Leading Edge Model," ASME J. Turbomach., **128**, pp. 564–571.
[2] Bons, J. P., Rivir, R. B., MacArthur, C. D., and Pestian, D. J., 1996, "The Effect of Unsteadiness on Film Cooling Effectiveness," Wright Laboratory Technical Report No. WLTR-96-2096.
[3] Ligrani, P. M., Gong, R., Cuthrell, J. M., and Lee, J. S., 1996, "Bulk Flow Pulsations and Film Cooling—I, Injectant Behavior, II. Flow Structure and Film Effectiveness," Int. J. Heat Mass Transfer, **39**, pp. 2271–2292.
[4] Seo, H. J., Lee, J. S., and Ligrani, P. M., 1999, "Effects of Bulk Flow Pulsations on Film Cooling From Different Length Injection Holes at Different Blowing Ratios," ASME J. Turbomach., **121**, pp. 542–550.
[5] Jung, I. S., Lee, J. S., and Ligrani, P. M., 2002, "Effects of Bulk Flow Pulsations on Film Cooling With Compound Angle Holes: Heat Transfer Coefficient Ratio and Heat Flux Ratio," ASME J. Turbomach., **124**, pp. 142–151.
[6] Bons, J. P., Sondergaard, R., and Rivir, R. B., 2002, "The Fluid Dynamics of LPT Blade Separation Control Using Pulsed Jets," ASME J. Turbomach., **124**, pp. 77–85.
[7] Schulte, V., and Hodson, H. P., 1998, "Prediction of the Becalmed Region for LP Turbine Profile Design," ASME J. Turbomach., **120**, pp. 839–846.
[8] Volino, R. J., 2003, "Separation Control on Low-Pressure Turbine Airfoils Using Synthetic Vortex Generator Jets," ASME J. Turbomach., **125**, pp. 765–777.
[9] Bons, J. P., MacArthur, C. D., and Rivir, R. B., 1996, "The Effect of High Free-Stream Turbulence on Film Cooling Effectiveness," ASME J. Turbomach., **118**, pp. 814–825.
[10] Burd, S., and Simon, T. W., 2000, "Effects of Hole Length, Supply Plenum Geometry, and Freestream Turbulence on Film Cooling Performance," NASA, CR-2000-210336.
[11] Schmidt, D. L., Sen, B., and Bogard, D. G., 1996, "Effects of Surface Roughness on Film Cooling," ASME Paper No. 96-GT-299.

[12] Pedersen, D. R., Eckert, E. R. G., and Goldstien, R. J., 1977, "Film Cooling With Large Density Differences Between the Mainstream and the Secondary Fluid Measured by the Heat-Mass Transfer Analogy," ASME J. Heat Transfer, **99**, pp. 620–627.
[13] Kohli, A., and Bogard, D. G., 1998, "Fluctuating Thermal Field in the Near-Hole Region for Film Cooling Flows," ASME J. Turbomach., **120**, pp. 86–91.
[14] Sinha, A. K., Bogard, D. G., and Crawford, M. E., 1991, "Film Cooling Effectiveness Downstream of a Single Row of Holes With Variable Ratio," ASME J. Turbomach., **113**, pp. 442–449.
[15] Pietrzyk, J. R., Bogard, D. G., and Crawford, M. E., 1990, "Effect of Density Ratio on the Hydrodynamics of Film Cooling," ASME J. Turbomach., **112**, pp. 437–443.
[16] Coulthard, S. M., Volino, R. J., and Flack, K. A., 2007, "Effect of Jet Pulsing on Film Cooling—Part II: Heat Transfer Results," ASME J. Turbomach., **129**(2), pp. 247–257.
[17] Coulthard, S. M., Volino, R. J., and Flack, K. A., 2005, "Effect of Unheated Starting Lengths on Film Cooling Experiments," ASME Paper No. HT2005-72392.

Effect of Jet Pulsing on Film Cooling—Part II: Heat Transfer Results

Sarah M. Coulthard
Department of Mechanical Engineering,
Stanford University,
Stanford, CA 94305

Ralph J. Volino
e-mail: volino@usna.edu

Karen A. Flack

Department of Mechanical Engineering,
United States Naval Academy,
Annapolis, MD 21402

Pulsed film cooling was studied experimentally to determine its effect on film-cooling effectiveness and heat transfer. The film-cooling jets were pulsed using solenoid valves in the supply air line. Cases with a single row of cylindrical film-cooling holes inclined at 35 deg to the surface of a flat plate were considered at blowing ratios of 0.25, 0.5, 1.0, and 1.5 for a variety of pulsing frequencies and duty cycles. Temperature measurements were made using an infrared camera and thermocouples. The plate was equipped with constant flux surface heaters, and data were acquired for each flow condition with the plate both heated and unheated. The local film-cooling effectiveness, Stanton numbers, and heat flux ratios were calculated and compared to baseline cases with continuous blowing and no blowing. Stanton number signatures on the surface provided evidence of flow structures, including horseshoe vortices wrapping around the film-cooling jets and vortices within the jets. Pulsing tends to increase Stanton numbers, and the effect tends to increase with pulsing frequency and duty cycle. Some exceptions were observed, however, at the highest frequencies tested. Overall heat flux ratios also show that pulsing tends to have a detrimental effect with some exceptions at the highest frequencies. The best overall film cooling was achieved with continuous jets and a blowing ratio of 0.5. The present results may prove useful for understanding film-cooling behavior in engines, where mainflow unsteadiness causes film-cooling jet pulsation. [DOI: 10.1115/1.2437230]

Introduction

Film cooling has been studied extensively in order to provide improved cooling of the airfoils in gas turbine engines and thus increase the life of the airfoils and allow for higher turbine inlet temperatures. Approximately 20–25% of compressor air is used for cooling of high-performance turbine engines [1]. If the amount of required coolant air could be reduced, engine efficiency would increase. The present study investigates whether pulsing the film-cooling bleed air might allow for a reduction in coolant flow while still providing adequate protection to the turbine airfoils.

Pulsing is of interest because it naturally occurs due to periodic unsteadiness in engines and because it might be used to deliberately control and improve film-cooling performance. Coulthard et al. [2], in Part I of the present study, discuss mechanisms by which pulsed film cooling could potentially be beneficial. As also discussed in Part I [2], only a few studies have considered pulsed film cooling, and only one previous study, Ekkad et al. [1], has considered pulsing for the purpose of improving film cooling. Ekkad et al. [1] studied a leading-edge model with a single film-cooling hole. They stated that pulsed jets increase the ability to effectively protect the surface and slightly lower heat transfer coefficients compared to continuous jets.

In the present study, film-cooling jets were pulsed using solenoid valves in the supply air line. The valves cycled between fully on and fully off positions. The geometry consisted of a flat plate with a single row of five round holes inclined at 35 deg to the surface and parallel to the streamwise direction. The holes were spaced $3D$ apart, center to center, with a length to diameter ratio $L/D=4$. The geometry has been used in several studies with continuous jets, as noted in Part I [2]. Among these are a few with surface heat transfer coefficient results such as Sen et al. [3]. Blowing ratios of 0.25, 0.5, 1.0, and 1.5 were investigated with varying frequencies and duty cycles. Phase-averaged jet velocity and flow temperature distributions, and film-cooling effectiveness results were presented in Part I [2]. Phase averaging shows the behavior of the flow as it changes during the jet pulsing cycle.

The results in Part I [2] show that pulsing generally caused film-cooling effectiveness to drop. Pulsing changed jet liftoff and left the surface unprotected during part of the pulsing cycle. At low blowing ratios (e.g., $B=0.5$), steady blowing resulted in effective cooling with little jet liftoff. Pulsing caused more liftoff, particularly during the initial transient at the start of each pulsing cycle. As pulsing frequency was increased, this transient occupied an increasingly significant fraction of the cycle, and effectiveness dropped. The trend began to reverse at the highest frequencies tested due to a lag between the response of the coolant supply plenum and the upstream valves. The lag resulted in some low-momentum flow during the valve-off portion of the cycle, which helped to improve the effectiveness.

At high blowing ratios (e.g., $B=1.0$), steady blowing resulted in considerable jet liftoff and low effectiveness. Pulsing at low frequencies does not help for the same reasons discussed above. At higher frequencies, however, the low momentum, valve-off flow, which did not lift off, raised the effectiveness above the steady $B=1.0$ case effectiveness while using less coolant mass flow. The effectiveness is much lower, however, than in the steady $B=0.5$ case.

These results are different than those presented by Ekkad et al. [1], presumably because of the geometry difference. In the present flat-plate study, jet liftoff lowers effectiveness at high blowing ratios and pulsing can affect liftoff. With a leading-edge geometry, as in Ekkad et al. [1], the impinging mainflow tends to keep the coolant near the surface even at high blowing ratios. The effectiveness tends to vary with the total coolant mass flow, whether pulsed or steady.

Film-cooling effectiveness only partially describes the effect of film cooling on heat transfer to a surface. Film cooling can also affect the heat transfer coefficient. In the present paper, heat transfer coefficients, shown as dimensionless Stanton number ratios,

Contributed by the International Gas Turbine Institute of ASME for publication in the JOURNAL OF TURBOMACHINERY. Manuscript received May 24, 2006; final manuscript received May 31, 2006. Review conducted by David Wisler. Paper presented at the ASME Turbo Expo 2006: Land, Sea and Air (GT2006), Barcelona, Spain, May 8–11, 2006. Paper No. GT2006-91274.

are presented for the steady and pulsed cooling cases of Part I [2]. The effectiveness and heat transfer coefficient results are then combined as overall heat flux ratios.

Experimental Facilities and Techniques

Experiments were conducted with an open-loop subsonic wind tunnel with a test plate attached at the exit of the contraction, and a plenum to supply the film-cooling jets. The wind tunnel, described more completely in Part I [2], was comprised of a blower, a diffuser with three screens, a heat exchanger to maintain air nominally at 20°C, a honeycomb, a settling chamber with three screens, and a nozzle with an 8.8 area reduction. The exiting mainstream air was uniform in temperature and velocity to within 0.1°C and 1%, respectively. The freestream turbulence intensity at the nozzle exit was 1%. Air exiting the nozzle formed a wall jet at $U_\infty = 8$ m/s along the flat test wall. The wall jet configuration is based on the facility of Burd and Simon [4].

The film-cooling supply plenum was a box with 0.38 m $\times$ 0.18 m $\times$ 0.36 m inside dimensions. It was supplied by a manifold connected to a high-pressure air source. The supply pressure was adjusted to vary the blowing ratio from $B = 0.25$ to 1.5. The air passed through small diameter, fast-response solenoid valves between the manifold and the plenum. The plenum contained a finned tube heat exchanger. Warm water at 30°C circulated through the tubes, and the air from the valves passed over the tubes in a cross-flow manner, maintaining the temperature of the coolant jets at ~27°C. As explained in Part I [2], the capacitance effect of the plenum volume and the mechanical response time of the valves resulted in a lag of ~0.004 s between the opening and closing of the valves and the corresponding response of the film-cooling jets. At the highest frequency considered (80 Hz), the pulsing period and valve-jet lag time were comparable, and the jets never fully turned on or off in response to the valve opening and closing. At lower pulsing frequencies, the period for a pulse was large compared to the valve-jet lag; thus, the effects of the lag were not as significant. Pulsing of the film-cooling flow from a gas turbine airfoil would similarly depend on the geometry of the internal passages upstream of the film-cooling hole and, in the case of controlled pulsing, would depend on the location of the actuator upstream of the hole.

The test wall was constructed of polyurethane foam with a thermal conductivity of 0.03 W/mK. The dimensions were 0.38 m wide, 44 mm thick, and 1.17 m long, with a starting length of 13.3D upstream of the row of film-cooling holes. Metal foil heating elements encapsulated in silicon rubber coatings (Minco, Inc.) were placed on the foam surface. Heaters covered the full surface of the wall upstream and downstream of the holes. The small areas between the holes were unheated. Coulthard et al. [5], using the same facility as the present study, showed that heating the wall upstream of the holes had a measurable effect on Stanton number ratios, $\mathrm{St}_f/\mathrm{St}_o$, particularly in the region just downstream of the holes. The ratio $\mathrm{St}_f/\mathrm{St}_o$ is a comparison of the Stanton number with film cooling (St_f) to the Stanton number without film cooling (St_o) in an otherwise equivalent flow with the same surface heating conditions. A heated starting length causes both St_f and St_o to drop due to a thicker thermal boundary layer at the start of the heated region. The effect on St_o is greater, however, so the ratio rises. Coulthard et al. [5] also showed that heating in the small regions between the film cooling holes has only a small effect on Stanton number ratios.

The heaters were covered with a 0.79 mm thick black sheet of Formica® laminate to provide a smooth test surface. The heaters provided a heat flux uniform to within 1.4%. Any small spatial nonuniformity in the heat flux at the test surface was quantified by examining the local surface temperature in a case with no film cooling and the cooling holes taped over (i.e., simple flow over a flat plate with an unheated starting length). This allowed for correction of the local heat flux in all subsequent tests for computation of Stanton numbers. Stanton number ratios were unaffected by the corrections, since the corrections canceled when the ratios were computed. The film-cooling geometry consisted of a single row of five round holes inclined at 35 deg to the surface and parallel to the streamwise direction. The sharp-edged holes had a diameter of $D = 19.05$ mm spaced 3D apart, center to center, and with a length to diameter ratio $L/D = 4$. A 1.6 mm thick trip was installed 11D upstream of the leading edge of the holes to ensure a turbulent boundary layer. The test plate was instrumented with type E thermocouples of 76.2 μm dia wire. The thermocouples were located between the heaters and Formica. Thermocouples were also placed in the film-cooling plenum, at the plenum-side end of the outermost film-cooling hole, at the wind tunnel exit, on the back of the test plate, in the ambient air, on the wall of the room to measure the surrounding temperature for radiation corrections, and in ice water as a reference. An infrared (IR) camera (FLIR Systems Merlin model) with a Stirling cooled detector was used to measure the surface temperature field of the test wall. The temperature resolution of the camera was 0.05°C. The camera had a 255 $\times$ 318 pixel detector and was positioned such that each pixel corresponded to a 1 mm $\times$ 1 mm area on the test wall. The field of view on the test wall corresponded to 13.4D $\times$ 16.7D. The emissivity of the test wall was determined to be 0.95 through comparison of IR images of the test wall and a surface of known emissivity (black electrical tape) at the same temperature.

The boundary layer 0.8D upstream of film-cooling hole leading edge had a momentum thickness Reynolds number of 550 and a shape factor of 1.48. The local skin friction coefficient at this location was 5.4×10^{-3}. With the upstream heaters active, the enthalpy thickness Reynolds number 0.8D upstream of the holes was 470. The Reynolds number based on hole diameter and mainstream velocity was 10,000.

The film-cooling jet flow uniformity was measured by traversing constant current and hot-wire probes over the hole exit. This is described in more detail in Part I [2]. The jet temperature was very uniform and matched the plenum temperature to within 0.2°C, indicating very little cooling of the jet flow as it passed through the hole channel. Since the jets were only heated to ~7°C above the main flow temperature, the density ratio of jets to main flow was 0.98. Hence, the blowing and velocity ratios were essentially equal. The temperature and velocity measurements were compared among the five film-cooling holes. The hole to hole variation in temperature was 2% of the jet to mainstream temperature difference, and velocity variation was 8% of the mainstream velocity.

The Stanton number, film-cooling effectiveness, and heat flux ratio were defined, respectively, as follows:

$$\mathrm{St} = \frac{q''_{\mathrm{conv}}}{\rho C_p U_\infty (T_w - T_{aw})} \tag{1}$$

$$\eta = \frac{T_{aw} - T_\infty}{T_{\mathrm{jet}} - T_\infty} \tag{2}$$

$$\frac{q''_f}{q''_o} = \frac{\mathrm{St}_f}{\mathrm{St}_o}\left(1 - \frac{\eta}{\phi}\right), \quad \phi = \frac{T_w - T_\infty}{T_{\mathrm{jet}} - T_\infty} = 0.6 \tag{3}$$

To determine the film cooling effectiveness and Stanton number, two tests were conducted for each experimental condition. The surface temperature, heat flux, and flow temperatures were measured with the plate unheated, and again with the heaters on. The convective heat flux was determined based on an energy balance at the plate surface.

$$q''_{\mathrm{conv}} = q''_{\mathrm{heater}} - q''_{\mathrm{rad}} - q''_{\mathrm{cond}} \tag{4}$$

The total power supplied to the heaters was known from the voltage applied and the electrical resistance. Conduction losses through the back of the test wall, q''_{cond}, were computed based on temperatures measured with thermocouples at the heaters and on

the back of the test wall. The conduction correction is applied uniformly to the whole surface and was a small (~1%) fraction of the total power supplied to the heaters. A larger (~15%) local radiation correction, q''_{rad}, was also subtracted from the heater power to determine the convective heat flux q''_{conv}. The radiation correction was computed on a pixel by pixel basis using the local surface temperature of the test wall measured with the IR camera, the temperature of the wall in the room opposite the test wall, and the emissivity of the test wall.

If q''_{conv} were exactly zero in the unheated wall case, T_{aw} would equal the measured T_w in this case, and η could be computed directly from Eq. (2). This is only approximately correct, however. Since q''_{rad} was not zero, $q''_{conv}=-q''_{rad}-q''_{cond}\neq 0$. Assuming $q''_{conv}=0$ was found to result in errors in η up to ~6%. Instead of assuming $q''_{conv}=0$ for the unheated case, Eqs. (1) and (2) were each written separately for the heated and unheated tests, and q''_{conv}, T_∞, T_{jet}, and T_w were measured independently for each test. The Stanton number and film-cooling effectiveness were assumed equal for the two tests, leaving four equations with four unknowns (St, η, $T_{aw\text{-unheated}}$ and $T_{aw\text{-heated}}$). The equations were solved simultaneously for the four unknowns. The measured flow temperatures need not be set exactly the same for the heated and unheated tests, and the computed T_{aw} for the two tests could be different at any given location. In the present study, however, T_∞ and T_{jet} were set consistently from test to test so T_{aw} for the unheated and heated cases typically agreed to within 0.2°C at every location.

The heat flux ratio was calculated based on the Stanton number ratio and film-cooling effectiveness. The constant 0.6 in Eq. (3) represents a dimensionless temperature ratio $\phi=(T_w-T_\infty)/(T_{jet}-T_\infty)$. The numerical value of 0.6 is taken from Sen et al. [3] and others, and is a typical value for this temperature ratio under engine conditions. Note that if $\eta>0.6$, q''_f/q''_o will be <0, indicating a reversal of the heat transfer direction. This is physically possible. Since airfoils are fabricated from metals, particularly effective localized cooling could cause heat to flow by conduction through the surface from adjacent warmer regions and then out into the fluid. Also possible, as explained by Mouzon et al. [6] is that the effective cooling would cause a local drop in the airfoil surface temperature, lowering the 0.6 in Eq. (3) and changing the actual heat flux ratio to a low-magnitude positive value.

The thermocouples and IR camera were calibrated against a precision blackbody source. The uncertainty in the measured temperature was 0.2°C, the uncertainty in the measured velocity and mass flow was 3%, and the uncertainty in the atmospheric pressure was 1%. The uncertainties in the film-cooling effectiveness and the Stanton number were determined using standard propagation of error with a 95% confidence interval. The uncertainty in the film-cooling effectiveness was determined to be 6%, and the uncertainty in the Stanton number was 8%. The uncertainty in the ratio of two Stanton numbers is 11%. The uncertainty in the heat flux ratio is 13%.

Baseline tests were conducted at blowing ratios of 0.25, 0.5, 1.0, and 1.5 with continuous cooling. Thermocouple data and the wall temperature distributions, as measured with the IR camera, were documented for each case for heated and unheated wall conditions. Pulsed-cooling cases were documented at nominal blowing ratios of 0.5 and 1.0. The nominal blowing ratio is given as the expected blowing ratio during the valve-open portion of the jet pulsing cycle. The jet velocity was set by measuring the jet velocity with a hot wire and adjusting the supply pressure to the solenoid valves with the valves fully open. The time-averaged blowing ratio for the full jet pulsing cycle is approximately equal to the specified nominal blowing ratio times the jet duty cycle. Pulsed cooling cases at $B=0.5$ were documented with a jet duty cycle of DC=0.5 and dimensionless pulsing frequencies of $F=fD/U_\infty$ =0.0119, 0.0238, 0.0476, 0.0953, and 0.1905 (corresponding to dimensional frequencies of 5 Hz, 10 Hz, 20 Hz, 40 Hz, and 80 Hz). The duty cycle is the fraction of the cycle that the valves are open. For example, a 10 Hz pulsing frequency with DC =0.25 means the valves are open for 0.025 s and then closed for 0.075 s each cycle. The dimensionless frequencies studied are in the range of expected wake passing frequencies in an engine. Pressure fluctuations due to wake passing cause natural pulsation in film-cooling flow, and the frequencies selected for controlled pulsing would likely be of the same order of magnitude as the wake passing frequency. Cases with $B=1.0$ and DC=0.5 were documented with $F=0.0238$, 0.0476, 0.0953, and 0.1905. To investigate duty cycle effects, additional cases with $B=0.5$ and F =0.0238 were documented with DC=0.25 and 0.75. At $B=1.0$, four additional cases were studied with $F=0.0238$ and 0.1905, and DC=0.25 and 0.75. For each of the pulsed flow cases, the same measurements were made as in the steady flow cases.

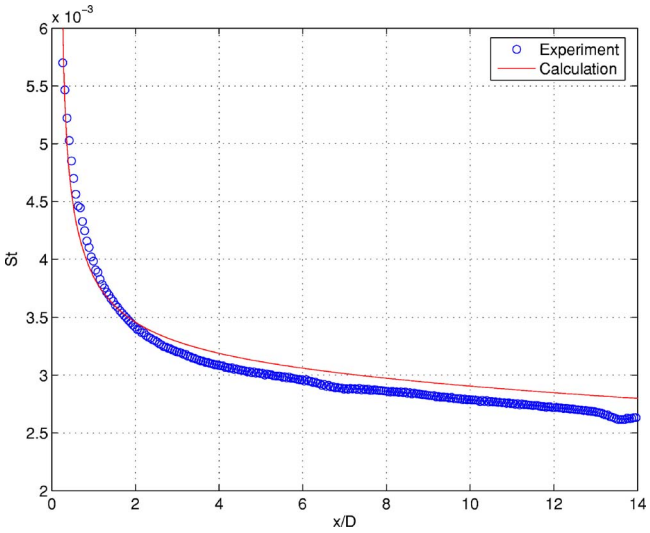

Fig. 1 Spanwise averaged Stanton number with no blowing, St_o

Results

Baseline experiments were conducted with no film cooling. For these experiments, the film-cooling holes were covered with tape. The experimental Stanton number distribution (St_o) for this case is shown in Fig. 1 along with values computed using a boundary layer code (TEXSTAN, [7]) using a mixing length turbulence model and heat transfer boundary conditions matching the experimental case. The calculated and experimental Stanton numbers agreed to within 6%, which is within the experimental uncertainty. The origin of the coordinate system for the measurement was taken as the trailing edge of the center film-cooling hole.

Steady Blowing Cases. Steady film-cooling cases were considered for blowing ratios of $B=0.25$, 0.5, 1.0, and 1.5, and Stanton numbers were computed for each case. Contours of the Stanton number ratio, St_f/St_o, are shown in Fig. 2. A few features are clear in these figures and show how the film-cooling flow enhances the heat transfer rate. Immediately downstream of the film-cooling holes, at x/D between 0 and 1, there are small regions of high St_f/St_o in all cases at $z/D=\pm 0.5$ around each hole. These regions are believed to be caused by the horseshoe vortex which forms when the mainflow boundary layer wraps around the film-cooling jet. Another feature is the pair of high St_f/St_o lines, which are symmetric about the centerline of each hole and extend downstream along the surface. These are believed to be caused by kidney vortices associated with the film-cooling jets, and were observed previously by Mayhew et al. [8], who referred to them as "fork tines." Between the high St_f/St_o lines, in the region directly downstream of the center of each hole, St_f/St_o is relatively low at the lower blowing ratios. As the blowing ratio increases, the fork

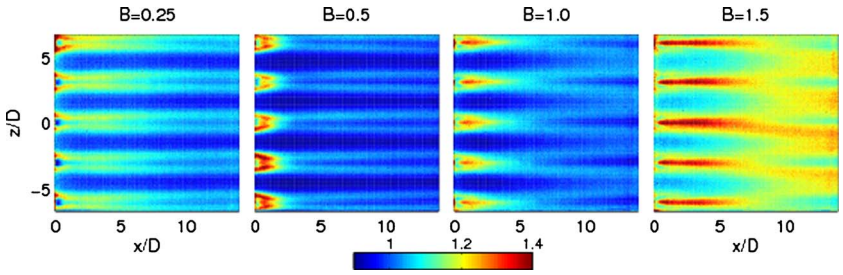

Fig. 2 St_f/St_o contours for steady blowing with $B=0.25$, 0.5, 1.0, and 1.5

tines spread outward in the spanwise direction, causing the tines of one hole to interfere with and merge with those of the adjacent film cooling holes. This merging occurs at approximately $x/D=13$ in the $B=1.0$ case and approximately $x/D=10$ in the $B=1.5$ case. The merging results in high heat transfer coefficients at the spanwise positions midway between the film-cooling holes, which could be particularly detrimental since this is where the film-cooling effectiveness is lowest. At the higher blowing ratios a narrowband of high St_f/St_o forms in the region between the tines, directly downstream of the center of the film cooling holes. This band extends to approximately $x/D=5$ for $B=1.0$ and approximately $x/D=7$ for $B=1.5$. The end of this band corresponds to the streamwise position where the fork tines begin to spread. The film-cooling jet in the $B=1.0$ and 1.5 cases experiences considerable liftoff, as shown through flow measurements in Part I [2]. The band of high St_f/St_o directly downstream of the holes and the subsequent spreading of the fork tines may be due to the liftoff. The strengthening of these effects between $B=1.0$ and 1.5 may be due to increasing liftoff at the higher blowing ratio.

The centerline and spanwise averaged Stanton number ratios are shown in Fig. 3 for the four blowing ratios. At $B=0.25$ the effect of the horseshoe vortices appears to be relatively weak, as seen by the lower centerline St_f/St_o immediately downstream of the hole. Farther downstream, the centerline St_f/St_o drops in all cases. The case with the lowest St_f/St_o is the $B=0.5$ case, which was shown in Figs. 2 and 3 of Part I [2] to be the case with the highest film-cooling effectiveness. The film-cooling fluid in this case remains near the wall with less interaction with the freestream than in the other cases. This appears to lead to a lower disturbance level and lower Stanton numbers. The $B=1.0$ case has a high upstream St_f/St_o region, which drops off gradually downstream of the holes. The high upstream St_f/St_o drops off even more gradually for $B=1.5$. The spanwise-averaged data again show St_f/St_o is significantly higher for the $B=1.5$ case, and unlike the other cases, the $B=1.5$ case exhibits a streamwise increase due to the spanwise spread of the high St region. As blowing ratio is varied, higher film-cooling effectiveness corresponds to lower Stanton numbers. At the lowest blowing ratio, the low mass flow results in rapid mixing with the main flow. The mixing apparently induces higher Stanton numbers, and the subsequent dilution of the coolant near the wall lowers the effectiveness. At the higher blowing ratios, liftoff results in low effectiveness and stronger interaction with the freestream. This presumably promotes turbulence, which increases Stanton numbers.

Figure 4 shows the centerline and spanwise averaged heat flux ratios for the four steady blowing cases. The heat flux ratio is dependent on the film-cooling effectiveness and the Stanton number ratio. Because the Stanton number ratios are close to 1, they do not affect the heat flux ratios as much as the effectiveness. Thus, for the steady film-cooling cases, the heat flux ratios are similar to the film-cooling effectiveness data, with $B=0.5$ being the best case, followed by the $B=0.25$, and $B=1.0$ cases. In the $B=1.5$ case, η is very low, so the high Stanton number ratio results in a heat flux ratio near 1.0 or higher. Hence, the film cooling has no positive effect in this case.

Pulsing Frequency Effects. Figure 5 shows the St_f/St_o contours at various pulsing frequencies for $B=0.5$ and DC=0.5. The shapes of the contours are similar to those of the steady pulsing cases, with high St_f/St_o directly downstream of the film-cooling holes attributed to the horseshoe vortices and the fork tine signature attributed to the kidney vortices. The general trend is that St_f/St_o increases as the frequency increases. The centerline and spanwise averaged St_f/St_o in Fig. 6 show this more clearly. The steady blowing $B=0.25$ case is also shown for comparison since this case has approximately the same time averaged coolant mass flow as the $B=0.5$, DC=0.5 pulsed flow cases. Flow temperature field measurements shown in Part I [2] suggest the appearance of

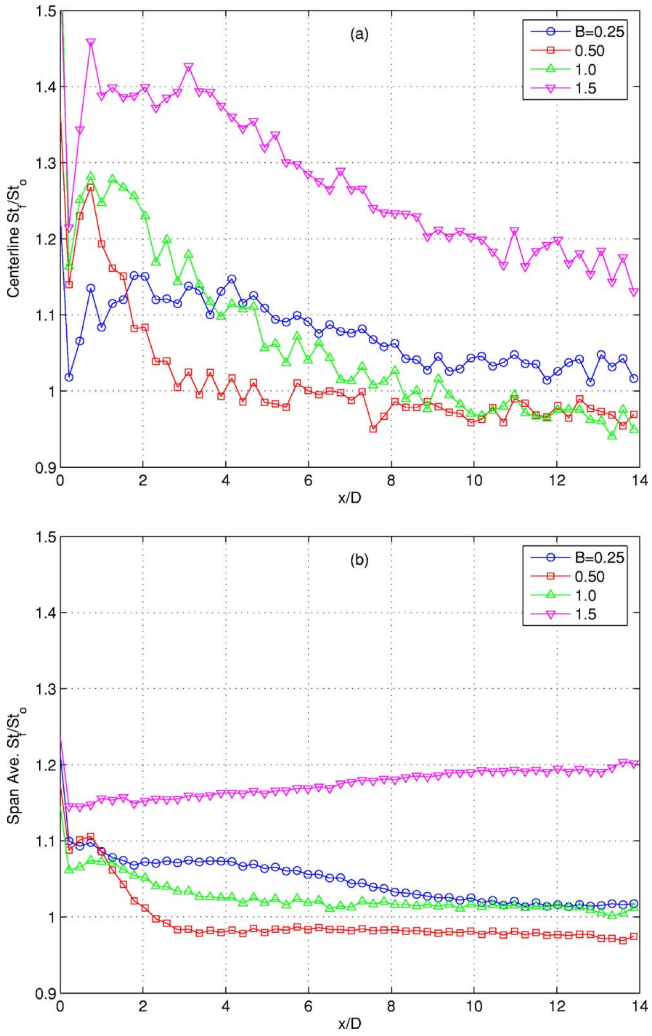

Fig. 3 St_f/St_o for steady blowing cases: (*a*) centerline and (*b*) spanwise averaged

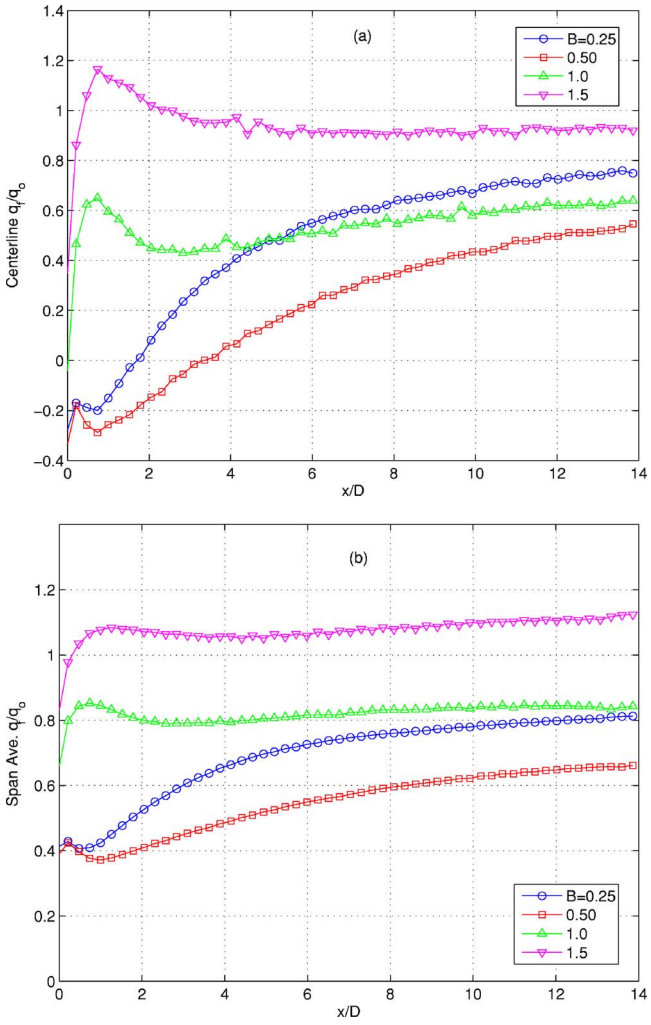

Fig. 4 q_f/q_o for steady blowing cases: (*a*) centerline and (*b*) spanwise averaged

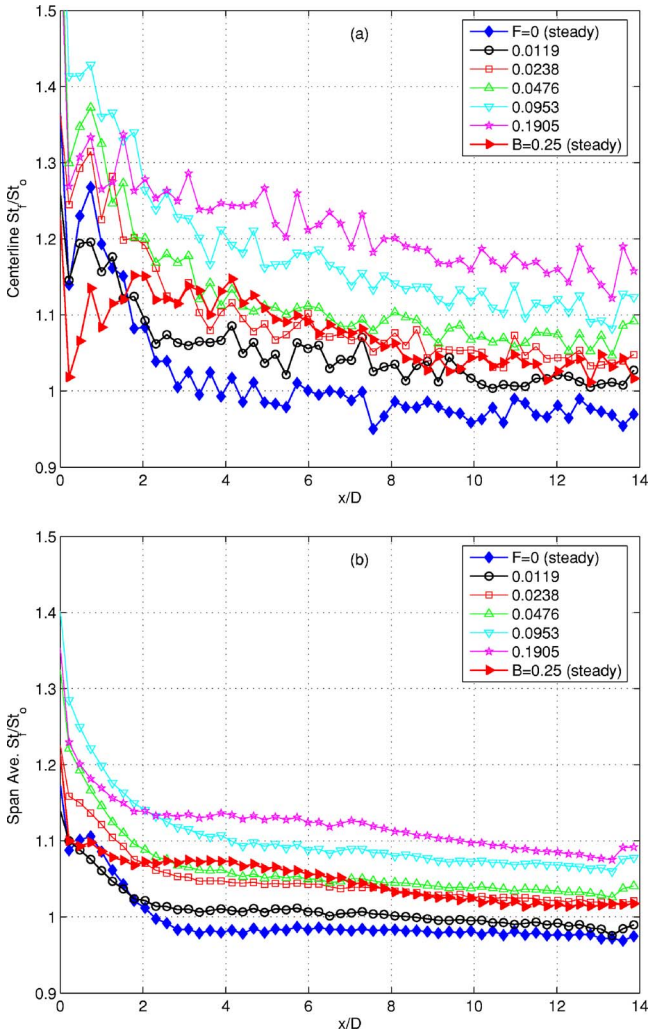

Fig. 6 St_f/St_o for nominal $B=0.5$, DC=0.5 and steady $B=0.5$ and $B=0.25$ cases: (*a*) centerline and (*b*) spanwise averaged

a starting vortex at the start of each pulsing cycle. The starting vortex could induce higher mixing and increase Stanton numbers. As frequency increases, the number of starting vortices increases per unit time; thus, St should tend to increase at higher frequencies. In contrast, during the off portion of the cycle, St should tend to drop toward the no-jet value of St_o. A lower frequency provides more time between pulses for the instantaneous St to drop. The instantaneous strength of the horseshoe vortex wrapping around the jet should also decrease during the jet off time. Hence, the St_f/St_o peak at $x/D \approx 1$,which was attributed to the horseshoe vortex, should be lower at low pulsing frequencies. This is observed for the $F=0.0119$ case, which has St_f/St_o slightly lower than the steady blowing case at $x/D=1$, although the difference is well within the experimental uncertainty. Weaker horseshoe vortex signatures can also be seen when comparing the contours in Figs. 2 and 5 for the $F=0.0119$ case. Comparison of the Stanton numbers of Figs. 5 and 6 with the corresponding film-cooling effectiveness plots (Figs. 11 and 12 of Part I [2]) shows the same trend observed in the steady cases noted above. Higher film-cooling effectiveness corresponds to lower Stanton numbers. The notable exception is the $F=0.1905$ case. Stanton numbers are highest in this case for the reasons given above. The high-frequency pulsing, however, results in jet-plenum dynamics, which raise the effectiveness. As explained in Part I [2], the jets are not able to respond fast enough to keep up with the high-

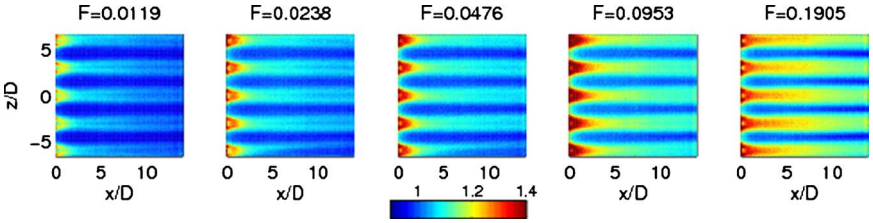

Fig. 5 St_f/St_o contours at various pulsing frequencies with nominal $B=0.5$ and DC =0.5

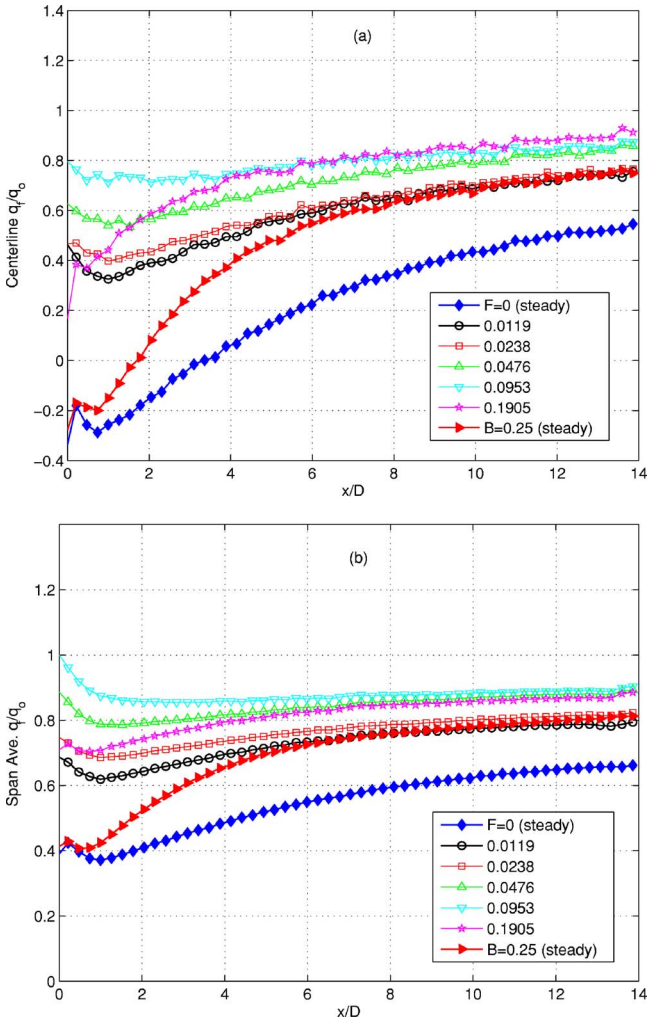

Fig. 7 q_f/q_o **for nominal** $B=0.5$, DC$=0.5$ **and steady** $B=0.5$ **and** $B=0.25$ **cases: (*a*) centerline and (*b*) spanwise averaged**

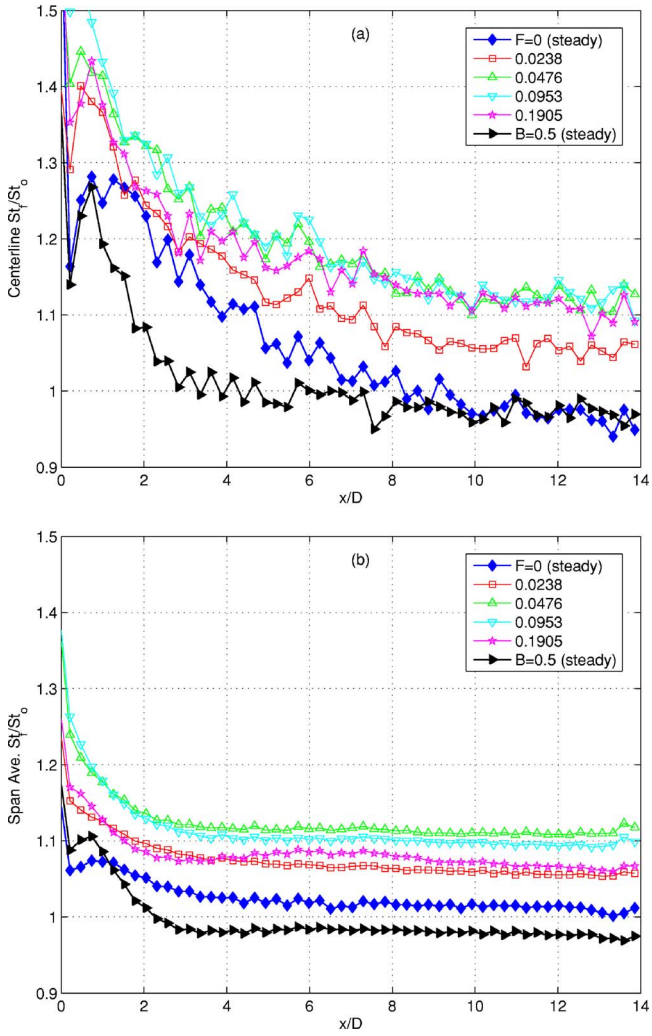

Fig. 9 St_f/St_o **for nominal** $B=1.0$, DC$=0.5$ **and steady** $B=0.5$ **and** $B=0.25$ **cases: (*a*) centerline and (*b*) spanwise averaged**

frequency opening and closing of the valves, and some low-momentum fluid leaves the film-cooling holes during the "valve-off" portion of the cycle, resulting in higher effectiveness.

Figure 7 shows the centerline and spanwise averaged heat flux ratio for $B=0.5$ and DC$=0.5$ at the various frequencies. The heat flux ratio follows the same trend as the film-cooling effectiveness. The pulsed flow cases have higher heat flux ratios than the steady $B=0.25$ case, which has approximately the same average coolant mass flow as the pulsed cases. This is particularly true near the hole, since near wall coolant is continuously supplied in the steady case. Farther downstream, after mixing has occurred, the heat flux ratios in the steady $B=0.25$ case and the best pulsed cases are equal. The steady $B=0.50$ case is superior to all the others, albeit with higher coolant mass flow.

The cases with $B=1.0$ and DC$=0.5$ were compared to determine the effect of varying frequency at higher blowing ratios. Figure 8 shows the St_f/St_o contours at various pulsing frequencies for these cases. It appears that the $F=0.0953$ case has the highest St_f/St_o directly downstream of the film-cooling holes; however, the $F=0.0476$ case has the highest St_f/St_o further downstream and the greatest amount of fork tine merging. These results are also seen in Fig. 9, which shows the centerline and spanwise averaged

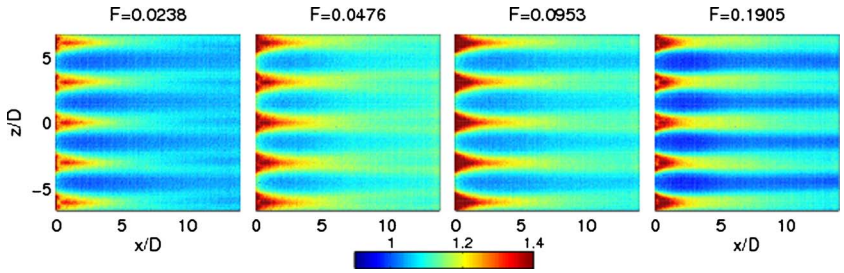

Fig. 8 St_f/St_o **contours at various pulsing frequencies with nominal** $B=1.0$, DC $=0.5$

St_f/St_o. The steady case has the best Stanton number ratio. All the cases have the initial St_f/St_o peak caused by the horseshoe vortices as explained earlier. Pulsing causes a 10 to 15% rise in St_f/St_o above the steady blowing case. The St_f/St_o ratio is slightly ($\sim$5%) higher in the $B=1.0$ cases than in the corresponding cases with $B=0.5$ (Fig. 6). Along the centerline, the general trend is increasing St_f/St_o at higher frequencies as in the $B=0.5$ cases, although the values at the highest frequencies are indistinguishable from each other. The spanwise-averaged values do not vary as much with frequency, and do not show the same trend of rising with frequency. Inspection of the flow temperature fields presented in Part I [2] suggests that the spread of the fork tines observed in Figs. 2 and 8 for the steady and pulsed $B=1.0$ cases may be related to the return of the film-cooling jet to the wall after initial liftoff. At the higher frequencies, as explained in Part I [2], the liftoff effect is more pronounced and there is less return of the jet to the near wall region. This reduces the spread of the fork tines and negates some of the rise in St_f/St_o across the span that was observed at the higher frequencies at $B=0.5$ (Fig. 6). Comparison of the Stanton numbers of Figs. 8 and 9 with the corresponding effectiveness plots (Figs. 17 and 18 of Part I [2]) shows little variation of η or St with frequency. The exception, as in the nominal $B=0.5$ cases, is the $F=0.1905$ case. Effectiveness is high for the $B=1.0$, $F=0.1905$ case due to the "valve-off" flow, which mitigates jet liftoff effects.

Figure 10 shows the centerline and spanwise averaged heat flux ratios for the various frequencies at $B=1.0$ and DC=0.5. The heat flux ratios follow the trend set by the film cooling effectiveness. As shown in Part I [2], liftoff results in a lower η with steady blowing at $B=1.0$, and η drops even further with pulsing as the mass flow for cooling is reduced. When coupled with the higher Stanton numbers resulting from pulsing, the heat flux ratio is near 1.0 at the centerline for frequencies of $F=0.0238-0.0953$. The spanwise averaged values are similar, indicating that pulsed jets have a detrimental effect and actually increase heat transfer to the surface. The $F=0.1905$ case is different and has lower q''_f/q''_o, particularly in the upstream region, where it is lower than in the steady $B=1.0$ case. As explained above, this is due to higher film-cooling effectiveness. It should be noted, however, that q''_f/q''_o with $B=1.0$, DC=0.5, and $F=0.1905$ is still between 0.2 and 0.6 higher than in the steady $B=0.5$ case, which has nominally the same coolant mass flow.

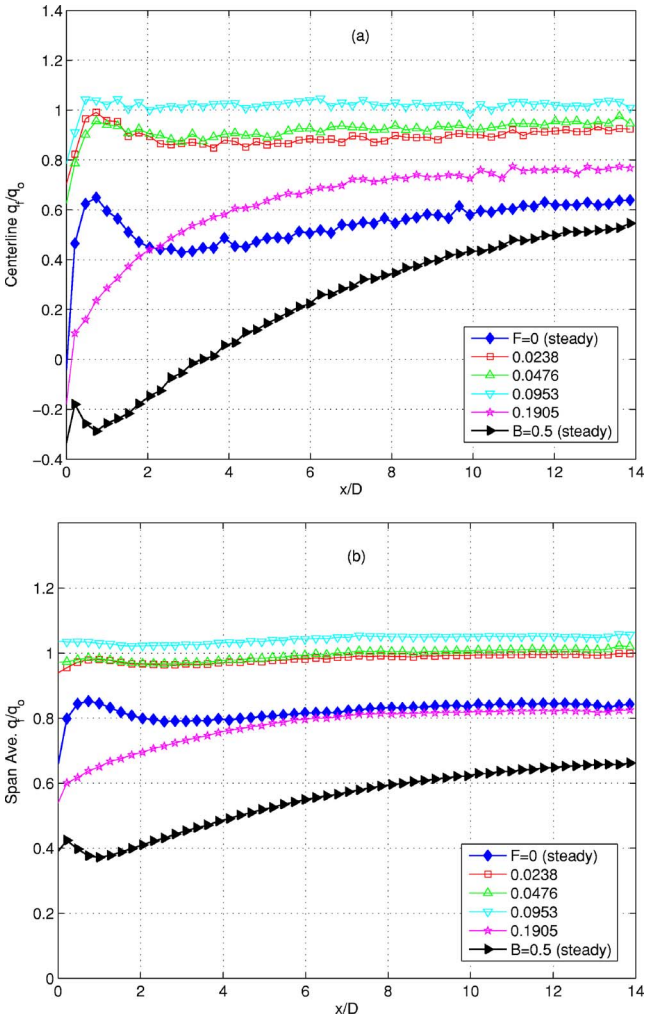

Fig. 10 q_f/q_o **for nominal** $B=1.0$, DC=0.5 **and steady** $B=0.5$ **and** $B=0.25$ **cases: (*a*) centerline and (*b*) spanwise averaged**

Duty Cycle Effects. Figure 11 shows the St_f/St_o contours with $B=0.5$ and $F=0.0238$ for varying duty cycles. The results follow the logical trend that as the duty cycles increases, the pulsed jet has more time to induce mixing and turbulence, and thus the Stanton number ratio increases. The Stanton number ratio is less for the steady case because it does not have the effect of the initial jet pulsations (starting vortices) disturbing the flow and increasing the mixing. The DC=0.25 case has the next best St_f/St_o because the jet is off for most of the cycling time, and St_f/St_o should drop toward 1.0 when the jet is off. The contour plots also show that as the duty cycle increases the effect of the horseshoe vortices increases and the fork tine tracks become more apparent. When the jets are off, there is no obstruction to the mean flow to cause the formation of the horseshoe vortex and no jets containing kidney-shaped vortices to produce the fork tine signature. The duty cycle effect is quantified in the centerline and spanwise averaged plots shown in Fig. 12. The DC=0.25 case has a slightly improved St_f/St_o over the steady case directly downstream of the film cooling holes ($x/D<2$) since the jets are off 75% of the time. Downstream, pulsing causes higher St_f/St_o with a slightly larger effect at the higher DC. It should be noted, however, that the differences from the steady case are all <10%, which is within the uncertainty of the measurements. Comparison of the Stanton numbers of Fig. 12 to the corresponding effectiveness plots (Fig. 21 of Part I [2]) shows that, although the duty cycle has a small effect on Stanton numbers, the resulting change to effectiveness is more significant. The heat flux ratios, shown in Fig. 13, are driven primarily by the film-cooling effectiveness, which was shown in Part I [2] to be directly proportional to the duty cycle.

The duty cycle was varied at $B=1.0$ with $F=0.0238$ and $F=0.1905$ to determine the effect at higher blowing ratios and frequencies. Figure 14 shows the St_f/St_o contours for $B=1.0$ and $F=0.0238$ at the various duty cycles, and once again the trend is

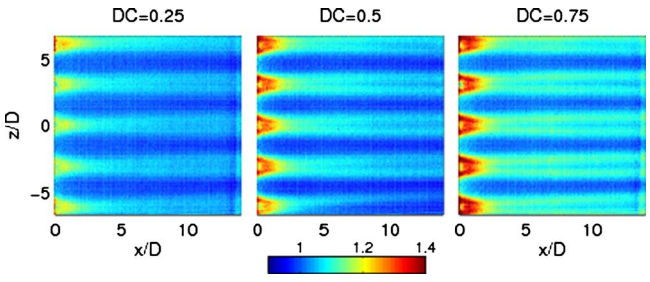

Fig. 11 St_f/St_o **contours at various duty cycles with nominal** $B=0.5$ **and** $F=0.0238$

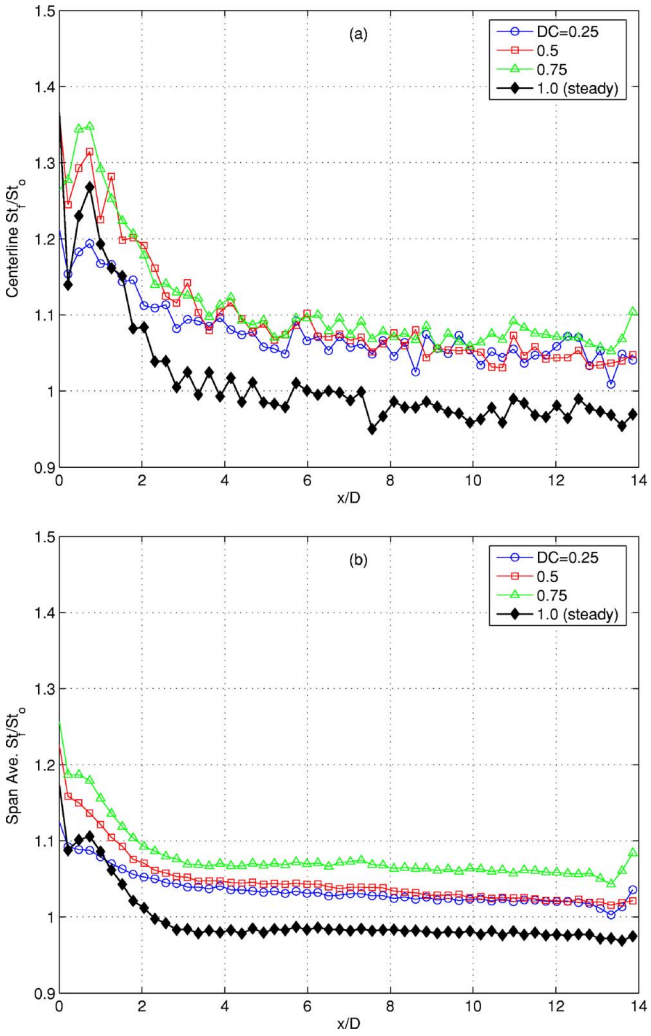

Fig. 12 St$_f$/St$_o$ for nominal B=0.5, F=0.0238 cases: (*a*) centerline and (*b*) spanwise averaged

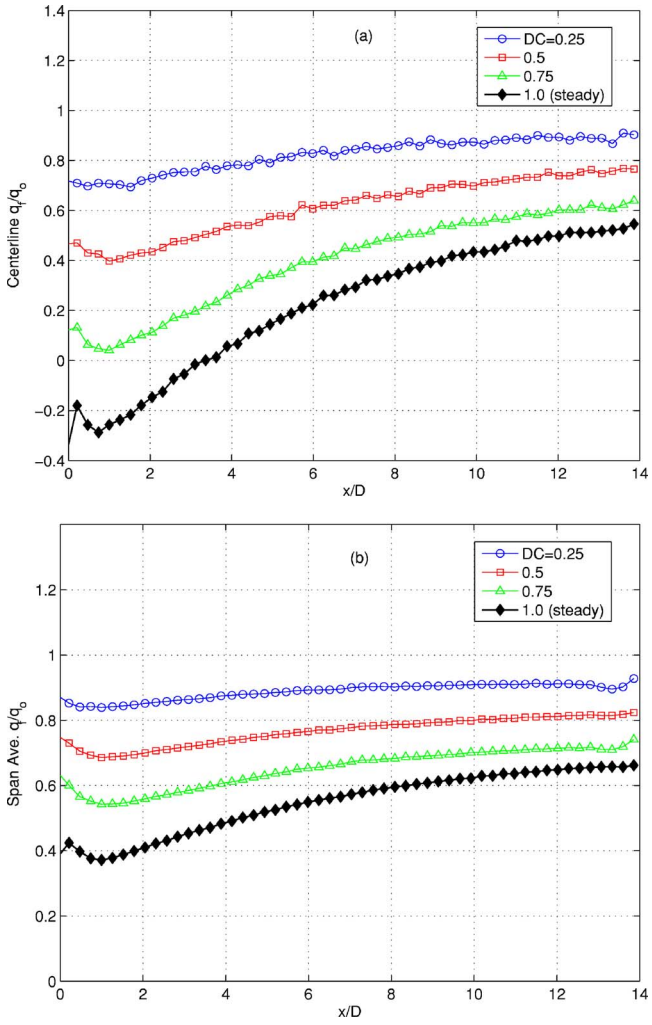

Fig. 13 q_f/q_o for nominal B=0.5, F=0.0238 cases: (*a*) centerline and (*b*) spanwise averaged

clear that the Stanton number ratio increases as the duty cycle increases for the pulsed cases. The three cases all have a separated fork tine signature. Figure 15 shows the centerline and spanwise averaged data for B=1.0 and F=0.0238. The DC=0.25 and 0.5 cases have similar results along the centerline with values ~10% higher than the steady case at x/D=14. The DC=0.75 case St$_f$/St$_o$ are ~5% higher than at the lower duty cycles. These differences are similar for the spanwise averaged data. As with the B=0.5 cases noted above, duty cycle has a small impact on Stanton numbers but a more significant effect on film-cooling effectiveness, as shown in Fig. 24 of Part I [2]. Figure 16 shows the heat flux ratio for B=1.0 and F=0.0238 with varying duty cycle. Both the centerline and spanwise-averaged heat flux ratio results reflect the film-cooling effectiveness results, with the steady case being the best, followed by DC=0.75, 0.5, and 0.25, respectively.

The B=1.0 and F=0.1905 cases have slightly different results due to the high frequency. Figure 17 shows the St$_f$/St$_o$ contours, and Fig. 18 shows the centerline and spanwise averaged Stanton number ratios for these cases. Along the centerline, pulsing increases Stanton numbers 10 to 15% above the steady blowing case values. The spanwise averaged values show smaller differences of 7% or less. Part I [2] of the paper showed that at this high of a frequency the jets never turn completely off, and the off-state blowing ratio is 0.4 at its lowest. At DC=0.75, the jet velocity is only fluctuating ~30% from its on-state to the off state; therefore, it behaves more like a continuous jet. Thus the fluctuations should not cause as much mixing and turbulence. This is the reason that the DC=0.75 case has a lower St$_f$/St$_o$ than the DC=0.5 case. The St$_f$/St$_o$ values in the DC=0.25 case are lower because the jet is off 75% of the time and therefore causes less of a disturbance, as in the lower-frequency cases discussed above. Figure 19 shows the centerline and spanwise-averaged heat flux ratio for B=1.0 and F=0.1905. All three pulsing cases have an improved centerline film-cooling effectiveness (see Fig. 29 of Part I [2]) over the steady case until x/D=1, with DC=0.5, 0.75, and 0.25 in the order from best to worst. The heat flux ratio results are analogous. As described above, the DC=0.5 case benefits from low momen-

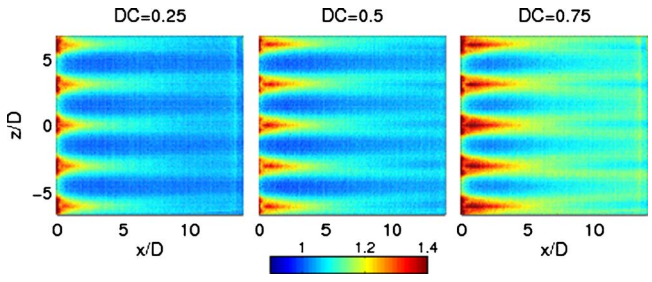

Fig. 14 St$_f$/St$_o$ contours at various duty cycles with nominal B=1.0 and F=0.0238

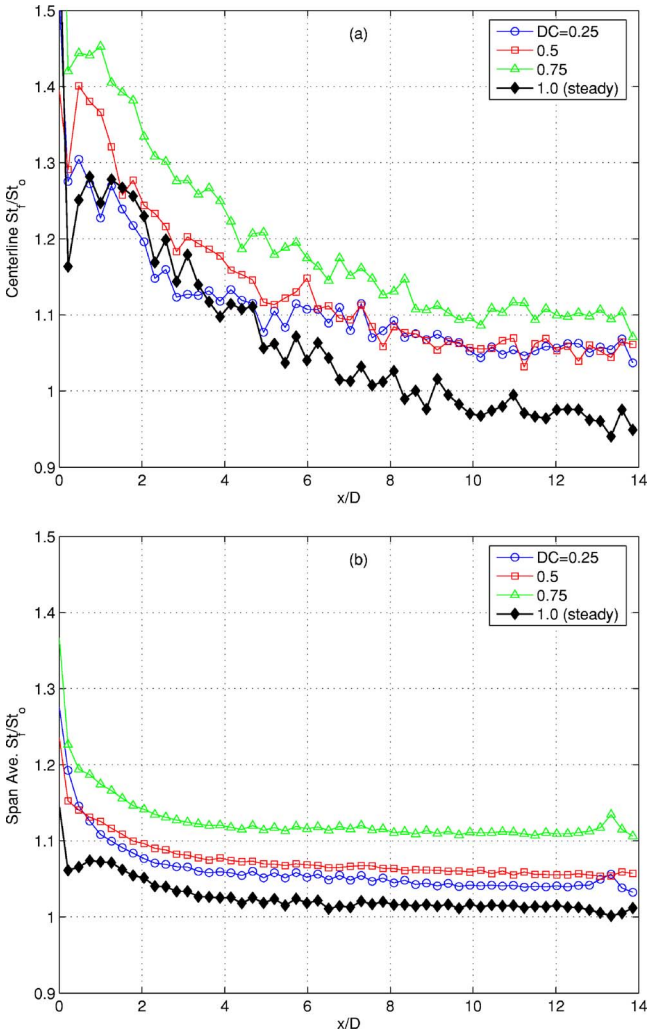

Fig. 15 St$_f$/St$_o$ for nominal B=1.0, F=0.0238 cases: (*a*) centerline and (*b*) spanwise averaged

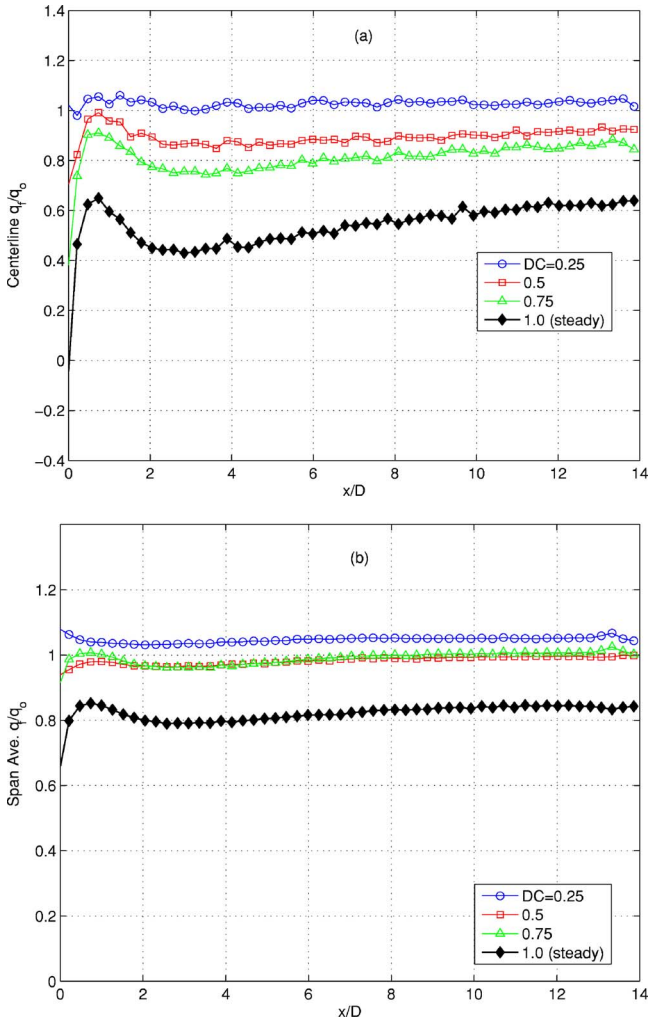

Fig. 16 q_f/q_o for nominal B=1.0, F=0.0238 cases: (*a*) centerline and (*b*) spanwise averaged

tum blowing during the valve-off portion of the cycle. With DC =0.75, the jets are more steady and the results are more like the steady blowing case. With DC=0.25 there is less cooling air so the heat flux ratio is higher. Further downstream, the steady case has the best results. The spanwise-averaged film-cooling effectiveness results showed an improvement over the steady case for DC=0.5, but only a small effect at $x/D>4$ for the other two duty cycles. The rise in St$_f$/St$_o$ for the DC=0.5 case counteracts the improved effectiveness and results in the spanwise-averaged heat flux ratio being ~0.2 better than the steady case directly downstream of the holes but equivalent to the steady case at $x/D>5$. The differences for the DC=0.25 and 0.75 cases are even smaller. Pulsing with B=1.0 at higher frequencies has the intended effect of providing equivalent or better film cooling with less mass flow than the B=1.0 steady blowing case. The results, however, are not as good as with steady blowing with a lower blowing ratio and even lower mass flow.

Conclusions

Heat transfer results were documented for cases with both steady and pulsed film cooling. The Stanton number ratio signatures provide insight into how the film-cooling flow enhances heat transfer rates. Regions of high heat transfer coefficient directly downstream of the film-cooling holes provide evidence of horseshoe vortices wrapping around the film-cooling jets. Pairs of high St$_f$/St$_o$ lines, extending downstream and symmetric about the centerline of each hole, are attributed to the effect of vortices within the film cooling jets. At high blowing ratios with strong jet liftoff, these lines spread in the spanwise direction, eventually merging with the lines from adjacent holes. With steady blowing, the cases with the lowest Stanton number ratios correspond to the cases with the highest film-cooling effectiveness. Pulsing tends to increase Stanton numbers, and higher frequencies and duty cycles increase the effect. Overall heat flux ratios depend most strongly on film-cooling effectiveness. Since pulsing tends to decrease ef-

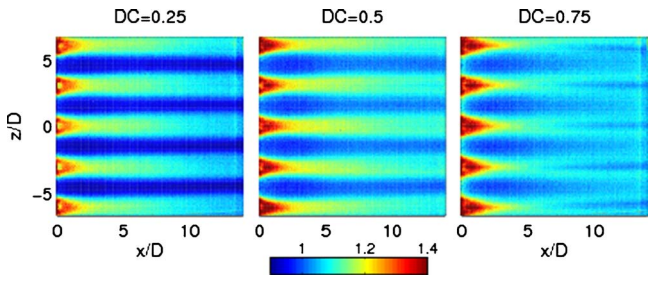

Fig. 17 Film-cooling effectiveness contours at various duty cycles with nominal B=1.0 and F=0.1905

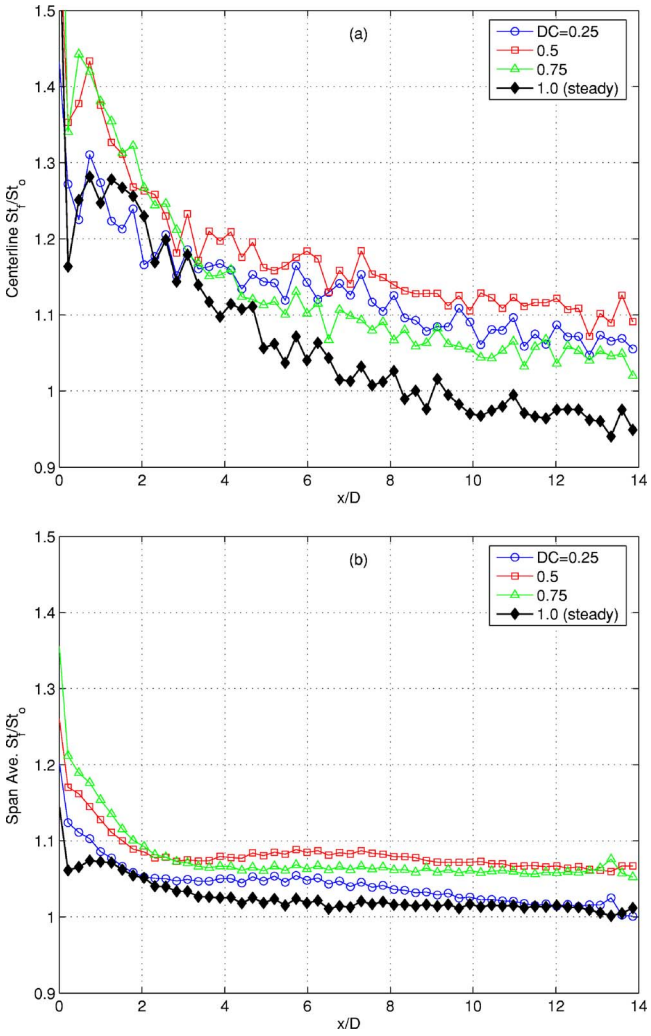

Fig. 18 St$_f$/St$_o$ for nominal B=1.0 and F=0.1905 cases: (*a*) centerline and (*b*) spanwise averaged

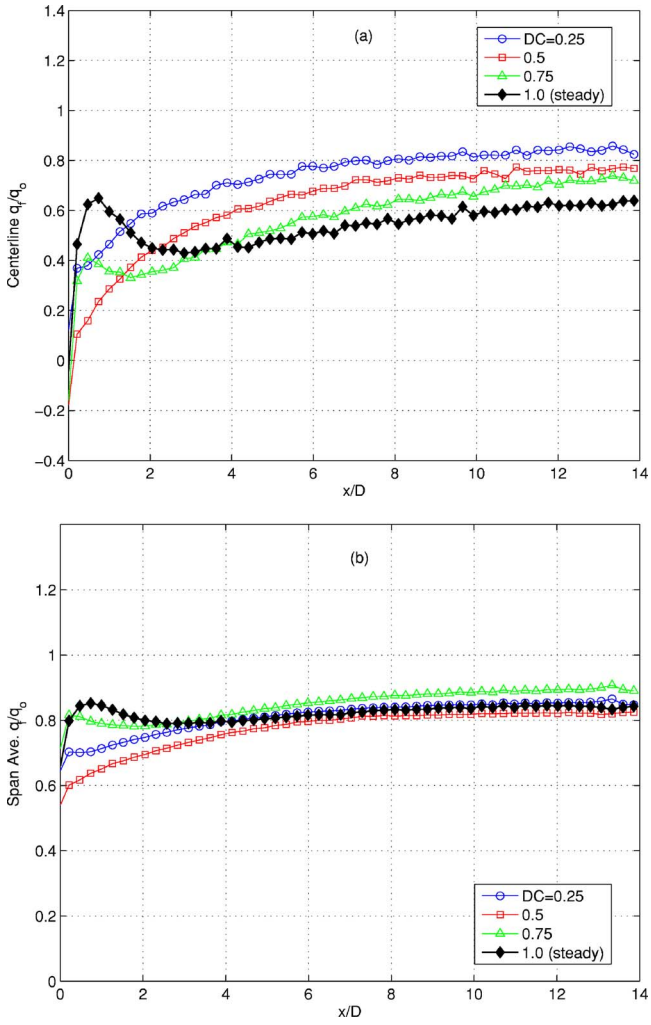

Fig. 19 q_f/q_o for nominal B=1.0 and F=0.1905 cases: (*a*) centerline and (*b*) spanwise averaged

fectiveness and increase heat transfer coefficients, the net effect is generally an increase in heat flux, with some exceptions at high pulsing frequencies and high blowing ratios.

Acknowledgment

This work was done under the Trident Scholar Program at the U.S. Naval Academy.

Nomenclature

B = $\rho_{\text{jet}}U_{\text{jet}}/\rho_\infty U_\infty$, blowing ratio
c_p = specific heat at constant pressure
D = film-cooling hole diameter
DC = duty cycle, fraction of time valves are open
F = dimensionless frequency, fD/U_∞
f = frequency, Hz
L = length of film-cooling hole channel
q'' = heat flux
St = Stanton number, $q''_{\text{conv}}/[\rho c_p U_\infty (T_w - T_{aw})]$
T = temperature
U = velocity
x = streamwise coordinate, distance from trailing edge of film-cooling holes
y = normal coordinate, distance from the wall
z = spanwise coordinate, distance from the centerline of the center hole
η = film-cooling effectiveness $(T_{aw}-T_\infty)/(T_{jet}-T_\infty)$
ρ = density

Subscripts

aw = adiabatic wall
cond = conduction
conv = convection
f = with film cooling
heater = total heater power
jet = film-cooling jet
o = without film cooling
rad = radiation
w = wall
∞ = mainstream

References

[1] Ekkad, S. V., Ou, S., and Rivir, R. B., 2004, "Effect of Jet Pulsation and Duty Cycle on Film Cooling From a Single Jet on a Leading Edge Model," ASME Paper No. IMECE2004-60466.
[2] Coulthard, S. M., Volino, R. J., and Flack, K. A., 2007, "Effect of Jet Pulsing on Film Cooling—Part I: Effectiveness and Flow-Field Temperature Results," ASME J. Turbomach., **129**(2), pp. 232–246.
[3] Sen, B., Schmidt, D. L., and Bogard, D. G., 1996, "Film Cooling with Compound Angle Holes: Heat Transfer," ASME J. Turbomach., **118**, pp. 800–806.
[4] Burd, S., and Simon, T. W., 2000, "Effects of Hole Length, Supply Plenum

Geometry, and Freestream Turbulence on Film Cooling Performance," NASA, CR-2000-210336.
[5] Coulthard, S. M., Volino, R. J., and Flack, K. A., 2005, "Effect of Unheated Starting Lengths on Film Cooling Experiments," ASME J. Turbomach., **128**, pp. 579–588.
[6] Mouzon, B. D., Albert, J. E., Terrell, E. J., and Bogard, D. G., 2005, "Net Heat Flux Reduction and Overall Effectiveness for a Turbine Blade Leading Edge," ASME Paper No. GT2005-69002.
[7] Crawford, M. E., and Kays, W. M., 1976, "STAN5—A Program for Numerical Computation of Two-Dimensional Internal and External Boundary Layer Flows," NASA CR 2742.
[8] Mayhew, J. E., Baughn, J. W., and Byerley, A. R., 2002, "The Effect of Freestream Turbulence on Film Cooling Heat Transfer Coefficient," ASME Paper No. GT-2002-30173.

Three-Dimensional Flow Prediction and Improvement of Holes Arrangement of a Film-Cooled Turbine Blade Using a Feature-Based Jet Model

André Burdet

Reza S. Abhari

Turbomachinery Laboratory,
Department of Mechanical and Process Engineering,
Swiss Federal Institute of Technology – ETH Zürich,
CH-8092 Zürich, Switzerland

A feature-based jet model has been proposed for use in three-dimensional (3D) computational fluid dynamics (CFD) prediction of turbine blade film cooling. The goal of the model is to be able to perform computationally efficient flow prediction and optimization of film-cooled turbine blades. The model reproduces in the near-hole region the macroflow features of a coolant jet within a Reynolds-averaged Navier-Stokes framework. Numerical predictions of the 3D flow through a linear transonic film-cooled turbine cascade are carried out with the model, with a low computational overhead. Different cooling holes arrangements are computed, and the prediction accuracy is evaluated versus experimental data. It is shown that the present model provides a reasonably good prediction of the adiabatic film-cooling effectiveness and Nusselt number around the blade. A numerical analysis of the interaction of coolant jets issuing from different rows of holes on the blade pressure side is carried out. It is shown that the upward radial migration of the flow due to the passage secondary flow structure has an impact on the spreading of the coolant and the film-cooling effectiveness on the blade surface. Based on this result, a new arrangement of the cooling holes for the present case is proposed that leads to a better spanwise covering of the coolant on the blade pressure side surface. [DOI: 10.1115/1.2437778]

Introduction

Modern gas turbine designs tend to push up the working gas temperature in order to increase the specific work and cycle efficiency. As a result, current and future heat management technologies of high-pressure turbine parts necessitate both full-coverage film cooling and locally specific film cooling for the hottest parts. In film cooling, coolant air is injected through rows of holes placed on the turbine blade leading edge, pressure and suction sides, as well as on the platform and casing. In some situations, several hundreds of cooling holes per blade can be used in order to ensure an efficient cooling. However, increasing cycle efficiency is counterbalanced by the losses induced by the cooling system. The designer has therefore to carefully balance the aerothermodynamics of the flow through high-pressure turbine blade passages to maximize turbine efficiency. This optimization induces a parametric study to be carried out. Hence, the designer needs a design tool that is both computationally efficient to shrink the turnover time so that design cost and accurate enough to ensure a useful final result. In this context, computational fluid dynamics (CFD) becomes a powerful tool to help the design and optimization of film-cooled high-pressure turbine blades. However, the accurate prediction of such flows faces several severe drawbacks inherent to the complexity of flow structures that appear. A coolant jet in cross flow (JICF) in a turbine is a multiscale flow problem. The coolant jet gradually mixes with the freestream at a characteristic length scale of the hole diameter (e.g., 0.5–1.0 mm). In contrast to this, the aerodynamics of the passage, e.g., passage vortex, have much larger length scales. These scales may differ by up to two orders of magnitude. Therefore, a relevant numerical simulation must be made with a mesh that allows at least the prediction of the important fluid structures of the smallest geometric scale, namely, the hole diameter.

Many authors [1–5] have shown that, in a flat-plate configuration, the accurate prediction of adiabatic film-cooling effectiveness necessitates meshing inside the hole and even inside the plenum chamber with a large number of grid nodes, i.e., about 7×10^5 grid nodes for one hole. In fact, the coolant flow inside the hole is three-dimensional (3D), with its structure rapidly changing at hole exit [6], the so-called near-hole region. In a film-cooled turbine blade, the specification of the coolant fluxes at the blade surface, where the hole would be located, leads an acceptable mesh size for the designer (e.g., 2.25 million grid nodes [7]), but results in an inaccurate prediction of heat load on the blade [7,8]. Thus, the meshing of the interior of the blade is also needed, leading to a complex multiblock grid structure. As an example, the computation of only the midspan region of a film-cooled blade, with symmetry boundary conditions at lower and upper sides with only two holes per row simulated, necessitated 1.2 million grid nodes and more than 2900 grid blocks to be connected together [9]. As a consequence, a full 3D film-cooled blade mesh using this numerical approach can be estimated to be of an order of about 50–100 million grid nodes when accounting for the surface of the blade, end walls, blade tip, as well as all the feeding plenums. This large number of grid points also substantially increases the preprocessing time as well as the computational time from the current day turnaround time for an uncooled configuration to many months for each design iteration. From a design perspective, numerical approach to solve entirely a film-cooled blade flow is hardly acceptable due to very large computational time requirements.

Contributed by the International Gas Turbine Institute of ASME for publication in the JOURNAL OF TURBOMACHINERY. Manuscript received June 1, 2006; final manuscript received June 6, 2006. Review conducted by David Wisler. Paper presented at the ASME Turbo Expo 2006: Land, Sea and Air (GT2006), Barcelona, Spain, May 8–11, 2006. Paper No. GT2006-91073.

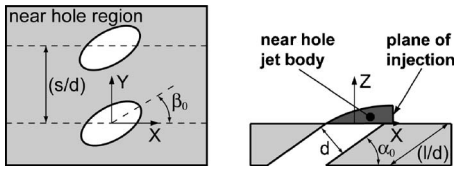

Fig. 1 Schematic of the near-hole region and the main geometrical parameters

In order to alleviate the meshing of the interior of blade while keeping an acceptable accuracy of the prediction, several authors [10–15] have proposed the application of a coolant jet model in a standard numerical scheme. However, none of these models are available for use in 3D RANS since they have been developed for two-dimensional (2D) boundary layer codes. As computational power per unit cost almost doubles every two to three years, development of more sophisticated numerical tools for the designer is critical to make full use of this increasing computational power. In this context, a 3D Reynolds-averaged Navier-Stokes-based (RANS-based) film-cooling model becomes a relevant option for the designer. Such a model has been proposed for use in 3D CFD by Burdet et al. [16] and validated with much film-cooled flat-plate experimental data. The modeling strategy is to model the near-hole macroflow features of the coolant jet and to experimentally anchor the model coefficients. The model is integrated in the computational mesh with the use of the implicit immersed boundary method (IBM) [17].

The goal of this paper is first to perform an evaluation of the computational performance and the predictive capability of the model in a film-cooled turbine blade configuration. Furthermore, it is aimed to make use of the model to improve the arrangement of the cooling holes. This improvement can be carried out because the model allows computing in a reasonable time scale so that dedicated time and iterative tests for the analysis of coolant jet flows interaction is enhanced. This improvement is made in the context of 3D optimization of the blade design, which generally occurs at the later stage of the design process. Thus, it is intended to demonstrate that the model is a relevant and useful numerical design tool for the designer of film-cooled turbine blade.

Film-Cooling Jet Model

Modeling Approach. The near-hole region and the main geometrical parameters that drive the coolant jet behavior are sketched in Fig. 1. Jets in cross-flow can produce a broad range of flow structures downstream of the injection site, depending on the geometrical arrangement, as well as on the difference of flow properties between the incoming freestream and the coolant fluid, quantified by density ratio (DR), blowing ratio (BR), and momentum flux ratio (IR). The current model covers cylindrical holes and a BR below 3.0. Long holes are assumed, i.e., the length of the hole is more than three to four times larger than its diameter. Approaches will be added in future to relax this current restriction.

The modeling approach is to experimentally anchor the near hole mixing, which has been shown by many researchers to be very difficult to resolve. The calibration of the model has been made with a large set of 3D particle image velocimetry (PIV) measurements of the flow structure in the near-hole region [18]. The model is simplified to a level that is resolved in RANS computation. The resultant flow field is injected in the CFD algorithm after the hole exit, in the so-called plane of injection, as shown in Fig. 1. Therefore, the model is only applied in the near-hole downstream region, on a two-dimensional cross plane.

Macroflow Features in Near-Hole Region. The jet flow behavior in the immediate vicinity of the hole exit is highly three-dimensional and contains flow features that are of primary importance for the downstream convection and diffusion of the coolant fluid with the freestream flow [6,19]. In Fig. 2, one can see the flow features near the hole that are included in the model [6]. Between the hole exit and the plane of injection, the coolant jet bends due to the inertial force of the freestream. The trajectory of the jet is the primary flow feature that affects the coolant fluid penetration. When flowing out of the hole, the coolant starts to mix with the freestream, on a length scale that is much smaller than the hole diameter. In addition, even at a moderate momentum flux ratio, a wake zone rapidly appears downstream of the hole trailing edge, in the lower part of the jet. This lowers the penetration velocity of the coolant fluid located near the wall, allowing the freestream fluid to penetrate more easily underneath the core of the jet. These two mixing processes are modeled using a superposition approach. The nonmixed freestream and coolant flow profiles are first derived and then they are superposed with the use of calibrated mixing functions so that the resulting flow profile at the plane of injection is found. The vorticity ring coming out of the hole (from the jet boundary layer) bends and squeezes, forming the well-known counterrotating pair of vortices. This counterrotating vortex (CVP) structure is modeled through an image vortex procedure.

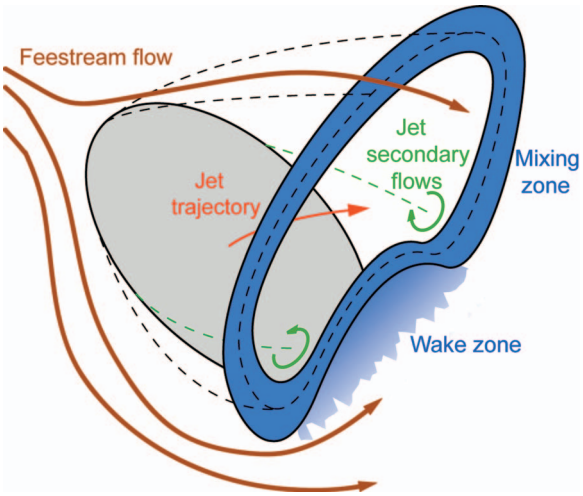

Fig. 2 Sketch of the near-hole coolant jet macro flow features

Numerical Integration of the Model. The model is numerically immersed in the computational mesh with the use of the implicit immersed boundary method (IBM) [20,21]. The strategy is to include the near-hole three-dimensional coolant jet body in the computational mesh, as shown in Fig. 3. The model is integrated as a separate module in the CFD code. In the computational procedure, the module only accounts in a 3D film-cooling box containing the computational cells that are only in the near-hole region. The feature-based film-cooling jet model is specified on the plane of injection. The numerical immersion of the near-hole jet body is done as follows. The jet surface is modeled with a toroidal shape. All the computational cells that are inside the toroidal shape are shut down during the calculation. The CFD algorithm takes account of the jet surface through the specification of immersed boundary conditions, where the jet surface lies. This jet surface can be viewed as the location of the thin, near-hole coolant to freestream mixing limit. The implicit IBM simulates the effect of the presence of the jet on the surrounding flow field. In the current modeling, slip and isothermal coolant boundary conditions are immersed. Indeed, vorticity cannot be created at the sides of the jet [6] and an averaged coolant to freestream mixing temperature is assumed at the jet surface. The numerical immersion of the jet body allows simulating the blockage of the freestream flow. Thus, the near-hole pressure field is realistically computed [16]. This is of primary importance since the near-hole

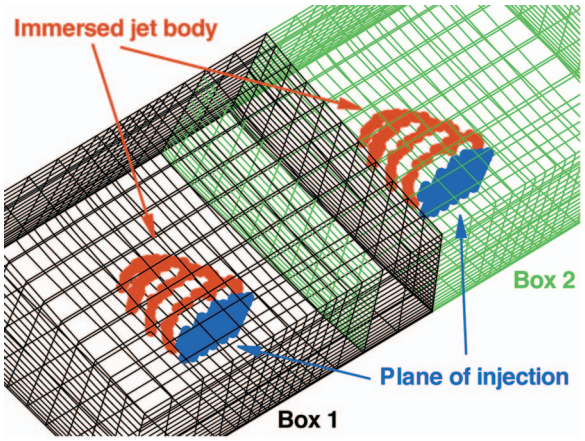

Fig. 3 Example of two 3D film-cooling boxes with the immersed jet body. The boxes can cross each other without any impact on the solution accuracy.

static pressure modulates the blowing of the coolant [22]. A complete description of the model and its validation can be found in Burdet [20].

Experimental Appartus

Cascade Geometry and Flow Conditions. A previously reported work from the Oxford University linear transonic turbine cascade test case is selected for application and further analysis. The turbine blades are placed in an isentropic light piston cascade, extensively described by Schultz et al. [23]. This is a short-duration facility ($\Delta t \approx 500$ ms), which produces a uniform (steady) flow condition for ~300 ms. A single-stroke isentropic piston compresses the test gas in the upstream cylinder. A turbulence grid generator is placed at five blade chords upstream of the blades row and produces a freestream turbulence level of ~3%. Just upstream of the blade row, a rotating bars device can be placed in order to simulate shock waves and wakes blade interaction. This option is not considered in this study; only a steady flow through the blade passage is investigated. The turbine cascade represents the midspan of typical gas turbine rotor blades. The geometry of the blade and the passage are shown in Fig. 4 and listed in Table 1.

The geometry of the 2D cascade blade profile is taken from Ashworth [24]. In the actual experiment, the blade height H_{HT} increases from the leading edge to the trailing of the blade. Unfortunately, the profile of the end-wall section was not known; thus, in the present study a linear increase of H_{HT} is assumed in the axial direction. Here, the flow and film cooling in this transonic cascade is investigated and compared to the experimental data provided by Rigby et al. [25]. The experimental conditions are outlined in Table 2.

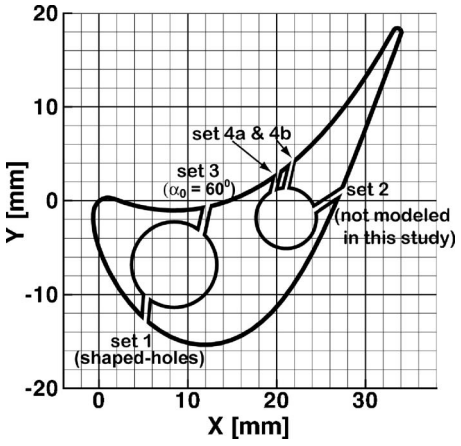

Fig. 4 Geometrical dimensions of the film-cooled turbine blade [24,25]

Table 1 Geometrical dimensions of the film-cooled turbine blade [24,25]

Geometrical dimension	Value
Axial chord C_{AC} (mm)	34.82
True chord C_{TC} (mm)	41
Solidity (-)	1.0
Turning (metal) (deg)	125
Span leading-edge H_{HT} (mm)	50
Span trailing-edge $H_{HT,TE}$ (mm)	56.095

Film-Cooling Hole Configurations. There are five rows of film-cooling holes drilled through the blade material, as shown in Fig. 4. There are two rows on the suction side (set 1 and set 2) and three rows on the pressure side (set 3), among which two are staggered (set 4a and set 4b). Except for set 1, every cooling hole has a cylindrical body from the plenum chamber to the blade surface. The diameter of every hole is $d=0.5$ mm. The cooling row in the first half of the suction side (set 1) contains only shaped holes. This means that the circular cross section of the holes at the plenum outer surface is expanded up to the blade surface, resulting in a trapezoidal cross-sectional shape at hole exit. The width of the hole exit area is larger than for cylindrical holes. Every cooling hole has a streamwise injection angle of $\alpha_0=30$ deg, except for those of set 3, where $\alpha_0=60$ deg. Rigby et al. [25] do not report the number of holes per row in their experimental setup. In order to demonstrate the capability of the model to simulate coolant jets issuing simultaneously from several dozens of holes, 17 holes per row (16 holes for set 4b) are placed. The hole-to-hole pitch distance is constant for every row and equal to $s/d=4.0$. This study limits the validation of the use of the jet model only near the midpsan section. Thus, there is no hole in the very near proximity of end-wall corners. As previously described, the first row in the suction side (set 1) is a collection of shaped holes. Since this hole configuration is not available in the present film-cooling jet model, it is replaced by a cylindrical hole configuration.

Coolant Injection Conditions. The coolant flow properties are not all explicitly provided. The freestream to coolant total temperature ratio is given ($T_T^c/T_T^f=1.6$), which results in a coolant total temperature in the plenum of $T_T^c=287.5$ K. The coolant total pressure P_T^c is not explicitly known. Instead, several blowing ratios are given. Thus, the definition of blowing ratio employed by many experimentalists is used. In a first step, an uncooled blade computation is carried out in order to determine the near-hole static pressure P_s. Based on the total freestream flow and coolant conditions, as well as the near-hole static pressure and given BR, the total pressure P_T^c of the coolant is computed using the following relation:

Table 2 Experimental flow conditions [25]

Flow quantity	Value
Inlet Mach number (-)	0.38
Outlet Mach number (-)	1.18
Reynolds number, based on axial chord and outlet flow (-)	1×10^6
Inlet stagnation temperature (K)	460
Inlet stagnation pressure (bar)	2.9

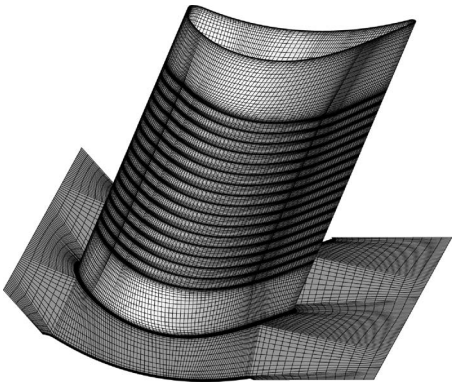

Fig. 5 Computational mesh

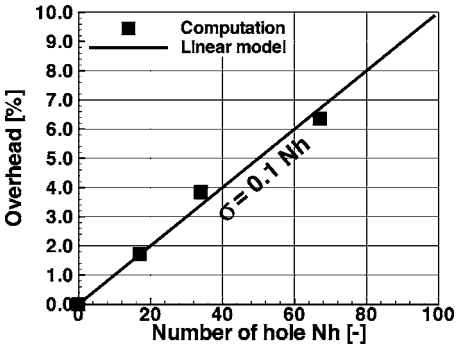

Fig. 6 Overhead σ as a function of the number of holes N_h

$$\mathrm{BR} = C_d \left(\frac{T_T^f}{T_T^c}\right)^{1/2} \left(\frac{P_T^c}{P_T^f}\right)^{(\gamma+1)/2\gamma} \sqrt{\frac{\left(\frac{P_T^c}{P_s}\right)^{\gamma-1/\gamma} - 1}{\left(\frac{P_T^f}{P_s}\right)^{(\gamma-1)/\gamma} - 1}} \quad (1)$$

A discharge coefficient C_d correlation has previously been implemented in the model [16]. The two reference flow regimes concern the uncooled blade with adiabatic or isothermal wall. For the isothermal wall computation, the wall temperature T_w is set to $T_w = 320$ K, approximately, as in the experiment (experimental uncertainty in fixing T_w is ±6 K). The different flow regimes with cooling are coolant injection with the two blowing ratios (BR $=[1.0, 1.5]$) combined with different arrangement of rows together (set 1, set 3, set 4a, and set 4ab). It is worth mentioning that set 2 is not considered since it is located in a transonic flow region, in which the current model has not been validated.

Computational Issues

Computational Method. The CFD code used in this study, MULTI3, is based on solving the unsteady compressible RANS equations. The solution method is based on an explicit, finite-volume, node-based, Ni-Lax-Wendroff time-marching algorithm developed by Ni [26]. The finite-volume formulation uses a central cell vertex variable location, meaning that the numerical scheme used in this study is a central scheme (contribution of fluxes same for each spatial direction) and the state variables are stored at the vertices of the computational cells. To prevent high-frequency oscillations and capture shock waves, a combined second- and fourth-order numerical smoothing is added, which is consistent with the second order accuracy in both space and time of the scheme. The eddy viscosity is determined with the help of the zero-equation Baldwin-Lomax turbulence model used in its low-Reynolds form.

Computational Mesh. The computational domain entirely covers the hub to tip span, through the whole blade passage (see Fig. 5). The inlet plane is placed at a distance of 0.27 axial chord upstream of the leading edge of the blade, whereas the outlet plane is located at a distance of 0.5 axial chord downstream of the trailing edge of the blade. The computational mesh contains 2.13×10^6 grid nodes in total. This is a relatively large grid to those generally employed in RANS-based numerical predictions of turbomachinery flows. A typical 3D grid for predicting an uncooled blade flow (not tip clearance nor shroud) has an order of magnitude of 5×10^5 grid nodes. There are several reasons that lead to this grid size. First, as a two-layer turbulence model is used (Baldwin-Lomax), it is needed to cluster the first cell near the blade wall so as to ensure a $Z+$ value of $Z+ \approx 1$. This leads to place a relatively large number of cells nearby the blade wall. In the current grid, there are approximately 12 to 20 grid nodes in the boundary layer region. Second, the use of the model necessitates having enough mesh resolution near the cooling holes in order to preserve an acceptable accuracy. A previous study made on the optimal use of the model in terms of grid-independent solution versus computational time [9] has shown that the mesh spacing near the hole should be of an order of $4 < N_X < 7$ and $7 < N_Y < 11$ grid nodes per hole diameter in the axial and lateral direction, respectively. Thus, the mesh density near the holes is controlled such that $N_X = 5$ and $N_Y = 7$–8 in this study.

As a comparison, in terms of overall grid size, the film-cooled turbine blade computed by Heidmann et al. [9], where the holes and plenum chamber are meshed, contains about 1.2×10^6 grid nodes with only two holes per row (only the midspan section is modeled). An extrapolation of this grid to the film-cooled turbine blade computed in this work leads to a mesh having about 25 to 40×10^6 grid nodes. Based on this benchmark, it is postulated that, the current jet model allows decreasing by a factor of over ten times the size of the mesh to be used to compute the flow in a film-cooled turbine. In addition, the preprocessing time spent to build up the entire film-cooled blade geometry and grid is significantly reduced because only the blade through-flow region is modeled.

Computational History. Computations of the different flow regimes have shown a very stable behavior. The following computational procedure has been employed. A generic flow solution is first computed with the blade uncooled. Numerical solutions of the different flow regimes with the blade film cooled are obtained by using the generic flow solution as the initial guess. The aggregate root-mean-square (rms) residual drops by more than three orders of magnitude for both restarted computations compared to the rms residual of the first iteration of the uncooled computation. At this stage, it is worth noting that the total coolant mass flow injected varies from 0.15% to 1.35% of the total freestream mass flow entering the turbine cascade, as a function of the number of holes. In all the presented cases, the coolant flow was injected upstream of the throat. As such, the reduction of freestream mass flow due to the blockage of the coolant jets is approximately counterbalanced by the injected coolant, resulting in a constant outlet mass flow ($\dot{m}_{\mathrm{out}}^f = 0.39$ kg/s for one passage). The global mass flow error ranges from −0.26% to 0.22% for all computations. The computational histories for the uncooled and film-cooled blade computations are similar. Hence, the numerical inclusion of the feature-based jet model does not significantly degrade the convergence rate and mass flow errors.

Computational Overhead. The overhead σ obtained when computing with the model is plotted in Fig. 6 as a function of the number of holes N_h. As it can be observed, the overhead σ is linearly increasing with the number of holes N_h,

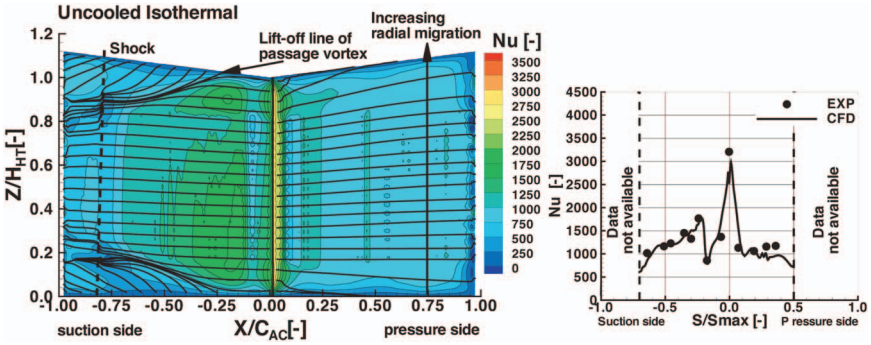

Fig. 7 Predicted contours of Nusselt number and surface flow streamlines (left); measured and predicted Nusselt number distribution at midspan (right); and *S* is blade surface length

$$\sigma = 0.1N_h \tag{2}$$

This result demonstrates that the treatment of each hole inside its corresponding 3D film-cooling box is independent of the others, so that the numerical procedure to immerse the near hole jet model is entirely local. Equation (2) scales the total amount of extra computational time (0.1% per hole) needed to calculate a film-cooled turbine with the model, compared to an uncooled blade computation with the same grid. Indeed, the rate of convergence is found to be similar for the uncooled and cooled computations.

Uncooled Blade Prediction: Description of the 3D Flow Field

In order to give an overview of the flow studied and to validate the computational method, the predicted contours of Nusselt number over the blade surface are plotted in Fig. 7 (left). The surface flow streamlines are superimposed. The predicted and measured profiles of Nusselt number at midspan section are also shown in Fig. 7 (right). Note that the rear part of the pressure and suction sides are not shown because only cooled blade experimental data are available at these locations.

The Nusselt number reaches its maximum level at the leading edge of the blade, from hub to tip. Indeed, this is where the boundary layer is the thinnest. On the pressure surface, the Nusselt number is pretty constant along blade axial direction ($750 < \mathrm{Nu} < 1000$). The surface flow streamline shows the upward radial migration of fluid due to the passage secondary flow structure. Overall, an under prediction of the Nusselt number of 10% to 20% on average is found. Several reasons may explain this discrepancy. The freestream turbulence (3%) is certainly enhancing the turbulent mixing in the pressure side, as well as the heat transfer. The current turbulence model (Baldwin-Lomax) is not taking into account the effect of freestream turbulence. Furthermore, the computational result (not shown here) shows that the eddy viscosity layer in the pressure side is not fully established. Near the middle of the pressure side surface ($S/S_{\max} \approx 0.5$), the eddy viscosity significantly reduces, to be almost zero. This might indicate that the boundary layer in the pressure side is in a transition regime. It is also worth noting that the experimental uncertainties are not known.

On the suction side surface, the prediction of Nusselt number is well in agreement with experimental data. It suddenly drops just after the leading edge ($-0.1 < X/C_{AC} < 0.0$). The increase of the Nusselt number level at ($X/C_{AC} \approx -0.1$) is commonly considered to be a marker of a laminar to turbulent boundary layer transition.

Further downstream, near the end walls, the liftoff line of the passage vortex is clearly identified with the surface flow streamlines. As a consequence, the Nusselt number (heat load) level reduces on the liftoff line of the passage vortex (locally thick boundary layer) and increases again in between the lift-off line and the blade corners, because of the new thin end-wall boundary layer forming. In addition, it is observed that the surface flow streamlines near the liftoff line are suddenly compressing toward midspan, at $X/C_{AC} = -0.8$. This is where the shock system, starting at the trailing edge of the blade, makes contact with the blade suction side, so that a shock-boundary layer interaction occurs. This shock system is also identified in the experiment of Rigby et al. [25] by Schlieren photographs. At this location, the compression of the surface flow streamline toward midspan indicates the sudden growth of the passage vortex due to the compression/dissipation effect of the shock. Eventually, it is noted that the contours of Nusselt number shows some wiggling artifacts. This is due to a lack of data of the blade geometry combined with the local refinement of the grid: the blade surface spline contains some small bumps near the refined grid regions.

Film-Cooled Turbine Blade

Blade Loading. The measured and predicted blade loading, in terms of isentropic Mach number M_{is}, are plotted in Fig. 8 for the two blowing ratios investigated; that is, BR=[1.0, 1.5]. The results are presented for coolant injection in set 1, set 3, and set 4ab.

As it can be expected, the blade loading is found almost identical for both blowing ratios, in the experimental and the CFD prediction. At the location of the holes, the blade loading could obviously not be measured. The CFD predictions give solutions that make sense in terms of the aerodynamics occurring near the hole. First, the blade loading level predicted a short distance before and after the holes are always found similar to the measured one. Second, a decrease of the isentropic Mach number Ma_{is} (or

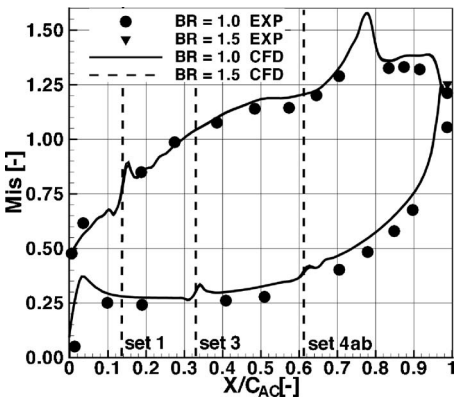

Fig. 8 Measured and predicted profiles of isentropic Mach number Ma_{is} at midspan

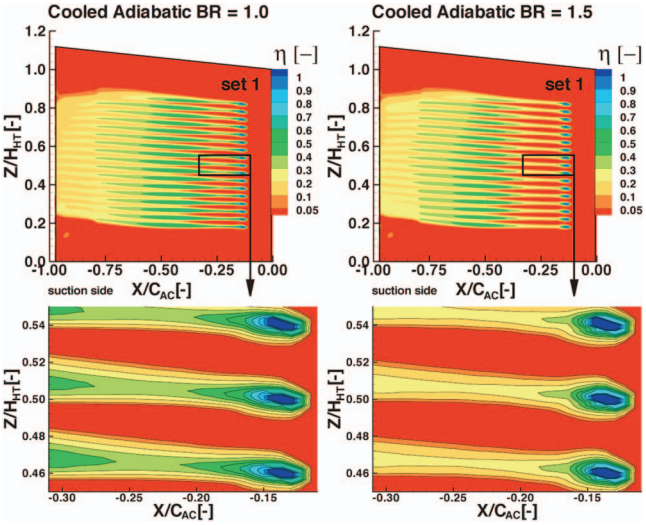

Fig. 9 Predicted contours of adiabatic film-cooling effectiveness η on suction side surface for BR=1.0 (left) and BR=1.5 (right)

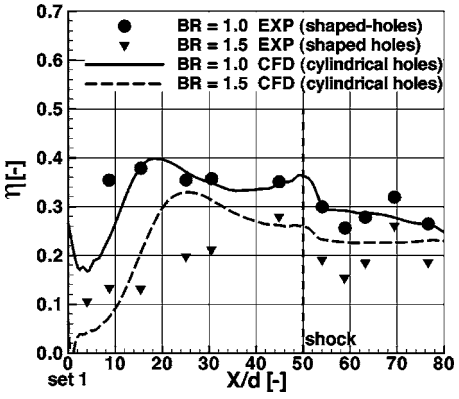

Fig. 10 Measured and predicted profiles of adiabatic film-cooling effectiveness η on suction side surface, at midspan, for BR=[1.0,1.5]

increase of static pressure) is systematically predicted just upstream of the holes, because of the jet blockage which is therefore well reproduced by the 3D jet model. Furthermore, an increase of the isentropic Mach number (or decrease of static pressure) just downstream of the holes is also systematically predicted because of the counterrotating vortex pair flow acceleration, also well reproduced by the model. It is worth noting that the isentropic Mach number distribution exhibits a higher gradient near the holes in the suction side than those in the pressure side. This means that the coolant counterrotating vortices are much more accelerated and stretched on the suction side of the blade when compared to pressure-side jets.

Film-Cooling Effectiveness on Suction Side. The adiabatic film-cooling effectiveness η is analyzed. Since no experimental data is available for adiabatic film-cooling effectiveness on the pressure side, only the suction-side surface is analyzed (injection from set 1). The predicted contours of adiabatic film-cooling effectiveness on the suction surface are plotted in Fig. 9 for the two blowing ratios investigated. The injection of the coolant with the use of the model is clearly seen. The downstream evolution of the coolant on the blade surface is observed with, in particular, a better cooling protection with BR=1.0 compared to BR=1.5. It is noted that the predictions suggest that there is some distance (more than 20 hole diameters) before a coolant jet issuing from one hole entirely mixes with its two neighbors. In fact, the flow is accelerating downstream of the holes of set 1 because of a positive streamwise pressure gradient. Thus, the stretching of the counterrotating vortex pair (CVP) better counterbalanced its diffusion. This can favor a pinching of the coolant jet further downstream, compared to a film-cooling flow without any streamwise pressure gradient. In the rear part of the suction side, the shock-boundary layer interaction provokes a blurring of the film-cooling protection. Indeed, the sudden deceleration of the flow just after the shock induces an intense viscous dissipation, hence, a reduction of the film cooling protection. In addition, the spanwise length covered by the coolant suddenly reduces just after the shock, due to the enlargement of the passage vortex. In order to quantify the accuracy of the numerical solution, Fig. 10 displays the measured and predicted adiabatic film-cooling effectiveness η at midspan, as a function of the non-dimensionalized axial distance X/d. The results with the two blowing ratios investigated are provided.

First, not too far downstream of the hole ($X/d<15$), a discrepancy in the CFD prediction is found when compared to the measurements. In this region, the numerical solution exhibits a lower adiabatic film-cooling effectiveness η than the measured one. Meanwhile, the fact that in the experiments, shaped-holes are used can be a major reason for the discrepancy. Indeed, in Fig. 9, it has been observed that the coolant mixes with the freestream not in the near downstream of the hole but far downstream. In general, shaped-holes having a large width, such as the ones in this experiment, induce a better mixing near the hole and also largely decrease the strength of the counterrotating vortex pair (see, for instance, [27]). Thus, the discrepancy of the numerical prediction can partially be explained by the fact that the cylindrical holes lead to a lower adiabatic film-cooling effectiveness in the near downstream of the holes because the penetration of the jet is stronger and the lateral mixing is reduced. Further downstream ($X/d>15$), the CFD prediction is in good agreement with the experimental data, especially for the low blowing ratio case (BR=1.0). However, an overprediction in the higher blowing ratio case (BR=1.5) remains.

Nusselt Number. The measured and predicted Nusselt number Nu distributions at midspan are compared in Fig. 11 for the two blowing ratios investigated (BR=[1.0,1.5]) and injection at set 1 and set 3. Near the leading edge, it is found that the Nusselt number is pretty similar both in the measurements and computations. On the suction side, the Nusselt number decreases down to a value lower than 0.0 just at the injection site of set 1. This is because the coolant temperature is lower than the wall temperature. Then, just downstream of the injection site, the Nusselt number rapidly increases both in the experiment and the computation.

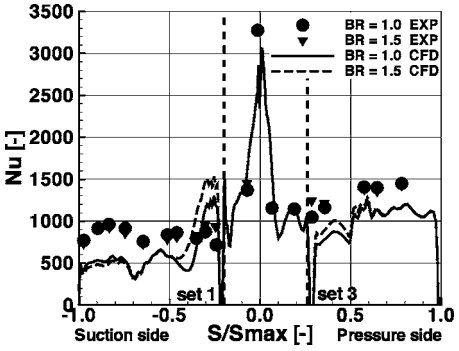

Fig. 11 Measured and predicted profiles of Nusselt number Nu at midspan for BR=[1.0,1.5]; injection at [set 1, set 3]; and *S* is blade surface length

Near this location, the peak of Nusselt number is too highly predicted, by ~20% on average for both blowing ratios. Further downstream, the heat transfer is reduced, compared to the uncooled blade, by ~25% in the experiment and by ~50% in the CFD prediction. The discrepancy of the prediction can be explained by the earlier comments made about the adiabatic film-cooling effectiveness prediction: the holes at the suction side are not the same in the experiment and in the computation. Meanwhile, the measured distribution of Nusselt number is qualitatively well predicted when using the model. This comments also applies at the pressure-side surface. Indeed, on the pressure-side surface, just of the injection site of set 3 the Nusselt number is slightly under predicted, by 10–15% on average for BR=1.0 and BR=1.5, respectively. Overall, these CFD predictions are in line with other prediction of film-cooled turbine using different higher order turbulence models [28,29].

Superposition Principle on Pressure Side

In the design of a film-cooled turbine, it is often useful to superpose different experimental or numerical results of adiabatic film-cooling effectiveness because it can shrink the turnover time. This superposition principle is a direct outcome of the linearity of the energy equation. This linearity would indicate that in the absence of property variation of the flow and for the same hydrodynamic flow distribution, any variation in the film temperature could be calculated by superimposing various solutions or experimental results. Given the above-stated conditions, then the optimization of the location of one hole can be independently done from the others. The goal of the present study is to first check for the limitations of this superposition rule in a typical 3D flow structure as in a cascade of airfoils. In addition, an attempt is made here to demonstrate how the present model can help the designer of a film-cooled turbine to improve the location of the film-cooling holes. Given the physically accurate nature of the model combined with extensive past experimental validation of the code, it is believed that useful design guidelines and trade-off studies from the present predictive design tool can be obtained.

Definition of Superposition Principle. The superposition model of Sellers [30] is selected here for application. This model assumes that the hydrodynamic of a cooling jet is not interacting with the other ones. This means that the superposition of the measurements or predictions of adiabatic film-cooling effectiveness η_r for different rows r gives the total adiabatic film-cooling effectiveness η_{tot}.

$$1 - \eta_{\text{tot}} = \prod_{r=1}^{r=R} (1 - \eta_r) \tag{3}$$

The main issue of the current investigation is to observe, on the pressure-side surface, if the superposition of the distribution of the predicted adiabatic film-cooling effectiveness with injection at set 3 only and with injection at set 4a only is the same as with injection at set 3 and set 4a together. If the superposition principle given by Eq. (3) applies, the design of a film-cooled turbine blade can be reduced to the addition of the individual design of each cooling row, i.e., the jet hydrodynamic does not need to be taken into account.

Results of Superposition on Pressure Side. The predicted contours of adiabatic film-cooling effectiveness on the pressure-side surface are plotted in Fig. 12, for BR=1.0. The same type of result is found for BR=1.5 (not shown here). At a first glance, the results seem to be pretty similar. However, a zoom downstream of the second row (set 4a) shows that the adiabatic film-cooling effectiveness is better spread over the surface of the pressure side, in the midspan region, for the two rows together (S34a) than for the superposition of the individual rows set 3 and set 4a (S3+S4a). However, near the hub the coolant appears to be better spread over the surface in the numerical solution obtained with the superposition of the two individual rows than for the two rows together. Thus, in order to verify Eq. (3), the hydrodynamics of the flow has to be taken into account. As a consequence, the application of Eq. (3) for design of a film-cooled turbine seems to be limited and not always accurately applicable. In the following, it is aimed to show the impact of the jet hydrodynamics, in particular, the impact of an upstream row of jet (set 3) on the cooling protection downstream of the second row (set 4a).

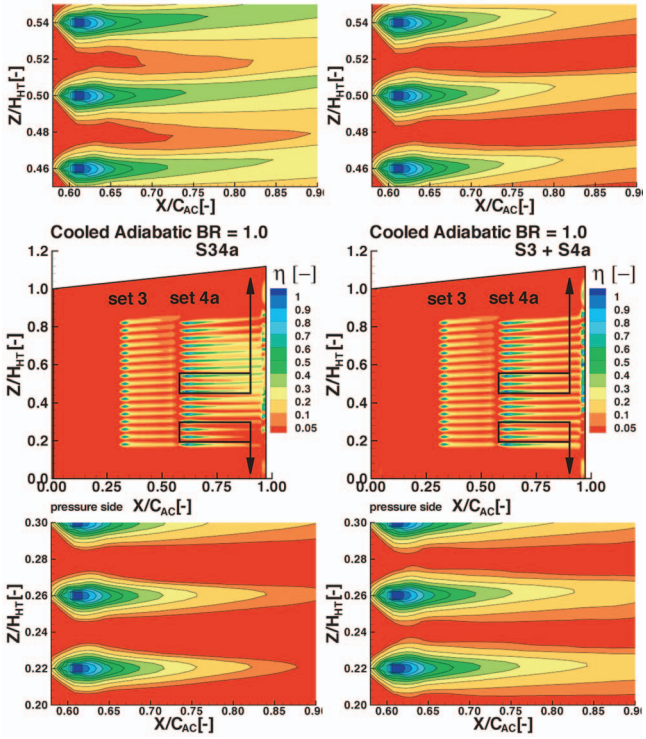

Fig. 12 Predicted contours of adiabatic film-cooling effectiveness η on pressure side with injection from set 3 and set 4a (left) and superposition of injection from set 3 only and injection from set 4a only (right)

Hydrodynamics Influence of an Upstream Row of Coolant Jets

Definition of Visualization. Plots of the predicted flow field on three cross planes near the pressure side surface are provided in Fig. 13. These three cross planes are denoted A, B, and C. Cross plane A is located three hole diameters upstream of set 4a, cross plane B is located one hole diameter downstream of set 4a and cross plane C is located 15 hole diameters downstream of set 4a. On all the cross planes, contours of the normalized total temperature θ superimposed with the coolant secondary flow vectors $\boldsymbol{U}_{2\text{nd}}$ are shown. The coolant secondary vectors $\boldsymbol{U}_{2\text{nd}}$ are found as follows. The predicted velocity vectors obtained in the cooled case are subtracted from the predicted velocity vectors calculated in the uncooled case. The resulting vectors are projected on the cross planes to give the coolant secondary velocity vectors $\boldsymbol{U}_{2\text{nd}}$

$$\boldsymbol{U}_{2\text{nd}} = (\boldsymbol{U}_{\text{cooled}} - \boldsymbol{U}_{\text{uncooled}}) \cdot (\boldsymbol{e}_b \boldsymbol{e}_b + \boldsymbol{e}_t \boldsymbol{e}_t) \tag{4}$$

where $\boldsymbol{e}_b$ and $\boldsymbol{e}_t$ are the two unity vectors defining the cross plane (A, B, or C). The coolant secondary vectors $\boldsymbol{U}_{2\text{nd}}$ represent the disturbance on the hydrodynamics flow field due to the presence of the coolant jets. The visualization of the predicted flow field near midspan is given in Fig. 13 (top) for injection from set 4a only (case S4a) in Fig. 13 (middle) for injection from set 3 and set 4a (case S34a) and the same visualization but near hub in Fig. 13

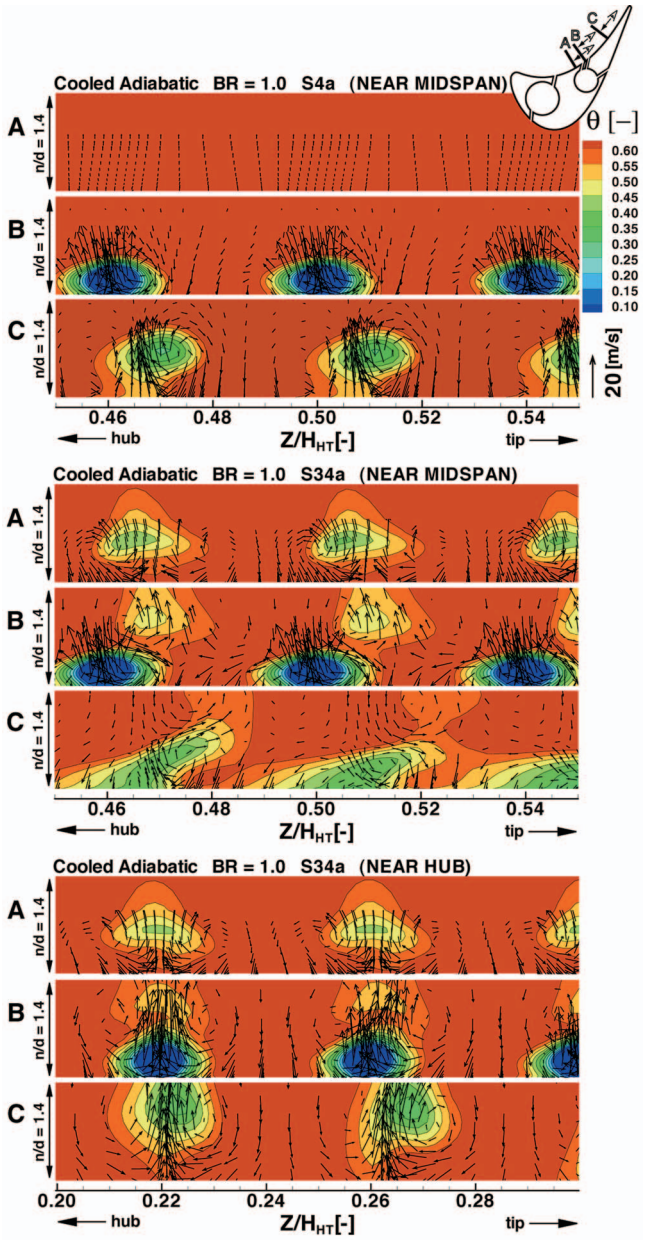

Fig. 13 Predicted contours of the normalized temperature θ and jet secondary flow vectors U_{2nd} near the midspan region for injection at set 4a only (top), for injection at set 3 and set 4a (middle) and near the hub region for injection at set 3 and set 4a (bottom). Only every second vector is represented.

(bottom) for injection from set 3 and set 4a.

Note that the near-hub flow field of case S4a is not plotted because it is similar to the one in the near-midspan region. These plots allow observing the hydrodynamic impact of the upstream jet, issuing from set 3, on the jet thermal field issuing from set 4a.

Near-Midspan Flow Field (Fig. 13 top and middle). On the cross plane upstream of set 4a (cross plane A), the flow field is undisturbed in the injection case S4a, whereas the counterrotating vortices (CVP) and coolant-mixing zone are clearly seen in the injection case S34a. At cross plane B, the newly injected coolant jets are observed. In particular, the counterrotating motion of the vortices and the coolant core are observed. In the injection case S34a, the upstream jets are located above, on the right of the new jets. Thus, the counterrotating vortices of the upstream jets are *phase shifted* compared to the counterrotating vortices of the new

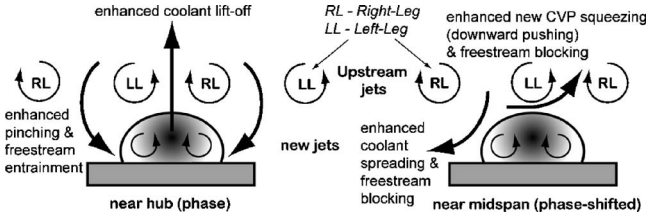

Fig. 14 Schematic of coolant jets interactions

jets. This induces a downward momentum push of the new jets due to the action of the CVP of the upstream jet. The consequence of this phenomenon is observed on cross plane C, further downstream. In the injection case S4a, the evolution of the jets issuing from set 4a are found, as can be expected: the coolant jets are lifting off and pinching due to the action of the CVP. In the injection case S34a, the flow field appears to be more complicated. The coolant jets issuing from set 4a are much more skewed with the presence of the phase-shifted upstream jets. Indeed, the action of the CVP of the upstream jet induces two main flow features. First, a migration of the coolant material toward the hub direction (left side of the newly injected jets) due to the action of the left-leg of the upstream CVP. This means that each newly injected coolant jet better spread toward the hub direction, close to the blade surface. Second, the right leg of the upstream CVP induces a blocking effect against the action of the CVP issuing from the new coolant jets, injected at set 4a. This blocking effect induces a squeezing of the right leg of the CVP of the new coolant jets toward the blade surface. Thus, the coolant material is forced to stay closer to the surface and the pinching effect is less pronounced. Overall, this explains the better film-cooling protection observed in the midspan region, downstream of set 4a, with the presence of the upstream row of jets (set 3).

Near-Hub Flow Field (Fig. 13 top and bottom). As previously, the flow field upstream of set 4a (cross plane A) is undisturbed in the injection case S4a whereas it is disturbed by the coolant jets issuing from set 3 in the injection case S34a. At cross plane B, in the injection case S34a, the upstream coolant jets are now located directly above the new coolant jets. Further downstream (cross plane C), still in the injection case S34a, the newly injected coolant jets from set 4a appear to have almost completely detached from the wall. Indeed, the presence of the upstream jets, just above appear to enhance both the upward motion in the center of the CVP of the newly injected jets and the freestream entrainment at their sides. As a consequence, the film-cooling protection becomes poor when the two coolant jets are in phase, as observed near the hub end-wall region for the current film-cooled turbine blade because the two jets act together.

Summary. A schematic of the previous analysis is given in Fig. 14. In this section, it is shown that the superposition of predicted values of adiabatic film-cooling effectiveness from different cooling holes configurations (Eq. (3)) does not always apply in a three-dimensional turbine environment due the interacting jet hydrodynamics. In particular, it is shown that the radial migration of the fluid particles induced by secondary flow structure has an impact of the trajectory of the coolant jets. The trajectory of the upstream coolant jets changes the incoming flow configuration at the downstream rows, having either a positive or a negative impact on the film-cooling protection as a function of the spanwise position. If the upstream coolant jets are appropriately phase shifted with the new coolant jets, then a positive impact on the film-cooling protection is found. If the upstream jets are in phase with the new coolant jet, then a negative impact on the film-cooling protection is found. Taking into account this result, an improved arrangement of the holes of the second row on the pressure side can therefore be proposed.

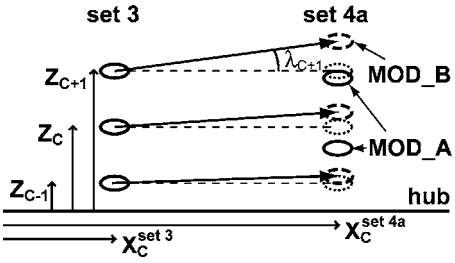

Fig. 15 Strategy for new hole arrangement

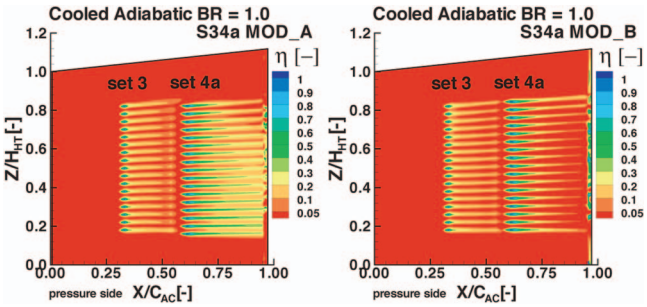

Fig. 16 Predicted contours of adiabatic film-cooling effectiveness η on pressure side obtained with the new hole arrangement in set 4a; MOD_A (left) and MOD_B (right)

Improvement of Holes Arrangement

Strategy. A prerequisite for the new arrangement of the holes in set 4a is that they should stay on the same row, i.e., at the same axial position. Indeed, it is aimed to show an improvement of the hole arrangement, which is not changing the global design of the blade, because it comes at the later stage of the design. Thus, the internal channel where the coolant is supplied should stay at the same location.

In order to improve the spreading of the coolant material downstream of the second row of holes, the previous flow analysis of the jets interaction is used. The holes of set 4 should therefore be relocated so that the coolant jets issuing from them should be phase shifted with the upstream coolant jets. This implies that the trajectory of the upstream jets should be first modeled in order to relocate the holes of set 4a. The current film-cooled turbine has an undisturbed incoming flow (no incoming vortices, hot streaks, etc.), and the analysis is done far enough from the end walls. The coolant jets trajectory is therefore only a function of the linearly increasing spanwise length of the blade, from leading edge to trailing edge (see Fig. 15). Hence, the trajectory of the upstream coolant jets is modeled as being a linear function of the axial distance. In detail, the change ΔZ_C of the spanwise position of the upstream jet issuing from hole C of set 3, as a function of its axial position X_C reads

$$\Delta Z_C = (X_C - X_C^{set3})\tan\theta_C \tag{5}$$

where θ_C is the pitch angle of the coolant jet trajectory. It is given by

$$\theta_C = (1-\varepsilon)\theta_h + \varepsilon\theta_t \quad \text{where} \quad \varepsilon = \frac{Z_C^{set3} - Z_h^{set3}}{Z_t^{set3} - Z_h^{set3}} \tag{6}$$

where θ_h is the pitch angle at the hub and θ_t is the pitch angle at the tip. The best modification (MOD_A) of the location of the holes in set 4a is to ensure that the jets issuing from them are phase shifted with the upstream jets. This means that the holes of set 4a should be located as follows:

$$Z_C^{set\ 4a\ MOD\_A} = 0.5(Z_{C-1}^{set3} + \Delta Z_{C-1}^{set3} + Z_C^{set3} + \Delta Z_C^{set3}) \tag{7}$$

The worst modification (MOD_B) of the location of the holes in set 4a is to make sure that the jets issuing from them are in phase with the upstream jets

$$Z_C^{set\ 4a\ MOD\_B} = Z_C^{set3} + \Delta Z_C^{set3} \tag{8}$$

The two proposed modifications of the holes arrangement in set 4a displace the center of the holes in the range of 0–1 mm (or two hole diameters). Manufacturing techniques to drill cooling holes, such as electrical discharge machining (EDM) have, in general, tolerances of 0.25 mm for positioning the center of the holes. Thus, the proposed modification of hole arrangement can be performed in terms of manufacturing.

Results. Predictions of contours of adiabatic film-cooling effectiveness on pressure side are plotted in Fig. 16 for the two modifications MOD_A and MOD_B of the hole arrangement in set 4a. The cooling protection is observed to be significantly better for the hole arrangement MOD_A, compared to MOD_B. Downstream of set 4a, the coolant material of a jet mixes with its two neighbors with case MOD_A all along the spanwise direction, whereas it never happened with the case MOD_B. Thus, the proposed modification of hole arrangement, given by Eqs. (7) and (8), based on the analysis of the jet hydrodynamics, is verified.

In order to verify if the modification of the hole arrangement MOD_A leads to an improvement of the cooling protection downstream of set 4a, the predicted profiles of lateral adiabatic film-cooling effectiveness, at $X/C_{AC}=0.80$, for the original and the modified (MOD_A) hole arrangement are compared in Fig. 17. The distribution of the adiabatic film-cooling effectiveness is observed to more uniform in the case MOD_A. Indeed, as it has previously been discuss, in the original hole arrangement, the coolant material does not spread enough near the hub because the upstream jet, coming from set 3 and the new jet, issuing from set 4a, are in phase. The modification of the hole arrangement MOD_A allows ensuring that for each holes in set 4a, the upstream jet and new jet are phase shifted. Hence, an improved arrangement of the holes in set 4a has been proposed.

This improvement could be made because a novel feature-based jet model is available for use in 3D RANS. The model can be used in a CFD code at a low computational cost and deliver useful prediction for the designer. This improvement is purely based on a numerical study so that additional experimental verifications are still needed. Eventually, it is well known that flows through high-pressure turbine exhibits much stronger flow distortions than only radial migration. These are, in particular, hot streaks and incoming vortices, which would have to be taken into account in any future optimization.

Conclusion

- The use of a novel feature-based jet model for predicting the 3D flow through a linear film-cooled turbine cascade has been demonstrated.
- In total, 67 cooling holes have been taken into account. There have been placed on the suction and pressure surface. A computational mesh of 2.13×10^6 grid nodes has been

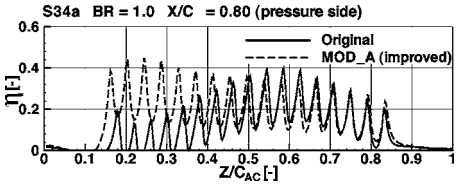

Fig. 17 Predicted profiles of lateral adiabatic film-cooling effectiveness η on the pressure side, at $X/C_{AC}=0.80$, for the original hole arrangement and the improved hole arrangement (MOD_A)

used. This grid size would be about one order of magnitude smaller than if a mesh, including the holes and plenum chamber, would be used. In addition, the geometrical and meshing complexity is alleviated. This reduction in the mesh size corresponds to between one to two order of magnitude reduction in the required computational time, when using the same computational scheme.

- Computational overhead when using the model is at 0.1% per hole compared to an uncooled computation on the same grid.
- Predictions of blade loading are in excellent agreement with experimental data. Predictions of adiabatic film-cooling effectiveness and of the Nusselt number are in agreement with experimental data.
- Different arrangements of the cooling rows are numerically investigated on the pressure side. It is observed that the hydrodynamics of the jets (i.e., interactions of jets issuing from different rows of holes) can enhance or lower the film-cooling protection, as a function of the arrangement of the holes on the rows. This is due to the flow distortions through the passage induced by the local secondary flow structure.
- Thanks to the computational efficiency of the model, a new arrangement of the cooling holes can be proposed to get a better film-cooling protection after the second row of holes on the pressure side. To the authors' knowledge, this study shows, for the first time, that taking into account the global 3D flow field can be quantitatively beneficial for the design of film-cooling holes.

Acknowledgment

The authors would like to acknowledge the support of this project by GE Aircraft Engines through their university strategic alliance program. Specifically, the technical interactions with Dr. Robert Bergholz and Dr. Fred Buck have been very helpful in the formulation of this project. We would also like to thank Bob Mischo and Dr. Martin Rose for fruitful discussions.

Nomenclature

X, Y, Z = axial, lateral, vertical (spanwise) coordinate
$\boldsymbol{U}$ = velocity vector
ρ = density
P = pressure
T = temperature
θ = normalized total temp. $=(T_T - T_T^c)/(T_T^f - T_T^c)$
d = hole diameter
α_0 = streamwise injection angle
β_0 = lateral injection angle
DR = density ratio $=\rho^c/\rho^f$
BR = blowing ratio $=\rho^c U^c/\rho^f U^f$
IR = momentum flux ratio $=\mathrm{BR}^2/\mathrm{DR}$
C_{TC} = blade true chord
C_{AC} = blade axial chord
H_{HT} = blade span (hub to tip height at leading edge)
C_d = discharge coefficient
γ = isentropic exponent
σ = overhead $=100[(\Delta t_{\text{cooled}} - \Delta t_{\text{uncooled}})/\Delta t_{\text{uncooled}}]$
Δt = time to iterate once the CFD algorithm
N_h = number of holes
$N_{X,Y}$ = grid density, per hole diameter
Nu = Nusselt number $=q_w' C_{TC}/\kappa(T_T^f - T_w)$
Ma = isentropic Mach $=\sqrt{2/(\gamma-1)[(P_T^f/P_s)^{\gamma-1/\gamma}-1]}$
q_w' = blade wall heat transfer rate $=-\kappa(\partial T/\partial n)_w$
h = heat transfer coefficient
κ = gas conductivity
η = wall adiabatic film-cooling effectiveness $=(T_{\text{rec}} - T_{aw})/(T_{\text{rec}} - T_T^c)$
R = total number of rows
λ = pitch (vertical to axial) angle

Subscripts/Superscripts

T = total
s = static
c = coolant fluid
C = cooling hole
f = freestream fluid
aw = adiabatic wall
rec = recovery

References

[1] Bergeles, G., Gosman, A. D., and Launder, B. E., 1981, "The Prediction of Three-Dimensional Discrete-Hole Cooling Processes—Part 2," ASME J. Heat Transfer, **103**, pp. 141–145.
[2] Demuren, A. O., Rodi, W., and Schönung, B., 1986, "Systematic Study of Film Cooling With a Three-Dimensional Calculation Procedure," ASME J. Turbomach., **108**(3), pp. 124–130.
[3] Lakehal, D., 2002, "Near-Wall Modeling of Turbulent Convective Heat Transport in Film Cooling of Turbine Blades With the Aid of Direct Numerical Simulation Data," ASME J. Turbomach., **124**(3), pp. 485–498.
[4] Leylek, J. H., and Zerkle, R. D., 1994, "Discrete-Jet Film Cooling: A Comparison of Computational Results With Experiments," ASME J. Turbomach., **116**(3), pp. 358–368.
[5] Walters, D. K., and Leylek, J. H., 2000, "A Detailed Analysis of Film-Cooling Physics—Part I: Streamwise Injection With Cylindrical Holes," ASME J. Turbomach., **122**(1), pp. 102–112.
[6] Morton, B. R., and Ibbetson, A., 1996, "Jets Deflected in a Crossflow," Exp. Therm. Fluid Sci., **12**, pp. 112–133.
[7] Garg, V. K., and Abhari, R. S., 1997, "Comparison of Predicted and Experimental Nusselt Number for a Film-Cooled Rotating Blade," Int. J. Heat Fluid Flow, **18**, pp. 452–460.
[8] Garg, V. K., and Gaugler, R. E., 1997, "Effect of Velocity and Temperature Distribution at the Hole Exit on Film Cooling of Turbine Blades," ASME J. Turbomach., **119**(2), pp. 343–445.
[9] Heidmann, J. D., Rigby, D. L., and Ameri, A. A., 2000, "A Three-Dimensional Coupled Internal/External Simulation of a Film-Cooled Turbine Vane," ASME J. Turbomach., **122**(2), pp. 348–359.
[10] Crawford, M. E., Kays, W. M., and Moffat, R. J., 1976, "Heat Transfer to a Full Coverage Film-Cooled Surface With 30° Slant-Hole Injection," NASA Contractor Report No. CR-2786.
[11] Schönung, B., and Rodi, W., 1987, "Predictions of Film Cooling by a Row of Holes With a Two-Dimensional Boundary-Layer Procedure," ASME J. Turbomach., **109**(4), pp. 579–587.
[12] Kulisa, P., Leboeuf, F., and Perrin, G., 1992, "Computation of a Wall Boundary Layer With Discrete Jet Injections," ASME J. Turbomach., **114**(4), pp. 756–764.
[13] Tafti, D. K., and Yavuzkurt, S., 1990, "Prediction of Heat Transfer Characteristics for Discrete Hole Film Cooling for Turbine Blade Applications," ASME J. Turbomach., **112**(3), pp. 504–511.
[14] Abhari, R. S., 1996, "Impact of Rotor-Stator Interaction on Turbine Blade Film Cooling," ASME J. Turbomach., **118**(1), pp. 123–133.
[15] Forest, A. E., White, A. J., Lai, C. C., Guo, S. M., Oldfield, M. L. J., and Lock, G. D., 2004, "Experimentally Aided Development of a Turbine Heat Transfer Prediction Method," Int. J. Heat Fluid Flow, **25**, pp. 606–617.
[16] Burdet, A., Abhari, R. S., and Rose, M. G., 2005, "Modeling of Film Cooling—Part II: Model for Use in 3D CFD," ASME Paper No. GT2005-68780.
[17] Burdet, A., and Abhari, R. S., 2006, "A Computationally Efficient Film Cooling Jet Model Using the Implicit Immerse Boundary Method," Comput. Fluids, submitted.
[18] Bernsdorf, S., Rose, M. G., and Abhari, R. S., 2006, "Modeling of Film Cooling—Part I: Experimental Study of Flow Structure," ASME J. Turbomach., **128**(1), pp. 141–149.
[19] Moussa, Z. M., Trischka, J. W., and Eskani, S., 1977, "The Near Field in the Mixing of a Round Jet With a Cross Stream," J. Fluid Mech., **80**(1), pp. 49–80.
[20] Burdet, A., 2005, "A Computationally Efficient Feature-Based Jet Model for Film-Cooling Flows Prediction," Ph.D. thesis No. 16163, ETH-Zürich, Switzerland.
[21] Majumdar, S., Iaccarino, G., and Durbin, P., 2001, "RANS Solver With Adaptive Structured Boundary Non-Conforming Grids," CTR Annual Research Briefs, pp. 353–366.
[22] Abhari, R. S., and Epstein, A. H., 1994, "An Experimental Study of Film Cooling in a Rotating Transonic Turbine," ASME J. Turbomach., **116**(1), pp. 63–70.
[23] Schultz, D., Jones, T. V., Oldfield, M. L. G., and Daniels, L. C., 1977, "A New Transcient Cascade Facility for the Measurement of Heat Transfer Rates," *High Temperature Problems in Gas Turbine Engines*, AGARD Conf. Proc. Vol. 229.
[24] Ashworth, D. A., 1987, "Unsteady Aerodynamics and Heat Transfer in a Transonic Turbine Stage," Ph.D. thesis, Osney Lab., St. John's College, University of Oxford, England.

[25] Rigby, M. J., Johnson, A. B., and Oldfield, M. L. G., 1990, "Gas Turbine Rotor Blade Film Cooling With and Without Simulated NGV Shock Waves and Wakes," ASME Paper No. 90-GT-78.
[26] Ni, R. H., 1981, "A Multiple Grid Scheme for Solving the Euler Equations," AIAA J., **20**(11), pp. 1565–1571.
[27] Hyams, D. G., and Leylek, J. H., 2000, "A Detailed Analysis of Film Cooling Physics—Part III: Streamwise Injection With Shaped Hole," ASME J. Turbomach., **122**(1), pp. 122–132.
[28] Garg, V. K., 1999, "Heat Transfer on a Film-Cooled Rotating Blade Using Different Turbulence Model," Int. J. Heat Mass Transfer, **42**, pp. 789–802.
[29] Medic, G., and Durbin, P., 2002, "Toward Improved Film Cooling Prediction," ASME J. Turbomach., **124**(2), pp. 193–199.
[30] Sellers, J. P., 1963, "Gaseous Film Cooling With Multiple Injection Stations," AIAA J., **1**, pp. 2154–2156.

Jongmyung Park

Matt Goodro

Department of Mechanical Engineering,
Convective Heat Transfer Laboratory,
University of Utah,
50 S. Central Campus Drive, MEB 2110,
Salt Lake City, UT 84112-9208

Phil Ligrani

Donald Schultz Professor of Turbomachinery
Department of Engineering Sciences,
Parks Road,
University of Oxford,
Oxford OX1 3PJ, UK

Mike Fox

Hee-Koo Moon

Aero/Thermal & Heat Transfer,
Solar Turbines, Inc.,
2200 Pacific Highway,
P.O. Box 85376,
Mail Zone C-9,
San Diego, CA 92186-5376

Separate Effects of Mach Number and Reynolds Number on Jet Array Impingement Heat Transfer

Limited available data suggest a substantial impact of Mach number on the heat transfer from an array of jets impinging on a surface at fixed Reynolds number. Many jet array heat transfer correlations currently in use are based on tests in which the jet Reynolds number was varied by varying the jet Mach number. Hence, this data may be inaccurate for high Mach numbers. Results from the present study are new and innovative because they separate the effects of jet Reynolds number and jet Mach number for the purposes of validating and improving correlations that are currently in use. The present study provides new data on the separate effects of Reynolds number and Mach number for an array of impinging jets in the form of discharge coefficients, local and spatially averaged Nusselt numbers, and local and spatially averaged recovery factors. The data are unique because data are given for impingement jet Mach numbers as high as 0.60 and impingement jet Reynolds numbers as high as 60,000, and because the effects of Reynolds number and Mach number are separated by providing data at constant Reynolds number because the Mach number is varied, and data at constant Mach number because the Reynolds number is varied. As such, the present data are given for experimental conditions not previously examined, which are outside the range of applicability of current correlations. [DOI: 10.1115/1.2437774]

Introduction

Impingement cooling is widely used to remove heat loads resulting from exposure to hot gases or hot liquids on components employed in a variety of applications. Impingement cooling is an attractive alternative for the use of such cooling fluids because its effectiveness is relatively high, thus providing a viable method for heat load management. The main objective of such cooling is maximum heat removal with minimal coolant mass flow rates. As a result, impinging jets are often delivered by orifices that have been cast or machined into internal structural members contained with components that are part of the particular application. For example, when employed for cooling leading-edge regions of turbine blades and vanes, the impingement air enters the leading-edge cavity from an adjacent cavity through a series of crossover holes on the partition wall between the two cavities. The crossover jets then impinge on the concave leading-edge wall and then exit either through film-cooling holes or though exit passages that lead to another part of the airfoil. With this arrangement, spanwise lines of impingement jets are produced, which direct cooling air on high external heat load regions, such as the stagnation region [1]. Impingement cooling is also often used to cool parts of the combustor in gas turbine engines, including combustion chamber liners, transition pieces, and splash plates. In each case, impinging jets are used individually or in arrays [2].

A wealth of papers are available in the literature on impingement cooling. Most existing investigations consider the effects of changing impingement plate geometric and configuration parameters, and physical parameters in flows with low Mach numbers, and relatively low speeds. Of these studies, Kercher and Tabakoff [3] present spatially averaged surface heat transfer coefficients beneath an array of impinging jets in low-speed flow for Reynolds numbers from 3×10^2 to 3×10^4, X/d and Y/d from 3.1 to 12.5, and Z/d from 1.0 to 4.8. Spent air flow from the impingement array exits the flow passage in one direction. According to these investigators, the spatially averaged heat transfer coefficients are dominated by the Reynolds number, and streamwise/spanwise hole spacing. In addition, increasing cross-flow decreases heat transfer performance, and heat transfer coefficients with cross-flow increase with decreasing Z/d. Of studies that consider heat transfer within airfoil leading-edge regions, Metzger et al. [4] and Chupp et al. [5] address heat transfer with a semi-circular concave region with a line of circular jets impinging on the apex. The effects of target spacing, hole spacing, and jet Reynolds number are considered. Metzger and Korstad [6] examine the influences of cross-flow on a single line of jets, emerging from circular holes, placed on one wall of a channel. The authors show that a number of parameters influence heat transfer on the target wall, including target spacing, jet Reynolds number, and the relative strengths of the jet flow and the cross-flow. Like the investigation of Kercher and Tabakoff [3], Chance [7] also investigates low-speed impingement cooling with spent air constrained to flow out only one side of the flow passage. He describes static pressure variations with the impingement passage that become larger with higher cross-flow velocities as Z/d decreases. Optimal values of Z/d are described, which depend on the ratio of total jet area to heat transfer area, for best heat transfer enhancement. Also addressed in this investigation are data at Reynolds numbers from 6×10^3 to 5×10^4, square, equilateral triangle, and rectangular jet arrays, Z/d values of 2, 3, 4, 6, and 8, and ratios of impingement to surface absolute temperature of 0.77, 1.27, and 1.54. In another paper, Metzger et al. [8] present heat transfer characteristics measured on a target surface beneath a two-dimensional array of impinging jets

Contributed by the International Gas Turbine Institute of ASME for publication in the JOURNAL OF TURBOMACHINERY. Manuscript received May 27, 2006; final manuscript received May 31, 2006. Review conducted by David Wisler. Paper presented at the ASME Turbo Expo 2006: Land, Sea and Air (GT2006), Barcelona, Spain, May 8–11, 2006. Paper No. GT2006-90628.

also in low-speed flow. Investigated are Z/d values of 1, 2, and 3, X/d and Y/d ranging from 6 to 32, and Reynolds numbers from 5×10^3 to 2×10^4. These investigators indicate that in-line jet impingement hole patterns provide better heat transfer than staggered arrangements. Florschuetz et al. [9] describe a continuation of this investigation, wherein Reynolds numbers from 2.5×10^3 to 7×10^4, inline and staggered hole patterns, Z/d from 1 to 3, X/d from 5 to 15, and Y/d from 4 to 8 are considered. As for the previous investigation, impinging air is again constrained to exit in a single direction from the channel formed between the impingement plate and the target plate. Included are data on channel cross-flow mass velocity and jet mass velocity (where ratios range from 0 to 0.8), as well as a correlation that gives Nusselt number dependence on these parameters, as well as on jet impingement plate geometry, Prandtl number, and Reynolds number.

More recently, Obot and Trabold [10] consider different cross-flow schemes on impingement heat transfer in low-speed flows. Impingement jet Reynolds numbers from 1×10^3 to 2.1×10^4, Z/d values from 2 to 16, X/d values of 5 and 10, and Y/d values of 4 and 8 are employed. According to these investigators, for a given cross-flow scheme and constant jet diameter d, higher heat transfer coefficients are obtained as the number of jets over a fixed target area increases. Unrestricted flow of spent air away from the target surface gives the best heat transfer performance in terms of magnitude and uniformity of cooling. Progressively lower performance is obtained as the cross-flow is restricted to exit through two opposite sides, and then, through one side of the passage between the impingement hole plate and the target plate. Bunker and Metzger [11] present detailed local heat transfer distributions due to line jet impingement for leading-edge regions, both with and without film extraction effects. Fox et al. [12] examine the effects of unsteady vortical structures on the adiabatic wall temperature distribution produced by a single impinging jet. Secondary vortex structures within the jet are described that alter adiabatic surface temperatures when the target plate is near the jet nozzle (i.e., Z/d of 1, 2, or 4). This is due to spatially varying total temperatures produced by these vortical structures, which result in relatively high total temperatures within jet central regions, with lower values near the edges of the jets. Also important are self-sustaining acoustic resonance events, which, when present, also alter adiabatic surface temperature distributions. Bailey and Bunker [13] investigate impingement arrays with inline jets in a "square array," with axial and lateral jet spacings of 3, 6, and 9. Reynolds numbers range from 1.4×10^4 to 6.5×10^4, Mach numbers are relatively low, and jet plate-to-target spacings range from 1.25 to 5.5 impingement hole diameters. Included are correlations developed from these data, which extend the range of applicability of the correlations presented by Florschuetz et al. [9]. Other recent studies considered the effects of jet impingement on a leading-edge/concave wall with roughness [14], and the effects of jets with mist and steam on a concave target surface [15]. Parsons et al. [16,17], Parsons and Han [18], Epstein et al. [19], and Mattern and Hennecke [20] show that rotational effects are important for jets impinging on flat surfaces at relatively low Reynolds numbers. For example, Parsons et al. [17] show a reduction in Nusselt numbers of the order of 30% at jet rotation numbers of around 0.0025, when jet Reynolds numbers are $<10{,}000$. However, there is little or no information available at higher jet Reynolds numbers and jet rotation numbers on concave surfaces relevant to engine conditions. Thus, it is evident that, aside from a few investigations, most of the impingement data from the open literature are obtained on flat, smooth surfaces. In another recent investigation that employs flat target plates, Brevet et al. [21] consider one row of impinging jets in a test section with low-speed flow in which the spent air is again constrained to exit in one direction. Effects of impingement distance, Reynolds number, and spanwise hole spacing on Nusselt number distributions lead to recommendations for optimal Z/d values of 2 to 5, and optimal spanwise hole spacings of 4 to 5 hole diameters. Data obtained at Reynolds numbers from 5×10^3 to 2×10^4, Z/d of 1, 2, 5, and 10, and X/d, Y/d values of 2, 4, 6, and 10 also show that local and spatially averaged Nusselt numbers increase substantially with Reynolds number.

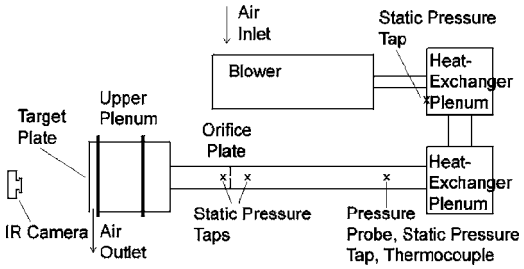

Fig. 1 Impingement flow facility

In one of the only known investigations to consider Mach number effects, Brevet et al. [22] describe recovery factors and Nusselt numbers measured on a flat target surface beneath a single, compressible impingement jet. Results are given for Z/d ratios from 2 to 10, at different Mach numbers from 0.02 to 0.69. Data sets with different Mach numbers and constant Reynolds number are obtained using different impingement hole plates with different hole diameters from 3 mm to 15 mm. According to these authors, increasing the Mach number (as the Reynolds number is constant) improves impingement heat transfer significantly, provided the impingement jet Mach number is >0.2.

In spite of the number of existing impingement cooling studies, newer and more specific cooling configurations are being used in gas turbines, which require additional information to account for a number of currently unexplored effects as they influence impingement heat transfer. Two of the most important of these unexplored areas are the *separate* effects of Mach number and Reynolds number for an array of impinging jets. The present study provides data on these effects for an array of impinging jets in the form of discharge coefficients, local and spatially averaged Nusselt numbers, and local and spatially averaged recovery factors. The data are unique because data are given for impingement jet Mach numbers as high as 0.60 and impingement jet Reynolds numbers as high as 60,000 and because the effects of Reynolds number and Mach number are separated by providing data at constant Reynolds number because the Mach number is varied, and data at constant Mach number because the Reynolds number is varied. As such, the present impingement jet array study can be thought of as a continuation of the investigation of Brevet et al. [22] wherein Mach number influences are considered only for a single impingement jet.

Experimental Apparatus and Procedures

Impingement Flow Facility and Impingement Plate. Schematic diagrams of the facility used for heat transfer measurements are presented in Figs. 1 and 2. The facility is constructed of 6.1 mm thick ASTM A38 steel plates and A53 Grade B ARW steel piping, and is open to the laboratory air at its inlet and exit. Depending on the required flow conditions, one of two blowers is employed. For the lower Reynolds numbers investigated, a New York Blower Co. 7.5 HP, size 1808 pressure blower is employed. For higher Reynolds numbers, a DRUM Industries, 50 HP, D807 pressure blower is employed. In each case, the air mass flow rate provided to the test section is measured (downstream of whichever blower is employed) using an ASME standard orifice plate, flow-mounted calibrated copper-constantan thermocouples, and Validyne DP15 pressure transducers (with diaphragms rated at 13.8 kPa or 34.5 kPa) connected to DP10D Carrier Demodulators. The blower exits into a series of two plenums arranged in series (the upstream plenum is 0.63 m to a side and the downstream plenum measures 0.63 m $\times$ 0.77 m $\times$ 0.77 m). A Bonneville cross-

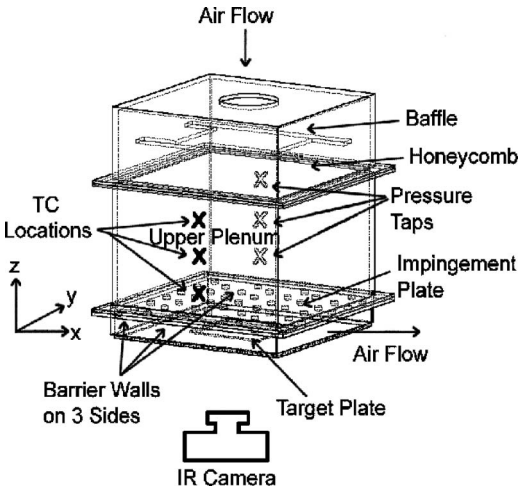

Fig. 2 Impingement flow facility test section, including impingement plenum and impingement channel

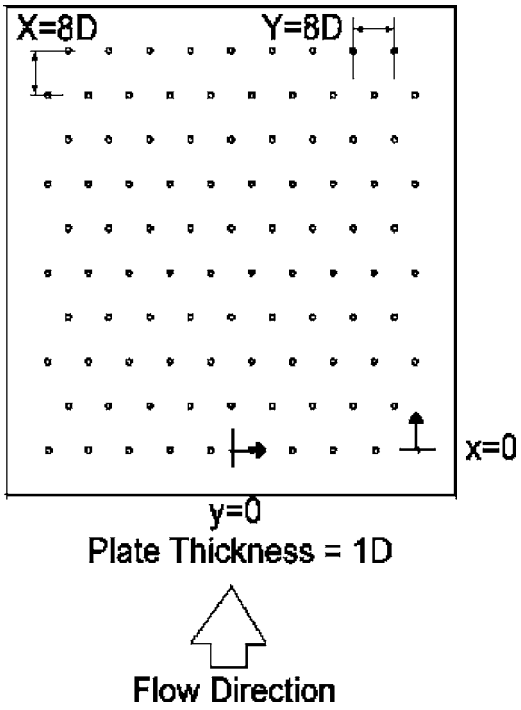

Fig. 3 Impingement test plate configuration

flow heat exchanger is located within the plenum, which is farther downstream. As the air exits the heat exchanger, and the second plenum, the air passes into a 0.22 m o.d. pipe, which contains the ASME Standard orifice plate employed to measure the air mass flow rate. This pipe then connects to the 0.635 m by 0.635 m side of a plenum. On entering this plenum, the air first encounters a flow baffle used to distribute the flow, a honeycomb, and other flow straightening devices. These are followed by the impingement plenum (or upper plenum, located below the honeycomb and flow straightening devices) whose top dimensions are 0.635 m and 0.635 m, and whose height is 0.40 m.

Individual plates with holes used to produce the impingement jets are located at the bottom of this plenum, as shown in Fig. 2 and is described in Table 1. The plenum is thus designed so that different impingement plates can be installed at this location using a 9.5 mm thick polyurethane gasket and 1/4 in SAE J429 Grade 5 bolts. Figure 3 shows that each impingement plate is arranged with ten rows of holes in the streamwise direction, arranged so that holes in adjacent rows are staggered with respect to each other. With this arrangement, either nine or ten holes are located in each streamwise row. The spacing between holes in the streamwise direction X is then $8D$, and the spanwise spacing between holes in a given streamwise row Y is also $8D$. The thickness of each impingement plate is $1D$. The spacing between the hole exit planes and the target plate is denoted Z and is equal to $3D$. Note that the coordinate system employed is also shown in Fig. 3. The impingement cooling flow, which issues from these holes is contained within the channel formed by the impingement jet plate and the target surface, and is constrained to exit in a single direction, which here, is denoted as the x direction. This channel is called the lower plenum. As different plates are employed with different-sized impingement holes, this is accomplished using different polycarbonate spacers that are exactly $3D$ in height and are sealed in place around three sides of the impingement channel. Plates with different impingement hole diameters are used to provide data at a variety of Mach numbers and Reynolds numbers. Specific hole sizes, mass flow rates, and pressure levels are employed so that data are obtained at different Mach numbers as the Reynolds number is constant, and at different Reynolds numbers as the Mach number is constant.

Table 1 Impingement test plate configurations

Hole Diameter, D	Plate Thickness	Hole Spacing, X,Y
2.5 mm	2.5 mm	20.0 mm
3.5 mm	3.5 mm	28.0 mm
4.5 mm	4.5 mm	36.0 mm
8.0 mm	8.0 mm	64.0 mm
15.0 mm	15.0 mm	120.0 mm
20.0 mm	20.0 mm	160.0 mm

Target Plate Test Surfaces for Measurements of Surface Recovery Factors and Surface Nusselt Numbers. Two different types of target plates are employed. Polycarbonate target plates are used for measurement of spatially resolved distributions of surface adiabatic surface temperature and surface recovery factor. Polycarbonate is chosen because of its strength, its low thermal conductivity (0.16 W/mK at 20°C), and to minimize streamwise and spanwise conduction along the test surface, and thus, minimize "smearing" of spatially varying temperature gradients along the test surface. Each plate is 1.58 mm thick and mounted on the bottom surface of the plenum using gray cloth tape with PVC cement, a solvent containing methyl ethyl ketone, tetrahydrofuran, and acetone to seal the edges so that no leaks are present along the flow passage. A mounting frame is also employed to hold the target plate in place, to keep it smooth (without bending or wrinkles), and normal to the impingement jets, as testing is underway. Ten calibrated, copper-constantan thermocouples are placed at different streamwise and spanwise locations within the polycarbonate so that each senses a different temperature as data are acquired. Each one of these thermocouples is mounted ~0.02 cm just below the surface adjacent to the air containing the impingement fluid, to provide measurements of local surface temperatures, after correction for thermal contact resistance and temperature drop through the 0.16 cm thickness of polycarbonate. Thermocouple lead wires are placed in grooves along the polycarbonate and bonded into place with epoxy to minimize thermal disturbances resulting from their presence.

Spatially resolved distributions of surface heat transfer coefficients and Nusselt numbers are measured on polystyrene target plates with heaters and thermocouples attached. The custom-made HK5184R26 thermofoil heaters employed are manufactured by Minco Products Inc. and have a temperature rating of 100°C. The

etched-foil heating element within this device is encased between two layers of DuPont Kapton polyimide film and used to provide a constant surface heat flux boundary condition. This heater is located adjacent to the air stream with the impinging air jets. Its thermal conductivity is 0.2 W/mK at 20°C. Polystyrene is chosen for the target plate because of its strength and because it does not deform in shape at temperatures as high as 80°C. It is also suitable because of its low thermal conductivity (0.09 W/mK at 20°C), which results in minimal streamwise and spanwise conduction along the test surface. The back side of this polystyrene plate is viewed by the infrared camera as spatially resolved measurements of surface temperature are obtained. Each polystyrene target plate is 1.27 mm thick and each heater is ~0.3 mm thick, giving a total target plate thickness of 1.57 mm. Like the recovery factor target test plates, and these plates are mounted on the bottom surface of the plenum using gray cloth tape with PVC cement to seal the edges so that no leaks are present along the flow passage. A mounting frame is also again employed to hold the target plate in place, to keep it smooth (without bending or wrinkles), and normal to the impingement jets, as testing is underway. In order to detect different surface temperatures as testing is underway, nine calibrated, copper-constantan thermocouples are placed at different streamwise and spanwise locations within the polystyrene. Each one of these is mounted just below the surface adjacent to the air containing the impingement fluid, between the thermofoil heater and the polystyrene portion of the target plate. Because each thermocouple is used to measure local surface temperature, corrections are made for thermal contact resistance and local temperature drop through the thermofoil heater. Thermocouple lead wires are placed in grooves in the polystyrene and bonded into place with epoxy to minimize thermal disturbances resulting from their presence. Because of the wear and degradation that results from exposure to different temperature levels as tests are conducted, these target plates are replaced with all new components after about three or four individual test sequences.

Local Impingement Air Pressure and Temperature Measurements. As shown in Fig. 2, three wall pressure taps are located on the surface of the upper plenum and eight wall pressure taps are located on the surface of the lower plenum for measurement of local static pressures. As tests are conducted, Validyne Model DP15-46 pressure transducers (with diaphragms rated at 13.8 kPa or 34.5 kPa) driven by DP10D Carrier Demodulators are used to sense pressures from these static pressure tappings. Local airflow recovery temperatures are measured using two calibrated copper-constantan thermocouples located in the central part of the lower plenum, and three calibrated copper-constantan thermocouples located in the central part of the upper plenum. In each case, readings from either multiple thermocouples or multiple pressure taps are used to obtain average values of measured quantities for a given plenum. In some cases, additional surface pressure taps are located on the exit side of the plate with the impingement holes. Voltages from the carrier demodulators and all thermocouples employed in the study are read sequentially using Hewlett-Packard HP44222T and HP44222A relay multiplexer card assemblies, installed in a Hewlett-Packard HP3497A low-speed Data Acquisition/Control Unit. This system provides thermocouple compensation electronically such that voltages for type-T copper-constantan thermocouples are given relative to 0°C. The voltage outputs from this unit are acquired by the Dell Precision 530 PC workstation through its USB port, using LABVIEW 7.0 software and a GPIB-USB-B adaptor made by National Instruments.

Because the overall volume and cross-sectional area of the upper plenum are large compared to the area of the impingement holes, the velocity and Mach number of the air in this plenum are both near zero. As a result, the static pressure measured at the wall static pressure taps is the same as the stagnation pressure and is denoted P_{oj}, the impingement air stagnation pressure. The measured air recovery temperature in the upper plenum is then the same as the upper plenum static temperature and upper plenum stagnation temperature. This resulting value is denoted T_{oj}, the impingement stagnation temperature. After measurement of the impingement air mass flow rate at the pipe orifice plate, the impingement air mass flux is determined using $\rho_a u_a = \dot{m}/A$.

An iterative procedure is then used to determine the impingement static temperature T_j, and the impingement flow Mach number Ma. The first step in this procedure is estimation of the value of T_j. The local recovery temperature, which is measured in the lower plenum, is used for this estimation. The impingement static density, and spatially averaged impingement jet velocity are then determined using $\rho_a = P_a/RT_j$, and $u_a = \dot{m}/\rho_a A$, respectively. Because the impingement flow vents to the laboratory, the local atmospheric pressure is used for P_a. Measurements of lower plenum static pressures using wall pressure taps confirm this approach. Next, the impingement air sonic velocity and Mach number are given by $c_a = (kRT_j)^{1/2}$ and $\mathrm{Ma} = u_a/c_a$, respectively. Iterations using these analysis steps are then continued until the impingement static temperature and impingement Mach number are consistent with the isentropic equation given by

$$T_j = \frac{T_{oj}}{1 + \mathrm{Ma}^2(k-1)/2} \tag{1}$$

with impingement static temperature T_j, impingement flow Mach number Ma, and other parameters known, the impingement Reynolds number is subsequently given by an equation of the form

$$\mathrm{Re}_j = \frac{\rho_a u_a D}{\mu} \tag{2}$$

A Kiel-type stagnation pressure probe is used to measure the total pressure in the pipe at a position that is located upstream of the orifice plate employed to measure mass flow rate. A wall pressure tap located on the surface of the pipe, and a calibrated copper-constantan thermocouple positioned within the air stream are used to sense static pressure and flow recovery temperature, respectively, at the same streamwise location. Pressures and temperatures measured using the thermocouple, probe, and tap are sensed and processed using the same types of instrumentation mentioned earlier. The velocities deduced from this arrangement are used to provide a cross-check on the velocities deduced from mass flow rates, which are measured using the ASME standard orifice plate.

Discharge Coefficient Determination. The discharge coefficient is determined using

$$C_D = \frac{\rho_a u_a}{\rho_i u_i} \tag{3}$$

The first step in determining the ideal impingement mass flux $\rho_i u_i$ is obtaining an ideal impingement Mach number Ma_i using

$$\frac{P_{oj}}{P_a} = \left[1 + \frac{\mathrm{Ma}_i^2(k-1)}{2}\right]^{k/k-1} \tag{4}$$

Next, impingement ideal static temperature T_i is determined using T_{oj}, the ideal Mach number Ma_i, and the appropriate ideal gas isentropic relationship. Impingement ideal static density is given by $\rho_i = P_a/RT_i$, and impingement ideal velocity is given by $u_i = \mathrm{Ma}_i(kRT_i)^{1/2}$. Note that, in most cases, discharge coefficients are determined that are based on P_a, the spatially averaged static pressure at the exits of the impingement holes. In some other cases, local discharge coefficients for different impingement holes located along the length of the plate are determined, which are based on measurements of local static pressure measured at different surface pressure taps located along the exit side of the impingement plate.

Local Recovery Factor Measurement. After the static temperature and stagnation temperatures of the impingement air are determined, the local surface recovery factor is determined at different target surface locations using

$$\mathrm{RF} = \frac{T_{AW} - T_j}{T_{oj} - T_j} \tag{5}$$

Here, T_{AW} represents the local adiabatic surface temperature which is present with zero heat flux on the target surface. Note that some small variations of local adiabatic surface temperature T_{AW} and local recovery factor RF are present due to streamwise and spanwise conduction along the test surface, but these are minimized by the use of the polycarbonate target plate and are included in the estimates of experimental uncertainty values for these two quantities. As tests are conducted and data are acquired, the impingement air jet stagnation temperature is maintained at or very near to the laboratory ambient temperature level $T_{oj} = T_{\mathrm{ambient}}$. This is accomplished using liquid nitrogen in the Bonneville heat exchanger to cool the impingement air to the appropriate level as it passes through the facility. This thermal condition, $T_{oj} = T_{\mathrm{ambient}}$, is then maintained for both the Nusselt number experiments and the recovery factor experiments to provide an appropriate basis of comparison between the data obtained from these two different types of experiments.

Local Nusselt Number Measurement. The power to the thermofoil heater, mounted on the target plate, is controlled and regulated using a variac power supply. Energy balances and analysis to determine temperature values on the two surfaces of the target plate then allow determination of the magnitude of the total convective power (due to impingement cooling) for a particular test. To determine the surface heat flux (used to calculate heat transfer coefficients and local Nusselt numbers), the total convective power level, provided by the particular thermofoil heater employed, is divided by the single surface area of this heater, denoted A_{ht}.

One step in this procedure utilizes a one-dimensional conduction analysis, which is applied between the surface *within* the target plate, where the thermocouples are located (between the heater and the polystyrene target plate), and the ambient air environment behind the target plate. This is used to determine T_b, the local temperature on the back surface of the polystyrene target plate, adjacent to the surrounding ambient air environment. Also required for this analysis is T_{tc}, the local temperature within the target plate between the heater and the polystyrene plate, which is determined from thermocouple measurements. With these temperatures known, the radiation heat flux and the convection heat flux from the back side of the target plate, q_{rb} and q_{cb}, respectively, are determined together using an equation of the form

$$q_{rb} + q_{cb} = h_{\mathrm{loss}}(T_b - T_{\mathrm{ambient}}) \tag{6}$$

where h_{loss} is assumed to be equal to 15 $\mathrm{W/m^2K}$ [21]. The radiation heat flux q_{rf} on the front (or impingement side) of the target plate is determined using

$$q_{rf} = \sigma\left(\frac{1}{\varepsilon_{\mathrm{inf}}} - \frac{1}{\varepsilon_f} - 1\right)^{-1}(T_W^4 - T_{\mathrm{ambient}}^4) \tag{7}$$

With this approach, the radiation heat flux is determined for an arrangement with multireflection between two infinite plates where each has a uniform temperature. ε_f and $\varepsilon_{\mathrm{inf}}$ are assumed to be equal to 0.9 for all conditions investigated. This approximate approach works well since $q_{rf}A_{ht}$ is generally only 3–6% of Q, the total amount of power provided to the thermofoil heater. Note that T_W, the local target surface temperature on the surface of the heater adjacent impingement air, must be known to determine q_{rf}. Because of the inter-dependence of T_W, q_{rf}, and q_{cf} (the convection heat flux from the front side or impingement side of the target plate), an iterative procedure is required to determine these quantities. The next part of this procedure uses a one-dimensional conduction model for the heater, which includes source generation of thermal energy, to provide a relation between T_W, T_{tc}, and q_{cf}. Also included in the analysis is thermal contact resistance between the internal thermocouples and the adjacent heater.

The convection heat flux from the front side (or impingement side) of the target plate is then given by

$$q_{cf} = \frac{Q}{A_{ht}} - q_{rf} - q_{rb} - q_{cb} \tag{8}$$

The local Nusselt number is then given as

$$\mathrm{Nu} = \frac{q_{cf}D}{(T_W - T_{oj})\alpha} \tag{9}$$

Modified local Nusselt numbers are also determined, which are based on the $(T_W - T_{oj}^*)$ and the $(T_W - T_{\mathrm{AW}})$ temperature differences. The determination of these parameters is discussed later in the paper.

Spatially resolved temperature distributions along the target test surface are determined using infrared imaging in conjunction with thermocouples, energy balances, digital image processing, and in situ calibration procedures. These are then used to determine spatially resolved surface Nusselt numbers. To accomplish this, the infrared radiation emitted by the heated interior surface of the channel is captured using a Thermacam PM390 Infrared Imaging Camera, which operates at infrared wavelengths from 3.4 μm to 5.0 μm. Temperatures, measured using the calibrated, copper-constantan thermocouples distributed along the test surface adjacent to the flow, are used to perform the in situ calibrations simultaneously as the radiation contours from surface temperature variations are recorded.

This is accomplished as the camera views the test surface from behind, as shown in Fig. 2. In general, six thermocouple junction locations are present in the infrared field viewed by the camera. The exact spatial locations and pixel locations of these thermocouple junctions and the coordinates of the field of view are known from calibration maps obtained prior to measurements. During this procedure, the camera is focused and rigidly mounted and oriented relative to the test surface in the same way as when radiation contours are recorded. Voltages from the thermocouples are acquired using the apparatus mentioned earlier. With these data, gray-scale values at pixel locations within video-taped images from the infrared imaging camera are readily converted to local Nusselt number values. Because such calibration data depend strongly on camera adjustment, the same brightness, contrast, and aperture camera settings are used to obtain the experimental data. The in situ calibration approach rigorously and accurately accounts for these variations.

Images from the infrared camera are recorded as eight-bit gray-scale directly into the memory of a Dell Dimension XPS T800r PC computer using a Scion Image Corporation Frame grabber video card, and Scion image v.1.9.2 software. One set of 15 to 20 frames is recorded at a rate of about one frame per second. All of the resulting images are then ensemble averaged to obtain the final gray-scale data image. This final data set is then imported into MATLAB version 6.1.0.450 (Release 12.1) software to convert each of 256 possible gray-scale values to local Nusselt number at each pixel location using calibration data. Each individual image covers a 256 pixel by 256 pixel area.

Experimental Uncertainty Estimates. Uncertainty estimates are based on 95% confidence levels and are determined using methods described by Kline and McClintock [23] and Moffat [24]. Uncertainty of temperatures measured with thermocouples is ±0.15°C. Spatial and temperature resolutions achieved with infrared imaging are ~0.1 mm to 0.2 mm, and 0.4°C, respectively. This magnitude of temperature resolution is due to uncertainty in determining the exact locations of thermocouples with respect to pixel values used for the in situ calibrations. Local Nusselt number uncertainty is then about ±4.8%. Uncertainty magnitudes of

Table 2 Experimental conditions employed in the present investigation

Experiment Number	Rej	Ma	D(mm)
2	59,700	0.21	15.0
6	11,100	0.20	3.0
7	13,100	0.20	3.5
8	17,300	0.20	4.5
9	30,500	0.20	8.0
16	30,000	0.11	15.0
17	30,500	0.20	8.0
18	30,000	0.35	4.5
19	31,000	0.45	3.5
20	30,000	0.60	2.5

local recovery factors and adiabatic surface temperatures are ±2.4%, and 0.5°C, respectively. Note that uncertainties of local Nusselt numbers, adiabatic surface temperatures, and recovery factors all include the effects of very small amounts of streamwise and spanwise conduction along the test surfaces employed. Reynolds number uncertainty is about ±2.0% for an Re_j value of 20,000. (See Table 2).

Experimental Results and Discussion

Table 2 gives a summary of the experimental conditions covered by the present investigation.

Impingement Hole Discharge Coefficients. Discharge coefficient data for the present experimental conditions, which represent average values for all of the impingement holes at a particular experimental condition, are presented in Fig. 4. Here, all discharge coefficients are based on P_a equal to the ambient pressure measured at the exit of the impingement flow facility. Here, data are presented that are measured at different impingement Mach numbers and a constant Reynolds number Re_j of 30,000, and at different impingement Reynolds numbers and a constant Mach number Ma of 0.2. The constant Mach number data decrease gradually as Re_j increases. The constant Reynolds number data then generally lie below the constant Mach number data. Overall, important variations are evident as the impingement Mach number varies, with lower discharge coefficients at higher values of the Mach number.

Determination of Spatially Averaged Adiabatic Surface Temperature T^*_{oj}. To determine an appropriate reference temperature to determine heat transfer coefficients and Nusselt numbers, the convective heat power from the front side (or impingement side) of the target plate q_{cf} is plotted as it varies with $(T_W - T_{oj})$. An example of such a plot for Re_j=30,500 and Ma=0.2 is shown in Fig. 5. Here, data are obtained at three different temperature differences. The largest temperature difference employed is always <30°C to avoid variations of measured Nusselt numbers with variable property effects. As a result, convective heat power data, such as presented in Fig. 5, vary linearly with $(T_W - T_{oj})$. Such linear data are extrapolated to the q_{cf}=0 axis to determine $(T_W - T^*_{oj})$. Note that the convective power is the value for the entire target plate. Consequently, the magnitude of T^*_{oj} is spatially averaged over the target plate heat transfer area, and as such, is the spatially averaged adiabatic surface temperature for the entire heated portion of the target plate at a particular experimental condition. Consequently, all Nusselt number data are obtained at three different values of $(T_W - T_{oj})$ to provide a means to determine T^*_{oj} for each experimental condition, and all Nusselt numbers are then calculated using

$$\mathrm{Nu} = \frac{q_{cf} D}{(T_W - T^*_{oj})\alpha} \tag{10}$$

Baseline Nusselt Numbers. Baseline Nusselt numbers are measured using a test plate and flow conditions that match ones used by Florschuetz et al. [9] with Re_j=34,500, Ma≅0, and an array of jets with $X=5D$, $Y=4D$, and $Z=3D$. In both cases, the effects of spent air cross-flow are considered, and the passage between the impingement plate and the target plate is closed on three sides. Figure 6 shows a comparison of results from the two investigations. The present data, line-averaged over Y/D from −8.0 to +8.0, and area-averaged also over Y/D from −8.0 to +8.0 and over $5D$ length segments in the streamwise direction, are compared to area-averaged data from Florschuetz et al. [9] in Fig. 6. The good agreement of the area-averaged data from the two sources validates the experimental procedures and apparatus employed in the present study. Also presented in this plot are local

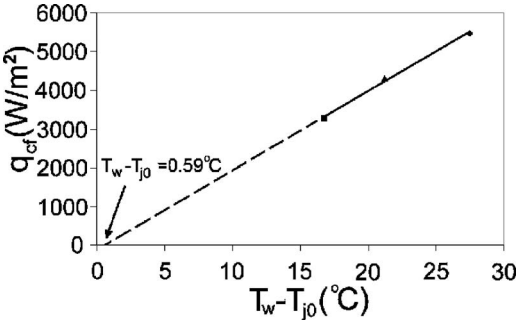

Fig. 5 Convection heat power from front side (or impingement side) of the target plate q_{cf} as it varies with $(T_W - T_{oj})$ for Re_j =30,500 and Ma=0.2

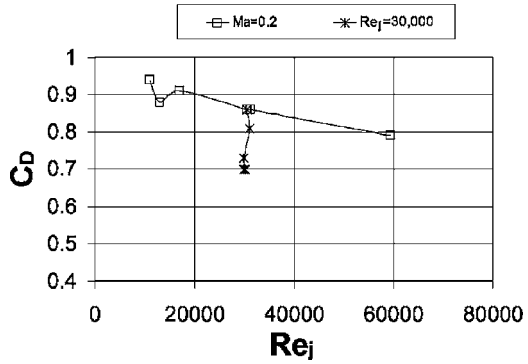

Fig. 4 Discharge coefficient data for Re_j=30,000 and different Mach numbers, and for Ma=0.2 and different Reynolds numbers

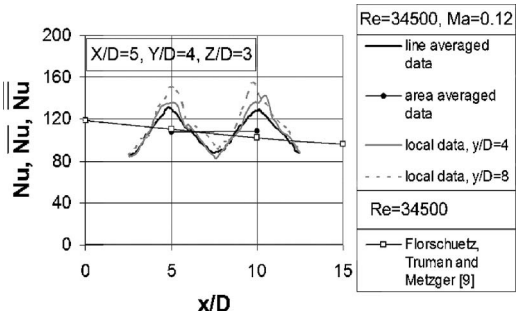

Fig. 6 Comparison of baseline Nusselt number data with correlation of Florschuetz et al. [9] for Re_j=34,500, Ma approximately equal to 0, and an array of jets with $X=5D$, $Y=4D$, and $Z=3D$

Nu data from the present investigation for $y/D=4$ and $y/D=8$.

Also investigated is the effect of the unheated starting length located upstream of the heated target plate. This is done by adding an extra heater upstream of the heater used on the target plate. Local and spatially averaged Nusselt numbers are then measured on the target plate, both with and without upstream heating, for $Re_j=34{,}500$ and $Ma=0.12$ with the same impingement hole plate as used for the other baseline data checks. The variation of local and spatially averaged Nusselt numbers between the two tests is only ~2%, at most, indicating minimal effect of thermal entry length on impingement heat transfer (for these particular experimental conditions).

Nusselt Number Variations With Reynolds Number. Surface Nusselt number distributions are presented in Fig. 7 for $Ma=0.20$, and Re_j values of 11,100, 17,300, 30,500, and 59,700. The different views of the test surface in the different parts of this figure are due to different infrared camera views of the target plate as impingement plates with different sized holes are employed on the opposite side. Note that, regardless of the Reynolds number, that the qualitative distributions of local Nusselt number produced by each impingement jet are similar, with good periodic repeatability in the spanwise direction for each streamwise row of impact locations. This spanwise periodicity is also illustrated by the local Nu data presented in Fig. 8(*a*) for $x/D=32$, and Re_j values of 11,100, 13,100, 17,300, 30,500, and 59,700.

Figure 7 also shows that only one local maximum value is present in the Nu distribution underneath each jet. Magnitudes of these local maximum values are about the same underneath the different impingement jets for the different Re_j values investigated, with occasional variations from one streamwise row to another. These variations with streamwise development are further illustrated by local Nusselt number data presented as it varies with x/D in Fig. 8(*b*) for $y/D=8$ and $y/D=0$. Here, the smaller peak values near $x/D=32$ and $x/D=48$, which are positioned between the larger peak values, are due to local Nusselt number increases at spanwise locations approximately halfway between the impact points of nearby impinging jets. However, in spite of these variations and differences, Figs. 7, 8(*a*), and 8(*b*) show that local maximum Nu values increase substantially as the Reynolds number increases.

Figure 9 presents Nusselt numbers for the same experimental conditions as they vary with x/D, which are line averaged over y/D from −8.0 to +8.0. Here, local maximum values are apparent, which are spaced ~8*D* apart, and are due to the impact of impingement jets from each different streamwise row of holes. Note that these local peak or local maximum line-averaged Nusselt number values become smaller at successive x/D locations for each value of impingement jet Reynolds number. However, in spite of these variations, the $\overline{Nu}$ data generally increase with Re_j at each x/D value.

Nusselt Number Variations With Mach Number. Figure 10 gives surface Nusselt number distributions for $Re_j=30{,}000$ and $Ma=0.20$, 0.45, and 0.60. As for the previous figures, the different views of the test surface in the different parts of this figure are due to different infrared camera views of the target plate as impingement plates with different sized holes are employed on the opposite side. Qualitative distributions of local Nusselt number produced by each impingement jet are also similar to each other and to the distributions shown in Fig. 7. Good periodic repeatability in the spanwise direction for each streamwise row of impact locations is also again apparent.

Figure 11(*a*) is given to further illustrate this spanwise periodicity as y/D varies for $x/D=32$, and Ma values of 0.11, 0.20, 0.35, 0.45, and 0.60. Streamwise variations for the same Mach number values are evident from local Nusselt number data presented as it varies with x/D in Fig. 11(*b*) for $y/D=8$. In both cases, important increases of local Nusselt numbers with Mach number are apparent at all x/D and y/D locations. The smaller peak values present in each distribution near $x/D=32$ and $x/D=48$, which are positioned between the larger peak values, are due to local Nusselt number increases at spanwise locations

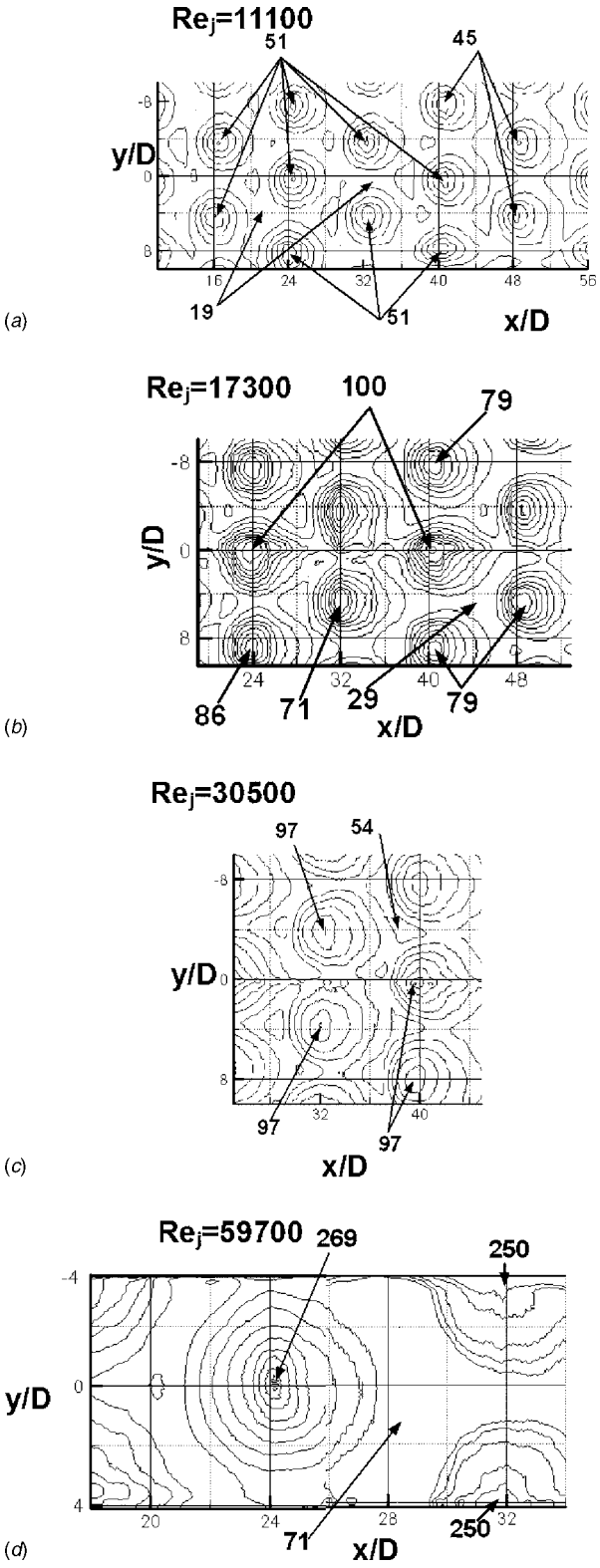

Fig. 7 Spatially resolved distributions of surface Nusselt number for Ma=0.20, and Re_j values of: (*a*) 11,100, (*b*) 17,300, (*c*) 30,500, and (*d*) 59,700

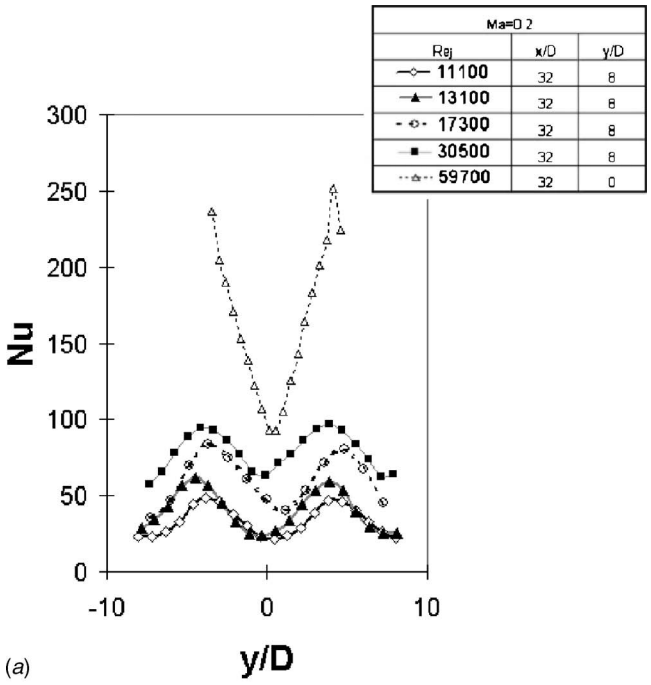

(*a*)

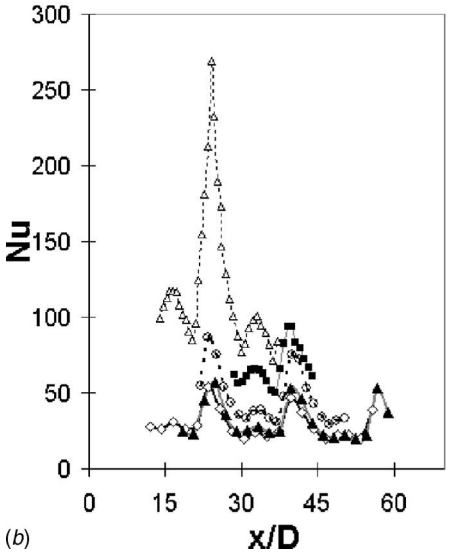

(*b*)

Fig. 8 Local surface Nusselt number variations for Ma=0.20, and Re_j values of 11,100, 13,100, 17,300, 30,500, and 59,700: (*a*) Variations with *y/D* for *x/D*=32 and (*b*) variations with *x/D* for *y/D*=8 and *y/D*=0

approximately halfway between the impact points of nearby impinging jets.

Corresponding line-averaged Nusselt number data are given in Fig. 12, also for Re_j=30,000 and Ma=0.20, 0.35, 0.45, and 0.60. Like the data presented in Fig. 9, these data are also obtained by line averaging over y/D values from −8.0 to +8.0. Figure 12 shows that local maximum $\overline{Nu}$ values have the same approximate streamwise spacing as the streamwise spacing of the holes located on the impingement jet plate. These local maximum values generally decrease at successive x/D locations for each value of impingement Mach number, Ma. Also evident in this figure are somewhat smaller maximum to minimum ranges of $\overline{Nu}$ as the Mach number increases, which gives higher spatially averaged values at higher values of the impingement Mach number.

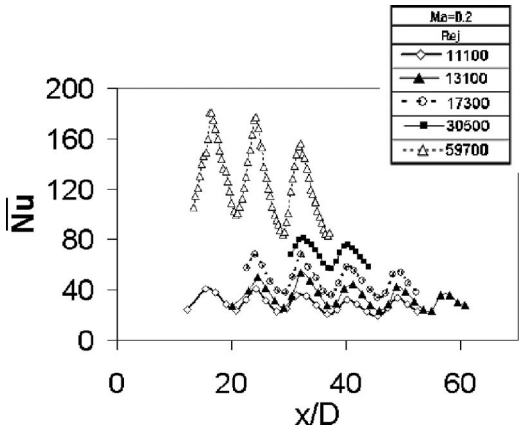

Fig. 9 Surface Nusselt number variations with *x/D*, which are line averaged over *y/D* from −8.0 to +8.0, for Ma=0.20, and Re_j values of 11,100, 13,100, 17,300, 30,500, and 59,700

Comparisons of Spatially Averaged Nusselt Numbers With Existing Correlations. Spatially averaged Nusselt numbers are compared to the correlation of Florschuetz et al. [9] in Figs. 13(*a*) and 13(*b*). The first of these figures shows Ma=0.20 data for Re_j values of 11,100, 13,100, 17,300, 30,500, and 59,700. Here, data from the present study show reasonably good matches to the correlation values from Florschuetz et al. [9] for all of these experimental conditions, except for Re_j=11,100, where the present data lie only slightly below correlation predicted values [9]. Figure 13(*b*) presents the present spatially-averaged data for Re_j=30,000, and Ma values of 0.11, 0.20, 0.35, 0.45, and 0.60. In this figure, data obtained at Ma=0.11 and Ma=0.20 show good agreement with the Florschuetz et al. [9] correlation. The present data then deviate from this correlation by larger amounts as the impingement Mach number increases further, with the largest deviation evident for Ma=0.60. This trend is also evident in other results measured at high Mach numbers at other Reynolds numbers, which confirms the need for a new correlation to represent high Mach number impingement data. The qualtitative trend shown by the data in Fig. 13(*b*) is also consistent with results from Brevet et al. [22] for a single impingement jet.

The variation of spatially averaged Nusselt numbers with Mach number is shown in Fig. 13(*c*). These data are for specific x/D locations. The correlation equation which best represents these data is given by

$$\frac{\overline{\overline{Nu}}}{\overline{\overline{Nu}}_F} = 1.0 + 0.58\ Ma^{1.35} \tag{11}$$

which is valid for Re_j=30,000, $0.2 \le Ma \le 0.6$, X/D=8, Y/D=8, Z/D=3, and $32 \le x/D \le 56$.

Recovery Factor Data. Recovery factor data provide information on the variation of adiabatic surface temperature over the test surface. Examples are shown in Figs. 14(*a*)–14(*c*) for Re_j=30,000 and Ma=0.60. The contour plot data show higher values of recovery factor RF beneath and in the vicinity of impact locations of the impingement jets. This is because T_{oj}=24.04°C, which is approximately equal to $T_{ambient}$ for these tests which gives T_j equal to 4.90°C. As a result, there is heat transfer to the impinging air streams from the surrounding air, an effect that is enhanced by the families of vortices associated with the jet, and the enhanced mixing and entrainment they produce of surrounding fluid to the jets [12]. Nearby jet impact locations, values of RF continue to be relatively high and >1.0, especially on the spanwise sides of impact locations. However, values are <1 at upstream and downstream locations. Such local variations and the quantitative variations associated with them are further illustrated

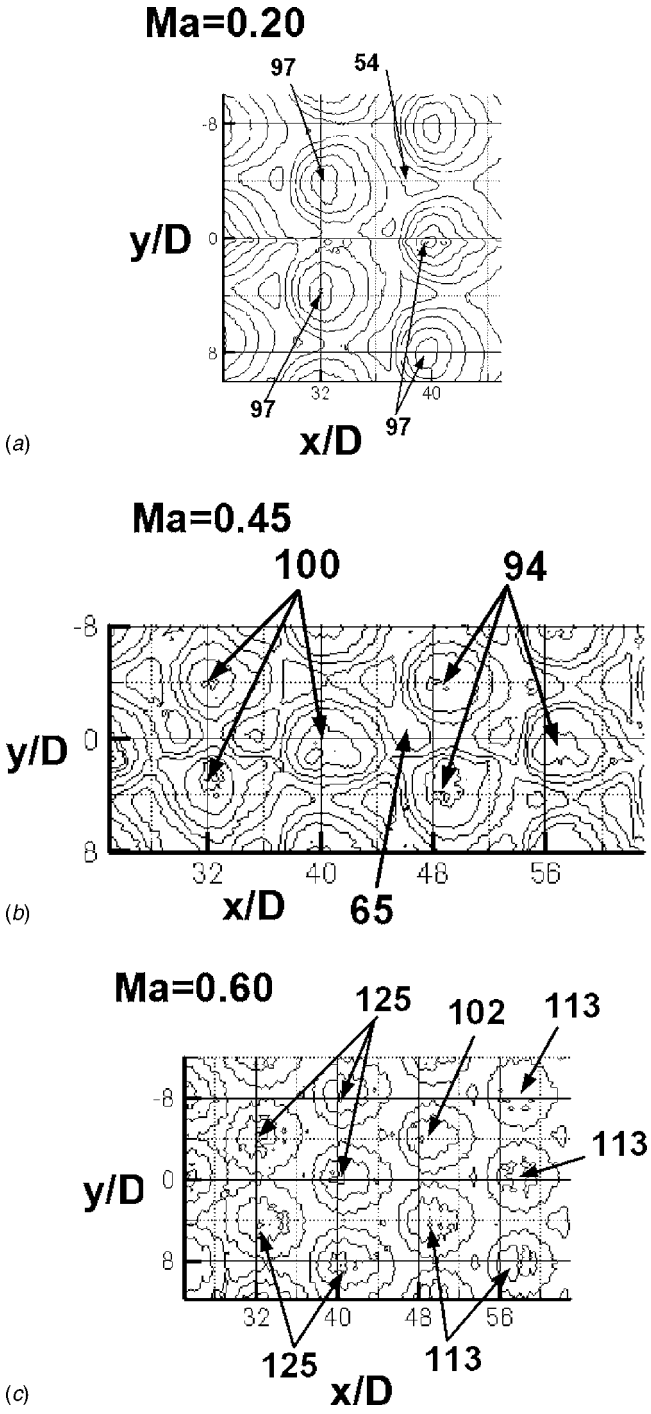

Fig. 10 Spatially resolved distributions of surface Nusselt number for Re_j=30,000 and Ma values of: (*a*) 0.20, (*b*) 0.45, and (*c*) 0.60

by the local RF data presented as it varies with x/D for $y/D=0$ and 4 in Fig. 14(*b*), and as RF varies with y/D for $x/D=32$ and 56 in Fig. 14(*c*). The similarity of the recovery factor distributions in Fig. 14(*c*) for $x/D=32$ and $x/D=56$ with results from Brevet et al. [22] for a single jet is notable. This is believed to be partially a result of the relatively large spacing between adjacent jets employed in the present investigation, which makes them behave with some similarity like individual, isolated jets. Also note that values of T_{AW}, determined from RF data and spatially averaged over the test surface, match magnitudes of T^*_{oj} for all experimental conditions where these data are measured.

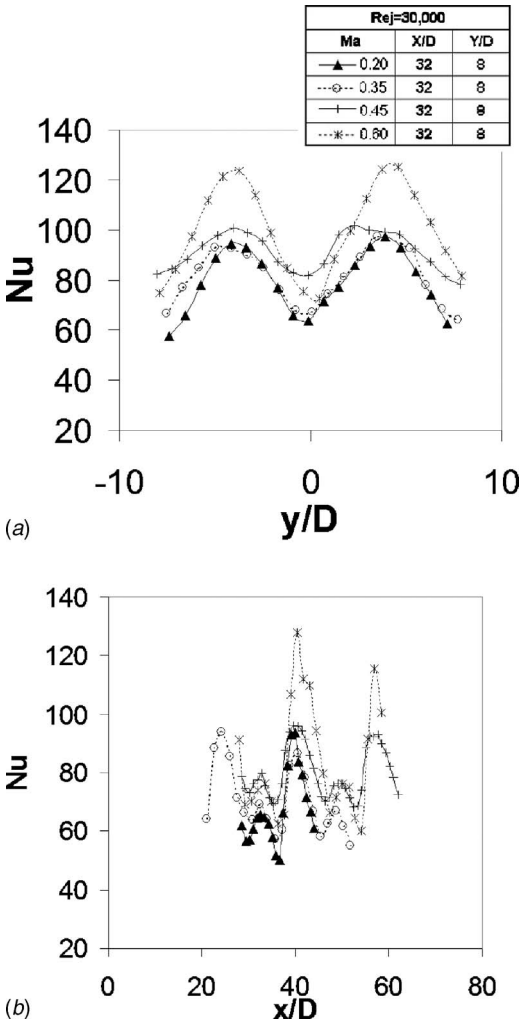

Fig. 11 Local surface Nusselt number variations for Re_j =30,000 and Ma values of 0.20, 0.35, 0.45, and 0.60: (*a*) variations with y/D for x/D=32 and (*b*) variations with x/D for y/D=8

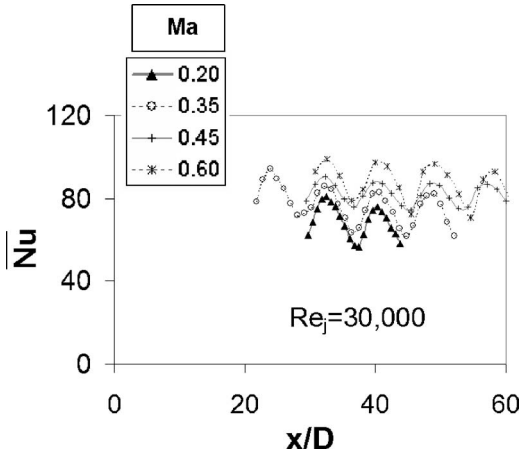

Fig. 12 Surface Nusselt number variations with x/D, which are line averaged over y/D from −8.0 to +8.0, for Re_j=30,000 and Ma values of 0.20, 0.35, 0.45, and 0.60

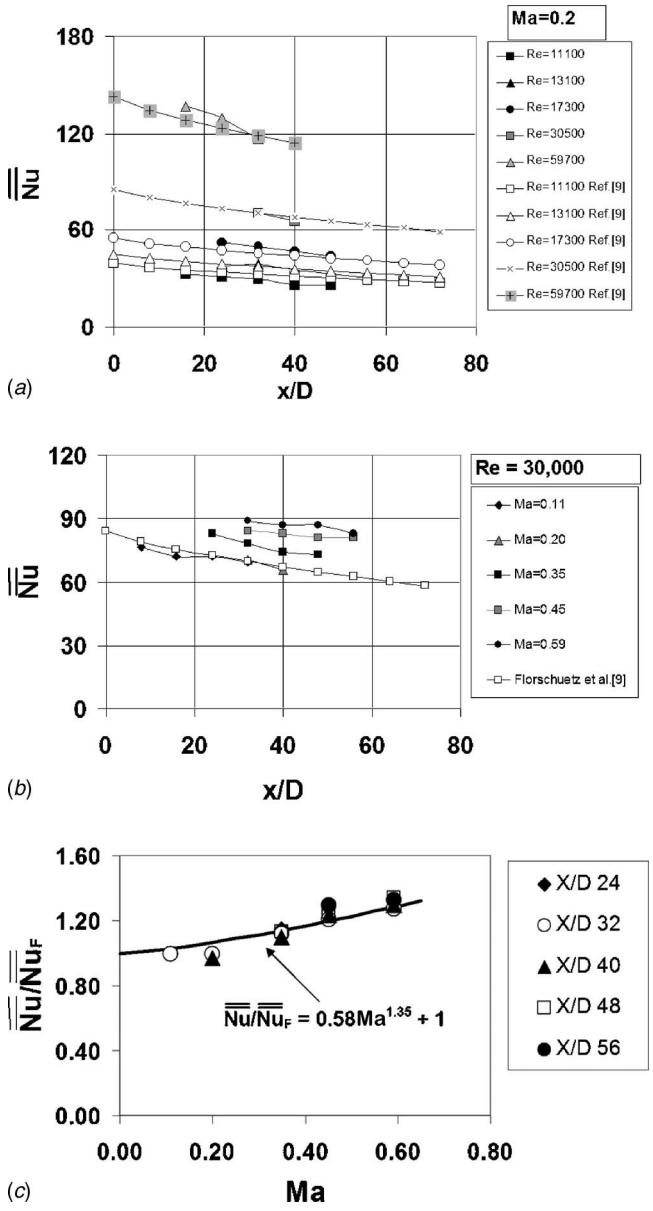

Fig. 13 Comparison of spatially averaged Nusselt numbers with correlation of Florschuetz et al. [9]: (*a*) Data for Ma=0.20 and Re_j values of 11,100, 13,100, 17,300, 30,500, and 59,700; (*b*) data for Re_j=30,000 and Ma values of 0.11, 0.20, 0.35, 0.45, and 0.60; and (*c*) Nusselt number correlation with Mach number

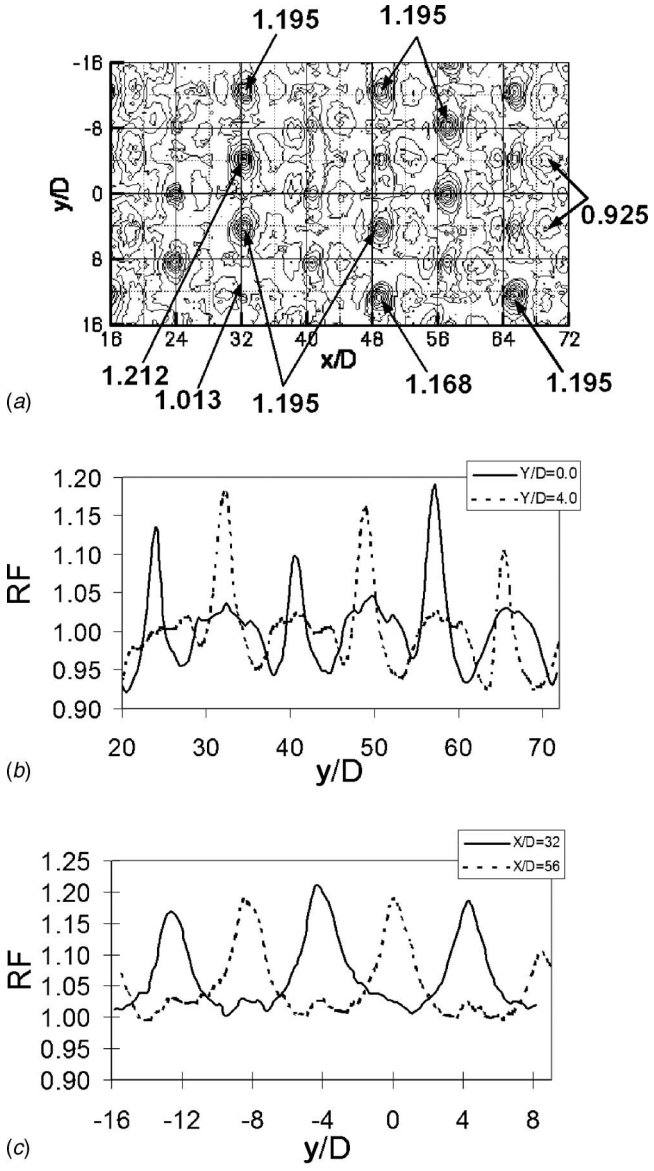

Fig. 14 Recovery factor data for Re_j=30,000 and Ma=0.60: (*a*) Local surface recovery factor distribution; (*b*) local surface recovery factor data as it varies with *x/D* for *y/D*=0 and 4; and (*c*) local surface recovery factor data as it varies with *y/D* for *x/D*=32 and 56

Nusselt Number Data Corrected Using Local Recovery Factors. The local and line-averaged Nusselt number data presented in Figs. 15(*a*)–15(*c*) are based on the difference between the local, spatially varying measured surface temperature T_W and the local adiabatic surface temperature T_{AW}, determined from recovery factor data given in Fig. 14(*a*). This is accomplished by correcting local Nusselt number values using the equation given by

$$Nu_c = \frac{Nu(T_W - T^*_{oj})}{(T_W - T_{AW})} \tag{12}$$

Recall that T^*_{oj} represents the adiabatic surface temperature, spatially averaged over the test plate. The results in Figs. 15(*a*)–15(*c*) are given for Re_j=30,000 and Ma=0.60. A comparison of Fig. 15(*a*) with results presented in Fig. 10(*c*) then shows that local corrected Nusselt numbers Nu_c based on local $(T_W - T_{AW})$ (i.e., Fig. 15(*a*)) have higher peaks and lower valleys than local Nu values based on $(T_W - T^*_{oj})$ (Fig. 10(*c*)). This trend is also illustrated by the local Nusselt number data presented as it varies with x/D (for y/D=4) in Fig. 15(*b*), as well as by the line-averaged Nusselt number data given in Fig. 15(*c*). Note that spatially averaged Nusselt numbers are the same regardless of whether they are based on $(T_W - T_{AW})$ or $(T_W - T^*_{oj})$.

Summary and Conclusions

The present study is unique because data are given for impingement jet Mach numbers as high as 0.60 and impingement jet Reynolds numbers as high as 60,000 and because the effects of Reynolds number and Mach number are separated by providing data at constant Reynolds number because the Mach number is varied, and data at constant Mach number because the Reynolds number is varied. These data are given for an array of impinging jets in the form of discharge coefficients, local and spatially averaged Nus-

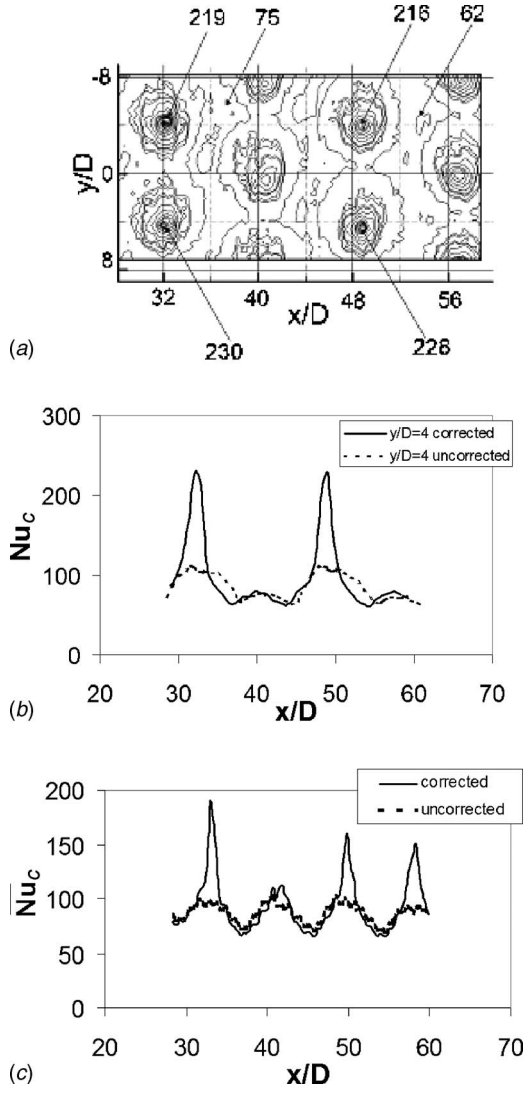

Fig. 15 Corrected and uncorrected surface Nusselt number data for Re_j=30,000 and Ma=0.60: (*a*) Local corrected surface Nusselt number distribution; (*b*) local surface Nusselt number data as it varies with *x/D* for *y/D*=4; and (*c*) surface Nusselt number variations with *x/D*, which are line averaged over *y/D* from –8.0 to +8.0

selt numbers, and local and spatially averaged recovery factors. The spacing between holes in the streamwise direction X is then $8D$, and the spanwise spacing between holes in a given streamwise row Y is also $8D$. The thickness of each impingement plate is $1D$, and the spacing between the hole exit planes and the target plate is denoted Z and is equal to $3D$. As such, the present data are given for experimental conditions not previously examined, which are outside the range of applicability of current correlations.

Experimental spatially averaged, surface Nusselt number data obtained for a constant impingement Mach number Ma of 0.2, and different Reynolds numbers Re_j from 11,100 to 59,700 show good agreement with the correlation of Florschuetz et al. [9], except for Re_j=11,100, where the present data lie below correlation predicted values [9]. Nusselt number data obtained at a constant Reynolds number of 30,000 and Ma=0.11 and Ma=0.20 also show good agreement with the Florschuetz et al. [9] correlation. Measured spatially averaged results for Re_j=30,000 then deviate from this correlation by larger amounts as the impingement Mach number increases further, with the largest deviation evident for Ma =0.60. A new correlation equation for spatially averaged Nusselt numbers is then presented for this range of Mach numbers.

Local spatially resolved Nusselt number data obtained at this Mach number, Ma=0.60, and Re_j=30,000 are also corrected to account for local variations of the adiabatic surface temperature, which are determined from local recovery factor data. Local corrected Nusselt numbers Nu_c based on local $(T_W - T_{AW})$ then have higher peaks and lower valleys than local Nu values based on $(T_W - T^*_{oj})$. This is because local recovery factor RF data are higher beneath and in the vicinity of impact locations of the impingement jets with values >1.0, including on the spanwise sides of impact locations. However, RF values are <1 at locations upstream and downstream of jet impact locations. Such local recovery factor distributions in the vicinity of jet impact locations are in qualitative and quantitative agreement with results from Brevet et al. [22] for a single jet. This is believed to be partially a result of the relatively large spacing between adjacent jets employed in the present investigation, which makes them behave with some similarity like individual, isolated jets.

Local, spatially resolved Nusselt number data show that only one local maximum value is present underneath each jet. Magnitudes of these local maximum values are about the same underneath the different impingement jets for Ma=0.20, and Re_j values of 11,100, 13,100, 17,300, 30,500, and 59,700, with local peak line-averaged $\overline{Nu}$ values, which generally decrease at successive x/D locations. However, regardless of the Reynolds number and Mach number, the qualitative distributions of local Nusselt number produced by the impingement jets show good periodic repeatability in the spanwise direction for each experimental condition and each streamwise row of impact locations. In all cases, important increases of local Nusselt numbers and line-averaged Nusselt numbers with Mach number are apparent at all x/D and y/D locations, provided Re_j=30,000 and impingement Mach number Ma >0.20.

Acknowledgment

The present investigation was supported by Solar Turbines Inc of San Diego, CA.

Nomenclature

A = impingement hole area
A_{ht} = heat transfer area on the target plate
c_a = impingement airflow sonic velocity
c_i = impingementc airflow ideal sonic velocity
C_D = discharge coefficient
D = diameter of an individual impingement hole
h_{loss} = heat transfer coefficient to account for convection and radiation loss from back side of target plate
k = ratio of specific heats
$\dot{m}$ = impingement air mass flow rate
Ma = impingement air flow Mach number
Ma_i = impingement airflow ideal Mach number
Nu = local Nusselt number
Nu_c = corrected local Nusselt number
$\overline{Nu}$ = line-averaged Nusselt number
$\overline{Nu_c}$ = corrected line-averaged Nusselt number
$\overline{\overline{Nu}}$ = spatially-averaged Nusselt number
$\overline{\overline{Nu}}_F$ = spatially-averaged Nusselt number from Florschuetz [9] correlation
P_a = impingement air static pressure
P_i = impingement air ideal static pressure
P_{oj} = impingement air stagnation pressure
Q = total power provided to the thermofoil heater
q_{rf} = radiation heat flux from front side (or impingement side) of the target plate

q_{rb} = radiation heat flux from back side of the target plate
q_{cf} = convection heat flux from front side (or impingement side) of the target plate
q_{cb} = convection heat flux from back side of the target plate
R = ideal gas constant
Re_j = impingement air flow Reynolds number
RF = recovery factor
T_{ambient} = ambient static temperature
T_b = local temperature on the back surface of the polystyrene target plate
T_W = local target surface temperature on the surface of the heater adjacent impingement air
T_{AW} = local adiabatic target surface temperature
T_i = impingement air ideal static temperature
T_j = impingement air static temperature
T_{oj} = impingement air stagnation temperature
T_{oj}^* = corrected impingement air stagnation temperature to give zero spatially averaged surface heat flux
T_{tc} = local thermocouple temperature between the heater and the polystyrene target plate
u_a = impingement air velocity
u_i = impingement air ideal velocity
x = streamwise coordinate
y = spanwise coordinate
z = normal coordinate
X = streamwise distance between centerlines of adjacent impingement holes
Y = spanwise distance between centerlines of adjacent impingement holes
Z = distance between target plate and impingement hole plate

Greek Symbols

α = air thermal conductivity
ρ_a = impingement air static density
ρ_i = impingement air ideal static density
μ = absolute viscosity
σ = Boltzmann constant
ε_f = emissivity of the front surface of the target plate
$\varepsilon_{\mathrm{inf}}$ = emissivity of a plate located opposite to the target plate

References

[1] Martin, H., 1977, "*Heat and Mass Transfer Between Impinging Gas Jets and Solid Surfaces*," Advances in Heat Transfer, Academic Press, New York, Vol. 13, pp. 1–60.
[2] Schulz, A., 2001, "Combustor Liner Cooling Technology in Scope of Reduced Pollutant Formation and Rising Thermal Efficiencies," Ann. N.Y. Acad. Sci., **934**, pp. 135–146.
[3] Kercher, D. M., and Tabakoff, W., 1970, "Heat Transfer by a Square Array of Round Air Jets Impinging Perpendicular to a Flat Surface Including the Effect of Spent Air," ASME J. Eng. Power, **92**, pp. 73–82.
[4] Metzger, D. E., Yamashita, T., and Jenkins, C., 1971, "Impingement Cooling of Concave Surfaces With Lines of Circular Air Jets," ASME J. Eng. Power, **91**, pp. 149–158.
[5] Chupp, R., Helms, H., McFadden, P., and Brown, T., 1969, "Evaluation of Internal Heat-Transfer Coefficients for Impingement Cooled Turbine Airfoils," J. Aircr., **6**(3), pp. 203–208.
[6] Metzger, D. E., and Korstad, R., 1972, "Effects of Crossflow on Impingement Heat Transfer," ASME J. Eng. Power, **94**, pp. 35–41.
[7] Chance, J. L., 1974, "Experimental Investigation of Air Impingement Heat Transfer Under an Array of Round Jets," Tappi J., **57**(6), pp. 108–112.
[8] Metzger, D. E., Florschuetz, L. W., Takeuchi, D. I., Behee, R. D., and Berry, R. A., 1979, "Heat Transfer Characteristics for Inline and Staggered Arrays of Circular Jets With Crossflow of Spent Air," ASME J. Heat Transfer, **101**, pp. 526–531.
[9] Florschuetz, L. W., Truman, C. R., and Metzger, D. E., 1981, "Streamwise Flow and Heat Transfer Distributions for Jet Array Impingement With Crossflow," ASME J. Heat Transfer, **103**, pp. 337–342.
[10] Obot, N. T., and Trabold, T. A., 1987, "Impingement Heat Transfer Within Arrays of Circular Jets—Part 1: Effects of Minimum, Intermediate, and Complete Crossflow for Small and Large Spacings," ASME J. Heat Transfer, **109**, pp. 872–879.
[11] Bunker, R., and Metzger, D. E., 1990, "Local Heat Transfer in Internally Cooled Turbine Airfoil Leading Edge Regions—Part I: Impingement Cooling Without Film Extraction," ASME J. Turbomach., **112**, pp. 451–458.
[12] Fox, M. D., Kurosaka, M., Hedges, L., and Hirano, K., 1993, "The Influence of Vortical Structures on the Thermal Fields of Jets," J. Fluid Mech., **255**, pp. 447–472.
[13] Bailey, J. C., and Bunker, R. S., 2002, "Local Heat Transfer and Flow Distributions for Impinging Jet Arrays of Dense and Sparse Extent," ASME Paper No. GT-2002-30473.
[14] Taslim, M. E., Pan, Y., and Bakhtari, K., 2002, "Experimental Racetrack Shaped Jet Impingement on a Roughened Leading-Edge Wall With Film Holes," ASME Paper No. GT-2002-30477.
[15] Li, X., Gaddis, J. L., and Wang, T., 2002, "Mist/Stream Heat Transfer With Jet Impingement Onto a Concave Surface," ASME Paper No. GT-2002-30475.
[16] Parsons, J. A., Han, J. C., and Lee, C. P., 1996, "Rotation Effect on Jet-Impingement Heat Transfer in Smooth Rectangular Channels With Four Heated Walls and Radial Crossflow," ASME J. Turbomach., **120**, pp. 79–85.
[17] Parsons, J. A., Han, J. C., and Lee, C. P., 2003, "Rotation Effect on Jet-Impingement Heat Transfer in Smooth Rectangular Channels With Four Heated Walls and Coolant Extraction," ASME Paper No. GT-2003-38905.
[18] Parsons, J. A., and Han, J. C., 2001, "Rotation Effect on Jet Impingement Heat Transfer in Smooth Rectangular Channels With Coolant Extraction," Int. J. Rotating Mach., **7**, pp. 87–103.
[19] Epstein, A. H., Kerrebrock, J. L., Koo, J. J., and Preiser, U. Z., 1985, "Rotational Effects on Impingement Cooling," Symposium on Transport Phenomena in Rotating Machinery, Honolulu.
[20] Mattern, C., and Hennecke, D. K., 1996, "Influence of Rotation on Impingement Cooling," ASME Paper No. GT-1996-161.
[21] Brevet, P., Dejeu, C., Dorignac, E., Jolly, M., and Vullierme, J. J., 2002, "Heat Transfer to a Row of Impinging Jets in Consideration of Optimization," Int. J. Heat Mass Transfer, **45**, pp. 4191–4200.
[22] Brevet, P., Dorignac, E., and Vullierme, J. J., 2001, "Mach Number Effect on Jet Impingement Heat Transfer," Ann. N.Y. Acad. Sci., **934**, pp. 409–416.
[23] Kline, S. J., and McClintock, F. A., 1953, "Describing Uncertainties in Single Sample Experiments," Mech. Eng. (Am. Soc. Mech. Eng.), **75**, pp. 3–8.
[24] Moffat, R. J., 1988, "Describing the Uncertainties in Experimental Results," Exp. Therm. Fluid Sci., **1**(1), pp. 3–17.

Experimental and Numerical Study of Mass/Heat Transfer on an Airfoil Trailing-Edge Slots and Lands

M. Cakan
Mechanical Engineering Department,
Istanbul Technical University,
34439 Istanbul, Turkey

M. E. Taslim
e-mail: m.taslim@neu.edu

Mechanical and Industrial Engineering
Department,
Northeastern University,
Boston, MA 02115

Proper cooling of the airfoil trailing edge is imperative in gas turbine designs since this area is often one of the life limiting areas of an airfoil. A common method of providing thermal protection to an airfoil trailing edge is by injecting a film of cooling air through slots located on the airfoil pressure side near the trailing edge, thereby providing a cooling buffer between the hot mainstream gas and the airfoil surface. In the conventional designs, at the breakout plane, a series of slots open to expanding tapered grooves in between the tapered lands and run the cooling air through the grooves to protect the trailing edge surface. In this study, naphthalene sublimation technique was used to measure area averaged mass/heat transfer coefficients downstream of the breakout plane on the slot and on the land surfaces. Three slot geometries were tested: (a) a baseline case simulating a typical conventional slot and land design; (b) the same geometry with a sudden outward step at the breakout plane around the opening; and (c) the sudden step was moved one-third away from the breakout plane in the slot. Mass/heat transfer results were compared for these slots geometries for a range of blowing ratios $[M=(\rho u)_s/(\rho u)_m]$ *from 0 to 2. For the numerical investigation, a pressure-correction based, multiblock, multigrid, unstructured/adaptive commercial software was used in this investigation. Several turbulence models including the standard high Reynolds number k-ε turbulence model in conjunction with the generalized wall function were used for turbulence closure. The applied thermal boundary conditions to the computational fluid dynamics (CFD) models matched the test boundary conditions. Effects of a sudden downward step (Coanda) in the slot on mass/heat transfer coefficients on the slot and on the land surfaces were compared both experimentally and numerically.*
[DOI: 10.1115/1.2436898]

Introduction

In today's advanced gas turbines, the limits of operating temperatures are continually pushed higher in order to meet present and future performance requirements. In fact, typical engine operating temperatures are much greater than the allowable turbine airfoil metal temperatures. This necessitates the requirement to provide thermal protection to the airfoils. A common method of providing thermal protection to an airfoil trailing edge (often the life limiting area) is by injecting a film of cooling air through slots located on the airfoil pressure side near the trailing edge, thereby providing a cooling buffer between the hot mainstream gas and the airfoil surface. To determine the extent of thermal protection and level of thermal stresses at the airfoil trailing edge, it is crucial to predict the film effectiveness as well as the heat transfer coefficients on the trailing-edge slots and lands.

Much research has been devoted to the topic of film cooling, and there exists a considerable amount of experimental data for film cooling with different slot geometries and various primary and secondary flow fields. A very comprehensive survey of film cooling was performed and compiled by Goldstein [1] which includes data for discrete holes as well as slots. It has been well established that the slot coolant to mainstream flow blowing ratio $[M=(\rho u)_s/(\rho u)_m]$ and normalized distance (x/s) downstream of slot breakout $(x=0)$ are key parameters to which film effectiveness and heat transfer coefficient are correlated. Other parameters, however, such as slot to mainstream flow density ratio (ρ_s/ρ_m), slot lip thickness to height ratio (t/s), slot width to height ratio (w/s), slot angle of injection relative to mainstream flow (α), and mainstream flow acceleration are recognized as having effects of various magnitudes on slot film effectiveness but are not as well established. A great majority of the slot cooling studies such as Wieghardt [2], Hartnett et al. [3], Seban et al. [4], Seban [5], Samuel and Joubert [6], Papell and Trout [7], Papell [8], Kacker and Whitelaw [9,10], Sivasegaram and Whitelaw [11], Goldstein et al. [12], Nicoll and Whitelaw [13], Burns and Stollery [14], Rastogi and Whitelaw [15], Patankar et al. [16], and Paxson and Mayle [17] are concentrated on film effectiveness.

A number of investigators have reported on the measurement of heat transfer coefficient in the region immediately downstream of slot breakout. Metzger et al. [18] reported the results of an experimental investigation on heat transfer with film cooling near flush, angled slots. Ballal and Lefebvre [19] conducted an experimental investigation in heat transfer coefficient and film effectiveness downstream of a slot in an annular geometry pertinent to film-cooled combustors. Pai and Whitelaw [20] developed a procedure for the prediction of adiabatic wall temperature and heat transfer coefficient downstream of two-dimensional film cooling slots and compared their predicted results with the experimental data obtained by a number of investigators. Most of the above-mentioned experimental studies on slot film cooling were for a single slot geometry and for large x/s values where flow has reached a fully developed turbulent boundary layer profile. Taslim et al. [21] conducted a parametric study to experimentally determine the effects slot exit geometries have on film effectiveness for five injection angles (α=0.0 deg, 5.0 deg, 8.5 deg, 11.5 deg, and 15.0 deg, four

Contributed by the Turbomachinery Division of ASME for publication in the JOURNAL OF TURBOMACHINERY. Manuscript received July 5, 2006; final manuscript received September 4, 2006. Review conducted by Ronald S. Bunker. Paper presented at the ASME Turbo Expo 2006: Land, Sea and Air (GT2006), Barcelona, Spain, May 8–11, 2006. Paper No. GT2006-91201.

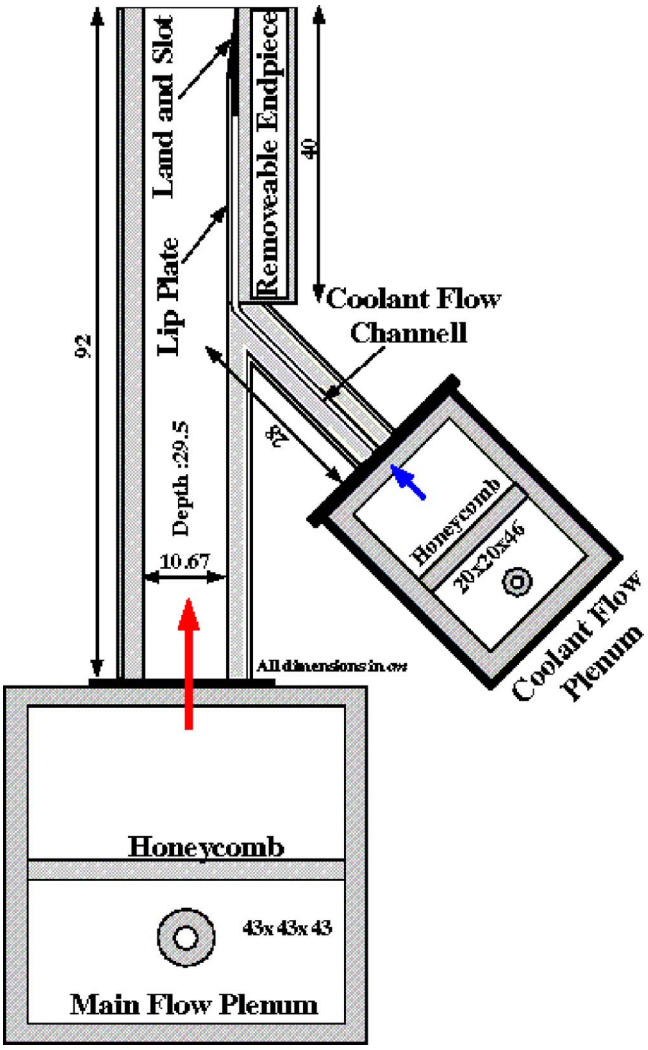

Fig. 1 Schematics of the test section

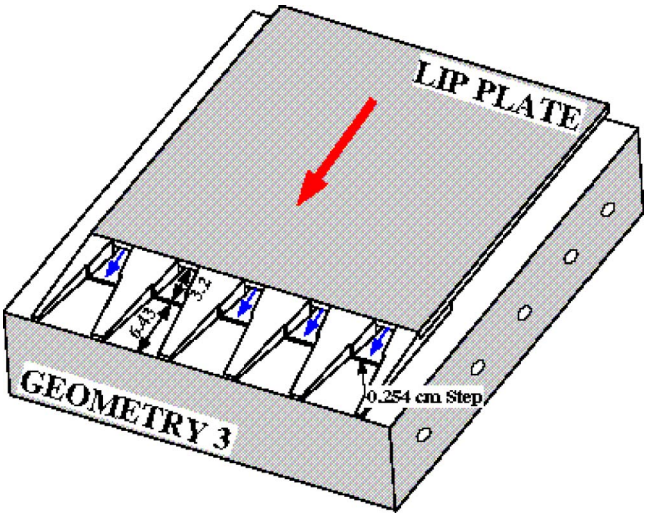

Fig. 2 Schematics of the end piece for Geometry 3

slot lip thickness to height ratios (t/s=0.5, 0.75, 1.0, and 1.25), three slot width to height ratios (w/s=2,5, and 17), and five density ratios (ρ_s/ρ_m=1.2, 1.3, 1.4, 1.5, and 1.6). Their results showed that: (a) the slot film effectiveness is highly sensitive to t/s, but not significantly sensitive to either w/s or ρ_c/ρ_h) and (b) an optimum injection angle equal to 8.5 deg exists for x/M_s values less than 60. The emphasis in this investigation was to study the effects that a sudden downward step along the coolant path downstream of the breakout plane (Coanda step, Korbacher [22]) have on the heat transfer coefficient in the vicinity of slot breakout region as well as on the land surfaces where the flow structure is quite complex. Film effectiveness measurements on the same slot geometries are underway and will be reported in a separate paper. It is in this region that the heat transfer coefficient results are directly applicable to turbine airfoil cooling design.

Experimental Apparatus

Plenums and Air Channels. A schematic of the experimental setup is shown in Fig. 1. The test rig, scaled based on a typical airfoil trailing-edge geometry, consisted of a mainstream air supply channel, a slot air channel, a multislot test module, and associated instrumentations. Plenums, main air and slot supply channels were made of 6.35-mm-thick aluminum sheets on the outside that were covered on the inside with 25.4-mm-thick polyurethane slabs. A compressor station supplied the mainstream and slot air to the test rig. The compressed mainstream air was filtered, dried, and directed through a flow measuring station, consisting of a pressure regulator and a critical venturimeter, into the main flow plenum chamber, a honeycomb flow straightener and to the main flow channel via a bell-mouth opening. Similarly, the slot air was filtered, dried, and routed through a pressure regulator and a critical venturimeter into the slot plenum chamber. The slot air then went through a honeycomb and a bell-mouth opening to the slot flow channel that fed a row of five parallel channels that formed the slots upon breakout into the mainstream flow as shown in Figs. 2 and 3. The main flow channel had a cross-sectional area of 10.67 cm by 29.5 cm while the slot supply channel's cross-sectional area was 0.71 cm by 29.5 cm. A 0.61-mm-thick polyurethane lip plate separated the main flow and slot supply channels. Both mainstream and slot channels were fed from the same air supply with the same temperature (typical of 24–25°C). No temperature variation was measured across the mainstream channel. Data were collected at ambient pressure for a range of pertinent nondimensional parameters such as blowing ratio and mainstream Reynolds number to match those of typical airfoils.

Trailing-Edge Slot Modules. Three slot geometries, typical of a high-pressure turbine, were tested. Therefore, three removable end pieces representing these geometries were machined out of polyurethane slabs. Figures 2 and 3 show the sketches of these modules for Geometries 2 and 3. These modules allowed simple assembly (gaskets and bolts) into the test rig. These three geometries were identical in all aspects except the presence and location of a 2.54 mm-step in the flow direction on the three walls of the trailing-edge slots. Geometry 1, the baseline geometry, had no step along the slot. Geometry 2, shown in Fig. 3, had the 2.54 mm-step around the three sides of the slot opening at the breakout plane. Geometry 3, shown in Fig. 2, had the 2.54 mm-step on the slot three walls at a distance of 3.2 cm (1/3 of the slot total axial length) from the breakout plane. All three geometries consisted of five slots and six lands with the slot diffusion half-angle (β) of 7.5°. The slot openings for the three geometries were 0.71 cm high corresponding to a lip thickness to the slot–height ratio (t/s) of 0.86 cm, and 1.83 cm wide, i.e., a slot width to height ratio (w/s) of 2.58. Lands were tapered from a thickness of 1.32 cm at the breakout plane to 0.254 cm at the trailing edge. The lands were extended into the coolant channel by 5.08 cm to create five rectangular channels for the ejection of the slot air. The lip plate, which separates the slot air from the mainstream flow upstream of the slot breakout location, rested on the six lands.

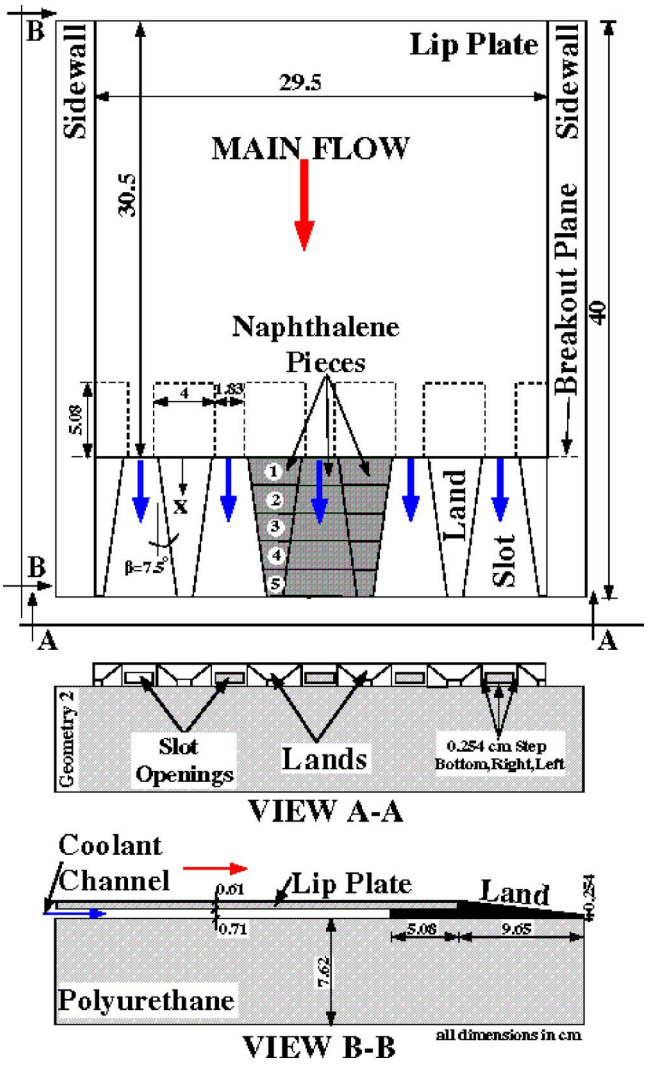

Fig. 3 Details of the end piece for Geometry 2

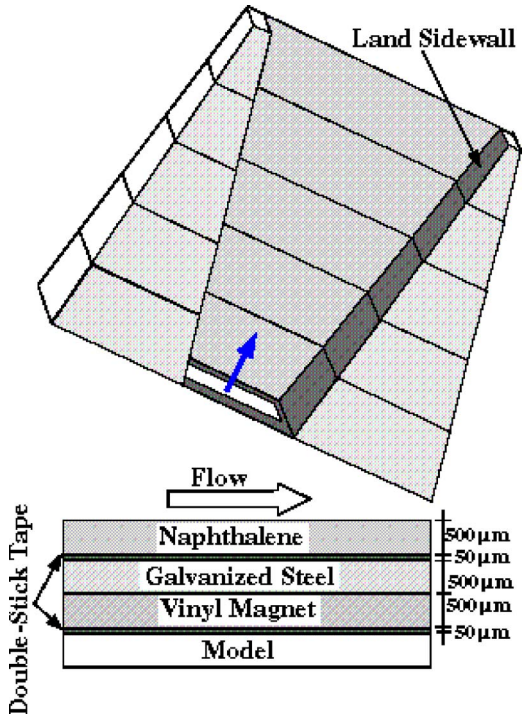

Fig. 4 Details of the naphthalene surfaces

Experimental Procedure

The naphthalene ($C_{10}H_8$) sublimation technique was used to determine quasi-local (localized average) mass/heat transfer coefficients. This technique consisted of coating the specimen with a layer of naphthalene and exposing it to the flow in the test rig. An area average mass transfer coefficient was obtained by weighing the test specimen before and after a run. An excellent review of the technique can be found in Goldstein and Cho [23]. All measurements were performed on the surfaces of the middle slot and the two adjacent lands. To accommodate the mounting of the naphthalene specimens, a 1.6-mm-thick layer of polyurethane was machined off the test surfaces such that, when a specimen was mounted on the test surface, the final geometry was identical to other slots and lands. As shown in Figs. 3 and 4, five naphthalene specimens were mounted on the slot surface, five on each land, five on each land sidewall inside the slot, one on the lip and three around the 0.254 mm-step for Geometries 2 and 3. The trapezoidal specimens had the same axial dimension along the flow direction x. Details of the specimen makeup are shown in Fig. 4. They were cut from a 500-μm-thick galvanized steel. Upper surfaces of the pieces that would be in contact with the flow were covered with a double-sided adhesive tape. They were then dipped into molten naphthalene at 80–85 °C. A naphthalene layer thickness of 500 $\mu\pm10$ μ, controlled by the number of dippings, was consistently used for all tests. After waiting for about 1/2 h to attain thermal equilibrium, they were cooled to solidify. The solidified naphthalene layer was then removed from the bottom surface of each piece. The pieces were then laid on the test surfaces that were previously covered with 500-μm-thick vinyl magnets. The vinyl magnets allowed easy installation and removal of the coated pieces.

Natural sublimation from each naphthalene-coated piece during a few minutes before and after the actual test run, when naphthalene modules were mounted or dismounted, were calculated based on a carefully conducted calibration procedure and recorded in order to account only for the sublimation due to forced convection effects of the flow field. The pieces were weighed on an analytical balance with 0.1 mg resolution. In order to obtain accurate results, the test run durations were chosen to be between 90 and 180 min. These time scales depended on the tested configurations and were established such that at least 5 mg of naphthalene had sublimated at the end of the test run. The duration of each run was also adjusted in such a way that the naphthalene sublimation did not lower the surface of solid naphthalene by more than 25 μm. Other variables recorded during the experiment include: (a) ambient temperature, (b) mainstream and slot air circuit pressures and temperatures, and (c) test section air temperatures. The last variables: slot and mainstream air temperatures in the test section are particularly important since the vapor density of naphthalene is very sensitive to temperature and varies about 10% per °C temperature change. Mainstream and slot air, supplied from the same source, were almost at the same temperature. The naphthalene vapor pressure and other properties were then evaluated at the arithmetic mean of the mainstream and slot air temperatures in the test section. For each test configuration, data were taken by holding all parameters constant throughout the run except the blowing ratio (M). To determine the air mass flow rate variation across the slots, a one-dimensional flow circuit of each test setup consisting of appropriate orifices, tubes, momentum, and pressure chambers was built and analyzed. Appropriate discharge coefficients for the orifices were calculated from correlations for sharp-corner holes. The results revealed that the air mass flow rate through the middle slot was very close to that of average mass flow through the five

slots, i.e., 20% each. The maximum difference in mass flow rate between the first and third slots was calculated to be 0.1%.

Mass/Heat Transfer Data Reduction. The mass transfer coefficient for a typical naphthalene-coated piece was evaluated from the following equation

$$K_i = m_i/[A_i(\rho_{nv,w} - \rho_{nv,b})] \quad (1)$$

In this equation, m_i is the rate of naphthalene sublimation per module; A_i is the mass transfer surface area per module; and $\rho_{nv,w}$ and $\rho_{nv,b}$ are the naphthalene vapor density at wall and at bulk conditions, respectively. The naphthalene vapor density at bulk conditions was assumed to be zero since the mainstream flow was naphthalene-vapor free. The naphthalene vapor density at the wall was determined from the perfect gas law [Eq. (2)] using the saturated vapor pressure and the surface temperature. The saturated vapor pressure which is a strong function of naphthalene surface temperature was based on the correlation [Eq. (3)] proposed by Kudchadker et al. [24]

$$\rho_{nv,w} = P_{nv}/RT \quad (2)$$

$$\log P_{nv} = [14.47884] - [8037.107/(410.77 - 273.15 + T)] \quad (3)$$

where P_{nv} is in bars and T is in K. Once the per-piece mass transfer coefficients were determined, they were represented in dimensionless form in terms of Sherwood number

$$Sh_i = K_i L/D_{naph} \quad (4)$$

where D_{naph} is the diffusion coefficient given by $D_{naph}=v\,.\mathrm{Sc}$ and L is the injection slot hydraulic diameter. During this investigation D_{naph} was calculated as a function of the mean air temperature and atmospheric pressure based on the following correlation given by Goldstein and Cho [23]

$$D_{naph} = 0.0681(T/298.16)1.93(1.013E - 5/P_{atm}) \quad (\mathrm{cm}^2/\mathrm{s}) \quad (5)$$

Sherwood number was then related to the Nusselt number through the following Colburn relation for both laminar and turbulent flows [23]

$$\mathrm{Nu/Sh} = (\mathrm{Pr/Sc})^{0.34} \quad (6)$$

Experimental Uncertainties. Flow and mass transfer measurement uncertainties were calculated using the method of Kline and McClintock [25]. The absolute uncertainty of the weight measurements was 0.4 mg which was obtained from analytical balance capability and weighing repeatability. The uncertainty on test duration was less than 90 s and temperature measurement uncertainty was 0.5 °C. The diffusion coefficient uncertainty was calculated as 3% based on the thickness of the bandwidth formed by various diffusion coefficient correlation curves given by Goldstein and Cho [23]. The overall uncertainties on both the mainstream and slot flow Reynolds numbers were determined as 3%, on the blowing ratio as 4%, and on Sherwood number as 5%.

Computational Models

The computational models were constructed for a representative repeated domain with two symmetric planes at the slot and land centerlines. In the axial direction, it extended from the inlets to the mainstream and slot flow channels to the exit plane (Fig. 1). Figure 5 shows this representative meshed domain around the slot region for Geometry 3. The computational domain size for the other two slot geometries were the same. The CFD analysis was performed using STAR-CD solver by Adapco, Inc., a pressure-correction based, multiblock, multigrid, unstructured/adaptive solver. Standard high Reynolds number k-ε turbulence model in conjunction with the generalized wall function was used for turbulence closure. Mesh density in the wall region was varied such that the average y^+ for the first layer of cells varied between 20 and 100 for all cases. Other available turbulence models in this commercial code, short of the two-layer model which required a change in mesh arrangement for each geometry and was beyond the scope of this investigation, were also tested and did not produce results significantly different from those of k-ε model. Mesh independence was achieved at about 700,000 cells for a typical model. Cells in all models were entirely hexagonal, a preferred choice for CFD analyses, and were varied in size bigeometrically from the boundaries to the center of the computational domain in order to have finer mesh close to the boundaries.

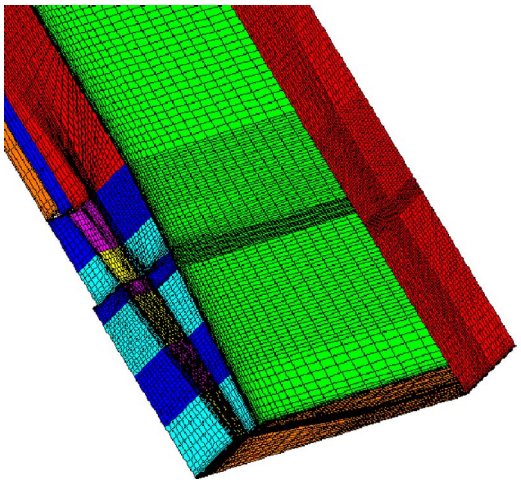

Fig. 5 Typical mesh arrangement around the computational domain periphery

Results and Discussion

Baseline Geometry. The combined effect of mainstream and slot air flow physics on the slot and land mass/heat transfer are initially evaluated for the baseline case where there is no sudden step at the breakout plane. This evaluation is carried out for two different mainstream flow Reynolds numbers and 6–7 different blowing ratios (M) depending on the magnitude of the mainstream flow Reynolds number. Zero blowing ratio cases correspond to no slot flow tests. Figure 6(a) shows the distribution of Sherwood number along the slot floor in the axial direction for seven blowing ratios at a mainstream Reynolds number of 35,750. For the $M=0$ case, the peak at the third naphthalene module proves the existence of the mainstream flow reattachment around $x/s=6$. At shorter axial locations, the slot surface must be covered with a recirculating bubble. After the flow reattachment, the Sherwood number starts decreasing due to boundary layer development. For $M=0.37$ and 0.47 the suddenly expanding laminar slot flow manages to keep the mass transfer rates low by forming a buffer layer between the surface and the mainstream flow. However as both flows proceed downstream, they mix and therefore mass transfer enhances slowly under the effect of the higher momentum mainstream flow. At higher blowing rates, the slot is filled more and more with laminar or transitional slot flow and this prevents effective entrainment of mainstream flow onto the slot valley bounded by lands on both sides. The decreasing mass transfer rates at higher x/s values are due to the thickening slot flow boundary layer. Figure 6(b) shows a very similar Sherwood number distribution for the mainstream Reynolds number of 53,350.

Figures 7(a) and 7(b) show the Sherwood number distribution on the land sidewalls inside the slot for two mainstream flow Reynolds numbers (35,750 and 53,350), respectively. Although the general shapes of the distributions are similar to those for the slot distribution given in Figs. 6(a) and 6(b), the presence of a sudden step around the slot opening causes the reattachment of the slot flow on the slot floor and on the land sidewall. Furthermore, the shearing effect formed by the differences between slot and main flow momentums may trigger the formation of axial second-

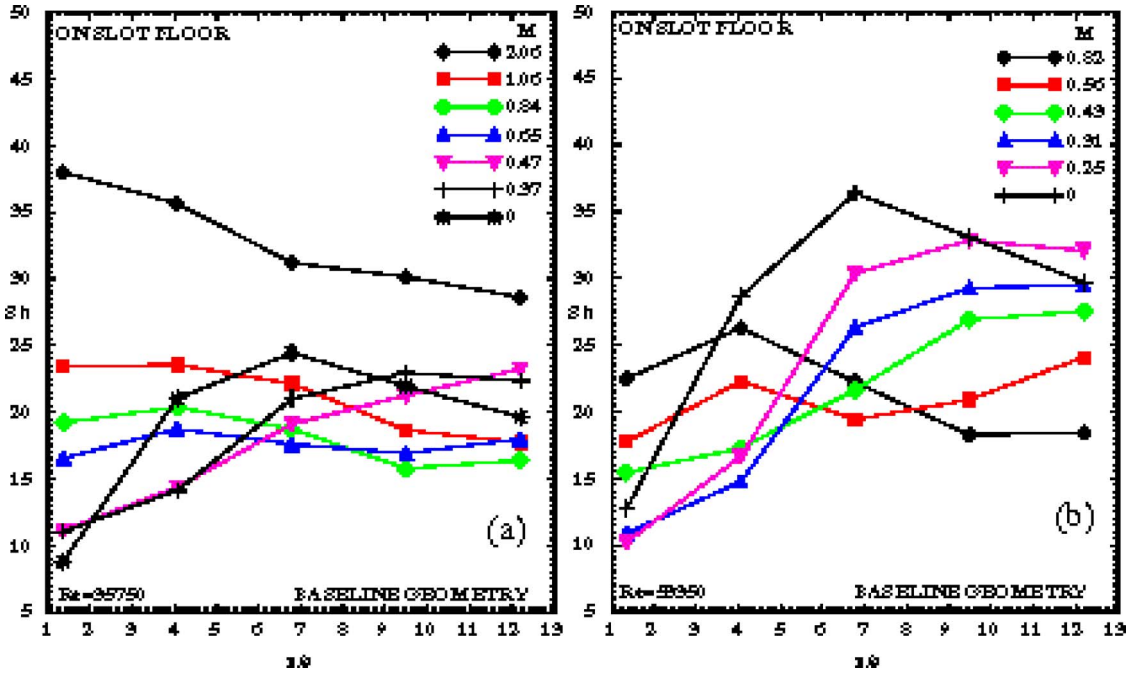

Fig. 6 Sherwood number variation on the slot floor downstream of the breakout plane, baseline geometry

ary flows which in return enhance mass transfer drastically on the sidewalls. The effect of this possible contribution is clearly reflected by the kinks seen on almost all the second pieces in both of the graphs. For $M=0$ cases, the parabolic Sherwood number distributions, as in the case of the distribution along the slot, still evoke the possibility of mainstream flow reattachment.

The Sherwood number distribution along the land pieces can be seen in Figs. 8(*a*) and 8(*b*). As one may expect, for all configurations, the distributions are characterized by a negative slope whose magnitude increases with increasing blowing ratio. This behavior is attributed to insufficient main air flow entrainment into the slot valley. As the main air flow is trapped and, therefore, routed over the lands, the boundary layer continues to grow thicker, thus decreasing the mass transfer on the land pieces.

Step at the Breakout Plane. Figures 9(*a*) and 9(*b*) show the effects of a sudden outward step (Coanda) at the breakout plane on the nondimensional mass transfer coefficient along the slot floor for the two mainstream Reynolds numbers. The first observation is that the first naphthalene module after the step is now under the effect of a subcirculation bubble especially for the high blowing ratio cases. Comparison between Figs. 6(*a*), 6(*b*) and

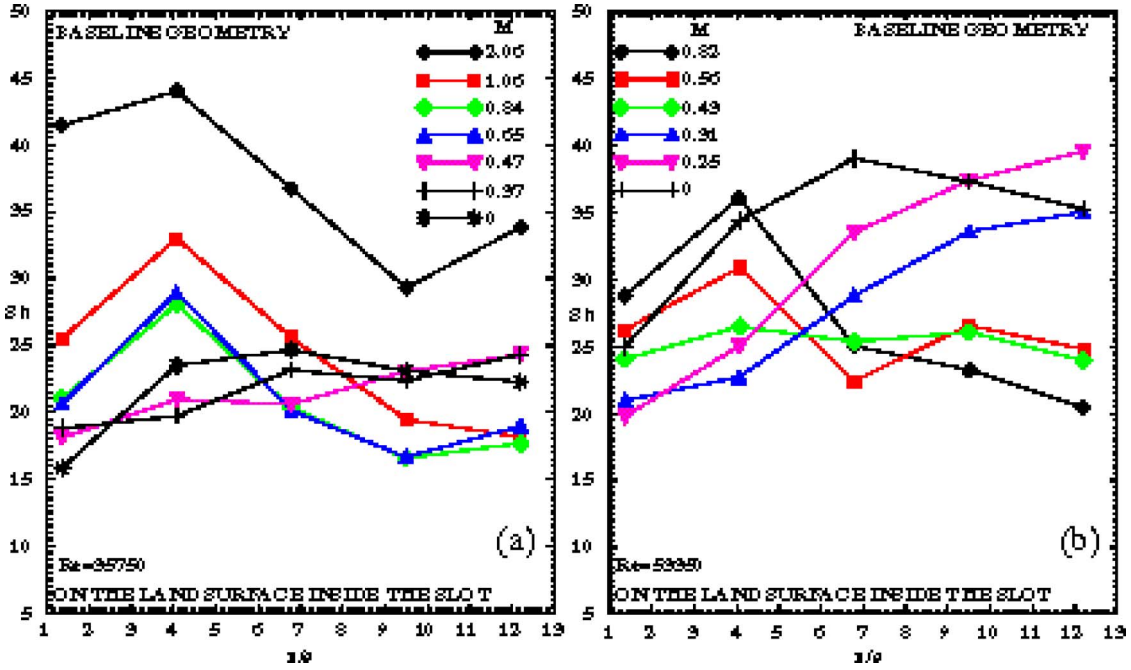

Fig. 7 Sherwood number variation on the land surface inside the slot downstream of the breakout plane, baseline geometry

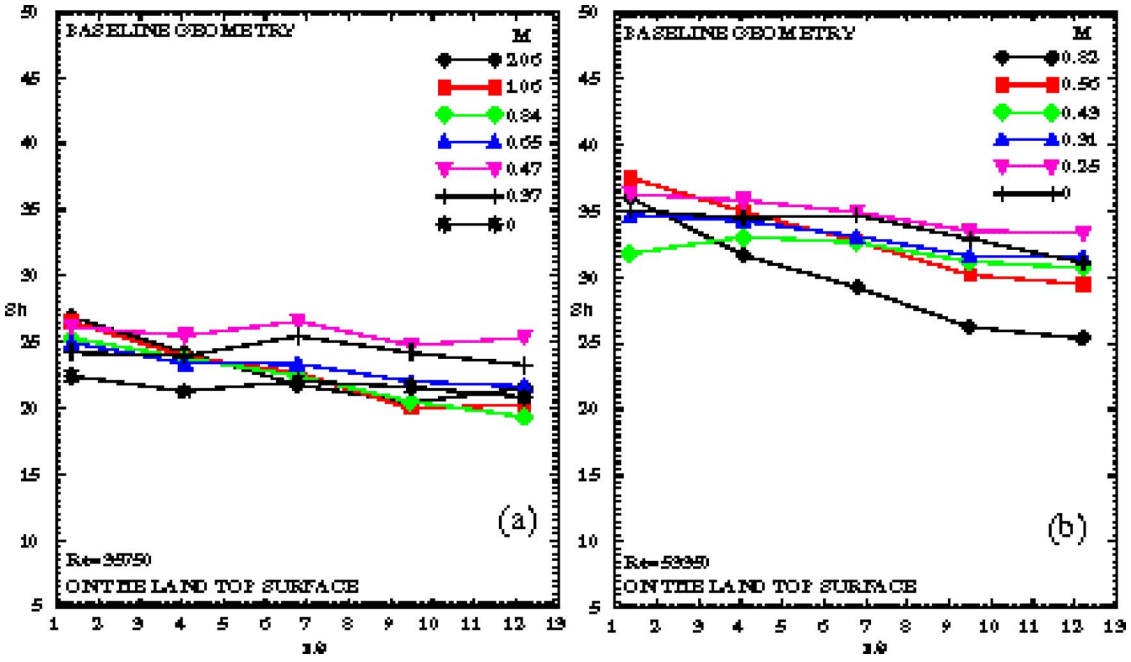

Fig. 8 Sherwood number variation on the land top surface downstream of the breakout plane, baseline geometry

Figs. 9(*a*), 9(*b*) shows that the slope of the Sherwood number variation on the first two naphthalene modules on the slot floor is generally steeper for the step-at-breakout configuration. Slot flow reattachment might be occurring around the second naphthalene piece. However, Sherwood number distributions after the reattachment are very similar to that of the baseline configuration especially for high blowing ratios. This behavior may be attributed to low mainstream entrainment due to high slot flow momentum.

The general trend of the Sherwood number distribution both along the land sidewalls and land top surface reflect similar attributes to baseline configuration (Figs. 6(*a*), 6(*b*) and 7(*a*), 7(*b*)). The kinks seen on the second land side piece is thought to be created under the effect of a very complex interaction of mainstream and slot flows merging into each other at a finite distance downstream of the lip. Depending on the variation in blowing ratio (*M*), the slot and mainstream side vortices forming behind the lip [26] may have different sizes which in return alter the initial merging point of the two aforementioned flows. Nevertheless, one might expect that the formation of an axial secondary flow structure effectively enhances mass transfer only after the first land piece (Figs. 10 and 11).

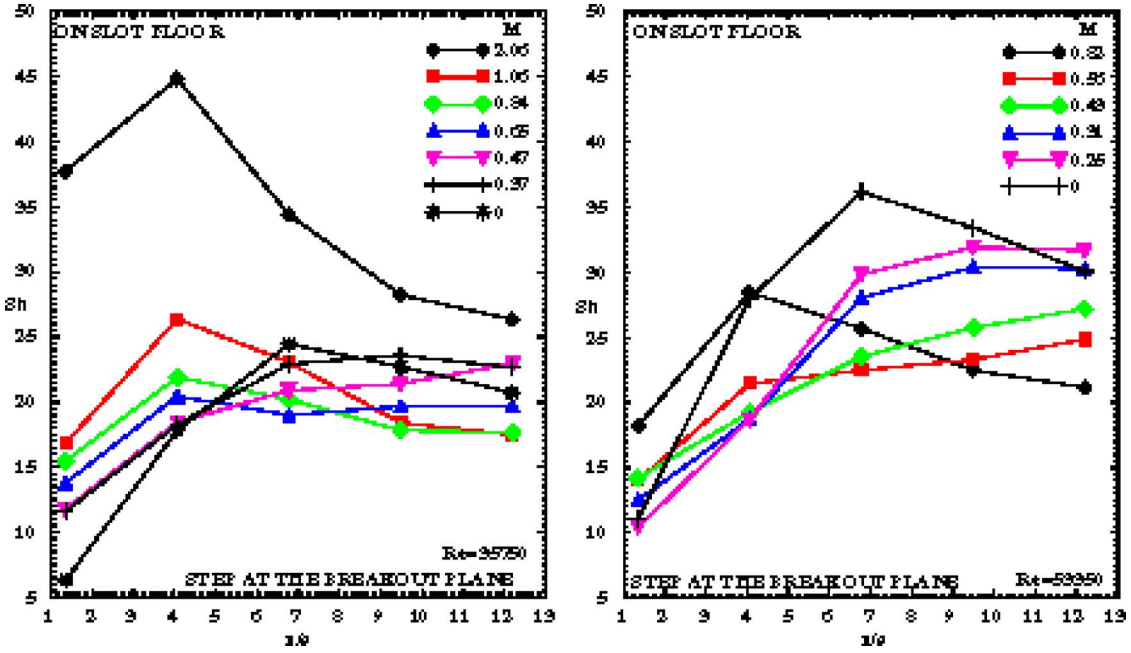

Fig. 9 Sherwood number variation on the slot floor downstream of the breakout plane, Geometry 2 (step at the breakout plane)

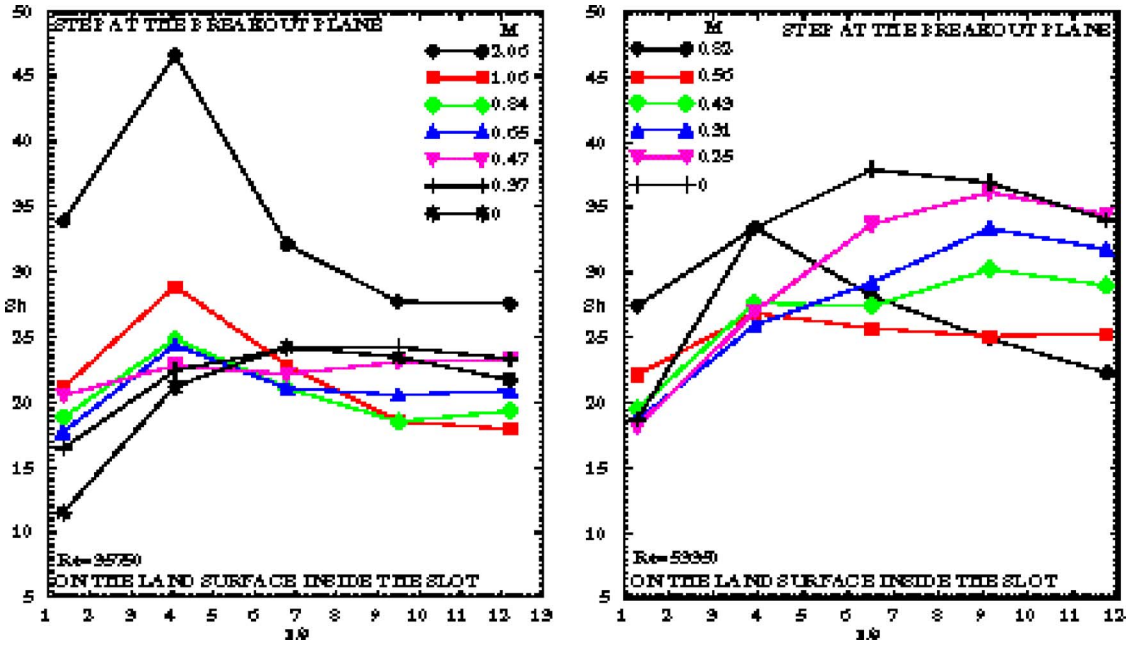

Fig. 10 Sherwood number variation on the land surface inside the slot downstream of the breakout plane, Geometry 2 (step at the breakout plane)

Step at 1/3 of the Slot Axial Length. The step being moved downstream by 1/3 of the total axial distance, Geometry 3 experiences a sudden and drastic decrease in mass transfer on the naphthalene modules right after the step (third piece). The relative importance of first slot piece mass transfer with respect to that of the second piece, monotonically increases as the blowing ratio increases for the smaller mainstream flow Reynolds number (Fig. 12(*a*)). This behavior may suggest that the mass transfer on the second slot piece is mainly due to axial secondary flow formation occurring under the effect of shearing flow behind the lip, whereas the mass transfer from the first slot piece stays unaffected by the secondary flows but is subject to laminar/transitional slot flow whose mass transferring ability increases with the increasing blowing rate. A similar behavior can also be observed for the set of Sherwood number distributions pertaining to the Baseline geometry at the lower mainstream Reynolds number (Fig. 6(*a*)). At the higher mainstream Reynolds number, the difference in module-average mass transfer for the first two modules is almost constant and is in favor of the second module (Fig. 12(*b*)). Step-free baseline geometry reflects the same features (Fig. 6(*b*)).

The kinks on the Sherwood number distribution concerning the second piece along the land sidewall are as well present for Geometry 3 (Figs. 13(*a*), 13(*b*). The sudden decrease in mass transfer right after the step must be due to the secondary flow separation

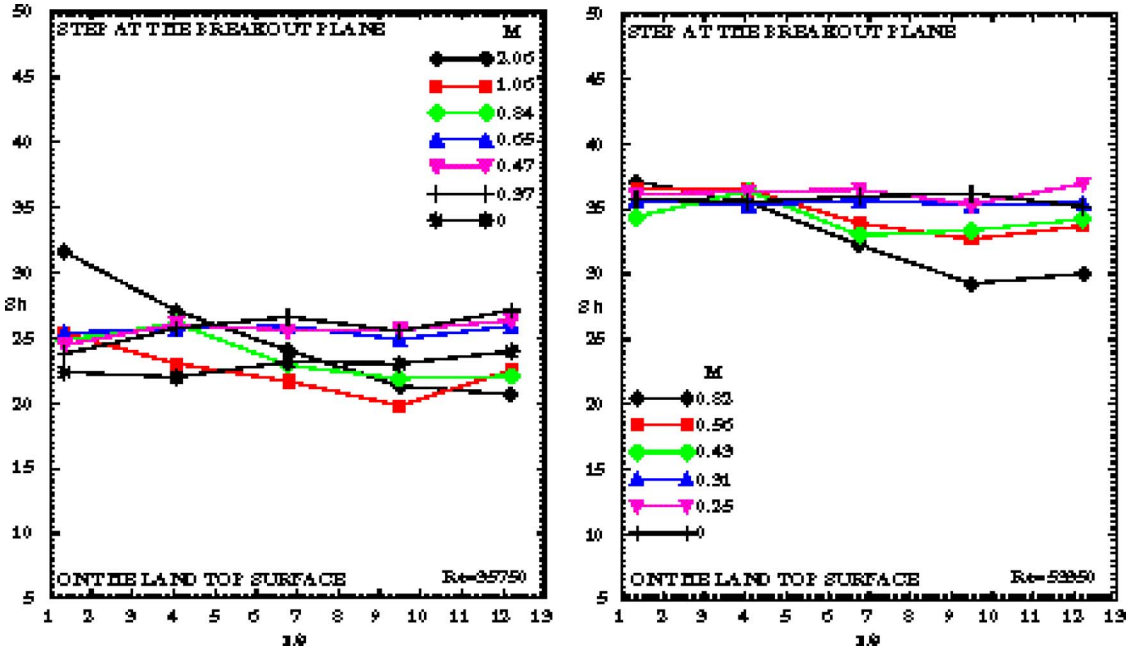

Fig. 11 Sherwood number variation on the land top surface downstream of the breakout plane, Geometry 2 (step at the breakout plane)

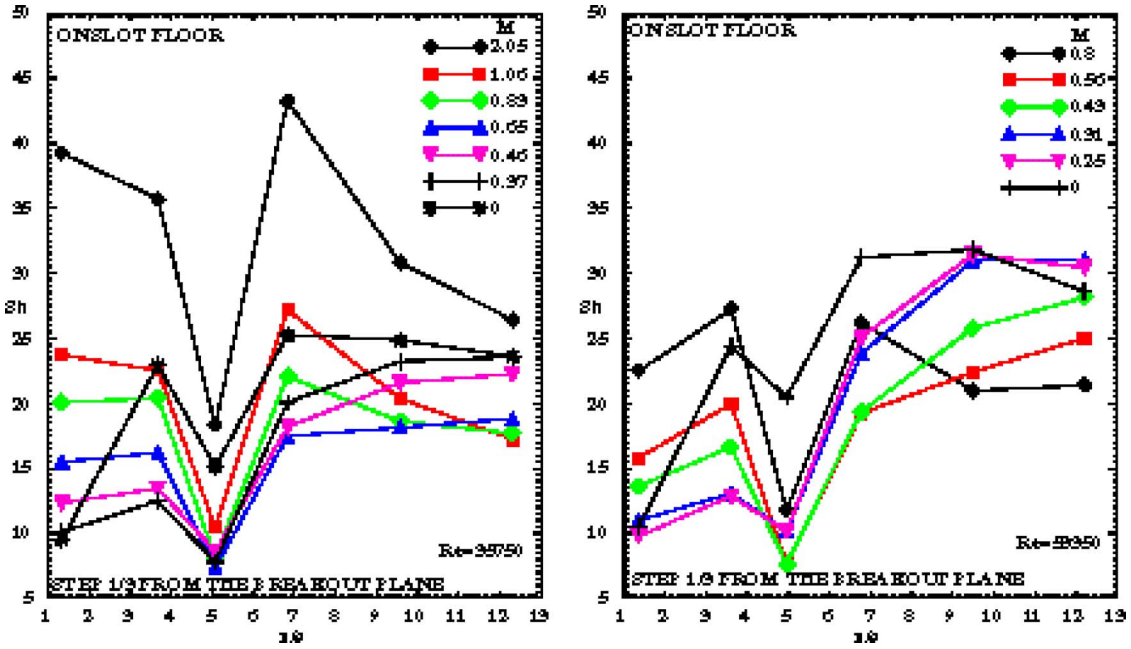

Fig. 12 Sherwood number variation on the slot floor downstream of the breakout plane, Geometry 3 (step at 1/3 of slot axial length)

along the sidewalls. The mass transfer rate consequently increases due to flow reattachment on the fourth sidewall piece and the mass transfer capability eventually decreases as the secondary flows enlarge in size towards the exit of the slot valley. The previously made observation about the fact that the mainstream flow entrainment lessens for increasing blowing ratios is also valid for Geometry 3.

Figures 14(*a*) and 14(*b*) shows the distribution of mass transfer along the land top surfaces. Besides the aforementioned general features of Sherwood number distribution along the land pieces, it is interesting to observe a slight decrease in mass transfer right after the slot step. This observation suggests that the sudden step in the slot region triggers a mainstream flow entrainment into the slot valley, temporarily aggravating the mass transfer enhancement on the land pieces.

Variations of area-weighted average Sherwood number with blowing ratio (M) are given in Fig. 15 for the two mainstream flow Reynolds numbers. On the slot floor surface, step at breakout geometry performs 8–11% better than Geometries 1 and 3 for almost all of the blowing ratios. This may be attributed directly to Coanda effect. On the land sidewalls, the baseline geometry mass transfer enhancement is generally about 10% higher than those for Geometries 2 and 3. On the land top surface, all geometries per-

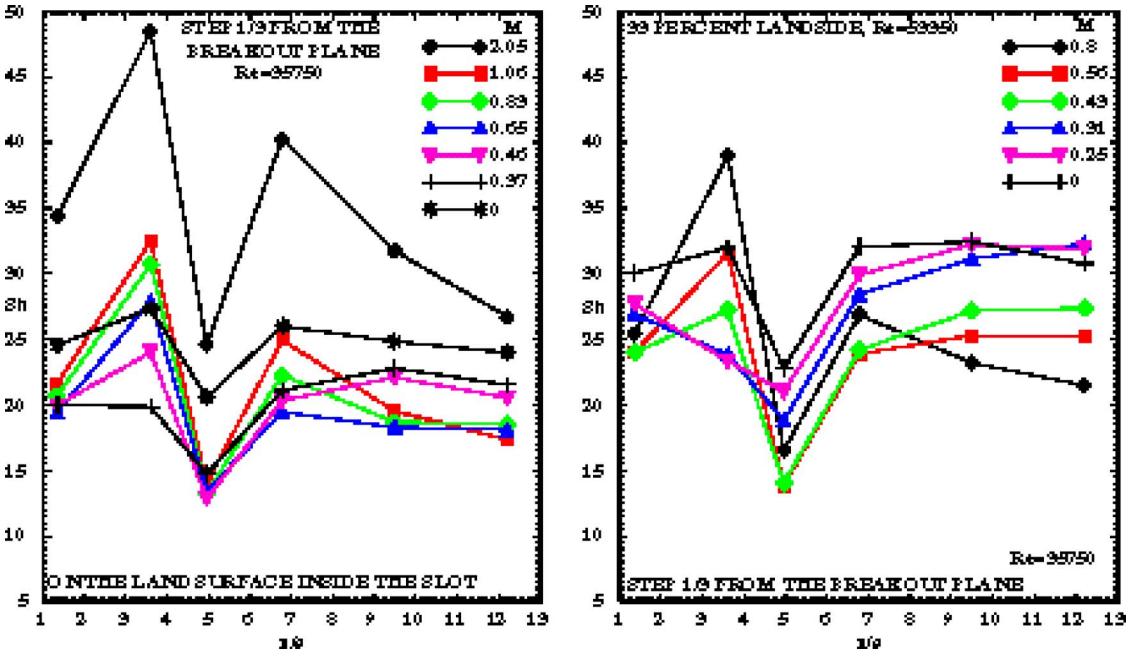

Fig. 13 Sherwood number variation on the land surface inside the slot downstream of the breakout plane, Geometry 3 (step at 1/3 of slot axial length)

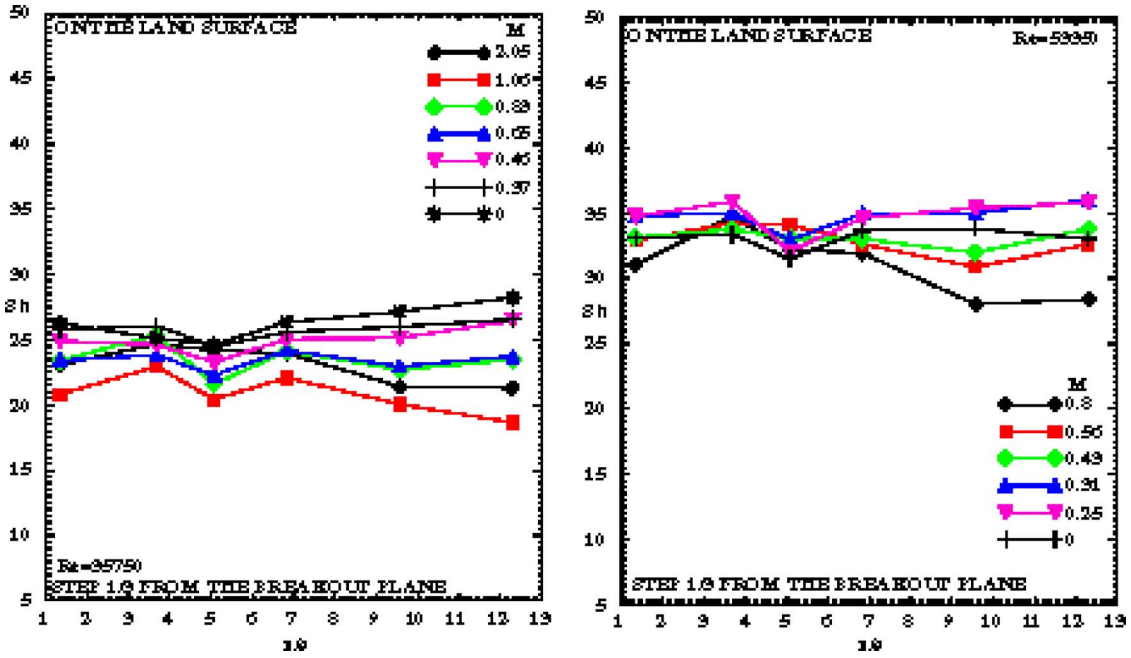

Fig. 14 Sherwood number variation on the land top surface downstream of the breakout plane, Geometry 3 (step at 1/3 of slot axial length)

form similarly with a peculiar wavy distribution. The Sherwood number distributions on slot floor surface and on land sidewalls exhibit parabolic feature and pass through minima around $M=0.5-0.7$.

For mainstream flow Reynolds number of 53,350 the difference in the distribution of area-weighted average mass transfer from one geometry to another vary within the measurement uncertainty band. Although there is no data point above $M=0.8$, the curves seem to pass through a series of minima between 0.5 and 0.7, similar to the behavior observed in low Reynolds number results. Likewise, the Sherwood number distribution on the land top surfaces show a similar character.

Lip and Step Mass Transfer. Figures 16(*a*) and 16(*b*) show variations of Sherwood number on the lip surfaces, for mainstream flow Reynolds numbers of 35,750 and 53,350, respectively. For the low Reynolds number case, the mass transfer increases monotonically with increasing blowing ratio for all the geometries. For the high Reynolds number case the flatness of the regression curves is a sign of the high momentum mainstream flow dominance.

Figures 17(*a*) and 17(*b*) show Sherwood number variations on the step surfaces of Geometries 2 and 3. As expected, the step at the breakout benefits from the increasing momentum intensity of the slot flow. However the explanation about the situation for the step of Geometry 3 might be more complicated. For the case of no slot flow ($M=0$), the high Sherwood value invokes the possibility of mainstream flow reattachment just downstream of the step. As laminar/transitional slot flow starts filling in the slot valley, mainstream flow reattachment becomes less effective causing the Sherwood numbers to drop temporarily. The mass transfer reclaims again its high values as the slot flow continues to increase above $M=1$.

Numerical Results. Representative CFD results are compared with the experimental data in Figs. 18 and 19. CFD models with constant heat flux boundary conditions were run on a unix workstation. A typical case took about 10,000 iterations and about 10–20 h to converge. The agreement between the measured and numerically calculated results on the land top surface for all three geometries is very good. On the slot floor and land sidewall, however, the numerical results, downstream of the breakout plane, fall below the test results with a steady increase until they become very close to the test results around the middle of the slot ($x/s=6-7$). It is speculated that the complicated flow field at the breakout plane and the strong interaction between the two flows are not captured by the numerical model. From the slot center to its exit, the numerical results are higher than the test results. The CFD results on the lip surface, shown in Fig. 19, are in excellent agreement with the tested results for the baseline and Geometry 3. However, when the step is at the breakout plane, the numerical results fall below the experimental data. Other turbulence models including the v2f model did not show any difference in the results. The discrepancy may be attributed to a more complicated flow structure due to the presence of two steps, one at the slot exit that is felt by both streams, and the step caused by the lip itself which is felt by the mainstream. As a result, two recirculating bubbles will form but the CFD analysis may not be able to capture their effects. A more dense mesh, combined with a different turbulence model, including a two-layer turbulence model, could improve the CFD results. That effort is underway and results will be reported later. Typical heat transfer coefficient and temperature variations on the slot and land surfaces are shown in Figs. 20 and 21. As expected, high temperature regions correspond to low heat transfer coefficients.

Conclusions

A practical naphthalene sublimation technique was used to measure mass/heat transfer on the slot and land surfaces of a test setup simulating typical airfoil trailing-edge slots. Test results were compared to numerical results obtained from a commercially available CFD software that could accommodate various turbulence models. The experimental results indicate that the average mass transfer from the land sidewalls are 9–14% higher than the average mass transfer from the slot floor surface for the two Reynolds numbers, respectively. The Coanda step increases mass transfer rates locally but does not cause a drastic change in area average mass transfer. For each geometry, regarding the slot surface and land sidewalls, there exists an optimum blowing ratio where the mass transfer exhibits a minimum. The range of these

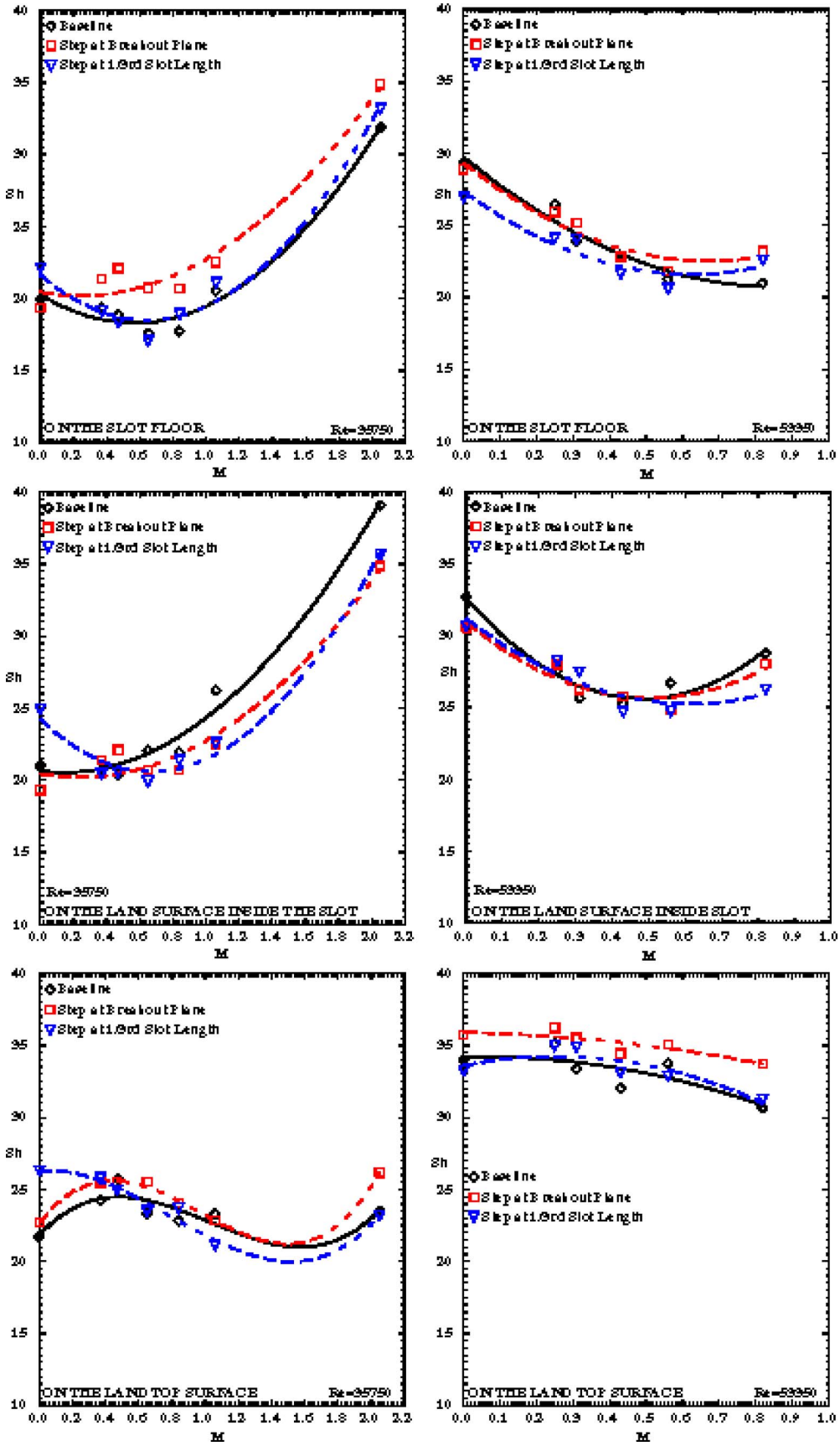

Fig. 15 Area-weighted average Sherwood number variation versus blowing ratio (*M*) for the three slot geometries and two mainstream Reynolds numbers

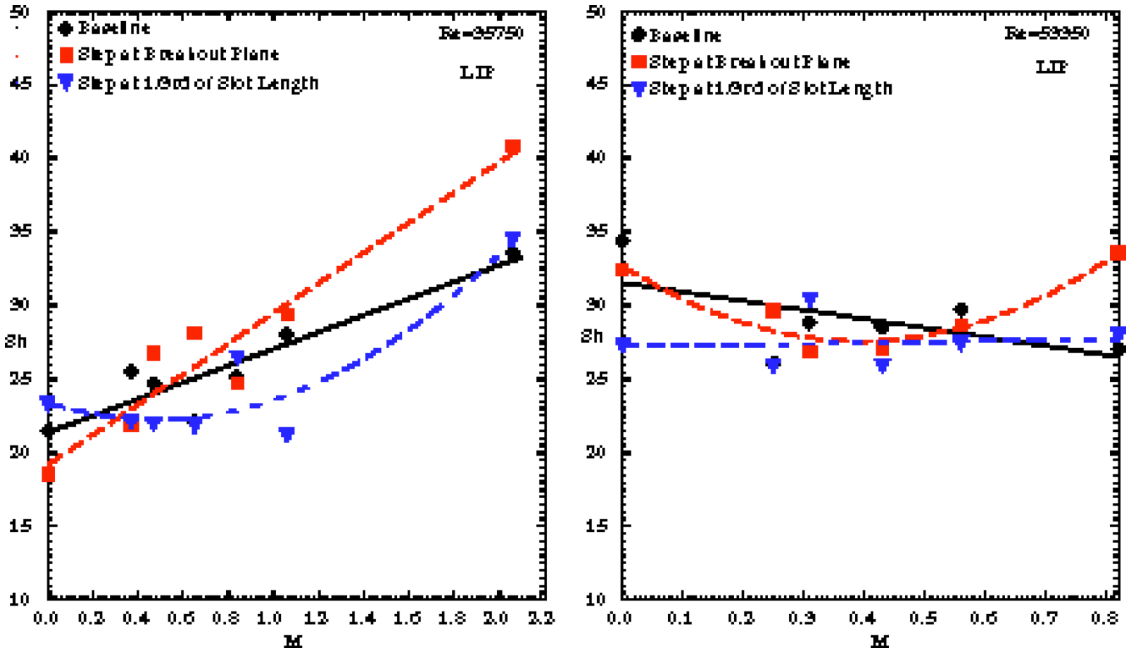

Fig. 16 Area-weighted average Sherwood number variation versus blowing ratio (M) on the lip surface

optima is between $M=0.5-0.7$ regardless of mainstream flow Reynolds number. Increasing mainstream flow Reynolds number by approximately 50% increases mass transfer from the slot surface, land sidewalls, and land pieces by 10%, 15%, and 40%, respectively. The agreement between the measured and numerical results were reasonably good on the land surface. Inside the slot, however, the numerical results were lower than the test results up to a distance of about 50% of the slot length from the breakout plane. Beyond that point, the numerical results were higher than the measured results.

Nomenclature

A_i = mass transfer area for module i (m^2)
D_h = injection slot hydraulic diameter $(2(w \cdot s)/(w+s))$
D_{naph} = diffusion coefficient (m^2/s)
H = mainstream channel height
h = heat transfer coefficient ($W/m^2\,K$)
K_i = mass transfer coefficient for module i (m/s)
L = characteristic length (m)

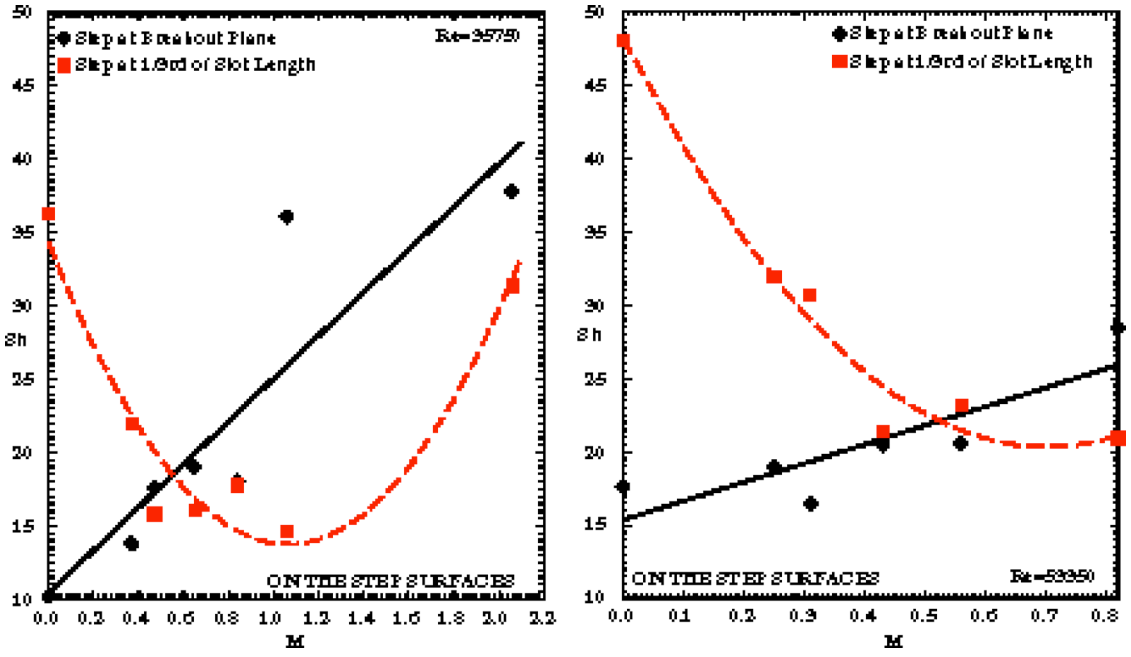

Fig. 17 Area-weighted average Sherwood number variation versus blowing ratio (M) on the step surfaces

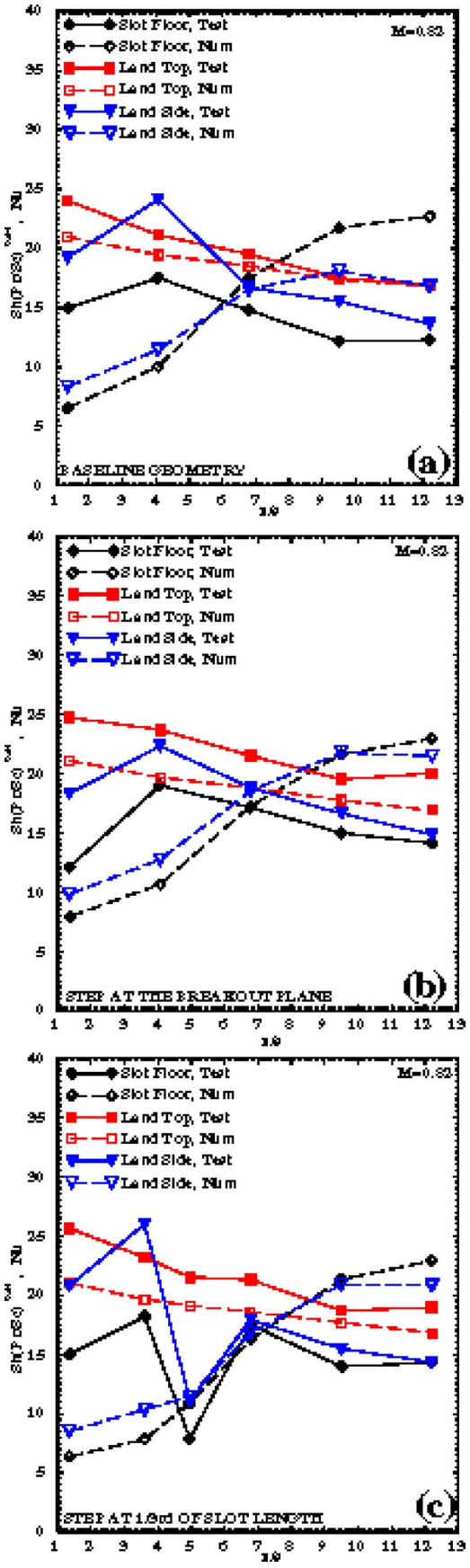

Fig. 18 Comparison between the experimental and numerical results for a blowing ratio of 0.82

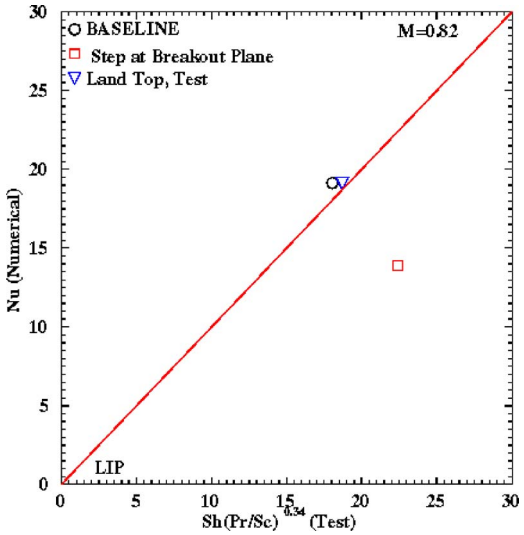

Fig. 19 Comparison between the experimental and numerical results for on the lip surface

M = blowing ratio (ratio of slot to mainstream mass flux), $(\rho u)_s/(\rho u)_m$
m_m = mainstream mass flow rate
m_s = slot mass flow rate
m_i = rate of naphthalene sublimation for module i (kg/s)
Pr = Prandtl number
Sh = Sherwood number
Sc = Schmidt number
Nu = Nusselt number
P_{nv} = naphthalene vapor pressure (Pa)
Re = Reynolds number based on the injection slot hydraulic diameter $(\rho u_m D_h/\mu)$
s = slot opening height
t = lip thickness
T_m = mainstream air temperature
T_s = slot air temperature
T = temperature (°C, K)
u_m = mainstream air velocity

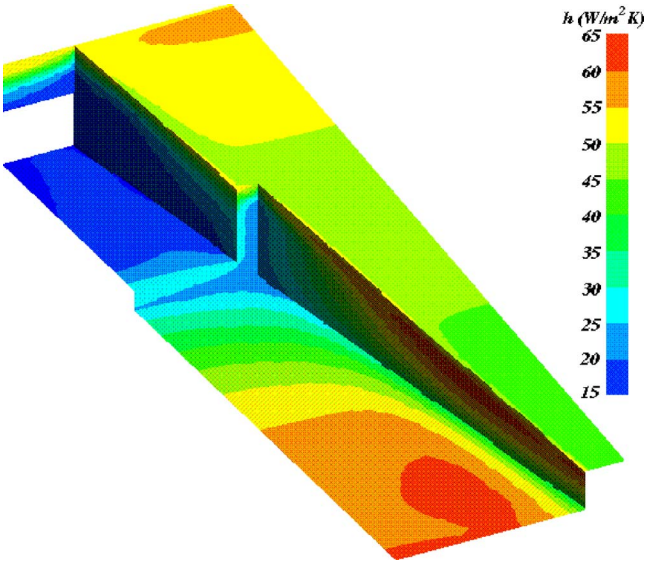

Fig. 20 Representative numerical heat transfer coefficient variation on the slot and land surfaces

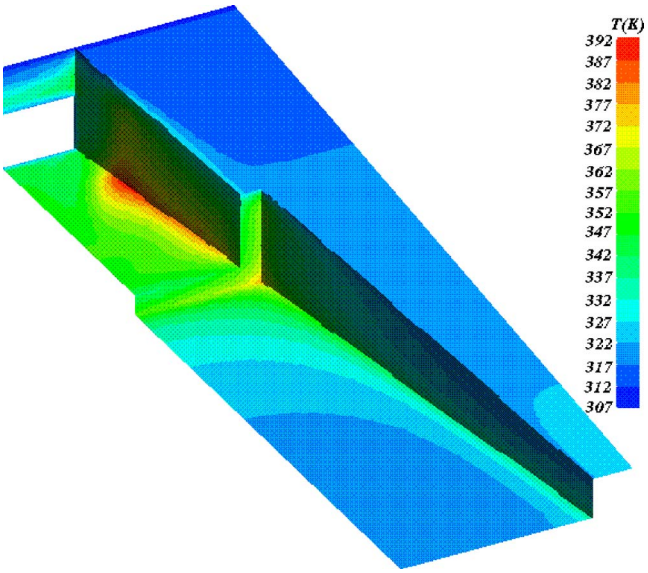

Fig. 21 Representative numerical temperature variation on the slot and land surfaces

u_s = slot air velocity
w = slot opening width
x = axial coordinate from the breakout plane (Fig. 3) (m)

Subscripts

m = mainstream (hot gas side in engine environment)
s = slot (cooling air side in engine environment)

Greek Symbols

α = slot injection angle
β = slot diffusion half-angle (Fig. 3)
ρ_m = mainstream air density
ρ_s = slot air density
$\rho_{\mathrm{nv},w}$ = naphthalene vapor density at the wall ($\mathrm{kg/m^3}$)
$\rho_{\mathrm{nv},b}$ = naphthalene vapor density in bulk flow ($\mathrm{kg/m^3}$)
μ_m = mainstream air dynamic viscosity
ν = kinematic viscosity ($\mathrm{m^2/s}$)

References

[1] Goldstein, R. J., 1971, *Film Cooling, Advances in Heat Transfer*, Academic, New York, Vol. 7, pp. 321–379.
[2] Wieghardt, K., 1964, "Hot-Air Discharge for De-Icing," American Astronautical Federation Translation F-TS-919-RE.
[3] Hartnett, J. P., Birkebak, R. C., and Eckert, E. R. G., 1961, "Velocity Distributions, Temperature Distributions, Effectiveness and Heat Transfer for Air injected Through a Tangential Slot Into a Turbulent Boundary Layer," J. Heat Transfer, **83**(3), pp. 293–306.
[4] Seban, R. A., Chan, H. W., and Scesa, S., 1957, "Heat Transfer to a Turbulent Boundary Layer Downstream of an Injection Slot," ASME Paper No. 57-A-36..
[5] Seban, R. A., 1960, "Heat Transfer and Effectiveness for a Turbulent Boundary Layer With Tangential Fluid Injection," J. Heat Transfer, **82**(4), pp. 303–312.
[6] Samuel, A. E., and Joubert, P. N., 1964, "Film Cooling of an Adiabatic Flat Plate in Zero Pressure Gradient in the Presence of a Hot Mainstream and Cold Tangential Secondary Injection," ASME Paper No. 64-WA-HT-48..
[7] Papell, S. S., and Trout, A. M., 1959, "Experimental Investigation of Air Film-Cooling Applied to an Adiabatic Wall by Means of an Axially Discharging Slot," NASA TN-D-9, NASA, Washington, D.C.
[8] Papell, S. S., 1960, "Effect on Gaseous Film Cooling Injection Through Angled Slots and Normal Holes," NASA TiN-D-299, NASA, Washington, D.C.
[9] Kacker, S. C., and Whitelaw, J. H., 1968, "The Effect of Slot Height and Slot Turbulence Intensity on the Effectiveness of the Uniform Density, Two Dimensional Wall Jet," J. Heat Transfer, **90**, pp. 469–475.
[10] Kacker, S. C., and Whitelaw, J. H., 1969, "An Experimental Investigation of the Influence of Slot-Lip-Thickness on the Impervious-Wall Effectiveness of the Uniform-Density, Two-Dimensional Wall Jet," Int. J. Heat Mass Transfer, **12**, pp. 1201–1206.
[11] Sivasegaram, S., and Whitelaw, J. H., 1969, "Film Cooling Slots: the Importance of Lip Thickness and Injection Angle," J. Mech. Eng. Sci., **11**(1), 22–27.
[12] Goldstein, R. J., Rask, R. B., and Eckert, E. R. G., 1966, "Film Cooling With Helium Injection into an Incompressible Air Flow," Int. J. Heat Mass Transfer, **9**, pp. 1341–1350.
[13] Nicoll, W. B., and Whitelaw, J. H., 1967, "The Effectiveness of the Uniform Density, Two-Dimensional Wall Jet," Int. J. Heat Mass Transfer, **10**, pp. 623–639.
[14] Burns, W. K., and Stollery, J. L., 1969, "The Influence of Foreign Gas Injection and Slot Geometry on Film Cooling Effectiveness," Int. J. Heat Mass Transfer, **12**, pp. 935–951.
[15] Rastogi, A. K., and Whitelaw, J. H., 1973, "The Effectiveness of Three-Dimensional Fflm-Cooling Slots: I Measurements," Int. J. Heat Mass Transfer, **16**, pp. 1665–1672.
[16] Patankar, S. V., Rastogi, A. K., and Whitelaw, J. H., 1973, "The Effectiveness of Three-Dimensionai Film-Cooling Slots: II Predictions," Int. J. Heat Mass Transfer, **16**, pp. 1673–1681.
[17] Paxson, D. E., and Mayle, R. E., 1988, "The Influence of a Main-Stream Mermal Boundary Layer on Film Cooling Effectiveness," ASME Paper No. 88-GT-17.
[18] Metzger, D. E., Carper, H. J., and Swank, L. R., 1968, "Heat Transfer With Film Cooling Near Nontangential Injection Slots," ASME J. Eng. Power, **90**, pp. 157–163.
[19] Ballal, D. R., and Lefebvre, A. H., 1972, "A Proposed Method for Calculating Film-Cooled Wall Temperature in Gas Turbine Combustion Chambers," ASME Paper No. 72-WA/HT-24.
[20] Pai, B. R., and Whitelaw, J. H., 1971, "The Prediction of Wall Temperature in the Presence of Film Cooling," Int. J. Heat Mass Transfer, **14**, pp. 409–426.
[21] Taslim, M. E., Spring, S. D., and Mehlman, B. P., 1992, "An Experimental Investigation of Film Cooling Effectiveness for Slots of Various Exit Geometries," J. Thermophys. Heat Transfer, **6**(2), pp. 302–307.
[22] Korbacher, G. K., 1962, "The Coanda Effect at Deflection Surfaces Detached From the Jet Nozzles," J. Canadian Aeronautical Institute, **8**(1), pp. 1–6.
[23] Goldstein, R., and Cho, H., 1995, "A Review of Mass Transfer Measurements Using Naphthalene Sublimation," Exp. Therm. Fluid Sci., **10**, pp. 416–434.
[24] Kudchadker, A. P., Kudchadker, S. A., and Wilhoit, R. C., 1978, *Naphthalene*, API Monograph Ser.707, American Petroleum Institute, Washington, D. C.
[25] Kline, S. J., and McClintock, F. A., 1953, "Describing Uncertainty in Single-Sample Experiments," Mech. Eng. (Am. Soc. Mech. Eng.), **75**, pp. 3–8.
[26] Holloway, D. S., Leylek, J. H., and Buck, F. A., 2002, "Pressure-Side Bleed Film Cooling, Part I—Steady Framework for Experimental and Computational Results," ASME Paper No. GT-2002–30471.

High-Resolution Film Cooling Effectiveness Measurements of Axial Holes Embedded in a Transverse Trench With Various Trench Configurations

Scot K. Waye
e-mail: scotwaye@hotmail.com

David G. Bogard

Mechanical Engineering Department,
University of Texas at Austin,
Austin, TX 78712

Adiabatic film cooling effectiveness of axial holes embedded within a transverse trench on the suction side of a turbine vane was investigated. High-resolution two-dimensional data obtained from infrared thermography and corrected for local conduction provided spatial adiabatic effectiveness data. Flow parameters of blowing ratio, density ratio, and turbulence intensity were independently varied. In addition to a baseline geometry, nine trench configurations were tested, all with a depth of 1/2 *hole diameter, with varying widths, and with perpendicular and inclined trench walls. A perpendicular trench wall at the very downstream edge of the coolant hole was found to be the key trench characteristic that yielded much improved adiabatic effectiveness performance. This configuration increased adiabatic effectiveness up to 100% near the hole and 40% downstream. All other trench configurations had little effect on the adiabatic effectiveness. Thermal field measurements confirmed that the improved adiabatic effectiveness that occurred for a narrow trench with perpendicular walls was due to a lateral spreading of the coolant and reduced coolant jet separation. The cooling levels exhibited by these particular geometries are comparable to shaped holes, but much easier and cheaper to manufacture.*
[DOI: 10.1115/1.2464141]

Keywords: transverse trench, film cooling, adiabatic effectiveness, vane

Introduction

In order to produce higher efficiency turbine engines, the exit gas temperature from the combustor needs to be increased. This causes an increased thermal load on the airfoils which decay the life and effectiveness of the engine as a whole. Cooler gas bled from the compressor stage of the engine is fed through the airfoil internally, cooling the airfoil with serpentine passages, ribs, pin fins, and impingement cooling. The gas is then ejected from the airfoil through discrete holes onto the surface. This film cooling provides an external cooling technique that helps protect the metal surface from the hot mainstream gases. Attempts to cool the airfoil surface more efficiently using less extracted gas from the compressor has led to various hole configurations and designs.

Bunker [1] investigated radial and axial holes that were embedded in an overlying transverse trench. The investigation was motivated by a previous study conducted by Wang et al. [2], which showed a uniform velocity distribution at the exit of a trench fed with discrete coolant holes. A similar approach of feeding a trench with discrete holes has been used for the combustor region of the engine, as studied in Klinger and Hennecke [3] and Schulz [4]. Ideally, holes imbedded within a trench will mimic a transverse slot. As shown by Goldstein [5], Teekaram et al. [6], and Papell [7], a slot has much better film effectiveness than a row of holes. Similar results were obtained with slots in endwalls and gaps between blade components by Blair [8], Chyu et al. [9], and Saban et al. [10].

The results from Bunker [1] indicated that a narrow and shallow trench performed better than deeper and wider trenches. The narrow trench filled with coolant and had less mixing with the hotter mainstream gas as compared to the wider trench. The narrow trench was shown to have increased centerline adiabatic effectiveness of 50–75% over conventional axial holes. The centerline adiabatic effectiveness was obtained by an array of surface thermocouples on a flat plate, but no off-centerline or spatial data was presented. For the shallow trench, the centerline effectiveness values were only reported for two blowing ratios, $M=0.97$ and 1.12. Lu et al. [11] built on the work of Bunker [1] using a transient infrared thermography technique that obtained spatial heat transfer coefficients and the adiabatic effectiveness measurements. Four trench configurations accomplished with inserts were tested in addition to a baseline, nontrench case. Measurements were made for $0 < x/d < 10$ on a flat plate at DR=1.1, and $M=0.5$, 1.0, and 1.5. Depending on blowing ratio, they found some configurations resulted in a 50% increase in film effectiveness and some caused a 40% decrease.

Experimental Facilities and Procedures

Experiments were conducted in a closed loop wind tunnel driven by a 50 hp adjustable speed fan. The test section shown in Fig. 1 consisted of a simulated three-vane linear cascade. The vane geometry replicated an actual engine geometry scaled up nine times. The center vane was the test vane and is shown in Fig. 2. The outer wall was adjusted to achieve a nondimensional pressure distribution around the vane that matched an inviscid computational fluid dynamics (CFD) simulation of the actual engine geometry and conditions. The cascade inlet velocity was 5.8 m/s and the exit velocity was 32 m/s, yielding an exit Reynolds number of 1.06×10^6 (based on a true chord length of $C=594$ mm) to

Contributed by the International Gas Turbine Institute of ASME for publication in the JOURNAL OF TURBOMACHINERY. Manuscript received July 12, 2006; final manuscript received July 14, 2006. Review conducted by David Wisler. Paper presented at the ASME Turbo Expo 2006: Land, Sea and Air (GT2006), Barcelona, Spain, May 8–11, 2006. Paper No. GT2006-90226.

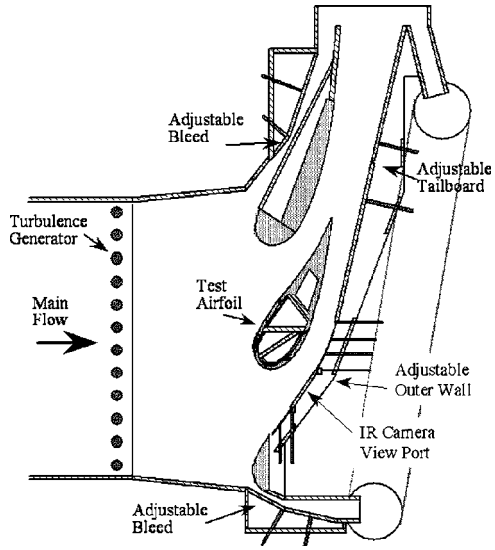

Fig. 1 Schematic of the simulated turbine vane test section

match realistic engine conditions. A removable passive turbulence generator located 0.5 m upstream of the vane cascade consisted of 12 rods with outside diameter of 38 mm and pitched 85 mm apart. Previous measurements [12] determined that, with the turbulence generator installed, the turbulence at $0.18C$ upstream of the test vane's leading edge was $Tu_{app}=21\%$ with and integral length scale of $\Lambda_f/d=10.0$. Without the turbulence generator installed, the turbulence was $Tu_{app}=5.2\%$ with $\Lambda/d=10.7$. The relatively high "low" mainstream turbulence condition was due to a simulated hot streak generator that was installed in the facility but not used in this study, although this low mainstream level is comparable to some power generating gas turbines. At the location of the holes tested, due to flow acceleration, high mainstream turbulence intensity was determined to be $Tu_{\infty}=3.9\%$ and the low mainstream turbulence level was $Tu_{\infty}=1.0\%$ with similar length scales. The boundary layer parameters of the approaching boundary layer were $\delta/d=0.56$ and 0.44, $\delta_1/d=0.05$ and 0.07, and $H=1.31$ and 1.67 for high- and low-mainstream turbulence, respectively. The shape factor for high mainstream turbulence indicated a turbulent boundary layer flow, while that for the low-mainstream turbulence indicated a transitional boundary layer.

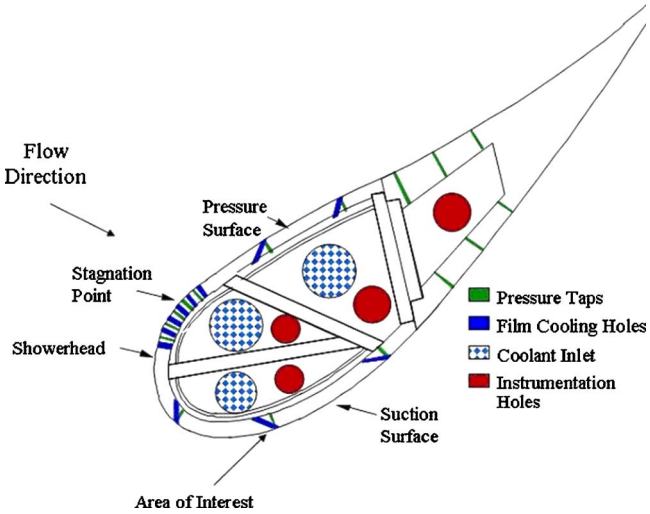

Fig. 2 Schematic of test vane details

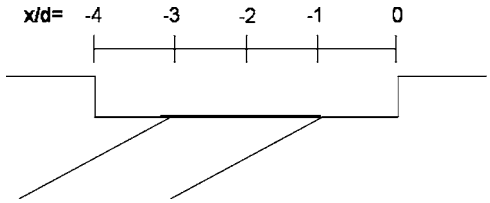

Fig. 3 Coordinate origin for trench configurations

The vane was constructed of a low conductivity polyurethane foam, $k=0.048$ W/m K, to facilitate measurement of adiabatic wall temperature. The second row of coolant holes on the suction side, used for the current study, was located at $s/C=0.367$. The baseline case implemented 30 deg round axial holes with a length of $L/d=6.7$ spaced $p/d=2.78$ apart, as described and tested in Ref. [13]. An overlying transverse trench was made over the second row of holes (reducing the hole length to $L/d=5.7$). For the current study, the trench was directly milled into the substrate, but other manufacturing methods are possible [14]. The trench dimensions were height $h/d=0.5$ and width $w/d=4.0$ with the holes centered in the trench. The coordinate origin, $x/d=0$, was defined as the trailing edge of the baseline axial hole. With the addition of the trench, the trailing edge of the hole moved upstream $1d$, but the x/d location was maintained. Therefore, $x/d=0$ for the trench cases was located at the edge of the downstream lip, as seen in Fig. 3. Experimental conditions are summarized in Table 1.

Machined styrene strips ($k=0.17$ W/m K) were used as inserts to form the lips of the trench configurations. No insert, a rectangular insert, or a triangular insert were used in the upstream and/or downstream locations. The triangular insert matched the injection angle of the hole (30 deg). Nine configurations were tested in addition to the baseline, as shown in Fig. 4, at one blowing ratio. The narrow and wide trench configurations (2 and 10) were tested for all flow parameters.

Adiabatic effectiveness was determined from the surface temperature distribution, measured via infrared thermography (a FLIR ThermaCAM P20 infrared camera calibrated in situ using ribbon type E surface thermocouples). The camera resolution was 1.5 pixels/mm at a focal length of 0.32 m. The viewing area was approximately 0.15 m in diameter through a circular salt window. The thermocouple data was acquired using a National Instruments Data Acquisition system (NI DAQ). Two mainstream thermocouples were located near the leading edge of the vane, suspended away from nearby walls. Two coolant thermocouples were located near the exit plane of coolant holes but were not in the camera's field of view. Two surface ribbon thermocouples were located just

Table 1 Test conditions

True chord length	59.4 cm
Vane span	54.9 cm
Vane pitch	45.7 cm
Inlet velocity	5.8 m/s
Exit Reynolds number	1.06×10^6
High-mainstream turbulence at inlet/test location	$Tu_{app}=21\%$ $Tu_{\infty}=3.9\%$ $\Lambda=4.1$ cm
Low-mainstream turbulence at inlet/rest location	$Tu_{app}=5.2\%$ $Tu_{\infty}=1.0\%$ $\Lambda=4.4$ cm
Coolant hole diameter	$d=4.11$ mm
Hole length (w/o trench)	27.5 mm ($L/d=6.7$)
Hole length (w/ trench)	23.4 mm($L/d=5.7$)
Coolant injection angle	$\alpha=30$ deg
Hole pitch	11.4 mm ($p/d=2.775$)
Trench depth	2.05 mm ($h/d=0.5$)
Trench width	16.4 mm ($w/d=4$)
Density ratio (ρ_c/ρ_{∞})	1.3, 1.5

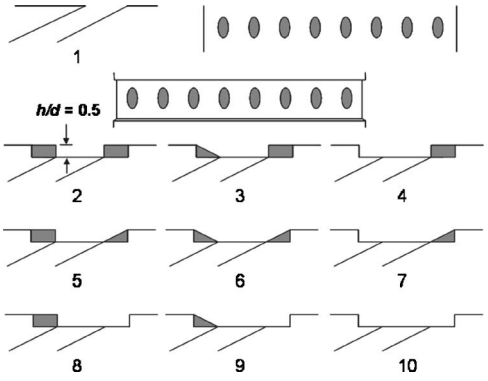

Fig. 4 Trench lip configurations

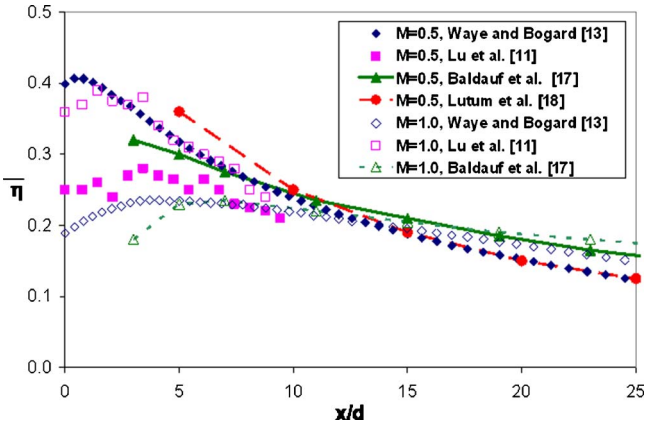

Fig. 5 Validation of baseline axial holes with literature

within the view of the camera but outside of the processed area. These were only used for the camera calibration. LabVIEW software was written to compute parameters in real time and write the data to disk. Adiabatic effectiveness, η, was determined using the following definition

$$\eta \equiv \frac{T_\infty - T_{\text{aw}}}{T_\infty - T_c} \tag{1}$$

Density ratios of DR=1.3 and 1.5 for the coolant were achieved using liquid nitrogen to cool the air in a secondary loop that was then used as the coolant of the test vane. A range of suction side blowing ratios was tested from $M=0.3$ to 1.4.

Although the vane was constructed of low thermal conductivity foam, conduction through the wall of the vane caused the measured surface temperatures to be slightly lower than what they would have been for a truly adiabatic surface. A steady-state analysis and experimental validation ensured that the wall temperatures were not transient. Radiation effects were calculated to be negligible during adiabatic effectiveness tests. The effect of conduction was corrected with a one-dimensional (1D) conduction model as described by Ethridge et al. [15]. An in situ conduction correction was found during each experiment by blocking the flow of coolant to the film cooling holes in view of the infrared (IR) camera, and allowing the other holes to flow freely. The decrease in surface temperature due to conduction was measured directly. Near the holes, the conduction was slightly higher due to 3D conduction around the holes. The conduction was nearly 1D when $x/d>3$. The wall temperature without film cooling, normalized like the adiabatic effectiveness, was designated η_0. The following equation was used to correct the other measurements for conduction

$$\eta = \frac{\eta_{\text{measured}} - \eta_0}{1 - \eta_0} \tag{2}$$

A typical value for the conduction correction was $\eta_0=0.04$.

In addition to the adiabatic effectiveness measurements, a hot wire anemometer was used to make velocity measurements. An A.A. Lab Systems Ltd. AN-1003 Hot Wire/Hot Film Anemometry System was employed, and the same NI DAQ hardware was used for data acquisition.

Uncertainties were calculated on a 95% confidence interval. Sources of uncertainty were the IR camera measurements, conduction correction, thermocouple measurements, and variation in the blowing ratio. Since comparisons of adiabatic performance done in separate tests of axial and compound angle holes was of primary importance, the precision of the experiments was the focus of the uncertainty analysis. The precision of the measurements was classified in two ways: test-to-test repeatability and within-test repeatability. Test-to-test uncertainties were used when comparisons were made for results obtained from separate experiments. Within-test uncertainties were used when evaluating the effects of parameters, such as blowing ratio and mainstream turbulence level, which were varied within a single experiment while holding other parameters constant. From multiple tests and through statistical analysis, the test-to-test uncertainties in the laterally averaged adiabatic effectiveness were $\delta\bar{\eta}=\pm0.04$ for $M=0.3$, $\delta\bar{\eta}=\pm0.02$ for $M=0.5$, and $\delta\bar{\eta}<\pm0.01$ for $M>1.0$. Similarly, the uncertainties for the spatially averaged adiabatic effectiveness were $\delta\bar{\bar{\eta}}=\pm0.03$ for $M=0.3$, $\delta\bar{\bar{\eta}}=\pm0.02$ for $M=0.5$, and $\delta\bar{\bar{\eta}}<\pm0.01$ for $M>0.7$. The uncertainty of the blowing ratio was found to range from $\delta M=\pm0.07$ for $M=0.3$ to $\delta M=\pm0.015$ for $M=1.4$ based on the uncertainty of the orifice meter reading, the mainstream velocity, and using the sequential perturbation method as suggested by Moffat [16]. During every experiment, various conditions were repeated in order to establish within-test repeatability. Statistical analysis showed the within-test uncertainty of $\bar{\eta}$ to be $\delta\bar{\eta}=\pm0.0075$ for moderate blowing ratios ranging from $M=0.6$ to 1.0.

The baseline axial hole data was compared with literature for experimental validation, as seen in Fig. 5. Baldauf et al. [17] and Lutum et al. [18] presented data for $\alpha=30$ deg cylindrical holes with $p/d=3$ on a flat plate. Baseline results from Lu et al. [11] are also included in Fig. 5 since their study also included transverse trenches. The current baseline results were consistent with those of Baldauf et al. [17] and Lutum et al. [18]. The results of Lu et al. [11] were inconsistent with all other studies, showing increasing $\bar{\eta}$ when the blowing ratio was increased from $M=0.5$ to $M=1.0$, while all other studies showed decreasing $\bar{\eta}$ over the range of $0<x/d<10$.

Results

The nine trench configurations were tested at $M=1.0$ and $\text{Tu}_\infty=1.0\%$. Figure 6 gives the quantitative values for all of the configurations as well as the baseline case with the same pitch. It is immediately obvious that one class of configurations yielded much higher adiabatic effectiveness values than all the rest. The other configurations were similar to the baseline case, providing little improvement to the $\bar{\eta}$ levels. All configurations with the rectangular insert situated downstream of the hole performed better, giving $\bar{\eta}$ values that were 50% higher near the hole and 20% higher downstream. The downstream insert had much more of an effect on the total cooling of the surface than did the upstream insert.

Configuration 2 gave the highest values of adiabatic effectiveness for all x/d locations compared to all the other configurations. This configuration was still 10% better than Configurations 3 and 4, which also had downstream rectangular insert.

Figure 7 shows the spatial distribution of η for all ten configurations. The jets were periodic, so only one pitch is included for

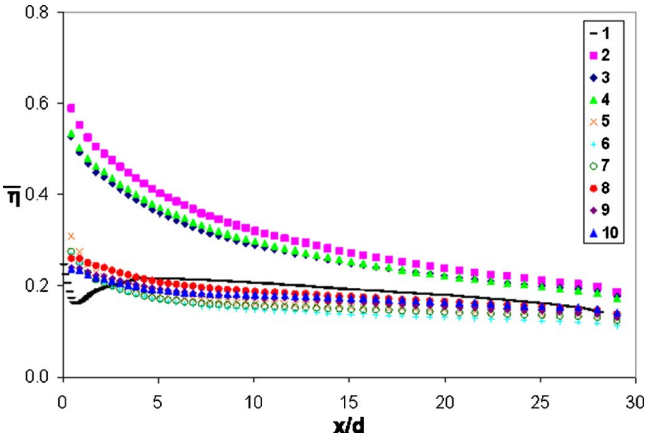

Fig. 6 Comparison of laterally averaged adiabatic effectiveness for trench lip configurations, $M=1.0$, $Tu_\infty=1.0\%$

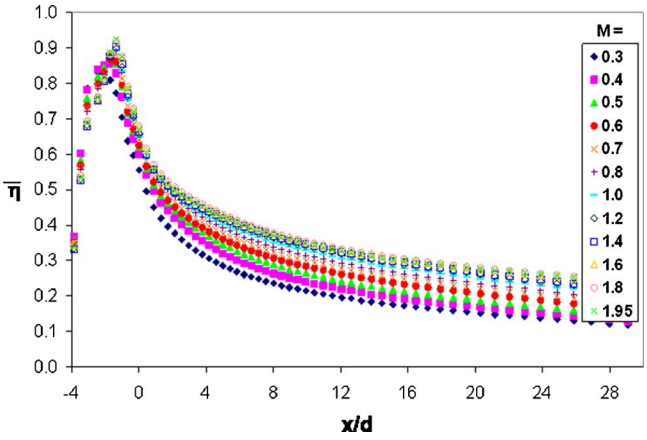

Fig. 8 Laterally averaged adiabatic effectiveness for narrow trench (configuration 2) for various M, $Tu_\infty=1.0\%$

comparison. The baseline case had a slight jet separation and reattachment. Configuration 2 can also be described as a narrow trench with a width of $w/d=2$. The coolant, when ejected from the hole, was obstructed by the downstream lip. This caused the coolant to fill the trench before it was ejected out of the trench onto the vane surface. This laterally spread the coolant, increasing the effectiveness values. Individual jet streaks were still evident. Mainstream gas entrainment warmed the coolant in the trench slightly for Configurations 3 and 4.

All of the configurations with the triangular insert downstream (5–7) showed similar laterally averaged adiabatic effectiveness levels and patterns on the surface. All three configurations had a nearly constant adiabatic effectiveness of $\bar{\eta}=0.15$ when $x/d>5$, which was lower than the baseline case by 25%. The angle of the triangular insert matched the angle of the hole, so the slope was matched and became a virtual continuation of the hole. Therefore, the cooling on the surface spread slightly in the trench area, but appeared more like the baseline axial hole case. Configuration 5, with the upstream rectangular insert, blocked mainstream gas entrainment upstream of the hole, so near the hole, effectiveness levels were about 7% higher than Configurations 6 or 7.

The configurations tested without an insert downstream of the hole (8–10) showed similar characteristics. A slight detachment and reattachment to the surface occurred, as suggested in the spatial contour plots. Configuration 10 can also be described as a wide trench, with $w/d=4$. The wide trench allowed for some coolant to fill the trench, but mainstream gas entrainment upstream of the hole lowered the cooling performance near the hole when compared to the other configurations. Downstream, Configurations 8–10 had 10–15% higher laterally averaged adiabatic effectiveness than the configurations with a triangular downstream insert, but still about 10% less then the baseline case. The upstream rectangular insert in Configuration 8 blocked some hot mainstream gas entrainment, evident in the contour plot.

As stated earlier, the narrow trench (Configuration 2) performed better than any other configuration tested in the current study. For all blowing ratios, the values of $\bar{\eta}$ within the trench were quite high, $\bar{\eta}=0.8-0.9$, as seen in Fig. 8. Downstream of the trench there was a monotonic increase in $\bar{\eta}$ of about 5–10% for every 0.1 increase of M from $M=0.3$ to 1.0. With increased blowing above $M=1.0$, the effectiveness levels plateaued. When $M=1.95$ for the low turbulence case, for example, there was only a 10% increase in adiabatic effectiveness over $M=1.0$, although 95% more coolant was used.

A verification of the effect of the density ratio was desired for the narrow trench, Configuration 2, since it had high effectiveness values. Figure 9 shows that there was almost no effect of the density ratio on the adiabatic effectiveness.

The spatial contour plots of the adiabatic effectiveness, shown in Fig. 10 for $M=0.4-1.4$, help explain why the narrow trench configuration was so effective in cooling the surface. The spatial distribution of the adiabatic effectiveness within $-3<x/d<-1$ suggests that the trench was mostly filled with coolant with little mainstream entrainment to heat the coolant. As the trench filled, the coolant ejected from the trench onto the surface. The spanwise

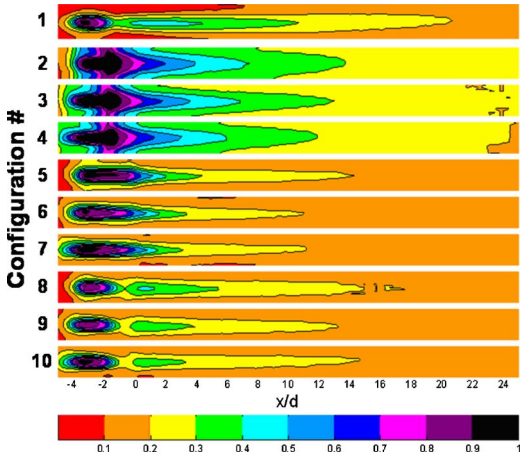

Fig. 7 Spatial plots of adiabatic effectiveness for trench configurations, $M=1.0$, $Tu_\infty=1.0\%$

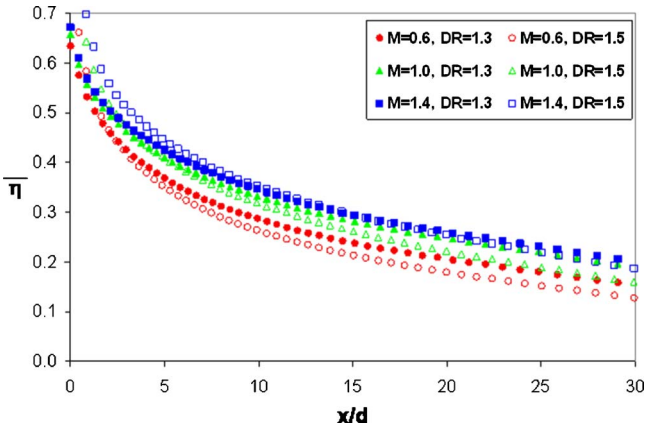

Fig. 9 Density ratio comparison for narrow trench configuration

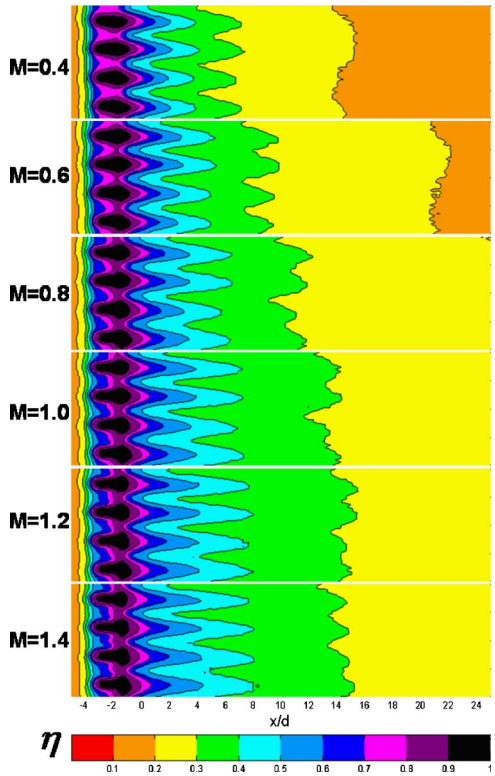

Fig. 10 Spatial plots of adiabatic effectiveness for the narrow trench (configuration 2) at various *M*, $Tu_\infty = 3.9\%$

peaks coincided with the coolant holes, so some coolant appears to have been forced over by the momentum of the jet.

When the narrow trench was compared to the baseline axial holes, the narrow trench performed better for all locations and conditions, as seen in Fig. 11. At low blowing ratios, the baseline axial holes and the narrow trench configuration exhibited similar cooling effectiveness downstream. Near the holes, however, the narrow trench configuration performed up to 35% better. This occurred only in the near hole region of $x/d < 5$ for $M < 0.6$. When blowing was increased, the narrow trench configuration had higher adiabatic effectiveness for all x/d. With increased blowing, the effectiveness levels of the baseline case steadily dropped due to jet separation, while the effectiveness values for the narrow trench configuration continued to increase, due to increased coolant mass flow.

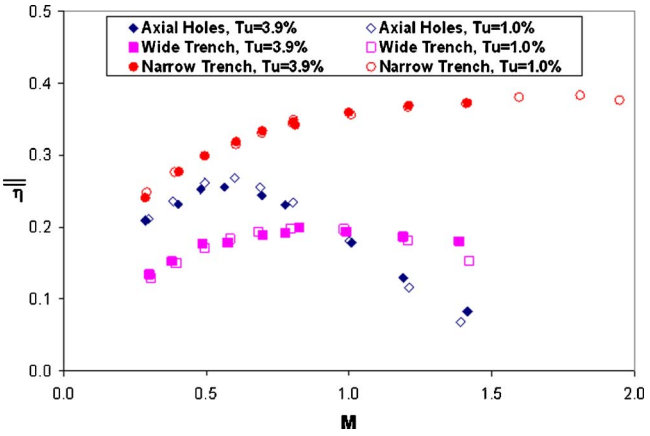

Fig. 12 Comparison of spatially averaged adiabatic effectiveness for axial and trench configurations

Figure 12 shows the spatially averaged adiabatic effectiveness, $\bar{\bar{\eta}}$, plotted against the blowing ratio for the baseline axial holes and the axial holes embedded within a wide trench and a narrow trench. For all configurations, results for $Tu_\infty = 1.0\%$ and $Tu_\infty = 3.9\%$ are presented. As is evident in Fig. 12, the effect of the mainstream turbulence was negligible.

At low blowing ratios, the baseline axial hole configuration and the narrow trench configuration had similar $\bar{\bar{\eta}}$ levels, but the wide trench configuration had lower $\bar{\bar{\eta}}$ values. With increased blowing ratio, the $\bar{\bar{\eta}}$ levels of the baseline case dropped due to jet separation, while the $\bar{\bar{\eta}}$ values for the wide and narrow trench configurations continued to increase. Consequently the wide trench configuration outperformed the axial hole configuration at high blowing ratios. The narrow slot configuration excelled over the axial holes at moderate and high blowing ratios. At $M = 1.0$, the narrow trench configuration had a 50% higher spatially averaged effectiveness than the axial holes. The narrow trench was nearly 300% better than the baseline axial hole configuration at $M = 1.4$, while the wide trench was 65% higher at this elevated blowing ratio.

The wide trench (Configuration 10) yielded cooling effectiveness similar to the baseline axial holes at $M = 1.0$. The wide trench geometry allows a contrast to the narrow trench, pointing out differences and further indicating how the narrow trench performs so well. Near the hole, $\bar{\bar{\eta}}$ for the wide trench increased until $M = 0.7$, then decreased with increased blowing, as seen in Fig. 13,

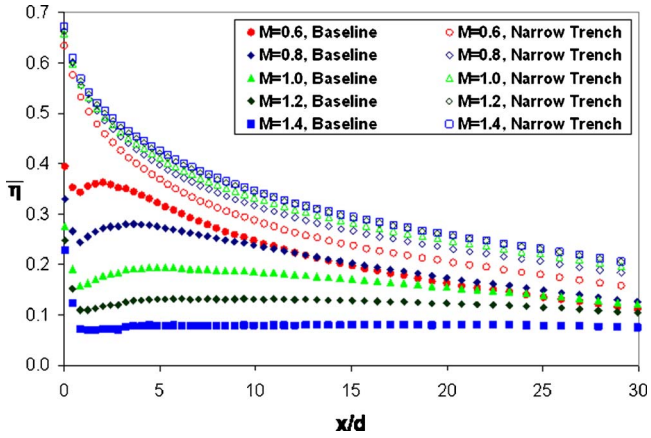

Fig. 11 Comparison of the narrow trench (configuration 2) and baseline axial holes, $Tu_\infty = 3.9\%$

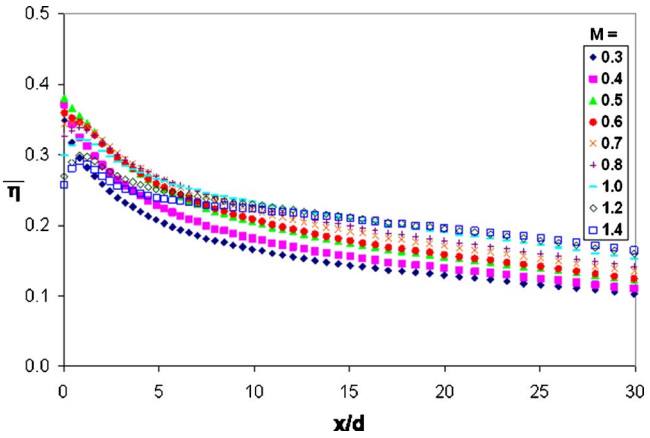

Fig. 13 Laterally averaged adiabatic effectiveness for wide trench (configuration 10), $Tu_\infty = 3.9\%$

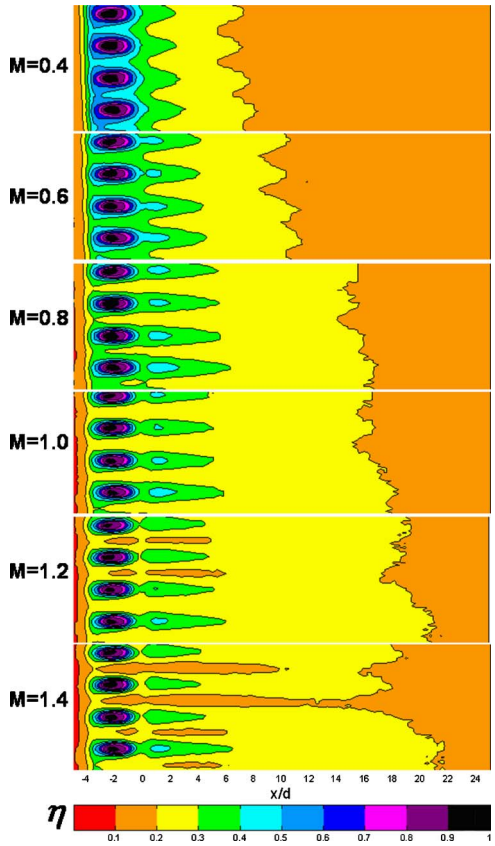

Fig. 14 Spatial plots of adiabatic effectiveness for wide trench configuration at various *M*, $Tu_\infty = 3.9\%$

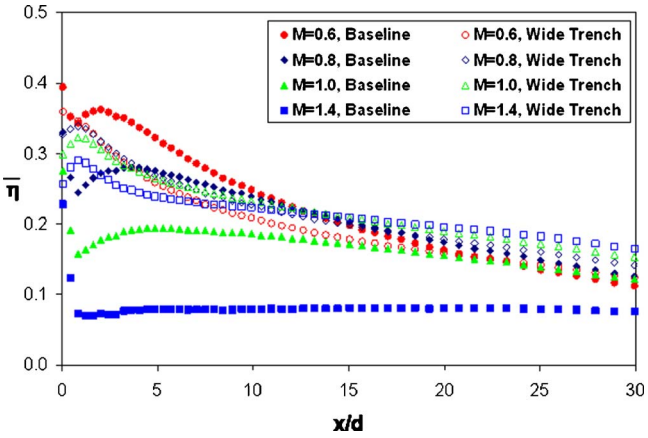

Fig. 15 Comparison of wide trench configuration and baseline axial holes, $Tu_\infty = 3.9\%$

which shows the laterally averaged adiabatic effectiveness levels for high mainstream turbulence. Downstream ($x/d > 8$), the laterally averaged effectiveness increased for all M, similar to the narrow trench configuration. Due to the generally tight band of the laterally averaged adiabatic effectiveness, the wide trench configuration also appears to be partially insensitive to blowing ratios, especially for moderate blowing ratios.

In order to understand the near hole and downstream effects for the wide trench configuration, the contour plots showing the spatial distribution of η were examined. Figure 14 shows the η distribution for a range of blowing ratios at high-mainstream turbulence. At low blowing ratios, such as $M = 0.4$, the contour plots indicate that the trench partially filled with coolant, increasing lateral spreading. As M increased, the higher effectiveness values within the trench, apparent for the narrow trench configuration, were not present. This most likely occurred because the coolant did not fill the trench, and the mainstream flow mixed with the coolant, warming it up within the trench. The narrow trench configuration contained the coolant while allowing minimal mainstream hot gas entrainment. Also, at higher blowing ratios, the coolant streak on the surface indicated that the jet was detaching from the surface. At around $M = 0.8$, this separation started to occur and by $M = 1.0$, the jet detachment and reattachment was more defined. With a further increase in blowing, the effectiveness levels downstream plateaued.

The variation of $\bar{\eta}$ levels due to blowing ratio for the wide trench configuration was smaller than for the baseline axial case, indicating that the wide trench was less sensitive to blowing ratio, as shown in Fig. 15. The adiabatic effectiveness for the baseline case increased until an optimal blowing ratio was reached, and thereafter decreased relatively rapidly due to jet separation. The wide trench configuration followed the same trend near the hole, but downstream, increased blowing increased $\bar{\eta}$. At low blowing ratios, like $M = 0.4$, values for the laterally averaged adiabatic effectiveness were about 35% lower for the wide trench configuration when compared to the baseline axial holes. With increasing blowing to moderate levels, this difference decreased. At $M = 1.0$, the wide trench configuration performed up to 25% better near the holes, but downstream, the baseline and wide trench cases were similar when $x/d > 10$. With even higher blowing, the wide trench configuration had higher cooling effectiveness than the baseline case. At $M = 1.4$, the adiabatic effectiveness for the wide trench configuration was over twice the value of the baseline axial holes.

The major overlying condition that helped the narrow trench configuration have high levels of cooling was that the coolant did not separate from the surface. Figure 16 shows the thermal profile of the axial hole configuration and the narrow trench configuration at a location $2d$ behind the trailing edge of the hole for $M = 1.0$. The coolant jet for the axial hole has separated, while the coolant for the narrow trench case was laterally spread and attached to the surface.

With the close proximity of the trench walls, some of the coolant injected into the mainstream flow hit the downstream trench lip. This caused the coolant jet to be blocked from direct injection and to fill the trench. As the trench was filled, the coolant exited the trench onto the surface more as a sheet than as individual jets. The close proximity of the upstream lip allowed the coolant to be contained in the trench with minimal warming from hot mainstream ingestion.

Figure 17, which shows the laterally averaged adiabatic effectiveness in the trench, gives insight as to why the cooling effectiveness plateaued at high blowing ratios. As the blowing ratio increased, the downstream half of the trench had higher adiabatic effectiveness values on the surface. At or around $M = 1.0$, the adiabatic effectiveness levels appear to level off. This suggests that the flow within the trench reaches a steady operation at higher blowing ratios, causing the coolant to exit the trench in the same manner for these higher blowing ratios. Any excess coolant presumably separates from the surface or does not contribute to the surface cooling.

Figure 18 show the development of the coolant distribution in the trench. The thermal profiles at locations of $x/d = -1.5$, -2.0, and -2.5 (1/4, 1/2, and 3/4 of the trench distance from $x/d = 0$) are shown. Through the series of the three profiles, it is evident that a portion of the coolant jet hit the downstream lip and circulated back into the trench, serving as the mechanism to help fill the trench. Figure 18(*b*) shows that some coolant wrapped back between two adjacent holes. Figure 18(*a*) shows that the two recirculating coolant masses from adjacent holes were combined at midpitch near the upstream part of the trench. Between the hole

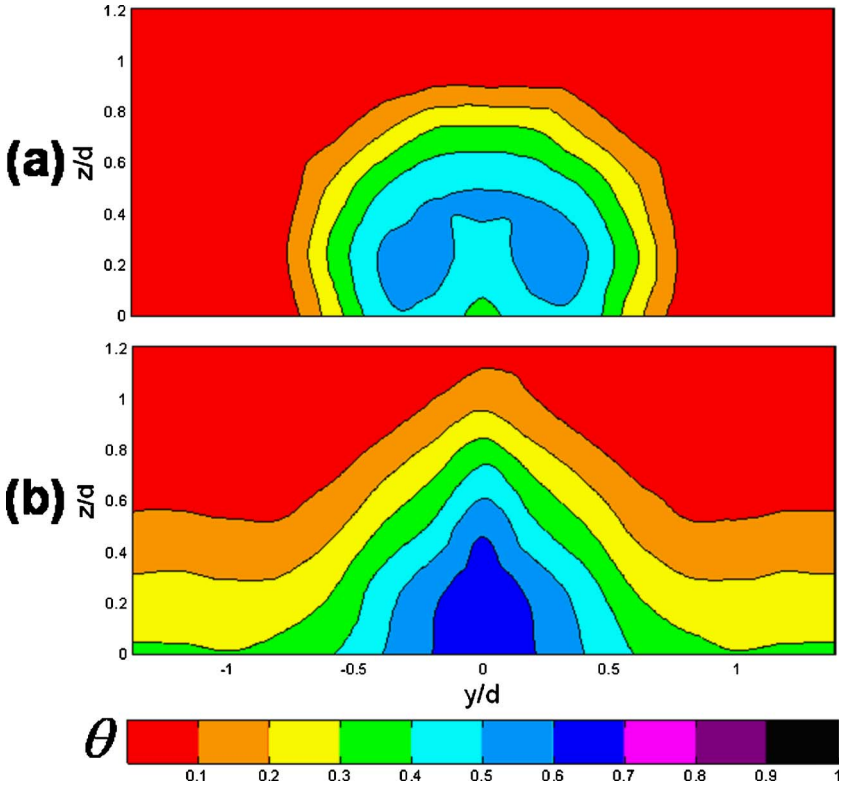

Fig. 16 Thermal profiles for: (*a*) axial hole, and (*b*) narrow trench configurations, $x/d=2$, $M=1.0$, $Tu_\infty=1.0\%$

and the midpitch location, there was slight mainstream entrainment, most obvious at the upstream position (Fig. 18(*a*)).

Shaped holes have been shown to outperform axial and compound angle holes, although at a manufacturing cost. Saumweber et al. [19] tested fan-shaped and laidback fan-shaped holes. The fan-shaped holes were laterally expanded 14 deg and the laidback fan-shaped holes were additionally forward diffused 15 deg. Both geometries yielded similar adiabatic effectiveness levels. The pitch of the holes was $p/d=4$, while for the current study, the pitch was $p/d=2.78$. The two shaped holes are compared to the narrow trench configuration in Fig. 19 with the round holes plotted as a reference. The axial holes embedded within a narrow transverse trench were comparable to the shaped holes when the difference in hole spacing is taken into account.

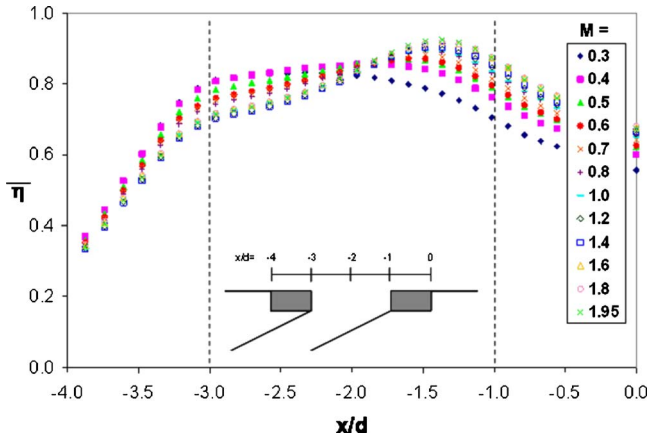

Fig. 17 Laterally averaged adiabatic effectiveness near the hole, $Tu_\infty=1.0\%$

Conclusions

An experiment was conducted to examine the effects of an overlying transverse trench on the film cooling effectiveness of axial holes. Nine trench configurations were tested. When comparing the various lip configurations, the key component to improved effectiveness was a rectangular lip immediately downstream of the trailing edge of the coolant hole, which dramatically increased the adiabatic effectiveness. The upstream geometry of the trench appeared to only slightly affect the cooling effectiveness, permitting varying levels of hot mainstream gas entrainment in the trench.

The narrow trench configuration provided the best adiabatic effectiveness performance. In fact, the increasing adiabatic effectiveness levels with increasing blowing ratio indicated that the trench suppressed coolant jet separation. At higher M, the values started to plateau, so increased coolant would not be warranted since only a slight increase in adiabatic effectiveness would occur. The mainstream turbulence levels and density ratios tested had no effect on the cooling effectiveness.

At low blowing ratios, the narrow trench had better adiabatic effectiveness than the axial holes near the hole and nearly the same effectiveness downstream. When blowing was increased, the adiabatic effectiveness levels peaked and then dropped for the axial holes, while they continued to increase for the narrow trench configuration. Therefore, for all M, the narrow trench performed better.

The wide trench configuration also was less susceptible to jet liftoff and blowing ratio when compared to the baseline axial holes. Although the adiabatic effectiveness was not as good as the narrow trench configuration, it did yield better cooling than the axial holes at high blowing ratios (although at low blowing ratios it performed worse).

The major overlying conditions that helped the narrow trench configuration have high levels of cooling were that the coolant did

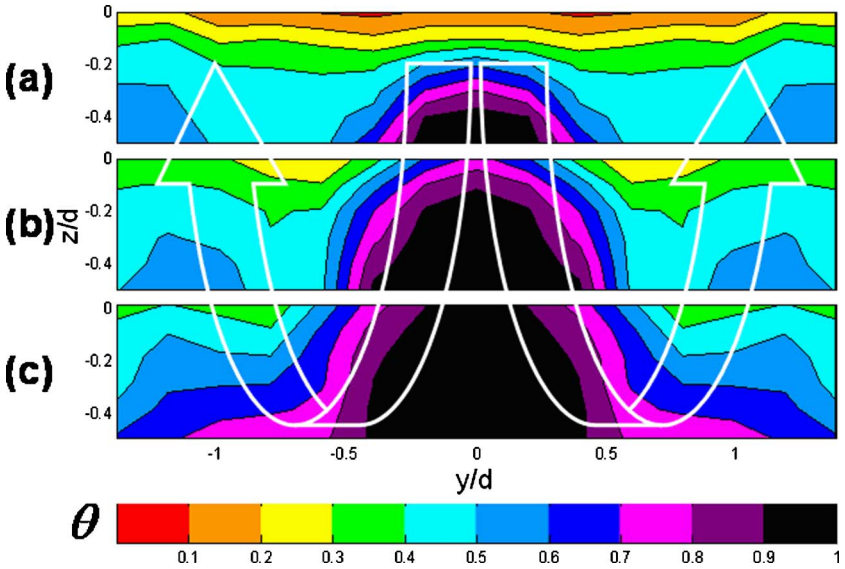

Fig. 18 Thermal profiles within the trench at: x/d=(*a*) −2.5, (*b*) −2.0, and (c) −1.5, M=1.0, Tu_∞=1.0%

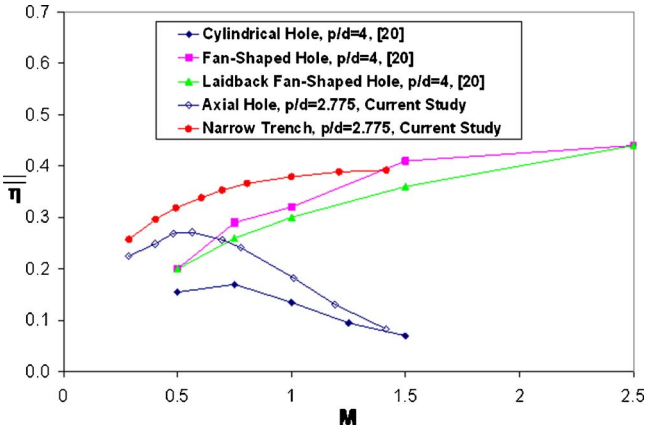

Fig. 19 Comparison of axial holes, shaped holes, and axial holes embedded within a narrow trench

not separate from the surface and the coolant exhibited lateral spreading. With the close proximity of the trench walls, the coolant was ejected and a portion of the jet hit the downstream lip. This caused some of the coolant jet to be blocked and to be distributed within the trench. The coolant laterally spread before ejecting onto the surface. The close proximity of the upstream lip allowed the coolant to be contained in the trench with minimal warming from hot mainstream ingestion.

The narrow trench configuration results compared favorably with shaped holes. The benefit to the trench is that it can be made by a slight modification to the thermal barrier coating process [14], which is much cheaper than manufacturing shaped holes. The results found in the current study are for adiabatic effectiveness only. Measuring the heat transfer for the same configurations would allow the heat flux reduction to be compared. It is expected that the trench configurations would not dramatically increase the heat transfer since the laterally spread coolant presumably would not induce strong vortex formation.

Acknowledgment

The authors gratefully acknowledge support from the UTSR program (Contract No. 03-01-SR110) directed through the South Carolina Institute for Energy Studies and the Office of Naval Research through the Electric Ship consortium.

Nomenclature

C = chord length
d = film cooling hole diameter
DR = density ratio, ρ_c/ρ_∞
h = trench height
H = shape factor, δ_1/δ_2
k = thermal conductivity
L = hole length
M = blowing ratio, $\rho_c U_c/\rho_\infty U_\infty$
p = coolant hole pitch distance
s = streamwise coordinate along vane
T = temperature
Tu = turbulence intensity, $u_{\text{rms}}/U_{\text{mean}}$
U = flow velocity
u = fluctuating velocity
w = trench width
x = streamwise distance from coolant holes
z = normal distance from vane wall

Greek

α = injection angle of coolant hole relative to surface
δ = uncertainty or change in a parameter boundary layer thickness
δ_1 = displacement thickness
δ_2 = momentum thickness
η = adiabatic effectiveness, $(T_\infty - T_{\text{aw}})/(T_\infty - T_c)$
ν = kinematic viscosity
Λ_f = integral length scale
θ = nondimensional temperature, $(T_\infty - T)/(T_\infty - T_c)$
ρ = density

Subscripts and Superscripts

app = approach condition
aw = adiabatic wall
c = coolant
rms = root mean square
∞ = local mainstream
0 = without film cooling
– = laterally averaged

= = spatially averaged

References

[1] Bunker, R. S., 2002, "Film Cooling Effectiveness due to Discrete Holes within a Transverse Trench," ASME Paper GT-2002-30178.

[2] Wang, T., Chintalapati, S., Bunker, R.S., and Lee, C.P., 2000, "Jet Mixing in a Trench," Exp. Therm. Fluid Sci., **22**, pp. 1–17.

[3] Klinger, H., and Hennecke, D. K., 1993, "The Effect of Main Stream Flow Angle on Flame Tube Film Cooling," *Proceedings AGARD Conference Heat Transfer and Cooling in Gas Turbines*, CP-527.

[4] Schulz, A., 2001, "Combustor Liner Cooling Technology in Scope of Reduced Pollutant Formation and Rising Thermal Efficiencies," Ann. N.Y. Acad. Sci., **934**, pp. 135–146.

[5] Goldstein, R. J., 1971, "Film Cooling," Adv. Heat Transfer, **7**, pp. 321–380.

[6] Teekaram, A., Forth, C., and Jones, T., 1989, "The Use of Foreign Gas to Simulate the Effects of Density Ratios in Film Cooling," ASME J. Turbomach., **111**, pp. 57–62.

[7] Papell, S. S., 1960, "Effect on Gaseous Film Cooling of Cooling Injection Through Angled Trenchs and Normal Holes," NASA Report No. NASA-TN-D-299, NASA, Washington, D.C.

[8] Blair, M. F., 1974, "An Experimental Study of Heat Transfer and Film Cooling on Large-Scale Turbine Endwalls," ASME J. Heat Transfer, **96**, pp. 524–529.

[9] Chyu, M. K., Hsing, Y. C., and Bunker, R. S., 1998, "Measurements of Heat Transfer Characteristics of Gap Leakage Around a Misaligned Component Interface," ASME Paper No. 98-GT-132.

[10] Seban, R. A., Chan, H. W., and Scesa, S., 1957, "Heat Transfer to a Turbulent Boundary Layer Downstream of an Injection Trench," ASME Paper No. 57-A-36.

[11] Lu, Y., Nasir, H., and Ekkad, S. V., 2005, "Film Cooling From a Row of Holes Embedded in Transverse Trenchs," ASME Paper No. GT2005-68598.

[12] Robertson, D. R., 2004, "Roughness Impact on Turbine Vane Suction Side Film Cooling Effectiveness," M.S. thesis, University of Texas at Austin, Austin, TX.

[13] Waye, S. K., and Bogard, D. G., 2006, "High Resolution Film Cooling Effectiveness Comparison of Axial and Compound Holes on the Suction Side of a Turbine Vane," ASME Paper No. GT2006-90225.

[14] Bunker, R. S., 2001, "A Method for Improving the Cooling Effectiveness of a Gaseous Coolant Stream," US Patent No. 6,234,755.

[15] Ethridge, M. I., Cutbirth, J. M., and Bogard, D. G., 2001, "Scaling of Performance for Varying Density Ratio Coolants on an Airfoil with Strong Curvature and Pressure Gradient Effects," ASME J. Turbomach., **123**, pp. 231–237.

[16] Moffat, R. J., 1988, "Describing the Uncertainties in Experimental Results," Exp. Therm. Fluid Sci., **1**, pp. 3–17.

[17] Baldauf, S., Scheurlen, M., Schulz, A., and Wittig, A., 2002, "Correlation of Film Cooling Effectiveness from Thermographic Measurements at Engine Like Conditions," ASME Paper No. GT-2002-30180.

[18] Lutum, E., and Johnson, B. V., 1999, "Influence of the Hole Length-to-Diameter Ratio on Film Cooling With Cylindrical Holes," ASME J. Turbomach., **121**, pp. 209–216.

[19] Saumweber, C., Schulz, A., and Wittig, S., 2003, "Free-Stream Turbulence Effects on Film Cooling With Shaped Holes," ASME J. Turbomach., **125**, pp. 65–73.

Kevin Reid[1]
Syncrude Canada Ltd.,
Edmonton,
AB Canada
e-mail: reid_kev@hotmail.com

John Denton

Graham Pullan

Eric Curtis

John Longley

Whittle Laboratory, Department of Engineering,
University of Cambridge,
Cambridge, UK

The Interaction of Turbine Inter-Platform Leakage Flow With the Mainstream Flow

Individual nozzle guide vanes (NGV's) in modern aeroengines are often cast as a single piece with integral hub and casing endwalls. When in operation, there is a leakage flow through the chord-wise interplatform gaps. An investigation into the effect of this leakage flow on turbine performance is presented. Efficiency measurements and NGV exit area traverse data from a low-speed research turbine are reported. Tests show that this leakage flow can have a significant impact on turbine performance, but that below a threshold leakage fraction this penalty does not rise with increasing leakage flow rate. The effect of various seal clearances are also investigated. Results from steady-state simulations using a three-dimensional multiblock Reynolds-averaged Navier-Stokes solver are presented with particular emphasis paid to the physics of the mainstream/leakage interaction and the loss generation. [DOI: 10.1115/1.2162592]

1 Introduction

The stationary vane in many gas turbine engines is cast as a single unit consisting of a blade with integral hub and casing endwalls. These individual units are then joined circumferentially to form a ring of vanes. When the engine is operating, there is inevitably a gap along the mating surfaces of the individual stator units. Leakage flow is pumped through this platform gap in order to avoid the ingress of combustion gases into the wheelspace. Chordwise slots can also be found in rotating blade rows; however, this study was concerned exclusively with stationary vanes. To the authors' knowledge, the effect of this leakage flow on machine performance has not been previously reported in the open literature, however several related studies have been completed.

Aunapu et al. [1] investigated the use of hub endwall jets to modify secondary flow in a cascade of turbine vanes. They modified the secondary flow both through the use of jets and through the use of a stationary fence. In both cases, the flow control resulted in the pressure side leg of the horseshoe vortex being deflected away from the suction surface of the adjacent blade, but did not affect the strength of the vortex. Compared with a baseline case, the fence resulted in a loss reduction of 10%. In order to achieve the same change in the path of the passage vortex as was observed in the fence study, approximately 2% of the mainstream flow was blown through the jets which were distributed over 44% of the chord. At this condition, the jets resulted in losses 30% greater than those observed in the baseline case. This study indicates that a leakage flow along the hub surface of a turbine passage can have a significant affect on performance.

Cardwell et al. [2] discussed the effect of a mid-platform gap on endwall film cooling effectiveness. With no applied sealant flow through the gap, they found that flow leaves the mainstream and enters the plenum beneath the gap along the front 50% of the gap, and then re-enters the main gas path along the trailing 50% of the gap. The presence of the mid-platform gap was found to significantly affect the endwall film cooling effectiveness by directing most of the coolant flow from the upstream hub rim seal onto the suction side of the blade, leaving the pressure side of the passage with less cooling air. This study did not investigate the effect of the mid-platform gap on the loss generation in the main passage.

Ranson et al. [3] also investigated the coolant effects of interplatform sealant flow in a linear cascade experiment. In this study, sealant flows of 0.25, 0.50, and 0.75% were used. It was found that increasing the sealant flow rate did not improve the cooling effectiveness on the blade platform. The increased radial momentum due to increased sealant flow rate caused the sealant flow to lift off of the hub surface and get caught up in the passage vortex, and this is what limited the cooling effect. It was found that the sealant flow issued from the trailing edge of the platform gap was swept across the passage by the secondary flow and therefore cooled the suction side of the endwall.

The effect of the leakage flow through the interplatform gaps on the hub surface of a low-speed axial flow turbine is presented in this study. A detailed understanding of the experimental results is obtained through three-dimensional steady-state CFD simulations.

2 Experimental Setup

The experimental results collected in this paper were obtained from a full-scale low-speed axial flow turbine. The same facility is described in a past ASME paper [4]; however, major modifications to both the annulus and the blading have been made since this time and the current configuration is briefly described here. A schematic of the facility is shown in Fig. 1. The machine is characterized by a significant radius change through the stage as well as by a low aspect ratio, low turning vane. Air was drawn through the turbine by a fan that was mounted on a separate shaft and driven by a 200 kW electric motor (not shown in schematic). An eddy current dynamometer controlled the shaft speed at 1100 rpm.

Inlet guide vanes (IGV's) were used to generate an inlet yaw angle distribution representative of engine conditions. An engine representative inlet stagnation pressure profile was generated using a wire gauze upstream of the IGVs and by selectively obstructing the flow at both the hub and the casing at the same axial location as the wire gauze.

Figure 1 shows the piping arrangement that was used to introduce leakage flow into the wheelspace of the rig. Leakage air was supplied by an industrial vacuum cleaner driven by a 2.4 kW electric motor (not shown in schematic). The mass flow of the secondary air was measured before it entered the rig in a long section of straight pipe using pitot and static tappings as outlined by Ower and Pankhurst [5]. The secondary air was introduced into a sealed plenum through perforations in the supply pipe. Due to the low

[1]Corresponding author.

Contributed by the International Gas Turbine Institute (IGTI) of ASME for publication in the JOURNAL OF TURBOMACHINERY. Manuscript received October 1, 2004; final manuscript received February 1, 2005. IGTI Review Chair: K. C. Hall. Paper presented at the ASME Turbo Expo 2005: Land, Sea and Air, Reno, NV, June 6–9, 2005. Paper No. GT2005-68151.

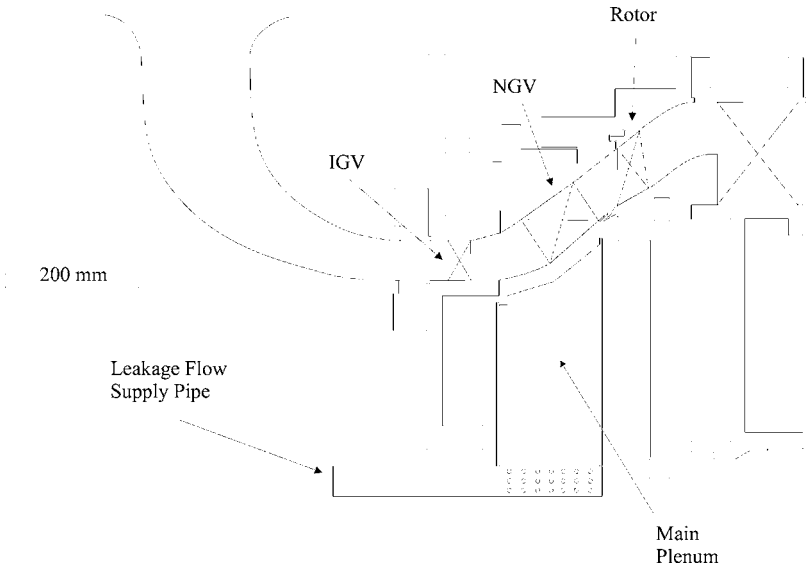

Fig. 1 Overview of the experimental apparatus

fluid velocity in the plenum, the total pressure of the leakage flow was taken as the static pressure. The total temperature of the leakage flow was measured in the supply pipe.

The temperature drop across the turbine is small. This means that small uncertainties in the temperature measurement lead to high overall uncertainties in the efficiency. For this reason, the work done by the turbine was determined by the shaft torque and speed. The efficiency definition also needs to account for the potential work of the leakage flow. The efficiency of the rig was therefore defined as

$$\eta_{br} = \frac{T_q \omega}{m_m c_p T_{01m}\left(1 - \left(\frac{\overline{P_{03}}}{\overline{\overline{P_{01m}}}}\right)^{\gamma-1/\gamma}\right) + m_s c_p T_{01s}\left(1 - \left(\frac{\overline{P_{03}}}{P_{01s}}\right)^{\gamma-1/\gamma}\right)} \tag{1}$$

The inlet total pressure was determined by a set of 10 pitot tubes located downstream of the IGVs. These probes were equispaced around the circumference at various radii (from 6% span to 96% span), and circumferential variations were measured by traversing them all over one IGV pitch. The exit total pressure was determined by a set of ten self-aligning pitot tubes located downstream of the rotor at various radii (from 5% span to 95% span), with an area average determined by traversing the probes over one nozzle guide vane (NGV) pitch. The torque was measured by a load cell which was connected through a lever arm to the dynamometer. The rotational speed was measured by an optical trigger located on the turbine shaft. The inlet total temperature was measured by the arithmetic average of six thermocouples located in the bell mouth inlet. At each condition investigated in this paper, the efficiency was measured four times and the average value of these measurements is reported. The scatter within these four measurements was never observed to be greater than ±0.10% even when measurements were conducted over several days. A detailed uncertainty analysis using the method outlined in [6] also resulted in a repeatability uncertainty of ±0.10%.

Area traverses could be conducted downstream of each blade row using a pneumatic five-hole probe as shown in Fig. 2. All traverses reported in this work were completed at Traverse Planes 2 and 3. An NGV loss coefficient can be determined by conducting area traverses both upstream and downstream of the stator. Again, this loss coefficient must account for the potential work of the leakage flow and is defined as

$$Y_p = \frac{[m_m \overline{\overline{P_{01m}}} + m_s P_{01s}] - (m_m + m_s)\overline{\overline{P_{02}}}}{(m_m + m_s)[\overline{\overline{P_{02}}} - \overline{P_{st2}}]} \tag{2}$$

Figure 3 shows the location of the slot in the blade to blade plane, along with a cross section of the leakage arrangement in a plane perpendicular to the slot axis (cross section plane illustrated in Fig. 2). The terms slot, plenum, and strip seal will be used often in the body of the paper and it is important to note their definitions from Fig. 3. The plenum is 25 mm deep and then exhausts into the larger plenum shown in Fig. 1.

3 Numerical Code

The numerical calculations were completed using TBLOCK, a Reynolds-averaged Navier–Stokes solver written by John Denton.

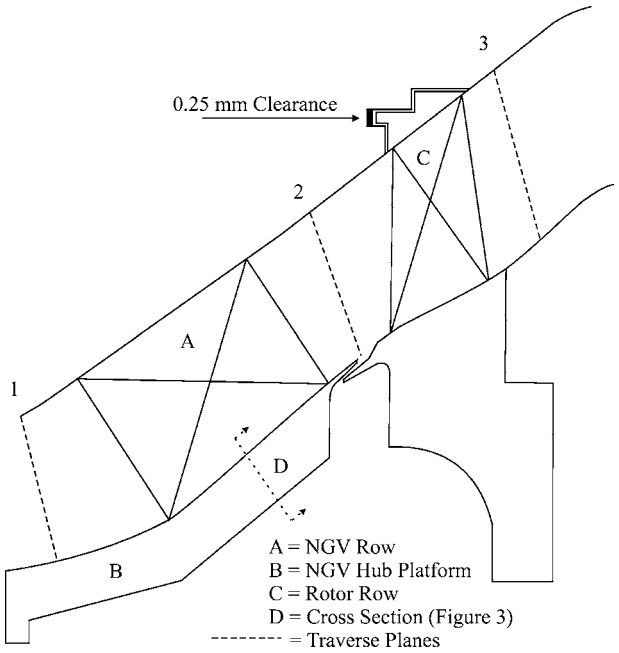

Fig. 2 Detail of the experimental turbine stage

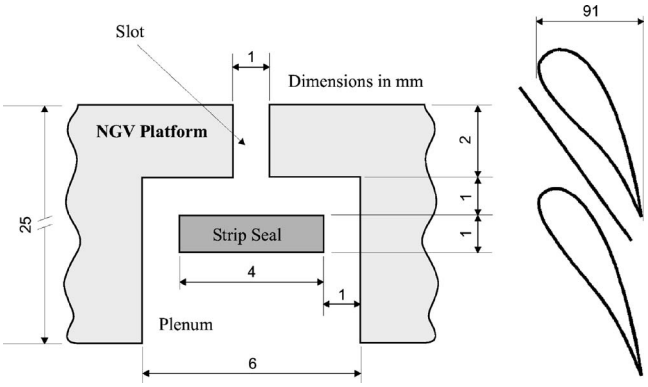

Fig. 3 Detail of the slot location and datum leakage arrangement

This code is an extension of Denton's MULTIP [7] and UNSTREST [8] turbomachinery codes but can be used to solve the flow in both the main blade path and any secondary gas paths. This is achieved using a multiblock approach where complex geometries are divided into a series of blocks, each of which is solved as a separate structured grid. Information is transferred between the various blocks via user defined patches. If the meshes on the two adjacent patches are identical, the flow variables are transferred directly from block to block.

TBLOCK is a finite volume code which uses the "Scree" scheme for time advancement [8]. Turbulence is modeled using a mixing length model with wall functions used to determine the surface skin friction. Laminar/turbulent transition can be modeled by assuming laminar boundary layers and viscosity until a specified location with turbulent boundary layers and viscosity downstream of this location. With a mixing plane at the interface between blade rows, the code is accelerated to a steady-state solution using multigrid and spatially varied time steps. By using dual time stepping, these same convergence acceleration techniques are also employed when the code is run in unsteady mode with a sliding interface between the blade rows.

The CFD geometry modeled the full annulus stage (NGV and rotor) using a mixing plane approach. The slot, strip seal, and plenum arrangement shown in Fig. 3 was also modeled. It was impractical to model the entire large plenum shown in Fig. 1; therefore, an additional 12 mm wide $\times$ 25 mm deep plenum was included beneath the 6 mm wide plenum, Fig. 4. This ensured that

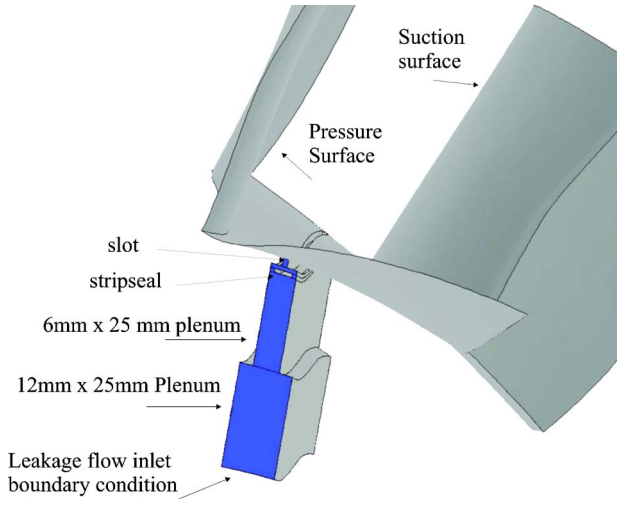

Fig. 4 CFD geometry (NGV passage and slot/seal/plenum arrangement)

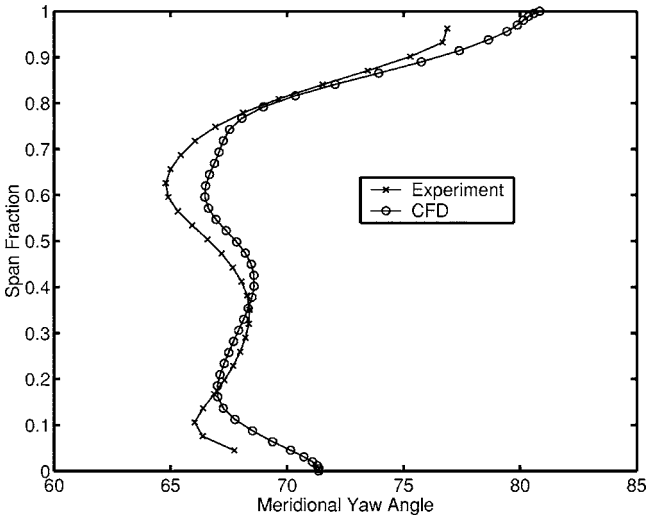

Fig. 5 Comparison of experiment and CFD with slot taped over—Meridional yaw angle at Traverse Plane 2

any mainstream flow entering the plenum was not influenced by the leakage flow inlet boundary condition. Unless stated otherwise, all boundary layers in this work were assumed to be fully turbulent.

Entropy is the best quantity to use when investigating loss in turbomachines [9]. Entropy is a convected quantity. This means that the entropy present at any particular location in a machine could have been created at that location or it could have been created upstream and convected into the downstream location. In order to clearly identify areas of high loss, entropy generation rates [10] have been added to TBLOCK. The rate of entropy production per unit volume is given by

$$\dot{s} = \frac{1}{T}\tau_{ik}\frac{\partial V_i}{\partial x_k} + \frac{k}{T^2}\frac{\partial T}{\partial x_i}\frac{\partial T}{\partial x_i} \tag{3}$$

4 Results

4.1 Verification of CFD. Figure 5 shows a comparison of experimental and numerical data of the pitchwise averaged meridional yaw angle distribution on Traverse Plane 2 with the interplatform slot taped over. The agreement between CFD and experiment is within 2° over the entire span.

Figure 6 shows a comparison of experimental and numerical data of the pitchwise averaged meridional yaw angle distribution on Traverse Plane 2 with no net leakage through the interplatform slot. Again the agreement between CFD and experiment is within 2° over the entire span. The CFD is also following the same trend over the bottom 20% of the span as the experimental results when the tape is removed from the slot. It is interesting to note that the agreement between CFD and experiment is better for the no net leakage configuration than it is for the taped over configuration. The reason for this is not clear. The CFD also predicts the efficiency of the no-slot case within 0.5% of the experimental result.

4.2 Effect of Leakage Mass Flow. Figure 7 shows the experimental normalized brake efficiency with increasing leakage mass flow. The efficiencies are normalized by the efficiency of the rig when the slot is taped over. It is clear that there is an approximately 1.2% drop in efficiency when the slot is opened, even when there is no applied leakage flow. It is also clear that increasing the leakage flow rate up to 1.5% causes no significant change in the efficiency. Figure 8 shows the normalized turbine efficiency obtained from CFD over the same range of leakage fractions. Again, it is evident that it is the presence of the slot that is causing the loss of efficiency and that increasing the mass flow has little

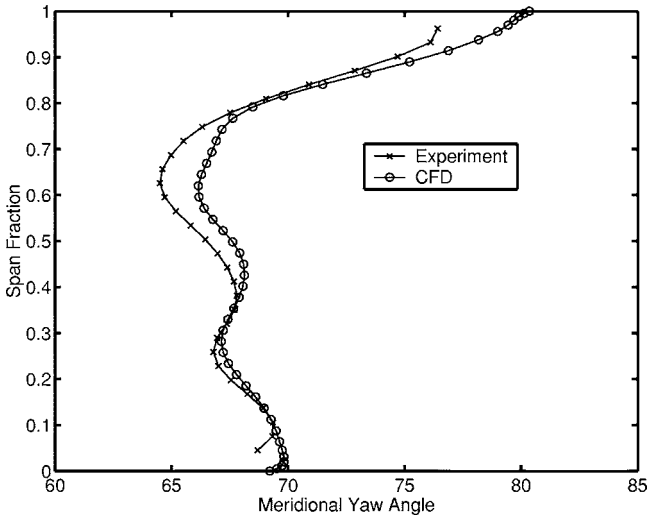

Fig. 6 Comparison of experiment and CFD with no net leakage—Meridional yaw angle at Traverse Plane 2

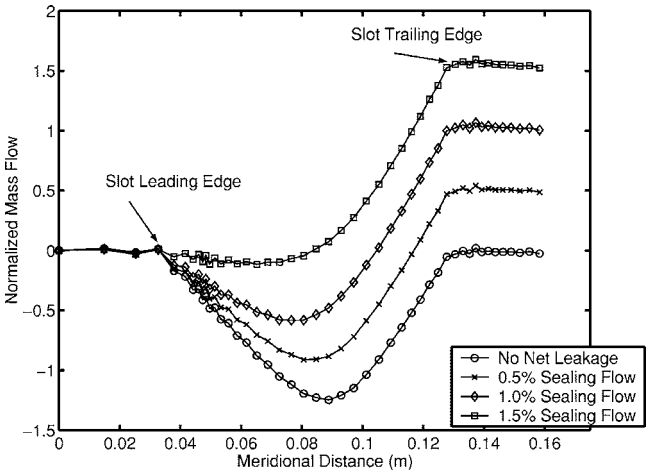

Fig. 9 Mass fraction of fluid exchanged between the mainstream and the plenum—Normalized mass flow = $m_{merid} - m_{inlet}/m_{inlet}$—(every third point shown for clarity)

effect.

Figure 9 shows the mass flow into and out of the slots obtained from the CFD solutions at various leakage mass fractions. The data has been normalized so that any change from zero indicates that mass is either entering (+ve) or leaving (−ve) the main blade passage. With no-net flow, approximately 1.25% of the mainstream flow is leaving the main annulus along the front 50% of the slot and then re-entering along the rear 50% of the slot. As the leakage flow is increased, less fluid leaves the mainstream annulus, but the net exchange of fluid between the plenum and the mainstream remains constant at approximately 1.5%. From this result, one would be tempted to conclude that the addition of leakage flow does not lead to a significantly higher efficiency penalty because the quantity of flow being reintroduced into the annulus from the plenum is approximately constant in all cases. In the next section, entropy generation rates will be used to show that the true picture is more complicated.

Figure 10 shows a comparison of the pitchwise-averaged loss coefficients for various leakage flows. These results were obtained from five-hole probe traverses and are independent of the efficiency results. They serve to reinforce the fact that increasing leakage flow does not create significantly more loss.

Figure 11 shows a comparison of experimental loss contours between a no leakage case (slot taped over) and a no net leakage case. The increased area of loss due to the mixing of the leakage flow and the mainstream is evident on the bottom left hand corner of Fig. 11(*b*). The leakage flow has also altered the structure of the wake.

Figure 12 shows that the flow entering the mainstream annulus along the rear half of the slot creates an air curtain that inhibits the

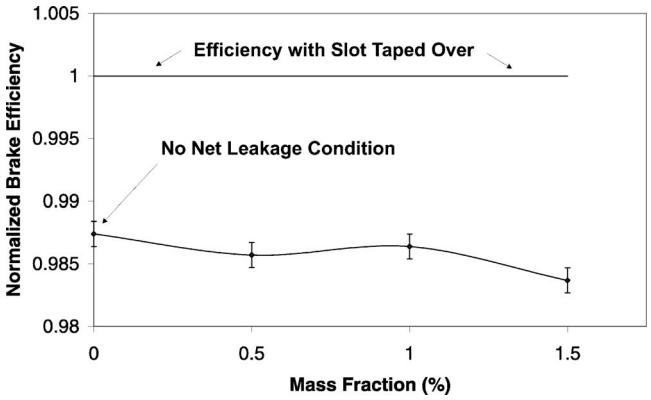

Fig. 7 Normalized brake efficiency with varying mass fraction—Experimental

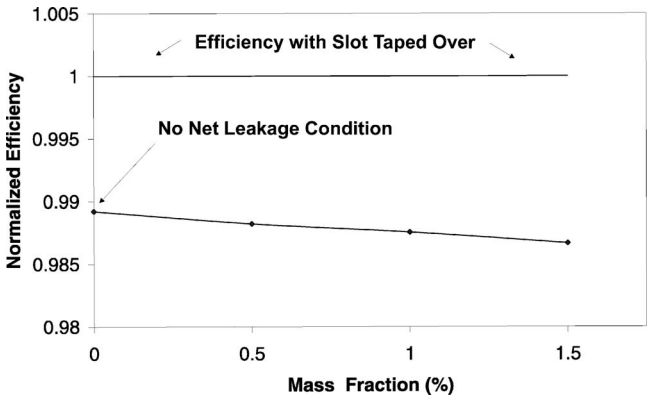

Fig. 8 Normalized efficiency with varying mass fraction—Computational

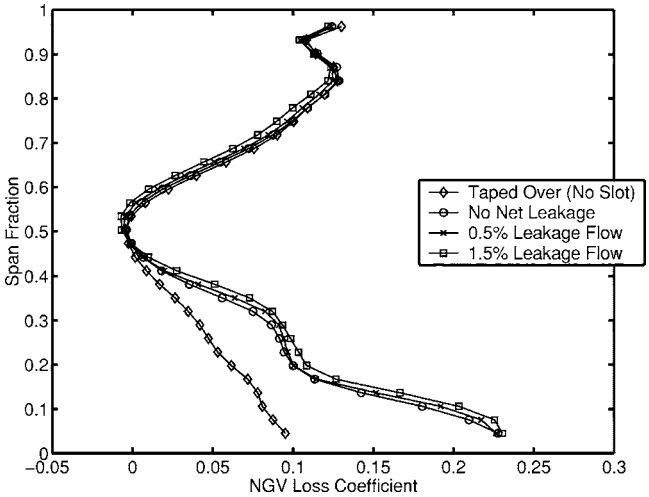

Fig. 10 Measured NGV loss coefficient with varying leakage flow

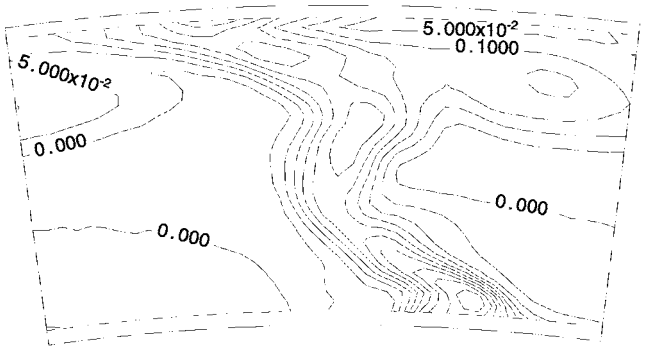

(a) No Leakage

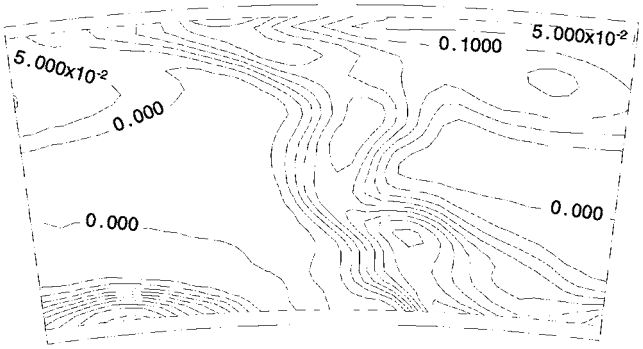

(b) No Net Leakage

Fig. 11 Measured NGV loss coefficient

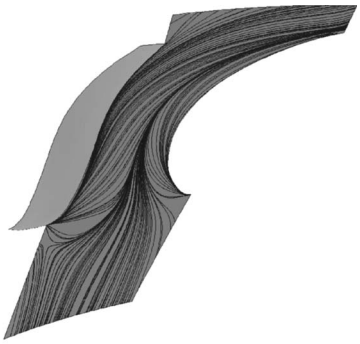

(a) No Leakage

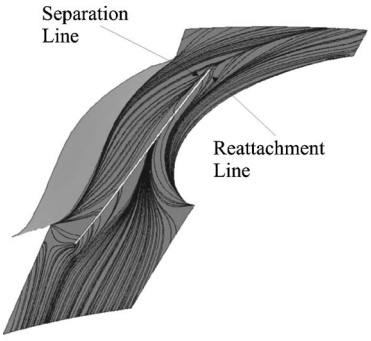

(b) No Net Leakage

Fig. 12 Computational NGV hub surface streamlines

secondary flow from sweeping along the hub endwall. It is this blockage that results in the reduction of loss in the wake near the hub of Fig. 11(*b*). The CFD NGV loss coefficient contours (not shown) do not show the area of increased loss at 30% span in the wake in the no-net leakage case. However, this is either boundary layer fluid that has been deflected up the span due to the air curtain, or is mixing loss created through the introduction of the leakage flow.

Five-hole probe traverses were also conducted downstream of the rotor and the pitchwise averaged relative meridional yaw angle is plotted in Fig. 13. The flow downstream of the rotor is little affected by the leakage flow and will not impact significantly on the flow in downstream stages.

4.3 Annulus Losses Versus Plenum Losses. CFD calculations along with entropy generation rates were used to compare the magnitude of the losses created by the mixing of the leakage flow when it re-enters the mainstream and the subsequent effect that this has on secondary flow, to the losses generated in the slot and plenum geometry, Fig. 14. The entropy generation rates defined by Eq. (3) are calculated per cell in the CFD calculation. To obtain the curves shown in Fig. 14 these cell values are summed at each meridional location, and these totals are then summed up along the length of the machine. The value at a given meridional location represents the total rate of entropy generation in the volume preceding that location. This quantity will be referred to as the cumulative entropy generation rate. The "plenum" lines represent the cumulative entropy generation rate in the slot/strip-seal/plenum geometry at each meridional location. The "annulus" lines represent the difference in the cumulative entropy generation rate in the annulus for a CFD calculation including a plenum and slot/strip-seal arrangement, and an annulus only calculation. The fact that these lines drop below zero entropy generation rate between $x=0.05$ and $x=0.1$ indicates that there is actually less loss generated in the annulus along the forward part of the slot in the calculation which included the slot/stripseal/plenum arrangement.

The key result from this plot is that the plenum losses are greater in the no-net leakage case than they are with 1.5% leakage flow, but that the annulus mixing and secondary flow losses are greater with 1.5% leakage flow. This shows that the nearly constant efficiency reported in Fig. 7 is due to the balance of losses occurring in the plenum and annulus, and is not due solely to the fact that a similar mass fraction is being injected into the mainstream flow along the trailing edge of the slot in both scenarios.

Figure 15 shows the variation in cumulative entropy generation

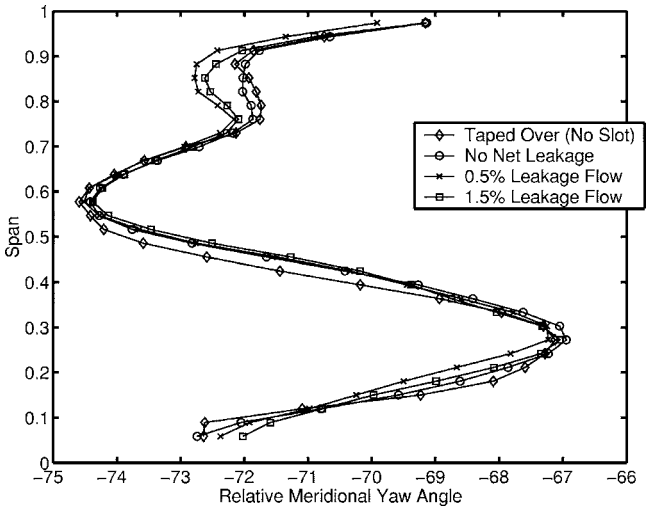

Fig. 13 Relative meridional yaw angle downstream of the rotor

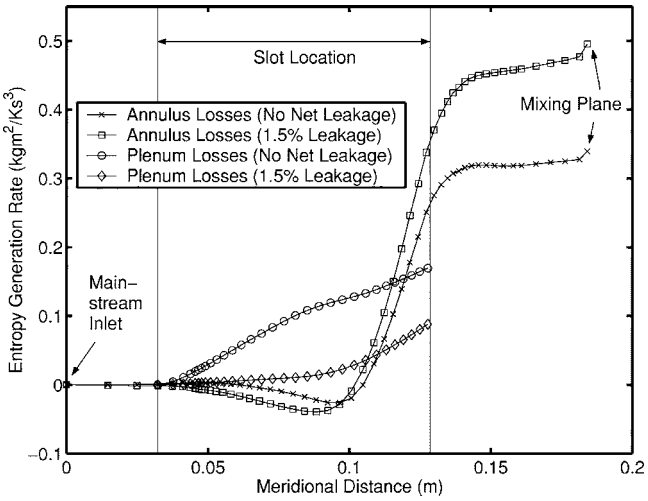

Fig. 14 Comparison of the cumulative entropy generation rates in the annulus and in the plenum

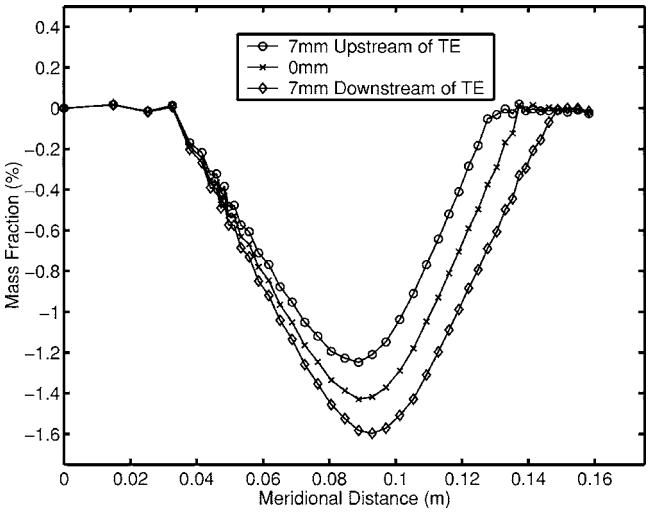

Fig. 16 Effect of slot length on mass flow

rate along the length of the six "blocks" shown on the right-hand side of the plot for all leakage fractions. With no-net leakage, the majority of the loss is occurring in Block 2, the 6 mm × 25 mm plenum. A more detailed investigation of the flow field shows that the majority of this loss occurs along the plenum walls and is due to the ingested mainstream fluid. As the leakage fraction is increased, less fluid is ingested into Block 2 and subsequently there is less loss.

Blocks 3 and 4 show different amounts of loss. More of the flow leaving the mainstream annulus enters the plenum through Block 4 than Block 3. This appears to be due to the fact that Block 4 is on the side of the plenum that is closest to the suction surface of the blade; the annulus secondary flow is driving more fluid through Block 4. It may be possible to capitalize on this preferential movement of the fluid through the slot in order to achieve a better seal.

4.4 Effect of Slot Length. Figure 3 shows that the datum slot ends 7 mm axially upstream of the trailing edge of the NGV. Calculations were conducted with the slot extended to the trailing edge of the vane and 7 mm axially downstream of the vane trailing edge. The resulting change in the annulus mass flow is shown in Fig. 16. By extending the slot 14 mm axially, an additional 0.4% mass flow is being exchanged with the plenum. This extra 0.4% mass flow leads to a predicted additional 0.6% drop in efficiency, showing that the length of the slot can have a significant effect on the loss.

Due to the geometry of the rig and the presence of the rim seal, it was impractical to conduct experiments to verify these results.

4.5 Effect of Varying Seal Clearance. The flow through the slot is determined by the pressure gradient along the length of the slot and by the quality of the seal between the plenum and the annulus. Experiments were conducted with various seal clearances to determine the range of efficiency penalty that can be incurred due to the sealing of the plenum. In addition to the datum configuration, three seal clearances were investigated and these are shown in Fig. 17 along with the measured efficiency penalty incurred by each. All of these results were obtained with no-net flow through the slot. The 0 mm clearance shown in Fig. 17(*c*) did not provide a perfect seal due to variations in the strip seal along its chordwise axis. For this reason, the geometry shown in Fig. 17(*d*) had a sealing foam placed beneath the strip seal. The largest drop in efficiency due to interplatform gaps was found to be 1.54% and the smallest drop in efficiency with only a 2 mm deep slot was found to be 0.46%. These results are only for a hub slot, there will likely be a similar penalty due to the slot at the casing; these slots could thus be responsible for a 1–3% drop in efficiency.

Figure 18 shows contours of NGV loss coefficient for the foam-backed zero-clearance case [Fig. 17(*d*)]. Comparing this plot with Fig. 11(*a*), it is clear that the slot leads to more loss in the loss core. When there is no large exchange of mass between the ple-

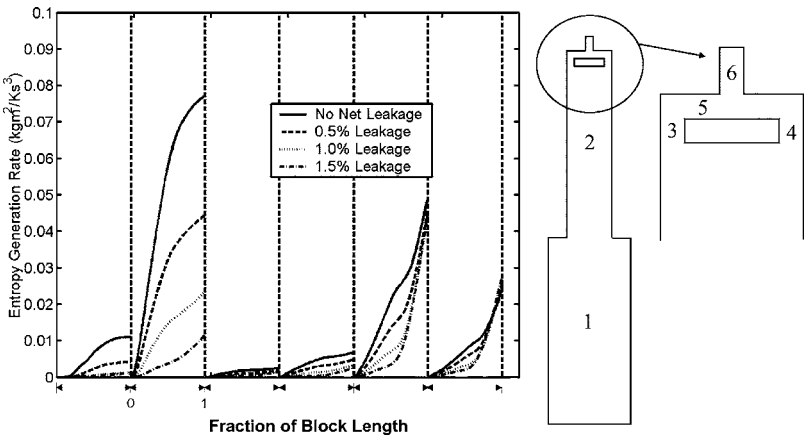

Fig. 15 Distribution of the cumulative entropy generation rate in the slot/strip-seal/plenum

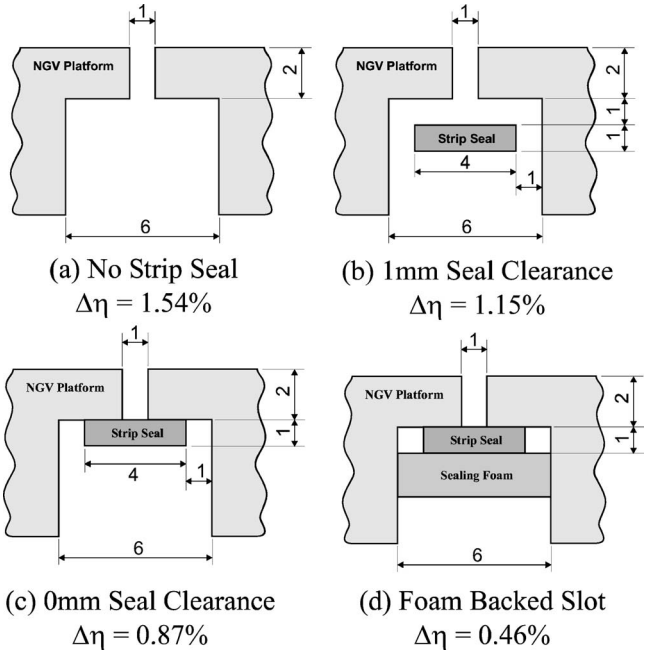

Fig. 17 Various seal clearances (dimensions in mm)

num and the annulus, it is proposed that the slot flow no longer creates a significant blockage to the secondary flow. Instead, the secondary flow incurs more loss as it crosses the slot, which leads to the deeper loss core. Neither the efficiency drop of this geometry nor the increase in the depth of the NGV loss core were predicted well by the CFD. Specifying laminar/turbulent transition to occur halfway along the slot led to no improvement in the agreement between the experiments and CFD. It is possible that improved transition modeling would improve the agreement. The flow in the region of the slot is likely dominated by small-scale turbulent mixing, and it is also possible that the mixing length model applied in TBLOCK is unable to model this flow accurately.

Without removing platform slots from engines, Fig. 17(*d*) offers the best case scenario. In engine installations, it is likely that these slots would extend along the entire length of the platform and cut through into the rim seal. As was shown earlier, the length of the slot can have a significant impact on the performance penalty. It was possible to extend the experimental 2 mm slot to the trailing edge of the NGV platform, and cut through into the rim seal, as shown in Fig. 19.

With the geometry of Fig. 17(*d*) on the portion of the slot upstream of the extension and with the platform cut through into the rim seal along the extension, an efficiency drop of 0.7% was measured. The small extension of the slot into the rim seal was therefore responsible for a drop of 0.24% over the configuration shown in Fig. 17(*d*). This again emphasizes the fact that small changes in the geometry of a turbine can have a relatively large effect on the efficiency.

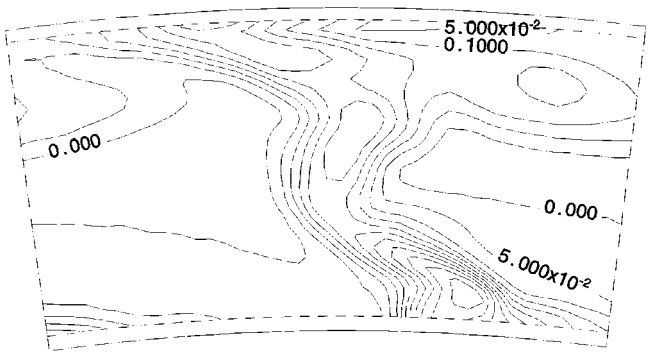

Fig. 18 Measured NGV loss coefficient with 0 mm clearance and foam backing

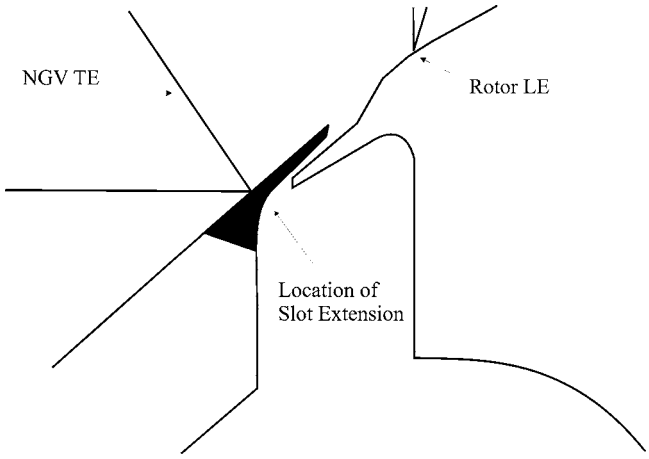

Fig. 19 Detail of the slot extension

5 Conclusions

This work has investigated the effect of chordwise hub platform slots on the performance of a low speed axial flow turbine. With a 1 mm seal clearance, the presence of the slots led to a significant performance penalty even with no-net leakage flow. The quality of the seal between the mainstream annulus and the wheelspace was found to be critical with a perfect seal resulting in a 1.08% efficiency improvement over an unsealed slot. Even when perfectly sealed, the presence of a 2 mm deep × 1 mm wide slot running along the chord of the blade resulted in a 0.46% drop in efficiency compared with a smooth annulus.

Acknowledgment

The authors would like to acknowledge the assistance of Nick Hooper of the Whittle Laboratory. The financial assistance of the Natural Sciences and Engineering Research Council of Canada, the Edmonton Churchill Society, and Rolls Royce is also gratefully acknowledged.

Nomenclature

c_v = specific heat capacity at constant volume
c_p = specific heat capacity at constant pressure
m = massflow
P = pressure
$\dot{s}$ = entropy generation rate
T = temperature
T_q = torque
V = velocity
Y_p = NGV loss coefficient
ω = rotational speed
ϕ = flow coefficient $= V_{merid2}/U_{mid2}$
γ = specific heat ratio $= c_p/c_v$
η = efficiency
τ = shear stress
$\bar{x}$ = area averaged x
$\dot{\bar{x}}$ = mass averaged x

Subscripts

br = brake
m = mainstream quantity
$merid$ = meridional

mid = midspan
s = leakage quantity
st = static quantity
0 = stagnation quantity
1,2,3 = downstream of the IGV, NGV, and rotor

References

[1] Aunapu, N., Volino, R., Flack, K., and Stoddard, R., 2000, "Secondary Flow Measurements in a Turbine Passage With Endwall Flow Modification," ASME Paper No. 2000-GT-0212.

[2] Cardwell, N., Sundaram, N., and Thole, K., 2005, "Effects of Mid-Passage Gap, Endwall Misalignment, and Roughness on Endwall Fil Cooling," ASME Paper No. GT2005-68900.

[3] Ranson, W., Thole, K., and Cunha, F., 2005, "Adiabatic Effectiveness Measurements and Predictions of Leakage Flows Along a Blade Endwall," ASME J. Turbomach., pp. 609–618.

[4] Pullan, G., Denton, J., and Dunkley, M., 2003, "An Experimental and Computational Study of the Formation of a Streamwise Shed Vortex in a Turbine Stage," ASME J. Turbomach., pp. 291–297.

[5] Ower, E., and Pankhurst, R., 1965, *Measurement of Air Flow*, 4th ed., Pergamon, New York.

[6] Beckwith, T., Marangoni, R., and Lienhard, J., 1993, *Mechanical Measurements*, 5th ed. Addison–Wesley, Reading, MA.

[7] Denton, J. D., 1990, "The Calculation of Three-Dimensional Viscous Flow Through Multistage Turbomachines," ASME Paper No. 90-GT-19.

[8] Pullan, G., and Denton, J., 2003, "Numerical Simulations of Vortex-Turbine Blade Interaction," *Conference Proceedings: 5th European Conference on Turbomachinery: Fluid Dynamics, and Thermodynamics*.

[9] Denton, J. D., 1993, "Loss Mechanisms in Turbomachines," ASME J. Turbomach., **115**, pp. 621–656.

[10] Dawes, W., 1987, "Application of a Three-Dimensional Viscous Compressible Flow Solver to a High-Speed Centrifugal Compressor Rotor-Secondary Flow and Loss Generation," IMECHE Paper No. C261/87.

Large Eddy Simulation of Transitional Boundary Layers at High Free-Stream Turbulence Intensity and Implications for RANS Modeling

Sylvain Lardeau

Ning Li
e-mail: n.li@imperial.ac.uk

Michael A. Leschziner

Department of Aeronautics,
Imperial College London,
Prince Consort Road,
South Kensington,
London SW7 2AZ, UK

Large-eddy simulations of transitional flows over a flat plate have been performed for different sets of free-stream-turbulence conditions. Interest focuses, in particular, on the unsteady processes in the boundary layer before transition occurs and as it evolves, the practical context being the flow over low-pressure turbine blades. These considerations are motivated by the wish to study the realism of a RANS-type model designed to return the laminar fluctuation energy observed well upstream of the location at which transition sets in. The assumptions underlying the model are discussed in the light of turbulence-energy budgets deduced from the simulations. It is shown that the pretransitional field is characterized by elongated streaky structures which, notwithstanding their very different structural properties relative to fully established turbulence, lead to the amplification of fluctuations by conventional shear-stress/shear-strain interaction, rather than by pressure diffusion, the latter being the process underpinning the RANS-type transitional model being investigated. [DOI: 10.1115/1.2436896]

1 Introduction

Bypass transition from the laminar to the turbulent state occurs when the linear growth of Tollmien–Schlichting waves, preceding natural transition, is bypassed by the penetration of disturbances into the boundary layer from a highly turbulent free stream. This process is especially pertinent to the flow over turbine blades. In modern low-pressure turbines, in particular, the Reynolds number, based on blade chord, is of the order 10^5. This relatively low value, in combination with the acceleration of the flow in the blade passages, can result in the blade suction-side boundary layer being laminar or transitional over 50–70% of the blade surface. In such circumstances, the transition process can have major operational consequences. In particular, early transition may prevent separation (stall) of the suction-side boundary layer, which is subjected, towards the rear of the blade, to a locally adverse pressure gradient. The consequence is a significant reduction in total-pressure loss. Furthermore, bypass transition plays an important role in the response of the suction-side boundary layer to passing wakes of preceding blade stages.

Turbomachine flows are almost invariably modeled within the Reynolds-averaged Navier-Stokes (RANS) framework with statistical closures that are applicable to fully established turbulence, and the representation of bypass transition within this framework presents a major challenge. Virtually all approaches return the transition process, in one way or another, as a rapid rise in turbulence activity at a specific transition location along the blade boundary layer, with consequent rapid rise in skin friction and heat-transfer coefficient. Transition is variously modeled with correlations for an intermittency parameter, with intermittency-transport equations or with low-Reynolds-number turbulence-transport equations that induce transition when the free-stream turbulence diffusing into the boundary layer is amplified by production to the extent of exceeding viscous dissipation. Reality is much more intricate, however.

Both experiments and simulations show that the boundary layer contains a significant level of "turbulence" well before the skin friction rises—the latter conventionally identifying transition. However, this turbulence does not comply with the usual concept of the condition in which the turbulence energy and the shear stress (and hence skin friction) are closely correlated. What is observed, rather, is that the fluctuation intensity rises in the intermediate-to-upper reaches of the boundary layer, well ahead of the rise in shear stress, giving a ratio of shear stress to turbulence energy, $\langle uv \rangle / k$ far below that associated with established turbulence. Turbulence models, either with or without transition corrections, are not able to return this "pretransitional" behavior [1].

Observing that the pretransitional velocity profile essentially adhered to laminar criteria, Mayle and Schulz [2] proposed an equation for the *laminar kinetic energy*, formally similar to the conventional form governing the turbulence energy, to represent the pretransitional rise in fluctuation level. This equation lacks the usual shear-stress/strain-related generation term, but contains a source term that is argued to arise from the pressure–diffusion correlation. Thus, the equation returns, upon calibration, the requisite rise in the fluctuation-energy level in the laminar regime, despite the absence of a shear stress, which is presumed to be zero. Mayle and Schulz's equation was used by Lardeau and Leschziner [1,3] to construct a transition-modified low-Reynolds number, nonlinear eddy-viscosity model, capable of returning the correct behavior of transitional as well as pretransitional features in laboratory configurations of the type shown in Fig. 1. These passing wakes generated by cylinders moving in pitch-wise direction upstream of the blades provoke, in conjunction with high free-stream turbulence, unsteady transition. However, an open question that was not addressed in that study is whether the pretransitional model for the *laminar fluctuation energy* is conceptually correct. To answer this question, highly resolved large eddy simulations have been performed for a boundary layer developing

Contributed by the Turbomachinery Division of ASME for publication in the JOURNAL OF TURBOMACHINERY. Manuscript received November 15, 2005; final manuscript received July 14, 2006. Review conducted by Greg Walker. Paper presented at the 4th International Symposium on Turbulence and Shear Flow Phenomena, 2005.

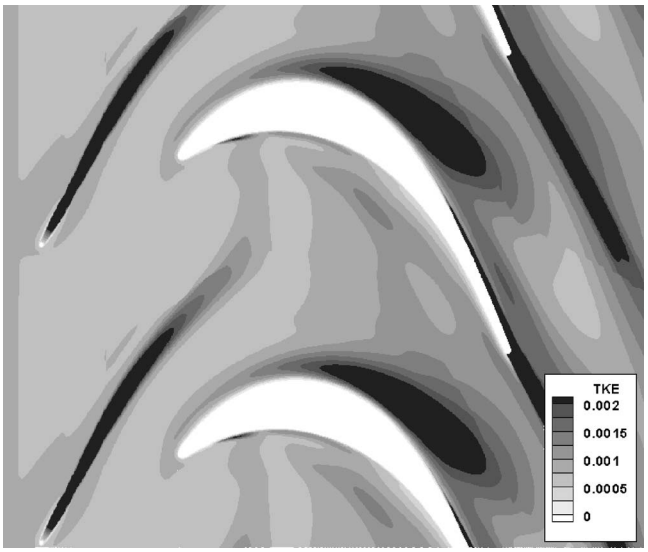

Fig. 1 Turbulence energy in blade passage, wake created by a moving rod, T106A blade profile

over a flat plate, subjected to free-stream turbulence. In particular, the influence of the turbulence structure in the free stream was examined, and turbulence budgets were obtained to study the implications of modeling the process within a statistical framework, and to examine the validity of Mayle and Schulz's [2] proposal. It is this study that is reported herein.

Several earlier simulations and experimental investigations, dealing with various aspects of bypass transition, have been published in the past. These consider, among other issues, the influence of free-stream turbulence intensity, the properties of the spectra of this turbulence, and the effects of pressure gradient (e.g., Refs. [4–6]). The studies by Brandt et al. [6] and Jonáš et al. [7], in particular, show that the details of the transition process are sensitive to the integral length scale in the free stream, and that receptivity of long streaky structures in the boundary layer to free-stream turbulence depends on the spectral distribution of modes in that stream. To the present authors' knowledge, only one study, namely that by Voke and Yang [8], includes considerations on how the budgets of the Reynolds stresses evolve before and during the transition. However, these simulations have been done with low numerical accuracy, and several processes of the budget have been agglomerated into groups, not allowing some important processes to be distinguished in isolation from others. The present study addresses, among other issues, the evolution of the budgets, with particular attention focusing on shear production relative to pressure-velocity interaction.

2 The Computational Framework

The simulations were performed with a staggered finite-difference scheme, combining a second-order Adams–Bashforth approximation for the time integration with a second-order central-difference scheme for the spatial derivatives. Subgrid-scale processes were represented by the localized Lagrangian-averaged dynamic eddy-viscosity model, proposed by Meneveau et al. [9]. This has been reported by Sarghini et al. [10] to perform especially well in transitional flows, and is thus held to be well suited to the present study.

The domain size and grid resolution are, respectively, $(L_x, L_y, L_z) = (400\delta_1^*, 35\delta_1^*, 40\delta_1^*)$, where δ_1^* is the displacement thickness at the inlet, and $(n_x, n_y, n_z) = (512, 80, 96)$ points in the three respective directions. The momentum-thickness Reynolds number, based on the inflow condition, was 425 for all the simulations. Statistical data, including budgets, have been obtained by integrating over a period of $2650\delta_1^*/U_{\text{in}}$ and over the homogeneous spanwise direction, with a time step $\Delta t = 0.04\delta_1^*/U_{\text{in}}$.

Table 1 Free-stream conditions for the transitional boundary-layer simulations (Tu is the turbulence intensity)

	Tu (%)	u'_{inlet}	v'_{inlet}	w'_{inlet}	BL perturbed
S_{iso}	4.3	Yes	Yes	Yes	Yes
S_{fs}	8	Yes	Yes	Yes	No
S_{uu}	2.5	Yes	No	No	Yes

The free-stream turbulence was superimposed onto the mean Blasius velocity profile at the computational inlet plane, and was synthetically generated by a Fourier-series method [11], which satisfies a prescribed spectrum, given by

$$E(k) = \frac{2}{3}\frac{a(\kappa/\kappa_p)^4}{[b + (\kappa/\kappa_p)^2]^{17/6}} \tag{1}$$

where $a = 1.606$ and $b = 1.350$; κ is the wave number; and κ_p is peak wave number. This method preserves spatial and temporal coherence and includes random sampling in respect of the phase of the Fourier components. The peak wave number in the spanwise and wall-normal direction was 12, while the peak wave number in the streamwise direction was 64, which gave the correct decay of the turbulent kinetic energy in the free stream (see later considerations). An alternative method, proposed by Jacobs and Durbin [5] and used by Brandt et al. [6], is to superimpose onto the free-stream the modes of the continuous spectrum of the linearized Orr–Sommerfeld and Squire operators. This method is appropriate if the goal is to study the detailed spectral mechanisms and receptivity issues over the full domain, including the stability region, where the small-amplitude perturbations are important. In contrast, the principal aim of the present study is to examine the statistical properties of the pretransitional region and the initial stages of the transitional region for different free-stream conditions. To this end, a refined spectral treatment of the free stream and the boundary layer is not needed.

Three simulations are discussed below. In one, denoted S_{iso}, isotropic turbulence is prescribed in the free stream and at the inlet plane, including within the boundary layer. In the second, identified as S_{fs}, isotropic turbulence is prescribed, but only above the Blasius boundary layer. Finally, in the third, denoted S_{uu}, only streamwise fluctuations are prescribed across the whole inflow boundary. The prescribed conditions for all three simulations are summarized in Table 1. The aim of the last is to re-examine more carefully Voke and Yang's observation [8] that low lateral fluctuations in the free stream inhibit transition, due to the weakness of pressure fluctuations induced by these lateral fluctuations. The results of these simulations appear not to have been published. As will be shown below, the absence of perturbations prescribed in the boundary layer at the inlet (case S_{fs}) inhibited the formation of the elongated streaky structures observed in the two other simulations, which are receptivity sites for free-stream turbulence and which eventually break down into turbulent spots [6]. As a consequence, transition was delayed beyond the end of the computational domain when the value of Tu used in S_{iso} was maintained for S_{fs}. Thus, for this case, the free-stream turbulence intensity at the inlet was raised to 8%. This is a permissible practice in view of the fact that the objective is here to examine the evolution of the statistical properties around and upstream of the transition onset. Finally, the inlet level of Tu in the simulation S_{uu} was lower than in S_{iso}, as $\langle uu \rangle$ was intentionally maintained at the same level in both simulations, while the other two components were nullified in S_{uu}.

The decay of the free-stream turbulence intensity in the streamwise direction for the three simulations is shown in Fig. 2. In all

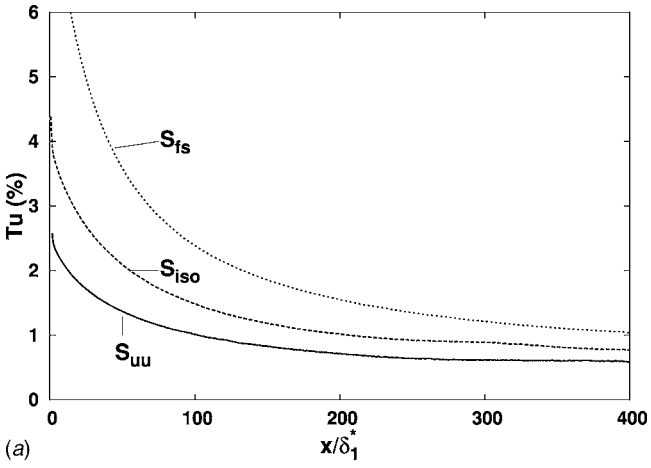

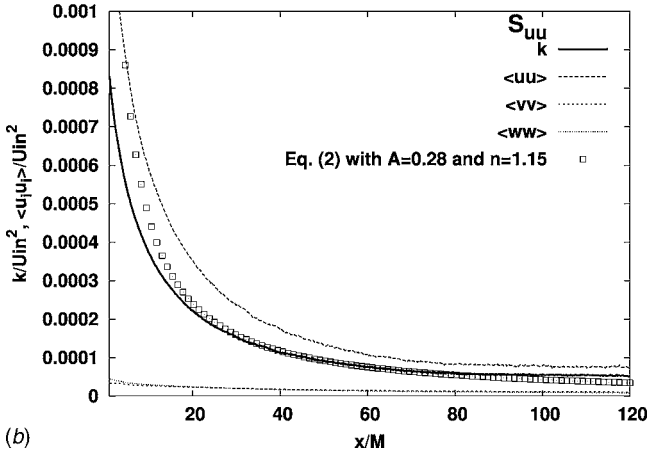

Fig. 2 Streamwise evolution of the freestream turbulence intensity: (*a*) comparison between all three cases; and (*b*) turbulence intensity and intensity of each normal stress for simulation S_{uu}. Symbols represents the theoretical decay of grid turbulence (Eq. (2)).

cases, even the one with streamwise fluctuations only, the free-stream turbulence is found to decay according to

$$\frac{k}{U_{\text{in}}^2} = A\left(\frac{x}{M}\right)^{-n} \tag{2}$$

where M is the grid size used to generate the turbulent field and A is an arbitrary constant. The grid size M is deduced here by dividing the lateral extent of the domain by the peak wave number κ_p used in that same direction: $M=40\delta_1^*/12$. The decay exponent $n=1.15$ is the same in all three cases, a value within the range reported in the literature [12]. Figure 2(*b*) also shows that, for S_{uu}, the free-stream condition remains highly anisotropic over the entire computational domain.

3 Results

An overall impression of the transition process is conveyed in Fig. 3, which shows contours of the streamwise fluctuations derived from the simulation S_{iso} at three time levels separated by the interval $45\delta_1^*/U_{\text{in}}$. These images are very similar to those observed experimentally by Matsubara and Alfredsson [4] and numerically by Brandt et al. [6]. Thus, elongated structures are visible right from the inlet, and these structures eventually break down into turbulent spots at around $x=110\delta_1^*$. As will be shown below, this is also roughly the location at which the skin friction

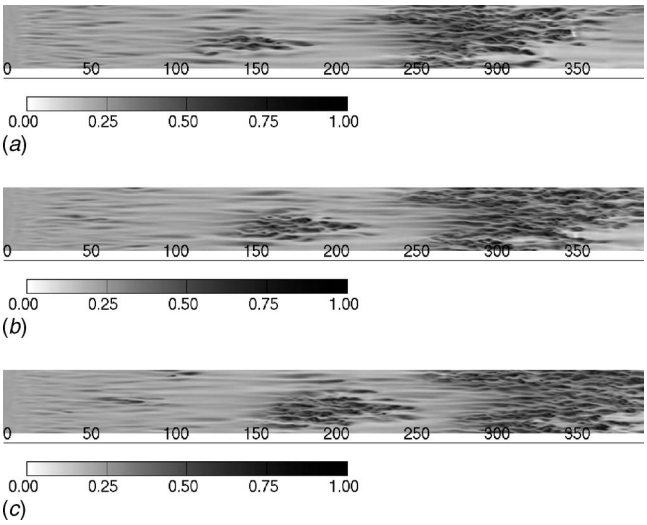

Fig. 3 Contours of the streamwise component of the velocity in the (x,z) plane at $y=0.39\delta_1^*$, simulation S_{iso}

rises. It is observed that the streaks are also present downstream of the spots. Even further downstream, the turbulent spots merge into a fully turbulent flow.

Figures 2(*a*) and 4 show, respectively, the streamwise decay of the free-stream turbulence intensity and the corresponding evolution of the skin friction. The transition process is clearly a strong function of the turbulence structure in the free stream and in the boundary layer. Conventionally, transition is considered to set in when the skin friction rises significantly. This occurs at around $x/\delta_1^*=130$, 180, and 300 for S_{iso}, S_{uu}, and S_{fs}, respectively, the first value being close to that at which the turbulent spots first develop in Fig. 3. In every case, the skin friction indicates a slow transition process. This is especially so with S_{fs}, despite the much higher free-stream-turbulence intensity than that applied in the other two cases. With no perturbations in the boundary layer, Hunt and Durbin [13] and later Zaki and Durbin [14] showed that "shear sheltering" prevents the high-frequency free-stream fluctuations from entering the boundary layer. In the other two simulations, the perturbations introduced into the boundary layer create long streamwise structures (Fig. 3), which are receptivity sites for the fluctuations entering the boundary layer. What may also be concluded from Fig. 4 is that the suppression of lateral free-stream fluctuations (i.e., the imposition of a high level of anisotropy) does indeed inhibit the transition process.

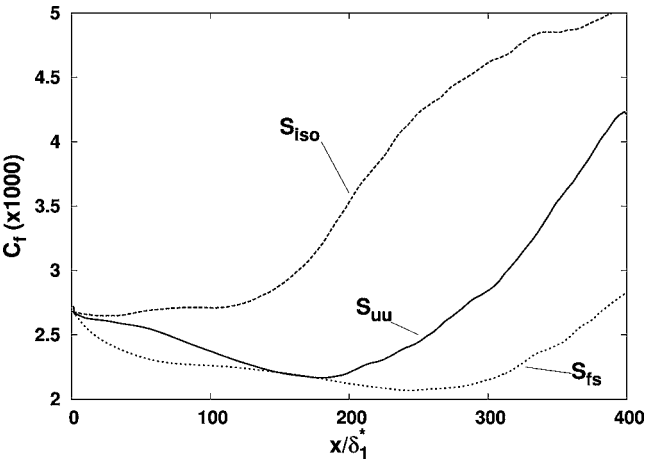

Fig. 4 Streamwise evolution of the skin-friction coefficient

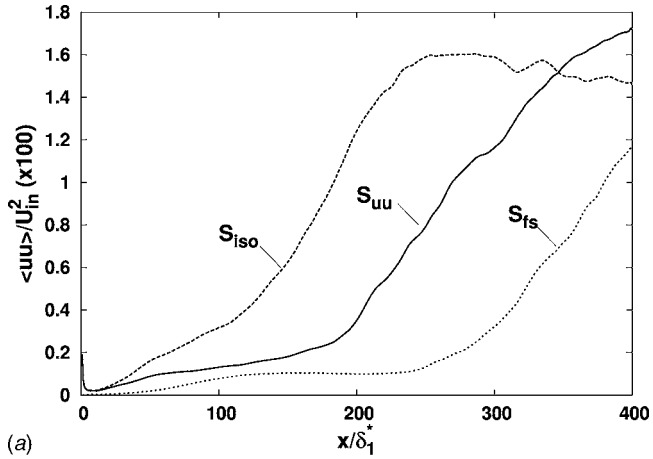

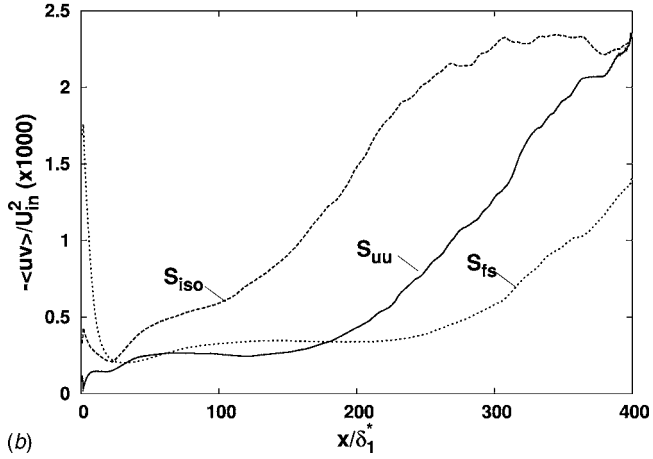

Fig. 5 (*a*) Streamwise evolution of the streamwise velocity fluctuations close to the wall ($y/\delta_1^*=0.34$); and (*b*) streamwise evolution of the shear stress

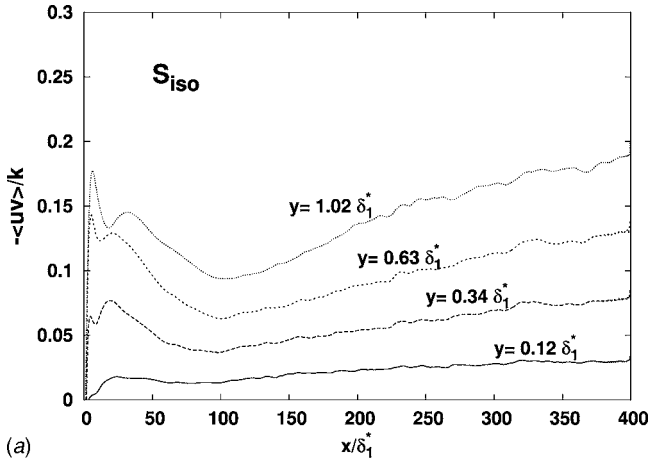

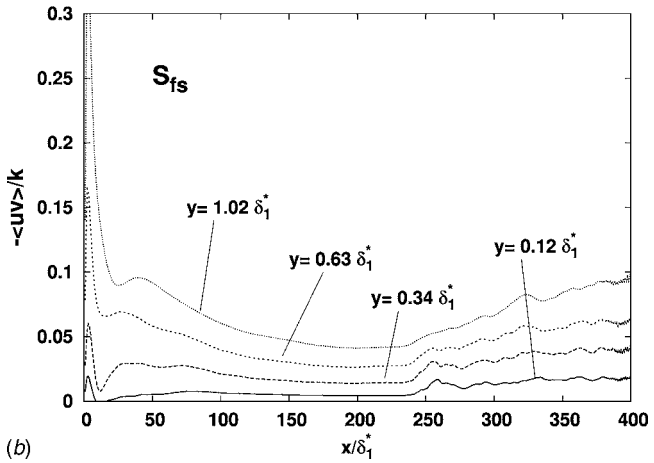

Fig. 6 Streamwise evolution of the ratio $-\langle uv\rangle/k$ at different distance from the wall, (*a*) simulation S_{iso} and (*b*) simulation S_{fs}

Figure 5 shows the streamwise evolution of $\langle uu\rangle$ and $\langle uv\rangle$ at a distance $y=0.34\delta_1^*$ from the wall. Although the imposed perturbation fields differ substantially, the respective evolutions of $\langle uu\rangle$ are qualitatively similar. As observed experimentally by Matsubara and Alfredsson [4], the energy rise is initially proportional to the distance from the leading edge. In the case S_{iso}, to which Fig. 3 relates, the streamwise-normal and shear stresses are seen to rise well upstream of the location at which C_f begins to increase. This rise is due to the long streaks that develop well upstream of the transition, while the turbulent spots are responsible for the elevation of C_f. The simulation S_{fs} shows an especially interesting behavior. Initially, the boundary layer is laminar and features no streaks, so the value of $\langle uu\rangle$ is very low. It then increases almost linearly between the inlet and $x=100\delta_1^*$, the level remaining low, because of low receptivity, until the onset of transition, at around $x=300\delta_1^*$.

Figure 6 gives streamwise distributions of the ratio $-\langle uv\rangle/k$ at four wall-normal locations. In this connection, it will be recalled that Mayle and Schulz's model rests on the assumption of zero shear-stress/shear-strain generation. As seen from the distributions relating to S_{iso}, this notion is incorrect. Clearly, the ratio is fairly high—of order 30–50% of the level in a fully turbulent boundary layer—signifying an elevated shear stress upstream of transition. While the ratio $-\langle uv\rangle/k$ declines sharply as the wall is approached, there is no fundamental or sudden change in this ratio as the flow undergoes transition at around $x=130\delta_1^*$, except for the distinctive rise in the boundary-layer portion remote from the wall. When turbulence is suppressed in the inlet boundary layer, as done in S_{fs}, so that receptivity is drastically reduced, the ratio is much lower, and this is consistent with the substantially delayed transition observed in Fig. 4.

Budgets for the turbulence energy are given in Figs. 7–9. The various curves correspond to the terms identified in Eq. (3) below

$$\underbrace{U_j\frac{\partial k}{\partial x_j}}_{\text{Conv}} = \underbrace{-\langle u_i u_j\rangle\frac{\partial U_i}{\partial x_j}}_{P_k} \underbrace{-\frac{\partial\langle k' u_j\rangle}{\partial x_j}}_{D_t} \underbrace{-\frac{1}{\rho}\frac{\partial\langle p u_j\rangle}{\partial x_j}}_{D_p} + \underbrace{\nu\frac{\partial^2 k}{\partial x_j \partial x_j}}_{D_\nu} - \varepsilon \quad (3)$$

These represent, respectively, convection, production, turbulent diffusion, pressure diffusion, viscous diffusion, and dissipation. The budgets are plotted at different streamwise locations, but in all cases before transition sets in, as identified by the skin-friction rise in Fig. 4. Also plotted, by way of square symbols, is the production term proposed by Mayle and Schulz [2] in their pre-transition *laminar kinetic energy* model. The transport equation is given by

$$\frac{Dk_l}{Dt} = P_{k_l} + \nu\frac{\partial^2 k_l}{\partial^2 y} - 2\nu\frac{k_l}{y^2} \quad (4)$$

where the last right-hand-side term represents the dissipation, and the production term is given by

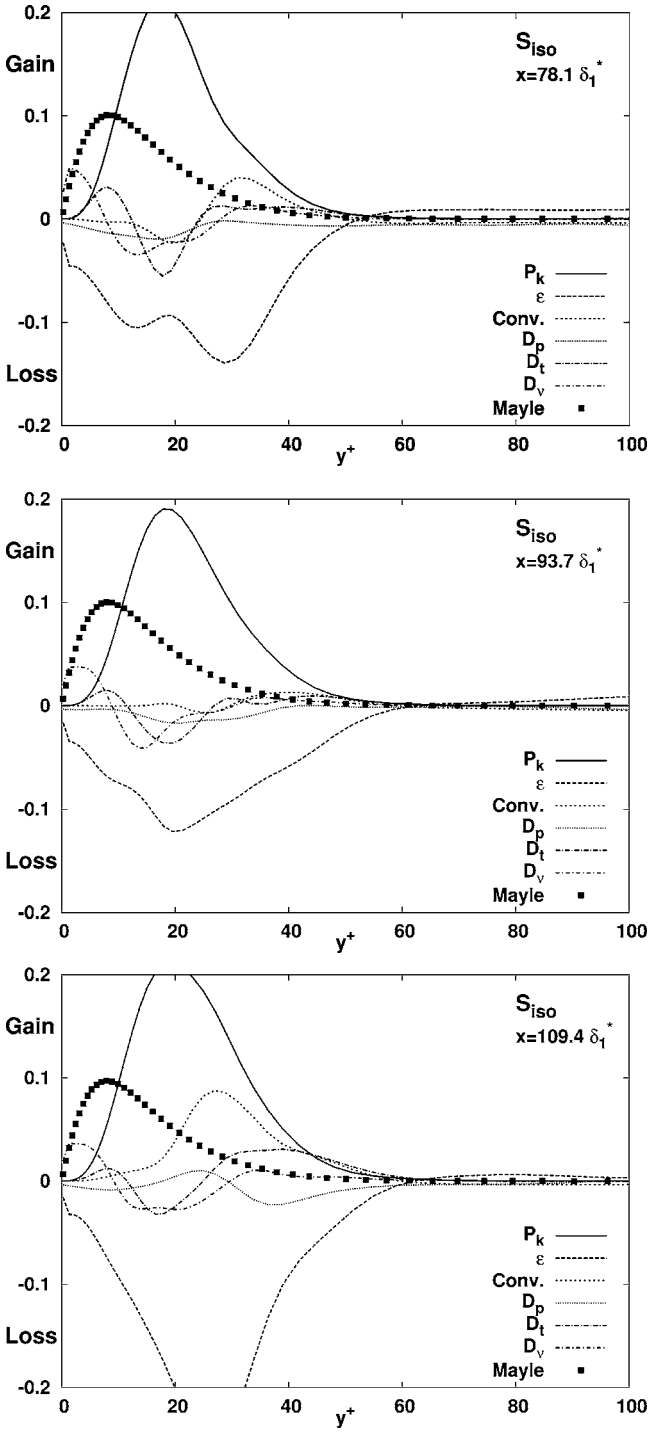

Fig. 7 Turbulence-energy budgets (Eq. (3)) for the S_{iso} test case

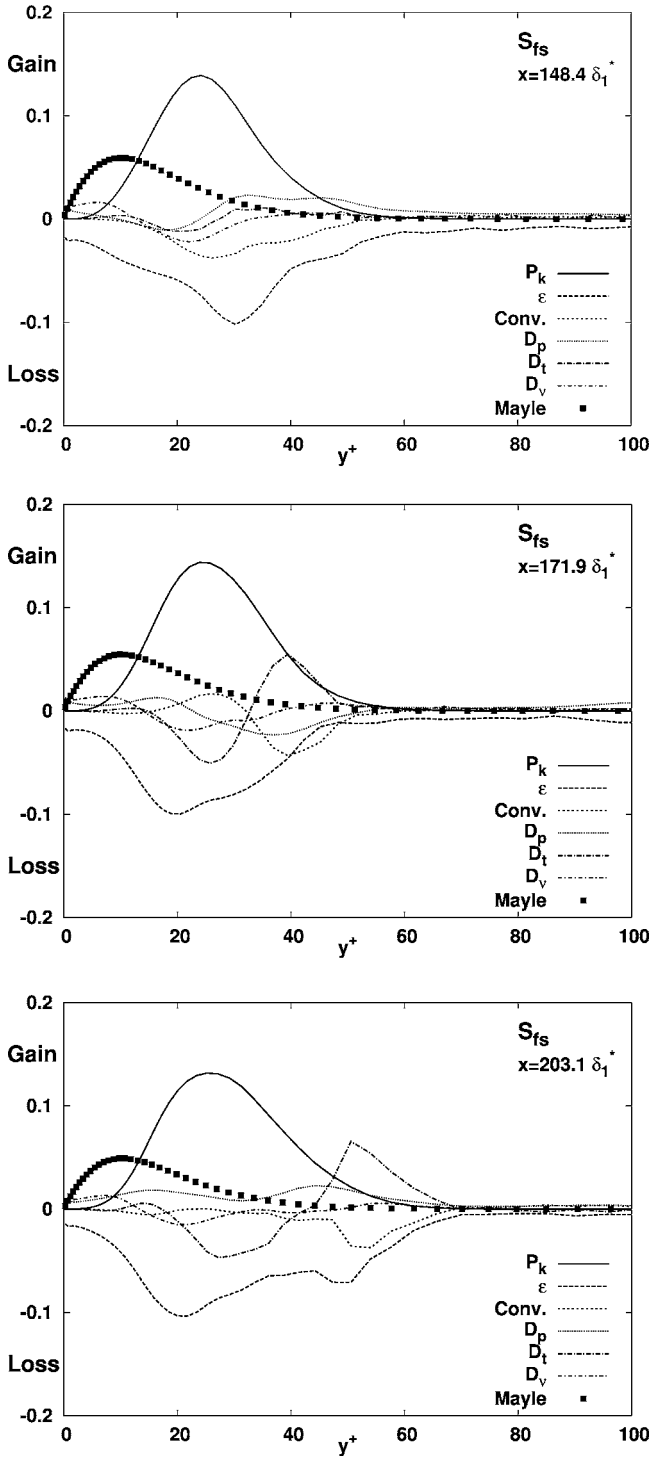

Fig. 8 Turbulence-energy budgets (Eq. (3)) for the S_{fs} test case

$$P_{k_l} = C_\omega \frac{U_{in}^2}{\nu} \sqrt{\overline{k \cdot k_\infty}} \exp(-y^+/C^+) \tag{5}$$

where C^+ is constant ($C^+ = 13$) and C_ω varies, depending on the velocity and the free-stream turbulence intensity, according to

$$C_\omega = 0.07 \left(\frac{u_\epsilon}{U_\infty} \right) \mathrm{Re}_\Lambda^{-1/3} \tag{6}$$

where u_ϵ is the Kolmogorov velocity scale and Re_Λ is the integral-length-scale Reynolds number. In contrast to the presentation adopted by Voke and Yang [8], the different processes featuring in Eq. (3) have here been separated. Attention is drawn to the fact that the dissipation rate ε in the budgets is that resolved by the simulation. This level is more than 95% of the total (with the subgrid-scale contribution estimated from the subgrid-scale model), illustrating the quality of the resolution and the relatively modest contribution of the unresolved processes.

As noted earlier, Mayle and Schulz's model is based on the hypothesis that shear-induced production is zero, while the amplification of the pretransitional fluctuation energy is effected by way of the pressure diffusion. As seen from Fig. 7, relating to S_{iso}, the

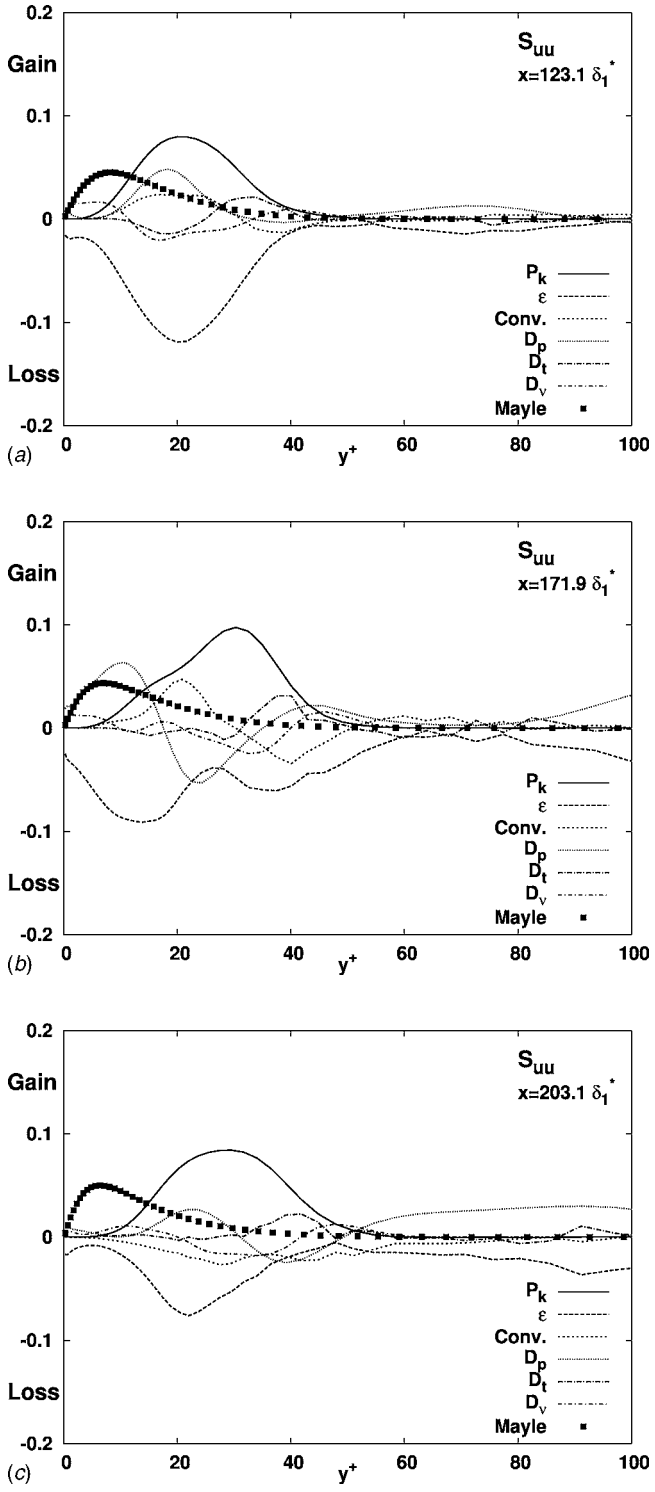

Fig. 9 Turbulence-energy budgets (Eq. (3)) for the S_{uu} simulation at three streamwise locations

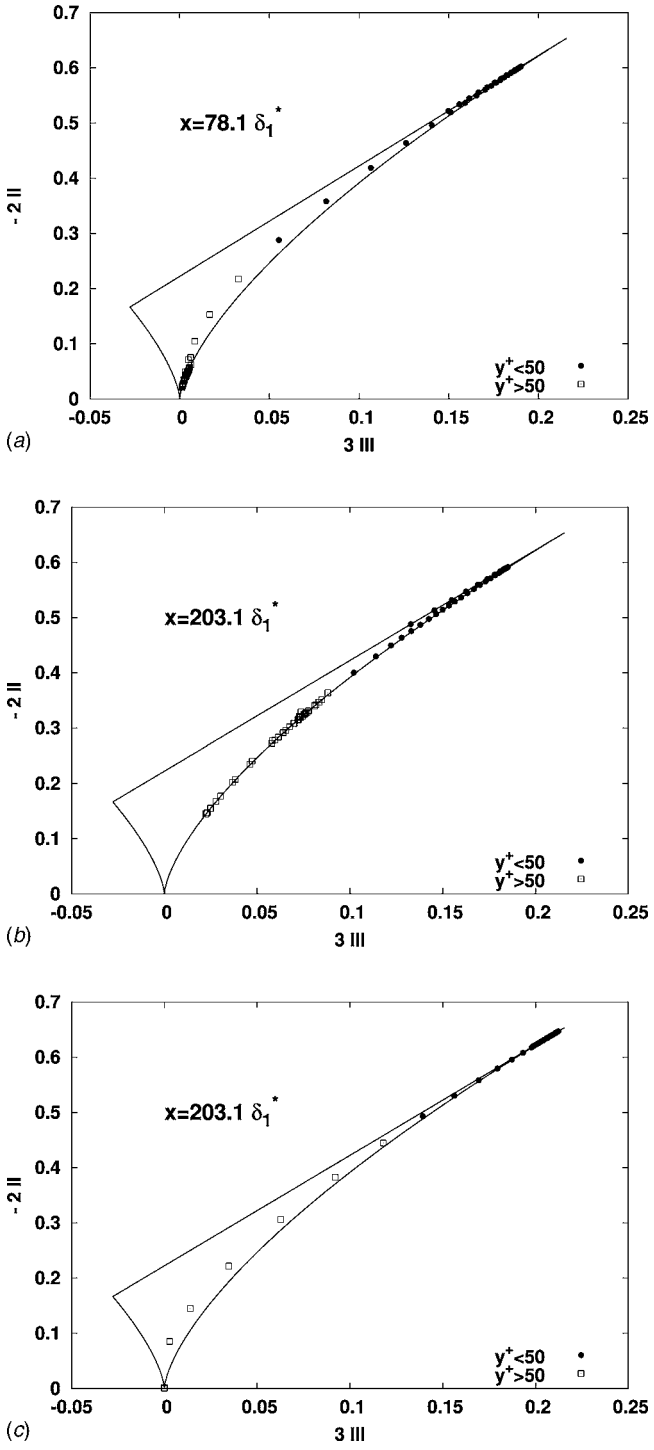

Fig. 10 Anisotropy-invariants map for (*a*) S_{iso}, (*b*) S_{uu}, and (*c*) S_{fs} simulations

simulation provides no evidence that this scenario is realistic. Thus, the elevation of fluctuation energy is due to shear production, despite the relatively low level of the shear stress. In contrast, pressure diffusion is minor—indeed, negative—over most of the boundary layer. While the balance is predominantly between production and dissipation, the budget clearly differs substantially from that of a fully turbulent layer. In particular, dissipation declines towards the wall due to the low level of diffusion. Thus, close to the wall, turbulence activity is insignificant.

The budgets derived from simulations S_{fs} and S_{uu} are qualitatively similar to that discussed above. A surprising observation, at first sight, is that the latter is characterised by significantly lower levels of production, and hence also dissipation, relative to those of the other two simulations. A partial explanation can be gleaned from Fig. 5. This shows the shear stress to be especially low in simulation S_{uu}, while the level of $\langle uu \rangle$ (and hence k) is higher than that of simulation S_{fs}. Thus, the $\langle uv \rangle$-related production is especially low in the pretransitional region, despite the presence of the elongated streaks is S_{uu}. This suggests that receptivity associated

with the streaky structure upstream of the spots is not the only feature that governs transition, but that highly anisotropic freestream fluctuations also play an important role—as has already been concluded by reference to Fig. 5. Despite these differences, the principal message is that the balance in all three simulations is mainly between shear production and dissipation, while pressure diffusion is negligible, except in some parts of the boundary layer of simulation S_{uu}, where it does seem to act in the same sense as the production term. Mayle and Schulz's model is seen to return a behavior which is bound to increase the pretransitional fluctuation energy, but the level is too low, and the maximum much too close to the wall.

Finally, plotted on Fig. 10 are anisotropy maps, which correlate the second and third anisotropy invariants, $II=b_{ij}b_{ij}$ and $III=b_{ij}b_{jk}b_{ki}$, respectively, with $b_{ij}=\langle u_i u_j\rangle/k-2/3\delta_{ij}$, across the flow at the same streamwise positions for which the budgets have been reported. The trajectories on the (III,-II) plane show that, before transition, the flow tends towards the one-component limit in the near-wall region, especially for the S_{uu} case for which the free stream is itself close to the one-component state. For the two cases, in which isotropic turbulence is prescribed in the free stream, there is a progressive departure from isotropy toward the one component state. An interesting feature is that, in the case S_{uu}, the conditions in the middle portion of the boundary layer first indicate a trend toward isotropy, with subsequent approach to the one-component limit.

4 Conclusions

Although the simulations reported herein are subject of some uncertainties arising from the lack of realism in the free-stream conditions, relative to those in a typical experiment, the results may be claimed to be relevant and informative. In particular, the principal objective of shedding light on the validity of the basic assumptions underlying the RANS closure for the high fluctuation level observed upstream of the transition location has been met. The simulations show that, from a statistical point of view, shear-stress/strain-induced production is mainly responsible for the elevation of the pretransitional *laminar fluctuation energy*—a process that is akin to that observed in the turbulent state, although effective here mainly in the upper (wall-remote) portions of the boundary layer. Indeed, the ratio $\langle uv\rangle/k$ is fairly high over a significant portion of the pretransitional boundary layer away from the wall, relative to the value 0.3 associated with an equilibrium boundary layer. This contradicts the basis of the model investigated herein, which rests on the assumption that the shear stress and the shear-effected production is zero. The simulations also show that the prescription of a highly anisotropic state in the free stream, wherein lateral fluctuations are very low, or the nullification of fluctuations in the laminar boundary layer subjected to isotropic free-stream turbulence, leads to a significant reduction in receptivity and a substantial delay in the formation of turbulent spots, which mark the onset of transition. The expectation is that lessons and data derived from this study will result in an improved model for the pretransitional processes.

Acknowledgment

The research reported herein was undertaken within the project "Unsteady Transitional Flows in Axial Turbomachinery," funded by the European Commission under Contract No. G4RD-CT-2001-00628.

References

[1] Lardeau, S., Leschziner, M., and Li, N., 2004, "Modelling Bypass Transition With Low-Reynolds-Number Non-Linear Eddy-Viscosity Closure," Flow, Turbul. Combust., **73**, pp. 49–76.
[2] Mayle, R., and Schulz, A., 1997, "The Path to Predicting Bypass Transition," ASME J. Turbomach., **119**, pp. 405–411.
[3] Lardeau, S., and Leschziner, M. (2006). "Unsteady RANS Modeling of Wake-Induced Transition in Linear LP-Turbine Cascades," AIAA J., **44**(8), pp. 1845–1865.
[4] Matsubara, M., and Alfredsson, P. H., 2001, "Disturbance Growth in Boundary Layers Subjected to Freestream Turbulence," J. Fluid Mech., **430**, pp. 149–168.
[5] Jacobs, R., and Durbin, P., 2001, "Simulations of Bypass Transition," J. Fluid Mech., **428**, pp. 185–212.
[6] Brandt, L., Schlatter, P., and Henningson, D., 2004, "Transition in Boundary Layers Subject to Free-Stream Turbulence," J. Fluid Mech., **517**, pp. 167–198.
[7] Jonáš, P., Mazur, O., and Uruba, V., 2000, "On the Receptivity of the By-Pass Transition Length Scale of the Outer Stream Turbulence," Eur. J. Mech. B/Fluids, **19**, pp. 707–722.
[8] Voke, P., and Yang, Z., 1995, "Numerical Study of Bypass Transition," Phys. Fluids, **7**(9), pp. 2256–2264.
[9] Meneveau, C., Lund, T., and Cabot, W., 1996, "A Lagrangian Dynamic Subgrid-Scale Model of Turbulence," J. Fluid Mech., **319**, pp. 353–385.
[10] Sarghini, F., Piomelli, U., and Balaras, E., 1999, "Scale-Similar Models for Large-Eddy Simulations," Phys. Fluids, **11**(6), pp. 1596–1607.
[11] Rogallo, R., 1981, "Numerical Experiments in Homogeneous Turbulence," Tech. Memo No. 81315, NASA, Washington, D.C.
[12] Pope, S. B., 2000, *Turbulent Flows*, Cambridge University Press, Cambridge, UK, pp. 160–161.
[13] Hunt, J. C. R., and Durbin, P., 1999, "Perturbed Shear Layers," Fluid Dyn. Res., **24**, pp. 375–404.
[14] Zaki, T. A., and Durbin, P. A., 2005, "Mode Interaction and the Bypass Route to Transition," J. Fluid Mech., **531**, pp. 85–111.

The Boundary Layer Over Turbine Blade Models With Realistic Rough Surfaces

Hugh M. McIlroy, Jr.
Department of Mechanical Engineering,
University of Idaho At Idaho Falls,
Idaho Falls, ID 83402
e-mail: mcieng@srv.net

Ralph S. Budwig
Department of Mechanical Engineering,
University of Idaho,
Moscow, ID 83844
e-mail: rbudwig@uidaho.edu

Results are presented of extensive boundary layer measurements taken over a flat, smooth plate model of the front one-third of a turbine blade and over the model with an embedded strip of realistic rough surface. The turbine blade model also included elevated freestream turbulence and an accelerating freestream in order to simulate conditions on the suction side of a high-pressure turbine blade. The realistic rough surface was developed by scaling actual turbine blade surface data provided by U.S. Air Force Research Laboratory. The rough patch can be considered to be an idealized area of distributed spalls with realistic surface roughness. The results indicate that bypass transition occurred very early in the flow over the model and that the boundary layer remained unstable (transitional) throughout the entire length of the test plate. Results from the rough patch study indicate the boundary layer thickness and momentum thickness Reynolds numbers increased over the rough patch and the shape factor increased over the rough patch but then decreased downstream of the patch. It was also found that flow downstream of the patch experienced a gradual retransition to laminar-like behavior but in less time and distance than in the smooth plate case. Additionally, the rough patch caused a significant increase in streamwise turbulence intensity and normal turbulence intensity over the rough patch and downstream of the patch. In addition, the skin friction coefficient over the rough patch increased by nearly 2.5 times the smooth plate value. Finally, the rough patch caused the Reynolds shear stresses to increase in the region close the plate surface. [DOI: 10.1115/1.2218572]

Introduction

Since 1939, when first introduced, gas turbine engines have steadily evolved. Today they are frequently the engine of choice for land, sea, and air applications. Refinements in engine design have resulted in high-efficiency compressors, combustors, and turbines. Great advances have been made in computer modeling of the gas flow through engine components, and the trend in the gas turbine industry appears to favor fewer turbine stages and wider airfoils. There has been a continuous effort to increase turbine inlet temperatures to their stoichiometric limit. This has led to the development of new metal alloys for turbine blades, blade cooling techniques, improved manufacturing techniques, and hybrid materials research [1]. One of the many issues facing engine designers and manufacturers relating to the heat transfer process that is ongoing inside a modern gas turbine engine is the impact of turbine blade roughness on engine performance. Koch and Smith [2] report an important method for the design of roughness. The authors calculate performance losses for axial flow compressors that are affected by several parameters including surface finish described by equivalent sand-grain roughness.

The impact of turbine blade surface roughness on aerodynamic performance and heat loads is well known. Over time, as the turbine blades are exposed to these huge heat loads, the external surfaces of the blades are degraded and become rough. Surface degradation results in an increase in heat loads and friction losses. Surface roughness on turbine airfoils can begin, and increase dramatically, from surface oxidation, surface corrosion, deposition of unburned fuel or foreign materials, spallation of thermal barrier coatings, and erosion and/or pitting during routine engine operation. Additionally, Boyle and Senyitko [3] report that new surfaces coated with a thermal barrier coating also suffer losses. In addition, for film-cooled blades, surface degradation can have a significant impact on film-cooling effectiveness.

Many studies have been conducted on the effects of surface degradation/roughness on engine performance, but most have investigated surfaces with *uniform* or *two-dimensional* roughness patterns in wind tunnels, with hot-wire anemometers and without matching *all* of the flow phenomena normally found in turbine engines (accelerating flow with elevated freestream turbulence over a realistic rough surface). There is a clear requirement to investigate and measure the effects of *realistic* surface roughness on the gas flow through a turbine stage. Bons [4] defines "realistic surface roughness" as the actual roughness that develops on turbine blades during in-service operation.

Average centerline roughness measurements from in-service gas turbine airfoils (blades and vanes) range from 1.6 to 85 μm [4–7]. Boyle estimated efficiency losses of 2.5% [8]. In addition, at the microscopic level, blade coating is porous to reduce its thermal conductivity. Surface depressions have been shown to affect heat transfer and skin friction, and can be expected to have comparable effects on flows over blades and vanes as well [9,10]. For high-pressure stages, the small sizes of the blades and vanes and their boundary layers make it difficult (if not impossible) to measure all flow characteristics accurately near their surfaces, particularly for the wall-normal component (v) and Reynolds shear stress ($\rho\overline{u'v'}$). On actual airfoils, boundary layer thicknesses as small as 0.1 mm may be found, while the smallest multi-sensor probes to measure the wall-normal component (v) are of the order of 1 mm or larger [11].

Consequently, there is an incentive to conduct experiments at larger scales to measure the effects of realistic surface roughness on the various boundary-layer parameters.

State of Knowledge Base—Previous Work. A tremendous volume of literature exists on the nature of the various fluid flow

Contributed by the International Gas Turbine Institute (IGTI) of ASME for publication in the JOURNAL OF TURBOMACHINARY. Manuscript received October 1, 2004; final manuscript received February 1, 2005. IGTI Review Chair: K. C. Hall. Paper presented at the ASME Turbo Expo 2005: Land, Sea and Air, Reno, NV, June 6–9, 2005. Paper No. GT2005-68342.

phenomena that are known to exist in gas flows through the three major components of a modern high-performance gas turbine engine. Although separate studies have been conducted on the effects that roughness, freestream turbulence intensity, and pressure gradients have on the turbulent boundary layer, to our knowledge, no comprehensive study on the simultaneous impact of all three effects has been conducted to date. Of the numerous studies reviewed for this paper, only 18 investigated the combined effects of more than one of the relevant phenomena on a turbulent boundary layer. Eight studies reported investigations that only included the effects of elevated freestream turbulence and a pressure gradient on a turbulent boundary layer, nine studies reported investigations on the effects freestream turbulence and a rough surface on a turbulent boundary layer, and only one study reported investigations on the effects of a pressure gradient and surface roughness on a turbulent boundary layer. Finally, because most of these studies used hot-wire anemometry in a wind tunnel, their spatial resolution near the surface was not as good as can be obtained with the laser Doppler velocimetry (LDV) system and matched-index-of-refraction (MIR) facility that was employed for this investigation. For a more detailed review of literature relating to this subject, see McIlroy [12].

Bunker [13] studied the effects of surface roughness levels on vane heat transfer with varied conditions of freestream turbulence and Reynolds number. He discovered that surface roughness tends to hasten transition on both the pressure and suction sides of a blade and increased turbulence intensity also hasten transition. Young et al. [14] studied the effects of jet-grid turbulence on a flat plate turbulent boundary layer. This investigation also concluded that increases in the freestream turbulence increase the skin friction, but the universal velocity and temperature profiles at the downstream developed region were unaffected by the jet-grid generated turbulence intensity. Additionally, the work of Bons et al. and others [15–18] provided valuable information on turbulence generation which was used to design the turbulence generator used in this study. Blair [19–21] studied boundary-layer transition and profile development in accelerating flows with free-stream turbulence. He reported that transition onset occurred upstream of the critical Reynolds number, the transition Reynolds number was insensitive to acceleration at even moderate turbulence levels, and that the ratio of u'/v' were about equal to those expected for equilibrium boundary-layer turbulence. Volino and Simon [22] reviewed experimental studies of two-dimensional boundary layers undergoing bypass transition to characterize the effects of freestream turbulence, acceleration, and curvature on bypass transition. This review concluded that, among other things, local coordinates (Re_{δ^*} and Re_{θ}) were useful in reducing and comparing data and that acceleration had a pronounced effect on both transition and on turbulent flow behavior. The authors also developed a formulation to capture the effects of pressure gradients [23]. Zhou and Wang [24,25] investigated the combined effects of freestream turbulence and streamwise acceleration on flow in transitional boundary layers. They determined that freestream turbulence has a greater effect than freestream acceleration on flow structures in transitional boundary layers. Keller and Wang [26–28] investigated the mean and fluctuation quantities of intermittent flow and thermal structures in accelerating transitional boundary layers. These investigations determined that the values for the friction coefficient in the nonturbulent and turbulent areas deviated significantly from laminar and turbulent correlations, that the fluctuating values in the turbulent portion of the transitional flows were higher than those values in the fully developed turbulent flow, and that streamwise acceleration delays the point of transition, both in terms of distance and Reynolds number based on downstream distance.

Mayle [29] provided a review of the effects of freestream turbulence and pressure gradient on transitional flows and a thorough review of transitional flow in high-pressure turbine stages. He concluded that throughflow turbulence levels in typical engines ranges from 5% to 10% and that bypass transition is the common mode of transition caused by disturbances in the external flow (freestream turbulence, pressure gradient, and the periodic, unsteady passing of wakes). He also reported that the length of the transitional region depends only on the freestream turbulence and pressure gradient, that transition can occur at two different locations on the same surface at the same time, and that transition can occur within the same general region on a surface as alternating and fluctuating turbulent spots. Finally, Dunn [30] reviewed the influence of axial flow turbine aerodynamics on heat transfer predictions. He reports findings from several investigations on turbine inlet turbulence intensity and that surface degradation results in decreased aerodynamic performance and increased heat transfer.

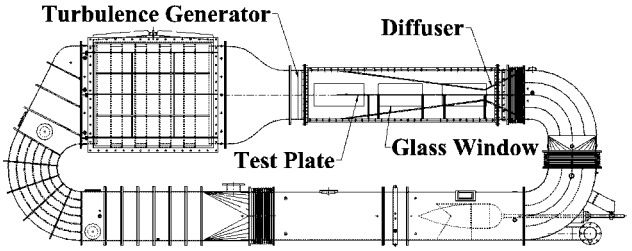

Fig. 1 Schematic diagram of matched-index-of-refraction flow facility with experimental apparatus

In this paper we present the results of our experimental investigation to examine how a *realistic rough patch* influences the flow over the front one third of the suction side of a turbine blade model *in the presence of elevated freestream turbulence and a favorable pressure gradient*.

Experimental Facility and Instrumentation

Measurements were obtained at the matched-index-of-refraction (MIR) closed-loop flow system located at the Idaho National Engineering and Environmental Laboratory (INEEL) in Idaho Falls, Idaho (see Fig. 1). This is the largest such MIR Facility in the world. Stoots et al. [31] provides a detailed description of this system.

Velocity and turbulence measurements were obtained with a two-component, TSI fiberoptic-based laser Doppler velocimeter operated in the forward scatter mode. A Model 9832 two-component fiber optic probe with a lens focal distance of 350 mm provided the transmitting optics. Included in the probe is a collimating lens that reduced the measurement control volume size to about 56 μm by 874 μm in the mineral oil. The laser is a water-cooled, 4-W argon-ion Model Lexel 95. A TSI Model CB-2F "Colorburst" provided beam splitting and frequency shifting. The receiving optic is connected to a Model 9320-2 "Colorburst Plus" multicolor receiver. Signal analysis and data processing were accomplished with a Model S65-2 two-component signal analysis system including a two-channel IFA 650 digital burst correlator and FIND-W Version 1.4 Windows-based software.

A traversing mechanism that can be operated either manually or automatically via the FIND-W software supported the LDV optics. This traversing mechanism could move the laser optics in all three directions relative to the mainstream flow direction (horizontally, vertically, and transversely) with a positional accurately of ±0.005 mm.

Optical flow measurement techniques, such as LDV, permit flow-field determination without locating transducers in the flow. By using transparent models, complex flow fields can be studied and the results can be used to assess the validity of computational fluid dynamic codes for difficult conditions. However, refraction of light beams can distort the views, introduce positioning errors and block measurements in some desired regions. Budwig [32] reports that a solution to these difficulties is to match the indices

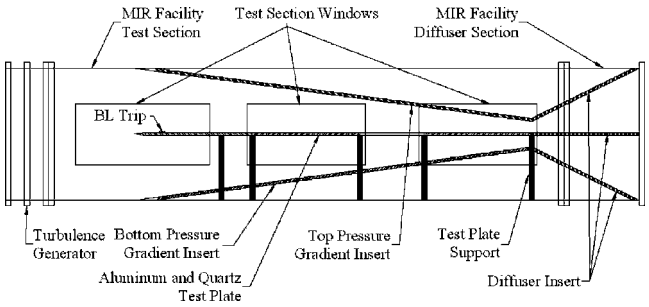

Fig. 2 Schematic drawing of test section

of refraction of the model and the fluid so that light rays are not deflected. While the INEEL MIR flow system has the refractive matching advantage that permits measurements that would otherwise be impossible, its innovation and technical significance is its large size. It is considerably larger than most other systems using the MIR technique; consequently, it provides significantly better spatial and temporal resolution at a given Reynolds number, typically by an order-of-magnitude.

The LDV velocity and turbulence data were obtained in the flowing oil in the test section with "natural seeding;" separate seeding was not necessary. Preliminary measurements demonstrated that the streamwise and spanwise mean velocity profiles and turbulence levels were essentially uniform and documented the freestream turbulence level at the model inlet. The average mean relative uncertainty for smooth plate measurements was estimated at 0.24% for the mean velocity (ε_1) and 8.96% for turbulence intensity (ε_2). For the rough patch case, mean relative uncertainty was estimated at 0.14% for the mean velocity (ε_1) and 7.01% for turbulence intensity (ε_2).

Measurements consisted of time series data collected at positions along the centerline of the test plate. These data are archived on disks and calculations of the profiles have been accomplished with TSI software, MS Excel, and MATHCAD.

Experimental Apparatus. Figure 2 is a schematic drawing of the experimental apparatus that was installed in the test section of the MIR Facility. The flow medium, light mineral oil, flows from left to right in the diagram. A turbulence generator is located upstream of the test section. The test plate is constructed of aluminum and quartz and is supported by five steel supports. An additional aluminum plate is installed above the test plate to achieve the desired streamwise pressure gradient in the flow, and a similar plate is installed beneath the test plate to provide balance and to control flows on the upper and lower surface of the test plate. Finally, a diffuser is installed at the end of the test plate to prevent excessive losses in the flow loop.

Pressure Gradient Inserts. The pressure gradient inserts are illustrated in Fig. 2. The top and bottom pressure gradient inserts are made of 1.3 cm thick aluminum plate and were placed in the test section to produce an acceleration parameter K of approximately 3×10^{-6}, which is in the range of K values reported by Blair [19], Keller and Wang [26], Volino and Simon [23], Zhou and Wang [25], and others who have conducted related boundary layer studies. We also estimated the value of K using a circular cylinder potential flow model with typical at-altitude high-pressure turbine inlet conditions which confirmed that a K value in the range of 1×10^{-6} to 4×10^{-6} is required.

Turbulence Generator. Figure 3 is a schematic drawing of the 21-tube parallel array active turbulence generator used in this experiment. The turbulence generator is located 45.72 cm (18 in.) upstream of the leading edge of the test section. The tubes are spaced on 2.54-cm centers (M=2.54 cm) and have 1/16-in. holes on the *downstream* side of the array for secondary flow injection.

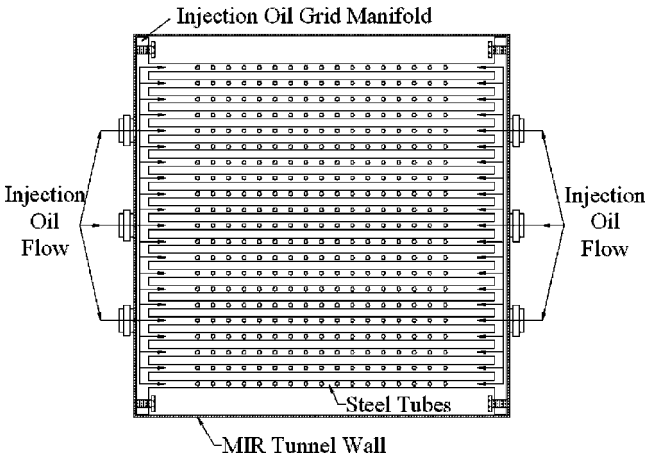

Fig. 3 Schematic drawing of turbulence generator

Injection oil is provided through a parallel auxiliary flow loop powered by a separate pump. Elevated freestream turbulence intensity is essential in this study because the flows exiting the combustor and entering the first stage of an actual turbine engine are highly turbulent as described by Bons et al. [15], Lake et al. [17], Giel et al. [16], and Radomsky and Thole [33]. The freestream turbulence intensity at the leading edge of the test plate was measured at between 6% and 7%. In addition, in accordance with the findings of Blair [19] and Young et al. [14], the turbulence at 20 grid mesh lengths downstream ($x/M=20$) was homogeneous. In the present apparatus the leading edge of the plate is located at $x/M=18$.

Test Plate. The test plate is shown in Fig. 4. The test plate is made of three sections of 1.3-cm-thick aluminum plate and two sections of 1.3-cm-thick GE124 clear fused quartz. The first section of the aluminum test plate section is 15.2 cm long with the leading edge machined into the shape of a NACA 009 airfoil. A turbulence trip is located in this section 118.7 mm downstream of the leading edge. The trip consists of four staggered rows of dowel pins across the plate. For the smooth plate base case a smooth, flat quartz plate was installed so that it was centered in the middle window section and the trailing edge of the test plate had a second smooth, flat quartz plate installed so that it was centered in the right glass window of the test section. The centerline locations at which velocity profile measurements were taken are indicated in the figure.

The rough patch was fabricated out of a 4 in. by 23 in. rectangular block of aluminum. Because of budget constraints we could only fabricate a small rough section that represented only about 5% of the test surface. The roughened surface would be much larger on an actual turbine blade. The rough patch model was patterned after Surface No. 22 (a suction-side surface) that was evaluated by Bons et al. [4]. Bons provided a detailed description of this surface in a single data file that contained a 1000×1000 data point matrix in MATLAB format. This matrix identified the distance in micrometers below a reference plane that describe the

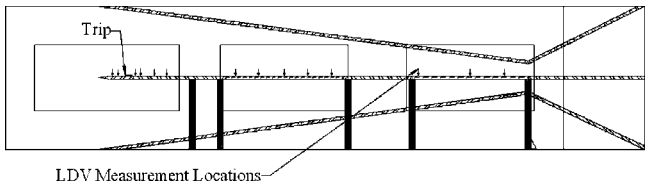

Fig. 4 Schematic drawing of the locations where LDV velocity profile measurements were obtained for the smooth plate base case

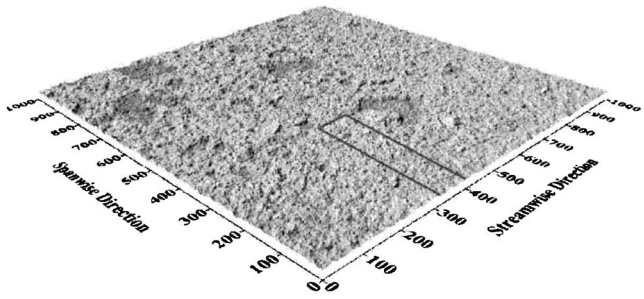

Fig. 5 Picture of the complete rough surface of the suction surface of a land-based power turbine rotor blade measured by Bons et al. [4]

rough surface at 15-μm intervals in the spanwise direction and 14.9-μm intervals in the streamwise direction. This surface was scaled for the present experiment in accordance with the technique reported by McIlroy et al. [34].

The rough patch data provided by Bons was analyzed and a small portion of the surface was selected for use in the aluminum model. Figure 5 is a picture of the complete rough surface measured by Bons. The small section highlighted by the rectangular box along the right side of the picture was selected for use in this study. This small area of the surface was selected because it was representative of the entire surface but did not include the large spallations or relatively tall peaks present in other areas.

Figure 6 is a picture of the rough surface that resulted from the scaling operation (see McIlroy et al. [34]).

The data for this rough patch was transferred to Microsoft Excel and subsequently reorganized/converted into a three-column x, y, z format via a C program code for transmission to the fabrication site (see Dalling [35]). This data was then used to generate a solid model of the surface using Rhino 3-D and saved as an.iges file. The.iges file was transferred to MasterCam in order to generate G-code to drive a CNC milling machine. The resulting 47-MB G-code file was subdivided into 45 segments for the actual milling operation, which took 27 h to complete. Figure 7 shows the results of this process. Figure 7 shows the rough surface machined in an aluminum plate with quartz plates on either side—all installed in the test section of the oil tunnel. The spanwise centerline of the rough patch was located at exactly 700 mm downstream of the leading edge of the test plate.

Table 1 lists the roughness parameters for this surface that were calculated from the scaled-up rough surface data.

Figure 8 is a schematic drawing of the test plate with the rough patch that was installed for the rough patch case study. The centerline locations at which velocity profile measurements were taken are indicated in the figure. Additional measurements were

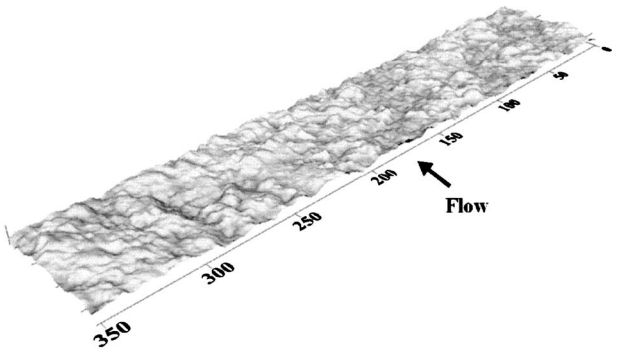

Fig. 6 Picture of the scaled rough surface used to fabricate the rough patch in a 4 in. by 20 in. aluminum plate

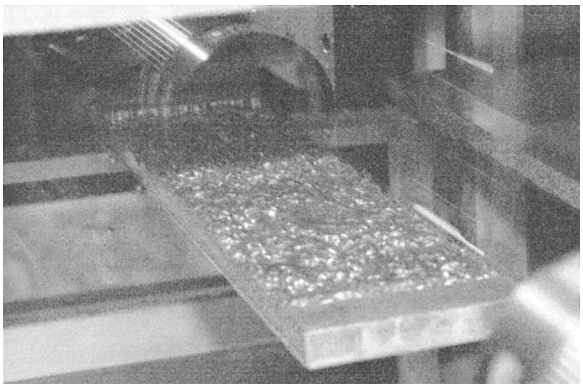

Fig. 7 The 4 in. by 20 in. realistic rough patch installed in the test section of the oil tunnel

taken about 44 mm off-center where a peak of the rough patch was within the vertical range of the horizontal LDV beams, but are not shown on this drawing.

Results of Smooth Plate Base Case Study

Figure 9 displays the measured freestream velocity, acceleration parameter (K), Reynolds number based on the downstream distance from the leading edge (Re_x), and the freestream turbulence intensity for the smooth plate case. This data establishes that the acceleration parameter is in the range identified by other investigations [19,23,25,26]. The figure also establishes that the Reynolds number based on the distance from the leading edge to the measurement location is consistent with the Reynolds numbers reported by Mayle [29], Dunn [30], and Bunker [13]. Additionally, the Reynolds numbers achieved here are in agreement with the Reynolds number calculated for a first stage high-pressure turbine blade for an aircraft gas turbine with the same engine operating conditions used to calculate the acceleration parameter. These calculations verify that the Reynolds number achieved in this experiment could adequately model the front 67% to 71% of an actual turbine blade with an axial chord length of 69 mm. The freestream turbulence intensity displayed is also in excellent agreement with the data presented by Mayle [29] and Dunn [30].

Figure 10 displays the velocity profiles measured at the locations shown in Fig. 4 for the smooth plate case. The data reveals profiles that, in the Cartesian (or outer) coordinates used in the figure, the velocity profiles generally resemble flow with a well developed turbulent boundary layer. The first four profiles (x =61, 82, 162, and 185) are quite flat and do not resemble the

Table 1 Rough patch parameters calculated from scaled up data

Parameter	Value
R_a	1.261 mm
R_{rms}	1.655 mm
R_z	10.219 mm
Sk	0.283
Ku	1.377

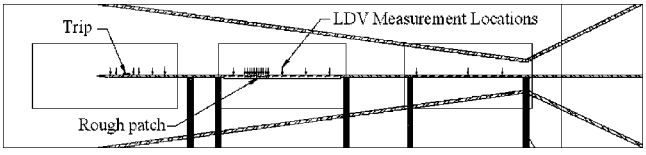

Fig. 8 Schematic drawing of the locations where LDV velocity profile measurements were obtained for the rough patch case

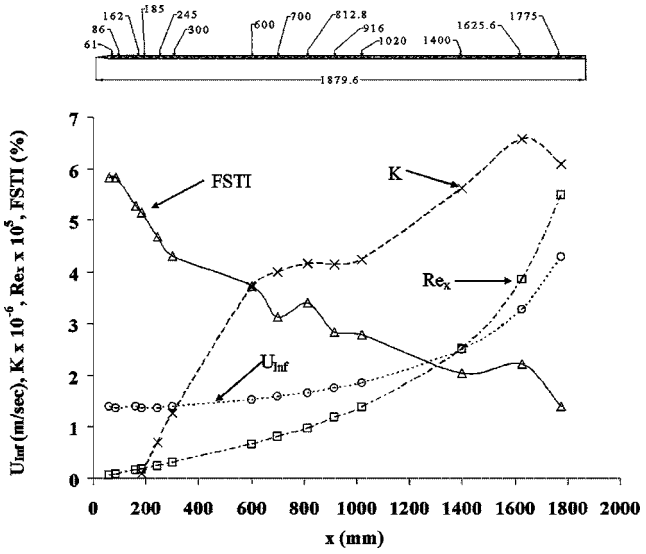

Fig. 9 Freestream velocity, acceleration parameter *K*, Reynolds number based on distance from the leading edge, and freestream turbulence intensity for the smooth plate case with sketch of test plate (dimensions in millimeters)

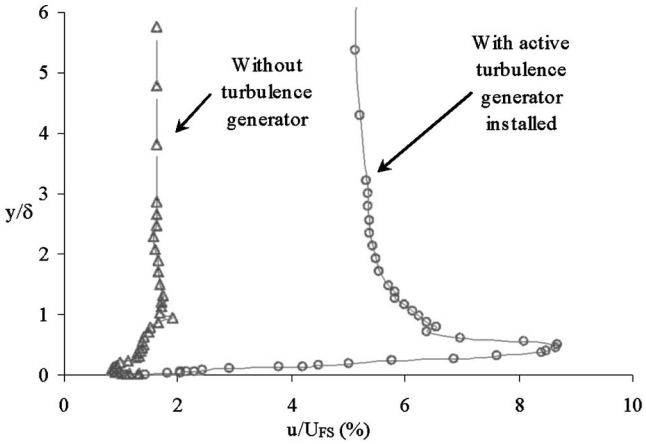

Fig. 11 Streamwise turbulence intensity for the smooth plate case at *x*=61 mm without a turbulence generator installed and with the turbulence generator installed and operating in the active, downstream injection mode

profile that could be expected at such an early stage of flow along the test plate if natural laminar-to-turbulent transition occurred. As reported by Blair [21] the interaction of the airfoil leading edge with an elevated freestream turbulence field may produce instantaneous, local separations and provide a path to transition. Accordingly, the shape of the velocity profiles just downstream of the leading edge indicates that the boundary layer is unstable very early in its flow over the test plate.

Figure 11 describes the streamwise turbulence intensity at $x=61$, the first measurement location. This position on the model represents flow on an actual airfoil only 0.5 mm downstream of the leading edge or stagnation point of the flow (based on a 69-mm blade chord length). The chart displays the streamwise turbulence intensity both with the turbulence grid installed (and operating with active, downstream auxiliary injection) and without a turbulence grid installed. The data establish that without a turbulence grid installed the streamwise turbulence intensity is nearly constant through the boundary layer and into the freestream at 1% to 2%. With the turbulence grid installed and operating in the active mode the streamwise turbulence intensity is almost 9% very near the surface and over 5% in the freestream. This high level of turbulence near the surface reinforces the indication that bypass transition occurred very early in the flow over the test plate. Also, this indicates that the flow in the first 0.8% of an actual blade may also be activated and very unstable.

Figures 12 and 13 display the velocity profiles measured at the locations shown in Fig. 4 for the smooth plate case in wall coordinates. Figure 12 displays velocity profiles for the first 6 measurement locations ($x=61$ to 300) and Fig. 13 displays the velocity profiles from $x=300$ to the end of the test plate. The profiles in Fig. 12 describe a boundary layer that displays laminar-like behavior near the leading edge of the test plate that gradually transitions to turbulent-like behavior at $x=300$. The profiles in Fig. 13 display a turbulent-like boundary layer at $x=300$ that then begins a gradual reverse transition to laminar-like behavior towards the end of the test plate.

Figure 14 displays the growth of the boundary layer thickness and integral parameters derived from measurements as the flow passes over the plate. This data confirms that the boundary layer thickness increases dramatically very early in the flow and continues to increase until measurement location $x=916$, where it begins to decrease almost as dramatically until the end of the test plate. The data also reveal that the trip mechanism, located at from $x=119$ mm to $x=144$ mm from the leading edge, had no apparent effect on the boundary-layer thickness or momentum thickness and only a slight effect on the displacement thickness. The curves for the boundary-layer thickness and momentum thickness appear

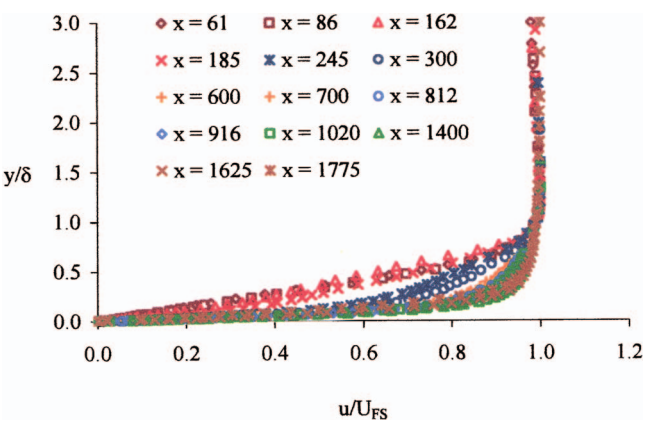

Fig. 10 Boundary-layer velocity profiles of smooth plate case in Cartesian coordinates

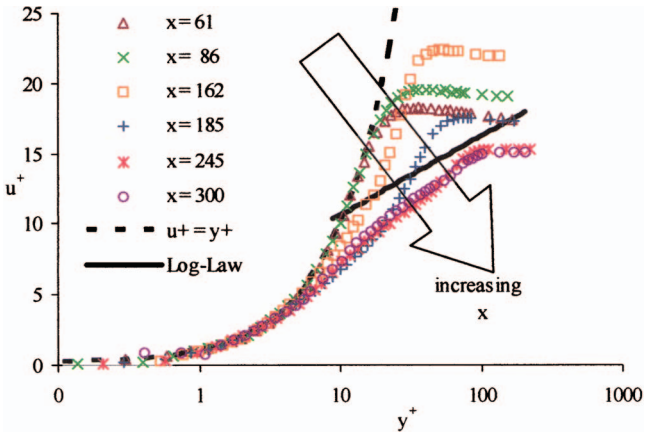

Fig. 12 Boundary layer velocity profiles at locations *x*=61 mm to *x*=300 mm in wall coordinates

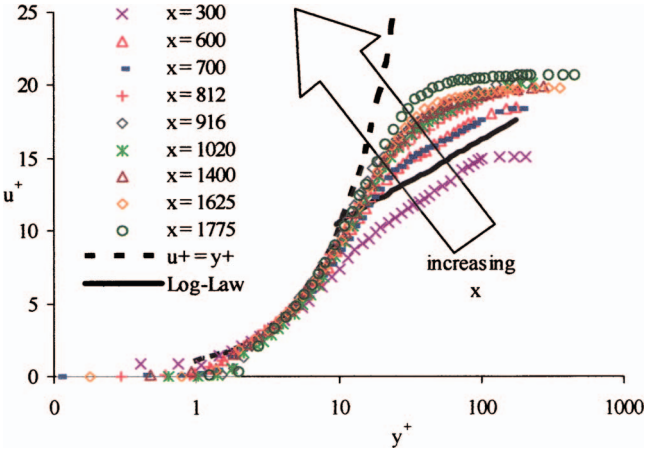

Fig. 13 Boundary-layer velocity profiles at locations x =300 mm to x=1775 mm in wall coordinates

to be generally smooth in Fig. 14 over the area where the trip is installed, but the displacement thickness curve displays a slight bump at measurement location $x=162$, which is the first measurement location downstream of the trip mechanism.

Figure 15 displays the momentum thickness Reynolds number (Re_θ) as it develops along the test plate. Blair [21] notes that at high freestream turbulence levels transition onset occurs at $Re_\theta \leqslant 154$. This observation appears to confirm, again, that transition onset occurred well forward on the test plate.

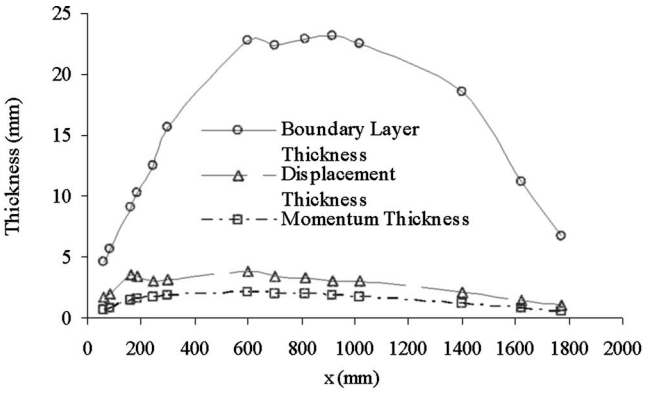

Fig. 14 Boundary-layer thickness and integral parameters for the smooth plate case

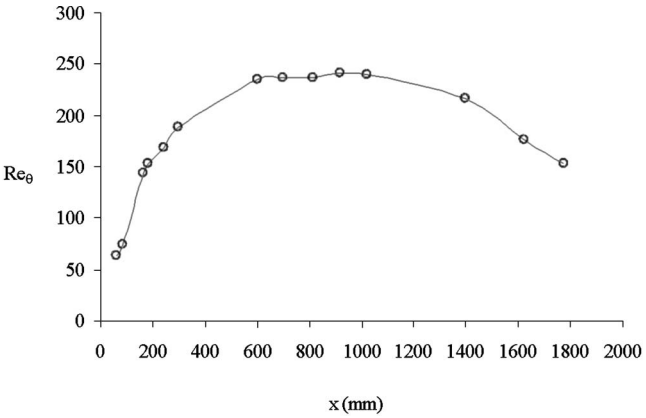

Fig. 15 Smooth plate case momentum thickness Reynolds numbers

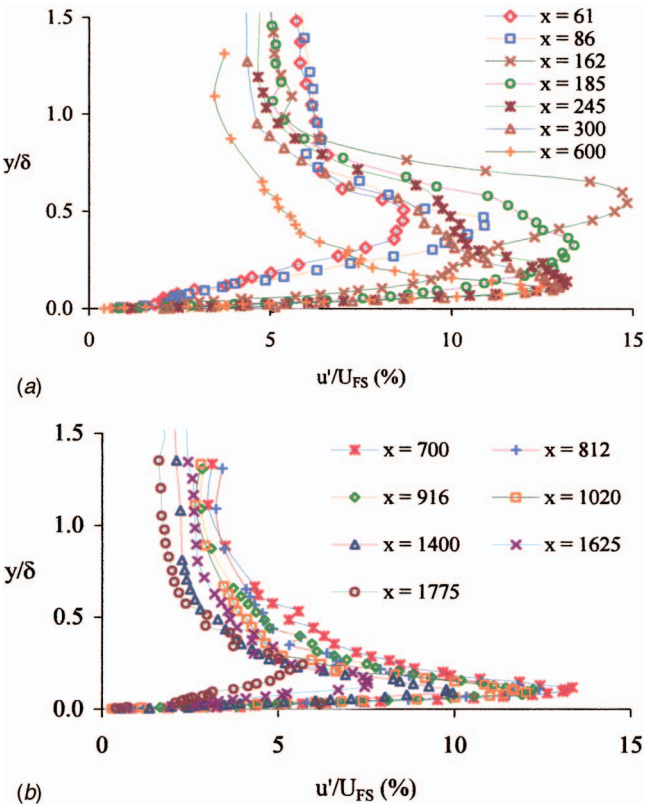

Fig. 16 (*a*) Measured streamwise turbulence intensity profiles for upstream half of test plate. (*b*) Measured streamwise turbulence intensity profiles for downstream half of the test plate.

Figures 16(*a*) and 16(*b*) display the measured streamwise turbulence intensity profiles at all measurement locations. The data is displayed in two charts so that the individual profiles are identifiable. These data confirm that there is significant turbulence in the boundary layer at every measurement location, and that even when the boundary layer velocity profile displays laminar-like behavior (see Fig. 12) the boundary layer is highly unstable and appears to be in transition.

Figures 17(*a*) and 17(*b*) display the measured normal turbulence intensity profiles at those measurement locations where the normal (v) velocity component could be measured. The data confirm that the normal turbulence intensity profiles are consistent with wall turbulent shear flows described in the literature.

Figures 18(*a*) and 18(*b*) display the absolute value of the Reynolds shear stress at the same measurement locations used in Fig. 17. These data establish that there is significant x-momentum transport in the direction normal to the plate surface deep within the boundary layer. The behavior displayed in Figs. 16–18 is consistent with the behavior of transitional boundary layers described by Fernholz and Warnack [36], Keller and Wang [26], Radomsky and Thole [37], and Zhou and Wang [24].

Figure 19 is a display of the friction coefficient that was calculated from measured data using the wall-slope method, the friction coefficients calculated with the Thwaites relationship for an accelerating, laminar, two-dimensional, steady flow over a smooth, flat plate, and the boundary layer shape factor also calculated from experimental data. The experimental values of the friction coefficient agree quite well with the Thwaites values for the first three measurement locations, then rise quickly to a maximum at x =300. The values of the friction coefficient then fall to values that approach the laminar predictions as the flow proceeds toward the end of the test plate. This trend is consistent with the behavior observed in Figs. 12 and 13 and confirm that the flow is in tran-

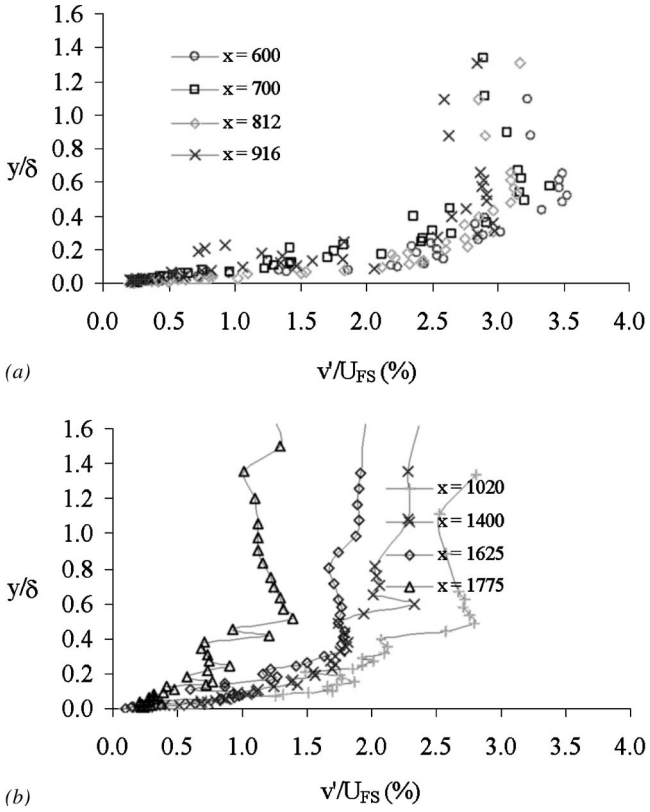

Fig. 17 (*a*) Measured normal turbulence intensity profiles at upstream measurement locations where the *v* component was available. (*b*) Measured normal turbulence intensity profiles at downstream measurement locations where the *v* component was available.

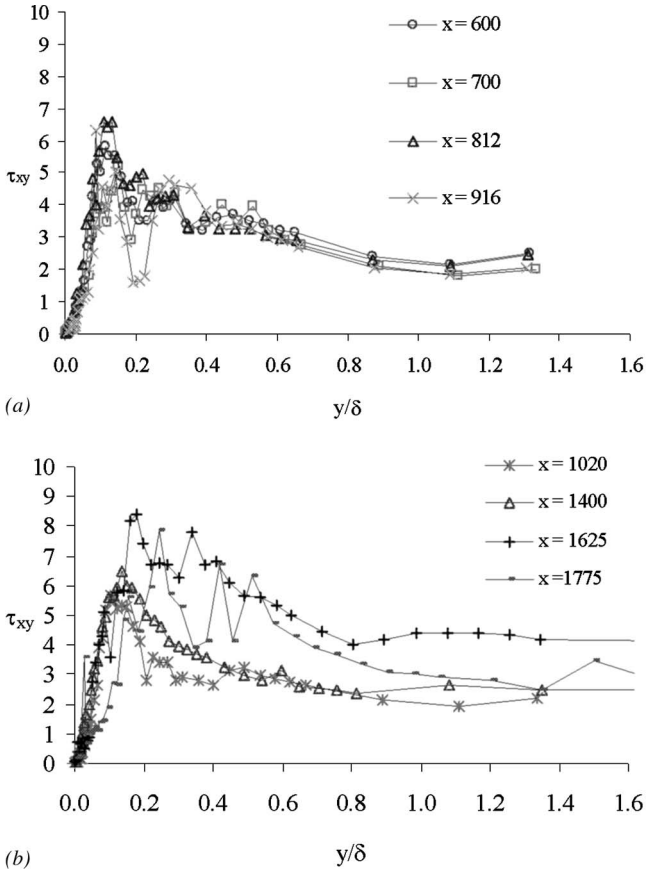

Fig. 18 (*a*) Absolute value of the Reynolds shear stress at upstream measurement locations where the *v* component was available. (*b*) Absolute value of the Reynolds shear stress at downstream measurement locations where the *v* component was available.

sition from laminar-like behavior to turbulent-like behavior up to $x=300$, and retransitioning from that point to laminar-like behavior at the end of the test plate.

Results of Rough Patch Study

The freestream flow for the rough patch case was established so that it was essentially identical to that of the smooth plate case with a similar acceleration parameter, Reynolds numbers (Re_x), and freestream turbulence intensity. Figure 20 displays three representative boundary layer velocity profiles measured along the flow centerline. The rough patch was located from $x=650$ to $x=750$. The profiles in this figure are very similar to those observed in Fig. 10 in that they are all quite "flat" and generally resemble the profiles of a well developed turbulent boundary layer. The data points below the horizontal axis near the origin are a result of measurements that were obtained over the rough surface where the LDV system could reach below the plane of the smooth surface.

Figures 21 and 22 display the boundary layer velocity profiles in wall coordinates of the flow measured where both velocity components were available to the LDV system. Figure 21 describes flow that has become turbulent again after beginning to retransition from turbulent-like behavior toward laminar-like behavior earlier in the flow at $x=300$ (see Figs. 12 and 13 for profiles upstream of $x=600$). Note that the flow at $x=600$ is essentially identical to the flow at $x=600$ described for the smooth plate case in Fig. 13 after it began to transition toward laminar-like behavior. However, in the rough patch case shown in Figs. 21 and 22, downstream of $x=600$ the rough patch appears to cause the flow to reverse the turbulent-to-laminar transition process observed in the smooth plate case and to begin transition, again, to turbulent-like behavior from $x=600$ to $x=795$. Additionally, the transition from turbulent-like behavior at $x=795$ to laminar-like behavior at $x=1775$ shown in Fig. 22 takes place in less time and distance than was observed in the transition from turbulent-like behavior to laminar-like behavior in the smooth plate case. In the smooth plate case, the transition from turbulent-like behavior to laminar-like behavior occurred from $x=300$ to $x=1775$ (see Fig. 13). In the rough patch case, the flow became turbulent-like again

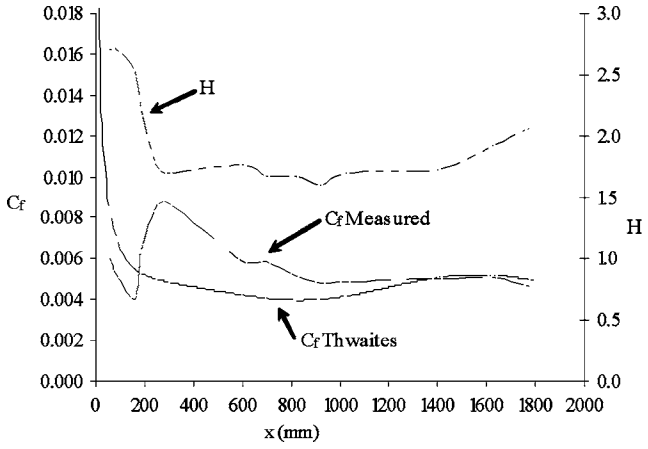

Fig. 19 Experiment and theoretical values of the friction coefficient and the boundary-layer shape factor

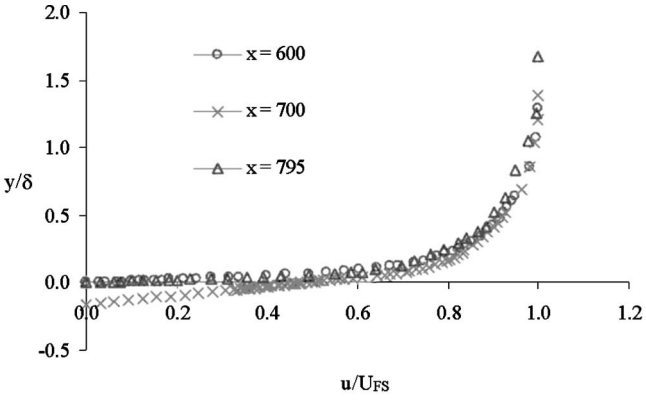

Fig. 20 Boundary-layer velocity profiles of the rough patch case in Cartesian coordinates

at $x=795$, but still completed transition to laminar-like behavior by $x=1775$. The retransition to laminar-like behavior in the smooth plate case occurred over a distance of about 1475 mm, whereas this same retransition downstream of the rough patch occurred over only 980 mm. The difference in the distance required (495 mm) represents roughly 28% of the test plate length. Additionally, close inspection of the profile for $x=1775$ for the rough patch case in Fig. 22 indicates that this profile is slightly more laminar-like than the profile at $x=1775$ for the smooth plate case shown in Fig. 13.

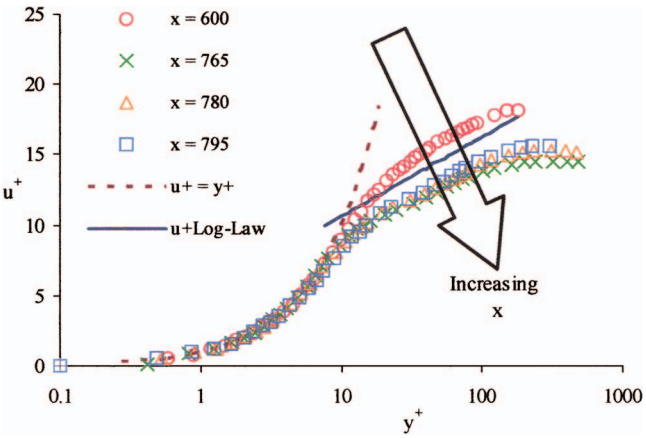

Fig. 21 Boundary-layer velocity profiles of the rough patch case for $x=600$ to $x=795$ in wall coordinates

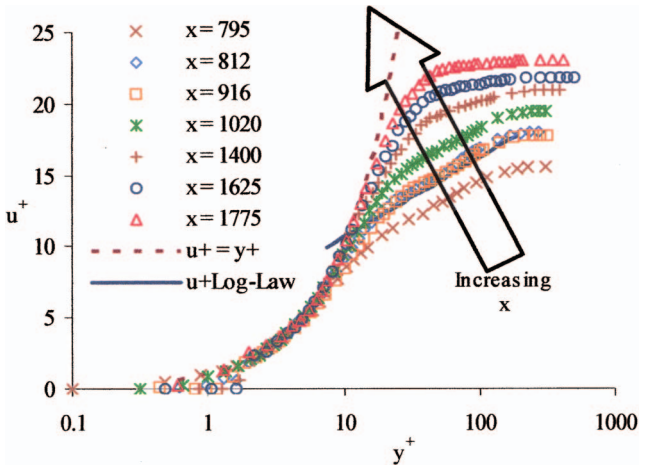

Fig. 22 Boundary-layer velocity profiles of the rough patch case for $x=795$ to the end of the test plate in wall coordinates

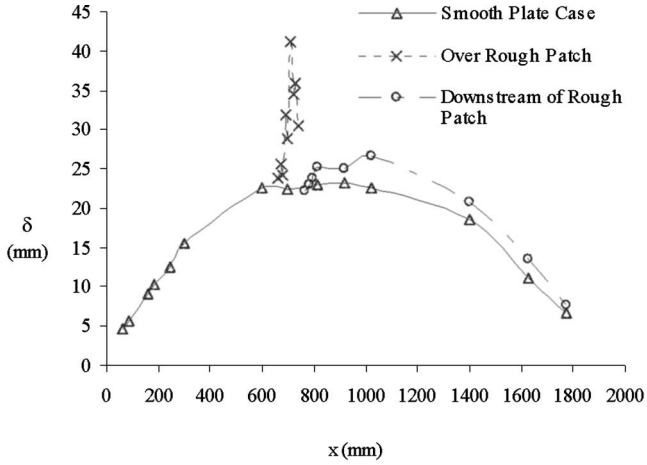

Fig. 23 Boundary-layer thickness for the rough patch case compared to the smooth plate case

Figure 23 displays the growth in the boundary layer thickness for the flow over the rough patch and the flow downstream of the rough patch compared to that of the smooth plate case. The red X's describe measurements over the rough patch (from $x=660$ to $x=740$ at 10-mm intervals) and the open circles connected by the green dash-dot line are measurements taken downstream of the rough patch starting at $x=765$. All of the values of the boundary layer thickness shown in Fig. 23, including the values for the boundary-layer thickness over the rough patch, were determined by using the plane of the smooth surface ($y=0$) as the reference plane. The data show a dramatic increase in the boundary layer thickness over the rough patch, then a similarly dramatic decrease to levels above the smooth plate case for the remainder of the flow. This large increase in boundary-layer thickness is consistent with the impact on boundary-layer flow that could be expected from the influence of the steep backward-facing step, the deep cavity that included a rough surface with dramatic elevation changes, and a second steep upstream-facing step that was encountered as the flow returned to the plane of the smooth surface (see Fig. 26).

Figures 24 and 25 display the boundary layer displacement thickness and the boundary layer momentum thickness that was calculated from measured data. As shown in the Fig. 24, the displacement thickness varies significantly over the rough patch

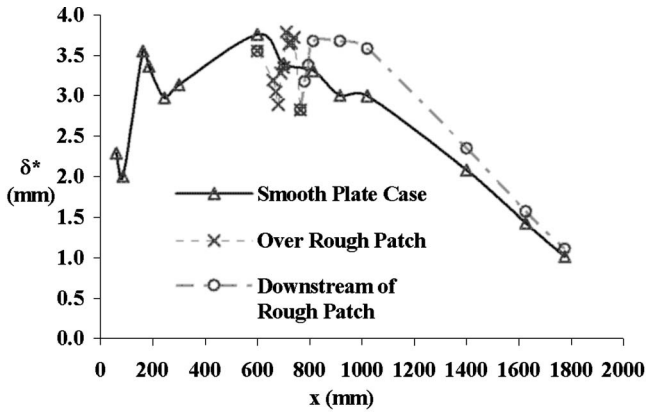

Fig. 24 Boundary-layer displacement thickness for the rough patch case compared to the smooth plate case

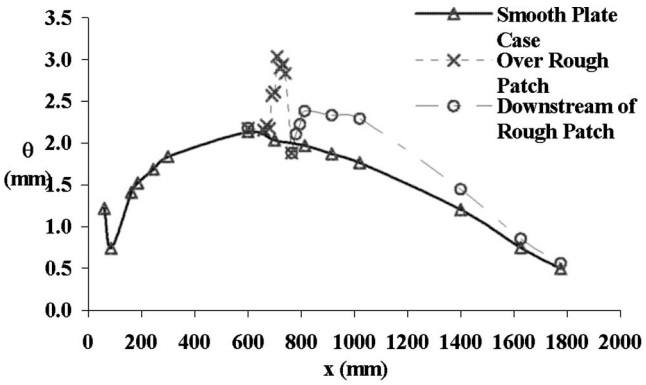

Fig. 25 Boundary-layer momentum thickness for the rough patch case compared to the smooth plate case

compared to the smooth plate values and remains greater than the smooth plate values for the remainder of the flow. In addition, the momentum thickness over the rough patch shown in Fig. 25 is greater than the smooth plate value then, similar to the displacement thickness, remains greater than the smooth plate value for the remainder of the flow. The values shown for the displacement thickness and the momentum thickness over the rough patch were calculated using the plane of the smooth surface as the reference plane ($y=0$) in order to provide a reference plane for these parameters that is consistent with the reference plane used in the smooth plate case. Therefore the integration limits used for these parameters were from the plane of the smooth surface (the reference plane ($y=0$) to the freestream. Again, the data appear to be consistent with what are likely to be expected as the flow *passes over the rough patch cavity*, as noted above. The variation observed in the displacement and momentum thickness profiles may be attributed to the rugged profile of the rough surface. As shown in Fig. 26, the displacement thickness and momentum thickness profiles are similar to the profile of the rough surface. The displacement thickness and momentum thickness decline as the rough surface drops away steeply from the plane of the smooth surface (vertical line on the left edge of the rough surface profile), then dives deeper into the cavity for about a third of the patch length. Both thicknesses then rise as the rough surface rises to a peak about half way through the cavity, then both drop again as the profile dives deeply before rising abruptly to the level of the smooth surface (vertical line on the right edge of the rough surface profile). These variations in elevation and the increased turbulence normal to the streamwise flow (see Fig. 28) are likely to affect the rate of change of the local streamwise velocity and therefore the

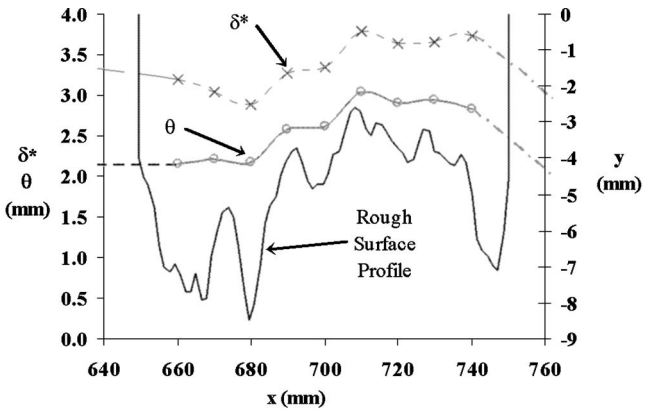

Fig. 26 Boundary-layer displacement thickness and momentum thickness over the rough patch with rough patch profile

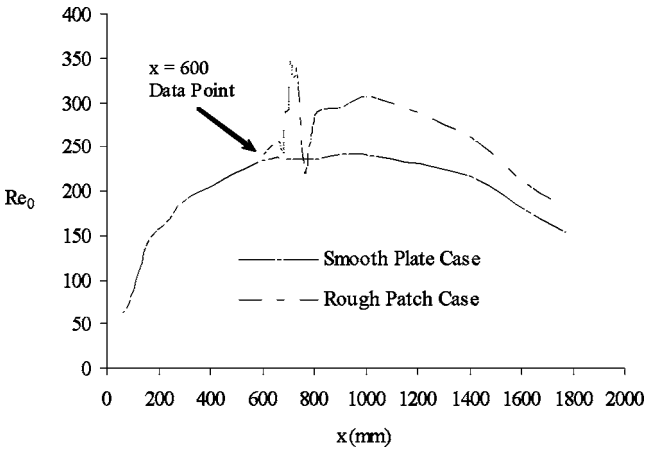

Fig. 27 Comparison of the momentum thickness Reynolds number (Re_θ) for the smooth plate case and the rough patch case

relative growth or shrinking of the integral parameters.

Figure 27 displays the Reynolds number based on momentum thickness (Re_θ) for the smooth plate case and the rough patch case. The chart establishes that Re_θ at measurement location $x=600$ for both the smooth plate case and rough patch case are in excellent agreement. Re_θ then drops below the smooth plate value at measurement location $x=765$. This drop in value of Re_θ is due to a sharp edge encountered by the flow at the trailing edge of the rough patch. Immediately downstream of measurement location $x=765$ Re_θ increases to values 22% to 28% greater than the smooth plate case and continues to remain 16% to 20% above the smooth plate case value for the remainder of the flow.

Figures 28(*a*) and 28(*b*) display the streamwise turbulence in-

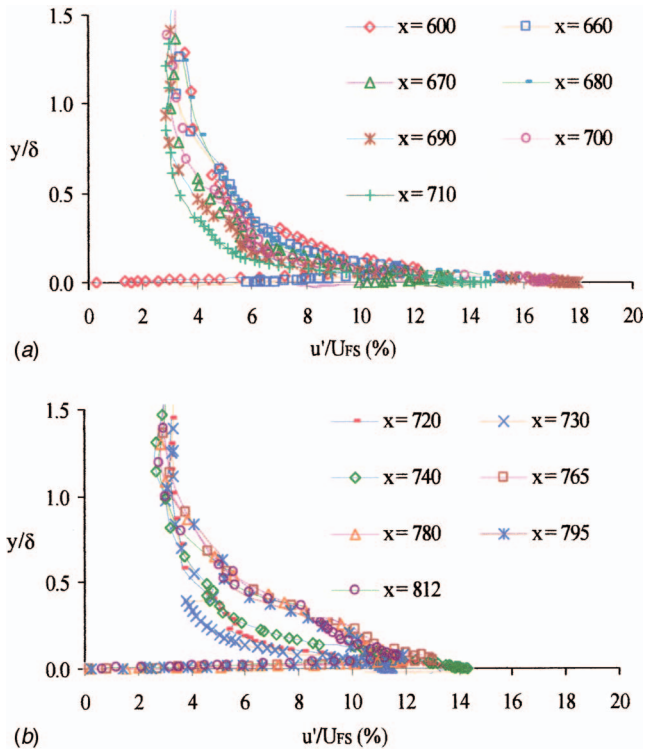

Fig. 28 (*a*) Streamwise turbulence intensity for the rough patch case. (*b*) Streamwise turbulence intensity for the rough patch case.

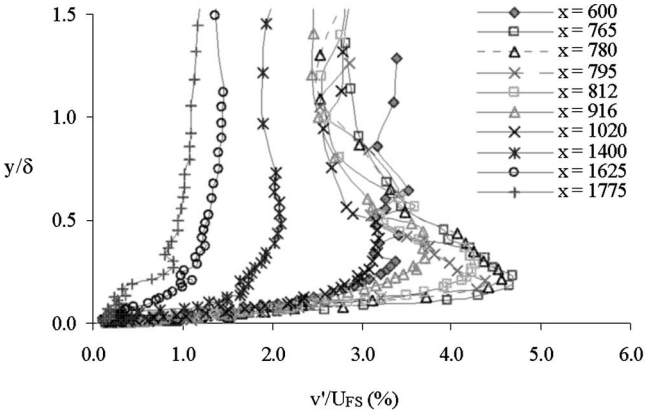

Fig. 29 Normal turbulence intensity for the rough patch case

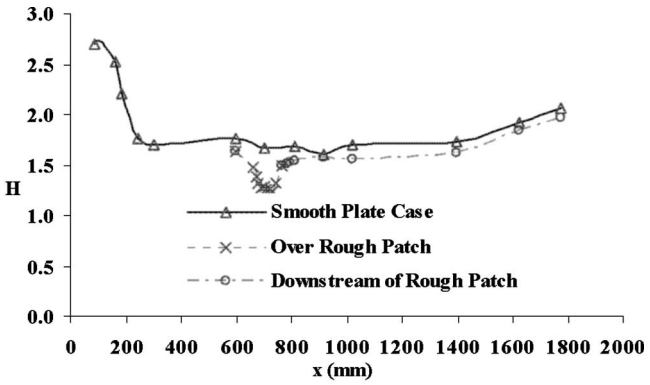

Fig. 30 Boundary layer shape factor for the rough patch case compared to the smooth plate case

tensity obtained from measured data over the rough patch and just downstream of the rough patch. As in the smooth plate case, the data establishes that there is significant streamwise turbulence in the boundary layer at every measurement location. In addition, as in the smooth plate case, even toward the end of the test plate where the flow exhibits laminar-like behavior, the boundary layer is highly unstable. These data confirm that the boundary layer in the rough patch case remains highly unstable over the entire length of the test plate. In addition, a comparison of the charts in this figure with those in Fig. 16 indicate that the maximum streamwise turbulence intensity measured within the boundary layer over the rough patch is 20% to 30% greater than the smooth plate value and 2% to 9% greater downstream of the rough patch compared to the same positions on the smooth plate. This finding indicates that the rough patch has significant effect on the streamwise turbulence intensity inside the boundary layer.

Figure 29 displays the normal turbulence intensity for the rough patch case for the same measurement locations displayed in Figs. 21 and 22. Note that the profiles for $x=600$ in this figure (solid green diamonds) are essentially the same as those for $x=600$ in Fig. 17. As in the smooth plate case, the data confirm that the normal turbulence intensity profiles are consistent with wall turbulent shear flows described in the literature. The normal turbulence intensity profiles at measurements locations $x=765$ through $x=1400$ describe substantially different profiles than those shown in Fig. 17 for the smooth plate case. The rough patch case normal turbulence intensity profiles at these locations describe obvious peaks that are both higher in turbulence intensity and slightly closer to the plate surface than those described for the smooth plate case. The maximum normal turbulence intensity at measurement location $x=812$ is over 38% higher and occurs slightly closer to the surface than its smooth plate counterpart. This trend continues toward the end of the plate with the maximum normal turbulence intensity about 25% higher than its smooth plate counterpart at measurement location $x=916$, about 14% higher at measurement location $x=1020$ and finally to only 12% higher at measurement location $x=1400$. The normal turbulence intensity profiles at the last two measurement locations closely resemble the profiles of the same measurement locations for the smooth plate case, but the maximum normal turbulence intensity is 16% below the smooth plate value at measurement location $x=1625$ and is about the same as the smooth plate value at measurement location $x=1775$. All of these maximum values of normal turbulence intensity occur at about the same or slightly lower locations in the boundary layer than the normal turbulence intensity peaks in the smooth plate case. This indicates that, similar to the indication for the streamwise turbulence, the rough patch has a substantial impact on the normal turbulence intensity inside the boundary layer.

Figure 30 displays the boundary layer shape factor of the flow over the rough patch and downstream of the patch compared to the smooth plate values. The data describe a variation in the shape factor consistent with the trends displayed in Figs. 24 and 25. The curve establishes that the shape factor declines early in the flow and declines further as the flow passes over the rough patch cavity. These data describe a trend toward turbulent behavior in the boundary layer.

Figure 31 displays the absolute values of the maximum Reynolds shear stresses for the smooth plate case and the rough patch case downstream of the rough patch. Figure 32 displays a comparison between the locations where these maximum Reynolds stresses occur in the boundary layer for the smooth plate case and rough patch case. The increases in the maximum absolute values of the Reynolds shear stresses and the increase in distance away from the surface where these maximums occur is consistent with the increase in turbulence within the boundary layer and establishes that the rough patch causes a significant increase in x-momentum transport of fluid away from the surface downstream of the rough patch.

Figure 33 displays friction coefficients calculated for the rough patch case compared to those calculated for the smooth plate case. All of these values were calculated from measured data using the wall-slope method. The data establishes excellent agreement between the friction coefficients calculated for the smooth plate case and rough patch case upstream of the rough patch (at $x=600$) where roughness should not affect the flow. The solid squares are the values of the friction coefficient at the off-centerline flow location where velocity measurements beginning at an exposed peak of the rough surface were possible. The remainder of the data points were measured along the centerline flow downstream of the

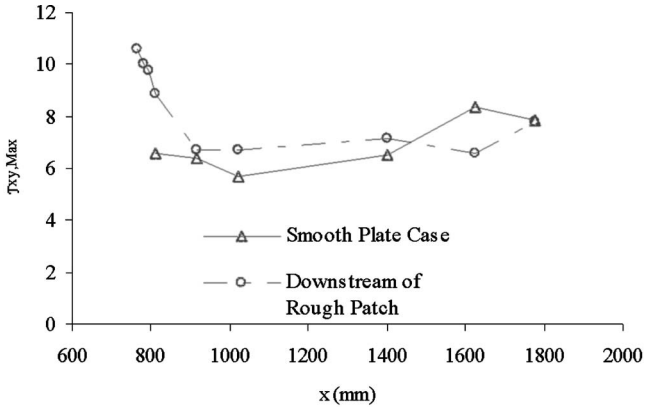

Fig. 31 Comparison of the maximum absolute value of the Reynolds stresses for the rough patch case and the smooth plate case

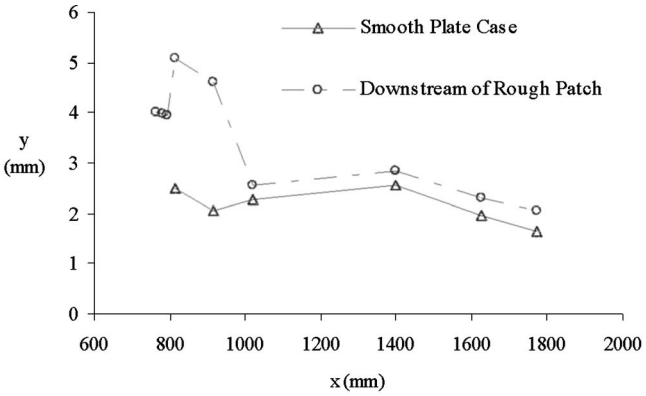

Fig. 32 Comparison of the *y*-location of the maximum absolute value of the Reynolds stresses for the rough patch case and the smooth plate case

rough patch. This data establishes that the friction coefficients over the rough surface are more than 2.5 times the smooth plate values and the rough surface causes the friction coefficients to remain well above the smooth plate values for 360 mm or 20% of the plate length downstream of the rough surface. Additionally, the friction coefficients at the last three measurement locations (trailing edge of the test plate) fall 10%–20% below the smooth plate values, which confirm a stronger return to laminar-like behavior in the rough patch case.

Figure 34 is a surface map of the rough patch that shows the location of the peak (solid squares in Fig. 32) that was available to the LDV system. As a result of the scaling and fabrication process the top of this peak was only about 1.2 mm below the smooth surface plane which was, because of the slight negative angle imposed on the LDV system during setup, within the vertical reach of the horizontal beams. Because of this situation, velocity measurements were possible all the way from the actual rough surface to the freestream. The three skin friction coefficients at this exposed peak were calculated from *measured* data and are described in Fig. 35. The friction coefficient on the slope just upstream of the peak is seen to be more than 2.5 times the value calculated for the smooth plate case near this location (see Fig. 19). The skin friction coefficient decreases very slightly at the peak then falls off dramatically to a value 57% less than the maximum value just downstream of the peak. This rather large drop in the value of the skin friction coefficient indicates the flow may experience separation on the downstream slope of the peak.

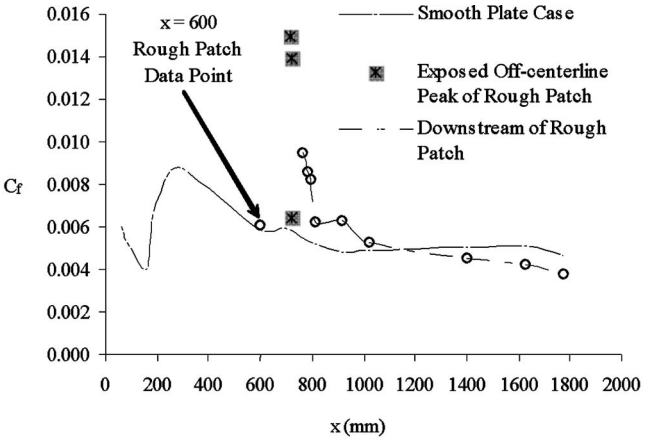

Fig. 33 Comparison of skin friction coefficients for the smooth plate case and the rough patch case

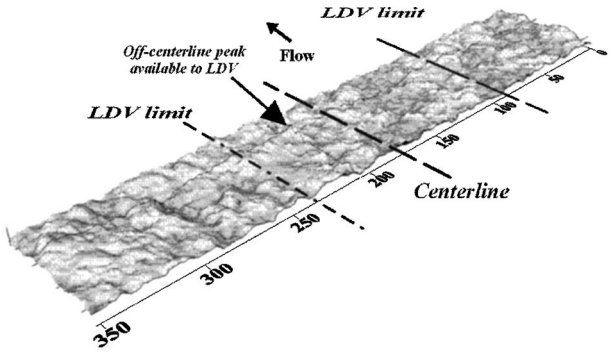

Fig. 34 Surface map of rough patch showing location of peak visible to the LDV system

Conclusions

The data and analysis presented establish that, when flow conditions such as elevated freestream turbulence and an accelerating freestream that are normally associated with flow over the front one third of the suction side of a turbine blade in an actual gas turbine engine are imposed on a flat plate model, the flow becomes highly unstable very early in its passage over the model. This indicates that the boundary layer flow over the front one-third of a high-pressure turbine blade in an actual turbine engine is, contrary to many reports in the literature, not a laminar flow that undergoes transition but in fact a flow that is transitional from a point very close to the leading edge of the blade. The addition of a realistic rough patch to this model was found to have a dramatic effect on the boundary layer flow over the rough patch and downstream of the patch. The boundary layer thickness, displacement thickness and momentum thickness increased, however, because of the elevated freestream turbulence, the trip mechanism had little effect on the boundary layer thickness and the momentum thickness and only slight impact on the displacement thickness. The shape factor increased then fell quickly downstream of the rough patch indicating that the flow was undergoing a gradual reverse transition to laminar-like behavior towards the end of the test plate. In both the smooth plate case and rough patch case reverse transition to laminar-like behavior was achieved by the time the flow arrived at the trailing edge of the plate. However, the reverse transition in the rough patch case occurred in less distance and less time than the reverse transition observed in the smooth plate case. This indicates that the rough patch had little effect on the ultimate reverse transition to laminar-like behavior near the end of the test plate. The rough patch was also responsible for an increase in streamwise and normal turbulence over the rough patch and downstream of the patch, a large increase in Reynolds shear stresses over the rough patch and downstream of the patch

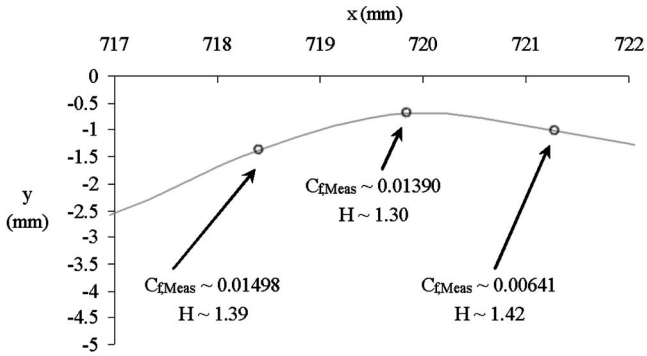

Fig. 35 Blow-up of the rough surface peak with calculated skin friction coefficients

and an increase in the skin friction coefficient over the rough patch by a factor of more than twice the smooth plate value. Finally, the boundary layer was transitional over the entire length of the plate but regions where the boundary layer was more turbulent-like and more laminar-like were clearly described by the shape factor (H) and the friction coefficient (C_f).

Acknowledgment

This research was funded by AFOSR Grant No. F49620-00-1-0265 and supported by DOE Field Office Contract No. DE-AC07-99ID13727. The authors wish to thank Dr. Donald M. McEligot of the Idaho National Laboratory, Prof. Jeffrey P. Bons of Brigham Young University (formerly of the U. S. Air Force Research Laboratory), Dr. Richard B. Rivir at the U. S. Air Force Research Laboratory, Prof. David G. Bogard of the University of Texas, and Dr. Ron S. Bunker of GE Global Research for their kind assistance in this work.

Nomenclature

C_f = skin friction coefficient ($2\tau_w/\rho_\infty U_\infty^2$)
FSTI = freestream turbulence intensity
H = boundary layer profile shape factor (δ^*/θ)
$H(x)$ = channel height at distance x from the leading edge $H(x)=0.115748x-0.3048$ (m)
h = half-width of flow channel ($h=H(x)/2$)
K = acceleration parameter ($(\nu_\infty/U_\infty^2)(dU_\infty/dx)$)
Ku = kurtosis ($(1/N)\Sigma_{i=1}^{N} z_i^4/R_{\text{rms}}^4$)
L_τ = integral time scale ($L_\tau=h/U_\infty$)
M = tube spacing in turbulence generator
N = number of points in profile record
$(\overline{pu'v'})$ = Reynolds shear stress (τ_{xy})
R_a = average centerline roughness height ($(1/N)\Sigma_{i=1}^{N}|y_i|$)
R_{rms} = rms roughness height ($\sqrt{1/N\Sigma_{i=1}^{N} z_i^2}$)
R_Z = maximum peak-to-valley roughness height
Re_x = Reynolds number based on distance from the leading edge (xU_∞/ν)
Re_{δ^*} = Reynolds number based on momentum thickness ($\delta^* U_\infty/\nu$)
Re_θ = Reynolds number based on momentum thickness ($\theta U_\infty/\nu$)
Sk = skewness ($1/N\Sigma_{i=1}^{N} z_i^3/R_{\text{rms}}^3$)
T = data run collection time (integration time)
TI = turbulence intensity (expressed as a decimal)
U_{Inf} = streamwise freestream velocity
U_{FS} = streamwise freestream velocity
u = instantaneous local streamwise velocity component
u' = instantaneous local streamwise velocity fluctuation
$\bar{u}$ = mean local streamwise velocity component
u_τ = friction velocity ($\sqrt{\tau_w/\rho_w}$)
u^+ = nondimensional mean streamwise velocity ($\bar{u}/u_\tau$)
v = instantaneous local normal velocity component
v′ = instantaneous local normal velocity fluctuation
x = horizontal (streamwise) length along surface measured from the leading edge
y = vertical (wall-normal) length measured from the surface
y^+ = nondimensional distance from surface (yu_τ/ν)
z = spanwise distance measured from the oil tunnel lengthwise centerline, vertical distance on rough surface

Greek Symbols

ε_1 = mean relative error for mean velocity ($\varepsilon_1=\sqrt{2TI^2L_\tau/T}$)
ε_2 = mean relative error for turbulence intensity ($\varepsilon_2=\sqrt{4L_\tau/T}$)
δ = boundary layer thickness
δ^* = displacement thickness
ρ = density
μ = dynamic viscosity
ν = kinematic viscosity
τ_{xy} = shear stress
τ_w = wall shear stress
θ = momentum thickness

Subscripts

FS = freestream
rms = root mean square
x = parameter evaluated at location x along the surface

References

[1] Archer, R. D., and Saarlas, M., 1996, *An Introduction to Aerospace Propulsion*, Prentice-Hall, Englewood Cliffs, NJ, pp. 14–24.
[2] Koch, C. C., and Smith, L. H., 1976, "Loss Sources and Magnitudes in Axial-Flow Compressors," J. Eng. Power, **98**(3), pp. 411–424.
[3] Boyle, R. J., and Senyitko, R. G., 2003, "Measurements and Predictions of Surface Roughness Effects on Turbine Vane Aerodynamics," ASME Paper No. GT2003-38580.
[4] Bons, J. P., McClain, S. T., Taylor, R. P., and Rivir, R. B., 2001, "The Many Faces of Turbine Surface Roughness," ASME Paper No. 2001-GT-163.
[5] Taylor, R. P., 1990, "Surface Roughness Measurements on Gas Turbine Blades," ASME J. Turbomach., **112**, pp. 175–180.
[6] Bogard, D. G., Schmidt, D. L., and Tabbita, M., 1998, "Characterization and Laboratory Simulation of Turbine Airfoil Surface Roughness and Associated Heat Transfer," ASME J. Turbomach., **120**, pp. 337–342.
[7] Tarada, F. H. A., 1987, "Heat Transfer to Rough Turbine Blading," Ph.D. thesis, University of Sussex, Falmer, Brighton, UK., pp. 40–42.
[8] Boyle, R. J., 1994, "Prediction of Surface Roughness and Incidence Effects on Turbine Performance," ASME J. Turbomach., **116**, pp. 745–751.
[9] Moon, H. K., O'Connel, T., and Glezer, B., 1999, "Channel Height Effect on Heat Transfer and Friction in a Dimpled Passage," ASME Paper No. 99-GT-163.
[10] Lin, Y. L., Shih, T. I. P., and Chyu, M. K., 1999, "Computation of Flow and Heat Transfer in a Channel With Rows of Hemispherical Concavities," ASME Paper No. 99-GT-263.
[11] Vukoslavčević, P. V., and Wallace, J. M., 2002, "The Simultaneous Measurement of Velocity and Temperature in Heated Turbulent Air Flow Using Thermal Anemometry," Meas. Sci. Technol., **13**, pp. 1615–1624.
[12] McIlroy, H. M. Jr., 2004, "The Boundary Layer Over Turbine Blade Models With Realistic Rough Surfaces," Ph.D. dissertation, Department of Mechanical Engineering, University of Idaho, Moscow, ID, pp. 5–24.
[13] Bunker, R. S., 1997, "Separate and Combined Effects of Surface Roughness and Turbulence Intensity on Vane Heat Transfer," International Gas Turbine & Aeroengine Congress & Exhibition, Orlando, FL., ASME Paper No. 97-GT-135.
[14] Young, C. D., Han, J. C., Huang, Y., and Rivir, R. B., 1992, "Influence of Jet-Grid Turbulence on Flat Plate Turbulent Boundary Layer Flow and Heat Transfer," J. Heat Transfer, **114**, pp. 65–72.
[15] Bons, J. P., Sondergaard, R., and Rivir, R. B., 1999, "Control of Low Pressure Turbine Separation Using Vortex Generator Jets," 37th AIAA Aerospace Sciences Meeting and Exhibit, Reno, NV, Paper No. AIAA 99-0367.
[16] Giel, P. W., Bunker, R., van Fossen, G. J., and Boyle, R. J., 2000, "Heat Transfer Measurements and Predictions on a Power Generation Gas Turbine Blade," NASA/TM-2000-210021, Glenn Research Center.
[17] Lake, J. P., King, P. I., and Rivir, R. B., 1999, "Reduction of Separation Losses on a Turbine Blade With Low Reynolds Number," 37th AIAA Aerospace Sciences Meeting and Exhibit, Reno, NV, Paper No. AIAA 99-0242.
[18] Roach, P. E., 1987, "The Generation of Nearly Isotropic Turbulence by Means of Grids," Am. Inst. Aero. Astro., **8**(2), pp. 82–92.
[19] Blair, M. F., 1982, "Influence of Free-Stream Turbulence on Turbulent Boundary Transition in Favorable Pressure Gradients," J. Eng. Power, **104**, pp. 743–750.
[20] Blair, M. F., 1992, "Boundary-Layer Transition in Accelerating Flows With Intense Freestream Turbulence: Part I. Disturbances Upstream of Transition Onset," ASME J. Eng. Ind., **114**, pp. 313–321.
[21] Blair, M. F., 1992, "Boundary-Layer Transition in Accelerating Flows With Intense Freestream Turbulence: Part II. The Zone on Intermittent Turbulence," ASME J. Eng. Ind., **114**, pp. 322–332.
[22] Volino, R. J., and Simon, T. W., 1995, "Bypass Transition in Boundary Layers Including Curvature and Favorable Pressure Gradient Effects," ASME J. Tur-

bomach., **117**, pp. 166–174.
[23] Volino, R. J., and Simon, T. W., 1997, "Velocity and Temperature Profiles in Turbulent Boundary Layer Flows Experiencing Streamwise Pressure Gradients," J. Heat Transfer, **119**, pp. 443–439.
[24] Zhou, D., and Wang, T., 1995, "Effects of Elevated Free-Stream Turbulence on Flow and Thermal Structures in Transitional Boundary Layers," ASME J. Turbomach., **117**, pp. 407–417.
[25] Zhou, D., and Wang, T., 1996, "Combined Effects of Elevated Free-Stream Turbulence and Streamwise Acceleration on Flow and Thermal Structures in Transitional Boundary Layers," Exp. Therm. Fluid Sci., **12**, pp. 338–351.
[26] Keller, F. J., and Wang, T., 1996, "Flow and Heat Transfer Behavior in Transitional Boundary Layers With Streamwise Acceleration," ASME J. Turbomach., **118**, pp. 314–326.
[27] Wang, T., and Keller, F. J., 1999, "Intermittent Flow and Thermal Structures of Accelerating Transitional Boundary Layers: Part 1—Mean Quantities," ASME J. Turbomach., **121**, pp. 98–104.
[28] Wang, T., and Keller, R. J., 1999, "Intermittent Flow and Thermal Structures of Accelerating Transitional Boundary Layers: Part 2—Fluctuation Quantities," ASME J. Turbomach., **121**, pp. 106–112.
[29] Mayle, R. E., 1991, "The Role of Laminar-Turbulent Transition in Gas Turbine Engines," ASME J. Turbomach., **113**, pp. 509–517.
[30] Dunn, M. G., 2001, "Convective Heat Transfer and Aerodynamics in Axial Flow Turbines," ASME J. Turbomach., **123**, p. 637–669.
[31] Stoots, C., Becker, S., Condie, K., Durst, D., and McEligot, D., 2001, "A Large-Scale Matched Index-of-Refraction Flow Facility for LDA Studies Around Complex Geometries," Exp. Fluids, **30**, pp. 391–398.
[32] Budwig, R., 1994, "Refractive Index Matching Methods for Liquid Flow Investigations," Exp. Fluids, **17**, pp. 350–355.
[33] Radomsky, R. W., and Thole, K. A., 2000, "Measurements and Predictions of a Highly Turbulent Flowfield in a Turbine Vane Passage," ASME J. Fluids Eng., **122**, p. 667.
[34] McIlroy, H. M. Jr., Budwig, R. S., and McEligot, D. M., 2003, "Scaling of Turbine Blade Roughness for Model Studies," ASME Paper IMECE2003-42167.
[35] Dalling, W. J., 2003, "An Experimental Study of Wall Shear Stress on Distributed Rough Surfaces in a Turbulent Boundary Layer," M.S. thesis, University of Idaho, Moscow Idaho, pp. 43–47.
[36] Fernholtz, H. H., and Warnack, D., 1998, "The Effects of a Favourable Pressure Gradient and of Reynolds Number on an Incompressible Axisymmetric Turbulent Boundary Layer. Part 1. The Turbulent Boundary Layer," J. Fluid Mech., **359**, pp. 343–345.
[37] Radomsky, R. W., and Thole, K. A., 2002, "Detailed Boundary Layer Measurements on a Turbine Stator Vane at Elevated Freestream Turbulence Levels," ASME J. Turbomach., **124**, pp. 116–117.

Film Effectiveness Performance of an Arrowhead-Shaped Film-Cooling Hole Geometry

Yoji Okita

Masakazu Nishiura

Aero-Engine and Space Operations,
Ishikawajima-Harima Heavy Industries (IHI),
Tokyo, Japan

This paper presents the first experimental and numerical work of film effectiveness performance for a novel film-cooling method with an arrowhead-shaped hole geometry. Experimental results demonstrate that the proposed hole geometry improves the film effectiveness on both suction and pressure surface of a generic turbine airfoil. Film effectiveness data for a row of the holes are compared to that of fan-shaped holes at the same inclination angle of 35 deg to the surface on a large-scale airfoil model at engine representative Reynolds number and Mach number in a high-speed tunnel with moderately elevated temperature mainstream flow. The film effectiveness data are collected using pressure-sensitive paint. Numerical results show that the coolant film with the proposed hole geometry remains well attached to the surface and diffuses in the lateral direction in comparison with the conventional laidback fan-shaped holes for coolant to mainstream blowing ratios of 0.6–3.5. [DOI: 10.1115/1.2437781]

1 Introduction

Film cooling is used extensively in modern gas turbine/aero-engines for cooling hot section components, such as turbine airfoils. Injecting cooler air through discrete holes and/or slots from inside the blade surface provides a coolant film that protects the outer blade surface from harsh environment of the hot combustion gases. The great majority of axial film holes are inclined along the streamwise direction at shallow centerline angles of 30–35 deg relative to the surface tangent to provide higher film effectiveness. Film effectiveness is highest when the coolant flow attaches to the surface and does not penetrate and dissipate in the hot mainstream.

There were numerous studies that focused on film cooling over flat surfaces with streamwise coolant injection in the past decades [1–3] and also some research in airfoil cascade environments in these couple of years that intended to simulate even better the flow mechanism at engine conditions [4–6]. Recently, efforts have been directed at seeking technologies that would enable enhanced film-cooling effectiveness.

Haven et al. [7] found that the kidney-shaped vortices formed by a jet in a cross-flow, which promote jet liftoff, can be weakened by introducing a canceling vortex pair into the jet. It was demonstrated in their particle image velocimetry (PIV) measurements that anti-kidney vortices generated by vanes in the hole causes the jet to reside closer to the plate surface. The idea of altering vortex structure was also reported by other researchers (e.g., [8]). Several research have investigated compound angle injection with cylindrical holes to provide increased film effectiveness (e.g., [9]). These studies showed that compound angle injection gives higher film effectiveness but also increases heat transfer coefficient in the region downstream of the jet. Also, there were a few results of shaped holes with compound angle injection (e.g., [10]). The shaped holes realize higher film effectiveness with minimum heat transfer enhancement compared to compound angle injection holes (e.g., [11]). Hole shaping provides 30–50 % higher film effectiveness and slightly lower heat transfer coefficients on the surface compared to a typical cylindrical hole at the same blowing ratio. Shaped holes control the mainstream-coolant jet interactions by reducing the jet momentum with keeping the mass flow rate constant. The resulting jets have lower penetration, thus, producing higher film effectiveness and lower heat transfer coefficients.

Several alternate geometries of shaped holes have been proposed recently that at least have demonstrated the comparable film effectiveness performance to the conventional shaped holes. Kohli et al. [12] reported a film hole with dimple or trench where the circular hole exits in a shallow depression machined on the blade surface. The flow is expected to impinge on the edge of this depression causing it to deflect and fill the depression prior to covering the blade surface. Bunker [13] also reported the similar idea of trenched film hole geometry. The intention of these geometries are the same, to increase the lateral spread of the coolant film downstream of the holes and to minimize the penetration of the coolant jet into the mainstream. While these ideas improve the uniformity of the film over the surface compared to discrete holes, the effect of depressions machined on the airfoil surface on the heat transfer coefficient and aerodynamic performance still remain to be further investigated.

The new arrowhead-shaped film-cooling hole presented in this paper is designed to offer the improved film effectiveness, without incurring detrimental effects on the heat transfer coefficient and/or aerodynamic loss. The cross section of the hole changes from a rectangular shape at inlet to an arrowheadlike shape at exit (Fig. 1(*b*)). In side view, the new hole has parallel walls from the inlet to the exit (not laid back) at the centerline section, while the walls diverge at other sections with the laid-back angle varied in the lateral direction. The minimum hole area (throat) and, hence, maximum flow velocity are at about the middle of the hole. Compared to a conventional fan-shaped hole with laid back (Fig. 1(*a*)), the new hole shows larger lateral expansion at exit with the same area ratio, AR, as the conventional one. The purpose of the proposed geometry is to increase the lateral coverage of the coolant film downstream of the holes and to minimize the penetration of the coolant flow into the mainstream. The invention may make it possible to increase the lateral spacing between discrete film holes, thus economizing on the use of coolant. It also minimizes the designer's incentive to reduce coolant supply pressure and accept the attendant risk of combustion gas backflow in an effort to promote film adherence.

In the course of this research, the proposed hole geometry proved to be machined by conventional electron-discharge ma-

Contributed by the International Gas Turbine Institute of ASME for publication in the JOURNAL OF TURBOMACHINERY. Manuscript received June 5, 2006; final manuscript received June 21, 2006. Review conducted by David Wisler. Paper presented at the ASME Turbo Expo 2006: Land, Sea and Air (GT2006), Barcelona, Spain, May 8–11, 2006. Paper No. GT2006-90108.

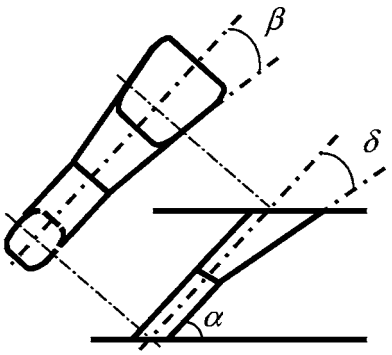

(a) fan-shaped hole with laidback (FSH)

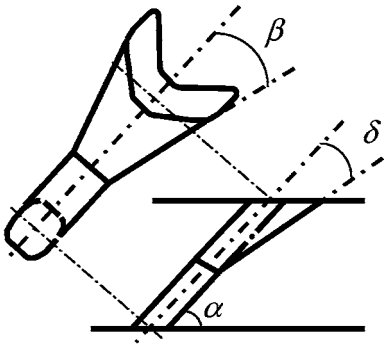

(b) arrowhead-shaped hole (ASH)

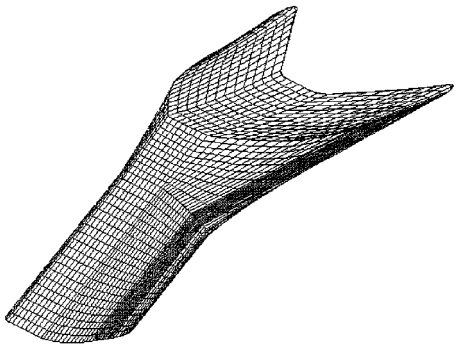

(c) 3-D surface definition of ASH

Fig. 1 Schematic of the laidback fan-shaped hole and the arrowhead-shaped hole

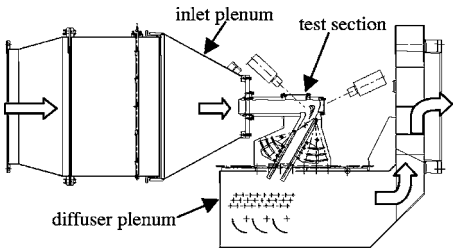

(a) General arrangement

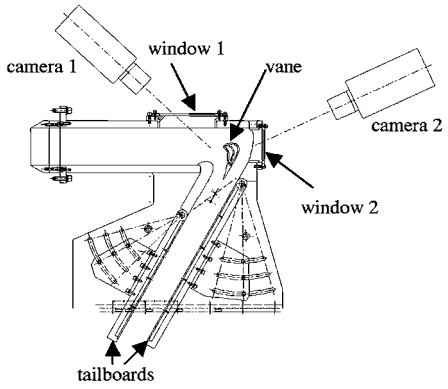

(b) Test section details

Fig. 2 Experimental apparatus

chining (EDM) with comparable drilling time as the conventional one. Thus, it never incurs any disadvantage in manufacturability, and furthermore, preliminary structural analysis shows that the new geometry exhibits slightly less stress concentration factor as the conventional fan-shaped hole.

The aim of this study is to measure the cooling performance of the proposed film hole on a generic turbine blade airfoil at engine representative flow conditions. Some numerical results are also carried out to understand the flow mechanism. The experimental setup is presented in Sec. 2 followed by a brief description of numerical method. The results of the conventional shaped hole and the arrowhead-shaped hole are then compared and discussed. Finally, the conclusions are summarized in Sec. 5.

2 Experimental Setup

2.1 Test Facility and Instrumentation. Figure 2 shows the cross section of the experimental apparatus. The test section is mounted to an inlet plenum duct (1.1 m dia $\times$ 1.8 m), which is connected to the laboratory facility air supply. Downstream of the test section, the mainstream passes through the diffuser plenum into a exhaust facility before it is dumped into the ambient. The flow rate of mainstream air is measured using an orifice. A perforated plate is located inside the inlet plenum to uniformly distribute the air. The inlet plenum is instrumented downstream of the perforated plate to measure the profile of mainstream temperature and supply pressure. Another total pressure probe is installed in the inlet of the test section. Ahead of the film-cooling experiment, the plenum pressure has been correlated with the pressure in the test section. The mainstream flow condition necessary to calculate the coolant-to-mainstream blowing ratio are obtained from the inlet plenum total pressure, temperature, and the airfoil surface static pressure at the film hole.

The test section consists of a straight entry duct and an airfoil section. The straight entry duct has a rectangular cross section of 0.103 m $\times$ 0.27 m. The interface between the inlet plenum and the entry duct is designed to form a knife edge to retard the boundary layer thickening at the end walls. In the airfoil section, an instrumented film cooled vane is centrally located in the two airfoil passage linear cascade. The airfoil is a scaled model of a generic aero-engine turbine blade. The vane is interchangeable to apply different film-cooling layout. Tailboards allow to adjust the pressure distribution along the airfoil. Bleed slots to remove boundary layer at the vane inlet are not applied in the present apparatus. Instead, the vane aspect ratio is designed to be on the large side, 3.0, to minimize the secondary flow effects on the midspan region where the main interest exists.

Cooling flow is provided through the end wall to the suction-surface (SS) and the pressure-surface (PS) film plenums inside the airfoil and is distributed through rows of film holes (see Fig. 3). The coolant plenum cross-sectional area is at least 20 times larger than the sum of cooling holes area to ensure that no significant plenum internal cross-flow exists. Each cooling plenum is instrumented with air thermocouples and pressure probes. The coolant and mainstream temperatures are equalized by heating the coolant supply. The coolant flow rate is adjusted by regulated valves and measured using calibrated mass flowmeter. Uncertainty for the

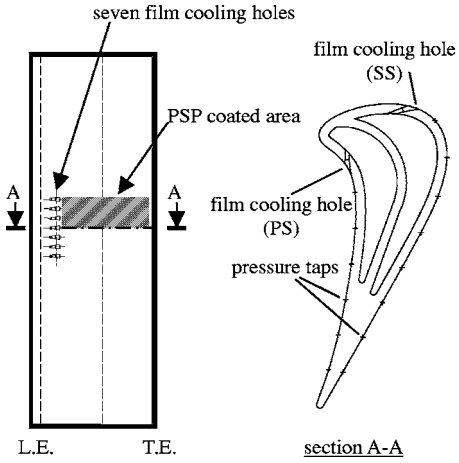

Fig. 3 Details of film-cooling instrumented vane

calculated blowing ratio is estimated to be 5%. Single-row cooling geometries on both SS and PS are investigated in the present test. There are seven film-cooling holes placed at the midspan in each row. The key dimensions of the hole geometry and layout are given in Table 1. The projections of the hole axes onto the airfoil surfaces are in-lined with the mainstream flow direction. The film holes are produced using electron-discharge machining (EDM) and the metering sections of the holes are nominally equal. Each airfoil is instrumented with 19 static pressure taps (1.0 mm dia) on the SS and 15 on the PS to record local static pressures during the test. The current test section does not have a turbulence grid in the mainstream passage, and the turbulence intensity is estimated to be on the order of 1% based on the experience of previous similar tests.

2.2 Test Conditions. The experiments are intended to mimic realistic aero-engine conditions. For the cascade inlet Mach number is 0.49 and slightly greater than 1 at around the airfoil throat. The flow parameters and cascade geometries are listed in Table 2, where typical values expected in modern medium-loaded high pressure turbine (HPT) blade are also shown. The exit Reynolds number in the table is based on airfoil chord length and exit velocity. The large aspect ratio adopted in the present experiment is to minimize the secondary flow effects on the midspan region as aforementioned.

Table 1 Key dimensions of hole geometry

	FSH SS	ASH SS	FSH PS	ASH PS
P/D		4.4		
L/D	3.7		2.7	
L_1/D	2.0		1.5	
AR	1.8	1.9	3.6	3.4
α		35		
β	10	22.6	10	22.6
δ	10	0–11	10	0–11

Table 2 Cascade geometries and flow parameters in the present experiment and in the typical medium-loaded HPT blade at design conditions (values in relative frame of reference)

Parameters	Present	Typical
Pitch to chord ratio	0.96	0.7–1.0
Aspect ratio	3.0	1.0–1.5
Turning angle	119	100–120
Inlet Mach number	0.49	0.3–0.5
Exit Mach number	0.75	0.8–1.1
Exit Reynolds number	1.82×10^6	10^5–10^6

For each cooling configuration, a series of experiments is conducted at exactly the same mainstream conditions. The blowing ratio (BR) for each case is calculated based on the film-hole metering section cross-sectional area, and tests are performed in a rage of BR=0.6–3.5 for the SS and 0.6–2.3 for the PS. In typical engine conditions, BR of 0.5–1.5 would be on the small side, 1.5–4.0 on the large side. Because nitrogen is supplied as coolant at the same temperature as the freestream in the present experiment, this results in an almost unity coolant to freestream density ratio.

2.3 Film-Cooling Effectiveness Measurement. Film-cooling effectiveness are measured using pressure-sensitive paint (PSP) techniques in the present experiment. The details of the techniques are well documented in, for example, Ahn et al. [14]. Only the summary relevant to the present application is briefly described in this section.

The techniques are based on oxygen quenched photoluminescence. Photoluminescence is the property of PSP to emit light after being illuminated by a light source. The intensity of the emitted light directly relates to the oxygen partial pressure of a surrounding gas. In this study, 460 nm LED light is used to excite PSP with the return signal in the 580 nm wavelength. To record the emitted light, charge coupled device (CCD) cameras are used. As a coolant, nitrogen gas is heated to the temperature of the mainstream and then injected through the film-cooling holes. The film-cooling effectiveness can be obtained from the mass concentration of the nitrogen/air mixture downstream of the injection using the mass transfer analogy. The oxygen sensitivity of PSP is used to indicate the oxygen mass concentration as well as measuring the static pressure profile.

A PSP setup includes targets (vane surfaces), CCD cameras, and light sources. The targets are coated with PSP (see Fig. 3) before mounting in the test section. Two transparent windows are installed in the test section to view the SS and the PS of the vane. The images of luminescence intensity distribution from the target surfaces, recorded by the CCD cameras, are originally grayscale. These images are then calculated by the data reduction program, which compares ratios of the recorded intensity to the calibration data to obtain the pressure and film effectiveness data.

For the film effectiveness measurement by PSP, four images are required: a dark image (image without illumination), a reference image (with no mainstream and coolant injection), an air injection image (mainstream air with air as coolant), and a nitrogen injection image (mainstream air with nitrogen as coolant).

The uncertainty in the measured film effectiveness, estimated to be 9% using the method of Kline and McClintock [15], is mainly due to the uncertainties in the paint calibration and errors due to model motion.

3 Numerical Method

The aim of numerical investigation is to give physical insight into the mechanism of interaction between the mainstream and film jet, especially for the newly developed arrowhead-shaped hole where the main interest of the present work exists.

The three-dimensional compressible RANS equations are solved using a pressure correction method with the FLUENT 6 software from Fluent, Inc. The equations are discretized using a finite volume method with the convective variables being basically resolved in a second-order upwind scheme. For the turbulent quantities, however, first-order upwind scheme is applied because of solution stability. The turbulent stresses and heat fluxed are modeled through the standard k-ε model with the standard wall function at near-wall cells. To quantify nitrogen injection and mixing in the experiment, a species concentration equation is also solved.

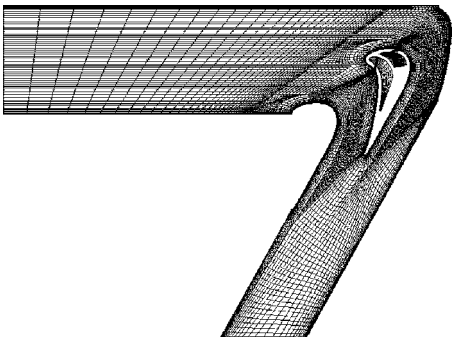

Fig. 4 Computational domain and mesh in the centerline section

The calculation is steady-state. Convergence of the iterative steady-state solution is declared when a reduction in normalized residuals of at least three orders of magnitude with the leveling off are achieved for all the solution variables.

The computational domain (Fig. 4) includes the plenum cavities inside the vane and the mainstream with the two airfoil passages. In the spanwise direction, only one-half of the hole pitch is solved assuming flow symmetry with symmetry conditions being imposed at the longitudinal centerline of the jet, as well as the line between the holes. No-slip and adiabatic conditions are applied on solid surfaces. At the coolant plenum inlet, the mass flux is set uniformly so as to give the required mass flow and the species concentration is set to unity. In the mainstream, the mass flow rate, total temperature, and a species concentration of zero are specified at the inlet. The turbulent kinetic energy is set with a turbulence intensity of 1% and the dissipation rate then obtained assuming turbulence Reynolds number equal to 100. At the flow exit, static pressure is specified and other variables are extrapolated from the interior of the solution domain. All the boundary conditions are set to be consistent as best with the experimental data.

The number of control-volume cells is ~140,000. The mesh growth rate is kept under 1.3 throughout the model. The converged solutions have near-wall mesh y^+ values in the range $10 < y^+ < 100$ in most regions. A centerline section of the computational mesh is shown in Fig. 4.

4 Result and Discussion

4.1 Inlet and Exit Conditions. To confirm a correct representation of the design conditions in the cascade, flow measurements are performed before the film-cooling test is initiated.

At the inlet of the cascade, mean flow quantities are measured across the duct to verify the flow uniformity. Variations in the measured total pressure and total temperature are 0.04 and 0.03%, respectively. At the exit of the cascade, limitations arise from the two airfoil passage arrangement. Although a great effort on tailboard adjustment has been made, complete flow uniformity and periodicity are not obtained.

4.2 Film-Cooling Effectiveness on the SS. The experimental results of film effectiveness distributions on the SS for lower blowing ratios, BR=0.6 and 1.2, using the PSP method are compared between the conventional laidback fan-shaped hole (FSH) and the arrowhead-shaped hole (ASH) in Fig. 5. The distributions are shown for the regions downstream of four holes of total 7 holes where the PSP is coated (see Fig. 3). Note that $X=0$ and 1 in the horizontal axis correspond to the leading- and trailing-edge positions, respectively, while another horizontal axis, x'/D, originates from the hole exit location. The results indicate that there is some uneven cooling flow distribution among the cooling holes. This is a result of the uncertainty of the manufacturing process of EDM. There also exists even broader spanwise nonuniformity. It is suspected that the flow rate between the film holes is not evenly distributed due to the design of coolant plenum or the secondary flow effect extends to the evaluated mid-span region.

In any of the BR cases, a high film effectiveness is observed at the centerlines near the point of the injection, while it is low between the holes. The difference in film effectiveness between the center line and the line between holes, however, becomes smaller at around $X=0.35$ and farther downstream. This indicates that the mixing between the film jet and the mainstream proceeds quickly on the SS, which is in contrast to the trend on the PS discussed in the next section.

In the lower BR cases, BR=0.6 and 1.2, the FSH shows better lateral spreading of the film than the ASH near the injection point. However, the higher effectiveness and good coverage of the FSH is confined within 8–9 hole diameters from the injection point and any considerable difference between the FSH and the ASH cannot be seen downstream.

The laterally averaged film cooling effectiveness is plotted in

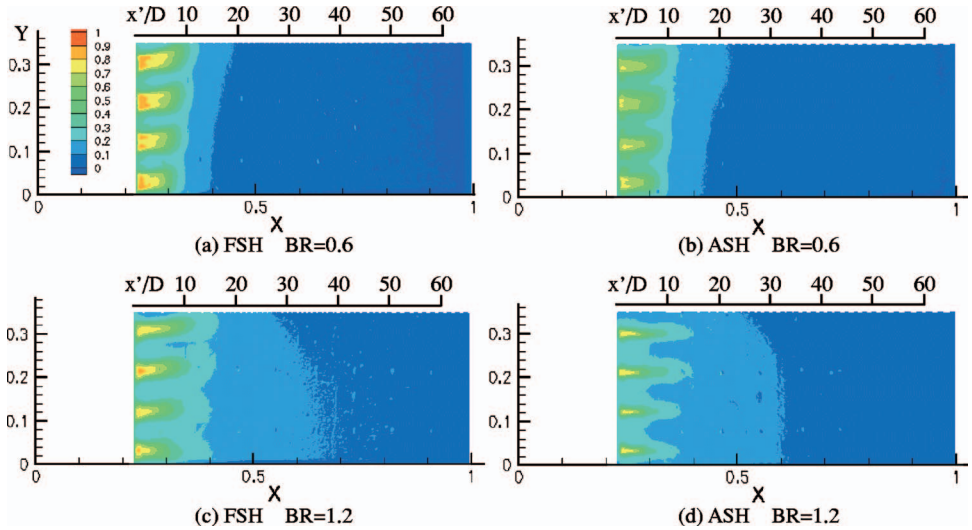

Fig. 5 Comparison of measured film effectiveness contours on the suction surface (SS) between the FSH and ASH, lower BR cases

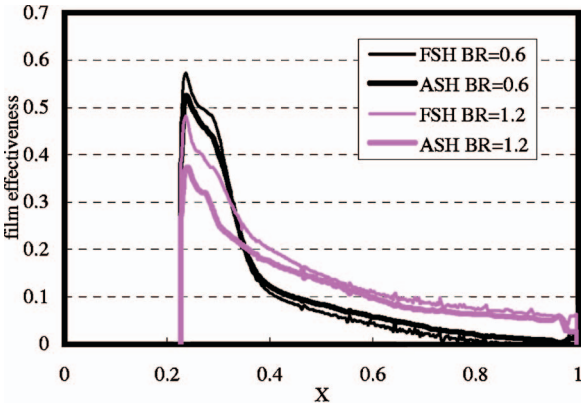

Fig. 6 Comparison of laterally averaged film effectiveness on the suction surface (SS) between the FSH and ASH, lower BR cases

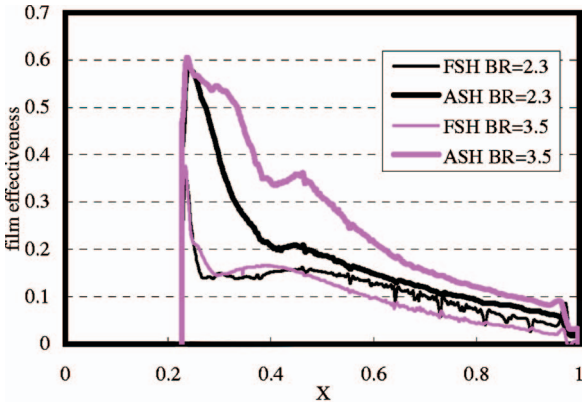

Fig. 8 Comparison of laterally averaged film effectiveness on the suction surface (SS) between the FSH and ASH, higher BR cases

Fig. 6 as a function of dimensionless distance (X). The slope of the effectiveness decrease in the streamwise direction seems less steep for the ASH. It is believed that the shaping of the ASH causes a reduction of jet penetration into the mainstream, as a result, mixing is retarded. Figure 6 illustrates that the FSH is superior for $X \lesssim 0.4$, but farther downstream overall film effectiveness is almost identical for the both hole geometries.

Figure 7 shows a completely different trend for the higher BR cases of BR=2.3 and 3.5. For the FSH effectiveness is significantly high near the hole exit at the aforementioned lower BR cases, but there is much less cooling effectiveness at the same region for these higher BR cases. The plot of laterally averaged effectiveness depicted in Fig. 8 also shows the dips of effectiveness for the FSH, just downstream of the injection point. The jet structure is suspected to exhibit a "blow off" near the hole exit, leading to weak presence of the coolant film along the wall. The jet penetration for these cases is higher, and thus, there may be also increased dispersion of the jet, leading to lower effectiveness overall. Therefore, the FSH geometry is more effective at low blowing ratios. On the contrary, the ASH hole exhibits much higher effectiveness than the FSH over the entire region for this BR range. Even with the highest BR case, where the FSH suffers the blow off, almost complete coverage is achieved near the hole exit with the ASH hole (note that the dips near $X=0.4$ for the ASH hole are caused by overexposure of the CCD camera). Higher blowing ratio does not monotonically contribute to the higher effectiveness with the FSH because of the effect of jet penetration. With the ASH hole, the jet penetration is reduced. Because the penetration of the coolant jet is reduced, higher film-cooling effectiveness and greater coverage are obtained.

Figure 9 presents the effect of blowing ratio on the overall-averaged film effectiveness for each hole. The figure suggests that the FSH has an optimum film effectiveness performance at around BR=1.2. Effectiveness is lowest for BR=3.5 due to jet blow off. On the contrary, the ASH shows a monotonous rising curve with the blowing ratio. Highest effectiveness is obtained for BR=3.5, while it is lowest for BR=0.6, where the jet spreading is limited due to lower coolant mass flux.

4.3 Film-Cooling Effectiveness on the PS. The experimental results of film effectiveness distributions on the PS for lower blowing ratios, BR=0.6 and 1.2 are compared between the two hole geometries in Fig. 10. A high film effectiveness is observed at the center lines and it is low between the holes, as same as on the SS. The difference in film effectiveness between the center line and the line between holes, however, does not smear quickly as on the SS. The footprints of film jet can be clearly traced even farther downstream. Also, the laterally averaged plot, Fig. 11, shows

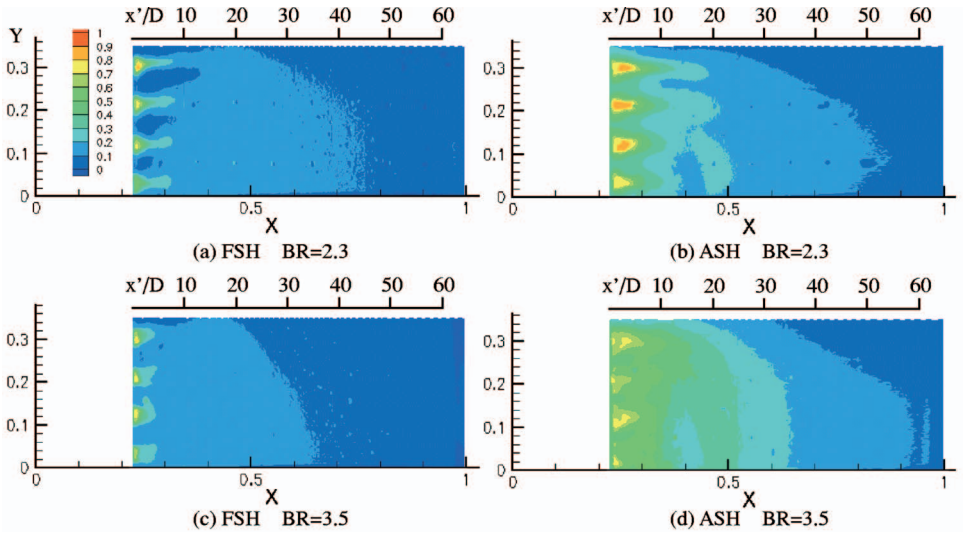

Fig. 7 Comparison of measured film effectiveness contours on the suction surface (SS) between the FSH and ASH, higher BR cases

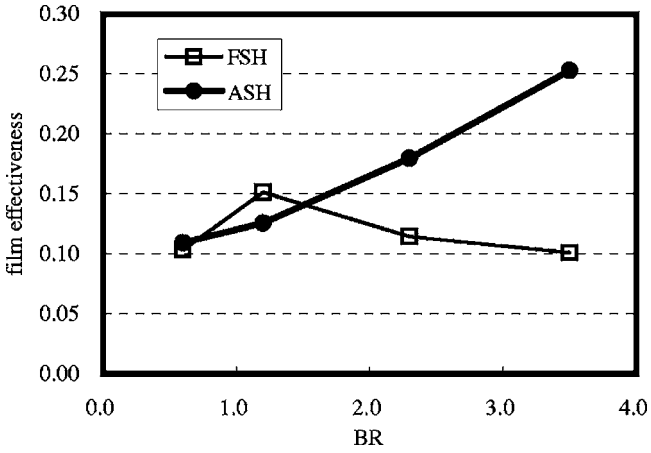

Fig. 9 Effect of blowing ratio on overall-averaged film effectiveness with FSH and ASH for the suction surface (SS)

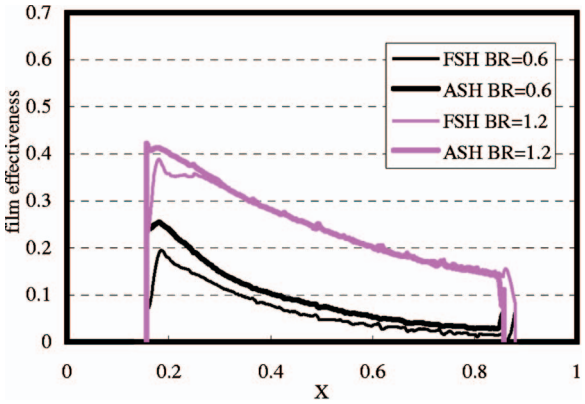

Fig. 11 Comparison of laterally averaged film effectiveness on the pressure side (PS) between the FSH and ASH, lower BR cases

more gentle slope of the effectiveness decrease in the streamwise direction, compared to the one on the SS. These trends are attributed to slower lateral mixing on the PS. In the current airfoil, the flow acceleration along the SS occurs mainly upstream of the film hole with a slight deceleration downstream, whereas on the PS there exists continuous acceleration over the entire surface. It is probable that this acceleration downstream of the film hole is related to the slower mixing on the PS. In such an accelerating boundary layer, the viscous sublayer thickening occurs and, consequently, the turbulence is suppressed. The reduced turbulence level leads to the less turbulent diffusion, which in turn, retards the mixing.

In this lower BR range, the FSH and the ASH give similar distribution of film effectiveness. The ASH shows slightly better lateral coverage. In the laterally averaged plot, Fig. 11, the ASH shows a considerable advantage over the FSH near the injection point owing to this better lateral coverage. Downstream there is slight (BR=0.6) or almost no advantage (BR=1.2).

For higher blowing ratio, only the results of BR=2.3 are available because supplying coolant more than BR=2.3 to the pressure surface holes is beyond the capability of the current facility. The measured effectiveness contours depicted in Fig. 12 indicate that the lateral coverage near the hole exit now shrink, compared with the BR=1.2 case. In this region ($X<0.3$) there exists almost no cooling effectiveness between the holes. Overall level of effectiveness and coverage seem better with the ASH. Figure 13 gives a plot with laterally averaged effectiveness. It clearly shows the dips in $X<0.3$ region, which is attributed to the shrinkage of the film coverage presented in the contours. The dips are similar to the one encountered with the FSH in higher flow cases on the SS, while the extent of decline is less severe. The jet structure is suspected to liftoff in some degree after issuing onto the mainstream surface. The plot shows an effective merit with the ASH over the entire surface in this higher blowing case. The performance improvement by the introduction of the ASH, however, is not so significant as the same BR case on the SS.

Figure 14 presents the effect of blowing ratio on the overall-averaged film effectiveness for the pressure surface. As same as for the suction surface, the FSH has an optimum performance at BR=1.2. For the ASH, the trend in lower BR range is similar to the FSH, but there is a slight increase even beyond BR=1.2.

4.4 Flow Mechanism Observed From Numerical Results.

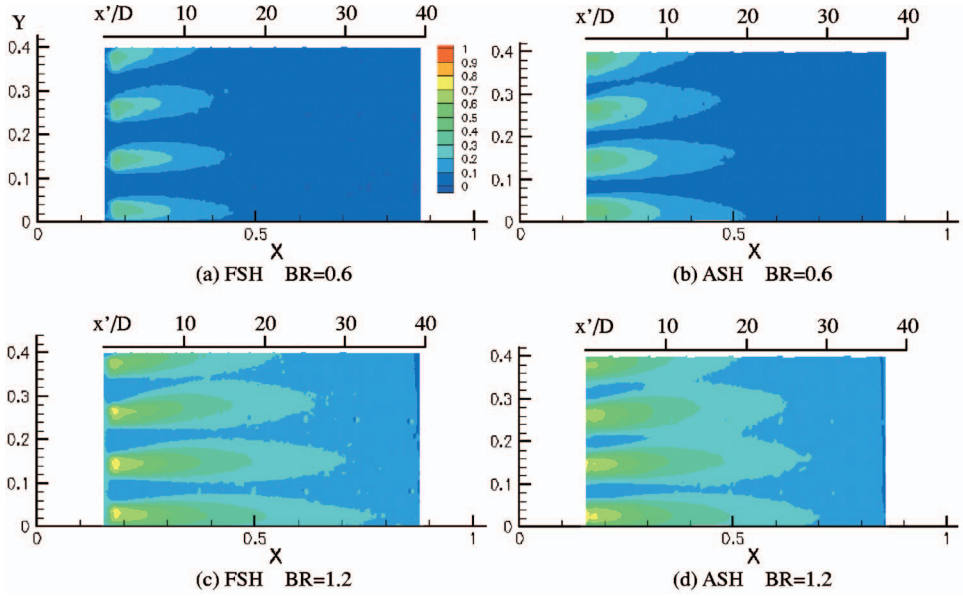

Fig. 10 Comparison of measured film effectiveness contours on the pressure side (PS) between the FSH and ASH, lower BR cases

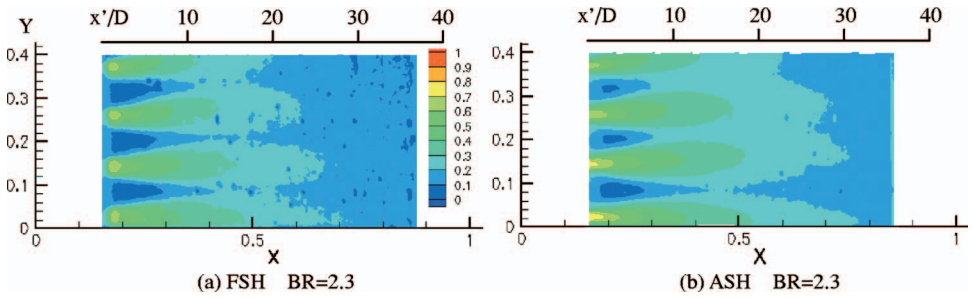

Fig. 12 Comparison of measured film effectiveness contours on the pressure side (PS) between the FSH and ASH, higher BR cases

A comparison of laterally averaged effectiveness for BR=2.3 case on the SS between the experiment, and the numerical result is plotted versus normalized surface distance in Fig. 15(*a*), indicates reasonably good agreement between experiment and computation for the FSH geometry, though the effectiveness is rather overpredicted. Qualitatively, the result show similar trends: significant plunge by blow off in the near field, and more gently decrease downstream. However, the experiment indicates that the case has only a slight effectiveness gain after the plunge, while the computation tends to give even more intense and broader recovery by film reattachment and consequently overpredicts the cooling per-

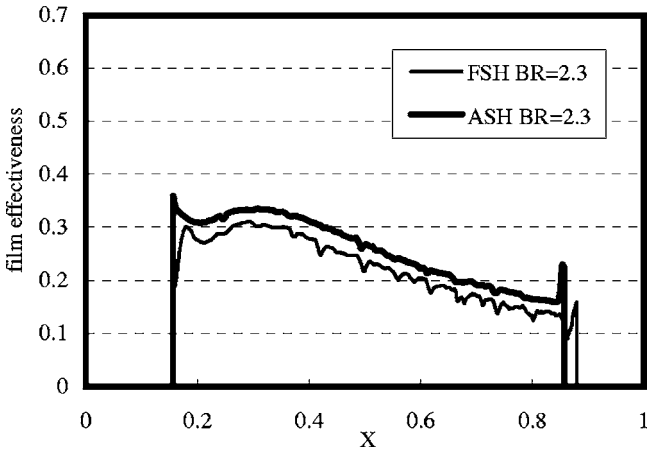

Fig. 13 Comparison of laterally averaged film effectiveness on the pressure side (PS) between the FSH and ASH, higher BR cases

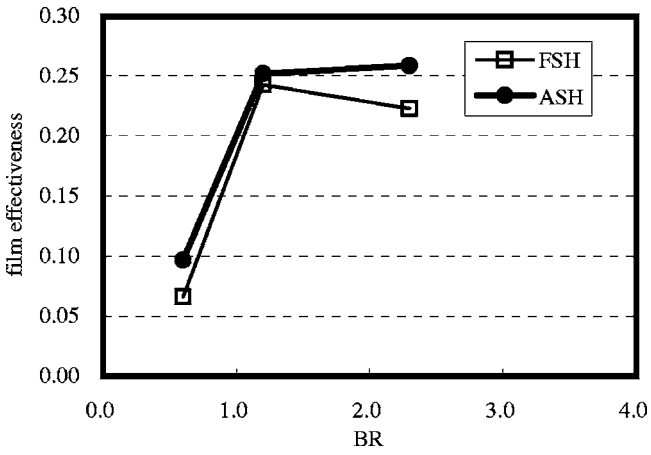

Fig. 14 Effect of blowing ratio on overall-averaged film effectiveness with FSH and ASH for the pressure surface (PS)

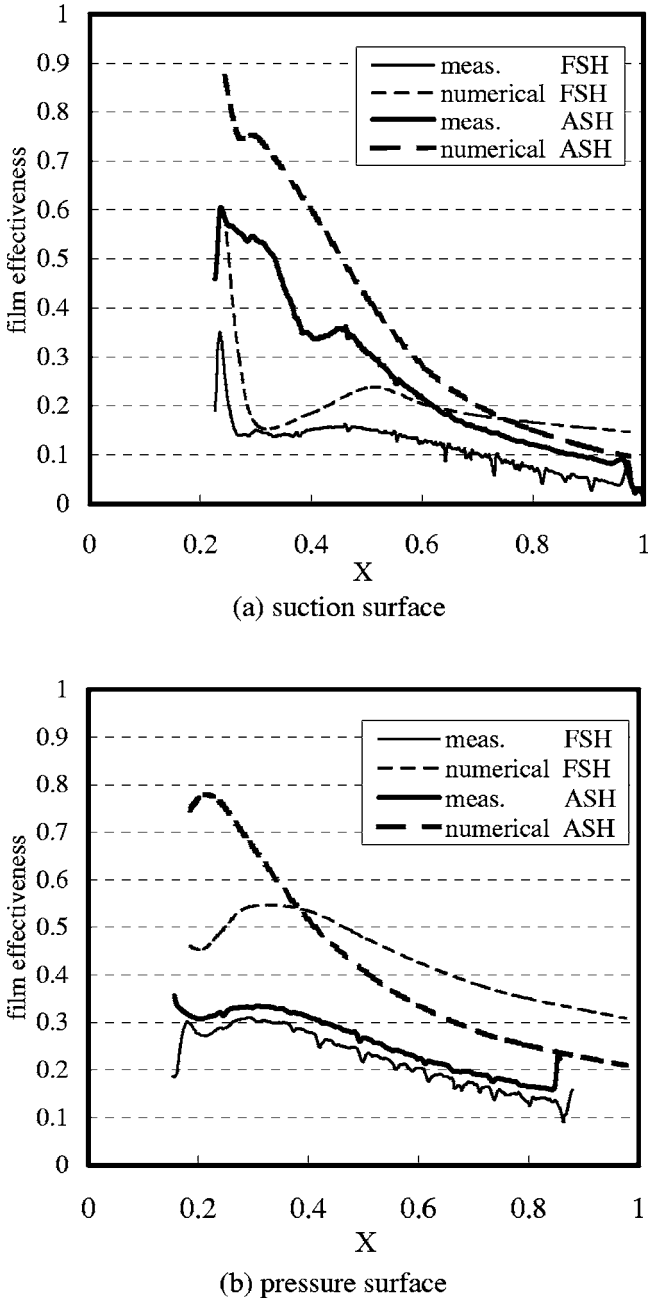

Fig. 15 Comparison of laterally averaged film effectiveness between experiment and computation, BR=2.3

formance downstream. As for the ASH, both experiment and computation show no trace of blow off in the near-hole exit field, almost monotonous decrease of effectiveness in the streamwise direction, and most importantly, a great advantage to FSH overall. The numerical result approaches the measured data far downstream, but overpredicts the effectiveness close to the film hole. Especially in the region close to the hole exit, several computational film-cooling studies have pointed out the need to accurately resolve the flow in the viscous sublayer and buffer region of turbulent boundary layer (e.g., [16]). Hence, an improvement to the near-hole region will probably be accomplished through the introduction of boundary layer resolving model instead of the wall function.

A comparison between the experiment and the numerical result on the PS with the FSH geometry, Fig. 15(*b*), shows a considerable discrepancy in the level of effectiveness. Both experiment and computation show the dip of effectiveness near the hole exit, recovery downstream, and monotonous decrease farther downstream. Again, recovery after the liftoff is intense for the computation, but insignificant for the experiment. A comparison for the ASH in Fig. 15(*b*) shows that the computation completely miss capturing both the magnitude and the qualitative trends of the measured film effectiveness. As a whole, the computation significantly overpredicts on the PS for BR=2.3. The reason for this is believed to be related the fact that in higher BR condition more of the coolant penetrates through the boundary layer into the mainstream flow. If the turbulent mixing in the mainstream is underpredicted, it will lead to the observed trends. Underprediction of turbulent mixing with the present physical model is from several sources: disability in capturing anisotropic nature of the diffusion, lack of terms to model the effect of streamline curvature on the turbulence field, etc.

Although agreement with the experimental data cannot be said to be complete, the computational results can be used to gain insight into the flow physics of film cooling for both FSH and ASH holes, at least on the suction surface where an acceptable level of agreement is obtained.

Figure 16 compares the calculated secondary velocity vectors and nitrogen mole fraction contours near the SS hole exit for BR=2.3. The FSH exhibits a strong secondary motion induced by interaction between inclined jet and crossflow, which is often referred as a pair of "kidney-shaped" vortices. Their sense of rotation is such that one vortex, by mutual induction, lifts the other off the surface. Additionally, the rotational motion of the vortices entrains the crossflow around the jet and down toward the wall surface. Both coolant liftoff and hot gas entrainment degrade the film effectiveness. A striking feature of the secondary motion for the case of ASH is that the vortices now rotate in the opposite direction of ordinary jet-cross-flow interaction vortices. The idea of achieving this "anti-kidney" vortex by shaping hole geometry was reported in several previous work (e.g., [7]). It is believed that the cross-sectional geometry of the ASH coolant passage causes the change in rotation direction (see Figs. 1(*b*) and 1(*c*)). The double-curved surfaces of the ASH should split the flow into two streams that produce a vortex pair structure within the coolant stream. Within the passage, the direction of this vortex rotation is from the center of the leeward flat surfaces toward the hole edge and out along the curved surfaces. This geometrically induced vortex rotation would influence the film effectiveness data. With the anti-kidney vortices, the coolant is spread laterally along the wall and negative induction lift is generated. Consequently, the coolant liftoff/blow off is prevented or minimized, better lateral film coverage is achieved, and the resultant better film effectiveness performance is obtained as shown in the experimental results.

The arrowhead shaping is originally intended to expand the hole exit in the lateral direction so as to achieve better lateral coverage of the coolant film. The numerical results reveal that the improved performance by the ASH shaping is also related to the generation of vorticity that rotates in the opposite direction of the kidney vortex, further encourages lateral film spreading, and reduces jet penetration keeping the coolant jet closer to the airfoil surface. One concern may be a poor agreement with the data especially on the PS, and thus, work to improve physical modeling of the numerical method is needed in the next step, which will help to explain even clearer the performance difference of the ASH between on the SS and on the PS.

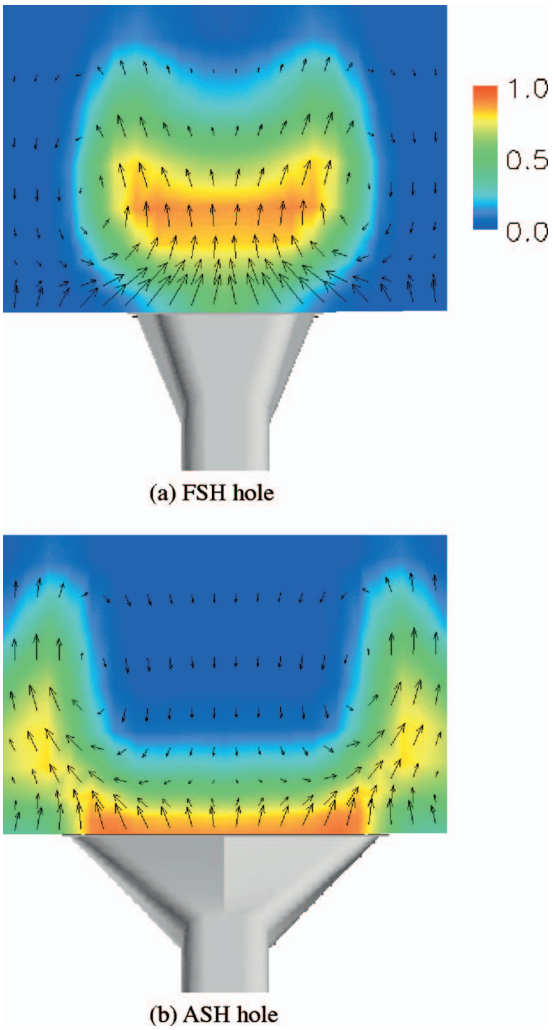

Fig. 16 Calculated secondary velocity vectors and nitrogen mole fraction contours near the hole exit (X=0.31) on the suction surface, BR=2.3

5 Conclusions

A new film-cooling hole shape, the arrowhead-shaped hole has been presented. The film effectiveness performance of the proposed film-cooling hole at engine representative conditions in a model of a generic turbine blade airfoil has been tested. The results have been compared to conventional laidback fan-shaped film-hole geometry.

On the suction surface of the airfoil the arrowhead-shaped hole shows greater increases in film effectiveness at the higher blowing ratios. For one thing, this is because of the tendency of the arrowhead-shaped hole to redirect the momentum of the film along the surface so that the penetration of jet, and consequently mixing, is reduced.

On the pressure surface, although the performance improvement is smaller than the suction surface, the new geometry consistently provides better film effectiveness performance in any of

the tested blowing ratios over most of the downstream surface with the greatest improvement in the near-hole region.

Numerical results have suggested that coolant jet liftoff and hot gas entrainment may be depressed by the arrowhead-shaped hole geometry that generates a counterrotating vortex pair structure in the coolant jet that rotates in opposition to the cross-flow generated vortex pair rotation. This flow mechanism is believed to contribute to the better performance of the proposed hole geometry as well.

Acknowledgment

The authors would like to express their thanks to the New Energy and Industrial Technology Development Organization (NEDO) and the Ministry of Economy, Trade and Industry (METI), who gave them the opportunity to conduct "Research and Development for Environmentally Compatible Engine for Small Aircraft (ECO Engine) Project."

Nomenclature

AR = area ratio ($=A_{\text{exit-plane}}/A_{\text{throat}}$)
ASH = arrowhead-shaped hole
BR = blowing ratio $[=(\rho U)_c/(\rho U)_g]$
C = oxygen concentration
c = distance from leading to trailing edge along the airfoil surface
D = film hole throat internal diameter
FSH = fan-shaped hole with laidback
L = film hole length
L_1 = film hole throat section length
P = spanwise pitch between film hole centerlines
PS = pressure surface
SS = suction surface
U = velocity
X = dimensionless chordwise distance ($=x/c$)
x = chordwise distance along airfoil surface from leading edge
x' = chordwise distance along airfoil surface from hole exit
Y = dimensionless spanwise distance ($=y/c$)
y = spanwise distance on airfoil surface from meanline
α = hole centerline angle relative to the surface tangent
β = hole lateral expansion angle
δ = hole laid-back expansion angle
η = film effectiveness $[=(C_{\text{air}}-C_{\text{mix}})/C_{\text{air}}]$
ρ = density

Subscript

air = mainstream with air as coolant
c = film coolant
g = mainstream
mix = mainstream with nitrogen as coolant

References

[1] Goldstein, R. J., 1971, *Film Cooling* (Advances in Heat Transfer, Vol. 7), Academic Press, New York, pp. 321–379.
[2] Walters, D. K., and Leylek, J. H., 1997, "A Detailed Analysis of Film-Cooling Physics—Part 1: Streamwise Injection With Cylindrical Holes," ASME Paper No. 97-GT-269.
[3] Mayhew, J. E., Baughn, J. W., and Byerley, A. R., 2003, "The Effect of Freestream Turbulence on Film Cooling Adiabatic Effectiveness," Int. J. Heat Fluid Flow, **24**, pp. 669–679.
[4] Drost, U., and Bolcs, A., 1998, "Investigation of Detailed Film Cooling Effectiveness and Heat Transfer Distributions on a Gas Turbine Airfoil," ASME Paper No. 98-GT-20.
[5] Zhang, L. J., and Pudupaty, R., 2000, "The Effects of Injection Angle and Hole Exit Shape on Turbine Nozzle Pressure Side Film Cooling," ASME Paper No. 2000-GT-247.
[6] Medic, G., and Durbin, P. A., 2002, "Toward Improved Film Cooling Prediction," ASME J. Turbomach., **124**, pp. 193–199.
[7] Haven, B. A., Yamagata, D. K., Kurosaka, M., Yamawaki, S., and Maya, T., 1997, "Anti-Kidney Pair of Vortices in Shaped Holes and Their Influence on Film Cooling Effectiveness," ASME Paper No. 97-GT-45.
[8] Shih, T. I.-P., Lin, Y.-L., Chyu, M. K., and Gogineni, S., 1999, "Computation of Film Cooling From Holes With Struts," ASME Paper No. 99-GT-282.
[9] Schmidt, D. L., Sen, B., and Bogard, D. G., 1994, "Film Cooling With Compound Angle Holes: Adiabatic Effectiveness," ASME Paper No. 94-GT-312.
[10] McGrath, E. L., Leylek, J. H., and Buck, F. A., 2002, "Film Cooling on a Modern HP Turbine Blade Part 4: Compound-Angle Shaped Holes," ASME Paper No. GT2002-30521.
[11] Gritsch, M., Schulz, A., and Wittig, S., 1998, "Adiabatic Wall Effectiveness Measurements of Film Cooling Holes With Expanded Exits," ASME J. Turbomach., **120**(3), pp. 549–556.
[12] Kohli, A., Wagner, J. H., and Aggarwala, A. S., 2005, "Film Cooled Article With Improved Temperature Tolerance," U.S. Patent No. 6,932,572 B2.
[13] Bunker, R. S., 2002, "Film Cooling Effectiveness due to Discrete Holes Within a Transverse Surface Slot," ASME Paper No. GT2002-30178.
[14] Ahn, J., Mhetras, S., and Han, J.-H., 2004, "Film-Cooling Effectiveness on a Gas Turbine Blade Tip Using Pressure Sensitive Paint," ASME Paper No. GT2004-53249.
[15] Kline, S. J., and McClintock, F. A., 1953, "Describing Uncertainties in Single-Sample Experiments," Mech. Eng. (Am. Soc. Mech. Eng.), **75**(1), pp. 3–8.
[16] Ferguson, J. D., Walters, D. K., and Leylek, J. H., 1998, "Performance of Turbulence Models and Near-Wall Treatments in Discrete Jet Film-Cooling Simulations," ASME Paper No. 98-GT-438.

Separation and Transition Control on an Aft-Loaded Ultra-High-Lift LP Turbine Blade at Low Reynolds Numbers: High-Speed Validation

Maria Vera

Xue Feng Zhang

Howard Hodson

Whittle Laboratory,
University of Cambridge,
UK

Neil Harvey
Compression Systems,
Rolls-Royce plc,
Derby, UK

This paper presents the second part of an investigation of the combined effects of unsteadiness and surface roughness on an aft-loaded ultra-high-lift low-pressure turbine (LPT) profile at low Reynolds numbers. The investigation has been performed using low- and high-speed cascade facilities. The low- and high-speed profiles have been designed to have the same normalized isentropic Mach number distribution. The low-speed results have been presented in the first part (Zhang, Vera, Hodson, and Harvey, N., 2006, ASME J. Turbomach., ***128****, pp. 517–527). The current paper examines the effect of different surface finishes on an aft-loaded ultra-high-lift LPT profile at Mach and Reynolds numbers representative of LPT engine conditions. The surface roughness values are presented along with the profile losses under steady and unsteady inflow conditions. The results show that the use of a rough surface finish can be used to reduce the profile loss. In addition, the results show that the same quantitative values of losses are obtained at high- and low-speed flow conditions. The latter proves the validity of the low-speed approach for ultra-high-lift profiles for the case of an exit Mach number of the order of 0.64. Hot-wire measurements were carried out to explain the effect of the surface finish on the wake-induced transition mechanism.* [DOI: 10.1115/1.2437220]

1 Introduction

At the inception of the aero gas turbine, the method of controlling the profile loss on the suction side of a low-pressure turbine (LPT) blade consisted of avoiding the occurrence of a laminar separation bubble and minimizing the boundary layer thickness at the trailing edge. Therefore, a large number of blades per row was necessary to compensate for the low rates of deceleration on the rear of the suction surfaces of the resulting aerofoils. For this family of profiles, moving the onset of transition upstream was detrimental in terms of loss because more surface was covered by turbulent flow. Hence, a polished surface finish was desirable to keep the suction-side boundary layer laminar as far downstream as possible.

The subsequent emergence of "high-lift" blading enabled significant reductions in blade count to be achieved. Hourmouziadis [1] was the first to describe in detail the issues surrounding their design. He showed that a primary element is the behaviour of laminar separation bubbles on the suction surface - inevitable for blading with high levels of back surface diffusion at low Reynolds numbers. While such blading of course has always operated in the unsteady, wake passing environment their design was largely undertaken using steady flow criteria, see Hourmouziadis [1] and Harvey et al. [2]. See also Zhang et al. [3].

Subsequent to this, the overwhelmingly important discovery has been that the key to achieving good aerodynamic performance in the engine is that the boundary layer separation and transition on these aerofoil surfaces must be optimised taking the unsteady environment fully into account. Research in this area includes that of Halstead et al. [4] and Schulte and Hodson [5]. The evolution of one family of profiles is described by Schulte and Hodson [6], Curtis et al. [7], and Howell et al. [8], in which the promotion of transition between the suction peak and the vicinity of the point of separation helps to control the size of the separation bubble and the losses. Their studies showed the beneficial effect of unsteadiness in controlling the suction-side separation bubble in high-lift profiles by promoting transition in the vicinity of separation. Nowadays, the use of unsteadiness to control the suction-side separation bubble in high-lift profiles is in common use. If a high-lift blade has been optimized to account for the unsteady inflow conditions, the use of a rough surface in addition to the unsteadiness could be detrimental in terms of losses. This is because the separation bubble is efficiently suppressed by the wakes. Therefore, the presence of a rough surface could increase the losses by covering more surface with turbulent flow [9].

The reduction of weight and cost of the LPT requires an increase of the lift coefficient up to limits where the effect of the unsteadiness caused by the wakes shed by an upstream blade row cannot, on its own, control the separation bubble, especially at low Reynolds numbers. Haselbach et al. [10] reported a 0.5% lower efficiency for an ultra-high-lift LPT blade at high altitude (low Reynolds number) when compared to a high-lift blade. At sea level, the ultra-high-lift blade had a performance that was similar to high-lift blades. Thus, for these ultra-high-lift blades, it is essential to complement the unsteadiness by another loss-reduction mechanism [11]. Zhang and Hodson [12] showed, for a particular pressure distribution style, that for a given roughness element a reduction in losses might occur only if the roughness is located between the suction peak and the point of separation. This is because, upstream of the suction peak, the acceleration is too strong, i.e., the favorable pressure gradient inhibits the onset of transition. Downstream of the separation point, the roughness could no longer affect transition, which starts within the shear layer of the separated flow. However, these observations also sug-

Contributed by the International Gas Turbine Institute of ASME for publication in the JOURNAL OF TURBOMACHINERY. Manuscript received May 17, 2006; final manuscript received May 30, 2006. Review conducted by David Wisler. Paper presented at the ASME Turbo Expo 2005: Land, Sea and Air (GT2005), Reno, NV, June 6–9, 2005. Paper No. GT2005-68893.

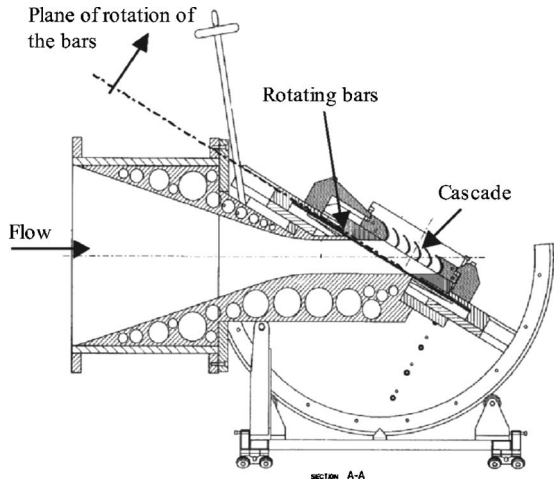

Fig. 1 Cross section of the high-speed bar rotating rig

gest that a uniformly rough surface will also only significantly affect the boundary layer between the suction peak and the separation. Therefore, the use of a rough surface finish on an ultra-high-lift blade could be beneficial in terms of the losses. In addition, the cost can be reduced by simplifying the surface treatment of the blades.

This paper presents the second part of an investigation of the combined effects of unsteadiness and surface roughness on an aft-loaded ultra-high-lift LPT profile at low Reynolds numbers. In this part, the effect of the surface finish at realistic LPT Mach and Reynolds numbers is presented. Two manufacturing routes were used to produce the casting waxes. The resulting blades underwent different finishing process to obtain a total of three surface finishes for each manufacturing process. The results are compared to the low speed data presented in Zhang et al. [3].

Experimental Apparatus

The experiments were carried out in the transonic cascade facility at the Whittle laboratory. This is a continuous-flow, closed-circuit, variable-density wind tunnel where the Reynolds and the Mach number can be fixed independently. Two vacuum pumps, working in parallel, are used to achieve subatmospheric pressures. A compressor is used to control the pressure ratio and, thus, the Mach number of the flow within the circuit. Before entering the cascade, the air passes through a honeycomb and screen. Before the entry into the cascade, the flow is accelerated in a convergent nozzle. At the exit, it is discharged into the large exit plenum that contains the test section. The inlet freestream turbulence is 0.5%.

The presence of the wakes shed from an upstream blade row is simulated using a wake generator. The high-speed bar wake generator consists of a number of cylindrical metal bars equally spaced at the outer periphery of a disk that rotates in a plane parallel to the leading-edge plane of the cascade. For the current case, the plane of rotation was located at ~0.8 axial chord lengths upstream of the leading edges of the cascade in the axial direction. A cover encloses the rotating disk and bar assembly, thus creating a sealed cavity containing the bars. The cover has a rectangular opening aligned with the exit of the convergent nozzle over which the cascade is mounted. A cross section of the high-speed bar passing rig is shown in Fig. 1. For the current study, the bars are made of 0.41 mm dia hypodermic tube. The bar passing frequency is 3600 Hz. This provides wakes of approximately the same strength and reduced frequency as an upstream stator [13]. In addition, the ratio of bar diameter to chord, 1.3%, closely matches that used for the low-speed experiments presented in Zhang et al. [3], 1.5%.

Table 1 HSU2 linear cascade and bar details

Chord (mm)	30.6
Axial chord (mm)	24.5
Pitch (mm)	28.3
Span (mm)	101.6
Design inlet flow angle (deg)	36.9
Design outlet flow angle (deg)	−60.0
Design exit Mach number	0.64
Zweifel coefficient	1.21
Bar diameter (mm)	0.41
Flow coefficient	0.87
Reduced frequency	0.52

The static pressures upstream and downstream of the cascade are measured using 0.3 mm dia wall pressure tappings. A conventional Pitot tube upstream of the row of bars measures the inlet total pressure. The inlet stagnation temperature is measured using a thermocouple placed within the inlet ducting upstream of the test section. A calculation procedure is used to calculate mixed-out conditions downstream of the bars. This calculation procedure and its validation are presented in [13]. It is based on the measured drag coefficient of the bars.

The profile used for the current test is the high-speed version of the U2 blade presented by Howell et al. [14] and, later, by Zhang et al. [3]. The U2 and the high-speed U2 (HSU2) profiles are not identical since they are designed to have the same distribution of nondimensional isentropic Mach number. This blade is an aft-loaded ultra-high-lift blade with ~100 deg of turning. Further information is given in Table 1. The cascade consists of seven blades. Adjustable bleed slots were placed on the top and bottom of the cascade in order to control the periodicity of the cascade.

Pitchwise traverses were performed behind the cascade to measure the profile loss. The traverse plane was placed at 0.5 axial chord lengths downstream of the trailing-edge plane of the cascade in the axial direction. The traverses extended across the wakes covering the three central pitches of the cascade. A fixed direction 4 hole Neptune probe was used to measure the exit flow field. The local flow conditions at the exit, i.e., Mach number, flow angle, and total pressure were used to provide the mixed-out values to calculate the profile loss coefficient. The kinetic energy loss coefficient, KSI, was calculated with an accuracy of ~0.1% of the exit dynamic kinetic energy at the design condition.

Hot-wire boundary layer traverses were performed over the rear part of the suction side of the HSU2 blade at 14 streamwise locations distributed between 45% and 99% S_0. At each position, the boundary layer traverses consist of 13 points exponentially distributed normal to the wall. The boundary layer traverses were performed up to a distance of 1.5 mm from the wall. The location of the wall was found with the method described by Hodson [15]. This process was performed at the operating conditions to account for the aerodynamic lifting of the probe and the small vibrations of the probe support. When the wall was found, the probe was moved 5 μm away from the wall in the perpendicular direction. This point has been taken as a reference (Y_n=0 mm) for the plots presented in this paper.

The hot-wire boundary layer traverses were carried out using a DANTEC 55P15 boundary layer probe with a 5 μm×1 mm Platinum-plated tungsten wire. The hot wire is operated in the constant temperature mode, using an overheat ratio of 1.8. A total of 128 ensembles were acquired at each point of the measurement grid. Each ensemble consists of 1024 points logged at 60 kHz. The method to process the hot-wire data was presented in [9]. When working with a hot wire in a compressible flow, three parameters contribute to the final output of the measurements, i.e., velocity, density, and temperature. Assumptions relating these parameters have to be made in order to interpret the data obtained with the hot wire at high subsonic Mach numbers. In this case, the assumptions to process the boundary surveys are that the static

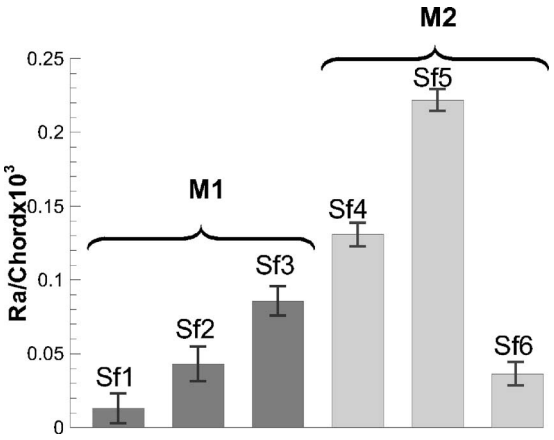

Fig. 2 Characterisation of the surface finish

pressure and the stagnation temperature are constant across the boundary layer. Furthermore, the small size of the high-speed blades reduces the spatial resolution of the measurements. The small scales also limit the time resolution. This is critical in the unsteady inflow measurements since the frequency response of the hot wire is only one order of magnitude larger than the wake passing frequency. Because of these restrictions, the hot-wire results are only used qualitatively. An overall picture of the flow field rather than quantitative values are sought.

Results

Two different manufacturing processes were used to produce the molds of the airfoils. The first process, M1, involves the production of the casting waxes using a stereolithography-based process. The second manufacturing process, M2, consists of a thermojet-based rapid prototyping of the casting waxes. As a result of this latter procedure, small spanwise ribs of $\sim 15\ \mu$m in depth are left on the surface of the blades. The blade material is a production engine alloy. The casting process M1 produces an industry standard "as cast" surface finish. The process M2, however, is not used for production engines. For both M1 and M2, different post casting finishing processes of the surface of the airfoils lead to the different surface finishes.

Figure 2 shows a bar chart with the characterization of the different surface finish presented in this paper. The surface finishes Sf1, Sf2, and Sf3 were achieved on blades manufactured by process M1, whereas the surface finishes Sf4, Sf5, and Sf6 were obtained on blades manufactured by process M2. The value of Ra, the centreline average roughness, is the arithmetic mean of the absolute departures of the roughness profile from the mean line. The values are normalised by the chord of the airfoil. For each of the surface finishes, several regions were measured along the surface to determine the size of the roughness. The consequent error bar is also shown in Fig. 2. The different surface finishes presented in this paper will be referred to using the labels of Fig. 2. The surface finishes Sf3 and Sf5 are as-cast surface finishes, and, to the touch, they resemble a very fine sandpaper. If these surfaces were then barreled, surface finishes Sf2 and Sf4 would be obtained. With further barreling a polished surface, Sf1, is achieved. The surface finish Sf6 was obtained by polishing by hand the barreled surface Sf4. Figure 3 shows a Sf5 blade and a close-up of the spanwise ribs.

At this point, a comparison between the normalized isentropic Mach number distributions around blades manufactured by the two methods has to be considered. Given the small size of the blades, the use of surface tappings was impracticable. Instead, blades representative of the Sf1 and Sf6 surface finishes were measured and the coordinates were used as an input to perform an inviscid calculation. Figure 4 shows the nondimensional isentropic Mach number distribution resulting from an inviscid calculation of the flow around the Sf1 and Sf6 profiles. The inviscid calculations presented in Fig. 4 suffer from a grid built from measured coordinates. However, the diffusion rate and the position of the suction peak do not differ significantly between the blades resulting from both manufacturing processes. Thus, a similar performance from the two blades is expected. The plot also presents the nondimensional velocity distribution measured in the low-speed cascade for the case of a smooth surface, $\mathrm{Re}=1.6\times10^5$ and unsteady inflow and a freestream turbulence of 4.0%. For this case, a separation bubble still exists downstream of the suction peak. From 5% to 40% of the suction surface, the low-speed profile presents a consistently lower nondimensional velocity distribution in comparison to its high-speed counterparts. This difference upstream of the suction peak is known to cause very little impact on the performance of the blade. On the other hand, the agreement around the position of the suction peak and the amount of diffusion presented for both high- and low-speed blades are indicative of an overall similarity between the profiles.

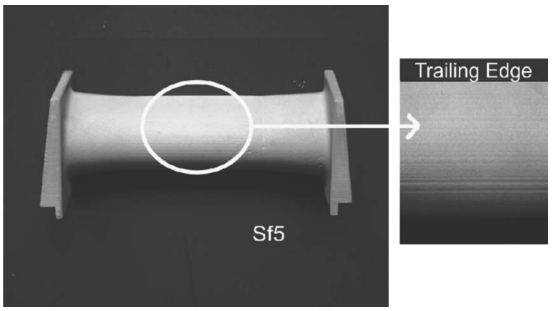

Fig. 3 Sf5 blade and close-up of the spanwise ribs

Results for Process M1. The blades of three cascades were manufactured following this procedure. The blades of each of these cascades underwent a different finishing process to obtain the surface finishes Sf1, Sf2, and Sf3 presented in Fig. 2. The normalized KSI of these blades is shown in Fig. 5. The data are presented against Reynolds number for steady and unsteady inflow conditions at the design exit Mach number, i.e., $\mathrm{Ma}_3=0.64$. The loss coefficients are normalized by the loss of the high-lift blade H presented by Howell et al. [8] at $\mathrm{Re}=1.3\times10^5$ and under unsteady inflow ($f_r=0.78$). In this way, the results can be compared to the data presented in Zhang et al. [3], which were obtained at low speed. Some of these data have been repeated in Fig. 5.

For the case of steady inflow, the curves corresponding to sur-

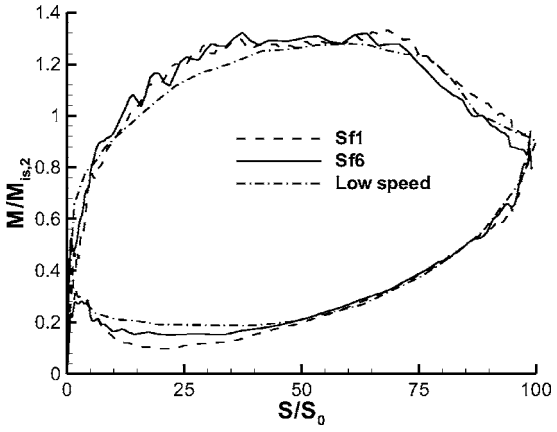

Fig. 4 Inviscid distribution of nondimensional isentropic Mach number around SF1 and SF6 profiles

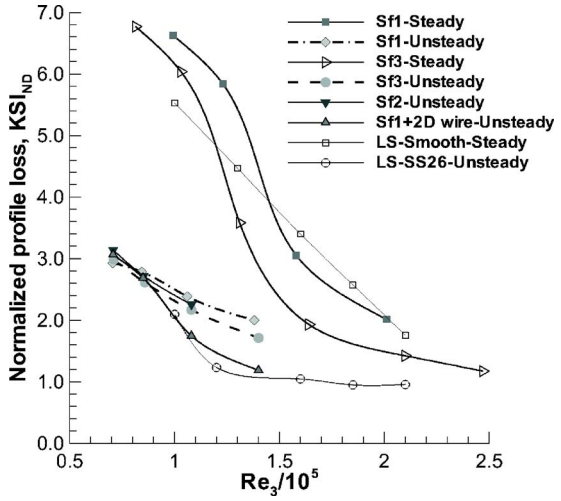

Fig. 5 Nondimensional profile kinetic energy loss coefficient against Reynolds number; $Ma_3=0.64$; manufacturing process M1

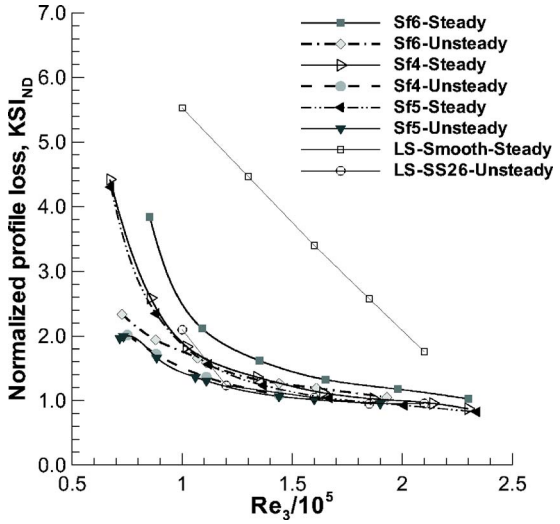

Fig. 6 Nondimensional profile kinetic energy loss coefficient against Reynolds number; $Ma_3=0.64$; manufacturing process M2

face finishes Sf1 and Sf3 show an extremely high level of losses. These results agree reasonably well with the low-speed measurements on a smooth surface under steady inflow. The steep increase in loss for Re_3 lower than 1.5×10^5 corresponds to the region where a large suction-side separation bubble occurs. At a Reynolds number Re_3 of about 1.1×10^5, the flow fails to reattach to the blade surface and, as the change of slope of the curves confirms, a further decrease of the Reynolds number increases the loss by a smaller amount. The larger loss shown by the high speed blades for $Re_3<1.1\times10^5$ in comparison to the low-speed counterparts could be due to, among other things, a larger blockage caused in the former blades by an open separation.

Under unsteady inflow and for $Re_3<9\times10^4$, the three curves corresponding to Sf1, Sf2, and Sf3 present very similar level of losses. According to the literature on the use of roughness elements, one of the critical parameters describing the effect of roughness on transition is the value of the local Reynolds number based on the size of the roughness element. Considering the latter, it seems as if for $Re_3<1.0\times10^5$, the size of the roughness is not large enough to have any effect upon transition. Hence, the three surface finishes become aerodynamically similar.

When the Reynolds number increases, the three roughnesses produce different results since the critical Reynolds number would be reached sooner for the case with the largest size of the grain, Sf3. This explains why the Sf3 blades have slightly lower losses than the Sf1 blades at a Reynolds number of 1.4×10^5. It also explains the differences between the two curves presented for the case of steady inflow.

However, the combination of unsteadiness and any of the surface finish does not result in a reduction in losses as large as the one obtained at low speed (see Fig. 5). The latter was obtained by combining unsteadiness and a discrete roughness element (in this case, a two-dimensional (2D) rectangular step). To simulate the low-speed measurements, a 2D wire was added to the surface finish with the smaller size of grain, i.e., Sf1. The criterion to chose the size, 65 μm, and the location of the wire, $64\%S_0$, was given by Zhang and Hodson [12]. The size of the wire is one order of magnitude larger than the roughness presented in Fig. 2. The presence of the 2D roughness element brings the level of the losses down to the values found in low speed measurements for Reynolds numbers larger than 9.0×10^4. When the Reynolds number is lower than 9.0×10^4, the curve corresponding to the case of the trip overlaps with the other three surface finishes. The latter indicates that for this particular location of the wire, a larger wire would have been needed to counterbalance the effect of a decrease in the Reynolds number.

Figure 5 shows that a larger benefit in terms of loss is obtained by using a 2D roughness element rather than a rough surface finish, i.e., a three-dimensional (3D) roughness. Several authors have reported the experimental evidence that for a given size of the surface element, a 3D roughness has less of an effect than a 2D roughness element. For a flat plate, Klebanoff et al. [16] found that the minimum Reynolds number based on the height of the roughness element below which there was no influence on transition was three times larger for the case of a 3D roughness element in comparison with the 2D counterparts. For the case of a LPT blade, the conclusions from Fig. 5 agree with the low-speed results presented in Zhang et al. [3] for the case of the ultra-high-lift profile U2. These authors showed that the case with a distributed (3D) roughness element presented higher losses than that with a 2D step.

In addition, Fig. 5 shows that a good agreement exists between the low- and the high-speed measurements. Hence, the validity of using low-speed experiments to study the effect of unsteadiness and/or roughness elements is confirmed for the case of ultra-high-lift profiles.

Results for Process M2. The blades of two cascades were manufactured following this procedure. Different means of post-processing the blades led to two different surface finishes, Sf4 and Sf5. As seen in previous sections, the surface finish Sf5 is an as-cast surface finish, whereas the surface finish Sf4 resulted from the barreling of the surface after casting, which results in a decrease of the size of the roughness in comparison to that of Sf5. For both of these surface finishes, small spanwise ribs were left on the surface by the manufacturing process. Once the experiments on the Sf4 cascade had finished, the blades were further polished by hand to reduce the size of the grain and obtain an additional surface finish. These latter blades will be referred to as Sf6. The size of the roughness corresponding to Sf6 is similar to that of Sf1. However, the polishing did not remove the spanwise ribs, but it did decrease their depth. A further polishing was considered inappropriate because it would probably have modified the pressure distribution around the profile.

Figure 6 shows the normalized profile loss coefficient against Reynolds number for steady and unsteady inflow conditions at the design exit Mach number, i.e., $Ma_3=0.64$. According to Fig. 6, the Sf4 and Sf5 blades present similar performance for the entire range of Reynolds numbers under consideration. The latter is

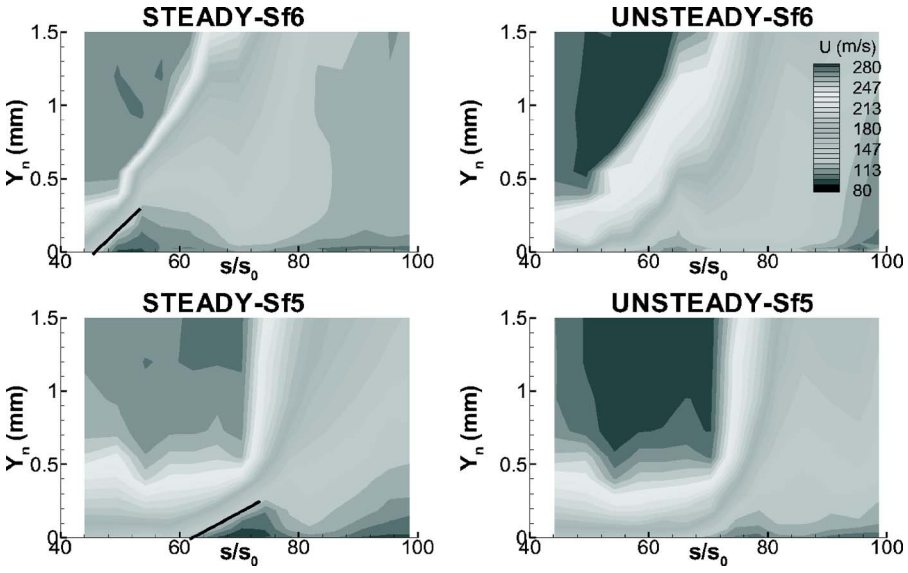

Fig. 7 Contours of mean velocity (left) and ensemble averaged velocity (right) on Sf6 (top) and Sf5 (bottom): $Ma_3=0.64$, $Re_3=9.0\times10^4$

valid for the two sorts of incoming flow, i.e., steady and unsteady. However, the size of the roughness is larger for the case of the Sf5 blades (see Fig. 2).

Figure 6 shows that the curves of Sf5-steady and Sf6-unsteady cross at a Reynolds number of about 1.1×10^5. This indicates that the permanent reduction of the size of the bubble and associated losses that are caused just by using a rough surface finish, Sf5-steady, equals the loss reduction on a smoother surface due only to the periodic suppression of the bubble by the upstream wakes, Sf6-unsteady. For Reynolds numbers lower than 1.1×10^5, the effect of the upstream wakes is more effective in reducing the losses than the effect of a rough surface. The opposite is true for Reynolds number larger than 1.1×10^5. The combined effect of both features can still reduce the profile losses as shown by the Sf5-unsteady curve.

The level of the losses of the Sf6 blades is larger than that corresponding to the Sf4 and Sf5 blades for both steady and unsteady inflow conditions. However, the benefit is less for the latter. This is consistent with the fact that under unsteady inflow, the size of the suction-side separation bubble is periodically reduced by the wakes. Therefore, there is less opportunity for a benefit to arise from the use of surface roughness.

The justification for the comments presented in the previous paragraphs can be seen in Fig. 7. In these plots, the vertical axis, Y_n, is exaggerated by a factor of 10. The figures on the left-hand side present the time mean velocity contours for the cases of Sf6 (top) and Sf5 (bottom) under steady inflow at $Re_3=9\times10^4$. A black line has been traced along the laminar shear layer of the separated flow. It is seen that the separation bubble is shorter in length and height for the case of the Sf5. At $Re_3=9\times10^4$, the Sf6 blades are operating within the range of Reynolds numbers corresponding to the steep increase in loss caused by a nearly open separation bubble. Under these conditions, the pressure distribution is altered, i.e., the peak Mach number and the point of separation move upstream (to $50\%S_0$). This can be seen by comparing the figures corresponding to Sf5 and Sf6 in steady flow. In addition, the velocity distributions presented in Zhang et al. [3] showed that the point of separation moved upstream to $55\%S_0$ for the case of $Re_3=1.3\times10^5$.

The plots on the right-hand side of Fig. 7 show the contours of ensemble averaged velocity at the phase of the wake-passing period when the size of the separation bubble reaches its minimum. At the time represented in Fig. 7, the wake has already left the test section. For both Sf5 and Sf6, the benefit from the wakes is evidenced from the reduction of the separation bubble and the slower growth of the boundary layer toward the trailing edge of the blade. In addition, for both cases, the maximum size of the separation bubble during the wake-passing period (not shown here) is smaller than that for the case of steady inflow shown on the left-hand side. For these reasons, the surface finish in Sf5 unsteady flow presents lower losses than Sf6 in either unsteady or steady flow.

Comparison Between M1 and M2. From Figs. 6 and 7, it is concluded that there is a benefit in terms of losses when using a rough surface finish of the type of the "as cast" ones, Sf3 and Sf5. The upper limit on the size of the roughness may be that which would promote (unwanted) transition within the acceleration region upstream of the suction peak—substantially increasing the surface area covered by turbulent flow and thus increasing the loss. It is important to note that this conclusion does not take into consideration the impact of the in-use degradation.

Nevertheless, the effect of surface roughness is of second order when comparing the variation of the level of losses between the blades manufactured with processes M1 and M2. The difference between the two manufacturing processes is that the blades manufactured with M1 present a uniform surface, whereas the M2 process produces an uneven surface with the appearance of 2D spanwise ribs. In addition, the curves corresponding to Sf4, Sf5, and Sf6 do not overlap at low Reynolds numbers. Hence, for the blades manufactured with the second process, there has been an effect on the profile losses over the entire range of Reynolds numbers. The surface finish Sf4 has a slightly larger size of the roughness than that of the Sf3 corresponding to the first manufacturing process. Also, the size of Sf6 is believed to be around the size of Sf1. This indicates that the differences in losses between the blades manufactured by the two different processes might not be due to the different size of the roughness presented in Fig. 2. This difference in losses could indicate that the dominant difference in surface finish is due to the presence of the spanwise ribs which act as 2D roughness elements. This is also indicated by observing the large effect on the loss of adding a 2D wire to Sf1, as seen in Fig. 5.

The difference between blades representative of both manufacturing processes can be also seen in Fig. 8. In this figure, the result of a hot-wire boundary layer survey on the blades with the pol-

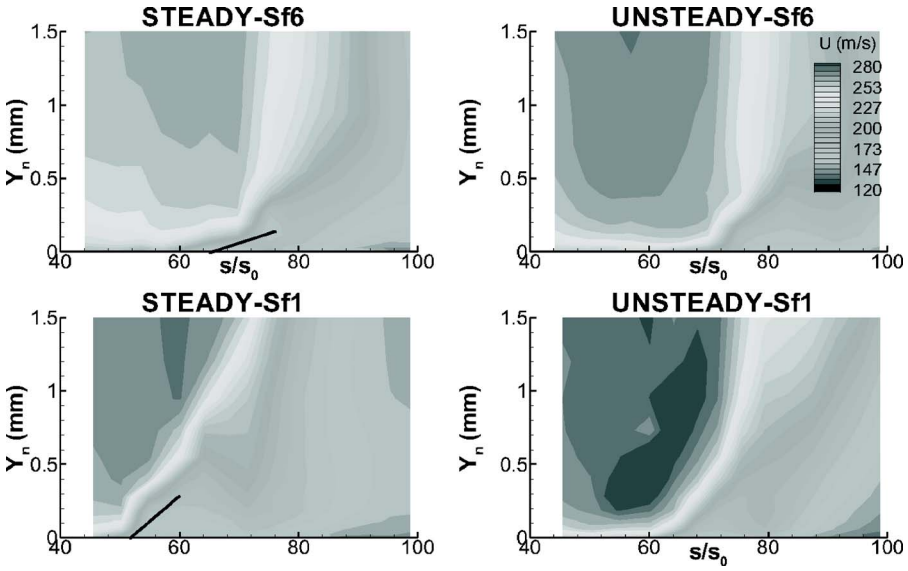

Fig. 8 Contours of mean velocity (left) and ensemble averaged velocity (right) on Sf6 (top) and Sf1 (bottom): $Ma_3=0.64$, $Re_3=1.45\times10^5$

ished finishes Sf1 (M1) and Sf6 (M2) is shown. The images on the left-hand side show the contours of mean velocity (steady inflow), whereas the images on the right-hand side show a phase of the wake-passing period equivalent to that shown in Fig. 7.

Figure 5 showed that the steep increase of losses at low Reynolds numbers for the case of Sf1 occurred when $Re_3 < 1.6\times10^5$. Therefore, in Fig. 8, the contours of mean velocity for the Sf1 finish show a flow field dominated by a large region of separated flow and where, consequently, the point of separation occurs further upstream in comparison to the equivalent plot for the Sf6 blade. For this latter profile, a smaller separation bubble exists. For the case of unsteady inflow, a thicker boundary layer is identified for the case of Sf1. This, among other differences that will be seen in the next section, explains the larger losses for the case of the Sf1 profile.

The similarities between the two isentropic Mach number distributions shown in Fig. 4 implied that the difference in performance between the two manufacturing processes is not caused by a different pressure distribution. Thus, the cause of the different performance must be related to the surface finish, which cannot be captured by an inviscid calculation.

It has already been argued that the 2D spanwise ribs left on the surface of the blade by the second manufacturing process cause an additional reduction in loss when the surface finishes Sf4, Sf5, and Sf6 blades are compared to those of the first manufacturing route Sf1, Sf2, and Sf3. The ribs are believed to be acting in the same way as the negative steps presented in Zhang et al. [3]. Zhang and Hodson [12] have previously shown that an optimum height of step exists for each Reynolds number. This is also true for the surface finish presented here. Also, in the current case, one single rib is smaller than the 60 μm wire presented in Fig. 5 but larger than the size of any of the rough finishes (see Fig. 2). The presence of several of these ribs between the suction peak and the separation point is believed to be the cause of the reduction of profile losses for the case of the second manufacturing process. Even though the ribs are present on the whole surface, and, given that the profile losses decrease with the presence of the ribs, only those ribs between the suction peak and the point of separation are believed to have an effect on the flow.

It has been shown that the ultra-high-lift profile HSU2 blade presents higher losses than an equivalent high lift profile under LPT Mach and Reynolds numbers representative conditions. The reason for the high-level losses can be found by considering the large back surface diffusion and the low reduced frequency typical of an ultra-high-lift blade. By modifying slightly the manufacturing process of the casting waxes, the losses could be reduced down to the level of a high lift blade. A further increase of the lift coefficient to a new generation of blades can be considered.

The experimental results presented in this paper have been carried out with a freestream turbulence of $\sim$0.5%. In real LPT engine conditions, the freestream turbulence is likely to be higher than this value, especially toward the last stages of the LPT. In Zhang et al. [3], the effect of a high freestream turbulence, 4.0%, has been presented for the case where a surface trip was also used. The results showed that although the profile losses increased slightly at high Reynolds numbers in comparison to the equivalent low freestream turbulent flow case, the blade performance was better for low Reynolds numbers. This is because the increased freestream turbulence intensity complemented the trip and the wakes in suppressing the separation bubble when the latter had not been completely suppressed. Hence, for this case, the increase of freestream turbulence has the same effect as an increase of the Reynolds number. The profile losses shown in Fig. 6 for the high-speed cases depend only marginally of the Reynolds number when $Re_3 > 1.5\times10^5$. This could indicate that, for the cases presented in Fig. 6, an increase of the freestream turbulence might not represent a large penalty in terms of losses at high Reynolds numbers. At low Reynolds number, a minor benefit from the increase of the freestream turbulence is still expected. However, in order to draw a final conclusion, an extended experimental investigation would have been needed.

Wake-Induced Transition Mechanism. This section presents a brief insight into the wake-induced transition mechanism. Even though the hot-wire results presented in this paper are of a qualitative nature, conclusions about the wake-induced transition mechanism can still be drawn. The cases of the blades Sf1 and Sf6, i.e., polished blades from the two different manufacturing processes, will be compared. The results will be also compared to the low-speed results presented in Zhang et al. [3].

Under certain conditions, the velocity perturbation associated to the wake, which can be thought of as being caused by the so-called negative jet, can induce the rolling up of the separated shear layer of the laminar separation bubble. This occurs by an inviscid Kelvin-Helmholtz mechanism [17]. Zhang et al. [18] argued that for Re_θ at the point of separation of about 185, the boundary layer

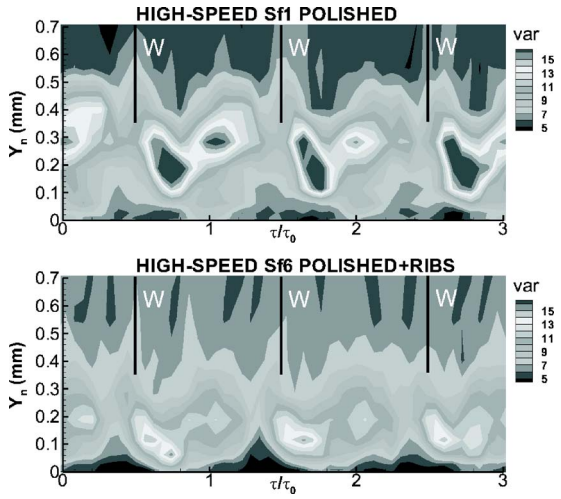

Fig. 9 Contours of variance of the velocity at 79% S_0, Sf1 (top) and Sf6 (bottom) blades: $Ma_3=0.64$, $Re_3=1.45\times10^5$

presents a low receptivity to the turbulence of the wake and the inviscid mechanism dominates the breaking down to turbulence. These authors also argued that when Re_θ is about 250 at the point of separation, transition could be initiated, most probably, by the turbulence in the wake in the proximity of the separation. Thus, the inviscid mechanism is inhibited. On the U2 blade, the Re_θ at the separation point is about 250 (see [3]), and thus, wake turbulence induced transition is believed to be the mechanism by which transition occurs in the current work.

Figure 9 shows the contours of variance of the velocity determined from the hot-wire data for the cases of the two polished blades, Sf1 (top) and Sf6 (bottom). The results are presented on a time-height plane at a surface distance of 79% S_0 and for a Reynolds number of 1.45×10^5. This position corresponds to a point within the unsteady separation bubble. The wake, which travels at freestream velocity, is label as W in Fig. 9. The position of the wake is known from the increased rms outside the boundary layer. For the cases presented in Fig. 9, the flow is separated underneath the wake. This is indicated by the displacement of the regions of highest variance away from the wall. The regions of low variance close to the surface lie within the separation bubble.

According to the figure corresponding to Sf1, the boundary layer reacts to the passing of the wake without any delay for values of $Y_n>0.35$ mm. For lower values of Y_n, a delay associated with the diffusion of the turbulence initiating wake-induced transition into the boundary layer occurs. This can be identified by the sloping trajectory of the region of high variance, which indicates the presence of transitional flow. This agrees with the detailed measurements presented in Zhang et al. [3], where the authors showed that the wake-induced transition lags behind the wake center. For the case of Sf6, there is instantaneous reaction to the wake passing for $Y_n>0.25$ mm, indicating the existence of a thinner boundary layer for this latter case. This means that the increase of variance near the surface occurs after a shorter delay. In this case, it occurs ~20% of the wake-passing period earlier in comparison to that of Sf1.

After the region of wake-induced transition has passed, Fig. 9 shows that the shear layer starts to recover the height that it would have without the presence of the wakes. Hence, a region of high variance, in this case associated with the shear layer of the reestablishing bubble, can be seen between the wakes. The high variance found in the shear layer corresponds to the separated boundary layer transition between the wakes. The region of lower variance between these two regions of higher variance is believed to be indicative of the calmed region that follows wake-induced transition. Before the arrival of the next wake, the size of the separation bubble reaches its maximum within the wake-passing period. Hence, the transition within the separated boundary layer is expected to start further downstream. The latter explains the low variance before the arrival of the wake. The reestablishment of the bubble is interrupted before completion by the arrival of the next wake. In the case of surface finish Sf1; the higher values of variance occur further from the surface, which indicates that the separation bubble is larger for this latter case in comparison to the case of Sf6. However, at no point within the wake-passing cycle does the height of the separated shear layer reach that corresponding to steady flow. The lack of full growth of the steady separation in either case is partly why the losses are reduced. Furthermore, a comparison between both blades shows that there is a larger boundary layer thickness during the entire wake-passing period for the case of the Sf1 blade. This is consistent with the greater production of loss by the Sf1 blade.

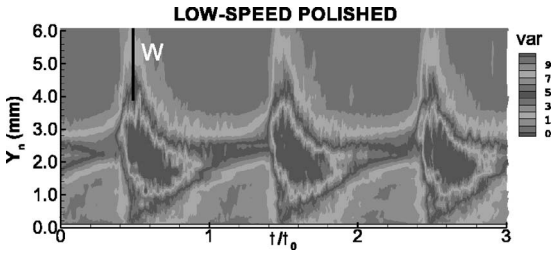

Fig. 10 Contours of variance of the velocity at 79% S_0 on the smooth surface at low speed: $Re_3=1.30\times10^5$

Figure 10 shows the contours of variance of the velocity determined from the hot-wire data for the case of the low-speed tests at a surface distance of 79% S_0 on a smooth (polished) surface and for a Reynolds number of 1.3×10^5. The detailed boundary layer development for this case has been discussed in Zhang et al. [3]. Overall, the contours shown in Fig. 10 are comparable to the high-speed result corresponding to the Sf1 smooth blade presented in Fig. 9 (top).

Some differences between Figs. 10 and 9 are evident. Even though there is no time-mean effect of the compressibility on the performance of the blade, this still plays a role and can cause differences between the high- and low-speed results. However, the effect of compressibility is of second order and does not change the main flow features. In addition, given the assumptions made to process the results of a hot wire in a compresible flow only qualitative data can be obtained. Nevertheless, phenomena, such as the wake-turbulence-induced transition, the delay in the diffusion of the turbulence initiating wake-induced transition into the boundary layer, and the reestablishment of the separation bubble between the wakes are evident in both Figs. 9 and 10. The comparison between the low- and high-speed tests shows that, not only the time mean quantities are comparable, but it also seems as if the boundary layer develops in the same manner.

Conclusions

The effect of surface roughness on an aft-loaded ultra-high-lift profile has been investigated at realistic LPT Mach and Reynolds numbers. By studying the same pressure distribution at low and high speeds, the validity of the low-speed studies on the effect of roughness and/or unsteadiness on an ultra-high-lift profile could be confirmed.

Even though the HSU2 blade is an aft-loaded profile, the large deceleration rate downstream of the suction peak causes the flow to separate soon after the deceleration starts. The consequences of this, i.e., large dissipation associated with the reattachment region, large portion of surface covered by turbulent flow, and a significant growth of the boundary layer downstream of the reattachment, contribute to the large level of losses of the nominal profile, i.e., a smooth/uniform profile, under steady inflow.

For the sizes of roughness used in this work, which represent an as-cast, barreled, and polished surface finishes, it has been found that a rough surface finish plays a secondary role in the reduction of the losses in comparison to a smoother surface finish. The positive results of these experiments being the fact that no loss penalty was found for the range of Reynolds numbers under consideration for either manufacturing process.

A new way of controlling the losses has been achieved by using an alternative manufacturing process. The presence of small, spanwise ribs left on the surface of the blade by one of the manufacturing processes causes a large reduction of the profile losses. The ribs between the suction peak and the point of separation act as negative steps that can control the size of suction-side separation bubble. This effect is of first order in comparison to the roughness characterizing the surface finish. Therefore, the cost can be reduced by removing the need to barrel or polish the blades.

Acknowledgment

The authors would like to thank T. Chandler for his work on the high-speed rotating bar rig. The authors would also like to thank Rolls-Royce plc for the funding of the project and their permission to publish this paper.

Nomenclature

C = chord
C_p = static pressure coefficient=$(P_{01}-Ps)/(P_{01}-P_{s2})$
f = bar-passing frequency
f_r = reduced frequency=$f(C/V_{2,\mathrm{is}})$
KSI = kinetic energy loss coefficient=$1-V_3^2/V_{3,\mathrm{is}}^2$ =$(T_{s3}-T_{3,\mathrm{is}})/(T_{01}-T_{s3})$
Ma = Mach number
P = pressure
Re = Reynolds number (based on chord)
Re_θ = Reynolds number based on momentum thickness
τ, τ_0 = time, wake-passing period
S_0 = Suction surface length
U, V = velocity
Y_n = coordinate normal to the wall (mm)

Subscripts

0 = stagnation
1 = inlet conditions to the cascade
2 = exit conditions from the cascade
3 = mixed-out conditions
is = isentropic
ND = nondimensional
s = static

References

[1] Hourmouziadis, J., 1989, *Aerodynamic Design of Low Pressure Turbines* (AGARD Lecture Series, 167), AGARD, pp. 8.1–8.40.
[2] Harvey, N. W., Schulte, V. S., Howell, R. J., and Hodson, H. P., 1999, "The Role of Research in the Aerodynamic Design of an Advanced Low Pressure Turbine," 3rd European Conference on Turbomachinery, I MechE, London, March.
[3] Zhang, X. F., Vera, M., Hodson, H. P., and Harvey, N., 2006, "Separation Control of an Aft-Loaded Ultra-High-Lift LP Turbine Blade at Low Reynolds Numbers: Low-Speed Investigation," ASME J. Turbomach., **128**, pp. 517–527.
[4] Halstead, D. E., Wisler, D. C., Okiishi, T. H., Walker, G. J., Hodson, H. P., and Shin, H. W., 1995, "Boundary Layer Development in Axial Compressors and Turbines. Parts 1-4," ASME Paper No. 95-GT-461/2/3/4.
[5] Schulte, V., and Hodson, H. P., 1994, "Wake-Separation Bubble Interaction in Low Pressure Turbines," AIAA Paper No. AIAA 94-2931.
[6] Schulte, V., and Hodson, H. P., 1998, "Unsteady Wake-Induced Boundary Layer Transition in High Lift LP Turbines," ASME J. Turbomach., **120**, pp. 28–35.
[7] Curtis, E. M., Hodson, H. P., Banieghbal, M. R., Denton, J. D., Howell, R. J., and Harvey, N. W., 1996, "Development of Blade Profiles for Low Pressure Turbines Applications," ASME Paper No. 96-GT-358.
[8] Howell, R. J., Hodson, H. P., Schulte, V., Schiffer, H. P., Haselbach, F., and Harvey, N., 2001, "Boundary Layer Development in the BR710 and BR715 LP Turbines-The Implementation of High Lift and Ultra High Lift Concepts," ASME Paper No. 2001-GT-0441.
[9] Vera, M., Hodson, H. P., and Vazquez, R., 2005, "The Effect of a Trip Wire and Unsteadiness on a High-Speed Highly-Loaded Low-Pressure Turbine Blade," ASME J. Turbomach., **127**, pp. 747–754.
[10] Haselbach, F., Schiffer, H. P., Horsman, M., Dressen, S., Harvey, N., and Read, S., 2001, "The Application of Ultra High Lift Blading in the BR715 LP Turbine," ASME Paper No. 2001-GT-0436.
[11] Ramesh, O. N., Hodson, H. P., and Harvey, N. W., 2001, "Separation Control in Ultra High Lift Airfoils by Unsteadiness and Surface Roughness," 15th International Symposium on Airbreathing Engines, September, Bangalore, India.
[12] Zhang, X. F., and Hodson, H. P., 2003, "Parametric Study of Surface Roughness and Wake Unsteadiness on a Flat Plate With Large Pressure Gradient," 10th ISUAAAT, Durham, NC, Sept. 7–11.
[13] Vera, M., Hodson, H. P., and Vazquez, R., 2003, "The Effect of Mach Number on LP Turbine Wake-Blade Interaction," 10th ISUAAAT, Durham, NC, Sept. 7–11.
[14] Howell, R. J., Ramesh, O. N., Hodson, H. P., Harvey, N. W., and Schulte, V., 2001, "High Lift and Aft Loaded Profiles for Low Pressure Turbines," ASME J. Turbomach., **123**, pp. 385–392.
[15] Hodson, H. P., 1984, "Measurements of Wake-Generated Unsteadiness in the Rotor Passages of Axial Flow Turbines," ASME Paper No. 84-GT-189.
[16] Klebanoff, P. S., Schubauer, G. B., and Tidstrom, K. D., 1955, "Measurements of the Effect of Two-Dimensional and Three-Dimensional Roughness Elements on Boundary Layer Transition," J. Aeronaut. Sci., **22**(11).
[17] Stieger, R. D., and Hodson, H. P., 2003, "The Transition Mechanism of Highly Loaded LP Turbine Blades," ASME Paper No. GT2003-38304.
[18] Zhang, X. F., Hodson, H. P., and Harvey, N. W., 2005, "Unsteady Boundary Layer Study on Ultra-High-Lift Low Pressure Turbine Blades," 6th European Turbomachinery Conference, Paper No. ETC6-145.

Unsteady Flow Physics and Performance of a One-and-1/2-Stage Unshrouded High Work Turbine

T. Behr
Turbomachinery Laboratory,
Swiss Federal Institute of Technology,
8092 Zurich, Switzerland
e-mail: behr@lsm.iet.mavt.ethz.ch

A. I. Kalfas
Deparment of Mechanical Engineering,
Aristotle University of Thessaloniki,
Greece

R. S. Abhari
Turbomachinery Laboratory,
Swiss Federal Institute of Technology,
8092 Zurich, Switzerland

This paper presents an experimental study of the flow mechanisms of tip leakage across a blade of an unshrouded turbine rotor. It shows the design of a new one-and-1/2-stage, unshrouded turbine configuration, which has been developed within the Turbomachinery Laboratory of ETH Zurich. This test case is a model of a high work ($\Delta h/u^2=2.36$) *axial turbine. The experimental investigation comprises data from unsteady and steady probe measurements, which has been acquired around all the bladerows of the one-and-1/2-stage, unshrouded turbine. A newly developed 2-sensor Fast Response Aerodynamic Probe (FRAP) technique has been used in the current measurement campaign. The paper contains a detailed analysis of the unsteady interaction between rotor and stator blade rows, with particular attention paid on the flow in the blade tip region. It has been found that the interaction of the rotor and the downstream stator has an influence on the development of the tip leakage vortex of the rotor. The vortex is modulated by the stator profiles and shows variation in size and relative position to the rotor trailing edge when it stretches around the stator leading edge. Thereby a deflection of the tip leakage vortex has been observed, which expresses in a varying circumferential distance between two neighboring vortices of* ±20% *of a rotor pitch. Furthermore, a significant influence of quasi-stationary secondary flow features of the upstream stator row on the secondary flow of the rotor has been detected. The geometry and flow field data of the one-and-1/2-stage turbine will be available to the turbomachinery community for validation and improvement of numerical tools.* [DOI: 10.1115/1.2447707]

Introduction

Modern gas turbine designs aim to reach highest possible turbine entry temperatures in order to increase cycle efficiency and turbine specific work. Due to the limitation of the material, rotating blade rows of high-pressure gas turbine stages are designed as unshrouded rotors to reduce mechanical stress. In addition, different cooling strategies have been developed in order to achieve adequate life for all parts that are exposed to these high-temperature gas flows. One critical region for cooling in a high-pressure turbine that remains is the blade tip area. Due to its function of sealing the rotating blade against the stationary casing flow path, this region experiences high thermal loads and is typically difficult to cool. Another way of increasing turbine cycle efficiency is the reduction of aerodynamic losses. The unshrouded design of high-pressure rotor blade rows introduces high losses due to tip leakage flows. Booth et al. [1] found them to be in the order of up to one third of the overall stage losses.

Several strategies for reducing losses due to blade tip gap flows have been subject to a number of investigations in the past decades. According to Denton [2] the loss related to over tip flows is proportional to a discharge coefficient. Further it scales with the velocity distribution around the blade tip, and thus with the loading of the blade tip.

One way of changing the discharge coefficient without effecting significantly the pressure distribution around the tip profile is through modifying the blade tip geometry. Contouring can be done by including squealer rims or radii on the edges of the tip. Booth [3] presented test series of different tip geometries and evaluated the related discharge coefficients. Bindon and Morphis [4] tested three different tip geometries in a linear cascade. They found the discharge coefficient is not necessarily representative for the overall loss created due to tip leakage flow. It does not account for losses due to mixing of the tip leakage flow downstream of the rotor. In an investigation of Kaiser and Bindon [5] in a 1.5-stage rotating rig the plain tip has shown the best performance compared to other geometries tested. With a tip containing a radius on the pressure side edge, the vena contracta that usually forms inside the tip gap could be almost completely eliminated. Other studies on rotating rigs concerning this area of research have been presented by Yoshino et al. [6] and Camci et al. [7]. A numerical analysis on the influence of improved tip concepts has been by Chander et al. [8].

The possibility of reducing tip leakage flows due to reduced loading of the tip region has been discussed in De Cecco et al. [9] and Yamamoto et al. [10]. Staubach et al. [11] realized the off-loading of the tip by applying three-dimensional (3D) design strategies to the profiles. Tip lean was found to be beneficial for this purpose, however its application is limited due to stresses within the rotor blade.

Offenburg et al. [12] investigated in the effect of different trenches within the casing around the rotor on efficiency of the stage. The function of trenches within the casing was found to depend on the tip gap height. Until a relative tip gap of 2.3% blade span the straight casing contour has shown the best results.

On the effect of tip leakage in a multi-stage environment, Harvey [13] concluded that no benefit can be gained out of the tip leakage flow once it has formed into a vortex. In order to limit the losses this vortex imposes on subsequent blade rows, the over tip leakage has to be reduced, and thus the strength of the vortex.

Contributed by the International Gas Turbine Institute of ASME for publication in the JOURNAL OF TURBOMACHINERY. Manuscript received June 7, 2006; final manuscript received June 8, 2006. Review conducted by David Wisler. Paper presented at the ASME, Turbo Expo 2006: Land, Sea and Air (GT2006), Barcelona, Spain, May 8–11, 2006. Paper No. GT2006-90959.

Another approach in order to reduce the losses due to tip leakage has been undertaken by Dey et al. [14] and Rao et al. [15,16]. Coolant has been injected from the blade tip into the tip gap in order to reduce the mixing losses due to the tip leakage. Jets at different discrete positions and blowing ratios have been evaluated. An influence of the injection rate on the radial position of the tip leakage vortex and of the injection position on its strength could be detected.

The design of the new test case focuses on the set research objectives and orientates on findings of previous investigation described above. A 1 1/2 stage turbine configuration, comprising a flat blade tip geometry and a straight rotor casing contour, has been implemented into a continuously operating test rig. Unsteady probe measurement techniques can be applied to measure the complete flow field around the blade rows. The existence of a second stator as well allows the evaluation of tip leakage effects on the performance of subsequent blade rows. The experimental investigation of the new test configuration creates the background for an upcoming study of tip leakage flow phenomena.

Experimental Method

The new research project required some substantial modification to the existing turbine rig of the turbomachinery laboratory. The previous two-stage, shrouded turbine configuration has been successfully used for a number of multi-stage, low-speed investigations, (i.e., Schlienger [17], Pfau [18], Porreca et al. [19], and Behr et al. [20]). A redesign of the entire turbine section made it possible to achieve more realistic flow conditions for the upcoming investigation and, at the same time, it increases the capabilities for measurement access. In the following sub section the new turbine rig will be introduced in more detail.

Research Turbine Facility.

Global System Design. The air loop of the facility is of a quasi-closed type and includes a radial compressor, a two-stage water to air heat exchanger, and a calibrated venturi nozzle for mass flow measurements. Before the flow enters the turbine section, it passes through a 3 m long straight duct, which contains flow straighteners to ensure an evenly distributed inlet flow field. Downstream of the turbine the air loop is open to atmospheric conditions. A dc generator absorbs the turbine power and controls the rotational speed of the turbine. A torque meter measures the torque that is transmitted by the rotor shaft to the generator. The turbine entry temperature (TET) is controlled to an accuracy of 0.3% and the rpm is kept constant within $\pm 0.5\ \text{min}^{-1}$ by the dc generator. The pressure drop across the turbine is stable within 0.3% for a typical measurement day. More information on the test rig can be found in Sell et al. [21].

For the current investigation the test rig turbine section has been redesigned to meet the following objectives:

1. Model of unshrouded, high-pressure gas turbine stage:
   - High-pressure gas turbine blade design;
   - High stage loading;
   - Compressibility effects;
   - Low aspect ratio; and
   - Realistic rotor exit flow field through second stator.
2. High accessibility for flow measurements:
   - Probe access to inlet and exit of each blade row; and
   - Optical access to all blade rows.
3. Flexibility for different research projects:
   - Modular design for fast hardware changes;
   - Universal measurement windows; and
   - Clocking of stator blade rows.

Table 1 Main parameter of "LISA" 1.5-stages axial turbine research facility at design operating point

Turbine	CFD	Exp.
Rotor speed (rpm)	2700	2700
Pressure ratio (1.5-stage, total to static)	1.58	1.60
Turbine entry temperature (°C)	55	55
Total inlet pressure (bar abs norm)	1.4	1.4
Mass flow (kg/s)	12.15	12.13
Shaft power (kW)	289	292[a]
Hub/tip diameter (mm)	660/800	660/800
First stage	CFD	Exp.
Pressure ratio (first stage, total to total)	1.35	1.35
Degree of reaction (-)	0.39	0.39
Loading coefficient $\psi=\Delta h/u^2$ (-)	2.21	2.36[b]
Flow coefficient $\phi=c_x/u$ (-)	0.63	0.65

[a]From torquemeter.
[b]From five-hole-probe measurement.

Given the fact that the compressor pressure ratio is limited to $\Pi_{c,\max}=1.5$, the new turbine contains only one highly loaded rotating blade row. This design was chosen in order to maximize flow Mach numbers and the loading coefficient of the turbine stage. The static pressure of the flow at exit of the first stage reaches almost the level of the atmospheric pressure, before it is further reduced by the second stator. The existence of a second stator has been set as a design intention in order to have the potential field of a subsequent stage. Since the turbine rig is open to atmosphere at the exit, a tandem de-swirl vane arrangement recovers the static pressure at exit of the second stator back to the ambient level. This design increases the available pressure ratio at the first stage to the maximum possible. The key parameters of the new turbine configuration are presented in Table 1 as a comparison between computational fluid dynamics (CFD) prediction and experimental validation.

Mechanical Design

A cross-section cut of the turbine section is shown in Fig. 1, as well as an expanded view of the test section in Fig. 2. The turbine mechanical design allows quick and precise assembly of all parts, which ensures a high level of repeatability and comparability between different builds.

First stator and rotor are manufactured as bladed disks (blisks) out of one piece (see Fig. 3). The manufacturing process ensures an accuracy of the profile shape of ±0.05 mm with respect to the design intention. The roughness of the profiles and flow channels are hand polished down to $Ra=0.8\ \mu$m. The second stator ring is divided into several segments, which gives the opportunity of individual instrumentation of single stator profiles.

The first stator row is fixed to a support ring that can be continuously positioned in circumferential direction. This feature opens the possibility to clock the two stator blade rows relatively to each other.

Measurement access for intrusive and nonintrusive techniques is provided around all blade rows. Aerodynamic probes can be automatically positioned inside the flow by a four-axis numerically controlled traversing system with high accuracy in every direction. In order to minimize the disturbance of the flow due to the probe access, only small holes are placed in the casing rings, which allow a probe to pass through. For the circumferential positioning, the casing ring is then traversed together with the probe.

Inside of the rotor casing ring a multi-purpose window has been implemented which covers around five rotor pitches. It can be traversed as well in a circumferential direction. Through that access it is possible to apply optical techniques, such as particle in velocity (PIV).

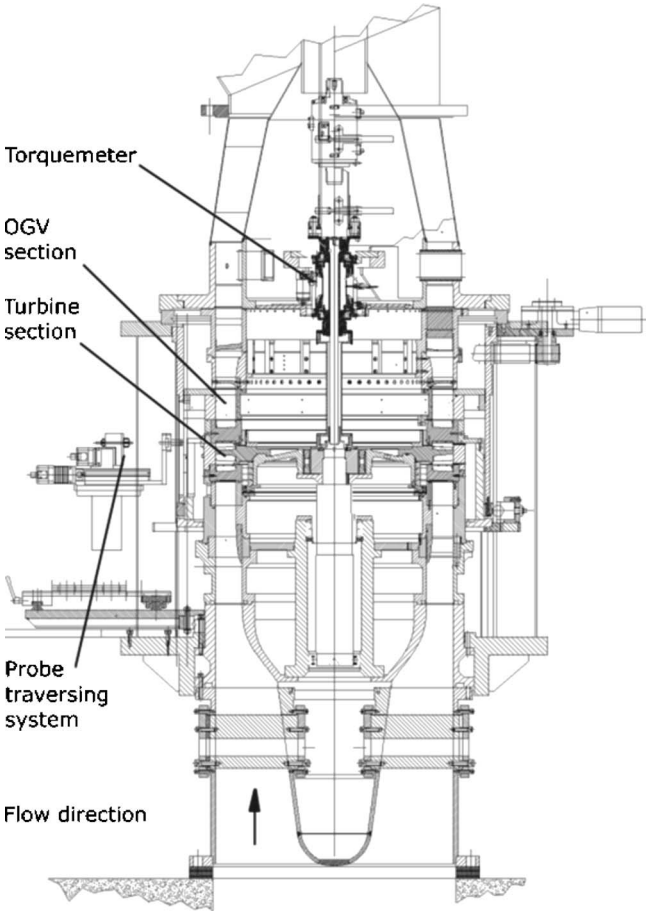

Fig. 1 "LISA" 1 1/2 stage axial turbine facility

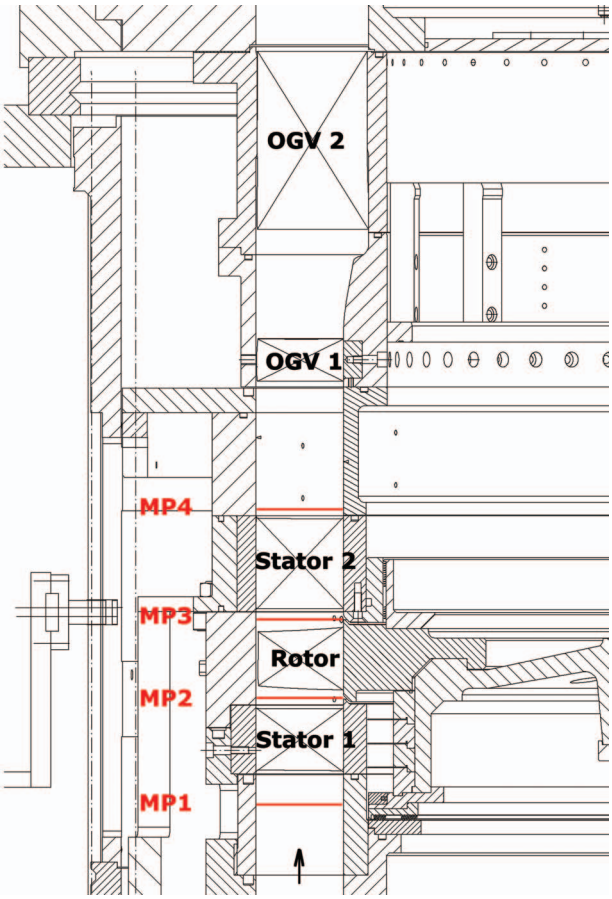

Fig. 2 1.5-stage turbine section with probe measurement planes and tandem exit guide vane section

Bladerow Design

All bladerows of the new 1 1/2 stage, unshrouded turbine have been designed at the Turbomachinery Laboratory. The geometry data are available to the public domain from Behr et al. [22]. A number of commercial and in-house design and validation tools have been combined to establish a development algorithm, which lead to the final design of four new turbine blade rows:

1. *1D design*: The meanline design of the new turbine has been done using an in-house tool of the Turbomachinery Laboratory of ETH Zurich (LSM). In addition the commercial tool Concepts NREC Axial has been applied.
2. *Profile generation*: The commercial tool Concepts NREC Axcad has been used for creating the baseline 2D profiles at different span positions and to define the stacking line of the 3D profiles. The implemented profile generator is based on an 11-parameter, axial turbine airfoil geometry model of Pritchard [23].
3. *Profile optimization*: The baseline 2D blade profiles have been optimized by running the industrial CFD code Stage3D in an inverse design mode. By defining the loading distribution of a 2D profile, the code corrects the geometry of the profile until it matches to the given distribution. The method has been developed and introduced by Troxler [24]. As a result of this optimization Fig. 4 shows the profile of the rotor at span positions hub, midspan and tip and its corresponding distributions of relative isentropic surface Mach number (Fig. 5).
4. *Aerodynamic design validation*: The industrial CFD code Stage3D has been used to validate the performance of the 3D blade geometries. All profiles have been modeled using grids created out of straight *H* meshes. Calculations were performed on single rows as well as in the multi-stage domain. The 3D steady and unsteady Navier–Stokes multistage solver Stage3D has been derived from the original Dawes code BTOB3D [25], running a discretization scheme from Jameson and Baker [26]. The one-equation turbulence models of Spalart and Allmaras [27] has been chosen in the current case. When running steady state the solver uses a so-called mixing-plane between rotating and nonrotating cascades, which mixes out circumferential variations. The averaging for the mixing planes is done, using a consistent

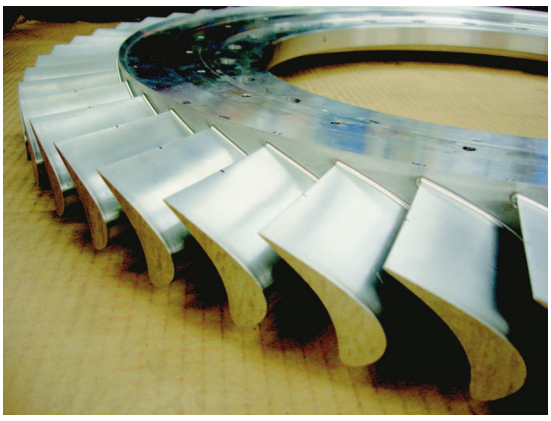

Fig. 3 Rotor blisk of the 1.5-stage unshrouded turbine

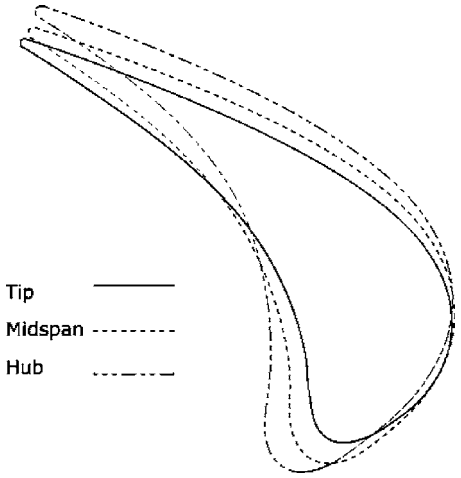

Fig. 4 Profile geometry of rotor blade at three span positions

approach from Denton [2]. The code has been further validated and improved by Mokulys et al. [28].

5. *Computer aided design (CAD) design*: The construction of 3D CAD models for manufacturing has been done using CATIA V5. It uses a cubic spline interpolation to connect the imported 2D profiles to a 3D model. Splines inbetween the profiles can be defined to prevent undesirable twisting of the 3D geometry. Important design geometry parameters, such as trailing edge radii, or throat areas, can be checked very accurately with this tool.
6. *Finite element method (FEM) validation*: To check the structural integrity of the rotor the FEM tool Abaqus has been applied.

The flow is turned by the first stator blade row to an average exit angle of about 73 deg. Thereby it reaches an average Mach numbers of $Ma_{av}=0.54$ at the exit of the first stator. The profiles of the both stators follow a constant exit angle design. Within the rotor the flow is redirected by an average turning angle of $\varepsilon=122$ deg, which results in a mean loading coefficient of $\psi=2.36$. The radial tip gap between rotor and casing has been selected to be of 1% of the blade span. The flow enters the second stator blade row at an average absolute flow angle of $\phi_{av}=-42$ deg and leaves it again at $\phi_{av}=64$ deg. It is thereby accelerated to an average exit Mach number of $Ma_{av}=0.48$. A more detailed list of profile parameters can be found in Table 2.

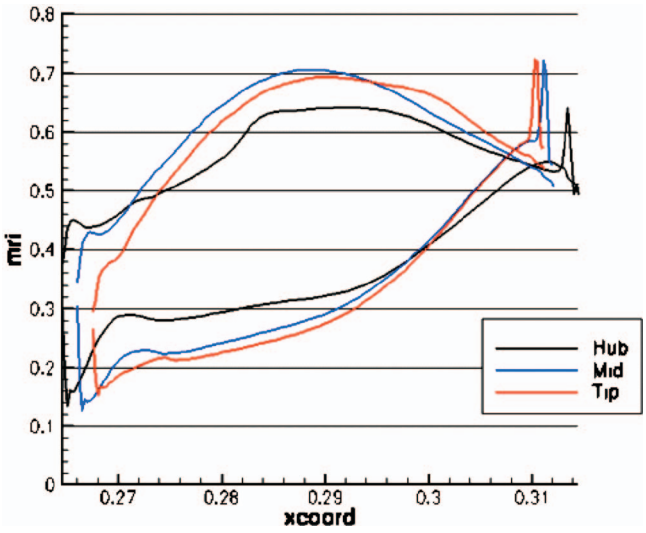

Fig. 5 Distribution of relative isentropic Mach numbers on the rotor at three span positions

Table 2 Characteristic geometry and performance parameters of the 1.5-stage turbine configuration (performance values derived from five-hole-probe measurements at design operating point)

	Stator 1	Rotor	Stator 2
Number of blades	36	54	36
Inlet flow angle (deg) (midspan)	0	54	−42
Exit flow angle (deg) (midspan)	73	−67	64
Solidity (chord/pitch)	1.27	1.41	1.34
Mean stagger angle (deg)	52.8	39.4	34.5
Aspect ratio (span/chord)	0.87	1.17	0.82
Zweifel number (-)	0.7	1.0	1.0
Profile stacking	LE	CoG	LE
Blade row relative exit Mach numbers (-) (average)	0.54	0.50	0.48
Reynolds number based on true chord and blade row relative exit velocity (-)	$7.1\cdot10^5$	$3.8\cdot10^5$	$5.1\cdot10^5$

During the design process it was decided to use a tandem outlet guide vane ensemble. The first outlet guide vane (OGV) row was designed to be adjustable in a range of stagger angle of ±10 deg. The second OGV row is fixed and turns the flow back to a 0 deg exit flow angle. Since the turbine exit is open to atmosphere, this design gives the possibility to throttle the exit of the turbine and hence to adjust the pressure ratio of the 1.5-stage turbine stages.

The first OGV has been design using the NACA profile definition of the Concepts AXCAD profile generator (see Fig. 6). The intended turning of this profile is in the order of 18 deg. In order to prevent flow separation at the endwalls and related unsteady flow instabilities, hub and tip lean have been applied for the profile stacking. At the hub a lean angle of 30 deg has been applied

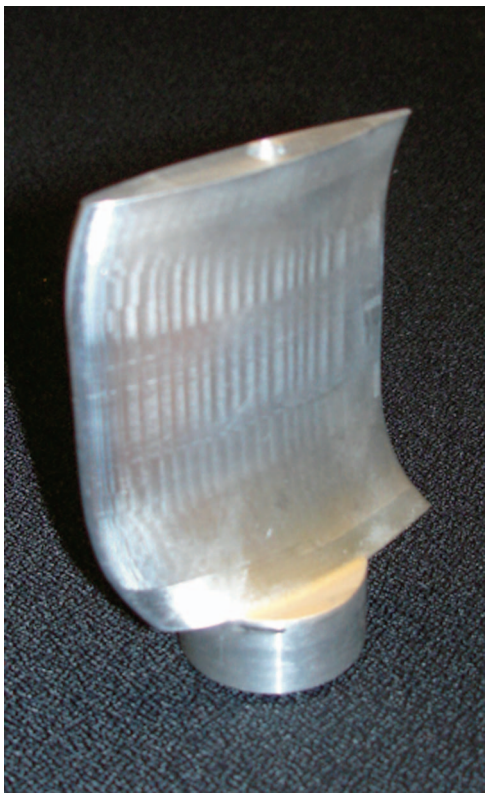

Fig. 6 Profile of first outlet guide vane row

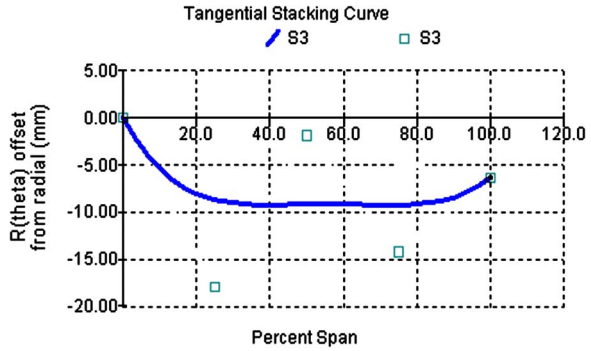

Fig. 7 Stacking definition of first OGV row

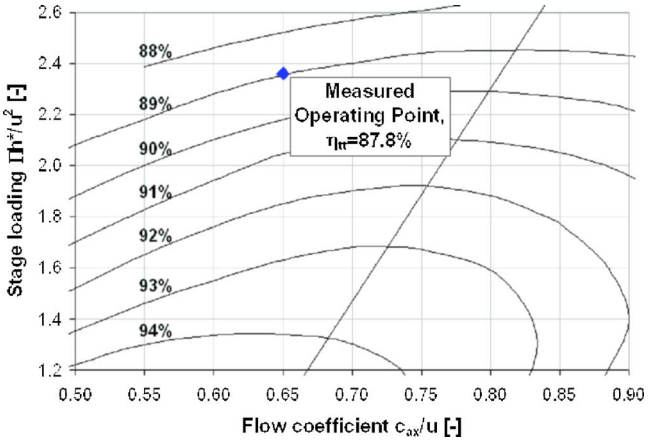

Fig. 8 Smith chart with measured operating point and determined total-to-total efficiency (reproduced after Ref. [32])

from 0% to 25% span. At the tip a lean angle of 15 deg has been applied from 90% to 100% span. The stacking definition is presented in Fig. 7.

The second OGV row comprises of a cylindrical profile which turns the flow from 46 deg to 0 deg. This extreme turning can be realized by the special shape of the profile, which accelerates the flow almost until the trailing edge, where a step diffuser releases it into the duct. With this design no separation and hence no blockage occurs (see Table 3).

Measurement Technology. The experimental flow field data presented in the paper originate from time-resolved probe measurement in planes downstream of each bladerow. The unsteady pressure measurement technology of the fast response aerodynamic probes (FRAP) has been developed at the LSM [29,30]. The mainstream flow field was measured using a novel 1.8 mm tip diameter, two-sensor FRAP probe in virtual-four-sensor mode providing 2D, time-resolved flow field information. Each measurement plane is resolved by a grid of 39 points in radial direction which are clustered close to the endwalls and 20 equally spaced points in circumferential direction, covering one stator pitch. The time-resolved pressures signal is acquired at each measurement point at a sampling rate of 200 kHz over a time of 2 s. The data sets are processed to derive basic flow quantities, i.e., total and static pressure, flow yaw and pitch angles, velocity components, and Mach number by applying a phase lock average over 85 rotor revolutions. For the data evaluation three consecutive rotor passages were selected. Each rotor passage is resolved in time by 82 samples. The frequency response of the probe allows capturing flow features at frequencies up to 35 kHz. With this new two-sensor probe technology it is possible to provide also flow turbulence information [31]. The FRAP probe technology provides also temperature data at a frequency of up to 10 Hz.

Results and Discussion

In the following section the analysis of the measured performance and flow field data will be presented. Particular attention will be paid on flow effects, which will influence the evolution of rotor tip leakage secondary flows.

Table 3 Characteristic geometry of the tandem outlet guide vane ensemble

	OGV 1	OGV 2
Number of blades	54	48
Inlet flow angle (deg) (midspan)	64[a]	46
Exit flow angle (deg) (midspan)	46[a]	0
Solidity (chord/pitch)	1.4	—
Mean stagger angle (deg)	53	—
Aspect ratio (span/chord)	1.16	—

[a]Adjustable stagger angle.

Performance Evaluation. The instrumentation of the test facility allows the measurement of rig operation parameters, such as torque of the second stage and massflow. This allows the calculation of mechanical efficiency. The integral character of this value does not resolve any spanwise efficiency distribution. It is defined as the ratio of specific shaft power over the enthalpy difference of the isentropic expansion

$$\eta_m = \left(\frac{\omega \cdot M}{\dot{m}}\right) \Big/ \left\{ c_p T_{\text{in}} \left[1 - \left(\frac{p_{t,\text{out}}}{p_{t,\text{in}}} \right)^{(\kappa-1)/\kappa} \right] \right\} \tag{1}$$

For the new turbine configuration a mechanical total-to-total efficiency value of the first stage of $\eta_{tt}=87.8\%$ has been derived. In order to relate this value to an empirical data basis, the operating point has been plotted in a Smith chart [32] (see Fig. 8). The actual value differs by about 1% from the expectation.

The performance of the tandem outlet guide vane ensemble has been a crucial design issue, since it is defining the pressure ratio and hence the overall performance of the 1.5-stage turbine. In the performance measurements of the final turbine it could be verified that the design of the OGV ensemble reached the intended recovery of static pressure. The comparison of design and experimental values is presented in Fig. 9. It was observed that the first OGV row recovers about 25% more static pressure than expected, which increases the range of possible pressure ratios of the turbine.

Flow Field of the First Stator. The flow field into the first stator has a uniform distribution of total pressure from 20% to

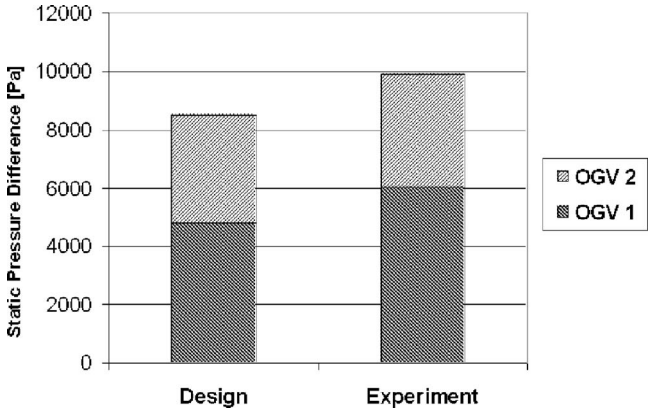

Fig. 9 Comparison of first OGV static pressure recovery between design and experiment

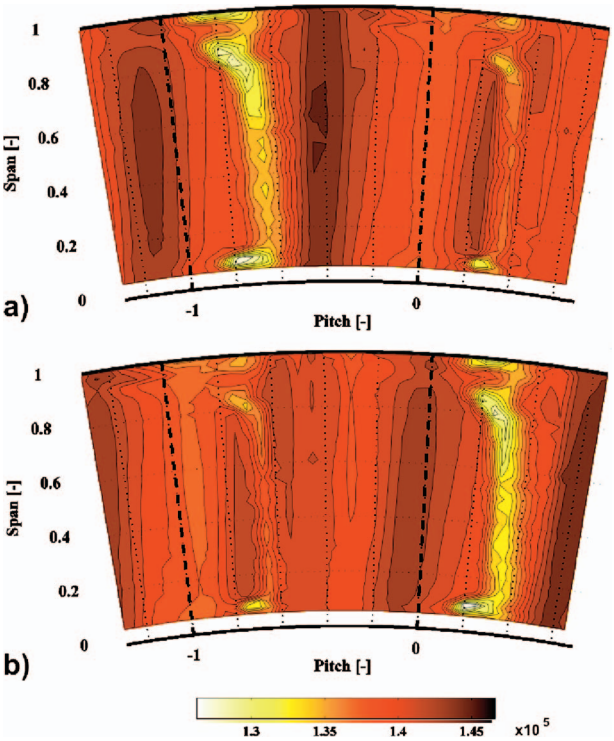

Fig. 10 Distribution of measured total pressure at exit of stator 1 at the time instants of a rotor blade passing period: (*a*) *t*/*T*=0.00; and (*b*) *t*/*T*=0.50

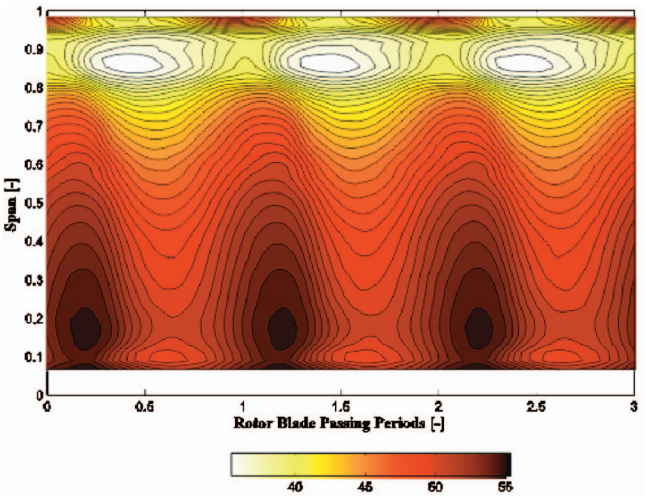

Fig. 11 Circumferentially mass-averaged distribution of measured relative flow yaw angle at exit of stator 1 versus time of three rotor blade passing periods

80% span. A region within 20% span from the endwalls is affected by boundary layers, which result from the inlet section of the turbine. The inlet flow field of the stator is symmetric between the hub and tip region.

In order to evaluate the flow field out of a stationary blade row it is usually sufficient to look at steady information of the flow properties. The general performance of a blade row can be captured well, when plotting time-averaged spanwise distributions of flow angles and pressures. With focus on the development of the rotor tip leakage flow it is important to consider the time-resolved flow field. The variation of the stator exit flow field over time will affect considerably the unsteady flow, especially in the rotor blade tip region.

The interaction between the stator exit flow field and the passing rotor is demonstrated in Fig. 10. On the area of two stator pitches, the distribution of total pressure is plotted for two time instants of one rotor blade passing period. In both figures the secondary flow features that leave the stator blade row can be identified. The core of the stator hub passage vortex reaches from the hub casing wall until 10% span. The stator passage vortex can be found between 80% and 90% span. Both vortices are connected by the stator wake, which shows a straight shape and is almost perfectly aligned in the radial direction. The fact that all main secondary flow features of the first stator are aligned along one circumferential position implies a high potential for improving turbine performance through clocking the stator blade rows. A dependency on the effect of clocking on the relative position of secondary flow features has been found by Behr et al. [20]. At the casing endwall the formation of an additional secondary flow feature can be identified. It originates at the casing endwall within the stator passage after the tip passage vortex has left the suction side and gives space to a formation of new boundary layer. This effect can be reduced by introducing a lean angle to the stacking of the profile in the tip region. In the current case this option has been discarded during the design process to create a baseline case that allows unrestricted probe access to all the stator passage. Generally, the flow field out of the stator shows a clear two-dimensional character over a range from 10% to 70% span. At both time instants, shown in Fig. 10, the secondary flow field of one stator pitch vanishes almost completely due to the vicinity of a rotor leading edge. In the contour plot: (*a*) the wake and both vortices are fully developed and approach the midpitch region of two rotor blades in an undisturbed manner. In this case the total pressure in these areas reaches its minimum value. Due to the 2:3 ratio between stator and rotor blade count, the secondary flow features of the adjoining stator pitch, oppose a static pressure field of a rotor leading edge. Thereby the pressure level rises in these regions such that the total pressure of secondary flow features reaches the level of the undisturbed main flow. Figure 10(*b*) shows the same area after the rotor has moved on by half a rotor pitch. The situation is analog to the one, which has been just described, except for the fact that the phenomena on the two stator pitches are switched.

The pulsation of the flow approaching the rotor blade can be also seen in the circumferentially mass-averaged distribution of relative flow yaw angle at the exit of stator 1. The mass averaging has been done intentionally on the area of one stator pitch, in order to see the local effect of the blade row interaction. In Fig. 11 these spanwise distributions are plotted for three rotor blade passing periods. It was found that in all span positions the rotor relative flow yaw angle varies by ±2.5 deg during the blade passing period. Hereby a linear phase shift between use tip and hub region of around 25% of a rotor blade passing period has been observed. This fact can be seen in the timewise shift of the locations of minimum and maximum flow angles at hub and tip in Fig. 11. The inclination of the contour lines in this plot also indicates the continuous rise toward flow overturning while the rotor leading edge pressure field approaches the wake region of the stator. As soon as it has passed, the flow yaw angles, especially the ones of the secondary flow, reduce quickly as the flow passes along the pressure side of the rotor. The periodic fluctuation of the relative rotor inlet angle also has a direct influence on the power created on a rotor blade. However, the timewise variation of global shaft power is rather low, since the ratio of stator and rotor blade count averages these individual unsteady effects on the rotor blades. Furthermore, Fig. 11 shows the trace of both passage vortices, by a constantly underturned region around 10% and 83% span, as well as an overturning at 93% span. The overturning of the hub passage vortex has not been captured by the probes, due to the vicinity to the wall. The variation of flow yaw angle during one rotor blade passing period, as it has been described on the mass-averaged

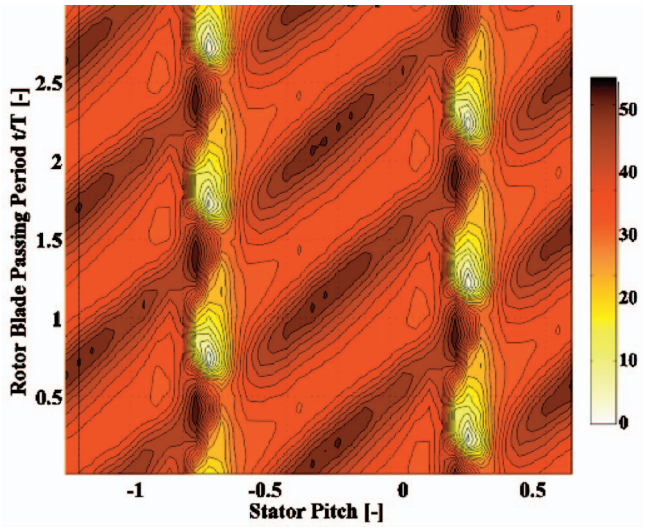

Fig. 12 Circumferential distribution of measured relative flow yaw angle at exit of stator 1 at 83% span versus time of three rotor blade passing periods

spanwise distribution, is much more intense in certain span positions. In the region of the stator tip passage vortex at 83% span, the variation of the relative flow yaw angle reaches locally up to 40 deg. This behavior is illustrated in a time–distance plot at this span position (see Fig. 12). In these kinds of plots, features that are fixed relative to the stationary frame appear as vertical lines. Features traveling with the rotor are visible as inclined parallel structures, which can be assigned to different rotor blades. The reaction of the flow during the interaction of rotor and stator can be seen in the crossing points of those lines.

The timewise variation of the rotor inlet flow angle in span positions near the casing endwall causes incidence on the rotor profile at this position. For this rotor blade profile, the design inlet angle in the tip region is around 40 deg. Due to the blade row interaction, this angle drops here for a short period of time to 0 deg. This variation of the rotor incidence angle will cause an unsteady, fluctuating pressure field around the rotor tip. Hence, the formation of the tip leakage vortex over the blade tip will be influenced according to the pressure variation.

Rotor Exit Flow Field. Within the rotor blade row the radial pressure gradient changes and the general direction of the streamlines is deviated toward the casing. The boundary layers of both hub and tip endwall are creating the passage vortices. At the same time the pressure gradient between pressure and suction side at the blade tip causes the flow in this region to pass through the tip gap. It results in a jet flow across the suction side edge of the blade tip, which mixes again with the main flow and rolls up into a vortex.

In Fig. 13 the time-resolved flow field out of the rotor is presented in the form of a relative total pressure coefficient distribution. All plots are views in the downstream direction on a sector covering two stator pitches. In order to show the variation of the flow field between two rotor blades, four equidistant time steps of one rotor blade passing period are plotted.

Both rotor passage vortices, the tip leakage vortex and the rotor wake, can be clearly identified in all pictures. All of these secondary flow features are traveling with the rotor blades. However, their relative position to the rotor trailing edges, as well as their strength, is not constant. The interaction with the downstream stator row and unsteady flow features originated by the first stator have an effect on their appearance.

The rotor hub and tip passage vortices are located between 18% and 28% blade span, and 65% and 80% blade span, respectively. Both vortices seem to be detached from the suction side of the

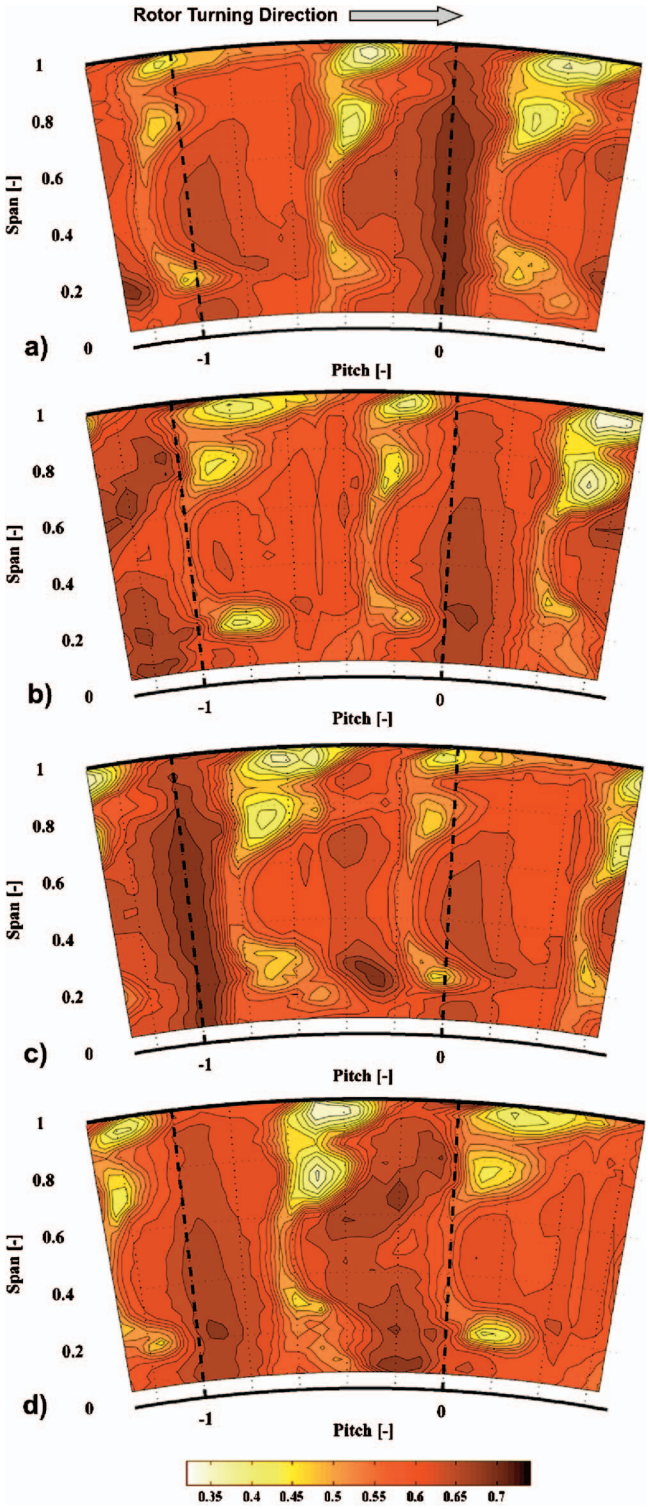

Fig. 13 Distribution of measured relative total pressure coefficient downstream of the rotor at four different rotor blade passing periods: (*a*) *t*/*T*=0.00; (*b*) *t*/*T*=0.25; (*c*) *t*/*T*=0.50; and (*d*) *t*/*T*=0.75

rotor blade, since the cores of these vortices are shifted by up to 20% rotor pitch in a circumferential direction relative to the wake position. This observation can be confirmed by the fact that their shape is almost elliptical, which indicates that there has been no recent restriction from the blade suction side surface. The tip passage vortex shows considerably lower relative total pressures than

the hub passage vortex.

The vicinity of the second stator has an impact on the secondary flow features coming out of the rotor. In Fig. 13 the position of the second stator leading edges is located around the stator pitch positions −1 and 0. In these locations the static pressure field of the second stators is maximal.

At time $t/T=0.00$ both passage vortices at stator pitch position −1.1 are just about to pass a leading edge of the second stator. Therefore in this moment the relative pressure of the passage vortices reaches its maximum value. At the same time the circumferential distance between the cores of the passage vortices and the rotor wake is minimal.

At time $t/T=0.25$ the passage vortices around stator pitch position −0.9 have passed the stator leading edge region and are becoming stronger, as the relative total pressure is reducing. The rotor wake has almost disappeared in this moment due to the influence of the second stator.

At time $t/T=0.50$ both passage vortices around the stator pitch position −0.7 and the corresponding rotor wake can pass unrestricted into the midpitch region of the second stator. At the same time the passage vortices of the preceding rotor blade around stator pitch position −0.1 stretch around the leading edge of the next stator profile. It is the same process as it has been described at $t/T=0.00$ for the other pair of passage vortices. This time shift of $t/T=0.5$ of a rotor blade passing period between the occurrences around two adjoining stator profiles is characteristic of the current 2/3 blade count ratio of stators and rotor.

At time $t/T=0.75$ both passage vortices at stator pitch position −0.5 are still unaffected by the stator leading edges. However, the passage vortex shows a discontinuity since it is leaving its radial position. This behavior will be addressed in the next paragraph. At the left side of the plot in Fig. 13(*d*) a next pair of rotor passage vortices is approaching the stator leading edge at stator pitch position −1.1. With this the loop of one rotor blade passing period is closed.

When observing the relative positions of passage vortices and wake of the rotor, it can be seen that both features show a different reaction to the potential field of the second stator leading edges. The closer the vortices and the wake come to the stator leading edge, the closer they come together. As soon as the vortices have passed the stator leading edge region, the circumferential distance between wake and vortices increases rapidly. Hereby the wake shows a more constant reaction to the potential field of the stator as it does not change the direction of the wake fluid. In contrast to that, the vortices change their flow direction rather quickly from suction to pressure side of the second stator.

Another flow feature has been observed, which is interacting with the hub passage vortex of the rotor. Due to the direction of the rotation of the hub passage vortex, the core of the hub passage vortex lifts up to 22% of the blade span until it reaches the measurement plane. It can be found in this position most of the time. In Fig. 13(*d*) it can be seen that this vortex moves outward up to around 32% span, as another low total pressure area appears close to the hub at −0.5 stator pitch. In the authors' opinion, this low −2 pressure area is a vortical structure which was originated in the first stator, since it always appears periodically at the same location. The hub passage vortex does not merge with this feature but goes around it. The fact that stationary features from the previous stator row can be clearly seen after the rotor indicates a high potential for optimizing stage efficiency by clocking both stator rows.

The behavior of the passage vortices due to the interaction with the second stator leading edge, as it has been described before, applies similarly to the tip leakage vortex. This can be found from the 90% blade span until the casing. The tip leakage vortex can be clearly distinguished from the tip passage vortex, which is located more radially inward at the same circumferential position. Within the rotor passage the tip leakage vortex covers the space around the rotor tip suction side corner. Due to its opposite direction of rotation it displaces the tip passage vortex, as it comes from the pressure side, to a more radially inward position.

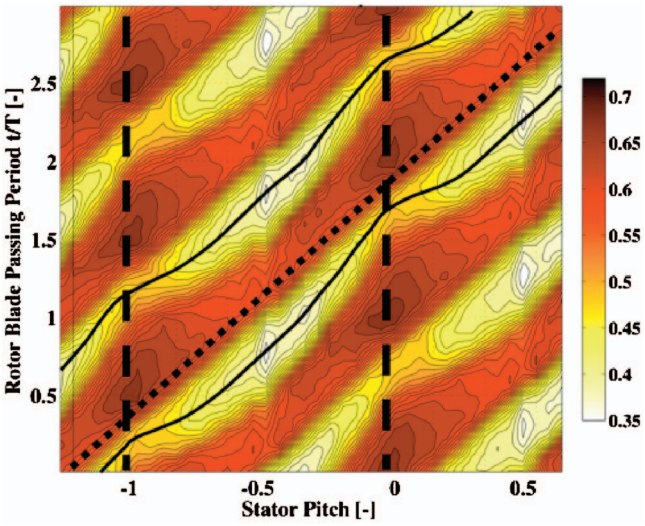

Fig. 14 Circumferential distribution of relative total pressure coefficient versus time at rotor exit at 95% span

The tip leakage vortex also experiences a modulation and deflection due to the second stator pressure field. In order to visualize the changes of the tip leakage vortex, the relative total pressure at the corresponding span position is plotted versus time in Fig. 14. The vertical dashed lines in the figure represent the position of the second stator leading edge. The approximate position of one rotor trailing edge is indicated by the dotted line. Accordingly, the rotor turning direction in the figure is from left to right. The region of the tip leakage vortex can be confined by the high-pressure gradient around it. The extension of the vortex in circumferential direction is minimal when it passes the stator leading edge. In this moment the vortex is being stretched to go around the leading edge of the stator. The stretching of the vortex can be seen in an increased velocity during this time (see Fig. 15). Right afterward the vortex slows down and occupies a larger area. These changes of the vortex size are visualized in Fig. 14. Since the vortex is confined on one side by the suction side surface, the low-pressure

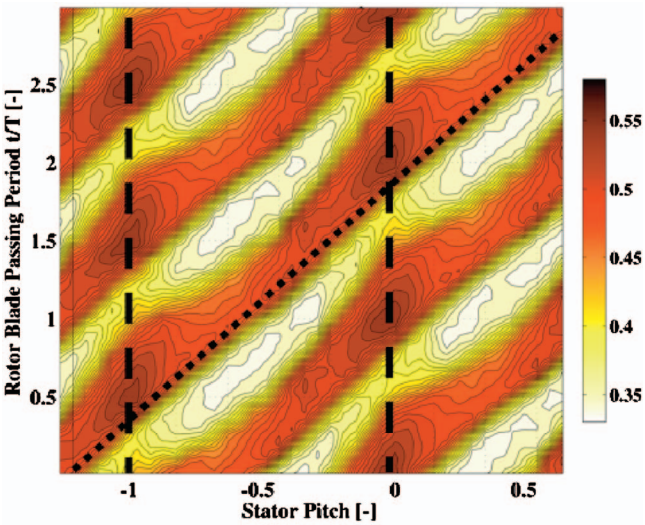

Fig. 15 Circumferential distribution of measured relative mach number versus time at rotor exit at 95% span

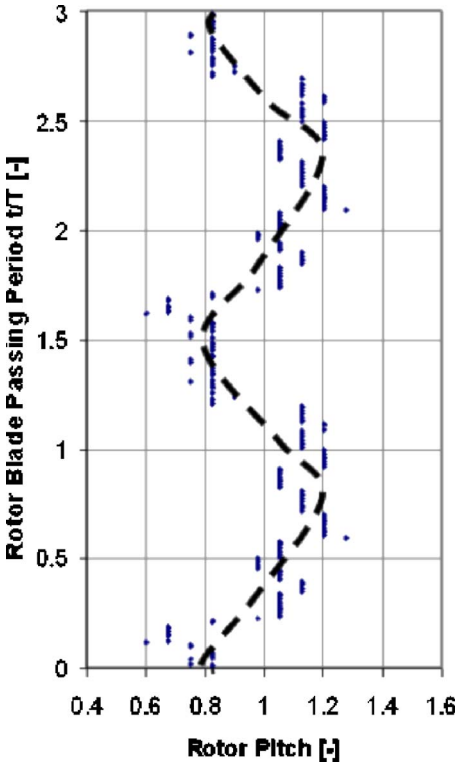

Fig. 16 Circumferential distance between the cores of two adjoining tip leakage vortices plotted versus time

area follows a straight line on its left boundary. The right boundary shows a nonlinear shape, according to the vortex size. The two splines in the figure follow the locations of minimum pressure, which are related to the core of the tip leakage vortex. They show that the residence time of the tip leakage vortex varies between different rotor relative positions. The mechanism of stretching of vortices due to blade row interactions and its relation to loss generation has been addressed in more detail in Chaluvadi et al. [33].

In Fig. 16 the circumferential distance between the two splines of Fig. 14 for each time instant is plotted versus time. These plot shows that the distance between the tip leakage vortices of two neighboring blades is changing by ±20% of a circumferential rotor pitch. This change in distance comes due to the time shifted deflection of the two vortices around the leading edges of the downstream stator.

This alternating deflection of the rotor vortices around the stator leading edge also expresses the instantaneous distribution of relative flow yaw angles at the rotor exit. Figure 17 shows the maximum and minimum deviation of circumferentially mass-averaged relative flow yaw angles from the time mean value. The rotor tip leakage vortex as well as both passage vortices can be clearly identified in the figure considering the considerably higher variation of the flow angle. Hereby the tip leakage vortex and the rotor tip passage vortex change the relative exit angle of the flow by up to ±2.5 deg during one rotor blade passing period. The hub passage vortex achieves ±2.5 deg, whereas the main flow is constant within ±0.7 deg. The change in exit angle contributes in addition to the variation of loading of each rotor blade.

The above mentioned effects show the influence of the pressure field of the downstream stator on the timewise circumferential variation within the rotor relative outlet flow field. An accurate unsteady CFD simulation of the rotor flow field, especially tip leakage secondary flows, should therefore apply to boundary conditions, which describe these circumferential variations, rather than radial profiles only.

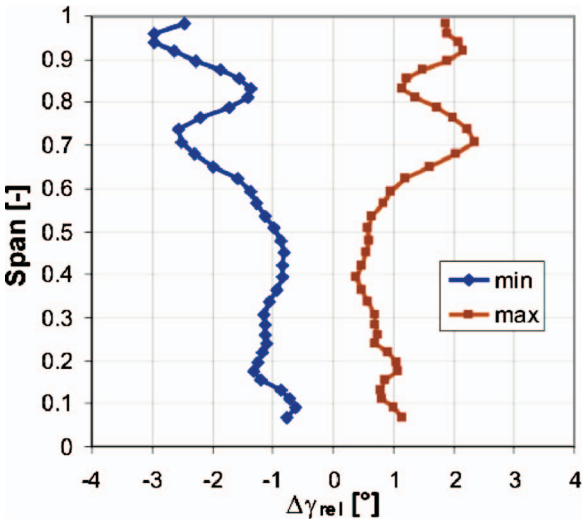

Fig. 17 Maximum and minimum deviation from time-averaged mean value of circumferentially mass-averaged spanwise distribution of relative flow yaw angles at rotor exit

Flow Field Behind Stator 2. The unsteady flow out of the rotor is going to be mixed and accelerated within the passage of the second stator. Any unsteadiness in the exit flow field of the second stator will be due to the flow of the upstream rotor, since no blade row is following downstream. Vortices of the rotor will be stretched around the stator leading edge, whereas remains may appear periodically at the stator exit. An impression of the highly three-dimensional flow field is given in Fig. 18. The distribution of total pressure coefficients is shown for two time instants of a rotor blade passing period. Considering the two neighboring stator

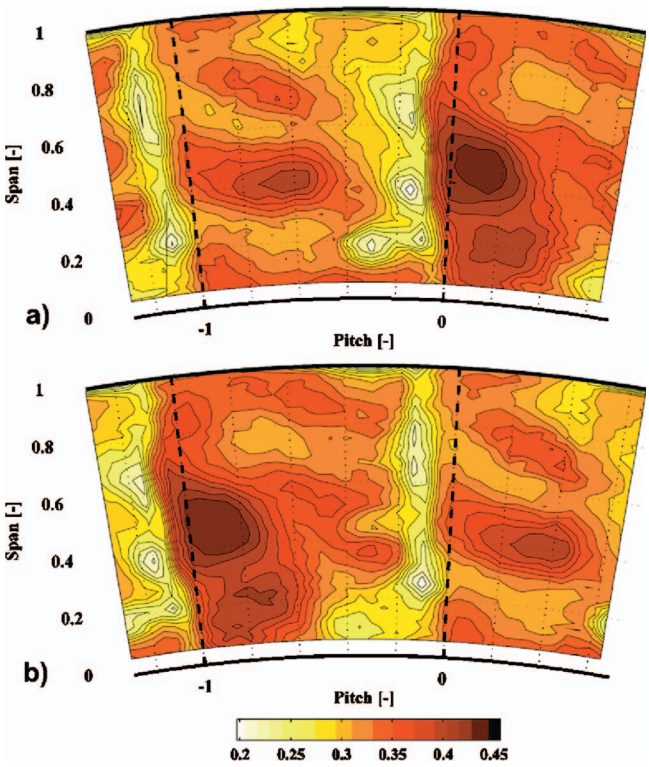

Fig. 18 Distribution of measured total pressure coefficient at the exit of stator 2 at rotor blade passing periods: (*a*) $t/T=0.00$; and (*b*) $t/T=0.50$

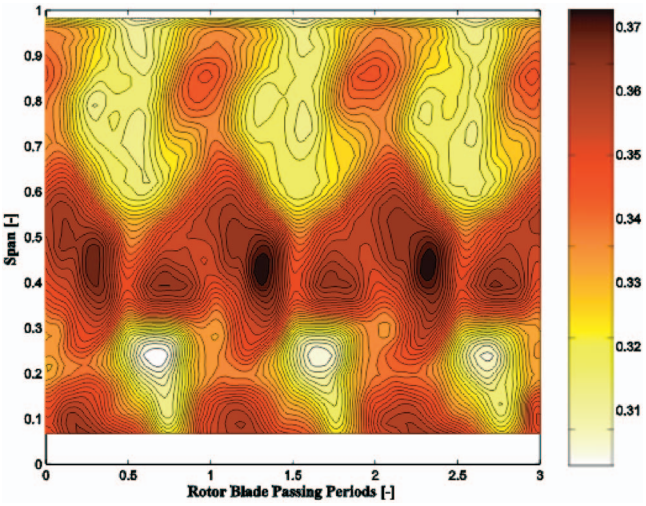

Fig. 19 Circumferentially mass-averaged distribution of measured total pressure coefficients at exit of stator 2, plotted versus time of three rotor blade passing periods

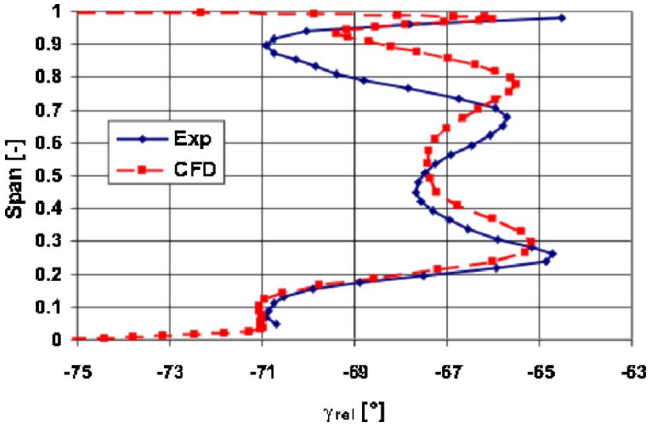

Fig. 21 Comparison of relative exit flow angle behind the rotor between time-averaged experimental results and CFD

pitches shown, the variation of total pressure between the two appears to be significant. Depending on how much secondary flow of the rotor is arriving at the stator exit the total pressure in the stator passage exit changes considerably. The change of total pressure over time would have an effect on the loading of a downstream rotor. In order to visualize the effective impact on a following blade row, Figs. 19 and 20 show the time-resolved evolution of circumferentially mass-averaged total pressure coefficient and absolute flow yaw angle. Since both plots show the exit flow field of a stationary blade row, any variation over time is due to secondary flows of the upstream rotor interacting with the stationary flow field of the stator. In Fig. 19 from 60% to 100% the *Cpt* values are reduced for about half of the time of a rotor blade passing period. This reduction originates from the interaction of the rotor tip passage vortex and tip leakage vortex with the secondary flow of the stator. An analogu behavior can be seen from 20% to 30% span, which relates to the rotor hub passage vortex.

In terms of flow angles the interaction of secondary flows creates a variation of circumferentially mass-averaged yaw angles over time of around ±2.5 deg (see Fig. 21). Hereby the maxima and minima are timewise shifted relative to each other. The inlet flow into a consecutive rotor would receive some incidence from the stator. However, the influence of the unsteady static pressure field of this rotor has to be taken into account as well in order to make a definite statement on the unsteady flow angle distribution.

Comparison of Numerical and Experimental Results. The evaluation of the experimental data has shown differences in the measured flow field with respect to the CFD prediction. In order to reduce the computational time, the calculations for the design of the turbine were done with a relatively coarse grid comprising 60 cells in a radial direction. Pressure levels inbetween the blade rows could be predicted very well. However, positions of secondary flow features, such as vortices, have shown larger deviations from the numerical prediction. In Fig. 21 the spanwise distributions of relative rotor exit flow angles from CFD and time-averaged experimental results are presented. The extension from the casing of the over–under turning region of the tip leakage and tip passage vortex is underpredicted by the CFD by about 10% span. An improvement of the CFD results could possibly be achieved by applying an improved grid definition, which is capable of resolving the complex flow features responsible for the tip leakage flow phenomena.

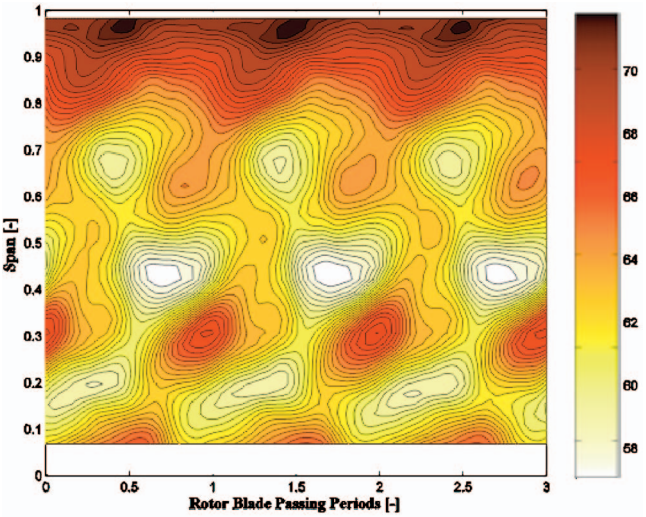

Fig. 20 Circumferentially mass-averaged distribution of measured absolute flow yaw angle at exit of stator 2, plotted versus time of three rotor blade passing periods

Conclusions

A new 1 1/2-stage, unshrouded research turbine test case has been designed and built within the Turbomachinery Laboratory of ETH Zurich in order study novel methods of reducing rotor tip leakage losses. The new turbine case has been extensively tested applying unsteady and steady probe measurement techniques. The results were analyzed with particular attention on the flow region at the rotor tip gap and the flow interactions between the different bladerows.

The geometry of the 1 1/2-stage turbine models a highly loaded, low aspect ratio gas turbine environment. The measured performance of the first stage reflects very well the design intent: loading coefficient of 2.36 and flow coefficient of 0.65 at a total pressure ratio of 1.35 and a degree of reaction of 0.39. Stator exit Mach numbers of up to Ma=0.58 ensure a realistic flow environment, which shows compressibility effects, but still allows the application of intrusive unsteady measurement techniques. Probe measurement access is provided at various locations around all bladerows. In addition a multi-purpose window inside the rotor casing covering a circumferential distance of five rotor pitches gives optical access to the inside of the rotor bladerow.

The results of the probe measurements represent a rare set of data, which describes the unsteady flow in a 1 1/2-stage turbine.

The geometry and flow field data of the turbine will be available to the turbomachinery community for validation and improvement of numerical tools.

The secondary flow features of the first stator are almost perfectly radially aligned. This implies that stator wake and passage vortices affect the rotor blade almost simultaneously. This is also the reason for a pulsation of total pressure in the rotor inlet flow field, modulated by the rotor leading edge.

The pulsation of the rotor inlet flow field manifests itself as well in the rotor inlet flow angles. Circumferentially mass-averaged flow yaw angles vary by ±2.5 deg during the time of one blade passing period. In the rotor tip region temporary negative incidence of 40 deg could be seen due to these blade row interactions. This phenomenon will introduce increased unsteadiness into the development of the rotor tip leakage flow.

Remnants of the first stator secondary flows have been found to affect the location of secondary flow features of the rotor. The rotor hub passage vortex shows a temporary radial inward migration of 10% blade span during the time of one blade passing period.

At the exit of the second stator the circumferentially mass-averaged flow yaw angles vary by ±2.5 deg. In this case this variation can only be attributed to the interaction between the rotor and the second stator, since no further bladerow is following downstream. The unsteadiness introduced upstream of the second stator propagates through the blade row and causes this high angle fluctuation.

The vortices of the rotor get modulated by the leading edges of the second stator. A variation of vortex size and relative position to the rotor trailing edge has been detected. Due to the 2:3 ratio of blade count between rotor and stators the interaction of the trailing edges of two neighboring rotor blades with the leading edges of the second stator is time shifted. This leads to a varying circumferential distance between the vortices of two neighboring rotor blades due to their deflection around the second stator leading edges. The variation in distance has been determined for the tip leakage vortices to be on the order of ±20% of a rotor pitch.

Nomenclature

c = absolute flow velocity (m/s)
c_p = specific heat capacity at constant pressure (J/kg K)
Cps = static pressure coefficient, $Cps=p-p_3/p_{t0}-p_3$ (-)
Cpt = total pressure coefficient, $Cpt=(p_t-p_3)/(p_{t0}-p_3)$ (-)
h = enthalphy (kJ/kg)
$\dot{m}$ = massflow (kg/s)
M = torque (N m)
p = pressure (Pa)
R = perfect gas constant (J/kg K]
r = radius (m)
T = temperature (K)
u = rotational speed (m/s)

Greek Symbols

ε = turning angle (deg)
ψ = loading coefficient ($\psi=\Delta h/u^2$) (-)
ϕ = flow coefficient $\phi=c_x/u$ (-)
ϕ = flow yaw angle (positive in rotor turning direction) (deg)
γ = flow pitch angle (positive towards casing) (°)
κ = isentropic coefficient ($\kappa=c_p/c_v$) (−)
ω = rotational velocity (1/s)

Abbreviations

5HP = five-hole probe
CFD = computational fluid dynamics
CoG = center of gravity
FRAP = fast response aerodynamic probe
LE = leading edge
MP = measurement plane
TE = trailing edge
TET = turbine entry temperature

Subscripts

av = average
m = mechanical
rel = relative frame of reference
t = total
th = thermal
x = axial direction

References

[1] Booth, T. C., 1982, "Rotor-Tip Leakage Part I—Basic Methodology," J. Eng. Power, **104**, pp. 154–161.
[2] Denton, J. D., 1993, "Loss Mechanisms in Turbomachines," ASME J. Turbomach., **115**, pp. 621–656.
[3] Booth, T. C., 1985, "Importance of Tip Leakage Flows in Turbine Design," VKI Lecture Series 1985-05, "*Tip Clearance Effects in Axial Turbomachines*," 1985.
[4] Bindon, J. P., and Morphis, G., 1990, "The Development of Axial Turbine Leakage Loss for Two Profiled Tip Geometries Using Linear Cascade Data," ASME Paper No. 90-GT-152, June.
[5] Kaiser, I., and Bindon, J. P., 1997, "The Effect of Tip Clearance on the Development of Loss Behind a Rotor and a Subsequent Nozzle," ASME Paper No. 97-GT-53.
[6] Yoshino, S., 2002, "Heat Transfer in Rotating Turbine Experiments," Ph.D. thesis, Oxford University, Oxford, UK.
[7] Camci, C., Dey, D., and Kavurmacioglu, L., 2003, "Tip Leakage Flows in Near Partial Squealer Rims in an Axial Flow Turbine Stage," ASME Paper No. GT2003-38979.
[8] Chander, P., Lee, C.-P., Cherry, D., Wadia, A., and Doughty, R., 2005, "Analysis of Some Improved Blade Tip Concepts," ASME Paper No. GT2005-68333.
[9] De Cecco, S., Yaras, M. I., and Sjolander, S. A., 1995, "Measurement of Tip Leakage Flows in Turbine Cascade with Large Clearances," ASME Paper No. 95-GT-77.
[10] Yamamoto, A., Tominaga, J., Matsunuma, T., and Outa, E., 1994, "Detailed Measurements of Three-Dimensional Flows and Losses Inside an Axial Flow Turbine Rotor," ASME Paper No. 94-GT-348.
[11] Staubach, J. B., Sharma, O. P., and Stetson, G. M., 1996, "Reduction of Tip Clearance Losses Through 3-D Airfoil Designs," ASME Paper No. 96-TA-13.
[12] Offenburg, L. S., Fischer, J. D., and Hoek, T. J. V., 1987, "An Experimental Investigation of Turbine Case Treatments," AIAA-87-1919.
[13] Harvey, N. W., 2004, "Aerothermal Implications of Shroudless and Shrouded Blades," VKI Lectures Series 2004-02, "*Turbine Blade Tip Design and Tip Clearance Treatment*."
[14] Dey, D., and Camci, C., 2000, "Development of Tip Clearance Flow Downstream of a Rotor Blade With Coolant Injection From a Tip Trench," *Proceedings of the 8th ISROMAC Conference*, Honolulu, Hawaii, pp. 572–579.
[15] Rao, N. M., and Camci, C., 2004, "Axial Turbine Tip Desensitization by Injection from a Tip Trench, Part 1: Effect of Injection Mass Flow Rate," ASME Paper No. GT2004-53256.
[16] Rao, N. M., and Camci, C., 2004, "Axial Turbine Tip Desensitization by Injection from a Tip Trench, Part 2: Leakage Flow Sensitivity to Injection Location," ASME Paper No. GT2004-53258.
[17] Schlienger, J., 2003, "Evolution of Unsteady Flows in a Multistage Shrouded Axial Turbine," Ph.D. dissertation No. 15230, ETH, Zurich, Switzerland.
[18] Pfau, A., 2003, "Loss Mechanisms in Labyrinth Seals of Shrouded Axial Turbines," Ph.D. dissertation No. 15226, ETH, Zurich, Switzerland.
[19] Porreca, L., Behr, T., Schlienger, J., Kalfas, A. I., and Abhari, R. S., 2005, "Fluid Dynamics and Performance of Partially and Fully Shrouded Axial Turbines," ASME J. Turbomach., **127**, pp. 668–678.
[20] Behr, T., Porreca, L., Mokulys, T., Kalfas, A. I., and Abhari, R. S., 2006, "Multistage Aspects and Unsteady Flow Effects of Stator and Rotor Clocking in an Axial Turbine with Low Aspect Ratio Blading," ASME J. Turbomach., **128**, pp. 11–22.
[21] Sell, M., Schlienger, J., Pfau, A., Treiber, M., and Abhari, R. S., 2001, "The 2-Stage Axial Turbine Test Facility LISA," ASME Paper No. 2001-GT-0492.
[22] Behr, T., Kalfas, A. I., and Abhari, R. S., 2006, "Geometry Data of Unshrouded 1.5-Stage Turbine Profiles," http://www.lsm.ethz.ch
[23] Pritchard, L. J., 1985, "An Eleven Parameter Axial Turbine Airfoil Geometry Model," ASME Paper No. 85-GT-219.
[24] Troxler, A., 2002, "Inverse Design of Gas Turbine Components," *Proceedings 4th International Conference on Inverse Problems in Engineering*, Rio de Janeiro, Brazil.
[25] Dawes, W. N., 1988, "Development of a 3-D Navier-Stokes Solver for Application to All Types of Turbomachinery," ASME Paper No. 88-GT-70.
[26] Jameson, A., and Baker, T. J., 1984, "Multigrid Solutions of the Euler Equations for Aircraft Configurations," AIAA Paper No. 84-0093.
[27] Spalart, P. R., and Allmaras, S. R., 1992, "A One-Equation Turbulence Model for Aerodynamic Flows," AIAA Report No. 92–0439.

[28] Mokulys, T., Dewhurst, S., and Abhari, R. S., 2005, "Numerical Validation of Characteristics and Linearized Unsteady Boundary Conditions for Non-Integer Blade Ratios in a Non-Linear Navier–Stokes Solver," ASME Paper No. GT2005-68670.
[29] Kupferschmied, P., Köppel, O., Gizzi, W. P., and Gyarmathy, G., 2000, "Time Resolved Flow Measurements With Fast Aerodynamic Probes in Turbomachinery," Meas. Sci. Technol., **11**, pp. 1036–1054.
[30] Pfau, A., Schlienger, J., Kalfas, A. I., and Abhari, R. S., 2002, "Virtual Four Sensor Fast Response Aerodynamic Probe (FRAP)," *Proceedings of the 16th Bi-Annual Symposium on Measuring Techniques in Transonic and Supersonic Flows in Cascades and Turbomachines*, Cambridge, UK, Sept. 23–24.
[31] Porreca, L., Hollenstein, M., Kalfas, A. I., and Abhari, R. S., 2007, "Turbulence Measurements and Analysis in a Multistage Axial Turbine," J. Propul. Power, **23**, pp. 227–234.
[32] Smith, S. F., 1963, "A Simple Correlation of Turbine Efficiency," J. R. Aeronaut. Soc., **69**, pp. 467–470.
[33] Chaluvadi, V. S. P., Kalfas, A. I., Hodson, H. P., Ohyama, H., and Watanabe, E., 2003, "Blade Row Interaction in a High-Pressure Steam Turbine," ASME J. Turbomach., **125**, pp. 14–24.

Unsteady Flow Field of an Axial-Flow Turbine Rotor at a Low Reynolds Number

Takayuki Matsunuma
National Institute of Advanced Industrial Science and Technology (AIST)
1-2-1 Namiki,
Tsukuba,
Ibaraki 305-8564, Japan
e-mail: t-matsunuma@aist.go.jp

The unsteady flow field of an annular turbine rotor was investigated experimentally using a laser Doppler velocimetry (LDV) system. Detailed measurements of the time-averaged and time-resolved distributions of the velocity, flow angle, turbulence intensity, etc., were carried out at a very low Reynolds number condition, $\mathrm{Re}_{out}=3.5\times10^4$. *The data obtained were analyzed from the viewpoints of both an absolute (stationary) frame of reference and a relative (rotating) frame of reference. The effect of the turbine nozzle wake and secondary vortices on the flow field inside the rotor passage was clearly captured. It was found that the nozzle wake and secondary vortices are suddenly distorted at the rotor inlet, because of the rotating potential field of the rotor. The nozzle flow (wake and passage vortices) and the rotor flow (boundary layer, wake, tip leakage vortex, and passage vortices) interact intensively inside the rotor passage.*
[DOI: 10.1115/1.2464143]

Introduction

Low Reynolds number flows have become increasingly important with the new generation of small gas turbines [1]. Blade Reynolds numbers for the turbine stage of such gas turbines can drop to below 10^5. For example, the Reynolds numbers of the turbine cascades of 300 kW industrial ceramic gas turbines [2] fall into the range of approximately 6×10^4 because of the increased viscosity caused by high turbine inlet temperatures and miniaturization of the cascade, which is considerably smaller than the Reynolds numbers of conventional gas turbines. At these low Reynolds numbers, the boundary layer is dominated by laminar flow and is susceptible to flow separation and strong secondary vortices that develop into increased loss, leading to reduced performance. Small and medium-sized gas turbines for aircraft propulsion also encounter the low Reynolds number problem at high altitudes, where the air density is low. Several studies focusing on the aerodynamics of turbine cascades at low Reynolds numbers have recently been published. In experiments on linear cascades by Curtis et al. [3], Murawski et al. [4], Lou and Hourmouziadis [5], Schulte and Hodson [6], Howell et al. [7], Volino and Hultgren [8], and Van Treuren et al. [9], flow separation occurred at the blade suction surface and the profile loss rapidly increased when the Reynolds number was reduced. Bons et al. [1] attempted to reduce the separation region on the suction surface at low Reynolds numbers using a method of intermittently blowing jets out from the blade surface. However, these studies were limited to linear two-dimensional cascades. There have been few studies on annular three-dimensional cascades at low Reynolds numbers.

Moreover, the flow field around the blades of a turbine is very unsteady and complex due to "rotor–stator interaction," the aerodynamic interaction between the turbine nozzle (stator) and the turbine rotor. Figure 1 illustrates the velocity triangles. When the flow is converted into a relative flow from the absolute flow, the velocity difference between the wake and the main stream in the absolute frame of reference appears as the slip velocity ("negative jet") in the relative frame of reference, and this affects the flow field in the downstream cascade. Hodson and Dawes [10] examined the negative jet effect using unsteady numerical analysis. Boundary layer behavior, loss generation, secondary vortex growth, and heat transfer in turbines are strongly affected by the rotor–stator interaction. Even though unsteady flow plays an important role in axial-flow turbines, turbines are designed using steady-flow calculations. Because few actual models exist for the loss-generating mechanisms seen in unsteady flow, empirical correlations are used to account for the effects of unsteadiness. One successful method for simulating the unsteady flow field within multistage turbomachinery has been actualized by the work of Adamczyk [11,12]. More knowledge on unsteady rotor–stator interaction is, however, essential to increase the performance of turbines [13,14], especially at low Reynolds numbers. Although a variety of measurement techniques can easily be applied to the flow field within the stationary blades, difficulties arise with measurements of the flow field within the rotating blades. Direct measurements of turbine rotor flows using rotating devices have been conducted by Hodson [15] and Chaluvadi et al. [16]. Binder et al. [17], Zaccaria and Lakshminarayana [18], Matsunuma and Tsutsui

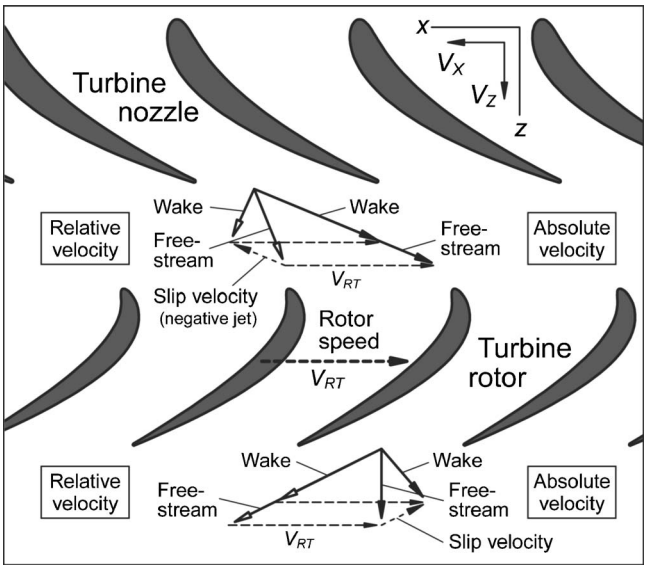

Fig. 1 Velocity triangles (absolute flow and relative flow)

Contributed by the International Gas Turbine Institute of ASME for publication in the JOURNAL OF TURBOMACHINERY. Manuscript received July 13, 2006; final manuscript received July 18, 2006. Review conducted by David Wisler. Paper presented at the ASME Turbo Expo 2006: Land, Sea and Air (GT2006), Barcelona, Spain, May 8–11, 2006. Paper No. GT2006-90013.

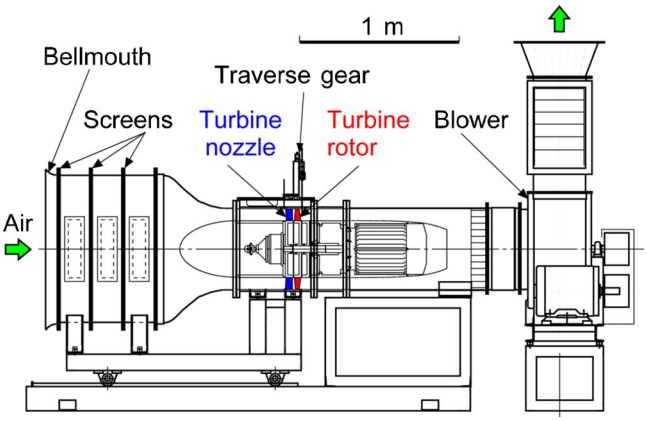

Fig. 2 Annular turbine wind tunnel

[19], and Göttlich et al. [20] used laser measurement systems, such as laser two-focus velocimetry (L2F), laser Doppler velocimetry (LDV) and particle image velocimetry (PIV). Sharma et al. [13], Binder et al. [21], and Gallus et al. [22] used hot-wire probes in a stationary frame downstream of the rotor. Since there have been few reports on unsteady rotor flow at low Reynolds numbers, and no reliable computational analyses are available to compute low Reynolds number turbine flows [23], detailed experimental data will make a major contribution to the establishment of theoretical studies of unsteady three-dimensional computational fluid dynamics (CFD) analysis.

This paper presents detailed LDV measurements of the unsteady flow field around an axial-flow turbine rotor. The blade geometries and measured data including movies can be obtained on request by e-mail to the author, and can be used for CFD code verification. The movies of the unsteady flow will also serve as effective resources for the education of gas turbine engineers.

Experimental Facility and Method

Annular Wind Tunnel and Turbine Cascade. Figure 2 shows the annular turbine wind tunnel used in the experiment. This wind tunnel is an air suction type, open circuit facility. The turbulence intensity of the free stream at the inlet of the test section is 0.5%. The total length of the wind tunnel is approximately 3.8 m. The outside and inside annular wall diameters of the test section are 500 mm and 350 mm, respectively. A single-stage axial-flow turbine designed using a free vortex method to attain radial equilibrium was installed at the test section. The geometries and specifications of the nozzle and rotor cascades are shown in Figs. 3 and 4 and Table 1.

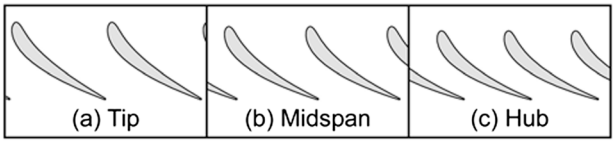

Fig. 3 Geometry of turbine nozzle

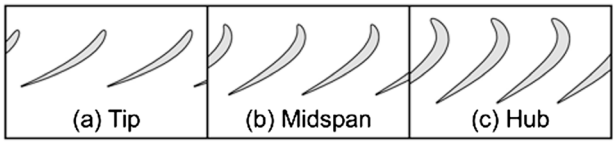

Fig. 4 Geometry of turbine rotor

Table 1 Specifications of turbine cascades

	Nozzle			Rotor		
	Tip	Mid	Hub	Tip	Mid	Hub
Number of blades, N		28			31	
Chord, C (mm)	69.2	67.6	66.2	58.6	57.5	58.7
Axial chord, C_{ax} (mm)	45.3	42.8	40.2	33.1	41.0	49.4
Blade span, H (mm)		75.0			74.0	
Blade pitch, S (mm)	56.1	47.7	39.3	50.5	43.1	35.5
Aspect ratio, H/C	1.08	1.11	1.13	1.26	1.29	1.26
Solidity, C/S	1.23	1.42	1.68	1.16	1.33	1.65
Inlet flow angle, α_1 (deg)	0.0	0.0	0.0	−16.2	22.1	51.9
Exit flow angle, α_2 (deg)	63.9	67.4	71.1	66.9	63.4	58.7
Turning angle, $\alpha_2-\alpha_1$ (deg)	63.9	67.4	71.1	50.7	85.5	110.6
Stagger angle, ξ (deg)	49.3	51.0	52.8	55.9	44.8	33.4
Inside diameter, D_1 (mm)		350			350	
Outside diameter, D_2 (mm)		500			500	
Hub/tip ratio, D_1/D_2		0.7			0.7	
Tip clearance, k (mm)		0.0			1.0	
Upstream axial gap, g (mm)		—		31.0	27.7	24.2
Flow coefficient, ϕ		—		0.43	0.50	0.61
Loading coefficient, ψ		—		0.88	1.20	1.77
Reaction, Λ		—		0.56	0.40	0.11

Pressure Probe Measurements. The nozzle inlet flow condition was measured using a three-hole pressure probe, with a 2.1 mm head width and 0.7 mm head height, at the axial position of $Z_{NZ}/C_{ax,NZ}=-0.706$, 30 mm upstream from the nozzle leading edge at midspan, where the potential influence of the nozzle is negligible. The number of spanwise measurement points was 73.

The wake traverse of the nozzle was carried out at a distance 6.6 mm axially from the nozzle trailing edge; i.e., $Z_{NZ}/C_{ax,NZ}=1.154$. The distributions of total pressure, velocity, flow angle, etc., were obtained using a five-hole pressure probe with a head diameter of 2.1 mm. The total number of measurement points was 819 (21 spanwise ×39 pitchwise locations). The traverse mechanisms had resolutions of 0.004 mm in the spanwise direction and 0.0036 deg in the pitchwise direction.

LDV Measurement System and Data Analysis Method. The LDV system was a standard two-color, four-beam, two-dimensional measuring system with a fiber-optic probe (System 90-3, TSI Inc.). The system consisted of a 4 W argon-ion laser tuned to 488 nm (blue) and 514.5 nm (green) output. The fiber-optic probe was mounted on a three-dimensional traverse gear. The half-angle between the beams was 4.29 deg, and the calculated dimensions of the measurement volume at e^{-2} intensity locations were 0.85 mm in length and 0.073 mm in diameter. Dantec Safex standard fog fluid with a mean particle diameter of 1.068 μm was used to seed the flow. The liquid was atomized using a Dantec Safex Model 2001 fog generator. Tracer particles were introduced into the test section from the wind tunnel inlet. An incremental rotary encoder (1800 pulses/revolution) was attached to the rotor shaft to detect the rotor angular position. An automatic measurement system controlled by a personal computer was adopted in this study, and all measured data were stored on a hard disk in the computer. Table 2 summarizes the uncertainty (99% coverage) of the LDV measurement, estimated according to ANSI/ASME performance test codes [24].

Figure 5 shows the LDV measurement locations around the rotor. Measurements were taken at 44 axial locations from immediately downstream of the nozzle to downstream of the rotor (an axial interval of 2 mm), 21 spanwise locations (from 3.3% span to

Table 2 LDV measurement uncertainty

		Time-averaged flow	Time-resolved unsteady flow
Relative velocity	V_{Rel}/V_2	0.0092 (0.92%)	0.0283 (2.83%)
Relative flow angle	θ_{Rel}	0.21 deg	0.69 deg
Turbulence intensity	Tu_{Rel}	0.41%	0.66%

96.7% span), and 32 pitchwise locations for one pitch of the nozzle. Ninety-seven pitchwise data (three nozzle pitches) were displayed in the subsequent data analysis to make the flow clearly intelligible. Since two-dimensional LDV was applied, the velocities in two directions (axial and circumferential velocities) were measured. At each measurement point, 10,000 instantaneous velocity samples were collected. Ensemble averaging of the instantaneous velocity data was performed with the help of the rotor encoder signal (see Fig. 8). It should be noted that this paper describes rotor synchronous unsteady effects because the ensemble averaging purges all nonrotational effects, such as instabilities, trailing edge vortex shedding, etc.

Figure 6 shows the data analysis method in the absolute frame of reference. As the rotor rotated, time-resolved data at different rotor positions were obtained at each measuring point. The number of time indexes in the absolute coordinate system $N_{T,Abs}$ is 29. This indicates that the time period T_{RT}, in which the rotor rotates one pitch, is divided into 29. Figure 7 shows the data analysis method in the relative frame of reference. Because of the relative coordinate system which rotates with the rotor, the nozzle moves from the top to the bottom in this figure. The number of time indexes in the relative coordinate system $N_{T,Rel}$ is 32. This indicates that the time period T_{NZ}, in which the nozzle moves one pitch is divided into 32. The time data number of $N_{T,Abs}$ and $N_{T,Rel}$, and the pitchwise data number of $N_{X,Abs}$ and $N_{X,Rel}$ differ in the absolute and relative coordinate systems. This is because the blade pitch of the rotor is different from that of the nozzle. Figure 8 shows an example of the data analysis at the rotor exit. The measurement position is the axial position of $Z_{RT}/C_{ax,RT}=1.096$ ($N_Z=36$, the 36th axial position in Fig. 5), and corresponds to the position at 9.6% of the rotor axial chord length downstream from the rotor trailing edge. The horizontal axis indicates the pitchwise width of one rotation of the rotor passage, which is divided into 29 locations and represents the different rotor positions. Phase-locked ensemble-averaged velocity and turbulence components were calculated from the instantaneous velocity data as shown in Fig. 8. The absolute velocity V_{Abs}, relative velocity V_{Rel}, and turbulence intensities Tu_{Abs} and Tu_{Rel} were calculated as follows

$$V_{Abs}=\sqrt{V_Z^2+V_{XAbs}^2}/V_1, \quad V_{Rel}=\sqrt{V_Z^2+(V_{X,Abs}+V_{RT})^2}/V_2$$

$$Tu_{Abs}=\sqrt{\frac{v_Z'^2+v_X'^2}{2}}\Big/V_1, \quad Tu_{Rel}=\sqrt{\frac{v_Z'^2+v_X'^2}{2}}\Big/V_2$$

All data presented in this paper are nondimensional. The time-averaged, pitchwise-averaged, and spanwise-averaged absolute velocity V_1 at the nozzle exit ($V_1=10.70$ m/s) made the velocity and turbulence intensity in the absolute frame of reference dimensionless. Similarly, the time-averaged, pitchwise-averaged, and spanwise-averaged relative velocity V_2 at the rotor exit ($V_2=9.27$ m/s) made the velocity and turbulence intensity in the relative frame of reference dimensionless.

Experimental Conditions. The Reynolds number used during the experiment was set at $Re_{in,NZ}=2.0\times10^4$ based on the nozzle chord length and nozzle inlet velocity. The reason for using the

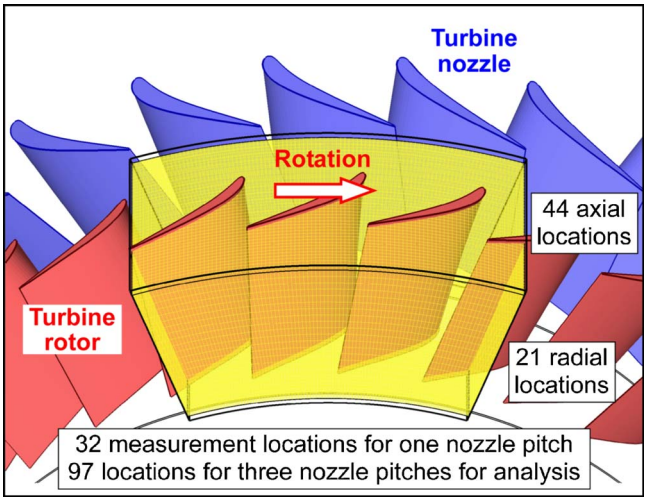

Fig. 5 LDV measurement locations

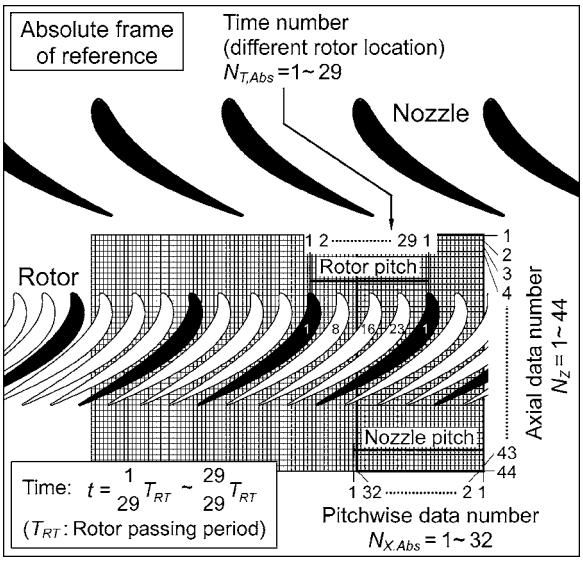

Fig. 6 Data analysis method in absolute frame of reference

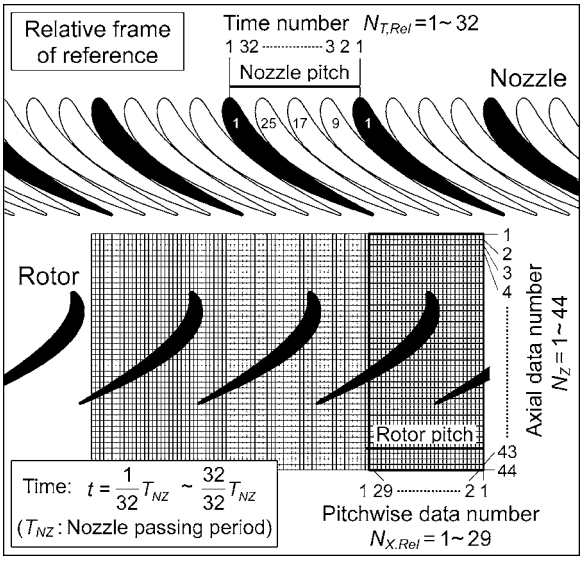

Fig. 7 Data analysis method in relative frame of reference

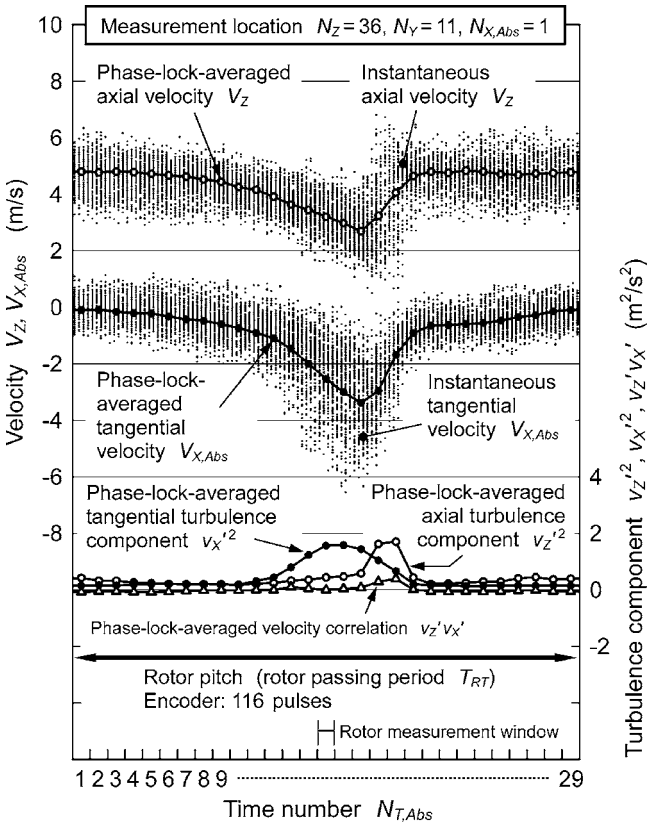

Fig. 8 Example of instantaneous data and ensemble-averaged data at rotor exit ($Z_{RT}/C_{ax,RT}=1.096$, $Y/H=0.5$ midspan)

Reynolds number of the nozzle inlet $Re_{in,NZ}$ was because the flow condition at the nozzle inlet is easy to measure. The Reynolds number based on the rotor chord length and rotor exit velocity $Re_{out,RT}$ was calculated as 3.5×10^4 from the measured LDV data. The axial velocity at the test section was 4.47 m/s and the rotor speed was set at 402 rpm to attain the design operating condition (design rotor inlet flow angle).

Regarding the performance of this turbine rotor, Fig. 9 shows the effect of low Reynolds numbers on total pressure loss (profile loss) at the rotor exit midspan. The total pressure loss was derived from hot-wire measurements of the boundary layer momentum thickness behind the rotor [25], using a control volume model for a trailing edge by Denton [26]. The measured loss (the pink circles in the figure) increases as the Reynolds number decreases. At higher Reynolds numbers, the measured data agree with the curve of the −0.2 power of the Reynolds number, as shown by the blue line in the figure. This result conforms with the well-known fact that losses in a turbine vary according to the −0.2 power of the Reynolds number [27], which is associated with the turbulent boundary layer. However, at lower Reynolds numbers below $Re_{out,RT}=6.0\times10^4$, the curve of the −0.5 power of the Reynolds number (the green line in the figure) fits more closely than the curve of the −0.2 power law for this turbine rotor. This steep increase in loss (or fall in performance) at lower Reynolds numbers would be caused by the change of the boundary layer on the blade surface from a turbulent regime to a laminar regime.

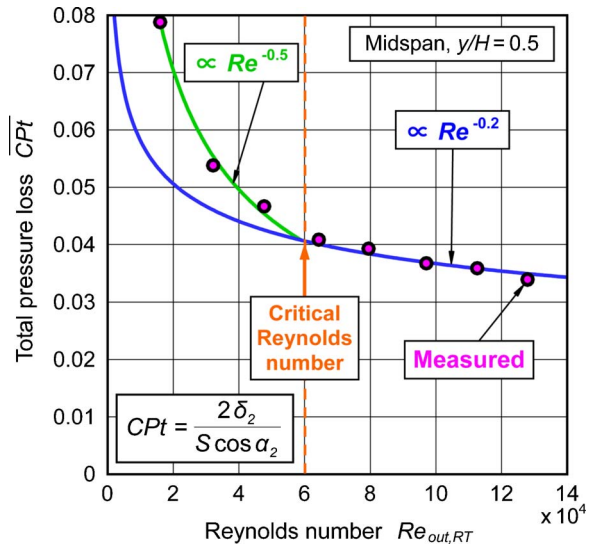

Fig. 9 Total pressure loss at rotor exit midspan

The flow in this experiment was considered to be incompressible because the Mach number was very low. The Mach numbers based on the mass-averaged velocities at the nozzle inlet, nozzle outlet, rotor inlet, and rotor outlet were $Ma_{in,NZ}=0.013$, $Ma_{out,NZ}=0.031$, $Ma_{in,RT}=0.014$, and $Ma_{out,RT}=0.027$, respectively. The author would like to note that the flow in actual gas turbines should be considered compressible because those Mach numbers are typically $Ma_{out}=0.5-1.2$. It is clearly impossible to simulate the many compressibility effects, such as shocks, expansion waves, and shock–boundary layer interactions, in this low-speed wind tunnel. With regard to flow compressibility effects, Moustapha et al. [28] and Predichizzi [29] reported that increases in the Mach number caused increased profile losses and secondary losses.

Results and Discussion

Nozzle Inlet Flow. Figure 10 shows the spanwise distributions of total pressure loss, static pressure, and velocity at the nozzle inlet. The main flow has constant values; i.e., no pressure and velocity gradient. The features of the inlet boundary layers are summarized in Table 3. The tip boundary layer is slightly thicker than the hub boundary layer. The shape factor H_{12} at both endwalls is approximately 2.3. In general, the shape factor has been reported to decrease from $H_{12}=2.6$ in the laminar regime to $H_{12}=1.4$ in the turbulent regime without a pressure gradient [30]. Therefore, the shape factor in this experiment is rather close to a laminar boundary layer condition.

Nozzle Exit Flow.

Time-Averaged Flow in Absolute Frame of Reference. Figure 11 shows an oil-film visualization of the suction surface flow of the nozzle. The surface textures from the leading edge, marked *A* in the figure, indicate a laminar boundary layer on the nozzle surface because of the very low Reynolds number flow. Radially inward-directed surface flow is apparent in the laminar regime. A laminar separation, marked *B*, forms behind the laminar flow and there is strong radial flow within the region. A reverse flow region, marked *C*, is observed to pass near the blade trailing edge from the tip endwall to the hub endwall. The effect of passage vortices of the nozzle ($PV_{tip,NZ}$ and $PV_{hub,NZ}$) exists near the tip and hub endwalls. The passage vortex occurs due to the distortion of the vortex filament of the inlet boundary layer passing with the flow through a curved passage [31]. Strong conflict between the passage vortex and the separated inward flow is observed near the hub endwall, marked *D*.

Figure 12 shows the flow distributions at the exit of the nozzle measured with a five-hole pressure probe (axial position $Z_{NZ}/C_{ax,NZ}=1.154$; i.e., 15.4% of the nozzle axial chord length downstream from the nozzle trailing edge). In Fig. 12(*a*), the boundary layer on the nozzle surface generates linear high total pressure loss regions (wake) from the tip endwall to the hub endwall behind the nozzle trailing edge. The regions of high total

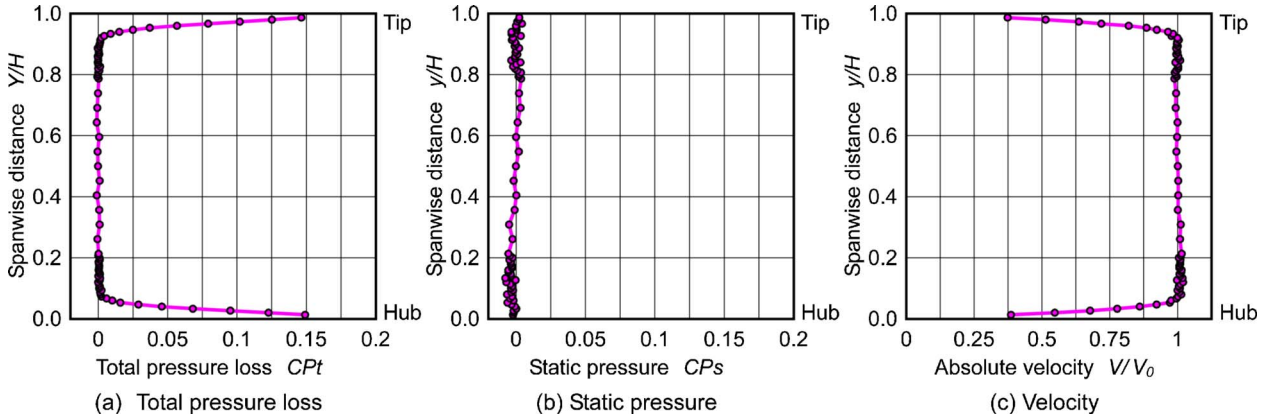

Fig. 10 Spanwise distributions of total pressure loss, static pressure, and velocity at nozzle inlet (axial position $Z_{NZ}/C_{ax,NZ}=-0.706$)

pressure loss extend to near the tip and hub endwalls of the suction surface, since passage vortices sweep up the inlet endwall boundary layer fluid on the suction surface. Figure 12(*b*) shows the distributions of secondary vectors. Passage vortices are observed near the suction side of both the tip and hub endwalls. In the nozzle wake region, the flow beside the trailing edge moves downward from the tip to the hub in the endwall direction due to the imbalance of the centrifugal force and the static pressure gradient. The radial difference of the static pressure reached 0.5 (50% of the exit dynamic pressure) from the tip to the hub, as shown in Fig. 12(*d*).

Figure 13 shows the time-averaged absolute velocity and turbulence intensity at the nozzle exit (axial position $Z_{NZ}/C_{ax,NZ}=1.154$) measured by LDV. A comparison of the absolute velocities in Figs. 12(*c*) and 13(*a*) shows good agreement between the five-hole pressure probe measurement and the LDV measurement. The wake and secondary vortices generate low-velocity and high turbulence intensity regions. In Fig. 13(*b*), there is a high-turbulence intensity region at the suction side of the wake (maximum value: 19%), which is caused by the reverse flow in the separation region, as shown in Fig. 11. The areas of high-turbulence intensity in Fig. 13(*b*) correspond to the areas of high-total pressure loss in Fig. 12(*a*).

Figure 14 presents the time-averaged distributions of absolute velocity and turbulence intensity at two axial positions ($Z_{NZ}/C_{ax,NZ}=1.295$ and 1.435) downstream of the distributions in Fig. 13 measured by LDV. Initially, the exit flow angle (yaw angle) at the hub side is larger than that at the tip side because the spanwise flow distribution of the turbine was designed using a conventional free-vortex method. Therefore, the nozzle wake (the black solid lines in the figure) becomes more aslant further downstream due to the spanwise difference of the exit flow angle. The nozzle wake near the tip and hub endwalls is gradually skewed by the rotating motion of the passage vortices (the black dashed circles). The same phenomenon of a slanted and skewed wake was observed in the experiment by Binder et al. [17].

Table 3 Endwall boundary layer data at nozzle inlet (axial position $Z_{NZ}/C_{ax,NZ}=-0.706$)

		Tip	Hub
Displacement thickness	δ_1	1.85 mm	1.68 mm
	δ_1/H	2.46%	2.24%
Momentum thickness	δ_2	0.832 mm	0.730 mm
	δ_2/H	1.11%	0.97%
Shape factor	H_{12}	2.22	2.30
Total pressure loss	CPt	0.0032	0.0020

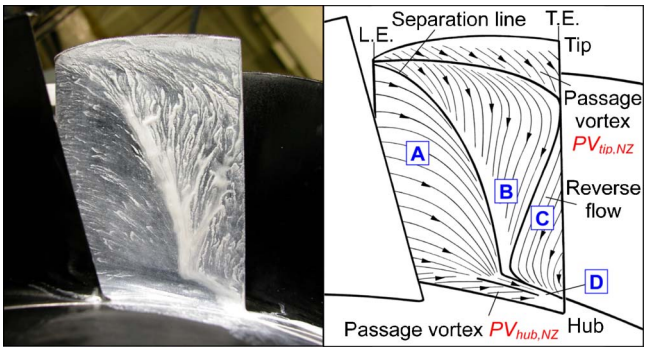

Fig. 11 Oil-film visualization of nozzle suction surface flow (view from downstream looking back up passages)

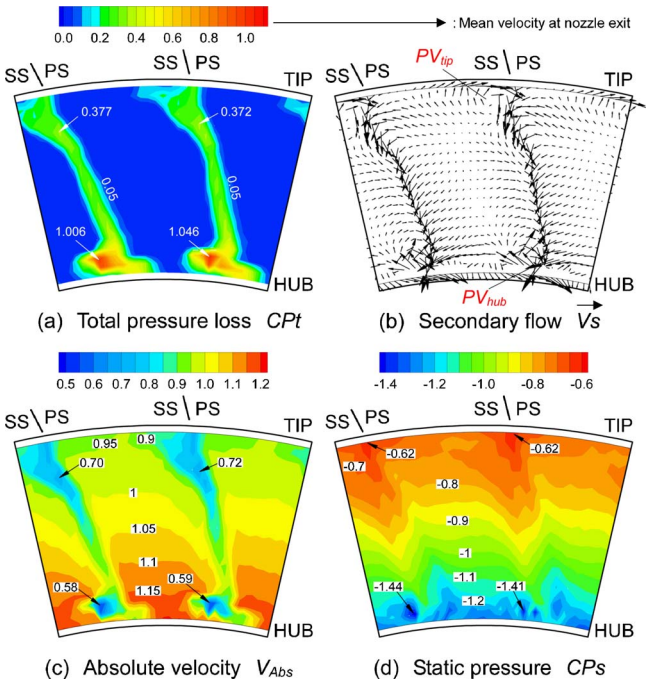

Fig. 12 Distributions of total pressure loss, secondary flow, absolute velocity, and static pressure at nozzle exit (at rotor inlet) measured with a five-hole pressure probe (axial position $Z_{NZ}/C_{ax,NZ}=1.154$)

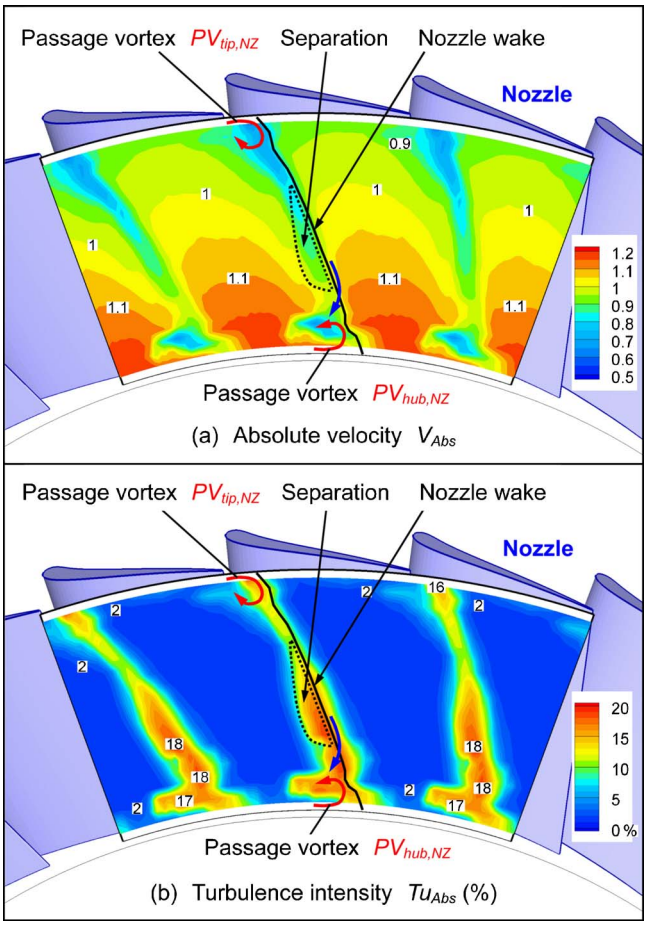

Fig. 13 Time-averaged absolute velocity and turbulence intensity at nozzle exit measured by LDV ($Z_{NZ}/C_{ax,NZ}$=1.154, absolute frame of reference)

Unsteady Flow in Absolute Frame of Reference. Figures 15 and 16 show the time-resolved unsteady distributions of absolute velocity and turbulence intensity at the nozzle exit observed from the absolute coordinate system (the axial position of $Z_{NZ}/C_{ax,NZ}$ =1.435, the same axial position as in Fig. 14(*b*), which also corresponds to 22.0% of the rotor axial chord length upstream from the rotor leading edge; i.e., $Z_{RT}/C_{ax,RT}$=−0.220). The distributions at four time-indexes (t=1/29T_{RT}, 8/29T_{RT}, 15/32T_{RT}, and 23/29T_{RT}) are shown in these figures. The red lines in the figures indicate the locations of the rotor leading edge moving from left to right. From one picture to the next, the rotor moves 2.9 deg, which corresponds to 1/4 of the rotor passing period T_{RT}. The interaction between the nozzle exit flow and the downstream passing rotor is clearly visible in these figures. The absolute velocity at the right side of the rotor leading edge (rotor suction side) is higher than that at the left side (rotor pressure side). Due to the interaction, the higher velocity region is generated at the mainstream region between the right side of the rotor leading edge and the left side (suction side) of the nozzle wake, marked *E*. The low-velocity and high-turbulence intensity regions due to the effect of the passage vortices (marked *F* and *G*) also fluctuate slightly due to the interaction.

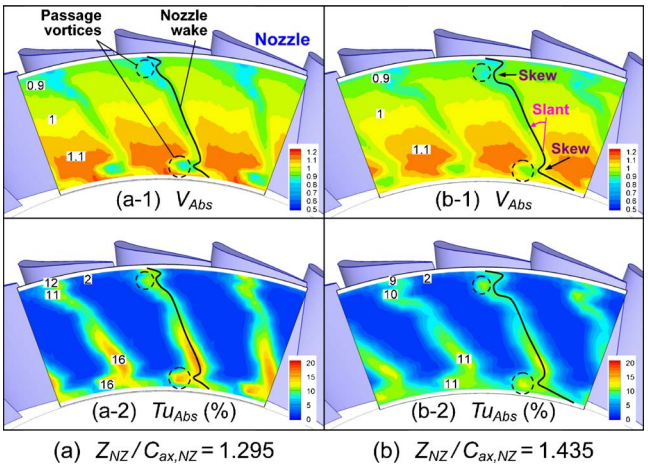

Fig. 14 Time-averaged absolute velocity and turbulence intensity at nozzle exit (two different axial positions)

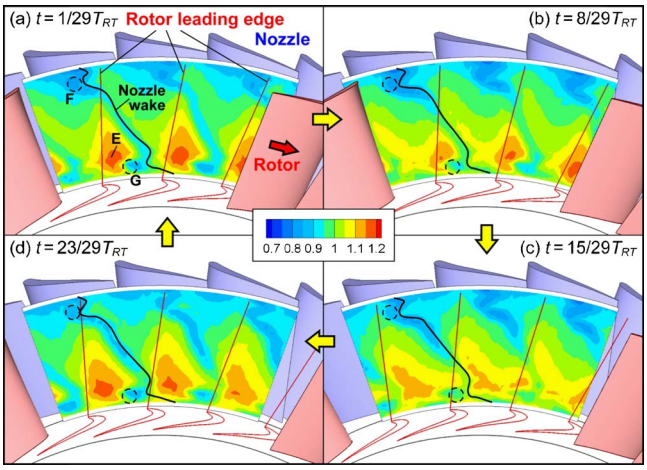

Fig. 15 Time-resolved absolute velocity at nozzle exit ($Z_{NZ}/C_{ax,NZ}$=1.435, $Z_{RT}/C_{ax,RT}$=−0.220, absolute frame of reference)

Unsteady Flow in Relative Frame of Reference. Figure 17 shows the time-resolved unsteady distributions of relative velocity at the nozzle exit observed from the relative coordinate system measured by LDV ($Z_{NZ}/C_{ax,NZ}$=1.435, $Z_{RT}/C_{ax,RT}$=−0.220, the same axial position as in Figs. 14(*b*), 15, and 16). In this figure also, the distributions at four time-indexes (t=1/32T_{NZ}, 9/32T_{NZ}, 17/32T_{NZ}, and 25/32T_{NZ}) are shown. Because the relative coordinate system rotates with the rotor, the rotor is fixed and the

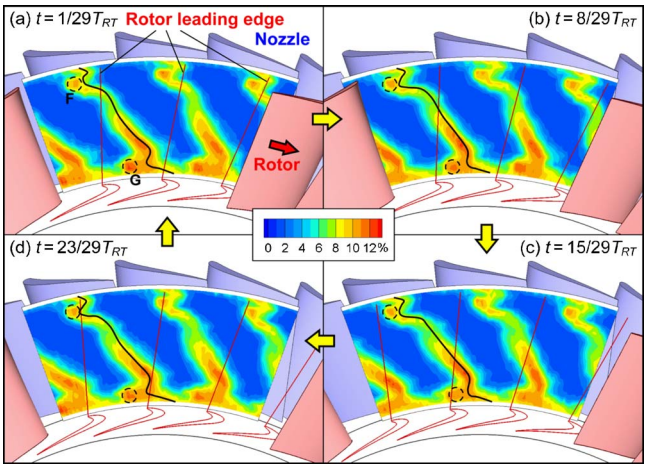

Fig. 16 Time-resolved turbulence intensity at nozzle exit ($Z_{NZ}/C_{ax,NZ}$=1.435, $Z_{RT}/C_{ax,RT}$=−0.220, absolute frame of reference)

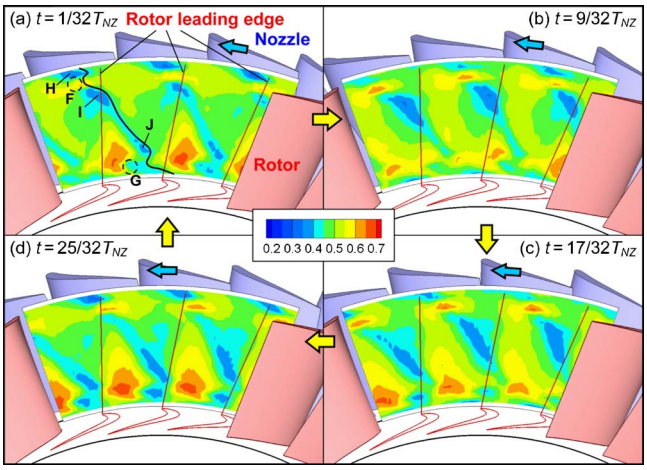

Fig. 17 Time-resolved relative velocity at nozzle exit ($Z_{NZ}/C_{ax,NZ}=1.435$, $Z_{RT}/C_{ax,RT}=-0.220$, relative frame of reference)

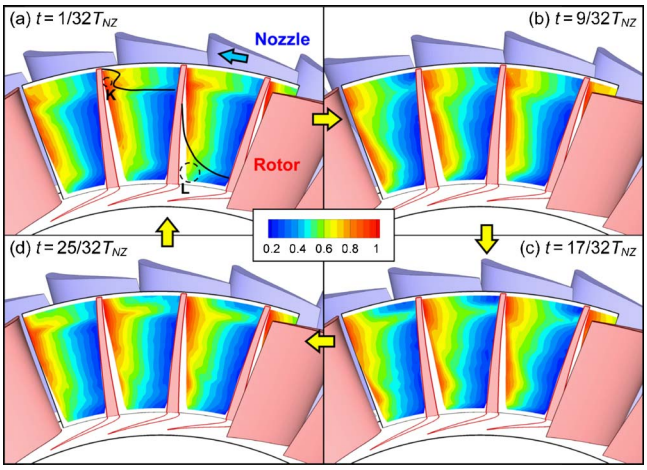

Fig. 19 Time-resolved relative velocity at rotor front ($Z_{RT}/C_{ax,RT}=0.121$, relative frame of reference)

nozzle moves from right to left as shown by the blue arrows in the figure. From one picture to the next, the nozzle moves 3.2 deg, which corresponds to 1/4 of the nozzle passing period T_{NZ}. The locations of the nozzle and the rotor at $t=1/32T_{NZ}$ in the relative coordinate system (Fig. 17(*a*)) are identical to those at $t=1/29T_{RT}$ in the absolute coordinate system (Fig. 15(*a*)). The distribution of the relative velocity in Fig. 17 is different from the distribution of the absolute velocity in Fig. 15 because of the transformation from absolute flow to relative flow (the velocity triangles in Fig. 1). The low relative velocity regions do not correspond to the low absolute velocity regions. For example, the low absolute velocity regions due to the tip-side passage vortex, marked *F* and *G* in Fig. 15(*a*), disappear at the same position in Fig. 17(*a*). Instead, three low relative velocity regions marked *H*–*J* are observed in Fig. 17(*a*). To understand the change of the low velocity regions between the absolute and relative velocity, the velocity triangles at marks *H*, *F*, *I*, *J*, and *G* in Figs. 16(*a*) and 17(*a*) are shown in Fig. 18. At the tip side in Fig. 18(*a*), the absolute velocity at *F* is lower than that at *H* and *I*. However, the relative velocity at *F* is higher than that at *H* and *I*. Similarly, the absolute velocity at *G* at the hub side in Fig. 18(*b*) is lower than that at *J* and the relative velocity at *G* is higher than that at *J*. This is because the axial velocity at *F* and *G* is higher than that at *H*, *I*, and *J*.

Rotor Inside Flow. Figures 19 and 20 show the time-resolved relative velocity and turbulence intensity distributions at the rotor front section in the relative frame of reference ($Z_{RT}/C_{ax,RT}=0.121$). There are white-colored shadow regions around the rotor where no measurements could be taken due to optical blockage.

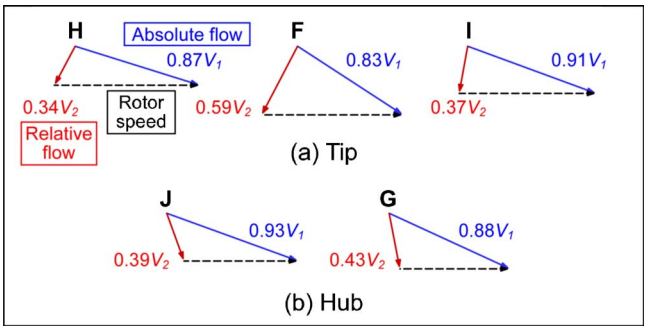

Fig. 18 Velocity triangles at marks *H*, *F*, *I*, *J*, and *G*

The relative velocity distribution in Fig. 19 is dominated by the rotor influence and the contours of the relative velocity have spanwise gradients between the suction and pressure surfaces of the rotor. However, the wake and secondary vortices of the nozzle generate sudden radial velocity gradients.

In Fig. 20, high-turbulence intensity regions due to the passage vortices exist near the endwalls, as indicated by *K* and *L* in the figure. The complicated deformation of the nozzle wake is clearly observed in the high turbulence intensity regions, as indicated by the black line in the figure. The distortion is caused by the three-dimensional flow distribution of the radially twisted rotor shape. The nozzle wake becomes considerably deformed compared with the wake immediately downstream of the nozzle and it is chopped by the rotor leading edge. Especially in Fig. 20(*a*), a curious tangential high-turbulence intensity region exists at the tip side of the center passage. Figure 21 shows the time-resolved turbulence intensity at the rotor inlet observed from the tangential–radial and axial–radial planes. Figure 21(*a*) provides an enlarged view of the center passage shown in Fig. 20(*a*). Figure 21(*b*) shows six axial–radial planes at the rotor inlet. In Planes 1 and 2, the shapes of the nozzle wake (the black lines in the figure) are similar to those at the nozzle exit in Fig. 14, although they display different slices through the flow domain. In Planes 3–6, the nozzle wake is axially stretched due to the effects of both the nozzle tip-side passage

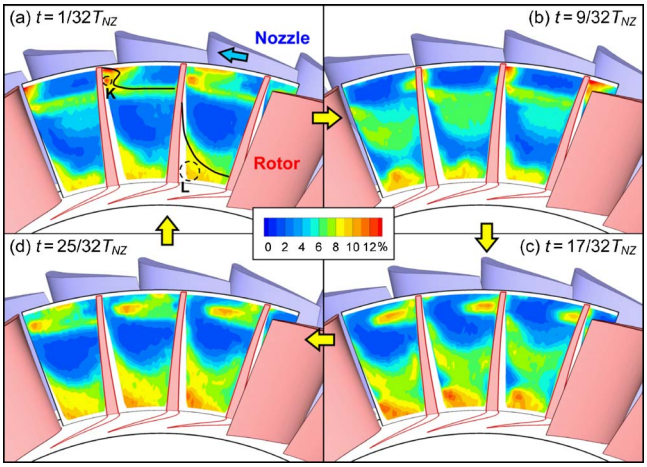

Fig. 20 Time-resolved turbulence intensity at rotor front ($Z_{RT}/C_{ax,RT}=0.121$, relative frame of reference)

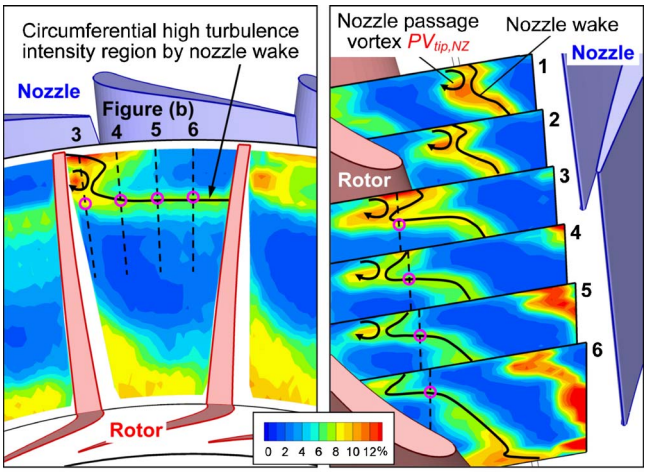

(a) Tangential-radial (X-Y) plane at $Z_{RT}/C_{ax,RT}=0.121$ [Fig. 20(a)] (b) Axial-radial (Z-Y) planes at rotor inlet

Fig. 21 Time-resolved turbulence intensity at *X-Y* plane and six *Z-Y* planes (time index $t=1/32T_{NZ}$)

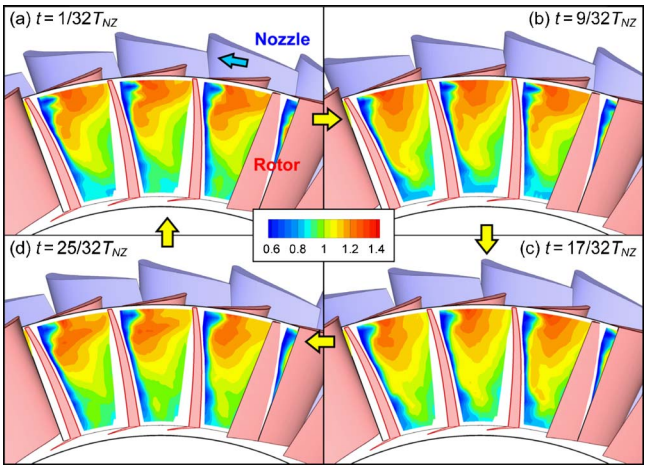

Fig. 23 Time-resolved relative velocity at rotor rear ($Z_{RT}/C_{ax,RT}=0.853$, relative frame of reference)

vortex $PV_{tip,NZ}$ and the rotor potential flow fields. The axial stretch of the nozzle wake generates the circumferentially spread high turbulence intensity region in Fig. 21(*a*).

To understand the deformation of the nozzle wake, observation from the tangential–axial planes is also effective. The time-resolved turbulence intensity distributions at three spanwise (radial) positions at $t=1/32T_{NZ}$ are shown in Fig. 22. Figures 22(*a*)–22(*c*) indicate the distributions at $Y/H=0.22$ (hub side), $Y/H=0.50$ (midspan), and $Y/H=0.87$ (tip side), respectively. The flow directions at the rotor inlet are indicated by the pink arrows in the figures. In each figure, the straight lines of high turbulence intensity caused by the nozzle wake and secondary vortices are distorted by the rotor. At the hub in Fig. 22(*a*), the high-turbulence intensity region generated by nozzle *N1* enters the passage between rotors *R1* and *R2*. At the tip in Fig. 22(*c*), however, the same high-turbulence intensity region of nozzle *N1* enters the passage between rotors *R2* and *R3*. At the midspan in Fig. 22(*b*), the high-turbulence intensity region of nozzle *N1* is chopped at the leading edge of rotor *R2*. The chopped high-turbulence intensity regions of the nozzle distort when they pass through the rotor passage. The distortion of the nozzle wake in the rotor passage occurs because the flow region near the rotor suction surface side moves faster than that near the rotor pressure surface side. Inside the rotor, the high-turbulence intensity regions concentrate at the rotor suction surface. This occurs because the nozzle wake and secondary vortices accumulate on the rotor suction surface due to the flow movement from the pressure side to the suction side caused by the negative jet effect [10,19]. At the rotor rear part, complex unsteady distributions of high-turbulence intensity were formed by the merging of the nozzle flow (wake and passage vortices) and the rotor flow (wake, passage vortices, and tip leakage vortex).

Figures 23 and 24 show the time-resolved distributions of relative velocity and turbulence intensity at the rotor rear section in the relative frame of reference ($Z_{RT}/C_{ax,RT}=0.853$). Figure 25 presents the time-resolved turbulence intensity distribution at $t=1/32T_{NZ}$ and $Z_{RT}/C_{ax,RT}=0.853$. This figure elucidates the flow mechanisms at the rotor rear section. A high-turbulence intensity region due to the thick boundary layer flow is observed on the rotor suction surface. A very high-turbulence intensity region widely spreads at the rotor suction surface near the tip endwall. This is caused by the rotor tip leakage vortex and the maximum peak of the region is as much as 40%. The tip leakage vortex also generates low relative velocity regions as shown in Fig. 23. High-turbulence intensity regions of the rotor passage vortices are observed near the endwalls as well. In the middle of the main flow region, nozzle wake and secondary vortices generate high turbulence intensity regions that have highly complex shapes.

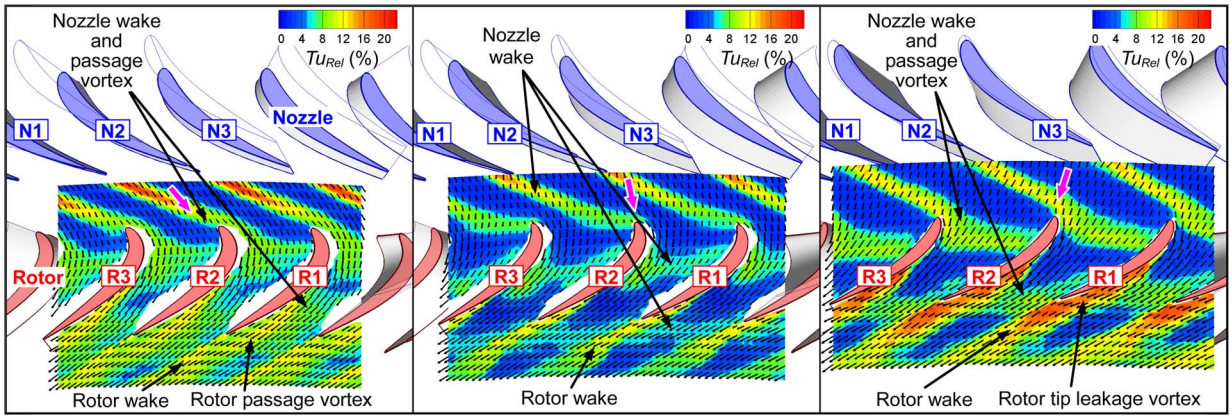

(a) Y/H = 0.22 (b) Y/H = 0.50 (midspan) (c) Y/H = 0.87

Fig. 22 Time-resolved turbulence intensity at three spanwise locations (time index $t=1/32T_{NZ}$)

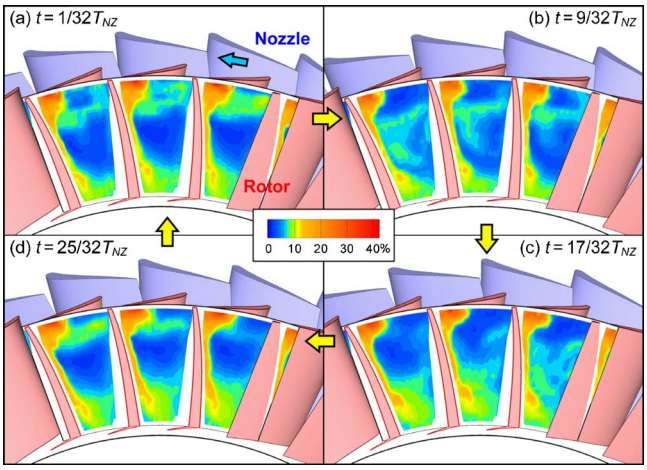

Fig. 24 Time-resolved turbulence intensity at rotor rear ($Z_{RT}/C_{ax,RT}=0.853$, relative frame of reference)

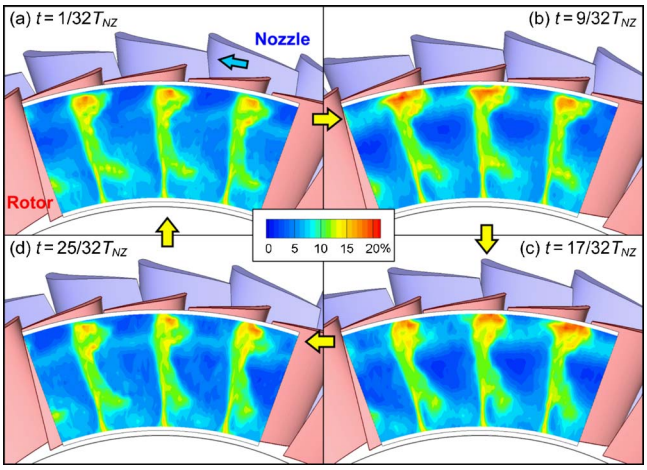

Fig. 27 Time-resolved turbulence intensity at rotor exit ($Z_{RT}/C_{ax,RT}=1.145$, relative frame of reference)

Rotor Exit Flow. Figures 26 and 27 show the time-resolved relative velocity and turbulence intensity distributions at the rotor exit in the relative frame of reference ($Z_{RT}/C_{ax,RT}=1.145$). Figure 28 presents the time-resolved turbulence intensity distribution at $t=1/32T_{NZ}$ and $Z_{RT}/C_{ax,RT}=1.145$. High-turbulence intensity regions are generated by the wake, tip, leakage vortex, and passage vortices of the rotor. In the middle of the main flow, the effect of the nozzle wake is clearly observed. In Fig. 26, the periodic fluctuation of the relative velocity due to the rotor–stator interaction is as large as 20% of the reference velocity V_2 (the mean relative velocity at the rotor exit). In Fig. 28, high-turbulence intensity regions due to the nozzle wake and secondary vortices spread at the mainstream region of the rotor. The turbulence intensity distribution at the middle of the rotor passage at $t=1/32T_{NZ}$ is shown in Fig. 29. Deformation of the high-turbulence intensity region of the nozzle wake and secondary vortices from the nozzle exit to the rotor exit is visible in the figure.

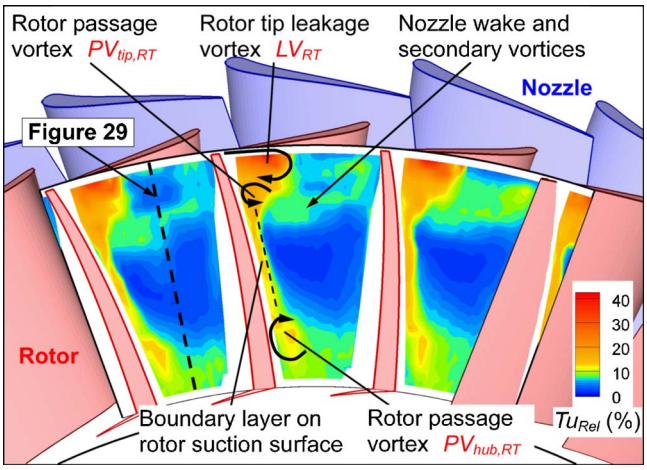

Fig. 25 Time-resolved turbulence intensity at rotor rear (time index $t=1/32T_{NZ}$, $Z_{RT}/C_{ax,RT}=0.853$)

Figure 30 shows the spanwise distributions of velocity and flow angle at the rotor exit ($Z_{RT}/C_{ax,RT}=1.145$). These distributions were obtained by calculating the time-averaged and pitchwise-averaged values at each spanwise position. The design relative velocity $V_{2,Des}$ at the midspan of the rotor exit ($V_{2,Des}=9.99$ m/s) made the velocity in this figure dimensionless. The measured relative velocity and flow angle are lower than the design values. This is because the thick boundary layer flow on the suction surface at the low Reynolds number condition reduces the flow turning at the rotor exit. The hub-side passage vortex causes

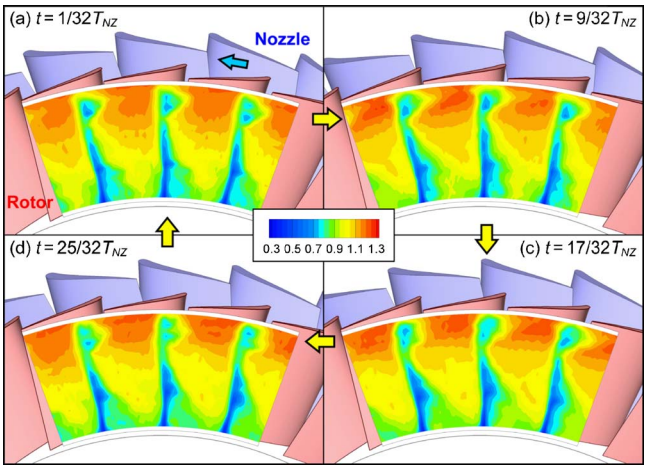

Fig. 26 Time-resolved relative velocity at rotor exit ($Z_{RT}/C_{ax,RT}=1.145$, relative frame of reference)

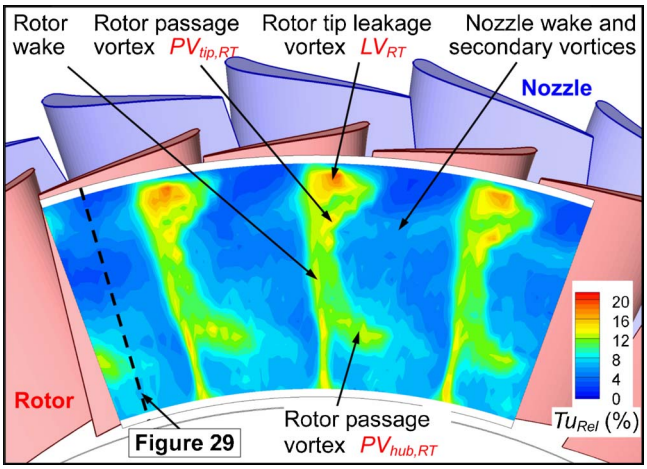

Fig. 28 Time-resolved turbulence intensity at rotor exit (time index $t=1/32T_{NZ}$, $Z_{RT}/C_{ax,RT}=1.145$)

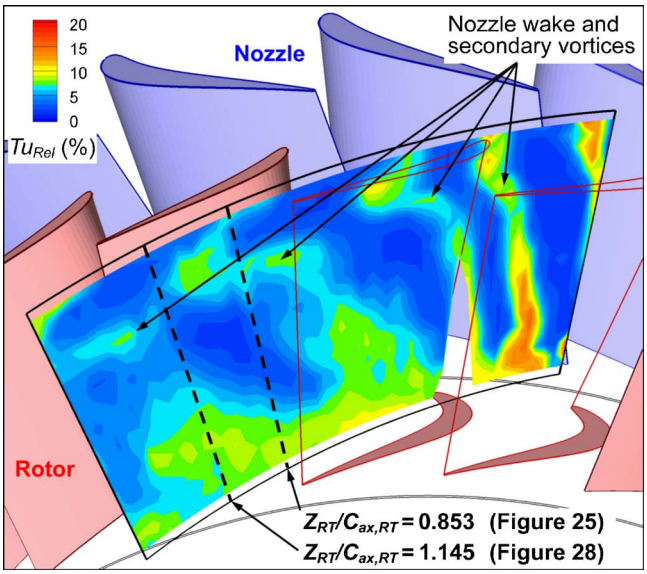

Fig. 29 Time-resolved turbulence intensity at rotor passage (time index $t=1/32T_{NZ}$)

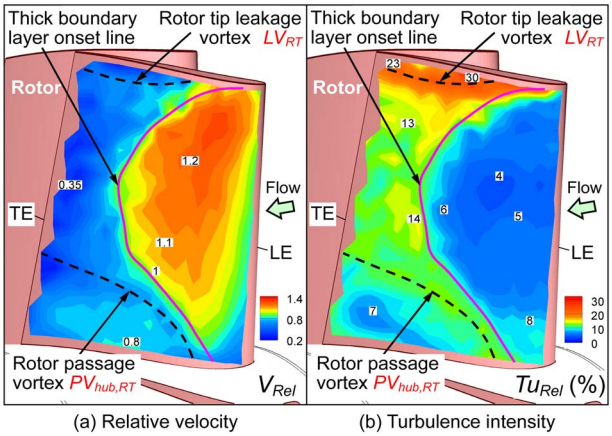

Fig. 31 Time-averaged flow on rotor suction surface

the underturning and overturning regions near the hub endwall. The rotor tip clearance vortex causes the underturning region near the tip endwall.

Rotor Suction Surface Flow. Figure 31 shows the time-averaged flow close to the rotor suction surface. Figures 31(*a*) and 31(*b*) show the relative velocity and the turbulence intensity, respectively. The main flow moves from right to left as indicated by the light green arrows in these figures. In Fig. 31(*a*), a large boundary layer region associated with the low relative velocity was observed at the rear section of the suction surface. This is because the thickness of the boundary layer developed from the rotor leading edge increases rapidly at the adverse pressure gradient region on the rear part of the suction surface. The existence of flow separation on the suction surface could not be confirmed from the LDV measurements because of insufficient measurement resolution in the boundary layer region. The pink solid line in the figure indicates the thick boundary layer onset line, which was defined as the position with the maximum velocity gradient (largest decrease in velocity). Low relative velocity regions due to the rotor tip leakage and passage vortex are observed near the tip and hub endwalls. In Fig. 31(*b*), the turbulence intensity increases dramatically behind the thick boundary layer onset line. The tip leakage vortex generates a high turbulence intensity region near the tip endwall. The maximum value of the turbulence at the tip leakage vortex region is approximately 30%.

Figures 32 and 33 show the time-resolved relative velocity and turbulence intensity close to the rotor suction surface, respectively. The pink solid lines in these figures indicate the time-resolved thick boundary layer onset lines. In order to observe the unsteady motion of the lines, the time-averaged thick boundary layer onset line in Fig. 31 is superimposed on the figures, as indicated by the pink dotted lines. The approximate positions of the nozzle wake and the nozzle passage vortices are shown by the black lines and circles in the figures. The black line was defined as the high-turbulence intensity position due to the nozzle wake and passage vortices. The nozzle wake and passage vortices generate large fluctuations of the relative velocity and turbulence intensity on the rotor suction surface. The range of periodical fluctuation of the relative velocity due to the nozzle effect is about 20% of the mean exit velocity V_2. The nozzle wake and passage vortices also have a moderate effect on the boundary layer region. The interaction between the rotor boundary layer flow and the nozzle wake and passage vortices generates complex local skews on the thick boundary layer onset line. It is evident that the thick boundary layer onset line locally moves upstream under the effect of the nozzle wake.

Conclusions

Laser Doppler velocimetry (LDV) was successfully applied to provide detailed experimental data on the time-resolved unsteady flow fields around the rotor of a single-stage axial-flow turbine at a low Reynolds number ($Re_{out,RT}=3.5\times10^4$). The complex aerodynamic interactions between the turbine nozzle and the turbine rotor were described in detail, as summarized below.

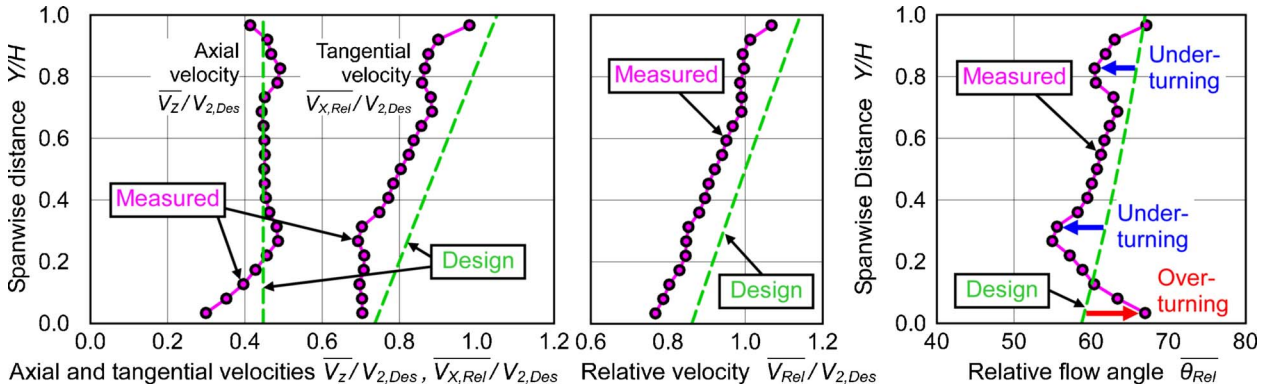

Fig. 30 Time-averaged, pitchwise-averaged spanwise distributions of velocity and flow angle at rotor exit in relative frame of reference ($Z_{RT}/C_{ax,RT}=1.145$)

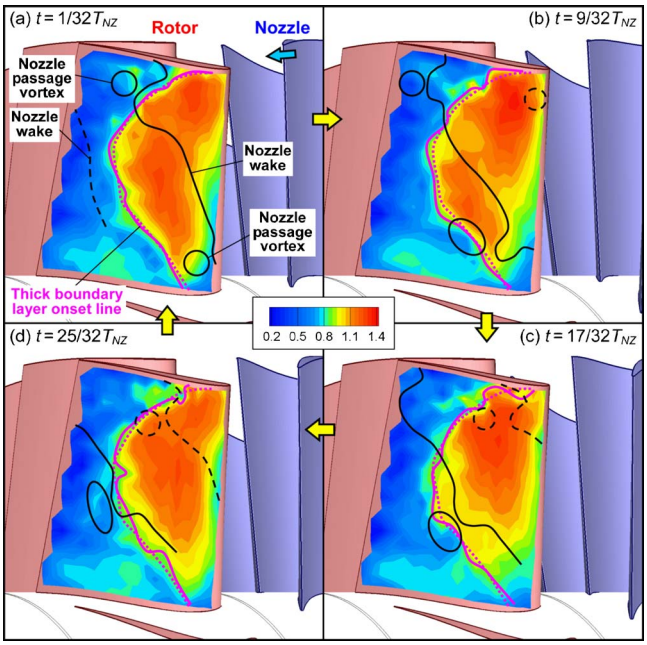

Fig. 32 Time-resolved relative velocity on rotor suction surface

1. The nozzle wake and secondary vortices are periodically and three dimensionally distorted at the rotor inlet because of the radial inclination of the nozzle wake relative to the rotor leading edge;
2. At the front part of the rotor passage, a curious tangential high-turbulence intensity region spread at the tip side. This was because of the axial stretch of the nozzle wake due to the effects of the nozzle passage vortex and rotor potential flow field. Observations from various planes revealed the mechanisms of the deformation of the nozzle wake and secondary vortices;
3. The nozzle flow (wake and passage vortices) and rotor flow (boundary layer, wake, tip leakage vortex, and passage vortices) interact intensively inside the rotor rear passage; and
4. The periodic fluctuation of the relative velocity on the rotor suction surface due to the nozzle effect is as much as 20% of the mean rotor exit velocity. The nozzle wake and passage vortices generate complex local skews of the thick boundary layer onset line.

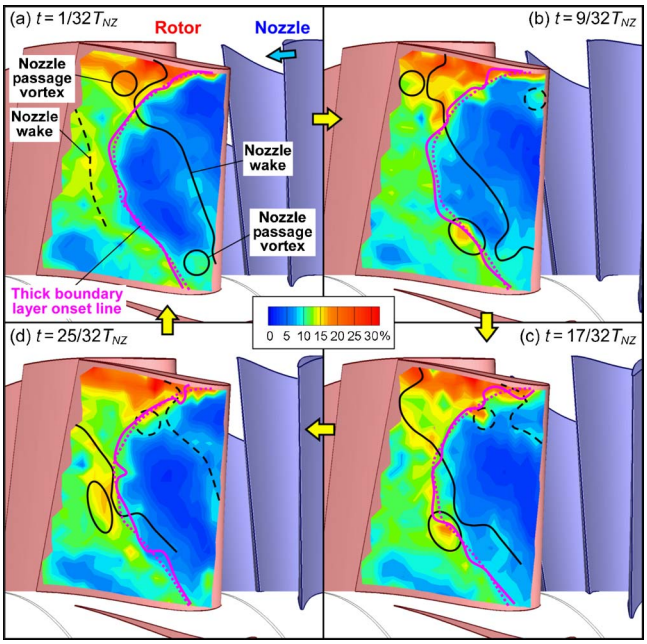

Fig. 33 Time-resolved turbulence intensity on rotor suction surface

The turbine geometry and the experimental data including movies of unsteady flows can be obtained on request by e-mail to the author, to support understanding of unsteady three-dimensional flows and the validation of unsteady CFD codes.

Acknowledgments

This study was supported by a grant from the "Micro Gas Turbine/Solid Oxide Fuel Cell Hybrid Cycle for Distributed Energy System" research project of the Department of Core Research for Evolutional Science and Technology (CREST) of the Japan Science and Technology Agency (JST). The author would like to thank Professor Haruo Yoshiki of the University of Tokyo, and Dr. Yasukata Tsutsui and Dr. Hiro Yoshida of the National Institute of Advanced Industrial Science and Technology (AIST), for their help during the course of this work.

Nomenclature

C = chord length
C_{ax} = axial chord length
CPs = static pressure $CPs=(Ps-Pt_{in,NZ,mid})/\frac{1}{2}\rho\overline{\overline{V_{out,NZ}}}^2$
CPt = total pressure loss $CPt=(Pt_{in,NZ,mid}-Pt)/\frac{1}{2}\rho\overline{\overline{V_{out,NZ}}}^2$
H = passage height
H_{12} = shape factor $(=\delta_1/\delta_2)$
LE = leading edge
LV = tip leakage vortex
Ma = Mach number
N_X = data divided number for tangential direction
N_Z = data divided number for axial direction
N_T = data divided number for time interval of one-pitch motion of blade
PS = pressure surface side
Ps = static pressure
Pt = total pressure
PV = passage vortex
Re = Reynolds number
SS = suction surface side
TE = trailing edge
Tu_{Abs} = turbulence intensity (random fluctuation component) in absolute frame of reference normalized by V_1
Tu_{Rel} = turbulence intensity (random fluctuation component) in relative frame of reference normalized by V_2
S = blade pitch
V_1 = time-averaged and pitchwise and spanwise mass-averaged absolute velocity at nozzle exit plane (axial distance $Z_{NZ}/C_{ax,NZ}=1.125$), $V_1=10.70$ m/s
V_2 = time-averaged and pitchwise and spanwise mass-averaged relative velocity at rotor exit plane (axial distance $Z_{RT}/C_{ax,RT}=1.145$), $V_2=9.27$ m/s
V_{Abs} = absolute velocity in absolute frame of reference normalized by velocity V_1
V_{Rel} = relative velocity in relative frame of reference normalized by velocity V_2
X = tangential (pitchwise) distance

Y = radial (spanwise) distance
Z_{NZ} = axial distance from nozzle leading edge at midspan
Z_{RT} = axial distance from rotor leading edge at midspan
δ_1 = boundary layer displacement thickness
δ_2 = boundary layer momentum thickness
θ = flow angle measured from axial direction

Subscripts

Abs = absolute flow or absolute frame of reference
Des = design value
Rel = relative flow or relative frame of reference
NZ = nozzle value
RT = rotor value
in = nozzle or rotor inlet value
mid = midspan value
out = nozzle or rotor outlet value

Superscripts

– = time average and pitchwise average
= = time average, pitchwise and spanwise average
’ = random fluctuation (turbulence) component

References

[1] Bons, J. P., Sondergaard, R., and Rivir, R. B., 2002, “The Fluid Dynamics of LPT Blade Separation Control Using Pulsed Jets,” ASME J. Turbomach., **124**, pp. 77–85.
[2] Arakawa, H., Suzuki, T., Saito, K., Tamura, S., and Kishi, S., 1997, “Research and Development of 300 kW Class Ceramic Gas Turbine Project in Japan,” ASME Paper No. 97-GT-87.
[3] Curtis, E. M., Hodson, H. P., Banieghbal, M. R., Denton, J. D., and Howell, R. J., 1997, “Development of Blade Profiles for Low Pressure Turbine Applications,” ASME J. Turbomach., **119**, pp. 531–538.
[4] Murawski, C. G., Sondergaard, R., River, R. B., Vafai, K., Simon, T. W., and Volino, R. J., 1997, “Experimental Study of the Unsteady Aerodynamics in a Linear Cascade with Low Reynolds Number Low Pressure Turbine Blades,” ASME Paper No. 97-GT-95.
[5] Lou, W., and Hourmouziadis, J., 2000, “Separation Bubbles Under Steady and Periodic-Unsteady Main Flow Conditions,” ASME J. Turbomach., **122**, pp. 634–643.
[6] Schulte, V., and Hodson, H. P., 1998, “Unsteady Wake-Induced Boundary Layer Transition in High Lift LP Turbines,” ASME J. Turbomach., **120**, pp. 28–35.
[7] Howell, R. J., Ramesh, O. N., Hodson, H. P., Harvey, N. W., and Schulte, V., 2001, “High Lift and Aft-Loaded Profiles for Low-Pressure Turbines,” ASME J. Turbomach., **123**, pp. 181–188.
[8] Volino, R. J., and Hultgren, L. S., 2001, “Measurements in Separated and Transitional Boundary Layers Under Low-Pressure Turbine Airfoil Conditions,” ASME J. Turbomach., **123**, pp. 189–197.
[9] Van Treuren, K. W., Simon, T., von Koller, M., Byerley, A. R., Baughn, J. W., and Rivir, R., 2002, “Measurements in a Turbine Cascade Flow under Ultra low Reynolds Number Conditions,” ASME J. Turbomach., **124**, pp. 100–106.
[10] Hodson, H. P., and Dawes, W. N., 1998, “On the Interpretation of Measured Profile Losses in Unsteady Wake-Turbine Blade Interaction Studies,” ASME J. Turbomach., **120**, pp. 276–284.
[11] Adamczyk, J. J., 1985, “Model Equation for Simulating Flows in Multistage Turbomachinery,” ASME Paper No. 95-GT-226.
[12] Adamczyk, J. J., 2000, “Aerodynamic Analysis of Multistage Turbomachinery Flows in Support of Aerodynamic Design,” ASME J. Turbomach., **122**, pp. 189–217.
[13] Sharma, O. P., Butler, T. L., Joslyn, H. D., and Dring, R. P., 1985, “Three-Dimensional Unsteady Flow in an Axial Flow Turbine,” J. Propul. Power, **1**, pp. 29–38.
[14] Kost, F., Hummel, F., and Tiedemann, M., 2000, “Investigation of the Unsteady Rotor Flow Field in a Single HP Turbine Stage,” ASME Paper No. 2000-GT-432.
[15] Hodson, H. P., 1985, “Measurements of Wake-Generated Unsteadiness in the Rotor Passages of Axial Flow Turbines,” ASME J. Eng. Gas Turbines Power, **107**, pp. 467–476.
[16] Chaluvadi, V. S. A., Kalfas, A. I., and Hodson, H. P., 2003, “Vortex Transport and Blade Interactions in High Pressure Turbines,” ASME Paper No. GT2003-38389.
[17] Binder, A., Forster, W., Mach, K., and Rogge, H., 1987, “Unsteady Flow Interaction Caused by Stator Secondary Vortices in a Turbine Rotor,” ASME J. Turbomach., **109**, pp. 251–257.
[18] Zaccaria, M. A., and Lakshminarayana, B., 1995, “Unsteady Flow Field Due to Nozzle Wake Interaction With the Rotor in an Axial Flow Turbine: Part I – Rotor Passage Flow Field; Part II – Rotor Exit Flow Field,” ASME J. Turbomach., **119**, pp. 201–224.
[19] Matsunuma, T., and Tsutsui, Y., 2003, “LDV Measurements of Unsteady Midspan Flow in a Turbine Rotor at Low Reynolds Number,” ASME Paper No. GT2003-38468.
[20] Göttlich, E., Woisetschläger, J., Pieringer, P., Hampel, B., and Heitmeir, F., 2006, “Investigation of Vortex Shedding and Wake-Wake Interaction in a Transonic Turbine Stage Using Lase-Doppler-Velocimetry and Particle-Image-Velocimetry,” ASME J. Turbomach., **128**, pp. 178–187.
[21] Binder, A., Schroeder, Th., and Hourmouziadis, J., 1989, “Turbulence Measurements in a Multistage Low-Pressure Turbine,” ASME J. Turbomach., **111**, pp. 153–161.
[22] Gallus, H. E., Zeschky, J., and Hah, C., 1995, “Endwall and Unsteady Flow Phenomena in an Axial Turbine Stage,” ASME J. Turbomach., **117**, pp. 562–570.
[23] Halstead, D. E., Wisler, D. C., Okiishi, T. H., Walker, G. J., Hodson, H. P., and Shin, H., 1997, “Boundary Layer Development in Axial Compressors and Turbines Part 4: Computations & Analyses,” ASME J. Turbomach., **119**, pp. 114–127.
[24] ANSI/ASME, 1985, *Measurement Uncertainty*, ASME Performance Test Codes, Supplement on Instruments and Apparatus, Part 1, ANSI/ASME PTC 19.1–1985.
[25] Matsunuma, T., and Tsutsui, Y., 2005, “Effects of Low Reynolds Number on Wake-Generated Unsteady Flow of an Axial-Flow Turbine Rotor,” Int. J. Rotating Mach., **2005**(1), pp. 1–15.
[26] Denton, J. D., 1993, “Loss Mechanisms in Turbomachines,” ASME J. Turbomach., **115**, pp. 621–656.
[27] Fielding, L., 2000, *Turbine Design*, ASME Press, New York, pp. 27–28.
[28] Moustapha, S. H., Carscallen, W. E., and McGeachy, J. D., 1993, “Aerodynamic Performance of a Transonic Low Aspect Ratio Turbine Nozzle,” ASME J. Turbomach., **115**, pp. 400–408.
[29] Perdichizzi, A., 1990, “Mach Number Effects on Secondary Flow Development Downstream of a Turbine Cascade,” ASME J. Turbomach., **112**, pp. 643–651.
[30] Schlichting, H., 1979, *Boundary Layer Theory*, McGraw–Hill, New York, pp. 455.
[31] Sieverding, C. H., 1985, “Recent Progress in the Understanding of Basic Aspects of Secondary Flows in Turbine Blade Passages,” ASME J. Eng. Gas Turbines Power, **107**, pp. 248–257.

Experimental Investigations of Clocking in a One-and-a-Half-Stage Transonic Turbine Using Laser Doppler Velocimetry and a Fast Response Aerodynamic Pressure Probe

O. Schennach
e-mail: oliver.schennach@tugraz.at

J. Woisetschläger
e-mail: jakob.woisetschlaeger@tugraz.at

A. Fuchs

E. Göttlich

A. Marn

R. Pecnik

Institute for Thermal Turbomachinery and Machine Dynamics,
Graz University of Technology,
Austria

The current paper presents experimental clocking investigations of the flow field in midspan in a high-pressure transonic turbine with a downstream vane row (1.5 stage machine). Laser-Doppler-velocimetry measurements were carried out in order to record rotor phase resolved velocity, flow angle, and turbulence distributions upstream and downstream of the second vane row at several different vane-vane positions. Additionally, a fast-response aerodynamic pressure probe was used to get the total pressure distribution downstream of the second vane row for the same positions. Altogether, the measurements were performed for ten different first vane to second vane positions (clocking positions) for measurements downstream of the second vane row and two different clocking positions for measurements upstream of the second vane row. The paper shows that different clocking positions have a significant influence on the flow field downstream of the second vane row. Furthermore, different measurement lines upstream of the second vane row indicate that clocking has nearly no influence on the flow field close to the rotor exit. [DOI: 10.1115/1.2464144]

Introduction

To meet the objective of reduced costs and more compactness of turbomachinery, it is advantageous to reduce the number of stages resulting in high-pressure (HP) ratios and transonic conditions for these stages. To keep the efficiency at a high level, a detailed understanding of the unsteady flow is necessary.

The flow unsteadiness in turbomachinery is highly related to the vane-rotor motion and the wake-wake interaction. Additionally, in HP low aspect ratio turbines the secondary flows, strong potential fields and trailing-edge shocks must be taken into account. These effects cause a time-varying, nonuniform flow field downstream the stage affecting the performance and boundary layer of the next vane row [1–3].

Hummel [4] performed a two-dimensional numerical simulation of a one-stage HP turbine and provided a guideline for positioning a second vane in order to minimize the effect of the trailing-edge shock strength on to the second vane.

The basic idea of clocking (also known as indexing) is to improve the overall efficiency by varying the circumferential and/or the axial position of adjacent vanes or blades. The most common method is to rotate the nozzle ring with respect to a downstream vane row, while the largest efficiency increase is achieved with equal blade counts. It is well known that a maximum of efficiency is achieved when the first vane's wake impinges the leading edges of the second vanes.

Much research work has been performed to investigate the influence of clocking in subsonic turbines. Experimental results reported by Huber et al. [5] for a two-stage turbine showed a 0.8% efficiency variation in midspan due to clocking of the second stage vane. Time accurate numerical studies by Arnone [6] in a three stage LP turbine showed a 0.7% efficiency variation due clocking. Furthermore, different investigated Reynolds numbers showed no major difference in the results. Reinmöller et al. [7] investigated the influence of clocking on the flow field between rotor and second vane as well as downstream the second vane using hot-wire probes and pneumatic probes supported by numerical simulations. The authors found 1% relative efficiency variation at midspan.

Recent research work focuses on clocking effects in transonic turbines. Billiard et al. [8] focused on to the heat transfer measurements on the second vane in a 1.5-stage HP turbine. It was found that clocking changes the mean levels of the heat transfer as well as the intensity and the trajectory of the fluctuations. Gadea et al. [9] investigated the influence of clocking on to the time-resolved pressure field of a second vane tested in a 1.5-stage HP turbine. It was shown that the optimum clocking position for aerodynamics is not the optimum for minimum unsteady forces. Haldemann et al. [10] performed aerodynamic measurements in 1.5-stage HP turbine indicating an overall efficiency increase of about 2–3 % using a variety of independent methods.

The current paper focuses on the flow field between rotor and second vane as well as downstream of the second vane of a highly loaded low aspect ratio transonic turbine stage with respect to different clocking positions. The investigations were performed under engine representative conditions in a continuously running cold-flow test facilty of the institute. Using nonintrusive optical measurement techniques, such as laser Doppler velocimetry (LDV), enables measurements close to the vane or blades and detect the interaction mechanisms.

Contributed by the International Gas Turbine Institute of ASME for publication in the JOURNAL OF TURBOMACHINERY. Manuscript received July 13, 2006; final manuscript received July 18, 2006. Review conducted by David Wisler. Paper presented at the ASME Turbo Expo 2006: Land, Sea and Air (GT2006), Barcelona, Spain, May 8–11, 2006. Paper No. GT2006-90264.

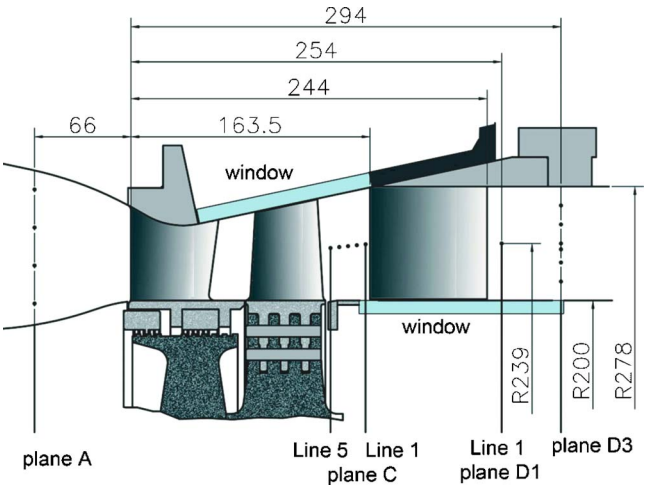

Fig. 1 Meridional flow path with measurement positions (indicated with dots)

Experimental Facility and Instrumentation

Test Facility. The transonic test turbine of the Institute for Thermal Turbomachinery and Machine Dynamics is a continuously operating cold-flow open-circuit facility, which allows the testing of turbine stages with a diameter up to 800 mm in full-flow similarity (corrected speed and pressure ratio). Pressurized air is delivered by a separate 3 MW compressor station. A membrane-type coupling directly transmits the turbine shaft power to a three-stage radial brake compressor and measures the torque. This brake compressor delivers additional air mixed to the flow from the compressor station and increases the overall mass flow. The air temperature in the mixing chamber (turbine stage inlet) can be adjusted by coolers between 40°C to 185°C. The maximum shaft speed of the test rig is limited to 11,550 rpm. Depending on the stage characteristic, a maximum coupling power of 2.8 MW at a total mass flow of 22 kg/s can be reached. Detailed information on the design and construction of the facility can be found in [11], on the operation in [12].

Turbine Stage Tested. The meridional section of the turbine stage is given in Fig. 1. To provide access for all types of optical measurements, the hub contour is cylindrical while the shroud contour is conical in the rotor section. The second vane has a simple cylindrical contour and is designed as an LP vane to prevent condensation of the humid air. Downstream of the second vane row, a deswirler takes out the circumferential velocity and reduces flow velocity and, therefore, exhaust losses (not shown in Fig. 1).

The optical access is realized with two glass windows for LDV measurements downstream and upstream of the second vane row. The rotatable stage inlet casing was instrumented with a pressure rake and a temperature rake, each with four kielheads, which allows one to traverse the turbine inlet flow. The stage outlet was also instrumented with a temperature rake and a pressure rake, each with five kielheads. Additionally, the pressure rake is equipped with a fast-response aerodynamic pressure probe at midspan. The circumferential measurements at the stage outlet were performed by turning the first and the second vane row while the probe remained at a fixed position. The measurement plane upstream the second vane row and the circumferential measurement line downstream the second vane as well as the rakes positions in plane A and plane D3 are shown in Fig. 1.

Some important operating conditions for this investigation and the geometrical data of the stage are given in Table 1. The profiles investigated are shown in Fig. 2 together with the trigger zero position.

Table 1 Stage geometrical data and operating conditions

Number of nozzle guide vanes	24
Number of rotor blades	36
Number of second guide vanes	24
Nozzle chord (midspan) (mm)	78.9
Nozzle axial chord (midspan) (mm)	56.1
Geometric turning angle nozzle (deg)	70
Nozzle aspect ratio (exit height/chord)	0.70
Blade chord (midspan) (mm)	55.9
Blade axial chord (midspan) (mm)	46.8
Geometric turning angle blade (deg)	107
Blade aspect ratio (exit height/chord)	1.24
Second vane chord (midspan) (mm)	88.3
Second vane axial chord (midspan) (mm)	80.1
Geometric turning angle second vane (deg)	53
Second vane aspect ratio (exit height/chord)	0.88
Rotor tip clearance/span (%)	1.4
Second vane hub clearance/span (%)	1.3
First vane-blade spacing [% nozzle axial chord (midspan)]	47
Blade-second vane spacing [% blade axial chord (midspan)]	73
Pressure ratio p_{tA}/p_C	3.30
Pressure ratio p_{tA}/p_D	4.27
Rotational speed (rpm)	10,600
Inlet total temperature T_{tA} (K)	413
Reynolds number nozzle guide vane exit	2.57×10^6
Reynolds number rotor blade exit	1.69×10^6
Isentropic first vane exit Mach number	1.13
Blade outlet Mach number, midspan	0.51
Relative blade outlet Mach number, midspan	0.87
Second vane outlet Mach number	0.69
Loading factor $\Delta h/u^2$	1.51

The vertical line indicates the position of a 0.8 mm gap between the first guide vane tip and the outer shroud contour. This gap is necessary to rotate the first vane ring and the guide vane casing during test run to change the relative position between vane and measurement system. The gap between rotor blade tip and shroud as well as the clearance of the second vane to the hub are 1 mm. The vanes, the rotor blades and the end walls were covered with a high-temperature flat black paint to reduce surface reflections. To allow a rotor-phase-resolved analysis of the measured velocities in the positions traversed, a reference signal provided by the monitoring system of the turbine was used to trigger the data sampling (uncertainty: blade pitch/300, a phase delay depending on speed was accounted for).

Droplets of DEHS oil (Di-Ethyl-Hexyl-Sebacin-Esther) with a nominal diameter of 0.3 μm were added by PALLAS AGF 5.0D

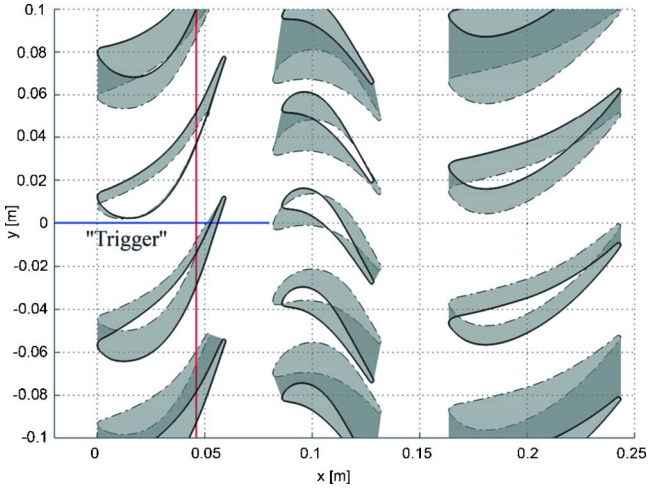

Fig. 2 Profiles at trigger zero position for clocking position 1 (CP1)

Table 2 Optical beam system

Velocity component	u	v
Focal length (mm)	400	400
Wavelength (nm)	514.5	488
Beam spacing (mm)	38	38
Beam diameter (mm)	2.2	2.2
Focal spot diameter (μm)	119.1	112.9
Number of fringes (-)	21	21

seeding generator 30 cm upstream of the first vane row as seeding material for the optical measurements. These particles guarantee sufficiently high particle response at transonic flow conditions. (In the region of the trailing-edge shocks, a smearing effect of 0.5 mm due to seeding particle inertia was estimated.)

Laser Doppler Velocimetry. The optical velocity measurement of the flow was performed by a two-component LDV system (DANTEC FiberFlow with two BSA processors) and by a 6 W argon-ion laser (COHERENT). Optical access upstream of the second vane row was realized through a small plane-parallel glass window of 9 mm thickness and 120×23 mm surface dimension, while downstream of the second vane row a convex-concave window of 9 mm thickness and 140×90 mm surface dimension was used. An anti-reflection coating was applied to both windows. The main optical parameters of the LDV system are presented in Table 2.

The optical probe head emitted four laser beams into the measurement volume. Light scattered by the tracer particles passing through the probe volume was collected in backscatter mode. Velocity data were recorded by pointwise detection along circumferential lines (at midspan) upstream as well as downstream of the second vane row (see Fig. 1, 0.12 mm probe volume diameter and 2.6 mm length in radial direction). The LDV system was mounted on a lightweight traverse in order to align the position of the probe head.

All circumferential LDV measurements for each clocking position were performed by turning both vane rows, while the probe volume remained in a fixed position. By varying the angular position of the second vane row relative to the first vane row different clocking positions were investigated. Altogether the measurements were performed for ten different clocking positions downstream of the second vane row and two different clocking positions upstream of the second vane row.

Figure 3 shows the investigated clocking positions as well as the LDV measurement locations upstream and downstream of the second vane row. Each circumferential line consists of 20 measurement positions and covers one vane pitch. To investigate the upstream influence of the second vane row, five circumferential lines were measured in plane C with an axial spacing of 6 mm. The measurement line 1 is located 3 mm upstream of the leading edge of the second vane.

The LDV system acquired velocity samples each time a seeding particle crossed the LDV probe volume. The reference signal of the turbine's monitoring system was used to sort the recorded velocity samples by the actual rotor position. Since a two-component LDV was applied, only the velocities in two different directions (i.e., axial and circumferential direction) were detected. In each measurement position, ~80,000 velocity bursts were collected. These samples were sorted with the help of the trigger signal provided by the shaft monitoring system to the proper rotor position. All data recorded were then mapped into one 10 deg section, i.e., into one blade passing period (time for one rotor blade to move over one rotor pitch). As a result, the data represent the average value over 36 rotor blade channels.

Such a velocity recording for a single position and the one component (BSA 2) is given in Fig. 4, with black dots indicating the single samples. The blade passing period was divided into 40

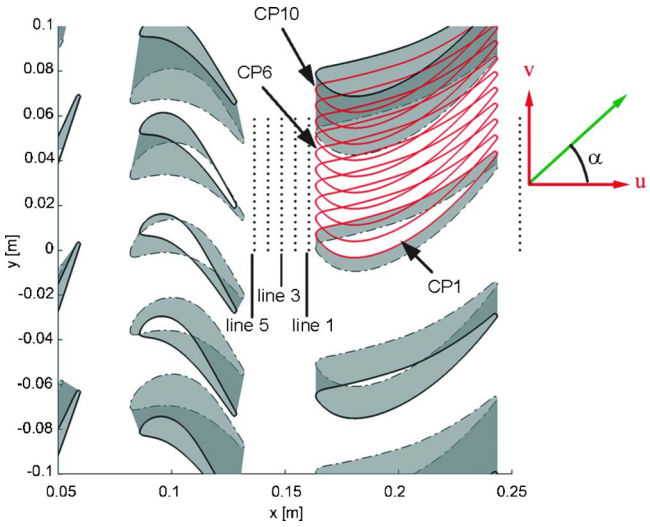

Fig. 3 LDV measurement locations in midspan and investigated clocking positions (CP1-CP10)

evaluation windows, which means that the averaged velocity samples were assigned to 40 different first vane-rotor positions per rotor blade pitch. The instantaneous velocity data were ensemble averaged for each evaluation window. A linear regression method presented in [13] was used. The instantaneous velocity vector $\mathbf{V}$ was decomposed as follows:

$$\mathbf{V} = \bar{\mathbf{V}} + \mathbf{V}' = \bar{\bar{\mathbf{V}}} + \tilde{\mathbf{V}} + \mathbf{V}' \tag{1}$$

The last term $\mathbf{V}'$ represents an unresolved fluctuating component after ensemble averaging and may contain coherent structures that are not a harmonic of blade passing. Here, it is used to quantify the level of turbulence in each evaluation window by means of the variance. With 40 evaluation windows, the number of velocity samples per window was still high enough to allow mean value and level of turbulence to be calculated with the data presented in Table 3. With a circumferential averaged velocity of 245 m/s in plane D1 and 165 m/s in plane C (line 1) and a confidence level of 95%, the errors for the ensemble averaged velocity and the unresolved fluctuation velocity listed in Table 3 are expected. The high-velocity uncertainty in the wake is due to

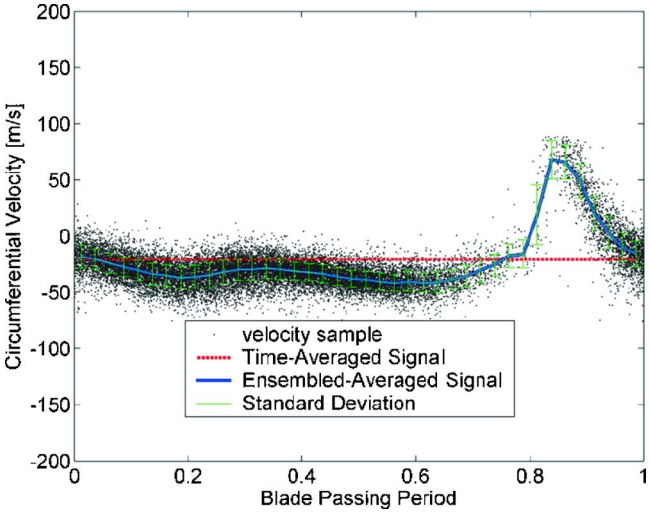

Fig. 4 Velocity decomposition for phase-averaged data (typical plot downstream of the rotor in line 5)

Table 3 LDV measurement uncertainties

Measurement position	$\bar{u},\bar{v}$ (%)	u',v' (%)
Inside the second vane row wake	±1.6	±5.5
Outside the second vane row wake	±0.7	±2.3
Inside the rotor wake (line 1)	±1.7	±6
Outside the rotor wake (line 1)	±0.4	±1.5

the low number of detected velocity bursts in the wake (the shedding boundary layer contains less seeding particles).

Fast-Response Aerodynamic Pressure Probe (FRAPP). The total pressure and total temperature measurements at outlet were carried out with two rakes each with five kielheads in plane D3 (see Fig. 1). The circumferential traversing was performed by turning the first and second vanes and consists 40 measurement positions over the vane pitch.

The total pressure rake was equipped with a fast-response pressure transducer Entran EPIH-411-0,7B to get the instantaneous total pressure at midspan (see Fig. 5). A protective grating with 16 holes (0.2 mm dia) protected the fragile sensor head against dust particles. The cutoff frequency of the pressure transducer was 40 kHz (1 dB deterioration). The amplified sensor signal and the trigger signal provided by the shaft monitoring system were fed to a National Instrument 4551 dynamic signal analyzer board (16 bit resolution, intern anti-aliasing filter) and were sampled with 204.8 kHz. The instantaneous pressure was ensemble averaged for each evaluation window (100 window sections within 10 deg blade pitch).

The steady pressure was measured with five kielheads, connected to a PSI intelligent pressure transducer with an accuracy of 0.05% FS (full scale 0.35 bar). The steady yaw angle variation in midspan was approximately ± 9 deg. The design of the probe head allows accurately measurements of the steady total pressure in an angle range of approximately ±11 deg.

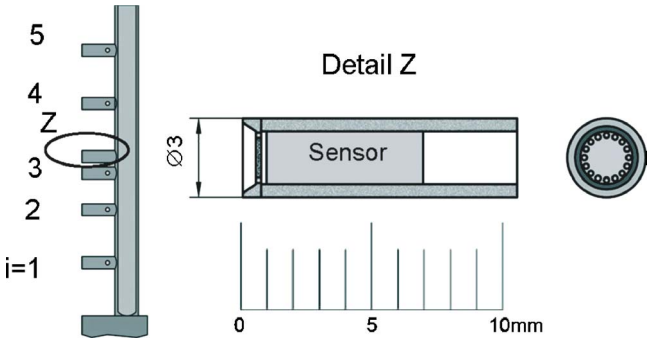

Fig. 5 Total pressure rake with FRAPP in midpan (plane D3)

Results and Discussion

Flow between rotor and second vane. Upstream the second vane two different clocking positions were investigated using LDV to record velocity, flow angle, and turbulence with respect to different rotor vane positions. Time-space plots are a suitable tool to visualize these instantaneous data. Because of the vane-blade ratio of 2:3 and the dimensions used in the data presentations, structures from the moving rotor trailing edge appear under an angle of 45 deg, where effects from the vanes are horizontal contours.

Since vane clocking is mainly attributed to the wakes of the vanes, time-space plots of the turbulent kinetic energy (TKE) are used to identify them. The TKE is calculated by the following equation from the two-component LDV data:

$$k = 0.75(\overline{u'^2} + \overline{v'^2}) \tag{2}$$

Equation (2) is based on the assumption that the third component w' (not recorded) is of the same magnitude than the u' and v' components (spatial isotropy of turbulence).

In Fig. 6, the time-space plots of the TKE for two opposite clocking positions are depicted over three blade-passing periods and two vane pitches (rotor phase is relating to first vane position). Three axial measurement lines were selected to show the upstream influence of the second vane row. In the time-space plots of this work, the positions of the profiles shown corresponds to the relative position of the rotor blades and the second vanes to the circumferential measurement line 1 and line 5 (see also Fig. 3).

In all plots of Fig. 6, the TKE level is dominated by the rotor wakes. In the measurement line 5 (closest to the rotor exit) a pronounced phase locking effect of the vortex shedding to the angular rotor position can be detected. The phase locking phenomena was also observed in early investigations (see [14]).

At a vane pitch of about ~1 (Fig. 6), only a low TKE is observed, whereas at a vane pitch of about ~1.4 higher turbulence

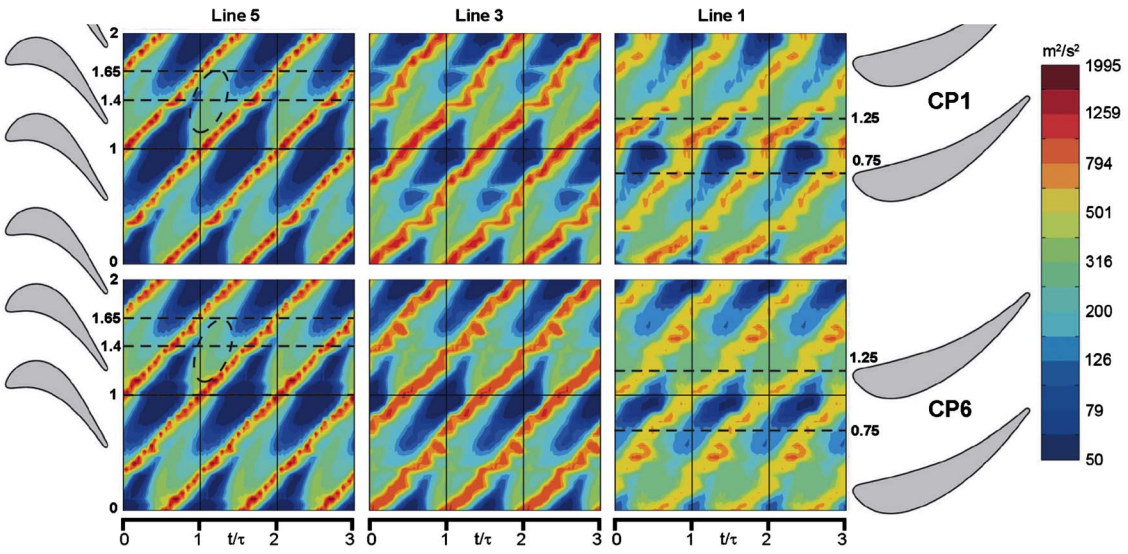

Fig. 6 Time-space plots of TKE in plane C for CP1 and CP6 for three different measurement lines

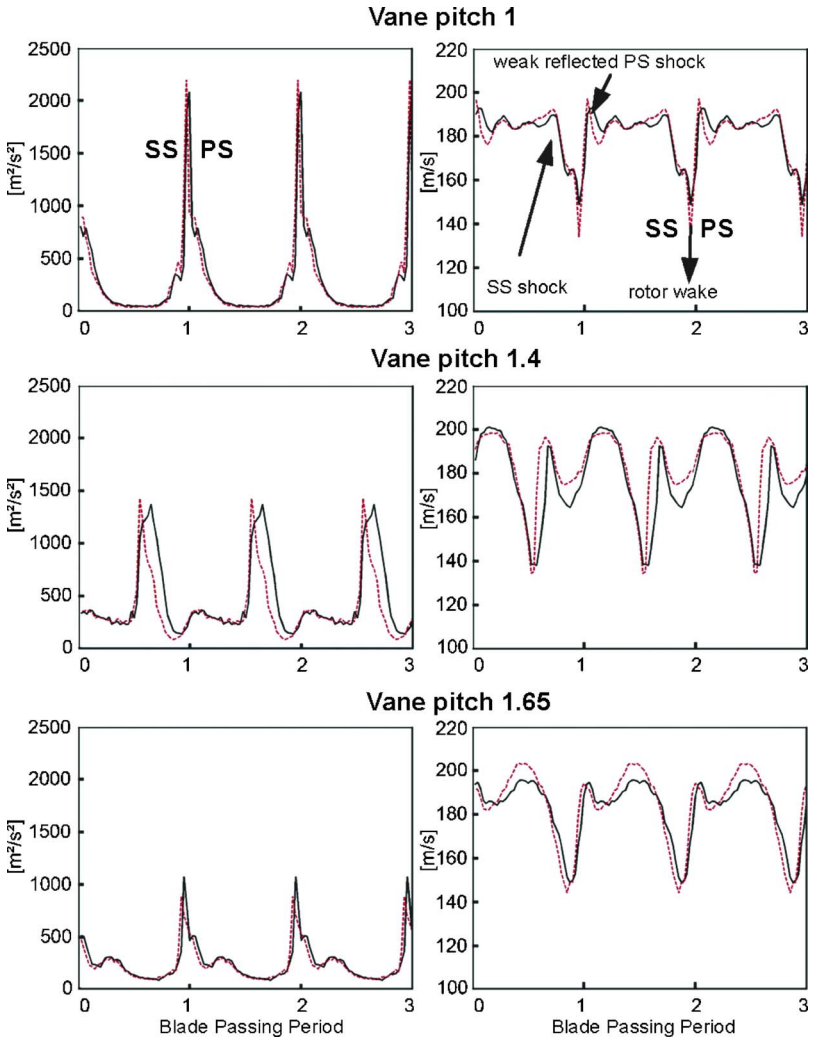

Fig. 7 Time-resolved TKE (left plot) and velocity magnitude in line 5, CP1 and CP6 ((red) dashed line)

occurs between the rotor wakes. This higher turbulence level is caused by the chopped first vane wakes, which passes the measurement lines at a constant vane pitch (first vane wake avenue is fixed relative to the first vane row). Details of wake-blade interactions are given by Hodson and Dawes [15].

In the region between a vane pitch of 1 and 1.4, a higher turbulence level of the rotor wake is observed, whereas at a vane pitch of 1.65 (first vane wake is close to rotor wake pressure side) a low turbulence level of the rotor wake and a significant reduction in the mean level is observed. Tiedemann and Kost [2] explained this decrease by the first vane wake-induced reduction of the "step" in the flow parameter levels between the rotor passage flow and the rotor wake flow. This results in a decrease of the wake mixing intensity and thus in the turbulence level.

Figure 7 compares the TKE (left plots) at vane pitches 1, 1.4, and 1.65 for the opposite clocking positions 1 and 6. From the top to the bottom plot, the maximum level (indicating the rotor wake) decreases by ~50%, whereas the base level has a maximum level in the center plot (core of the first vane wake) for both clocking positions. The TKE close to the rotor exit presented in these graphs indicates a weak influence for different clocking positions.

The time-space plot of the velocity magnitude shown in Fig. 8 is dominated by the rotor wakes, the periodic first vane wakes and the trailing-edge shocks. The dotted lines parallel to the rotor wake mark the reflected pressure-side shocks (reflected by the rotor blades, A) and the suction-side shocks (B, see also Fig. 7). Periodically, the strength of the shocks changes. Since the modulation is a horizontal line in the time-space plot, it is likely that the first vane cause this variation [4]. The comparison of both clocking positions presented here (CP1 and CP6) indicated that clocking had only a small influence onto the velocity field close to the rotor outlet. The upstream influence of the second vane row becomes stronger at measurement line 3, particularly in the velocity magnitude. This is due to the strong static pressure field induced by the leading edge of the second vane row (Fig. 8).

The region of low velocity seen in measurement line 1 (close to the socond vane row) identifies the circumferential position of the second vane's leading edge. The time-periodic impingement of the rotor wakes on the leading edge of the second vane caused distinct maxima and minima in the velocity magnitude, whereas these maxima are more pronounced at CP1 than at CP6.

Figure 9 shows the time-resolved velocity magnitude and TKE at the measurement position in line 1 close to the leading edge of the second vane for both clocking positions. The second maximum in the TKE at CP6 indicates the wake of the first vane, whereas at CP1 this second maximum does not appear. Furthermore, CP6 shows less periodic fluctuations in TKE, whereas the time-averaged TKE level is increased.

The plot of the velocity magnitude in Fig. 9 indicates an amplitude decrease by roughly 11% for CP6, whereas the minimum level remains constant. Assuming a constant dissipation coefficient and a low speed flow the boundary layer loss could be esti-

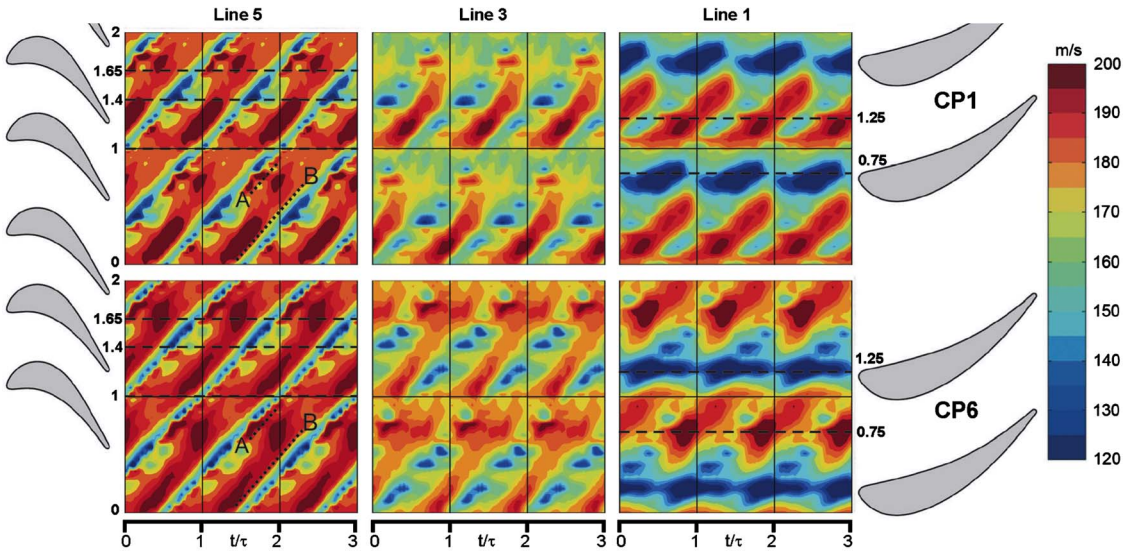

Fig. 8 Time-space plots of velocity magnitude in plane C for CP1 and CP6 for three different measurement lines

mated to be proportional to the cubic of the blade surface velocity [16]. Griffin et al. [17] found that reduced surface velocities and less large-scale unsteadiness are the reasons for the improved second vane performance. Therefore at CP6, the efficiency should be higher compared to CP1, supposing that a lower inlet velocity would result in lower surface velocities.

In contrast, Fig. 10 presents the time-resolved velocity magnitude and the TKE at midspan between two blades of the second vane. CP6 gives higher midpassage velocities, while minimizing the velocity close to the leading edge (compare to Fig. 9). An increased turbulence level for both positions was observed, whereas at CP1 the turbulence level was slightly higher.

Note that the blade passing period in Figs. 9 and 10 is related to the first vane row according to Fig. 2. For different positions relative to the vane pitch a phase-delay of the rotor wake is observed (see also Fig. 6). This is shown in Figs. 9 and 10 for VP 0.75 and 1.25 (dashed line).

An additional effect of clocking is the change in yaw angle. The time-averaged yaw angle distribution close to the leading edge of the second vane is given in Fig. 11. CP1 shows a higher yaw-angle variation over the vane pitch, whereas the mean yaw angle is nearly not affected by clocking the vanes.

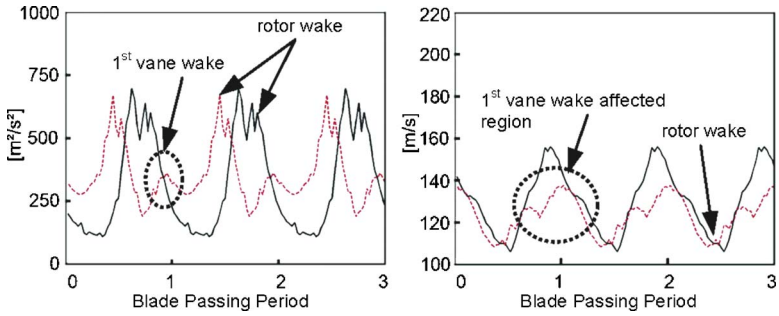

Fig. 9 Time-resolved TKE (left plot) and velocity magnitude in line 1, leading edge of the second vane row at VP 0.75 for CP1 and VP 1.25 for CP6 ((red) dashed line)

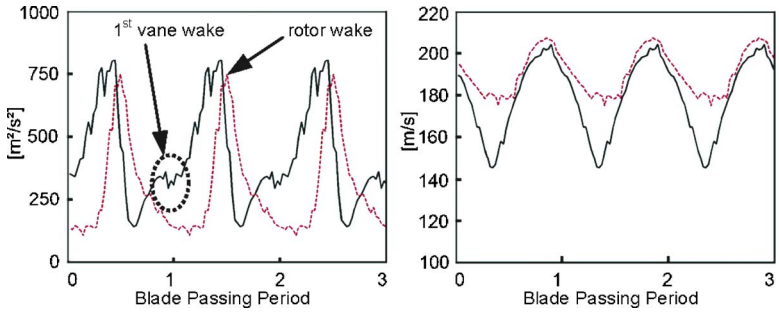

Fig. 10 Time-resolved TKE (left plot) and velocity magnitude in line 1, mid channel of the second vane row at VP 1.25 for CP1 and VP 0.75 for CP6 ((red) dashed line)

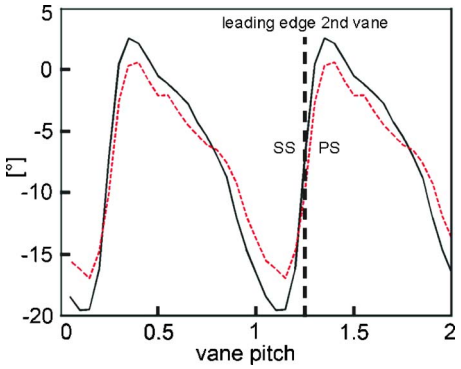

Fig. 11 Time-averaged yaw angle distribution in line 1 for CP1 (shifted in space) and CP6 ((red) dashed line)

Flow Downstream of the Second Vane Row. The time-averaged velocity magnitude and the TKE are shown in Fig. 12. The area of high TKE amplitude in the left plot indicates the wake of the second vane, whereas the second maximum denotes the wake of the first vane. The TKE for CP1 shows a higher turbulence level for the second vane wake as well as for the wake of the first vane. The right plot in Fig. 12 shows a smoother velocity distribution for the CP6.

Figure 13 compares CP6 and CP7. In CP7, the first vane wake directly impinges the leading edge of the second vane. The strong interaction of the first vane wake with the boundary layer at the second vane leads to a remarkable increase in the TKE of the wake of the second vane.

Figure 14 shows the TKE, yaw angle, and the velocity magnitude at midspan (plane D1, line 1) for four selected clocking positions. The measured data for each clocking position were shifted in space in that sense that the wake of the second vane remained at a fixed position. This means that effects generated by the first vane change their circumferential position while clocking the vanes. In all plots, the second vane wake is the dominant structure and appears as horizontal line (marked with A in the upper plot). A pronounced phase-locking effect of the vortex shedding (locked to the rotor phase) can be detected easily in the plot of the TKE and in the plot of the yaw angle. Areas of low and high yaw angle in the wake of the second vane indicate the vortex shedding. It seems that the pressure-side vortex is much stronger (low yaw angle) due to the stronger velocity gradient on the pressure-side boundary layer.

Between the second vane wakes, areas of higher turbulence indicate the interaction between first vane wake segments and rotor wake (marked with B in the TKE plot). While clocking the first vane row, the wakes change their circumferential position. In CP9, it appears at the second vane suction side and is shifted continuously over CP1, CP4, and CP6 to the pressure side. The occurrence of the first vane wakes changes with respect to the rotor phase. CP1 and CP4 show a higher level of turbulence of the first vane segments, whereas at the other clocking positions a lower turbulence level is observed.

A further comparison of all investigated clocking positions shows a higher TKE in the regions affected by the wake of the first vane when the wake passes near the suction side of the second vane other than near the pressure side (see CP1 and CP6). It seems that the first vane wakes have a major influence on the second vane suction-side boundary layer state.

Effects in Fig. 14 that are related to the moving rotor blades appear as structures under 45 deg, e.g., the rotor wake flow. In the time-space plot of the TKE, the rotor-wake-influenced region is marked with C. The middle plot shows the yaw angle distribution, which is strongly influenced by clocking. Because of the negative jet effect [15], the passing rotor wakes appear as regions of high yaw angle. CP6 shows a more uniform yaw angle distribution in circumferential direction, indicating a weak influence of the first vane wake. Again the velocity magnitude is strongly influenced by different vane-vane positions. Particularly at CP1, the velocity changes periodically by more than 10% in the main flow field. Clocking positions where the first vane wake passes close to the second vane surface (CP6) clearly shows the inclined structures related to the moving rotor blades over the whole flow channel.

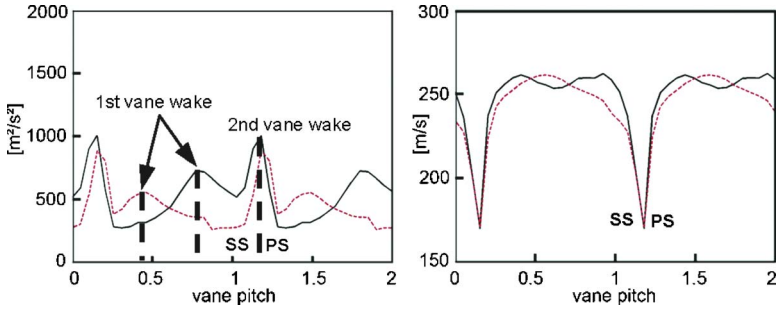

Fig. 12 Time-averaged TKE (left plot) and velocity magnitude downstream of the second vane row (plane D1) for CP1 and CP6 ((red) dashed line)

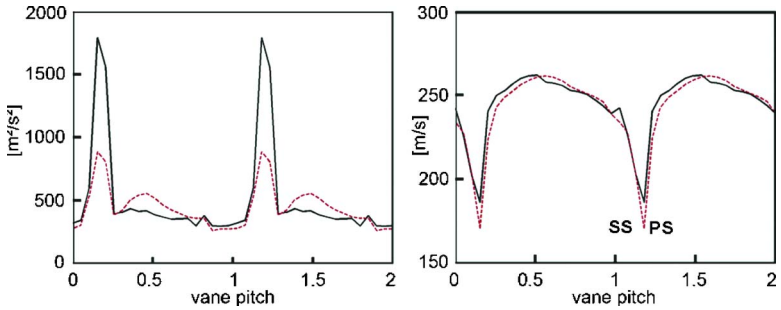

Fig. 13 Time-averaged TKE (left plot) and velocity magnitude downstream of the second vane row (plane D1) for CP6 ((red) dashed line) and CP7

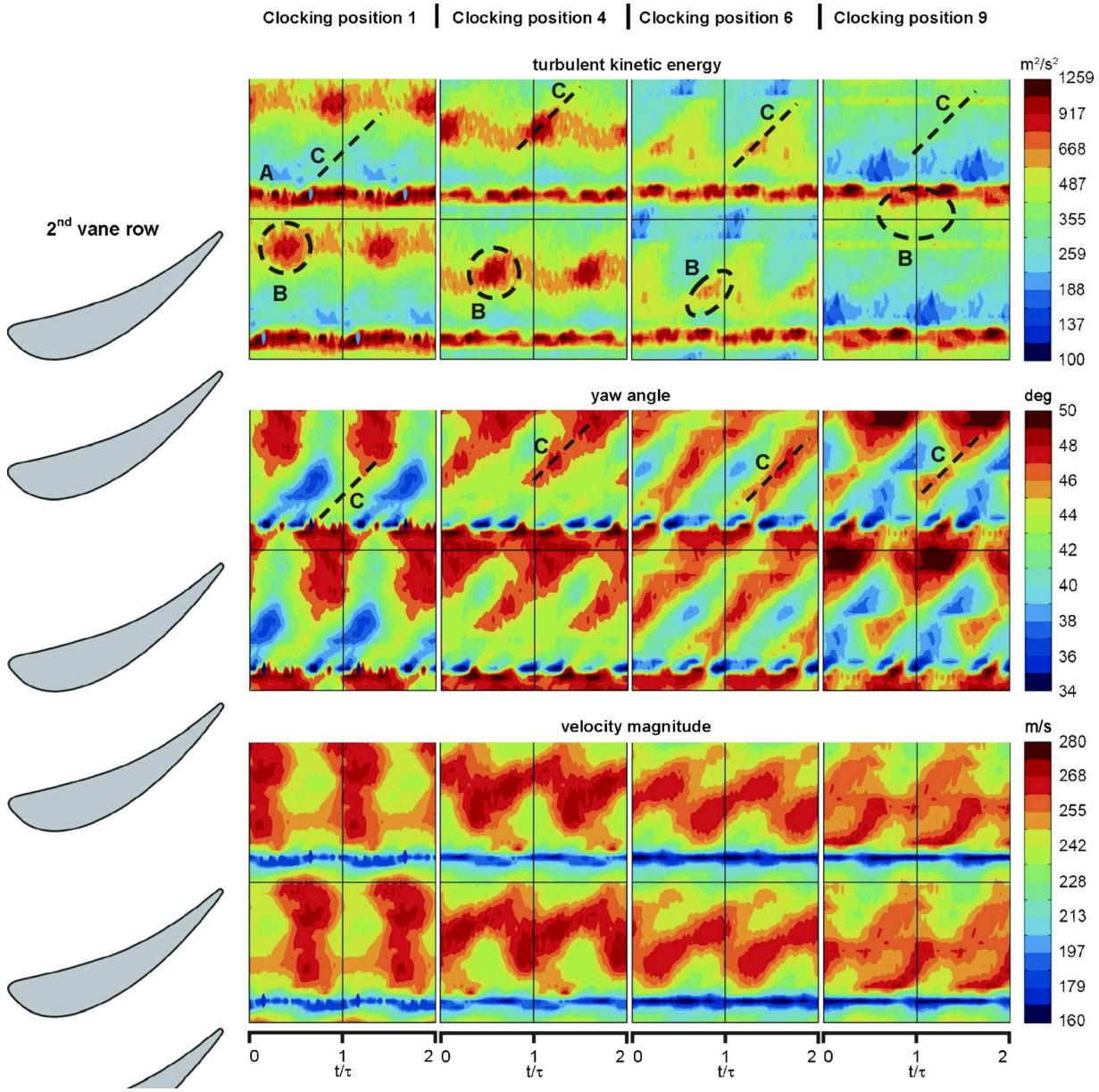

Fig. 14 Time-space plots of TKE, yaw angle, and velocity magnitude at midspan for four different clocking positions downstream of the second vane row (plane D1, line 1)

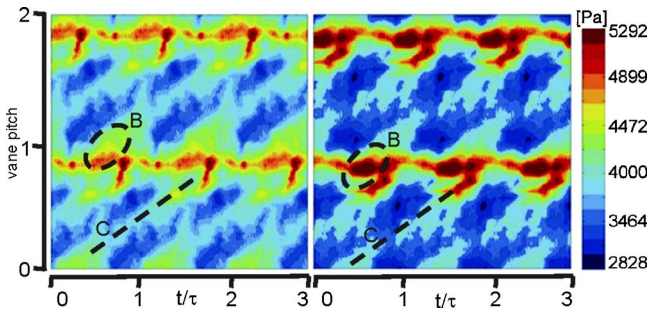

Fig. 15 Time-space plot of the total pressure fluctuation (rms) for CP6 (left plot) and CP7 downstream of the second vane (plane D3, midspan)

The time-space plot of the total-pressure rms (detected with the FRAPP probe in plane D3) presented in Fig. 15 again shows diagonal regions of high rms values, indicating the time-periodic rotor wake passing (marked with C), while the wakes of the first vane appear at a fixed circumferential position (B). At CP7, where the first vane wake directly impinges the leading edge of the second vane, a higher rms value of the second vane wake is observed, but the difference is less pronounced compared to TKE gained by LDV (see also Figs. 13 and 16).

The spanwise total-to-total efficiency was used to quantify the clocking effect on the turbine efficiency, which is defined as

$$\eta_{j,i} = \frac{1 - \frac{T_{tD3,i}}{T_{tA,i}}}{1 - \left(\frac{p_{tD3,i}}{p_{tA,i}}\right)^{(\kappa-1)/\kappa}} \quad \text{and} \quad \eta_{\text{rel},j,i} = \frac{\eta_{j,i}}{0.1\sum_{j=1} \eta_{j,3}} \tag{3}$$

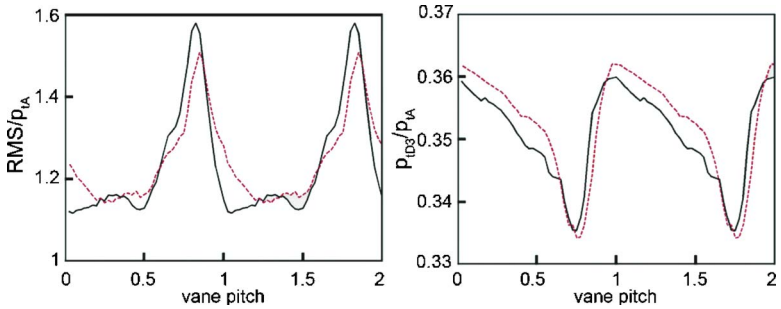

Fig. 16 Time-averaged total pressure fluctuation (rms) and total pressure for CP6 ((red) dashed line) and CP7 downstream of the second vane row (plane D3, midspan)

Because of the lack of data, the total temperature T_t and the total pressure p_t are pitchwise area averaged quantities. The measurement uncertainty of the efficiency is approximately ±0.35%.

The applied second vane row was designed cylindrically. Therefore, optimized clocking over the whole span is not possible and a distinct maximum in the overall total efficiency is not expected. In order to comment on the degree of three-dimensionality, spanwise efficiency is discussed for the positions of the five kielheads. Because of the coarse radial spacing of the rakes, no averaging over the span was performed.

Figure 17 gives the spanwise relative efficiency variation with respect to the clocking position. At a relative span of $h/H=0.17$, 0.33, and 0.45, pronounced maxima and minima in the efficiency are observed, while closer to the tip the effect of clocking is less pronounced. However, maximum efficiency is shifted to different clocking positions. At a relative span of $h/H=0.45$ (near midspan) a relative efficiency variation of about ±1.6% is observed with a maximum at CP6.

A further calculation of the efficiency based on torque, shaft speed, and mass flow (mechanical method) showed no clocking effect due to the slight upstream influence of the second vane row (see also Figs. 6 and 8). This type of efficiency measurement would be more informative in a two stage turbine because, downstream of the second vane, the clocking effect would be more pronounced (see Fig. 14).

Figure 18 presents the total pressure distribution for six different clocking positions downstream of the second vane row. The plots were shifted, so that the wake of the second vane remained at a fixed position.

Regions of low total pressure over the span indicate the second vane wake. Near the pressure side a loss core is present. While clocking the first vane row, the loss core changes the radial position, while the circumferential position remains nearly constant. In CP1, the loss core appears at a relative span of $h/H=0.17$ and is shifted continuously over CP1, CP4, CP5, and CP6 to $h/H=0.33$. This indicates that the clocking phenomena are strongly influenced by the secondary flow field with strong radial migration effects due to the low aspect ratio of the turbine investigated in this work. Because of the very coarse radial spacing of the rake (five kielheads over the span, marked with lines in Fig. 17), a more detailed discussion of the secondary flow field is not yet possible.

A complete 3D design of the vanes in a low aspect ratio turbine has to be applied to benefit from the clocking effect. It should be noted that in a real engine the vane's three-dimensionality is limited. It has an immediate effect on losses generated by the vane, stresses in the vane and on the exit flow distribution. In practice, the blade shape is a tuned balance of many terms, any potential clocking benefit will have to compete with other more powerful factors.

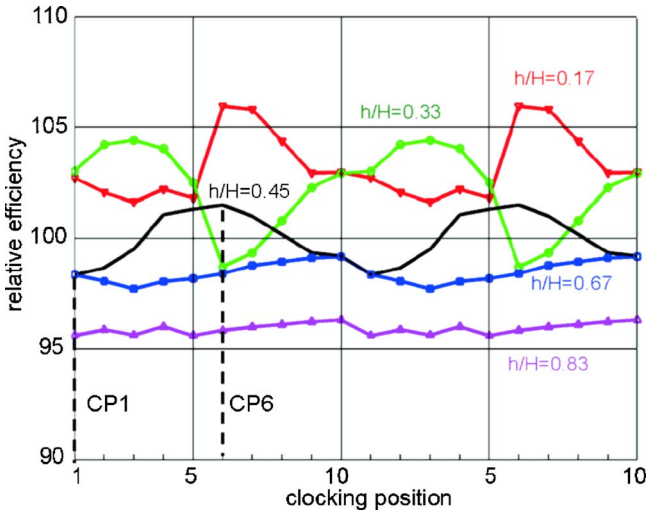

Fig. 17 Spanwise relative efficiency versus clocking position

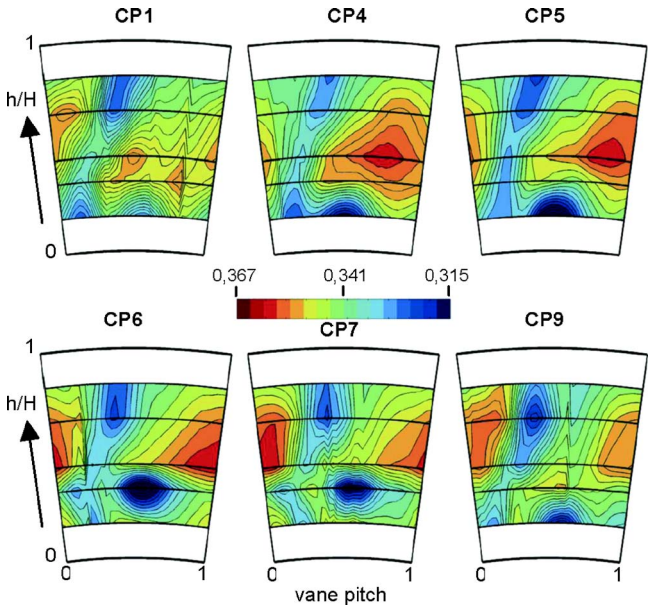

Fig. 18 Time-averaged total pressure distribution (P_{tD3}/P_{tA}) for six different clocking positions downstream of the second vane in plane D3

Conclusions

Laser Doppler velocimetry and a fast-response aerodynamic pressure probe were used to perform a detailed investigation of the flow field in midspan during clocking of the two vanes in a HP 1.5 turbine stage. It was found that clocking the first and second vanes have no significant influence on the velocity field close to the exit of the first rotor. In the TKE close to the rotor exit, hardly no difference due to clocking was recorded.

In the clocking position where the first vane wake passes close to the second vane's leading edge (at pressure side), an amplitude decrease of the velocity magnitude by roughly 11% close to the leading edge of the second vane was observed compared to other clocking positions. Additionally, less periodic fluctuations in the TKE were found close to the leading edge of the second vane. Over the vane pitch, less yaw angle variations were detected when averaged over the blade-passing period. The mean yaw angle, averaged in time and over the vane pitch, was nearly not affected by clocking.

The clocking position where the first vane wake directly impinges the leading edge of the second vane leads to a strong interaction between wake and the boundary layer and caused an increase in TKE and pressure fluctuations in the second vane's wake.

The spanwise total-to-total efficiency plots indicated a significant influence of the three-dimensionality of the flow while clocking. Close to the tip, the clocking effect is hardly recordable. At different spanwise positions, maximum efficiency is shifted to different clocking positions. These results show that the secondary flow field has a major influence on the clocking phenomena in a low aspect ratio turbine.

The investigations presented herein mainly focus on the midspan. A detailed understanding of the clocking phenomena in a HP turbine requires the experimental investigation of the three dimensional flow field supported by numerical simulations.

Acknowledgment

This work was made possible by the Austrian Science Fund (FWF) within the Grant No. P16521-N07, "Experimental Investigation of the Stator-Rotor-Stator Interaction in a Transonic Turbine." The support of Dr. H. P. Pirker in the operation of the compressor station is also gratefully acknowledged.

Nomenclature

h, H = span (m)
k = turbulent kinetic energy (m^2/s^2)
p = absolute pressure (bar)
t = time(s)
T = absolute temperature (K)
$\mathbf{V}$ = velocity vector (m/s)
u, v = velocity components (m/s)
x, y, z = Cartesian coordinates (m)

Greek

α = yaw angle (deg)
κ = ratio of specific heats (c_p/c_v) (-)
η = total to total efficiency (-)
τ = rotor blade passing period (s)

Subscripts

A = first vane inlet
C = rotor outlet
$D1, D3$ = second vane outlet
i = spanwise measurement location
j = indices for clocking position
rel = relative
t = total

Superscripts

$\bar{}$ = ensemble-averaged properties
$=$ = time-averaged properties
$\sim$ = periodic quantity
$'$ = unresolved fluctuating quantity

Acronyms

BSA = burst spectrum analyzer
CP = clocking position
FRAPP = fast response aerodynamic pressure probe
LDV = Laser Doppler velocimetry
HP, LP = high-pressure, low-pressure
PS = pressure surface
rms = root mean square
SS = suction surface
TKE = turbulent kinetic energy
VP = vane pitch

References

[1] Miller, R. J., Moss, R. W., Ainsworth, R. W., and Horwood, C. K., 2003, "Time-Resolved Vane-Rotor Interaction in a High-Pressure Turbine Stage," ASME J. Turbomach., **125**(1), pp. 1–13.

[2] Tiedemann, M., and Kost, F., 2001, "Some Aspects of Wake-Wake Interactions Regarding Turbine Stator Clocking," ASME J. Turbomach., **123**(3), pp. 526–533.

[3] König, S., Heidecke, A., Stoffel, B., Fiala, A., and Engel, K., 2004, "Clocking Effects in a 1.5-Stage Axial Turbine—Boundary Layer Behaviour at Midspan," ASME Paper No. 2004-GT-54055.

[4] Hummel, F., 2002, "Wake-Wake Interaction and Its Potential for Clocking in a Transonic High-Pressure Turbine," ASME J. Turbomach., **124**(1), pp. 69–76.

[5] Huber, F. W., Johnson, P. D., Sharma, O. P., Staubach, J. B., and Gaddis, S. W., 1996, "Performance Improvement Through Indexing of Turbine Airfoils: Part 1-Experimental Investigation," ASME J. Turbomach., **118**(4), pp. 630–635.

[6] Arnone, A., Marconcini, M., Pacciani, R., Schipani, C., and Spano, E., 2002, "Numerical Investigation of Airfoil Clocking in a Three-Stage Low-Pressure Turbine," ASME J. Turbomach., **124**(1), pp. 61–68.

[7] Reinmöller, U., Stephan, B., Schmidt, S., and Niehuis, R., 2002, "Clocking Effects in a 1.5 Stage Axial Turbine-Steady and Unsteady Experimental Investigations Supported by Numerical Simulations," ASME J. Turbomach., **124**(1), pp. 52–60.

[8] Billiard, N., Paniagua, G., and Dénos, R., 2005, "Effect of Clocking on the Heat Transfer Distribution of a Second Stator Tested in a One and a Half Stage HP Turbine," ASME Paper No. 2005-GT-68462.

[9] Gadea, J., Dénos, R., Paniagua, G., Billiard, N., and Sieverding, C. H., 2004, "Effect of Clocking on the Second Stator Pressure Field of a One and a Half Stage Transonic Turbine," ASME Paper No. 2004-GT-53463.

[10] Haldeman, C. W., Dunn, M. G., Barter, J. W., Green, B. R., and Bergholz, R. F., 2004, "Experimental Investigation of Vane Clocking in a One and $\frac{1}{2}$ Stage High Pressure Turbine," ASME Paper No. 2004-GT-53477.

[11] Erhard, J., and Gehrer, A., 2000, "Design and Construction of a Transonic Test Turbine Facility," ASME Paper No. 2000-GT-480.

[12] Neumayer, F., Kulhanek, G., Pirker, H. P., Jericha, H., Seyr, A., and Sanz, W., 2001, "Operational Behavior of a Complex Transonic Test Turbine Facility," ASME Paper No. 2001-GT-489.

[13] Glas, W., Forstner, M., Kuhn, K., and Jaberg, H., 2000, "Smoothing and Statistical Evaluation of LDV Data of Turbulent Flows in Reciprocating Machinery," Exp. Fluids, **29**, pp. 411–417.

[14] Göttlich, E., Woisetschläger, J., Pieringer, P., Hampel, B., and Heitmeir, F., 2005, "Investigation of Vortex Shedding and Wake-Wake Interaction in a Transonic Turbine Stage Using Laser-Doppler-Velocimetry and Particle-Image-Velocimetry," ASME Paper No. 2005-GT-68579.

[15] Hodson, H. P., Dawes, W. N., 1998, "On the Interpretation of Measured Profile Losses in Unsteady Wake-Turbine Blade Interaction Studies," ASME J. Turbomach., **120**(2), pp. 276–284.

[16] Denton, J. D., 1993, "Loss Mechanisms in Turbomachines," ASME J. Turbomach., **115**(4), pp. 621–656.

[17] Griffin, L. W., Huber, F. W., and Sharma, O. P., 1996, "Performance Improvement Through Indexing of Turbine Airfoils—Part 2: Numerical Simulation," ASME J. Turbomach., **118**(4), pp. 636–642.

Experimental Evaluation of an Inlet Profile Generator for High-Pressure Turbine Tests

M. D. Barringer
Mechanical Engineering Department,
Virginia Polytechnic Institute and State University,
Blacksburg, VA 24061
e-mail: mbarringer@vt.edu

K. A. Thole
Department of Mechanical and Nuclear Engineering,
The Pennsylvania State University,
University Park, PA 16802
e-mail: kthole@psu.edu

M. D. Polanka
Air Force Research Laboratory,
Turbines Branch,
WPAFB, OH 45433
e-mail: Marc.Polanka@wpafb.af.mil

Improving the performance and durability of gas turbine aircraft engines depends highly on achieving a better understanding of the flow interactions between the combustor and turbine sections. The flow exiting the combustor is very complex and it is characterized primarily by elevated turbulence and large variations in temperature and pressure. The heat transfer and aerodynamic losses that occur in the turbine passages are driven primarily by these spatial variations. To better understand these effects, the goal of this work is to benchmark an adjustable turbine inlet profile generator for the Turbine Research Facility (TRF) at the Air Force Research Laboratory. The research objective was to experimentally evaluate the performance of the nonreacting simulator that was designed to provide representative combustor exit profiles to the inlet of the TRF turbine test section. This paper discusses the verification testing that was completed to benchmark the performance of the generator. Results are presented in the form of temperature and pressure profiles as well as turbulence intensity and length scale. This study shows how a single combustor geometry can produce significantly different flow and thermal field conditions entering the turbine. Engine designers should place emphasis on obtaining accurate knowledge of the flow distribution within the combustion chamber. Turbine inlet conditions with significantly different profile shapes can result in altered flow physics that can change local aerodynamics and heat transfer. [DOI: 10.1115/1.2436897]

Introduction

Increasing the thrust to weight ratio of a gas turbine aircraft engine can be accomplished by increasing the turbine working temperature. This has put great emphasis on understanding just how the combustor exit flow interacts with and affects the performance of the downstream turbine. The complex temperature and pressure profiles exiting combustors have forced engine designers to prepare for the worst case without knowing exactly how the profiles affect the hardware. The variations in pressure, temperature, and turbulence that are present in the radial and circumferential spatial directions at the combustor exit all combine to yield a very complex exit flow structure. The temperature variations migrate through the combustion chamber and impose nonuniform heat transfer on the downstream high pressure turbine vanes that can result in local melting and cracking of the vane metal and in some circumstances result in total failure of the part. Elevated turbulence can intensify this heat transfer by increasing local convection heat transfer coefficients to the vane surface. The spatial variations in pressure at the combustor exit result in nonuniform aerodynamic loading on the vanes. Turbine designers currently use a pressure profile consistent with a standard turbulent boundary layer as the inlet condition to the turbine while designing their vanes and blades. The nonuniformity of the combustor exit pressure profiles can result in turbine inlet profiles and secondary flow development that is different than what is expected when using uniform profiles.

Combustion chambers in aircraft gas turbine engines consist of annular liners, inlet swirlers, fuel nozzles, dilution holes, film cooling holes and slots, and an overall exit contraction. The design of combustion chambers centers on the division of mass flow into separate flow paths to establish continuous stable combustion, to dilute the combustion products before they enter the turbine stage, and to form a protective layer of insulating air that shields the liner metal from the relatively hot combustion gas. The interaction of the flow streams passing through these combustor components results in a complex flowfield exiting the combustor.

A better understanding of how the combustor exit flow affects the flow development and heat transfer within the downstream turbine is needed. It is for this reason that a device was designed to simulate the conditions exiting typical engine combustors. The primary research objective was to perform benchmark tests on a nonreacting combustor simulator device. The simulator, documented in Barringer et al. [1], was designed to provide representative combustor exit pressure and temperature profiles, with realistic turbulence levels, to the inlet of the true scale, fully annular, high pressure turbine rig located in the Turbine Research Facility (TRF) at the Air Force Research Laboratory (AFRL). The focus of this paper is to present the benchmark test results. The effects of these different profiles on turbine vane heat transfer and aerodynamics are presented in a separate research paper [2].

Research Focus and Past Studies

Several nonreacting and reacting studies have been performed experimentally and computationally to analyze and model combustor flows. Very few of these studies, however, have focused on the effects that the exit flowfield has on the downstream turbine stage. The following is a review of several past combustor studies as well as several combustor–turbine interaction studies. The combustor studies pertain to analyzing and correctly modeling the flow and thermal fields within the combustion chamber itself whereas the combustor–turbine interaction studies focus on researching the effects of the combustor exit flow on the downstream turbine.

Combustors. Dilution holes were studied by Holdeman [3] using a nonreacting combustor model. Experiments and computations were conducted on the mixing of single, double, and opposed rows of dilution jets. The principle finding was that the jet momentum flux ratio dictated the combustor exit velocity and

Contributed by the International Gas Turbine Institute of ASME for publication in the JOURNAL OF TURBOMACHINERY. Manuscript received July 24, 2006; final manuscript received July 31, 2006. Review conducted by David Wisler. Paper presented at the ASME Turbo Expo 2006: Land, Sea and Air (GT2006), Barcelona, Spain, May 8–11, 2006. Paper No. GT2006-90401.

temperature profiles. The opposed rows of jets resulted in the most effective and rapid mixing. Computational models using the standard k-ε turbulence model did not accurately predict the mixing of the opposed dilution jet injection, but predicted the jet penetration very well.

High-intensity, large-scale turbulence in a nonreacting combustor simulator was studied by Ames and Moffat [4]. Their experimental model contained two rows of in-line dilution holes, and a 50% exit contraction that generated turbulence intensity levels up to 19% and integral length scales that scaled well with the dilution hole diameters. Barringer et al. [5] and Stitzel and Thole [6] also tested and computationally modeled a nonreacting combustor simulator containing liners with film cooling holes and two rows of in-line dilution jets that produced similar turbulence intensity levels near 18%. The computational models used the renormalization group (RNG) k-ε turbulence model and the results agreed with those found by Holdeman [3] in that turbulence was under predicted.

Swirl driven inlet flow was studied by Cameron et al. [7] in nonreacting and reacting model combustors with wall injection. They concluded that the strong recirculation zone located upstream of the primary jets present in the nonreacting case was dissipated in the case of reaction. Velocity measurements in the exit plane indicated turbulence levels near 25% for the reaction case, which is consistent with the studies without reaction.

Turbulence was also studied in two reacting models by Bicen et al. [8] that included liner cooling slots and two rows of dilution jets. The results indicated nonuniform distributions of velocity in the combustor exit plane and turbulence levels near 20% over the majority of the exit plane. These levels are consistent with the results presented earlier for the nonreacting combustor studies indicating that reactions do not significantly contribute to turbulence levels. The temperature profiles at the combustor exit plane were also found to be nonuniform.

Combustor-Turbine Interactions. A combustor exit radial temperature simulator (CERTS) was used by Schwab et al. [9] at the NASA Lewis Research Center to conduct analytical and experimental studies of flow through a full turbine stage with uniform and nonuniform inlet radial temperature profiles. The profiles were generated by adjusting the coolant air mass flow rate injected through circumferential slots in the hub and tip endwalls upstream of the stator vanes. In addition to measuring nonuniform temperature profiles, nonuniform total pressure profiles were indicated at the turbine vane inlet. Cattafesta [10] conducted similar experiments to study the effects of turbine inlet radial temperature profiles on the aerodynamic performance of a transonic turbine stage using the M.I.T. Blow Down Turbine Facility. Tests with similar corrected flow conditions but with different temperature profiles affected the overall turbine efficiency by 2%. Results also showed that the turbine inlet profiles were nearly mixed out at the exit plane of the rotor. Chana et al. [11] also designed and tested a nonuniform inlet temperature generator for the QinetiQ transient turbine research facility. Cold gas was injected upstream of the turbine section at the hub and tip to shape the temperature profile in the radial direction and through turbulence rods inserted into the main flow to shape it in the circumferential direction. Results showed vane heat transfer was affected by the presence of the nonuniform temperature profiles on the vane suction surface.

Krishnamoorthy et al. [12] investigated the effect of combustor turbulence on a downstream turbine vane cascade. Their results indicated that the effect of high turbulence at the combustor exit was to reduce the cooling effectiveness on the vane by 10%. It was also shown that the effect of temperature non-uniformities at the combustor exit was to reduce the overall cooling effectiveness on the vane by as much as 21%. Van Fossen and Bunker [13] studied heat transfer augmentation in the stagnation region of a flat plate with an elliptical leading edge. The test article was located downstream of an arc segment of a dual-annular combustor. The swirl driven combustor flow produced turbulence intensities

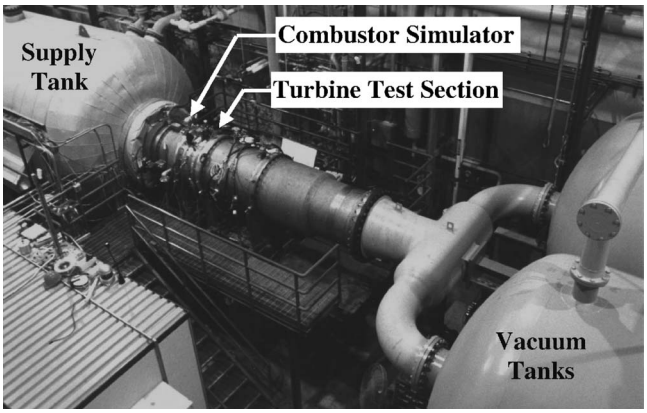

Fig. 1 Photograph of the TRF facility

up to approximately 32% with length scales near 1.3 cm. Augmentation of heat transfer was found to be very significant in the range of 34–59%. No effect of circumferential position with respect to the upstream swirlers was found.

Colban et al. [14] studied the effects of varying the film cooling flow through the liner and exit junction slot in a large-scale ($9\times$), low-speed combustor simulator on the adiabatic effectiveness and secondary flow development within a downstream turbine cascade. Results showed that varying the coolant injection through the liner led to different total pressure profiles entering the downstream turbine section. Measurements showed that the coolant exiting the liner and slot accumulated along the suction side of the vane and endwall and that increasing the film cooling flow through the liner did not result in a continual increase in adiabatic effectiveness values.

In summary, the literature indicates that the most significant components that contribute to the nonuniform exit thermal and pressure fields are swirlers, film cooling slots and holes, and dilution holes. The studies also indicate that the flow field downstream of the primary dilution zone is very similar with or without reaction. The only noteworthy differences occur upstream of the primary zone where combustion is stabilized. This is important because it allows a flow field representative of one exiting a real gas turbine combustor to be simulated under nonreacting conditions without swirl. There is insufficient research to date, however, that incorporates the effects of realistic combustor flow and thermal fields on downstream turbine vanes and endwall regions. Very little experimental data exist that document total pressure profiles at the combustor exit. This information is paramount since it has been shown in Hermanson and Thole [15] and Colban et al. [14] that the total pressure field is a driving force in the development of secondary flows and heat transfer present in the downstream turbine vane passages.

Experimental Facility

The TRF is a turbine test facility located within the Turbine Engine Research Center at the AFRL at Wright-Patterson Air Force Base in Dayton, Ohio. The TRF, documented in Haldeman et al. [16], is a short duration blow-down test facility that is capable of matching several aero-thermal engine parameters. These parameters include Reynolds number, Mach number, pressure ratio, gas to metal temperature ratio, corrected speed, and corrected mass flow.

The facility, shown in Fig. 1, consists primarily of a large supply tank, a turbine test section, and two large vacuum tanks. The test section is a true scale, fully annular, single turbine stage consisting of vanes and rotor blades. Prior to testing, nitrogen gas is pressurized and heated within the supply tank while the main turbine section and vacuum tanks are evacuated to near vacuum conditions. The turbine rotor is then driven by a starting motor to

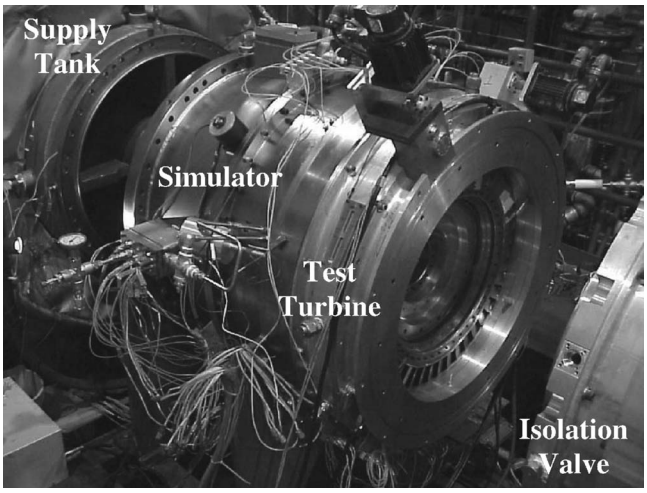

Fig. 2 Photograph of the TRF combustor simulator

a speed slightly higher than the desired test speed. This motor is then turned off allowing the turbine rotor to decelerate to the test speed at which time an electrical eddy current brake is used to hold the rotor speed constant. Testing begins by activating a fast acting valve that connects the supply tank to the turbine test section. The gas then flows from the supply tank through the turbine test section and into the vacuum tanks. The mass flow rate is set by controlling the turbine pressure ratio using a variable area isolation valve located downstream of the main test section. The duration of a typical test is between 1 and 5 s, depending on the size of the turbine that is being tested. All testing in the current study was performed in a vane-only configuration (without rotating turbine blades).

Recently a combustor simulator was designed and installed into the TRF facility to allow turbine testing to be performed with realistic turbine inlet profiles of pressure and temperature. Prior to installing the simulator, the temperature and pressure profiles at the inlet of the turbine section were nearly uniform in the radial and circumferential directions. The simulator, shown in Fig. 2 and documented in Barringer et al. [1], divides the supply tank flow into three concentric annular flow paths. The center annulus is further divided into three concentric annuli to direct a portion of the supply tank flow to the inlet of the central annular chamber, shown in Fig. 3, and to the first of two rows of dilution holes. The inner and outer annular flow paths are used to thermally condition portions of the supply tank flow by directing the flow through finned-tube heat exchangers and then into the central chamber

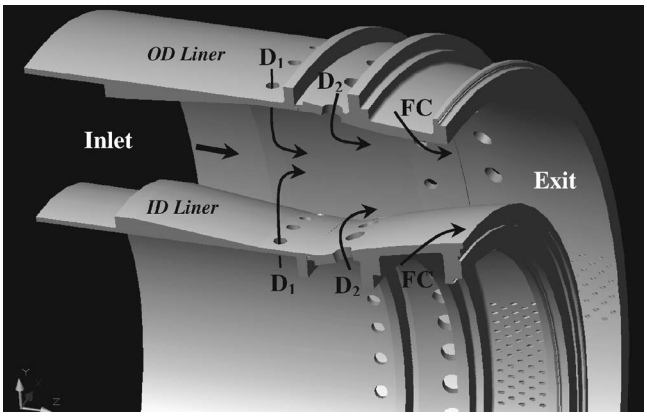

Fig. 3 Drawing of the central annular chamber (inlet shutter not shown)

through secondary dilution holes and film cooling holes located within the contraction section. The first row of opposing dilution jets acts as the primary turbulence generator by injecting flow at relatively large local momentum flux ratios. The second row dilution jets and film cooling jets were designed to inject flow at lower momentum flux ratios to tailor the exit temperature profile.

Direct flow control is accomplished through the use of five adjustable shutter systems. Each system consists of one rotating disk and one nonrotating disk that both contain the exact same slot pattern. By positioning the rotating disk with respect to the nonrotating disk the blockage in a particular flow stream can be increased or decreased. This controllable flow blockage acts as an adjustable pressure drop that allows the flow in a particular path to be controlled. The center shutter system is located at the inlet of the central chamber and it is used to establish the primary flow blockage required to achieve the various flow splits and momentum flux ratios.

Instrumentation

Traverse rings are used to measure the turbine inlet and exit conditions. Each traverse ring contains multiple instrumentation rakes for mounting thermocouples and pressure transducers. The probes on each rake are spaced to obtain measurements over equal annular flow areas and during testing these rakes are traversed circumferentially by approximately 90 deg to obtain both radial and circumferential profiles. Due to the short test duration, measurements of temperature and pressure as well as velocity, heat flux, and rotor speed are all recorded simultaneously in real time onto data storage units. The facility is capable of simultaneously acquiring data across 200 12-bit channels with a maximum sampling frequency of 100 kHz and 200 16-bit channels with a maximum sampling frequency of 200 kHz. Signal conditioning on each channel takes place using low pass filters and built-in amplifiers. All data processing and reduction is performed at a later time.

For the current tests, three temperature rakes were used each containing 0.0254-mm-diameter thermocouple beads with a thermal time constant of approximately 1.1 ms. The three rakes included one containing five beads, one with seven beads, and one with nine beads. The different number of beads provides more spatial radial locations to perform ensemble averaging. Two pressure rakes were used each containing nine pressure transducers. All flow and thermal field measurements taken during testing were sampled at 20 kHz. To benchmark the performance of the simulator, measurements of total pressure, static pressure, velocity, flow temperature, and surface temperature were taken. An instrumentation plan was developed to locate the places within the simulator to perform these measurements. Figure 4 shows a drawing of the simulator highlighting these positions and their measurements.

Total pressure measurements were made using in-house custom Kiel probes that were positioned within the plenums of the second row dilution holes and film cooling holes to help quantify mass flow splits between the various flow paths. Kiel probes were also positioned at the exit of several dilution holes to help verify the amount flow passing through both dilution rows. Static pressure measurements were made on the surface of the inner and outer diameter contraction liners at an axial location upstream of the film cooling holes to help determine the amount of flow exiting the film cooling holes. These static pressure measurements were made using high-temperature, miniature, Kulite pressure transducers. Velocity measurements were also made using several custom pitot-static pressure probes placed upstream and downstream of each heat exchanger and the central chamber shutter system.

The pressure transducers were calibrated in situ prior to each run. A Ruska standard was used to monitor the test section pressure while it was filled and evacuated. A typical calibration uncertainty for the static transducers was less than 0.05% of full scale. The overall uncertainty for these transducers was raised 0.40%

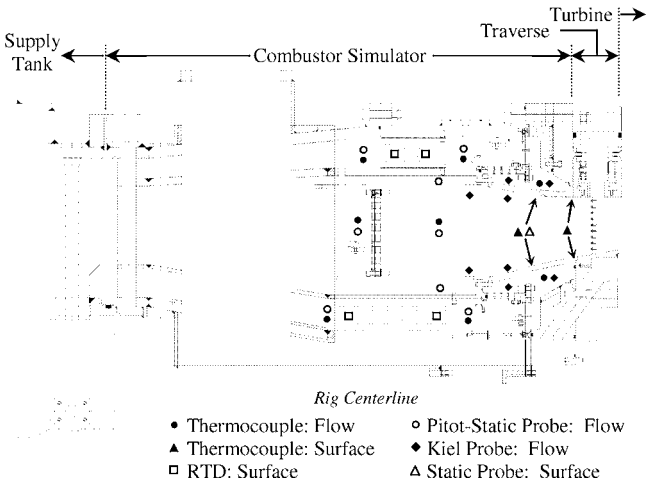

Fig. 4 General instrumentation locations

due to short term drift known to exist between time of calibration and time of the run. The velocity measurements were more uncertain. This was attributed to the very small delta pressures (less than 6000 Pa) that were measured at these locations coupled with the fact that these transducers were not able to be calibrated each run resulting in a long term drift uncertainty as well. This was further compounded by the fact that these are single point measurements both across the annuli and around the circumference making it difficult to know what the true average annulus velocity was. Converted to mass flow, uncertainties up to 10% were possible.

The flow temperature at various locations within the simulator was measured using in-house type E thermocouple probes containing 0.127-mm-diameter beads. These thermocouple probes were used to monitor the flow temperature within the film cooling plenums as well as upstream and downstream of the heat exchangers. The heat exchanger metal temperatures were monitored before and during testing using Omega RTDs (resistance temperature detectors). The metal temperatures of the inner and outer diameter contraction rings were monitored using type E thermocouples with 0.076-mm-diameter beads. The thermocouple wire that made these beads was calibrated in a Kaye temperature bath against a platinum RTD standard accurate to 0.01 K. The 0.127 mm beads were calibrated and found to be within 1.0 K of the standard E type curve. The 0.0254 mm beads in the rakes were calibrated to an accuracy of 1.5 K but had a noticeable shift from the standard E type thermocouple curve due to the imperfections of the wire.

In addition to measuring the pressure and temperature profiles exiting the simulator, the traverse ring located upstream of the turbine test section was modified to incorporate a special hotwire rake to allow measurements of velocity at the simulator exit. The rake allowed for the mounting of two hot-film probes with their sensing elements positioned near vane midspan at $Z/S=0.45$ and 0.55. The hotwire probes were calibrated outside of the main test rig at ambient temperature and pressure using a TSI flow calibration unit. The calibration curves for the probes both follow a power law curve fit for wire Nusselt number versus Reynolds number. Since the velocity at the simulator exit is near $M=0.1$ during testing, a simple density correction was applied to the experimental test data in order to apply the curve fits to the higher density flow exiting the simulator. Due to the transient nature of the test rig and the varying elevated flow temperatures, hotwire measurements were conducted under separate isothermal test conditions (unheated supply tank) where all flow streams were approximately at the same temperature near ambient conditions.

Table 1 High and low values of system inputs

System inputs	Units	Low	High
Initial pressure—Supply tank	kPa	207	552
Initial temp—Supply tank	K	366	478
Initial temp—ID heat exchangers	K	297	422
Initial temp—OD heat exchangers	K	259	422
Porosity—Central chamber shutter	%	30	90
Porosity—ID film cooling shutter	%	12	89
Porosity—OD film cooling shutter	%	10	90
Porosity—ID 2nd row dilution shutter	%	13	93
Porosity—OD 2nd row dilution shutter	%	14	98

Test Matrix

A series of benchmark tests was developed to determine the overall performance of the simulator device. These tests were determined by performing a Taguchi style analysis, described in Ref. [17], to help reduce the number of experimental runs needed to produce a performance map for the combustor simulator. Nine factors were selected as the system inputs including the initial supply tank temperature and pressure, the initial metal temperatures of the two heat exchangers, and the porosities of the five adjustable shutters. Porosity refers to the percentage of total open flow area of the shutter. Each of the input factors was assigned an upper and lower limit, shown in Table 1, which was based on component operating limits.

The system outputs are the pressure and temperature profiles at the combustor simulator exit, and therefore consist of a set of pressure probes and a set of thermocouple probes that are mounted on separate instrumentation rakes. These probes were traversed approximately 90 deg in the circumferential direction during testing to determine both radial and circumferential variations in pressure and the temperature. The benchmark tests that were determined from the analysis are shown in Table 2 and they provided a large data set that includes over two dozen different combinations of combustor exit temperature and pressure profiles. The test cases shown in Table 2 that are in bold correspond to the baseline experiments where the mean flow conditions at the simulator exit (turbine vane inlet) are $\mathrm{Re}=2.1\times10^5$ and $M=0.1$. Additional tests were performed at different Reynolds numbers to create a more complete performance map of the simulator, including $\mathrm{Re}=0.8\times10^5$, 1.1×10^5, and 2.7×10^5. These additional Re tests are shown in Table 2 in italics. All experimental data associated with a particular test configuration was acquired during a single blow-down test.

The knowledge gained from these tests comes in the form of a sensitivity coefficient for each input factor and how it affects the exit profiles at certain radial locations. Determining the sensitivities of all nine inputs was accomplished by performing a statistical analysis of variance. This analysis mapped each system input setting to the measured system outputs and also estimated the sensitivity of interactions between individual system inputs. The procedure for performing this analysis is also outlined in Ref. [17].

Radial Pressure Profile Range

The radial pressure profiles measured at the simulator exit for the baseline test cases are shown in Fig. 5 (test numbers are shown in Table 2). These radial profiles have been circumferentially (spatially) averaged across one full vane pitch along lines of constant radius that correspond to equal annular flow areas. Data was analyzed across several vane pitches that are all equally spaced around the entire 360 deg annulus. The local total pressure has been normalized into the form of a pressure coefficient C_p, defined as the local total pressure subtracted by the midspan total pressure all divided by the mean dynamic pressure at the simulator exit. Radial pressure profiles are often referenced with respect to a span location, for example inner diameter (ID) peaked, outer diameter (OD) peaked, or midspan peaked. The normalization

Table 2 Experimental test matrix (baseline and *additional Re* tests)

	Supply tank		Percent of total mass flow (%)							Heat exchanger: initial temp (K)	
Test	T (K)	P (kPa)	Central chamber inlet	ID 1st row dilution	OD 1st row dilution	ID 2nd row dilution	OD 2nd row dilution	ID film cooling	OD film cooling	Inner annulus	Outer annulus
104	*480*	*200*	*54*	*8*	*7*	*5*	*14*	*0*	*12*	*300*	*300*
105	*480*	*200*	*6*	*13*	*12*	*20*	*24*	*1*	*24*	*300*	*400*
106	*480*	*200*	*12*	*13*	*12*	*7*	*27*	*9*	*20*	*400*	*300*
107	**480**	**550**	**14**	**12**	**11**	**14**	**22**	**8**	**19**	**300**	**300**
108	**480**	**550**	**52**	**7**	**7**	**4**	**14**	**4**	**12**	**300**	**400**
109	**480**	**550**	**48**	**7**	**7**	**9**	**15**	**0**	**14**	**400**	**300**
110	*340*	*200*	*50*	*7*	*8*	*7*	*15*	*2*	*11*	*300*	*300*
111	*340*	*200*	*15*	*12*	*12*	*8*	*22*	*9*	*22*	*300*	*400*
112	*340*	*200*	*52*	*8*	*8*	*5*	*14*	*1*	*12*	*400*	*400*
113	*340*	*200*	*9*	*14*	*13*	*16*	*23*	*3*	*22*	*400*	*300*
114	*340*	*550*	*53*	*8*	*7*	*9*	*10*	*1*	*12*	*300*	*400*
115	**480**	**550**	**15**	**14**	**13**	**9**	**24**	**0**	**25**	**400**	**400**
116	*480*	*200*	*54*	*9*	*8*	*9*	*11*	*5*	*4*	*400*	*400*
117	*340*	*550*	*15*	*15*	*15*	*12*	*32*	*3*	*8*	*300*	*300*
118	*340*	*550*	*57*	*9*	*8*	*5*	*12*	*5*	*4*	*400*	*300*
119	*340*	*550*	*8*	*13*	*12*	*13*	*25*	*8*	*21*	*400*	*400*
120	*340*	*200*	*15*	*17*	*16*	*13*	*22*	*13*	*4*	*300*	*400*
121	*340*	*200*	*53*	*9*	*9*	*8*	*15*	*2*	*4*	*400*	*400*
122	**480**	**550**	**14**	**15**	**14**	**18**	**27**	**8**	**4**	**300**	**300**
123	**480**	**550**	**56**	**8**	**8**	**9**	**18**	**0**	**1**	**400**	**300**
124	**480**	**550**	**40**	**11**	**11**	**4**	**20**	**4**	**10**	**300**	**300**
125	**480**	**550**	**37**	**11**	**11**	**6**	**21**	**4**	**10**	**400**	**400**
126	**420**	**550**	**64**	**7**	**8**	**7**	**14**	**0**	**0**	**400**	**400**
127	**420**	**550**	**61**	**6**	**6**	**2**	**9**	**4**	**12**	**400**	**400**
133	**420**	**550**	**36**	**13**	**13**	**14**	**15**	**9**	**0**	**300**	**400**
134	**420**	**550**	**32**	**11**	**10**	**5**	**22**	**0**	**20**	**400**	**300**
135	**480**	**550**	**23**	**13**	**12**	**5**	**13**	**10**	**24**	**300**	**300**

used here is consistent with this idea in that it compares each local total pressure to that at the midspan. Note that in using this definition, C_p=0 at the midspan.

The measured C_p values near the endwalls on both the ID and OD are consistent with those exiting real combustors. Figure 6 shows an example of a pressure profile at the exit of an aero-engine combustor, as well as three pressure profiles generated using the TRF simulator and two generated using the Virginia Tech simulator. The TRF simulator was designed using this engine profile and the Virginia Tech (VT) simulator profiles, documented in Barringer et al. [5] and Colban et al. [14]. Figure 6 also shows the pressure profile at the TRF turbine inlet prior to installing the simulator. It can be seen from the figure that the TRF simulator can produce turbine inlet pressure profiles similar to those of the VT simulator and the engine profile. The test conditions shown here were not configured to specifically match any of these engine cases, but show that these different profiles can be achieved within the simulator's range. For example, the profiles corresponding to Tests 108 and 127 result in pressure profiles similar to the VT Simulator C_p 0.0 curve on the ID side and the VT Simulator C_p 2.0 curve on the OD side. The TRF simulator can easily shift the profile peak near the endwalls from C_p=0 to 2 to be consistent with the engine profile. It is important to note that the VT and TRF combustor simulators are completely different experimental

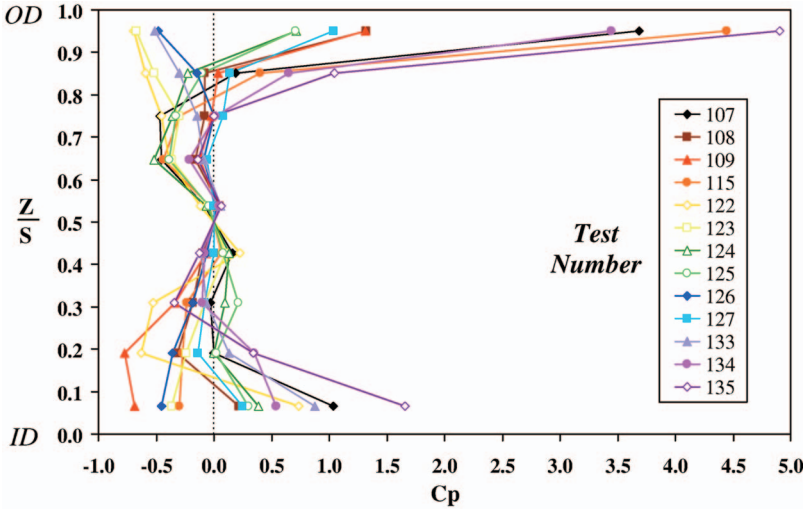

Fig. 5 Plot of several radial pressure profiles measured at the simulator exit for the baseline tests

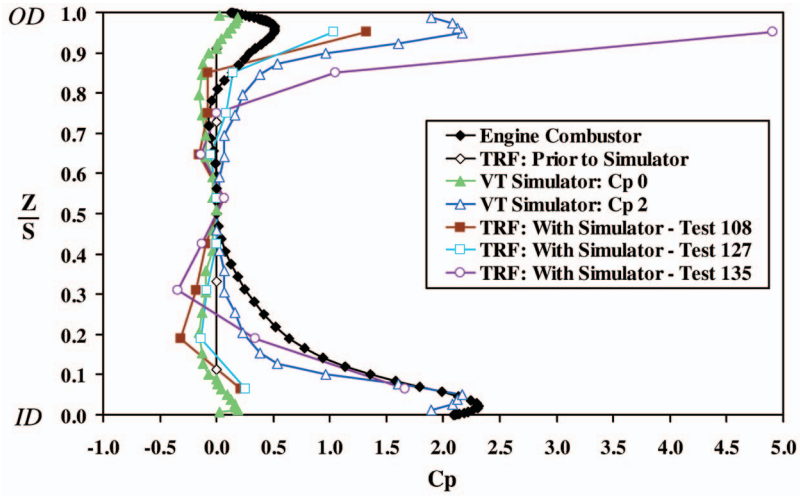

Fig. 6 Plot of several engine and combustor simulator exit pressure profiles

rigs. The VT simulator is a large-scale linear device that operates at relatively low pressure, low speed, and low temperature, while the TRF simulator is a true-scale fully annular device that operates at high pressure, high speed, and elevated temperatures.

The pressure profiles that are plotted in Fig. 5 vary greatly in overall shape, especially near the ID and OD endwalls. Some of the profiles are peaked along the ID and OD endwalls and some are peaked in the midspan region. At the baseline flow conditions, the simulator is capable of producing pressure profiles in the near ID endwall region between $-0.7 < C_p < 1.7$ and in the near OD endwall region between $-0.6 < C_p < 5.0$. It is important to note that a negative C_p does not mean that flow is in the opposite direction or that the pressure is negative, it simply means that the local pressure is less than the midspan pressure. For example, the pressure profile corresponding to Test 126 is midspan peaked. The pressure profile operating range is larger on the OD side than the ID side. This was expected due to the outer annulus possessing less overall flow resistance compared to the inner annulus and the fact that the central chamber contraction is larger on the ID side than the OD side, which was an original design constraint to accommodate the radial dimensions of the turbine being tested. But nonetheless, the simulator is capable of achieving C_p values consistent with the range of the real engines, i.e., up to 2.0.

To create a more complete performance map of the simulator, several tests were also conducted where the flow conditions at the simulator exit were at different Reynolds numbers. These tests, corresponding to $\mathrm{Re} = 0.8 \times 10^5$, 1.1×10^5, and 2.7×10^5, are given in Table 2 in italics. The measured radial pressure profiles for some of these tests are shown in Fig. 7. These radial profiles have also been circumferentially averaged over one vane pitch. The results shown in this figure highlight that the inlet profile generator is capable of producing realistic turbine inlet profiles over a wide range of operating points. This is important for future tests as it shows the flexibility of the simulator to generate any desired inlet condition throughout a turbine operating map. Pressure profiles measured in the near ID endwall region ranged from $-0.6 < C_p < 2.0$ while near the OD endwall region they ranged from $-0.6 < C_p < 5.0$.

The wide range of C_p values in the near endwall regions is directly attributable to the relative amount of upstream film-cooling flow. When the film cooling mass flow is significantly low the local total pressure at span locations near the endwalls results in a negative C_p value. As the film cooling mass flow is increased the momentum flux ratio of the film cooling jets increases, which forces more flow out into the mainstream along the endwalls. This results in a higher total pressure near the endwall relative to midspan. As the film cooling flow is increased even further, the local total pressure near the endwall becomes significantly higher than that in the midspan region resulting in the sharp gradients seen in some of the profiles. The spanwise variation in the pressure coefficient was found to be less in the span region from $0.25 < Z/S < 0.75$. This smaller variation is explained by the intense mixing process of the upstream dilution jets that inject large amounts of flow into the central chamber producing high turbulence levels. As this flow progresses down the axis of the central chamber the individual dilution jets expand and merge into one another. This turbulent process results in a large mixing zone over the majority of the chamber span, thereby reducing spatial variations. This effect was also confirmed by the computational fluid dynamics (CFD) computations of Kunze et al. [18] for these same test runs.

The measured peak in the C_p pressure profile near the endwalls is scaled in Fig. 8 to the film cooling momentum flux ratio as well as the combustor simulator exit Reynolds number. The figure shows that as the momentum flux ratio is increased, the measured peak in the C_p pressure profile increases in a parabolic but nearly linear manner. The curves that are shown are parabolic best fits of the data points. The figure shows that the ID film cooling possesses a slightly less powerful trend than the OD for a given momentum flux ratio. This is explained by the fact that as the film cooling on the ID side exits the holes it must pass over a large contracting surface, relative to the OD side. This ID contraction forces the film cooling flow to move outward in the radial direction and by the time it reaches the axial location of the instrumentation rake its momentum has been reduced relative to the film

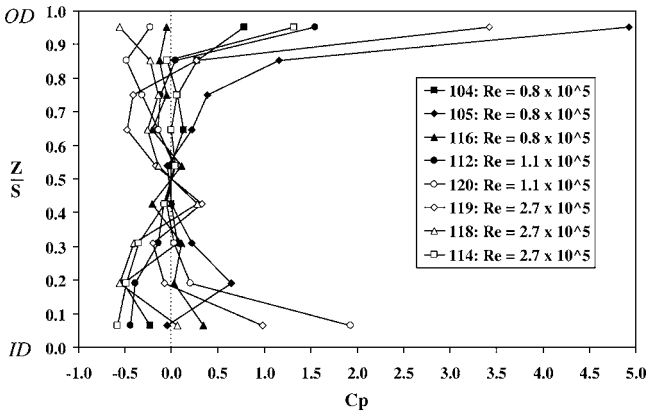

Fig. 7 Several pressure profiles measured at the simulator exit at different Reynolds numbers

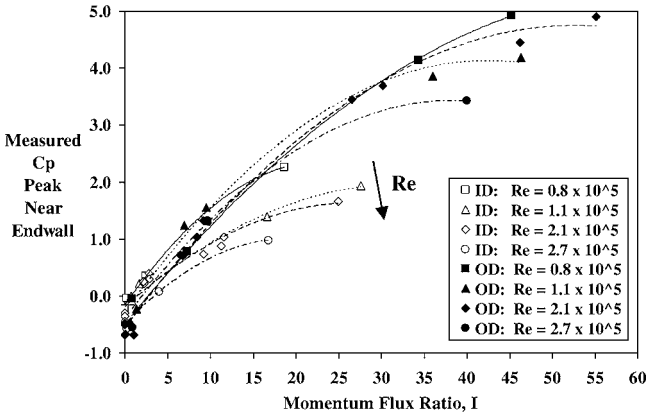

Fig. 8 Plot of the pressure profile peak (measured) near the ID and OD endwalls scaled to the film cooling momentum flux ratio and simulator exit Re number

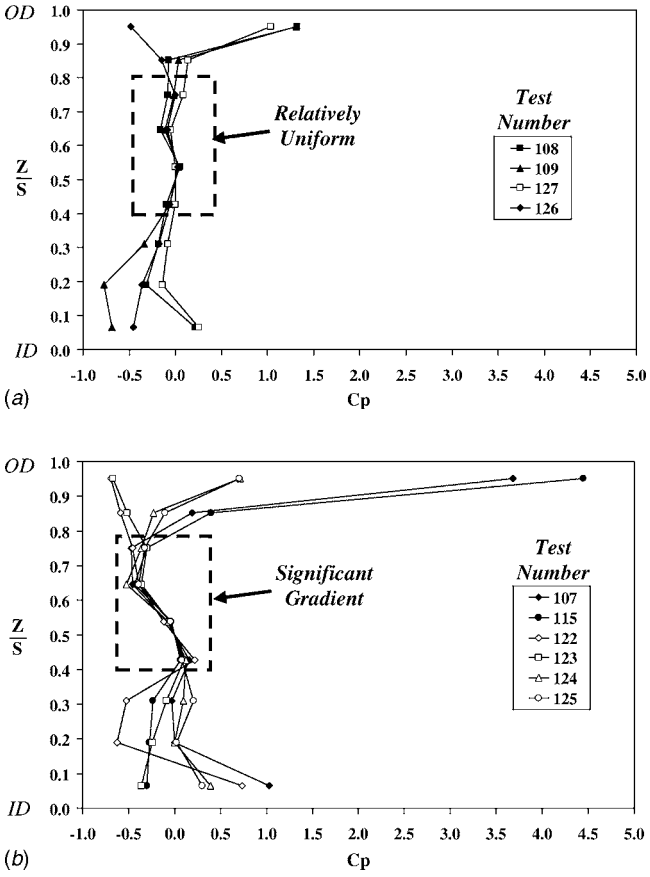

Fig. 9 Plots of pressure profiles at the simulator exit when the total dilution mass flow is: (*a*) 23–38%, and (*b*) 43–74% of the total combustor exit flow

cooling flow along the OD side. As the film cooling on the OD side exits the holes, it sees a relatively constant annular flow area and a relatively short direct path to the instrumentation rake. Figure 8 also shows that as the Reynolds number at the combustor simulator exit increases the measured peak in the C_p pressure profile along the endwall has a slightly decreasing trend for a given film cooling momentum flux ratio. Overall, the results were similar for both the ID and OD endwall regions.

An attempt was also made to scale the pressure profiles at the exit of the simulator to the dilution flow conditions which primarily affects the midportion of the flow path. Figure 9 shows two distinct patterns that were observed between $0.4 < Z/S < 0.8$ that scaled to the total amount of dilution mass flow. The first group consists of tests in which the total dilution mass flow was in the range of 23–38% of the total combustor flow, and the second group was tests in which the total dilution mass flow was in the range of 43–74% of the total combustor flow. The first group is relatively uniform in this span, while the second group contains a significant backward facing gradient in the span direction. It can be seen that this gradient exists for tests cases with little to no film cooling on the OD side as well as test cases with large amounts of film cooling on the OD side, as indicated by the C_p values near the OD. This is important because it indicates that the gradient truly is a direct result of the dilution flow. This effect was further confirmed by investigation of the CFD results of Kunze [18] which highlighted that the second row of OD dilution jets has a strong influence in shaping the flow profile in this region.

Radial Temperature Profile Range

The combustor exit temperature profile can be arranged in several nondimensional forms. Engine manufacturers typically use the pattern factor $(\mathrm{PF}) = (T_{\max} - T_{\mathrm{ave}})/\Delta T_{\mathrm{combustor}}$ to document the performance of their combustors. This pattern factor definition, however, only applies to actual combustors as it references the temperature rise across the combustor. In a simulator, the inlet condition is irrelevant and only the profiles entering the turbine are of interest. The radial temperature profiles measured at the simulator exit for the baseline tests are shown in Fig. 10 for the seven-headed thermocouple rake. These radial profiles have also been circumferentially averaged across one full vane pitch. The local total temperature has been normalized into the form of the temperature coefficient θ, defined as the local total temperature subtracted by the average temperature at the simulator exit all divided by the same average temperature.

The average temperature at the simulator exit was determined by performing an integration from hub to tip of the spanwise profile. To obtain a better approximation of this average temperature, the temperature profile data were extrapolated to the endwalls using a constant slope between the outermost and second outermost data points. The figure shows a variety of temperature profiles including some that are midspan peaked (107), some that are peaked more toward the ID (109), some that are peaked more toward the OD (108), and some that are nearly uniform in the midspan region (125 and 127). The temperature profiles near the ID and OD endwalls show large differences, some are nearly uniform (133 and 134), and some possess sharp gradients (108, 109, and 135). The test case numbers refer to the test conditions given in Table 2.

The measured θ profiles are similar to those exiting real combustors. Figure 11 shows several temperature profiles at the exit of aero-engine combustors, as well as temperature profiles at the TRF turbine inlet prior to and after installing the simulator. These aero-engine profiles were used to help design the TRF simulator. The figure shows that the TRF simulator is capable of producing turbine inlet temperature profiles similar to those of the engine profiles. While these profiles are not identical to the engine cases (and again efforts were not made in this program to tailor the profile to a particular case) they do enable researchers and designers the ability to understand the effects that these profiles have on vane and rotor heat transfer better than conventional uniform inlet profiles.

The maximum radial temperature variation that was observed using the seven-headed thermocouple rake for the baseline tests was approximately $\Delta\theta = 0.10$ or 10%, which corresponds to Test 109 between the vane span locations of $0.08 < Z/S < 0.94$. The minimum radial temperature variation that was observed was approximately $\Delta\theta = 0.01$ or 1% corresponding to Test 126. It was decided that the results for the seven-headed thermocouple rake would be reported rather than the nine-headed since the inner

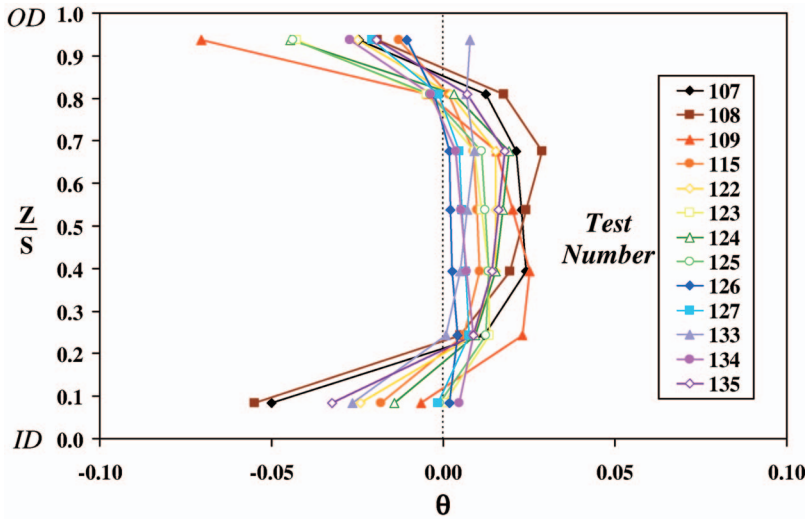

Fig. 10 Plot of several radial temperature profiles measured at the simulator exit for the baseline tests

most diameter thermocouple on the nine-headed rake was damaged during the first blow-down test and therefore temperature data for this rake at the innermost diameter was unavailable for all tests.

The conditions corresponding to the tests where the combustor simulator exit Re=0.8×10^5, 1.1×10^5, and 2.7×10^5, were given in Table 2 in italics. The measured radial temperature profiles for some of these tests are shown in Fig. 12. These radial profiles have also been circumferentially averaged over one vane pitch. The results shown in this figure highlight that the inlet profile generator is capable of producing realistic turbine inlet profiles at any inlet Reynolds number. The measured temperature profiles show a wide range of shapes in the near ID and OD endwall regions, some having nearly uniform profiles and some having very sharp gradients. Some of the thermal profiles are peaked near the ID, some are peaked near the OD, and some are peaked near midspan.

The temperature profiles at the simulator exit were also found to be significantly influenced by the film cooling flow. Figure 13 shows a schematic of a generic exit temperature profile and it illustrates some important parameters. These include the film coolant temperature, the film coolant momentum flux ratio, the near endwall temperature, and the midspan temperature. The temperature difference, $\Delta T=T_{MS}-T$, between the midspan and the near endwall flows is related to the film cooling momentum flux ratio as well as the film cooling temperature relative to the core flow near midspan. The midspan temperature is a good estimate of the core flow temperature above the film cooling holes as the flow collectively exits the simulator. The average temperature across the span at the simulator exit, T_{AVE}, is not a good choice as a scaling parameter since its value is affected by the coolant flow temperature on opposite sides of the span. The coolant exiting the film cooling holes on the ID side only sees the fluid temperature that it is being injected into locally near the ID liner, and therefore the midspan temperature is a more suitable scaling factor than the spanwise average temperature.

The thermal scaling for the baseline tests can also be seen in Fig. 13 where ΔT has been normalized by the midspan temperature and has been plotted as a function of film cooling momentum flux ratio. Several curves are shown for different ratios of the film cooling to the midspan temperature, T_{FC}/T_{MS}. Note that the curves shown are based on the experimental data indicating the general behavior that exists for tests that resulted in a positive ΔT parameter. For a given film cooling momentum flux ratio, as the film cooling temperature is reduced relative to the midspan tem-

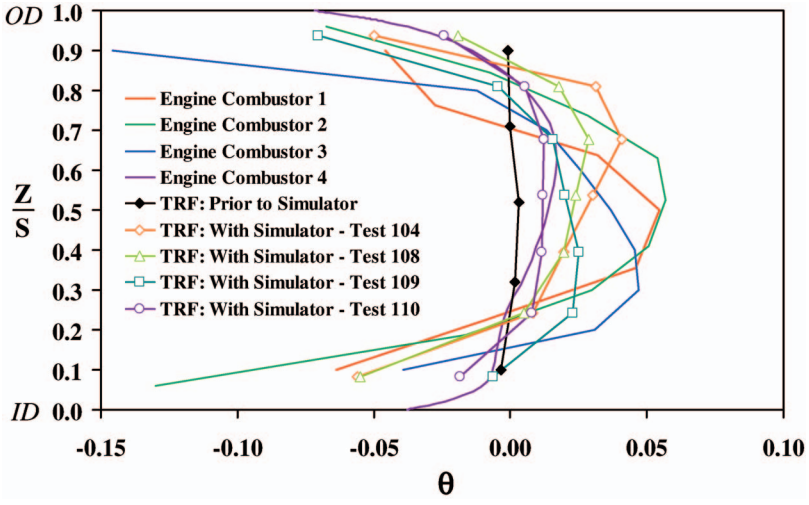

Fig. 11 Plot of several engine and simulator combustor exit temperature profiles

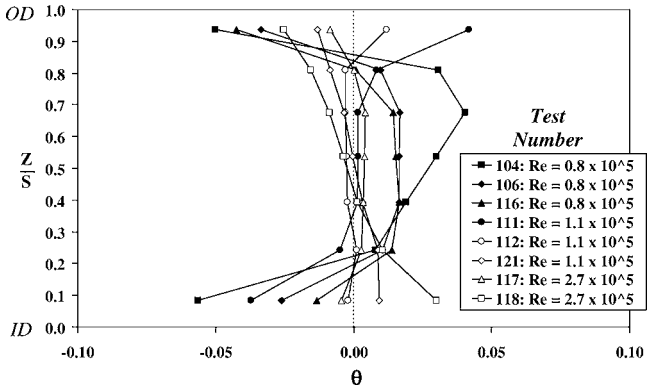

Fig. 12 Several temperature profiles measured at the simulator exit at different Reynolds numbers

perature, the larger the $\Delta T/T_{MS}$ that can be achieved. This results in increased temperature gradients near the endwall, and thus a greater potential for keeping the endwall cool. For example, when the film cooling momentum flux ratio is near $I=5$, $\Delta T=1\%$ of T_{MS} when $T_{FC}/T_{MS}=97\%$, which corresponds to a nearly uniform exit temperature profile. However, $\Delta T=9\%$ of T_{MS} when $T_{FC}/T_{MS}=76\%$, which corresponds to an exit temperature profile with significant gradients near the endwalls. The figure also shows that for a given T_{FC}/T_{MS}, the relationship between ΔT and I is more sensitive for $I<10$ and then gradually levels out as the momentum flux ratio is increased. These thermal trends were found for both the ID and OD film cooling.

Turbulence Intensity and Length Scale

Turbulence intensity and length scale were investigated using TSI hotwire probes and a TSI thermal anemometry system. The integral length scale Λ_X was determined by multiplying the mean velocity of the signal by the integral time scale T of the turbulent eddies. The integral time scale was determined by integrating the autocorrelation function $R(\tau)$ of the hotwire signal from $\tau=0$ to a τ value corresponding to $0.00<R(\tau)<0.05$.

A summary of the measured turbulence intensities and length scales for three of the isothermal tests is shown in Table 3. The measured turbulence intensities were found to be in an elevated range from $20\%<\mathrm{Tu}<30\%$, which is consistent with real combustor exit flows as reported by Cameron et al. [7], Goebel et al. [19], and Van Fossen and Bunker [13]. The main difference between these three tests was the position (porosity) of the center shutter at the inlet of the central chamber. The position of this shutter was varied in an attempt to force different amounts of flow through the dilution holes thereby affecting the turbulence production. The integral length scales for these tests were found to scale very well with the dilution hole diameters of the simulator. The axial position of the dilution holes with respect to the location of the hotwire probes is approximately $x/D_1=21$ and $x/D_2=11$. The turbulence intensity results are consistent with some of the computational results presented in Kunze et al. [20] who performed a study that modeled the central chamber flow and thermal fields of the simulator device in this study. Note that the test numbers displayed in Table 3 correspond to the separate isothermal tests that were conducted and discussed earlier in the instrumentation section.

Table 3 Summary of turbulence intensities and length scales for the isothermal tests

Test	Tu (%)	Λ_x (m)	Λ_X/D_2
011	21.3	0.0155	0.82
013	29.8	0.0160	0.84
017	22.5	0.0190	0.99

Circumferential profiles of turbulence intensity and integral length scale near midspan are shown in Fig. 14 for one of the isothermal tests. Both profiles are plotted versus vane pitch location Y/P. The alignment of the hotwire probes with respect to the upstream dilution holes is indicated on each plot. It can be seen that as the hotwires are traversed from a circumferential position corresponding to a first row dilution hole to a circumferential position corresponding to a second row dilution hole, the turbulence intensity remains relatively constant and increases only slightly from 20% to 23%. This small increase is explained by the fact that the second row dilution holes are physically larger and closer to the hotwire probes than the first row, and therefore the turbulence associated with the second row jets is more prevalent.

Three curves are shown for both turbulence and length scale corresponding to different time averaging windows of 100 ms, 200 ms, and 300 ms. For example, the 100 ms time window means that *each* data point in that curve represents the average turbulence intensity or length scale over 100 ms and the result is plotted at the center of the time window. Three different time windows were used to determine if the calculation results would turn out consistent with one another, and from viewing Fig. 14 it

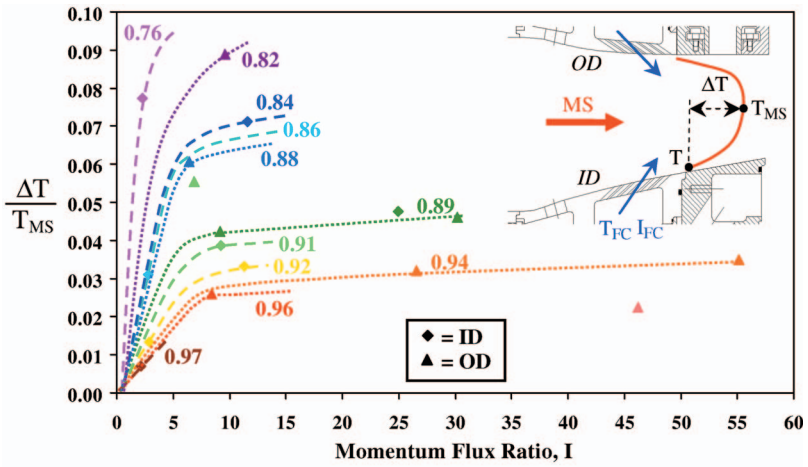

Fig. 13 Plot of the near endwall temperatures as a function of film cooling temperature and momentum flux ratio for the baseline tests

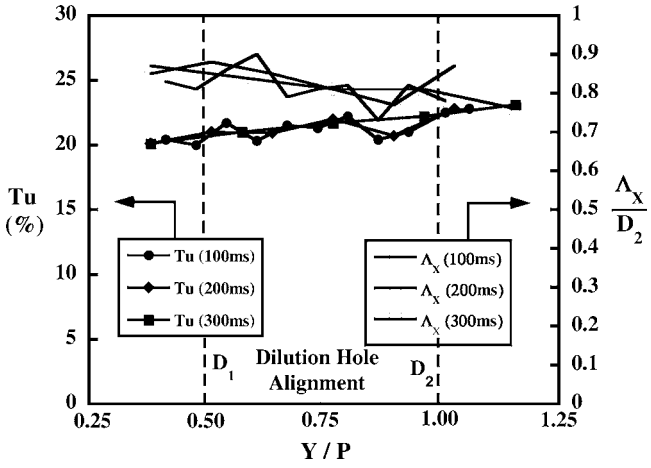

Fig. 14 Plot of Tu and Λ_x at the midspan for hotwire Test 011

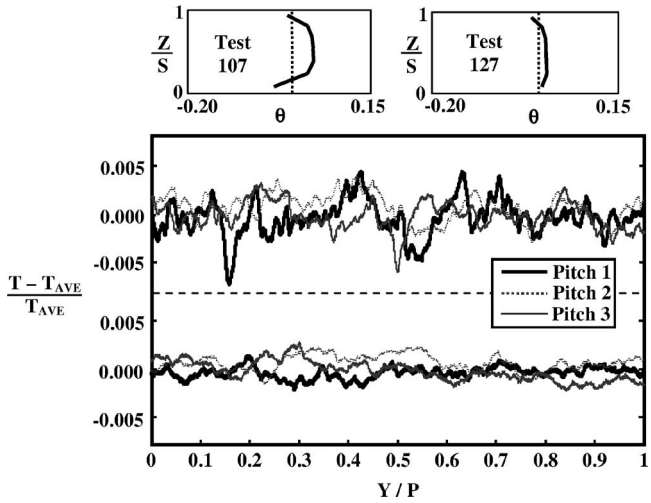

Fig. 16 Circumferential temperature near midspan over three vane pitches for Tests 107 (top) and 127 (bottom)

can be seen that this is the case. It is noted that these three time windows are much less than the overall test time window of approximately 4.0 s. In the same figure, the integral length scale consistently scales well with the dilution hole diameters within the range of 80–90% of D_2 or 110–130% of D_1.

Circumferential Variations

The circumferential variation in measured pressure near midspan is shown in Fig. 15 over three full vane pitches for Tests 107 and 123, respectively. These two tests correspond to cases that produced spanwise pressure profiles nearly opposite of one another. Test 107 produced a spanwise pressure profile at the simulator exit that contained sharp gradients near the ID and OD endwalls with a relatively lower pressure region near midspan, while Test 123 produced a spanwise pressure profile that was peaked in the midspan region. The total pressure has been normalized by the average pressure across the span. This normalization is more appropriate at this location than the previously defined C_p pressure coefficient which is by definition equal to zero at midspan. This pressure ratio varies up to approximately 1.0% for Test 107 and 1.5% for Test 123. Relative to the spanwise pressure profile variation discussed earlier, however, no significant patterns in the pitch direction were distinguishable within the pressure wave forms. This result indicates that flow in the circumferential direction is being significantly mixed out by the highly turbulent dilution jets.

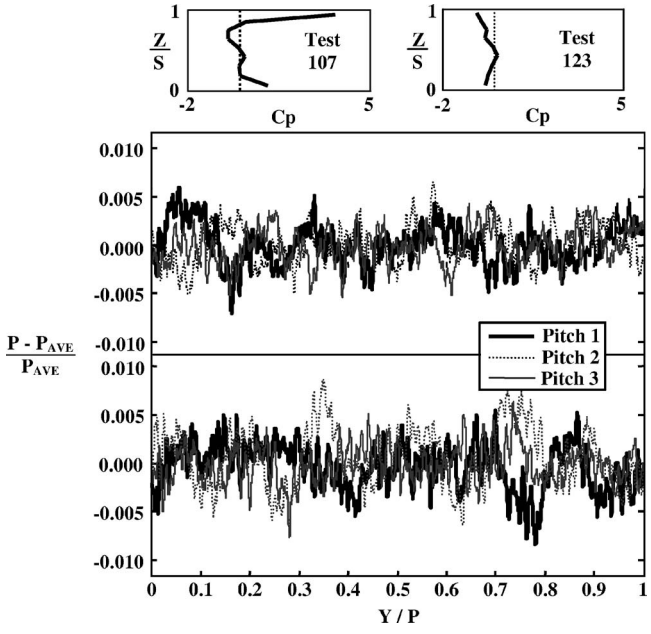

Fig. 15 Circumferential pressure near midspan over three vane pitches for Tests 107 (top) and 123 (bottom)

The circumferential variation in measured temperature near midspan is shown in Fig. 16 over three full vane pitches for Tests 107 and 127. The measured temperature has been normalized by the average temperature across the span. This temperature ratio varies up to approximately 1.0% for Test 107 in which the spanwise temperature profile at the simulator exit possessed significant shape with $\Delta\theta$ near 0.1. The same temperature ratio varies by only about 0.5% for Test 127 in which the spanwise temperature profile at the simulator exit is relatively uniform over the vane span. Relative to the spanwise temperature profile variation discussed earlier, no significant pitchwise patterns were distinguishable within the thermal wave forms. This result is also caused by the intense dilution mixing process which dominates the midspan region.

The circumferential variation in pressure and temperature near the endwalls was observed to be similar but slightly higher than that at the midspan. The higher variation was attributed to the highly turbulent film cooling flow being located relatively closer to the exit plane than the upstream dilution holes which dominate the behavior of the profiles in the near midspan region. While the dilution holes are clocked with the vane passages, meaning that the flow for each passage is periodic, the film-cooling holes are not exactly periodic for each passage due to manufacturing limitations. However, the film-cooling hole periodicity, clocked with the vanes, is not relevant given that the very large number of closely spaced film-cooling jets merge in the pitch direction as the coolant flow approaches the vane, whose leading edge is approximately 25 cooling hole diameters downstream of the last row of film cooling holes.

It is important to note that the original design intent of this simulator device was to produce significant variations of pressure and temperature in the radial direction while also producing some variation in the circumferential direction. The results show that the central chamber configuration of the generator used in this study produced variations much more powerful in the radial direction as compared to the circumferential direction. The mean circumferential variation of pressure and temperature within most real combustors is quite low compared to that in the radial direction. In fact, as combustor designs move towards operating near stoichiometric conditions, these circumferential variations in temperature will become even less. Fuel injectors can have uneven

fuel distributions, can become partially or totally clogged, misaligned, or even damaged, which can all create hot streaks and larger more significant variations in the circumferential direction, however studying these scenarios was not the goal of the current work.

Conclusions

The benchmark tests revealed that the inlet profile generator can produce a variety of turbine inlet profiles that are representative of actual engine conditions with realistic turbulence levels. Turbulence intensities from 20% to 30% were measured with integral length scales from 1.5 to 1.9 cm ($0.82 < \Lambda_X/D_2 < 0.99$). Pressure and temperature profiles were measured with peaks near the ID endwall, midspan, and OD endwall. When testing at the baseline conditions, the simulator is capable of producing ID endwall pressure peaks between $-0.7 < C_p < 1.7$, OD endwall pressure peaks in the range of $-0.6 < C_p < 5.0$, and radial thermal variations up to $\Delta\theta = 10\%$ (for the seven-headed thermocouple rake). Overall, the measured results show that the variation of pressure and temperature was more significant in the radial direction compared to the circumferential direction which was attributed to the high turbulence mixing out the variations.

It was shown that the exit pressure profiles in the near endwall regions scaled very well with the momentum flux ratio of the upstream film cooling flow and the combustor exit Reynolds number. The exit temperature profiles in the near endwall regions also scaled very well with the film cooling momentum flux ratio, as well as the ratio of the film cooling temperature to the midspan temperature. The liner film cooling affected the simulator exit pressure and temperature profiles between approximately $0.0 < Z/S < 0.2$ on the ID and $0.8 < Z/S < 1.0$ on the OD.

The significance of this research resides in its contribution to improving turbine engine hardware by evaluating the behavior of different combustor exit profiles. There are very few facilities that can simulate combustor profiles as inlet conditions to a full stage rotating turbine. Data sets, whether aerodynamic or heat transfer, that can be obtained from this facility will be of high value to the design community. These data sets can be used to baseline CFD codes allowing more confident extrapolation of the codes to the specific profiles and turbine that the designer wishes.

The results from the current study are useful to engine designers of both aircraft and power generation turbines since they show how a single combustor geometry can produce widely different flow and thermal field conditions entering the downstream turbine. The results show that great emphasis should be placed on obtaining accurate knowledge of the flow distribution within the combustion chamber at all operating conditions. This distribution is paramount and the results show that analyzing the performance of turbine hardware should be conducted using more precise profiles rather than uniform inlet conditions typically used in the past. Turbine inlet profiles possessing significantly different shapes can alter the flow physics in the turbine vane and blade passages thereby changing local aerodynamics and heat transfer.

This study will be used as a launching point for future studies. For example, future testing of the inlet profile generator will involve modifying hole patterns to allow studies with increased circumferential variations of pressure and temperature to be performed with the specific goal of studying combustor hot streaks and migration patterns.

Acknowledgments

The authors would like to thank Robert Free and John Finnegan for their help with instrumentation and assembly. The authors would also like to thank Michael Kobelak, Terry Gillaugh, and Douglas Rabe in the Technology Evaluation Branch at AFRL/PRTE. The authors would like to thank the AFRL for funding and sponsoring this research effort.

Nomenclature

- C = vane axial chord length
- C_p = pressure coefficient, $C_p = P_0 - P_{0_{ms}}/0.5\rho_{AVE}U^2_{AVE}$
- D = dilution hole diameter
- I = momentum flux ratio, $I = \rho_{jet}U^2_{jet}/\rho_\infty U^2_\infty$
- M = Mach number
- P = pressure or vane pitch
- R = autocorrelation coefficient
- Re = Reynolds number, $\mathrm{Re} = U_{AVE}\cdot C/\nu$
- S = vane span
- T = temperature
- Tu = turbulence intensity, $\mathrm{Tu} = U_{RMS}/U_{AVE}$
- U = velocity
- X, Y, Z = axial, pitch, and span directions

Greek Symbols

- T = integral time scale, $T = \int_0^\infty R(\tau)d\tau$
- Λ = integral length scale, $\Lambda = T\cdot U_{AVE}$
- ν = kinematic viscosity
- ρ = density
- τ = autocorrelation time lag
- θ = temperature coefficient, $\theta = (T - T_{AVE})/T_{AVE}$

Subscripts

- ∞ = freestream or mainstream
- 1,2 = dilution row number
- AVE = average
- FC = film cooling
- jet = flow exiting hole
- max = maximum
- MS = midspan
- RMS = root-mean-square

References

[1] Barringer, M., Thole, K., and Polanka, M., 2004, "Developing a Combustor Simulator for Investigating High Pressure Turbine Aerodynamics and Heat Transfer," ASME Paper No. GT2004–53613.
[2] Barringer, M., Thole, K., and Polanka, M., 2006, "Effects of Combustor Exit Profiles on High Pressure Turbine Vane Aerodynamics and Heat Transfer," ASME Paper No. GT2006–90277.
[3] Holdeman, J. D., 1993, "Mixing of Multiple Jets with a Confined Subsonic Crossflow," Prog. Energy Combust. Sci., **19**, pp. 31–70.
[4] Ames, F. E., and Moffat, R. J., 1990, "Effects of Simulated Combustor Turbulence on Boundary Layer Heat Transfer," *Heat Transfer in Turbulent Flow 1990: Proceedings AIAA/ASME Thermophysics and Heat Transfer Conference*, Seattle, WA, June 18–20.
[5] Barringer, M., Richard, O., Stitzel, S., Walter, J., and Thole, K., 2002, "Flow Field Simulations of a Gas Turbine Combustor,"ASME J. Turbomach., **124**, pp. 508–516.
[6] Stitzel, S., and Thole, K. A., 2004, "Flow Field Computations of Combustor-Turbine Interactions Relevant to a Gas Turbine Engine," ASME J. Turbomach., **126**, pp. 122–129.
[7] Cameron, C., Brouwer, J., Wood, C., and Samuelsen, G., 1989, "A Detailed Characterization of the Velocity and Thermal Fields in a Model Can Combustor With Wall Jet Injection," J. Eng. Gas Turbines Power, **111**, pp. 31–35.
[8] Bicen, A., Tse, D., and Whitelaw, J., 1988, "Flow and Combustion Characteristics of an Annular Combustor," Combust. Flame, **72**, pp. 175–192.
[9] Schwab, J., Stabe, R., and Whitney, W., 1983, "Analytical and Experimental Study of Flow Through an Axial Turbine Stage With a Nonuniform Inlet Radial Temperature Profile," AIAA Paper No. 83–1175.
[10] Cattafesta, L., 1988, "An Experimental Investigation of the Effects of Inlet Radial Temperature Profiles on the Aerodynamic Performance of a Transonic Turbine Stage," Masters thesis, M.I.T., Cambridge, MA.
[11] Chana, K., Hurrion, J., and Jones, T., 2003, "The Design, Development and Testing of a Non-Uniform Inlet Temperature Generator for the QinetiQ Transient Turbine Research Facility," ASME Paper No. 2003-GT-38469.
[12] Krishnamoorthy, V., Pai, B., and Sukhatme, S., 1988, "Influence of Upstream Flow Conditions on the Heat Transfer to Nozzle Guide Vanes," ASME J. Turbomach., **110**, pp. 412–416.
[13] Van Fossen, J., and Bunker, R., 2002, "Augmentation of Stagnation Region Heat Transfer Due to Turbulence from an Advanced Dual-Annular Combustor," ASME Paper No. GT2002–30184.
[14] Colban, W., Thole, K., and Zess, G., 2003, "Combustor Turbine Interface Studies—Part 1: Endwall Effectiveness Measurements," ASME J. Turbomach., **125**, pp. 193–202.
[15] Hermanson, K., and Thole, K., 2000, "Effect of Inlet Conditions on Endwall

Secondary Flows," J. Propul. Power, **16**(2), pp. 286–296.
[16] Haldeman, C. W., Dunn, M. G., MacArthur, C. D., and Murawski, C. G., 1992, "The USAF Advanced Turbine Aerothermal Research Rig (ATARR)," NATO AGARD Propulsion and Energetics Panel Conference Proceedings 527, Antalya, Turkey.
[17] Roy R., K., 2001, *Design of Experiments Using the Taguchi Approach*, Wiley, New York.
[18] Kunze, V., Wolff, M., Barringer, M., Thole, K., and Polanka, M., 2006, "Numerical Insight Into Flow and Thermal Patterns Within an Inlet Profile Generator Comparing to Experimental Results," ASME Paper No. GT2006–90276.
[19] Goebel, S., Abuaf, N., and Lee, C., 1993, "Measurements of Combustor Velocity and Turbulence Profiles," ASME Paper No. 93-GT-228.
[20] Kunze, V., Wolff, M., Barringer, M., Thole, K., and Polanka, M., 2005, "Numerical Modeling of Flow and Thermal Patterns Within a Combustor Simulator," ASME Paper No. GT2005–68284.

Movement of Deposited Water on Turbomachinery Rotor Blade Surfaces

John Williams
Department of Engineering Science,
University of Oxford,
Parks Road,
Oxford OX1 3PJ, UK and
Whittle Laboratory,
Cambridge University Engineering Department,
Cambridge University,
Cambridge CB2 1PZ, UK
e-mail: john.williams@eng.ox.ac.uk

John B. Young
Hopkinson Laboratory,
Cambridge University Engineering Department,
Cambridge University,
Trumpington Street,
Cambridge CB2 1PZ, UK
e-mail: jby@eng.cam.ac.uk

A theoretical approach for calculating the movement of liquid water following deposition onto a turbomachine rotor blade is described. Such a situation can occur during operation of an aero-engine in rain. The equation of motion of the deposited water is developed on an arbitrarily oriented plane triangular surface facet. By dividing the blade surface into a large number of facets and calculating the water trajectory over each one crossed in turn, the overall trajectory can be constructed. Apart from the centrifugal and Coriolis inertia effects, the forces acting on the water arise from the blade surface friction, and the aerodynamic shear and pressure gradient. Nondimensionalization of the equations of motion provides considerable insight and a detailed study of water flow on a flat rotating plate set at different stagger angles demonstrates the paramount importance of blade surface friction. The extreme cases of low and high blade friction are examined and it is concluded that the latter (which allows considerable mathematical generalization) is the most likely in practice. It is also shown that the aerodynamic shear force, but not the pressure force, may influence the water motion. Calculations of water movement on a low-speed compressor blade and the fan blade of a high bypass ratio aero-engine suggest that in low rotational speed situations most of the deposited water is centrifuged rapidly to the blade tip region. [DOI: 10.1115/1.2437780]

Keywords: turbomachinery, water ingestion, water films, water deposition, water movement

Introduction

Water may deposit on a rotor blade as a result of spontaneous nucleation in steam turbines [1], inlet "fog boosting" in industrial gas turbines [2], condensation of humid air in aero-engine intakes [3], or ingestion by aero-engines of rain [4]. The current work addresses the behavior of water deposited on aero-engine compressor blades due to rain ingestion but the approach taken is equally applicable to the other problems. The main focus is on aircraft descent at idle power settings when rain ingestion can have adverse effects on engine performance [4]. The objective is to calculate the path of deposited water over a blade surface in order to determine whether the water is centrifuged to the casing or re-entrained into the gas flow from the blade trailing edge.

The motion of water on a rotor blade is influenced by inertia, blade friction, aerodynamic drag, and aerodynamic pressure gradient. The inertia "force" comprises the centrifugal and Coriolis components resulting from the blade rotation. A previous study by Gyarmathy [5] concluded that the centrifugal effect dominates the motion of water on steam turbine blades and provided some justification for this. In another study, Kirillov and Yablonik [6] modeled a steam turbine rotor blade as a flat plate and analyzed the motion of water on the plate for different stagger angles. The blade friction force was assumed to act in the opposite direction to the water velocity relative to the blade, with magnitude proportional to the water speed. It was acknowledged, however, that the actual magnitude of the friction force would depend on whether the water was in the form of a droplet, a rivulet or a film. Kirillov and Yablonik also stated (although it was not justified by calculation) that the aerodynamic drag would be small in comparison with the centrifugal and Coriolis forces and so could be neglected. The effect of the aerodynamic pressure gradient was not mentioned.

The current work extends that of Kirillov and Yablonik [6] by considering water motion on a rotor blade of arbitrary shape. Also, the blade friction and aerodynamic forces are examined in greater detail leading to conclusions very different from those of Ref. [6]. Quantifying the effects of water ingestion on engine performance is beyond the scope of this paper and has been addressed by Day et al. [7].

Derivation of the Equation of Motion

The total force *per unit mass* acting on an arbitrarily shaped "packet" of water moving on a rotor blade surface comprises an inertial (centrifugal and Coriolis) "force" $\mathbf{F}_I$, a frictional resistive force due to the water contact with the blade $\mathbf{F}_B$, an aerodynamic shear force from the external gas flow $\mathbf{F}_S$, and a force caused by the gas flowfield pressure gradient $\mathbf{F}_P$. Shock wave effects are neglected since the focus is on aircraft engines operating at idle power. Evaporative effects are thought to be small at this power setting [4] and are also neglected.

The frictional force per unit mass of water is assumed to be given by

$$\mathbf{F}_B = -k\mathbf{W} \tag{1}$$

where $\mathbf{W}$ is the water packet velocity relative to the blade and k is a constant, termed the "friction factor." The value of k will depend on whether the water packet is a droplet, part of a rivulet or part of a film, and must be determined either empirically or via appropriate theory.

The analysis of Kirillov and Yablonik [6] is here extended to predict water motion on a rotor blade of arbitrary shape. The rotor blade is considered to be made up of a number of plane triangular facets, as shown in Fig. 1. This grid may represent either the suction or pressure surface of a blade, since both appear identical

Contributed by the International Gas Turbine Institute of ASME for publication in the JOURNAL OF TURBOMACHINERY. Manuscript received May 29, 2006; final manuscript received June 16, 2006. Review conducted by David Wisler. Paper presented at the ASME Turbo Expo 2006: Land, Sea and Air (GT2006), Barcelona, Spain, May 8–11, 2006. Paper No. GT2006-90792.

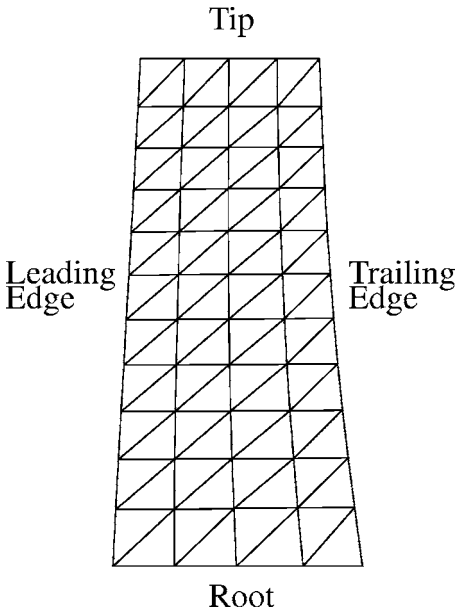

Fig. 1 Representation of a rotor blade surface as a collection of triangular facets (2D meridional view)

when projected onto the meridional plane. As the water moves over the blade, the equation of motion is solved for each facet crossed in turn, thus allowing the complete trajectory to be constructed. The accuracy of the facet calculation does not depend on the facet size and the grid density need only be high enough for the blade curvature to be well captured. For each facet, a local coordinate system rotating at a constant angular velocity ω about the machine axis is used, as shown in Fig. 2. Figure 3 shows how the facet stagger angle β may be positive or negative for a turbine blade, but is generally negative for a compressor blade. The sign of β is determined by the convention that positive swirl velocity is

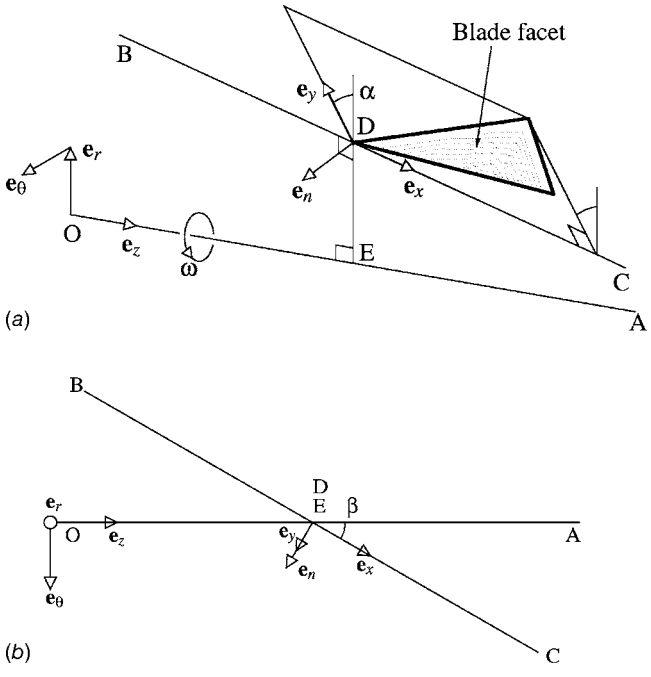

Fig. 2 Definition of coordinate system local to facet: (*a*) 3D representation; and (*b*) view along line *D-E* (2D representation with facet omitted)

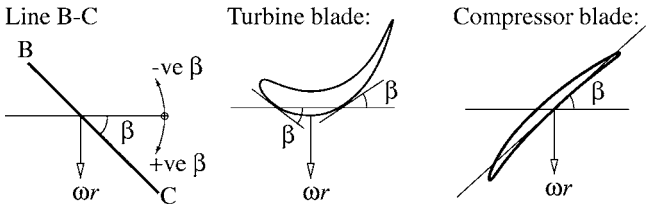

Fig. 3 Relationship between Fig. 2 and turbo-machinery rotor blade sections

in the direction of blade rotation. This paper focuses on compressor blades with negative β over the whole blade surface.

The components of the water packet acceleration in the local coordinate system are obtained by writing down the packet position vector $\mathbf{r}$ with respect to the origin O (see Fig. 2), and then differentiating twice with respect to time. Thus

$$\mathbf{r} = z_0\mathbf{e}_z + r_0\mathbf{e}_r + x\mathbf{e}_x + y\mathbf{e}_y \tag{2}$$

$$\begin{aligned}\ddot{r} = {} & \mathbf{e}_x[\ddot{x} - x\omega^2 \sin^2\beta + 2\dot{y}\omega\cos\alpha\sin\beta - y\omega^2\sin\alpha\sin\beta\cos\beta] \\ & + \mathbf{e}_y[\ddot{y} - y\omega^2(1 - \sin^2\alpha\sin^2\beta) - 2\dot{x}\omega\cos\alpha\sin\beta \\ & - x\omega^2\sin\alpha\sin\beta\cos\beta - r_0\omega^2\cos\alpha] + \mathbf{e}_n[\ldots]\end{aligned} \tag{3}$$

where the $\mathbf{e}_n$ component is not required because the water is assumed to remain in contact with the blade. In Eq. (2), z_0 and r_0 define vertex D of the facet (see Fig. 2), and x and y define a general point in the local coordinate system. The facet lean and stagger angles, α and β, are also shown in Fig. 2. The time derivatives of the unit vectors $\mathbf{e}_x$ and $\mathbf{e}_y$ are required in the derivation of Eq. (3) and can be obtained using the relations

$$\mathbf{e}_x = \sin\beta\mathbf{e}_\theta + \cos\beta\mathbf{e}_z \tag{4}$$

$$\mathbf{e}_y = \cos\alpha\mathbf{e}_r + \sin\alpha\cos\beta\mathbf{e}_\theta + \sin\alpha\sin\beta\mathbf{e}_z \tag{5}$$

$$\mathbf{e}_r = \cos\alpha\mathbf{e}_y - \sin\alpha\mathbf{e}_n \tag{6}$$

$$\mathbf{e}_\theta = \sin\beta\mathbf{e}_x + \sin\alpha\cos\beta\mathbf{e}_y + \cos\alpha\cos\beta\mathbf{e}_n \tag{7}$$

Equations (4) and (5) allow the time derivatives of $\mathbf{e}_x$ and $\mathbf{e}_y$ to be obtained in terms of the time derivatives of $\mathbf{e}_r$, $\mathbf{e}_\theta$, and $\mathbf{e}_z$, which are standard results. The expressions obtained include $\mathbf{e}_r$ and $\mathbf{e}_\theta$ terms, and these can be re-expressed in terms of $\mathbf{e}_x$ and $\mathbf{e}_y$ using Eqs. (6) and (7). This method of performing coordinate transformations is applicable to other problems and is very succinct. Attempting to perform the transformations in terms of scalar components quickly generates a large number of terms.

The equations of motion in the x and y directions are obtained from Newton's second law using Eqs. (1) and (3). Thus

$$\begin{aligned}\frac{dW_x}{dt} + kW_x - \omega^2[x\sin^2\beta + y\sin\alpha\sin\beta\cos\beta] \\ + 2\omega W_y\cos\alpha\sin\beta = F_{S,x} + F_{P,x}\end{aligned} \tag{8a}$$

$$\begin{aligned}\frac{dW_y}{dt} + kW_y - \omega^2[y + r_0\cos\alpha - y\sin^2\alpha\sin^2\beta \\ + x\sin\alpha\sin\beta\cos\beta] - 2\omega W_x\cos\alpha\sin\beta = F_{S,y} + F_{P,y}\end{aligned} \tag{8b}$$

with $W_x = dx/dt$ and $W_y = dy/dt$. The terms on the right are the x and y components of the aerodynamic shear and pressure forces.

For analytical and computational work Eqs. (8) are nondimensionalized by substituting

$$X = \frac{x}{L}, \quad Y = \frac{y}{L}, \quad R_0 = \frac{r_0}{L}, \quad T = \omega t, \quad K = \frac{k}{\omega}, \quad \bar{F} = \frac{F}{\omega^2 L} \quad (9)$$

where L is an appropriate length scale. The trajectory across a facet is then calculated by numerical integration of the dimensionless equations, choosing a suitable nondimensional time step ΔT and assuming that the water acceleration remains constant over this period. Suitable values for K and the components of $\bar{\mathbf{F}}_S$ and $\bar{\mathbf{F}}_P$ must be specified and these can vary from facet to facet if desired. When the trajectory crosses a facet edge, the position and velocity are communicated to the next facet by recording the edge crossed, the fractional distance along the edge, and the velocity components parallel and perpendicular to the edge. In this way, the trajectory is built up until it reaches the blade boundary at the tip, trailing edge or leading edge.

Water Flow on a Rotating Flat Plate

The study of the water flow on a flat plate is a good starting point for understanding the mechanisms responsible for water movement on a real blade. For a rotating flat plate, the angles α and β are constant and initially it will be assumed that the lean angle α and the aerodynamic force terms are zero. This is the model originally analyzed by Kirillov and Yablonik [6]. Equations (8) for the water motion therefore reduce to

$$\frac{dW_x}{dt} + kW_x - \omega^2 x \sin^2\beta + 2\omega W_y \sin\beta = 0 \quad (10a)$$

$$\frac{dW_y}{dt} + kW_y - \omega^2 (y + r_0) - 2\omega W_x \sin\beta = 0 \quad (10b)$$

and the contributions from the centrifugal and Coriolis "forces" are now very obvious.

Nondimensionalizing as in Eq. (9) with L equal to the plate "hub" radius r_0 gives

$$\ddot{X} + K\dot{X} - X \sin^2\beta + 2\dot{Y} \sin\beta = 0 \quad (11a)$$

$$\ddot{Y} + K\dot{Y} - (Y + 1) - 2\dot{X} \sin\beta = 0 \quad (11b)$$

where the dot notation indicates differentiation with respect to nondimensional time $T = \omega t$. Clearly, a trajectory in a $(X\text{-}Y)$ plot is fully determined by the stagger angle β, the dimensionless friction factor $K = k/\omega$, and the initial conditions.

In their work, Kirillov and Yablonik [6] assumed that K varied between 0 and 1. As will be shown later, this assumption is incorrect: K can, and indeed does, take values much higher than unity. Nevertheless, the lower limiting case of zero blade friction is still worth considering because it defines the water movement when controlled by inertia alone.

Zero Blade Friction. For constant K, Eqs. (11) are two simultaneous linear ordinary differential equations (ODEs) which can be solved analytically to give trajectories in the form, $X = X(T)$, $Y = Y(T)$. This was the procedure followed in Ref. [6] but in the present work it was found more convenient to solve the equations numerically, even in simple cases. Accordingly, Fig. 4 shows water packet trajectories on a radial flat plate for $K = 0$ and various stagger angles β, calculated by numerical integration of Eqs. (11). For comparison, the results of Ref. [6] are also shown.

In Fig. 4(*a*), the water is assumed to lose all its momentum on deposition and to start from rest relative to the plate. For $\beta = 0$ the Coriolis force acts normal to the plate surface and does not affect the water motion which, being controlled solely by the centrifugal force, is in the outward radial direction. As β becomes more negative, the effect of the Coriolis force increases with the result that the water is displaced towards the plate trailing edge. For stagger angles of −40 deg and −60 deg this effect is very marked indeed. Although not shown here, for positive β (as on parts of a turbine blade), the Coriolis force displaces the water toward the *leading* edge.

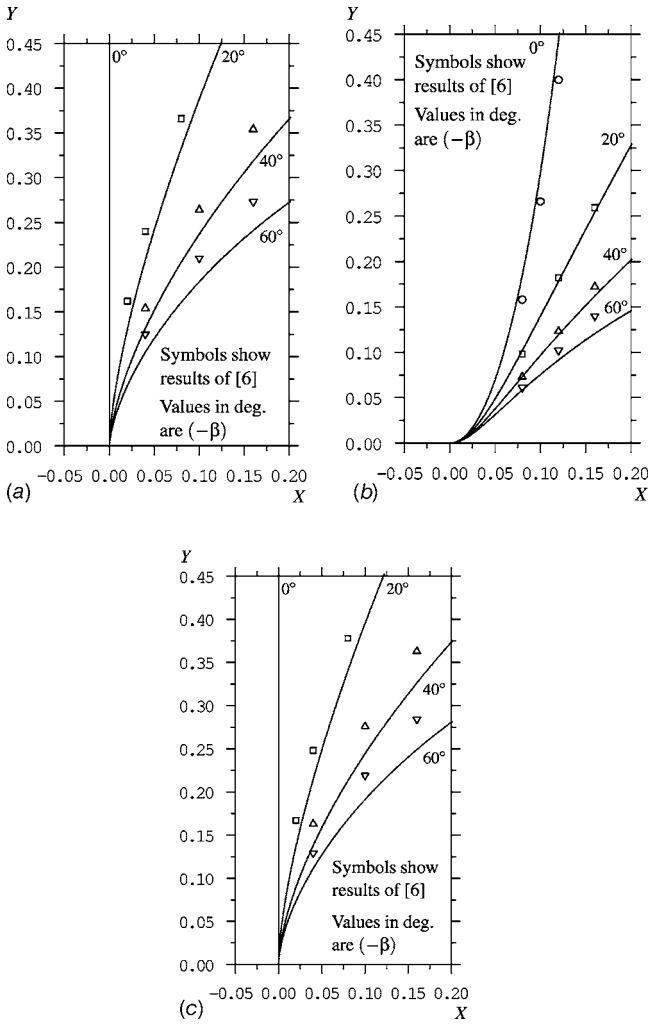

Fig. 4 Water packet trajectories on a rotating flat plate set at various stagger angles β. Zero friction ($K = 0$), zero lean angle, and zero aerodynamic forces. Initial velocity is: (*a*) $\dot{X}_0 = 0$, $\dot{Y}_0 = 0$; (*b*) $\dot{X}_0 = 0.1$, $\dot{Y}_0 = 0$; and (*c*) $\dot{X}_0 = 0$, $\dot{Y}_0 = 0.1$.

The calculations shown in Figs. 4(*b*) and 4(*c*) differ from those in Fig. 4(*a*) in that the water packet is assumed to start with a finite initial velocity due to the retention of some momentum after deposition. In Fig. 4(*b*), the initial nondimensional velocity is $(\dot{X}_0 = 0.1, \dot{Y}_0 = 0)$, corresponding to a relative velocity of $(W_{x0} = 0.1U_0, W_{y0} = 0)$, where $U_0 = \omega r_0$ is the plate speed at the root $(r = r_0)$. A comparison with Fig. 4(*a*) shows that this initial X component of velocity has a very strong effect on the water trajectories which are displaced markedly towards the trailing edge. In contrast, Fig. 4(*c*) shows that an initial radial velocity of $(\dot{X}_0 = 0, \dot{Y} = 0.1)$ has almost no effect on the trajectories.

Kirillov and Yablonik [6] showed trajectories for $K = 1$ but these will not be discussed as $K = 1$ does not represent the upper limit on blade friction. For $K = 0$ it will be noted that the trajectories of the present work display reasonable, but by no means perfect, agreement with the calculations of Ref. [6]. The reasons for the discrepancies are unknown, although a study of the figures in Ref. [6] shows that the symbols for $K = 0$ and $K = 1$ have, in some cases, been reversed. It is also possible that a different nondimensionalizing length L was used.

In summary, for $K = 0$ both the Coriolis force and the X com-

ponent of the initial water velocity exert a strong influence on the water movement by displacing the trajectories toward the trailing edge (for negative β). In reality, of course, as a water packet moves over the blade surface it may acquire extra X momentum more or less continuously due to coalescence with further deposited water. This effect has not been included in the calculations of Fig. 4 but would clearly enhance the tendency of the trajectories to deflect toward the trailing edge.

The implicit conclusion of Kirillov and Yablonik that (subject to the precise operational conditions and blade geometry), much of the deposited water will reach the blade trailing edge before the tip is very dependent on the assumption of low blade friction. This will now be demonstrated by considering the opposite extreme where K takes high values.

High Blade Friction. For the case of high blade friction, Eqs. (11) simplify considerably because the second derivatives $\ddot{X}$ and $\ddot{Y}$ may be neglected in comparison to the other terms. For $\beta=0$ it is easy to show that this approximation is valid if $K^2 \gg 1$ but the derivation of a general condition is difficult. Neglecting $\ddot{X}$ and $\ddot{Y}$, the resulting simultaneous equations may be solved to give

$$\dot{\tilde{X}} = \frac{\tilde{W}_x}{U_0} = \frac{K(X \sin^2 \beta) - 2 \sin \beta (Y+1)}{(K^2 + 4 \sin^2 \beta)} \tag{12a}$$

$$\dot{\tilde{Y}} = \frac{\tilde{W}_y}{U_0} = \frac{2 \sin \beta (X \sin^2 \beta) + K(Y+1)}{(K^2 + 4 \sin^2 \beta)} \tag{12b}$$

where the tilde denotes the "high-friction approximation." It should be noted that $\tilde{W}_x$ and $\tilde{W}_y$ are independent of the initial conditions and are defined completely by the position on the plate, the parameters K and β, and the local aerodynamic forces.

The physical interpretation of the high-friction approximation is as follows. When the water packet is deposited, the actual velocity components (W_{x0} and W_{y0}) will generally not be equal to the values ($\tilde{W}_{x0}$ and $\tilde{W}_{y0}$) given by Eqs. (12). As the water moves, however, the velocity differences ($W_x - \tilde{W}_x$) and ($W_y - \tilde{W}_y$) decay exponentially according to $\exp(-KT)$. During this period, the packet moves distances ΔX and ΔY on the order of

$$\Delta X \approx \frac{\dot{X}_0 - \dot{\tilde{X}}_0}{K} \quad \Delta Y \approx \frac{\dot{Y}_0 - \dot{\tilde{Y}}_0}{K} \tag{13}$$

which are small as K is large. The high-friction approximation neglects this initial relaxation and assumes instantaneous adjustment to the local values given by Eqs. (12).

Figure 5 shows trajectories for $K=20$ and the same values of β as in Fig. 4. The calculations were carried out first with the full Eqs. (11) and then with Eqs. (12) in order to examine the accuracy of the high-friction approximation. The initial conditions are the same as in Fig. 4, namely $(\dot{X}_0=0, \dot{Y}_0=0)$, $(\dot{X}_0=0.1, \dot{Y}_0=0)$, and $(\dot{X}_0=0, \dot{Y}_0=0.1)$ for Figs. 5(*a*)–5(*c*) respectively. A study of these figures shows that, in all cases, the water flow on the plate is much closer to the radial direction than in Fig. 4. It can also be seen that Eqs. (12) provide a good approximation to Eqs. (11) and that the high friction damps the initial motion very quickly.

An expression for the slope of the trajectories in the high-friction approximation can be obtained from Eqs. (12). Thus, if ϕ is the angle between a trajectory and the radial direction

$$\tan \phi = \frac{\tilde{W}_x}{\tilde{W}_y} = \frac{K(X \sin^2 \beta) - 2 \sin \beta (Y+1)}{2 \sin \beta (X \sin^2 \beta) + K(Y+1)} \tag{14}$$

Figure 6 shows contours of constant trajectory angle ϕ calculated from Eq. (14) with $\beta=-40$ deg, $K=20$. In keeping with Fig. 5, it will be seen that ϕ is small everywhere, the maximum value

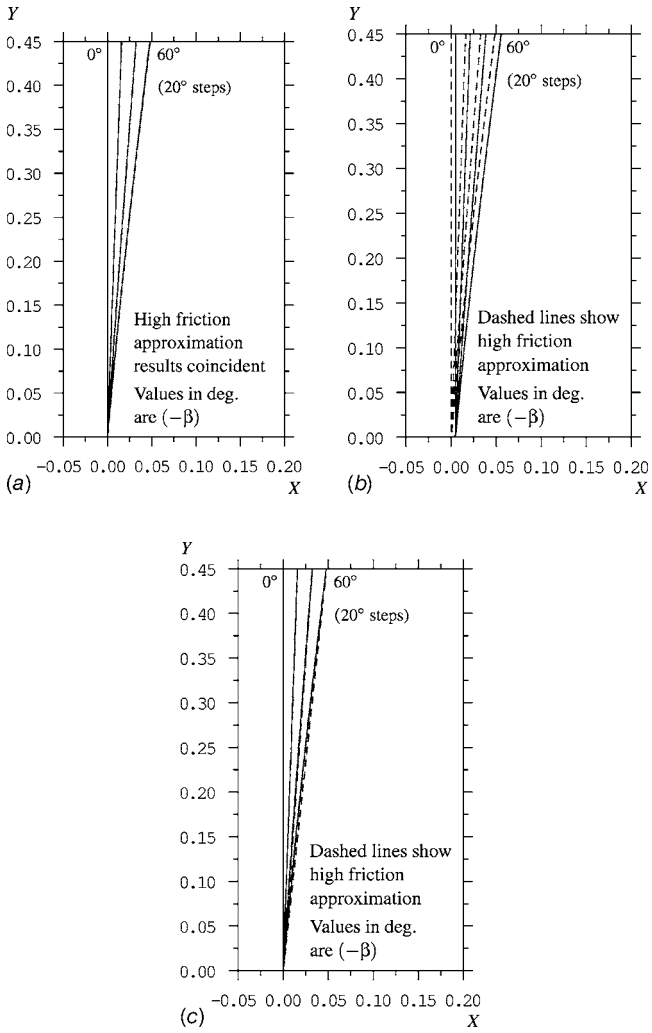

Fig. 5 Water packet trajectories on a rotating flat plate set at various stagger angles β. High friction ($K=20$), zero lean angle and zero aerodynamic forces. Initial velocity is: (*a*) $\dot{X}_0=0$, $\dot{Y}_0=0$; (*b*) $\dot{X}_0=0.1$, $\dot{Y}_0=0$; and (*c*) $\dot{X}_0=0$, $\dot{Y}_0=0.1$.

being about 8 deg at the bottom right hand corner of the plate. Equation (14) also shows that ϕ tends to decrease (i.e., the water flow becomes more radial) as K increases.

In summary, if K is large the trajectories lie much closer to the radial direction and are less sensitive to changes in stagger angle and initial water velocity than when K is small. This implies that more water reaches the tip of the blade than in the case of low blade friction.

Estimation of the Friction Factor. One of the main difficulties in computing the water movement on rotating blades is in estimating the dimensionless friction factor K. Unfortunately, there is no universal prescription for K because its magnitude depends on the form of the water (droplets, rivulets, or film) and varies with position on the plate or blade.

There is, however, one situation which responds to analysis. This is the case of a laminar water film moving in steady flow on a rotating flat plate. In laminar film theory, the "low Reynolds number approximation" is invoked, whereby the fluid acceleration is neglected in comparison with the other force terms. This assumption is identical to the high-friction approximation discussed above and hence the two analyses should be compatible.

The analysis of a moving water film on a rotating plate is given in the Appendix where an expression for K in terms of the local

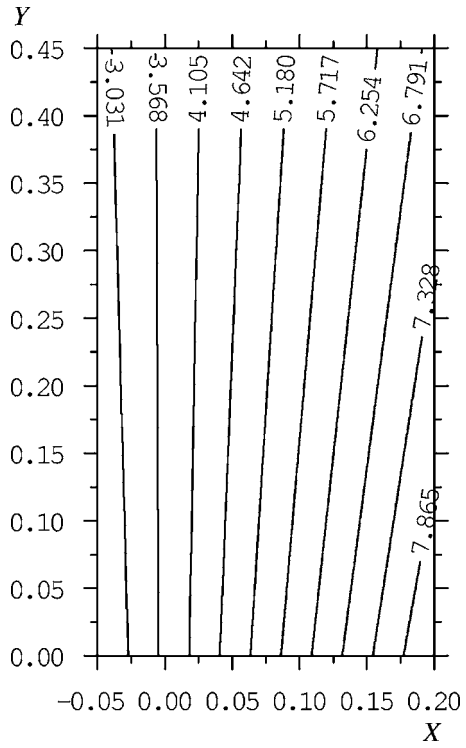

Fig. 6 Contours of constant trajectory angle ϕ from Eq. (14) with $K=20$, $\beta=-40$ deg, $\alpha=0$ deg, and zero aerodynamic forces

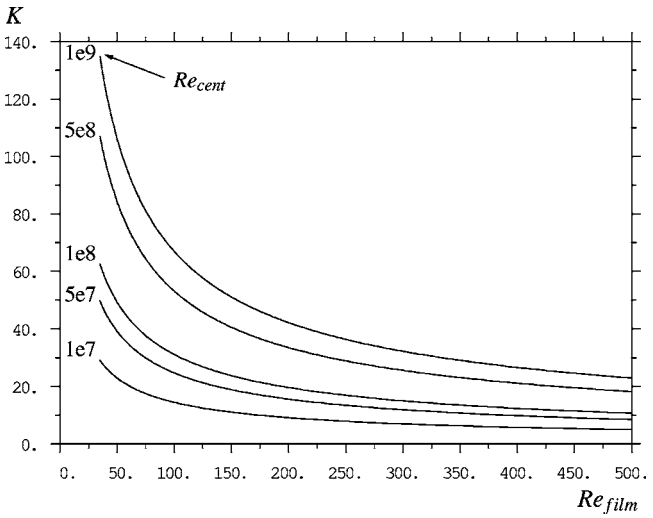

Fig. 7 Laminar film flow on a rotating plate: variation of K with Re_{film} for various values of Re_{cent} from Eq. (16)

film thickness h is derived, namely Eq. (A5). Two interesting results then follow for the special case of zero stagger angle when the water film moves radially. The first is that, if $\bar{W}_r$ is the *mean* radial velocity of the water in the film and U_r is the plate speed (both at radius r), K is given by

$$K = \frac{U_r}{\bar{W}_r} \tag{15}$$

This interpretation of K is not, however, restricted to film flow because an identical result (for $\beta=0$) is obtained directly from Eq. (12*b*), an equation which is valid for *any* form of water subject only to the high-friction approximation. In turbomachinery applications with high rotational speeds, it seems likely that $\bar{W}_r$ will be considerably smaller than U_r and Eq. (15) is therefore a strong indication that K will be substantially greater than unity.

The second interesting result (also restricted to the case of $\beta=0$) is that K can alternatively be expressed in the form

$$K = \left(\frac{3\,\mathrm{Re}_{\mathrm{cent}}}{\mathrm{Re}_{\mathrm{film}}^2}\right)^{1/3} \tag{16}$$

where $\mathrm{Re}_{\mathrm{cent}}=r^2\omega\rho_w/\mu_w$ is a centrifugal Reynolds number and $\mathrm{Re}_{\mathrm{film}}=G/\mu_w$ is a film Reynolds numbers (ρ_w and μ_w being the density and dynamic viscosity of water and G being the local water mass flowrate per unit width of film). Equation (16) allows quantitative predictions to be made because the film mass flowrate at any radius, say $r=r_1$, must equal the total rate at which water is deposited in the region $r<r_1$. Hence, if the deposition rate over the plate surface is known, $\mathrm{Re}_{\mathrm{film}}$ can be calculated at any location and K follows from Eq. (16).

Figure 7 shows K as a function of $\mathrm{Re}_{\mathrm{film}}$ for various values of $\mathrm{Re}_{\mathrm{cent}}$ in the range appropriate for turbomachinery, $10^7<\mathrm{Re}_{\mathrm{cent}}<10^9$. In keeping with rough estimates of the rate of deposition of ingested rain in aero-engines, the abscissa covers the range $\mathrm{Re}_{\mathrm{film}}<500$. Even at $\mathrm{Re}_{\mathrm{film}}=500$ the body-force driven film flow would probably remain laminar because (by analogy with pressure-gradient driven channel flow which has a similar parabolic velocity profile) transition to turbulence should occur at around $\mathrm{Re}_{\mathrm{film}}\approx 1000$. For most practical situations, Fig. 7 shows that high values of K are to be expected and Eq. (14) then implies that the water trajectories will only deviate by a few degrees from the radial direction. Figure 7 also shows that the choice of $K=20$ when calculating the trajectories in Fig. 5 is representative of operation at midrange values of both $\mathrm{Re}_{\mathrm{cent}}$ and $\mathrm{Re}_{\mathrm{film}}$.

Because of the difficulty of estimating K theoretically, a simple experiment was conducted in an attempt to obtain some empirical information. To this end, a horizontal plane circular disk was mounted on a vertical shaft. When the disk was stationary, a droplet of water was placed close to the axis of rotation, and the disk was then rotated by an electric motor. The subsequent trajectory of the droplet could be determined after bringing the disk to rest because the droplet left a trail of tiny subdroplets over the disk surface. Calculations of the droplet trajectory were made and Fig. 8 shows that excellent agreement between theory and experiment

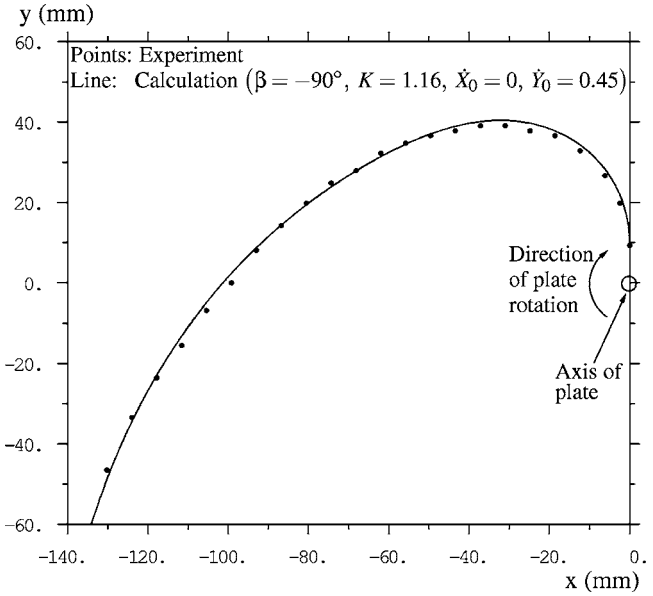

Fig. 8 Droplet moving on the surface of a horizontal flat disk rotating about a vertical axis: comparison of experimentally measured trajectory with calculation

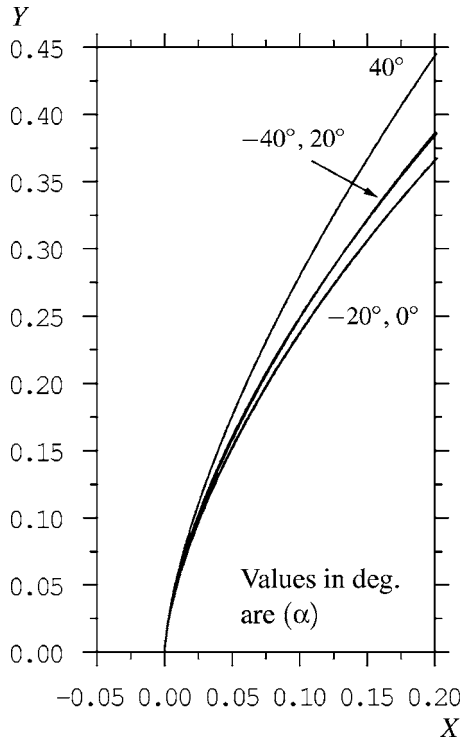

Fig. 9 Water packet trajectories on a rotating flat plate set at $\beta=-40$ deg and various lean angles α: zero blade friction ($K=0$), zero aerodynamic forces, and zero initial velocity

was obtained with $K=1.16$. It was, however, necessary to prescribe a nonzero initial velocity in the y direction because of the phenomenon of "stiction." At the instant when the droplet starts to move, its acceleration is high so that, in effect, it does not start from rest.

It might be thought that the experimentally determined value of $K=1.16$ tends to negate the conclusion drawn above that K is likely to be high in turbomachinery applications. In fact, this is not so because the centrifugal Reynolds number in the experiment was several orders of magnitude lower than typical turbomachinery values. Indeed, it is encouraging that the simple theory presented in this paper, even with a constant value of K, allows such an accurate prediction of the droplet trajectory to be made.

The Effect of the Plate Lean Angle. Kirillov and Yablonik did not consider the possibility of "leaning" the blades, although it is now common design practice (at least for stator blades). However, as shown by Eqs. (8), the derivation of the equations incorporating a lean angle α is straightforward.

For the case of a flat plate and zero blade friction, $K=0$, Fig. 9 shows the effect of varying the lean angle (0 deg, ±20 deg, ±40 deg) with zero initial velocity. Leaning the surface in either direction causes the trajectories to deviate slightly towards the blade tip. Even for values as large as ±40 deg, the influence of α is small.

In the case of high blade friction, Eqs. (12) and (14) may easily be modified to include the effect of lean, thus giving analytical expressions for the water velocity components and the trajectory angle ϕ. It is then easy to show that the lean angle has even less effect on the water trajectories than in the case of zero friction.

The Aerodynamic Forces

Attention is now directed toward compressor blades so that the aerodynamic shear and pressure forces must be considered. It is assumed that the high-friction approximation $K \gg 1$ is appropriate. Equations (12) for the X and Y water velocity components therefore become

$$\dot{\bar{X}} = \frac{\tilde{W}_x}{U_0} = \frac{K(X\sin^2\beta + \bar{F}_{S,X} + \bar{F}_{P,X}) - 2\sin\beta[(Y+1) + \bar{F}_{S,Y} + \bar{F}_{P,Y}]}{(K^2 + 4\sin^2\beta)} \tag{17a}$$

$$\dot{\bar{Y}} = \frac{\tilde{W}_y}{U_0} = \frac{2\sin\beta(X\sin^2\beta + \bar{F}_{S,X} + \bar{F}_{P,X}) + K[(Y+1) + \bar{F}_{S,Y} + \bar{F}_{P,Y}]}{(K^2 + 4\sin^2\beta)} \tag{17b}$$

The counterpart of Eq. (14) for the trajectory angle ϕ is

$$\tan\phi = \frac{\tilde{W}_x}{\tilde{W}_y} = \frac{K(X\sin^2\beta + \bar{F}_{S,X} + \bar{F}_{P,X}) - 2\sin\beta[(Y+1) + \bar{F}_{S,Y} + \bar{F}_{P,Y}]}{2\sin\beta(X\sin^2\beta + \bar{F}_{S,X} + \bar{F}_{P,X}) + K[(Y+1) + \bar{F}_{S,Y} + \bar{F}_{P,Y}]} \tag{18}$$

The Aerodynamic Pressure Force. The aerodynamic pressure force will have components in both the X and Y directions. The latter is unlikely to be significant compared with the centrifugal force but the former does require consideration. In a compressor, the pressure rises through a blade passage and the effect on the water trajectories is to deflect them toward the leading edge of the blade.

With $L=r_0$, the dimensionless pressure force per unit mass of liquid is

$$\bar{\mathbf{F}}_P = -\frac{\nabla p}{\rho_w \omega^2 r_0} \tag{19}$$

where ∇p is the local pressure gradient in the gas flow at the blade surface. Introducing ρ_{g1} and V_{g1} (the gas density and relative speed at blade inlet), and defining a dimensionless pressure gradient $\overline{\nabla p} = r_0 \nabla p / \rho_{g1} V_{g1}^2$, Eq. (19) may be written more informatively as

$$\bar{\mathbf{F}}_P = -\left(\frac{\rho_{g1}}{\rho_w}\right)\left(\frac{V_{g1}}{U_0}\right)^2 \overline{\nabla p} \tag{20}$$

An estimate of the average value of $|\bar{F}_{P,X}|$ can now be obtained easily. Thus, if $(p_2 - p_1)$ is the pressure rise across the blade row and c is the true chord length

$$|\bar{F}_{P,X}| \approx \left(\frac{\rho_{g1}}{\rho_w}\right)\left(\frac{V_{g1}}{U_0}\right)^2\left(\frac{r_0}{c}\right)\left(\frac{p_2 - p_1}{\rho_{g1} V_{g1}^2}\right) \approx 0.001 \times 1^2 \times 6 \times 0.5 \approx 0.003 \tag{21}$$

where the values are representative for a high bypass-ratio engine operating at idle power. This suggests that the maximum value of $|\bar{F}_{P,X}|$ is unlikely to exceed about 10^{-2}. From Eqs. (17), it can be seen that $|\bar{F}_{P,X}|$ is to be compared with the centrifugal term $X\sin^2\beta$ which takes values from zero to about 10^{-1} depending on the location. This indicates that the pressure force is unlikely to have much influence on the water trajectories, a conclusion corroborated later by some numerical calculations using the full equations of motion.

The Aerodynamic Shear Force. Unlike the pressure force, the aerodynamic shear force depends on the form of the water on the blade surface and a general expression cannot be obtained. For the special case of a water film, however, it is possible (as in the Appendix) to consider a water packet of film thickness h so that the dimensionless shear force per unit mass of water can be written

$$\bar{\mathbf{F}}_S = \frac{\boldsymbol{\tau}_S}{\rho_w \omega^2 r_0 h} \tag{22}$$

where $\boldsymbol{\tau}_S$ (a vector quantity) is the shear stress exerted by the gas flow on the liquid surface. Expressing the shear stress in terms of a friction coefficient c_f in the usual way

$$|\bar{\mathbf{F}}_S| = \frac{c_f \rho_g V_g^2}{2\rho_w \omega^2 r_0 h} \tag{23}$$

where ρ_g and V_g are the local gas density and velocity at the blade surface (actually just outside the gas boundary layer). Using Eq. (A5) in the Appendix for the film thickness h, Eq. (23) can be written after some manipulation as

$$|\bar{\mathbf{F}}_S| = \frac{c_f \mathrm{Re}_c^{1/2}}{2\sqrt{3}} \left(\frac{\rho_{g1}}{\rho_w}\right)^{1/2} \left(\frac{r_0}{c}\right)^{1/2} \left(\frac{V_{g1}}{U_0}\right)^{3/2} \left(\frac{\rho_g V_g^2}{\rho_{g1} V_{g1}^2}\right) \left(\frac{\mu_g}{\mu_{g1}}\right)^{1/2} \tag{24}$$

where $\mathrm{Re}_c = \rho_{g1} V_{g1} c / \mu_{g1}$ is the Reynolds number based on the blade chord length and inlet relative flow conditions. Assuming that the aerodynamic shear stress acts predominantly in the X direction and inserting some approximate typical values for a high bypass-ratio engine operating at idle power gives

$$|\bar{F}_{S,X}| \approx \frac{0.005 \times 10^{5/2}}{2\sqrt{3}} \times 10^{-3/2} \times 6^{1/2} \times 1^{3/2} \times 1 \times 1^{1/2} \cong 0.04 \tag{25}$$

According to Eqs. (17), this is to be compared with $|\bar{F}_{P,X}|$ and the term $X \sin^2 \beta$ which, it was noted above, takes values from zero to about 10^{-1}. Evidently, the aerodynamic shear force is likely to exert a much greater influence on the water trajectories than the pressure force and may play a rôle comparable to the centrifugal term $X \sin^2 \beta$. Further, the aerodynamic shear force will be larger when the water is in the form of discrete droplets and rivulets which project further into the air flow.

Little more progress can be made analytically but the effect of aerodynamic shear is examined below using numerical calculations.

Water Flow on Compressor and Fan Blades

By considering the various simplified situations discussed in the previous sections, it has been possible to build up a picture of how water moves on rotating surfaces and to highlight the main factors influencing the water trajectories, these being the dimensionless blade friction factor K, the aerodynamic shear friction coefficient c_f, and possibly the fraction of momentum retained by the water after deposition. When the water is in the form of a laminar film K and c_f can be estimated with some confidence but when the water exists as droplets or thin rivulets analysis is more or less impossible. In these situations, the best strategy is to conduct parametric studies with a range of values of K and c_f in an attempt to establish upper and lower bounds of the operational behavior.

Water Flow on a Model Compressor Rotor Blade. As part of a more general study on the effects of rain ingestion on aeroengine performance, calculations of water movement on a laboratory low-speed compressor rotor blade following deposition were undertaken using the methods described in this paper. In the computational fluid dynamics (CFD) simulation, the compressor operated at a rotational speed of 4300 rpm with a midspan flow coefficient (axial air velocity/mean blade speed) of 0.54. Full details of the compressor and the water injection experiments are given by Day et al. [7].

The deposition rates and impact velocities over the blade surface were estimated using a particle tracking computer program. Upstream of the blade, 100 μm-diameter water droplets were "computationally launched" with zero slip velocity relative to the air and a uniform distribution over the inlet area. Subsequently,

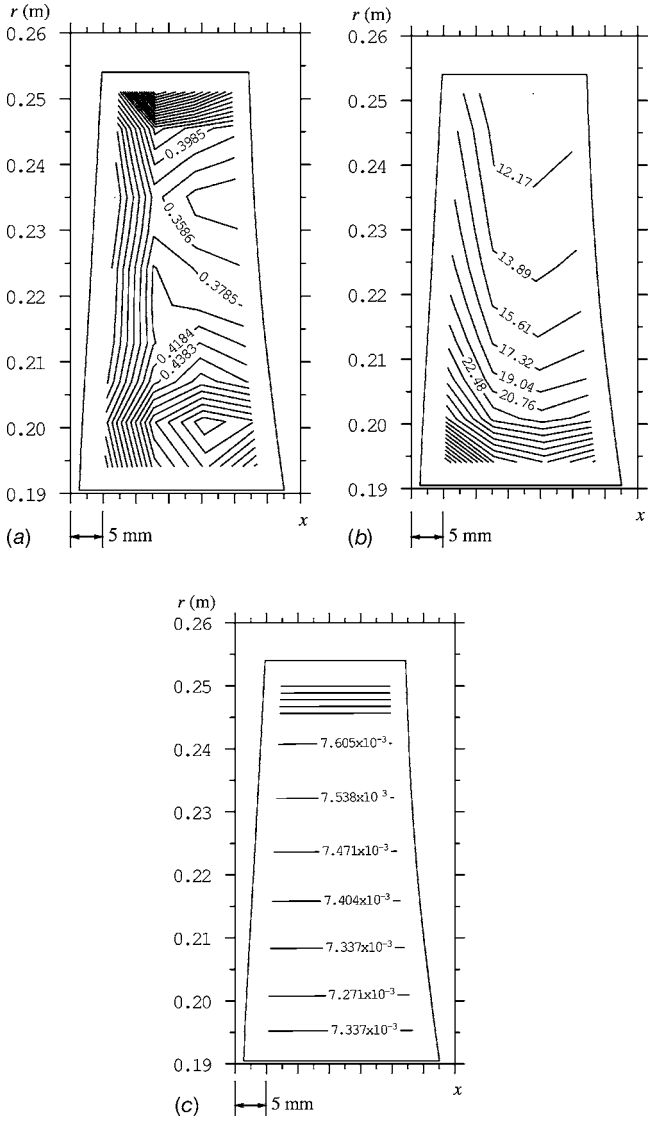

Fig. 10 Water movement on a model compressor rotor blade pressure surface (200,000 100-μm-diameter droplets tracked with uniform inlet distribution, water-to-air mass flowrate ratio =0.1, ϕ=0.54). Contours of: (*a*) deposition rate (g/cm²/s); (*b*) dimensionless friction factor *K*; and (*c*) blade skin friction coefficient c_f.

the droplets developed a slip velocity due to the curvature of the air streamlines within the blade passage with the result that deposition on the pressure surface occurred. For this size of droplet, the trajectories were scarcely affected by the air flow and could be well approximated by straight lines. Smaller droplets would deviate less from the gas streamlines due to their lower inertia thus giving less deposition. However, the size of the tracked droplets is unimportant since this paper is concerned solely with the behavior of water on the blade surface. It was assumed that the droplets did not break up during their motion.

Figure 10(*a*) shows how the deposition rate varies over the blade surface. The overall water-to-air mass flowrate ratio was 10% and 200,000 droplets were tracked. In total, 67% of the water approaching the blade was predicted to deposit. The blade curvature is higher close to the hub and hence the deposition rate is higher in this region. Assuming that the water on the blade coalesces into a laminar film, the deposition rates can be used to estimate local values of dimensionless friction factor K and film thickness h using the analysis given in the Appendix. In calculat-

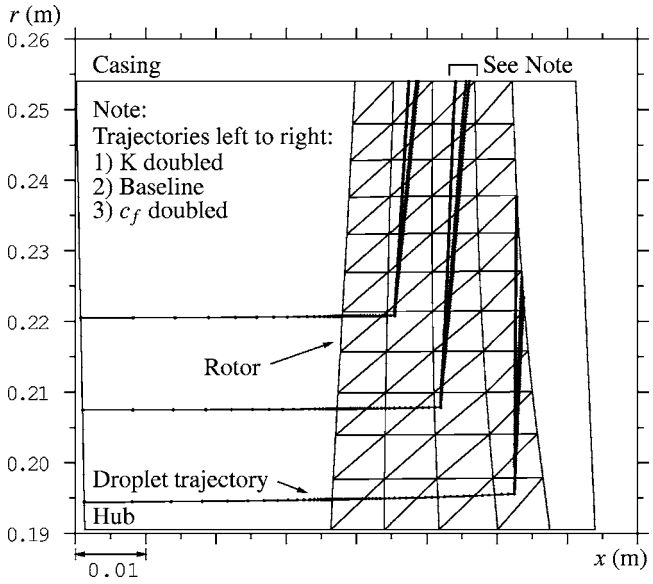

Fig. 11 Droplet trajectories on model compressor rotor blade pressure surface (baseline conditions: K=12.0, c_f=0.008, ϕ =0.54)

ing K from Eq. (A7), the water is assumed to move radially outward over the blade surface, with the flowrate over each surface grid cell equal to the sum of the deposition flowrate on that cell and the flowrate entering the cell from the adjacent cell at lower radius. Using standard correlations [8] and assuming turbulent flow in the boundary layers, local values of c_f were obtained from a Navier–Stokes CFD solution of the flow through the blade passage without water present. An estimate of the aerodynamic shear force then follows from Eq. (23). The variations of K and c_f over the blade pressure surface are shown in Figs. 10(b) and 10(c). It can be seen that K is relatively large and increases toward the hub. This is because the water flowrates are lowest in surface grid cells close to the hub, which do not "pickup" water flowing outward from cells at lower radius. The value of G in Eq. (A7) is therefore lower at the hub and this dominates over the reduction in centrifugal Reynolds number due to the lower radius, thus giving a higher K. The value of c_f is nearly constant over the blade surface, reflecting the relatively small variation in freestream Reynolds number. The contours do not extend to the blade edges because the data are defined on a relatively coarse surface grid with cell-centered storage. The angular nature of the contours again results from the coarseness of the grid.

Calculations of the water trajectories were made using the equations of motion both with and without the acceleration terms. However, because the values of K were high (see Fig. 10(b)), there was essentially no difference between the results of the two calculations. Figure 11 shows the water trajectories using the minimum value of K from Fig. 10(b) (12.0) and the maximum value of c_f from Fig. 10(c) (0.008). Taking these values, the effects of friction in driving the trajectories toward the radial direction are not overestimated and the effects of the aerodynamic shear force in moving the trajectories toward the blade trailing edge are not underestimated. It was assumed that all the momentum of the impacting droplets was given up to the blade, which was shown to be reasonable when K is large and the high friction rapidly damps the initial motion. This assumption is also supported by empirical evidence, such as observations of rain droplets striking a car windscreen when traveling at speed. It can be seen that the water flow is predominantly in the radial direction and it is predicted that about 86% of the deposited water reaches the tip of the blade before the trailing edge.

Figure 11 also shows water trajectories where the value of K has been doubled (maintaining the same value of c_f) but this has a relatively small effect in as much as 92% of the deposited water now reaches the tip. Finally, Fig. 11 shows trajectories where the value of c_f has been doubled (maintaining the original value of K) and this also has a small influence, with 85% of the water now reaching the tip. This suggests that earlier concerns about the potential magnitude of this force may be unjustified. The effect of the streamwise pressure gradient was included in the calculations using data from the CFD solution, but was found to be negligible, with a doubling of the pressure gradient term making no noticeable difference to the trajectories. Since the water motion on the blade is effectively independent of the aerodynamic forces, it is unnecessary to account for changes in the flow field that may result from the disturbance caused by the water. The effect of the lean angle was also unimportant. In all cases the flow is predominantly radial, thus justifying the assumption to this effect that was made when calculating K.

Water Flow on an Aero-Engine Fan Blade. Similar calculations were undertaken for an aero-engine fan blade. The operating condition was close to the design point since CFD convergence difficulties were experienced at idle speeds. Contours of deposition rate, dimensionless friction factor K, and skin friction coefficient c_f are shown in Fig. 12 and water trajectories are shown in Fig. 13. In obtaining the baseline trajectories, values of K=2.75 and c_f=0.004 were used based on the data of Figs. 12(a)–12(c) and using the same arguments as described above. The closely spaced contours near the hub at the trailing edge arise because the curvature of the blades effectively prevents deposition there. It then follows from Eq. (A7) that K is large in this region.

In general, the values of K are smaller for the aero-engine fan blade than for the model compressor blade, suggesting values of film Reynolds number significantly higher than 500 (from Fig. 7). This is due to the high-power condition at which the fan is operating. Larger values of K, perhaps more similar to those calculated for the model compressor, might be expected at idle conditions. However, despite these lower values of K, Fig. 13 shows that the water movement is still predominantly radial.

The same parametric studies of K and c_f were conducted for the aero-engine fan blade as for the model compressor blade and Fig. 13 shows that similar results were obtained. The percentages of deposited water that reach the tip are now 38% (baseline), 35% (c_f doubled), and 70% (K doubled). The lower value of K means that doubling its value has a much greater effect than for the model compressor blade. However, although the percentages of deposited water reaching the tip are lower than for the model compressor blade, it should be noted that the fan blade has a very much larger span. Further, the calculations predict that all of the water that leaves the fan blade trailing edge will enter the bypass duct rather than the core engine. In total, 54% of the water approaching the fan is deposited, but the higher blade curvature at the hub effectively catches all the water that might otherwise enter the core engine. Smaller droplets that can follow the gas streamlines more effectively will enter the core but the core water mass flowrate will still be low, since the majority of the water mass is in the larger droplet sizes. At idle speeds, reduced air velocities will lead to lower deposition rates as larger water droplets will be more able to follow the curved gas streamlines. Thus, the core water mass flowrate will be higher.

Figure 13 also shows results obtained using the high friction approximation, i.e., neglecting the acceleration terms. The lower value of K means that the results are now noticeably, although still not greatly, different. The effect of the streamwise pressure gradient was again found to be negligible as was the effect of the lean angle α.

Conclusions

A method has been presented for calculating the trajectories of liquid water moving on a general rotating surface. After first in-

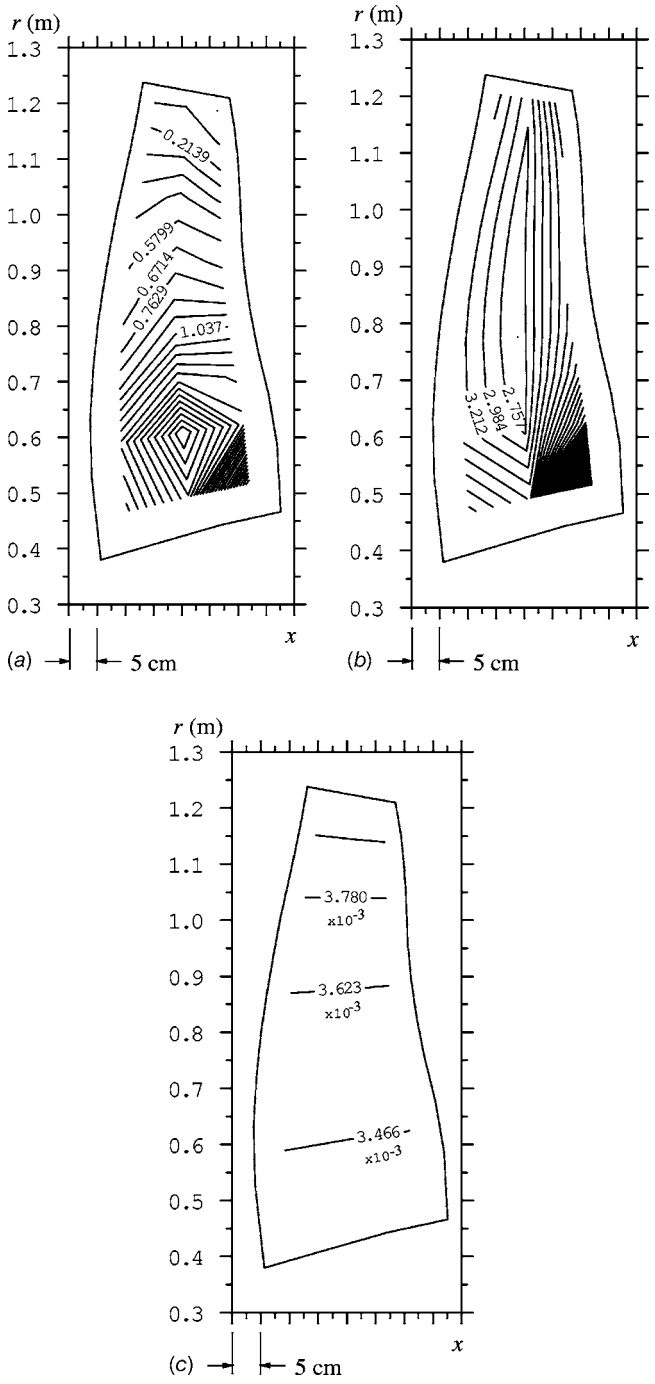

Fig. 12 Water movement on an aero-engine fan blade pressure surface (200,000 100 μm-diameter droplets tracked with uniform inlet distribution, water-to-air mass flowrate ratio=0.1, engine close to design point). Contours of: (*a*) deposition rate (g/cm^2/s); (*b*) dimensionless friction factor *K*; (*c*) blade skin friction coefficient c_f.

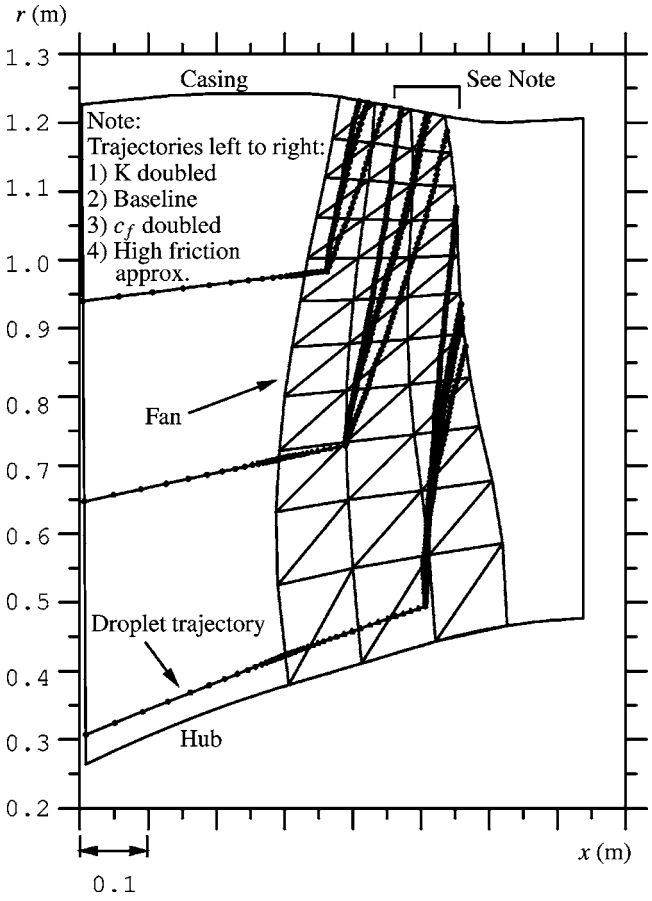

Fig. 13 Droplet trajectories on an aero-engine fan blade pressure surface (baseline conditions: K=2.75, c_f=0.004, engine close to design point)

vestigating the dynamics of the motion for the simplest possible case of a rotating flat plate, the method has been applied to a model compressor rotor blade and an aero-engine fan blade. The blade surface was divided into a collection of triangular facets and the water trajectories calculated for each facet crossed in turn. The motion was found to be dominated by the inertia forces (centrifugal and Coriolis) and the frictional resistance force opposing motion on the blade. The streamwise aerodynamic shear force was modeled assuming a laminar film of water on the blade surface and found to have an insignificant effect. However, the effect may be larger if the water is in the form of discrete droplets and rivulets. The pressure gradient had a negligible effect on the water trajectories.

The important parameters were found to be the blade stagger angle, the magnitude of the frictional resistance force, and the initial water velocity on the blade. The blade lean angle had almost no effect. Representative values of the frictional resistance force were calculated for the model compressor rotor blade and the aero-engine fan blade and the motion was shown to be relatively insensitive to variations about these values. Further, the values were sufficiently high that: (i) the sensitivity to stagger angle is reduced; (ii) the second derivative acceleration terms in the equations of motion can reasonably be neglected; and (iii) the depositing water droplets can be assumed to give up all of their momentum to the blade. It has subsequently been shown that, to a good approximation, water will move radially outward across rotating turbomachinery blade surfaces during low-speed operation. The implications for high bypass ratio aero-engine designers are that: (i) during low-speed operation, any ingested rainwater will mostly enter the bypass duct; and (ii) any water that enters the core engine will be rapidly centrifuged to the casing from where it could be removed through bleed slots. Both of these conclusions are supported by engine test evidence [4].

Acknowledgment

The work was carried out in the Hopkinson and Whittle Laboratories of Cambridge University Engineering Department and was jointly funded by Rolls-Royce plc and the Civil Aviation Authority. J.C.W. is grateful for financial support from RR and a

CAA Air Registration Board Fellowship. The authors wish to thank Professor J. D. Denton and Professor W. N. Dawes of Cambridge University Engineering Department for allowing the use of their CFD codes. The assistance of Dr. S. J. Gallimore and Dr. J. J. Bolger of Rolls-Royce plc in providing the CFD input data for the model compressor and aero-engine fan is also gratefully acknowledged as is the assistance received from Dr. I. J. Day of the Whittle Laboratory.

Nomenclature

c = blade chord length
$\mathbf{e}$ = unit vector defining coordinate direction
$\mathbf{F}_B$ = blade friction force per unit mass of water
$\mathbf{F}_I$ = inertia (centrifugal and Coriolis) force per unit mass of water
$\mathbf{F}_P$ = aerodynamic pressure force per unit mass of water
$\mathbf{F}_S$ = aerodynamic shear force per unit mass of water
G = film mass flowrate per unit width
h = film thickness
k = friction factor
K = dimensionless k (k/ω)
L = length-scale
n = normal distance from plate or blade
$\mathbf{r}$ = position vector
r,θ,z = cylindrical polar coordinate system
R = dimensionless r (r/L)
$\mathrm{Re}_{\mathrm{cent}}$ = centrifugal Reynolds number $(\rho_w \omega r^2/\mu_w)$
$\mathrm{Re}_{\mathrm{film}}$ = film Reynolds number (G/μ_w)
t = time
T = dimensionless t (ωt)
U = blade or plate speed (ωr)
$\mathbf{V}$ = gas velocity relative to blade
$\mathbf{W}$ = water velocity relative to rotating blade
x,y = coordinate system on plate or blade facet
X,Y = dimensionless x and y $(x/L, y/L)$
α = lean angle of plate, blade or facet
β = stagger angle of plate, blade or facet
ϕ = trajectory angle (from radial)
μ = dynamic viscosity
ρ = density
$\boldsymbol{\tau}$ = shear stress (treated as a vector)
ω = angular velocity

Subscripts

g = gas
w = liquid water
0 = trajectory initial condition, hub radius
1, 2 = blade inlet and outlet

Appendix: Estimation of K for a Laminar Film on a Rotating Plate

The "low Reynolds number approximation" of film theory allows the water acceleration to be neglected. Ignoring the aerodynamic shear and pressure forces, the force balance on an elemental control volume is

$$\frac{\partial}{\partial n}\left(\mu_w \frac{\partial \mathbf{W}}{\partial n}\right) + \rho_w \mathbf{F}_I = 0 \tag{A1}$$

where ρ_w and μ_w are the density and dynamic viscosity of water, $\mathbf{F}_I$ is the inertia force per unit mass, and $\mathbf{W}$ is the water velocity which varies with the normal distance n from the plate. Integrating with respect to n gives the wall shear stress $\boldsymbol{\tau}_B$ (treated as a vector quantity) as

$$\boldsymbol{\tau}_B = \rho_w h \mathbf{F}_I \tag{A2}$$

Further integrations then give the mean water velocity as

$$\bar{\mathbf{W}} = \frac{\rho_w h^2}{3\mu_w}\mathbf{F}_I \tag{A3}$$

Consider now a water "packet" in the film, this being of unit width, full film thickness h, and extent δz in the direction of $\bar{\mathbf{W}}$. From Eqs. (A2) and (A3) the wall frictional force per unit mass $\mathbf{F}_B$ acting on this packet is

$$\mathbf{F}_B = -\frac{\boldsymbol{\tau}_B \delta z}{\rho_w h \delta z} = -\frac{3\mu_w}{\rho_w h^2}\bar{\mathbf{W}} \tag{A4}$$

Hence, from Eq. (1) in the main text

$$K = \frac{k}{\omega} = \frac{3\mu_w}{\rho_w h^2 \omega} \tag{A5}$$

Insight can be obtained by considering a purely radial flow on a plate with $\beta=0$ (so that the Coriolis force is zero). The magnitude of $\mathbf{F}_I$ is now $r\omega^2$ and Eqs. (A3) and (A5) give

$$K = \frac{\bar{\mathbf{W}}_r}{U_r} \tag{A6}$$

where $\bar{W}_r$ is the mean radial water velocity and $U_r = r\omega$ is the local plate speed. Defining $G = \rho_w h \bar{W}_r$ as the local water mass flowrate per unit width of plate, K can also be written as

$$K = \left[\frac{3\,\mathrm{Re}_{\mathrm{cent}}}{(G/\mu_w)^2}\right]^{1/3} = \left(\frac{3\,\mathrm{Re}_{\mathrm{cent}}}{\mathrm{Re}_{\mathrm{film}}^2}\right)^{1/3} \tag{A7}$$

where $\mathrm{Re}_{\mathrm{cent}} = \omega r^2 \rho_w/\mu_w$ and $\mathrm{Re}_{\mathrm{film}} = G/\mu_w$ are local centrifugal and film Reynolds numbers.

References

[1] Young, J. B., Yau, K. K., and Walters, P. T., 1988, "Fog Droplet Deposition and Coarse Water Formation in Low Pressure Steam Turbines: A Combined Experimental and Theoretical Analysis," ASME J. Turbomach., **110**, pp. 163–172.
[2] Meher-Homji, C. B., and Mee, T. R., 1999, "Gas Turbine Power Augmentation by Fogging of Inlet Air," *Proceedings 28th Turbomachinery Symposium*, Texas A&M University, Houston, TX, September.
[3] Young, J. B., 1995, "Condensation in Jet Engine Intake Ducts During Stationary Operation," ASME J. Eng. Gas Turbines Power, **117**, pp. 227–236.
[4] AGARD, 1995, "Recommended Practices for the Assessment of the Effects of Atmospheric Water Ingestion on the Performance and Operability of Gas Turbine Engines," AGARD Advisory Report No. 332.
[5] Gyarmathy, G., 1962, "Bases of a Theory for Wet Steam Turbines," Technical Report Bulletin 6, Inst. for Thermal Turbomachines, Federal Technical University, Zurich (English translation by U.K. Central Electricity Generating Board, No. T-781).
[6] Kirillov, I. I., and Yablonik, R. M., 1968, *Fundamentals of the Theory of Turbines Operating on Wet Steam*, Mashinostroyeniye Press, Leningrad (English translation by NASA, No. TT F-611).
[7] Day, I. J., Williams, J. C., and Freeman, C., 2005, "Rain Ingestion in Axial Flow Compressors at Part Speed," ASME Paper No. GT2005-68582.
[8] Massey, B. S., 1989, *Mechanics of Fluids*, 6th ed., Chapman and Hall, London, p. 247.

The Effect of Stagger Variability in Gas Turbine Fan Assemblies

Mark J. Wilson

Mehmet Imregun

Imperial College London,
United Kingdom

Abdulnaser I. Sayma
University of Sussex,
Brighton, United Kingdom

Fan blades of high bypass ratio gas turbine engines are subject to substantial aerodynamic and centrifugal loads, producing the well-known phenomenon of fan blade untwist. The accurate prediction of the running geometry, as opposed to the cold geometry at rest, is crucial in the assessment of aerodynamic performance, vibratory response, and noise production of the fan. The situation is further complicated by the fact that some geometric variation is inevitable even for the state-of-the-art manufacturing processes used. The aim of this paper is to investigate the effect of static stagger variability on the dynamic untwist behavior of fan assemblies. An aeroelastic model was used to show that under certain conditions the stagger pattern changes significantly, both in form and amplitude, relative to the static configuration. At other conditions, a strong correlation between the running and static patterns is demonstrated. [DOI: 10.1115/1.2437776]

Keywords: stagger variability, stagger pattern, untwist

1 Introduction

As an assembly of high aspect ratio, thin, flexible aerofoils rotates, the centrifugal and aerodynamic loads deform the blades relative to their stationary shape. Such assemblies are typically found in the fan system of gas turbine engines powering large civil airframes. The deformation induced by the running forces can reduce the tip stagger of the blades by ~5 deg, producing the well-known phenomenon of fan blade untwist. Untwist is defined as the difference between the static and running tip stagger of the fan,

$$U = U_{CF} + U_p = \phi_s - \phi_r$$

where the symbols are defined in the Nomenclature. Typically, fan blades open up under the aerodynamic and centrifugal loads, resulting in a positive value of untwist. At sea-level, where the aerodynamic loads are high, the deformation induced is greatest.

The accurate prediction of the running geometry of a fan is a crucial step in the design process. Incorrectly predicting the untwist of a fan will result in the blades assuming the wrong aerodynamic shape under running conditions. Geometric variation due to manufacturing and assembly processes are ignored during design, and it is inherently assumed that all blades in the assembly are identical.

Blade-to-blade geometric variability has been theoretically shown to alter the vibratory response to aerodynamic excitation [1], enhance flutter stability [2], and generate multiple pure tone or buzz saw noise [3]. Experimentally, the performance of a fan assembly has been shown to be influenced by blade-to-blade geometric variations [4]. It has also been noted during shock visualization experiments that the position of the shock waves forming on the suction side of transonic aerofoils may be sensitive to geometric variations [5]. However, to the best of the authors' knowledge, all analyses of geometric variability ignore the additional change in blade shape induced by the varying aerodynamic loads arising from geometric blade-to-blade variability. The aim of this paper is to investigate the effect of static stagger variability on the dynamic untwist behavior of fan assemblies.

The remainder of this paper is structured as follows. First, a discussion of the aeroelastic model used in the computational study is given, followed by a description of the transonic fan analyzed. The untwist results of a nominal assembly are then presented, followed by a discussion of the behavior of a misstaggered fan assembly.

2 Aeroelastic Formulation

To determine the running geometry of a fan blade, the deflections arising from the aerodynamic and structural loads must be calculated. There are three major computational methods that can be applied to this problem: fully coupled, closely coupled, and loosely coupled analyses [6]. Fully coupled analyses involve simultaneously integrating the structural and aerodynamic equations, and are computationally very expensive. The loosely coupled analysis technique involves iteratively applying aerodynamic and structural solvers, a method adopted by Yamamoto and August [7] and Srivastava et al. [8]. This method involves passing surface pressures derived from the aerodynamic solution to the structural solver. Blade displacements can then be calculated, and a new blade shape generated for aerodynamic analysis. This process is repeated until the change in blade displacements from one iteration to the next falls below a predetermined convergence level.

Alternatively, the structure and the fluid can be closely coupled through the use of an integrated aeroelastic code. The closely coupled method is an efficient technique for solving complex nonlinear problems and is the most widely used method in the field of aeroelasticity. Guruswamy [9] and Marshall [10] have successfully applied the integrated technique, which is the method adopted here. The computational study presented in this paper was performed using an integrated nonlinear aeroelastic code that couples a nonlinear CFD model to a linear modal model of the structure. The details of the code along with case studies are reported by Sayma et al. [11,12].

The first step in the application of the aeroelastic code to the problem of untwist prediction is as follows. A finite element structural code is used to calculate the blade deformations induced when the assembly is rotating in a vacuum. A modal analysis is also performed, and the dominant low-frequency vibration modes extracted, forming the basis of the linear modal model of the structure implemented in the aeroelastic code.

Next, the steady-state flow solution around the centrifugally displaced blades is calculated. At this stage, the blades are held fixed and are not allowed to deform in response to the aerodynamic loads. Such a configuration can be viewed as modeling very low-density flow around the assembly, in which the interac-

Contributed by the International Gas Turbine Institute of ASME for publication in the JOURNAL OF TURBOMACHINERY. Manuscript received May 25, 2006; final manuscript received June 6, 2006. Review conducted by David Wisler. Paper presented at the ASME Turbo Expo 2005: Land, Sea and Air (GT2006), Barcelona, Spain, May 8–11, 2006. Paper No. GT2006-90434.

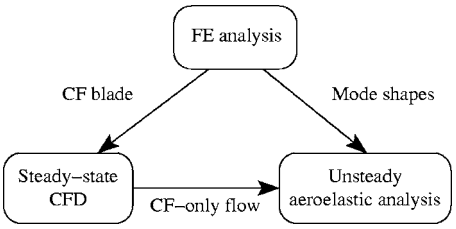

Fig. 1 Untwist prediction method

tion between the aerodynamics and the structure is very weak. Once the steady-state solution is obtained, corresponding to the geometry deformed by centrifugal loads but not aerodynamic loads, the system can be marched forward in a time-accurate fashion to find the effect of the real aerodynamic loads. In this, the pressure loads and blade displacements are exchanged between the aerodynamic and structural models at every time step. When the system reaches equilibrium, that is the steady deformation with no further vibrational motion, the untwist of the blade is determined. The structure is usually damped just below critical levels so that the untwist position can be obtained with minimum oscillation about the final position of equilibrium. Figure 1 summarizes the adopted untwist prediction method.

The aerodynamic mesh used for this computational study is semi-structured in form, being structured in the radial direction and unstructured in the axial and tangential directions [13]. The blade surface is treated as a viscous boundary and surrounded by a structured hexahedral O-mesh to resolve the large gradients normal to the wall effectively. The near-wall flow is approximated through the application of wall functions with a slip velocity at the wall. The one equation turbulence model of Spalart and Allmaras [14] is used to calculate the eddy viscosity. For the cases including the gap between the tip of the blade and the casing, the hub and casing are treated as viscous walls. When the tip gap is omitted from the model, the end walls are treated as inviscid boundaries.

During the unsteady aeroelastic calculation, the blade deforms under the aerodynamic loads. To accommodate this motion, the CFD mesh needs to be deformed at each time step. To achieve this, each edge of the mesh is assigned a stiffness and treated as a spring, a method first developed by Batina [15] and Robinson et al. [16]. As the blade moves, a Jacobi iteration scheme is used to calculate the displacement at each node from force balance considerations. To maintain the integrity of the mesh as the blade moves, the stiffness of an edge is set to be inversely proportional to the square of its length. This ensures that the bulk of the blade motion is absorbed in the larger cells that can tolerate the largest deformation without collapse. To maintain mesh integrity during large-scale deflections, the points on the casing must be allowed to slide along the casing surface.

As well as large displacements in the circumferential direction as the blade deforms in response to the aerodynamic loads, the tip will move radially relative to the casing. For the inviscid end-wall model, the motion of the blade normal to the casing is ignored, ensuring that the blade tip remains on the casing line. For the cases including the tip gap, the extent of the tip gap will vary as the blade untwists. As a result, the mesh above the blade is redistributed to maintain an even distribution of points radially. Figure 2 shows the projection of the mesh onto a plane normal to the tip stagger line before and after a typical deformation.

3 Case-Study Description

The coupled aeroelastic code presented above was applied to a typical transonic fan designed to power a large civil airframe. The details of the blading are listed in Table 1. The dominant low-frequency mode shapes spanning frequencies from 50 Hz to 200 Hz used in the analysis are shown in Fig. 3.

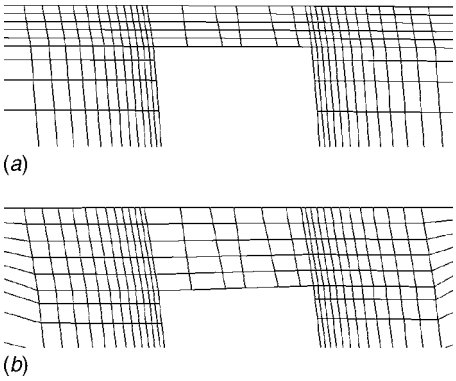

Fig. 2 Projection of tip-gap mesh onto plane normal to tip stagger line at 7% chord: (*a*) before and (*b*) after a typical deformation

A characteristic feature of the flow around a transonic fan is the presence of a shock wave near the tip of the blade. The position of the shock wave changes as the rotational speed of the fan is varied, producing complex shock structures. The position of the shock strongly influences the lift distribution over the aerofoil surface and, hence, impacts the untwist generated by the aerodynamic loads, the "pressure untwist." At low shaft speeds, the shock forms on the suction surface of the blade ahead of the passage; the shock is "expelled" from the blade passage and the flow is "unstarted." At high rotational speeds, the shock moves rearward and forms in the blade passage itself; the shock is "swallowed" and the flow is "started." To investigate the dynamic untwist behavior of the fan, three operating points will be used: unstarted, started, and an intermediate condition between the two flow regimes. A schematic diagram depicting the shock structure on the casing of the fan at the three flow regimes is shown in Fig. 4.

Aside from the position of the shock relative to the blade, the altitude at which the fan operates greatly influences the aerodynamic loads and, hence, the pressure untwist. The low-pressure, low-density air at a typical cruise altitude near the edge of the troposphere induces only a small pressure untwist. Operating the fan at sea level greatly increases the aerodynamic forces on the aerofoil, generating higher levels of pressure untwist. Hence, the blade-to-blade variation in aerodynamic loads arising from geo-

Table 1 Transonic fan parameters

Aspect ratio (height/midheight chord)	2.3
Bypass ratio	5 to 7
Number of blades	26
Tip stagger	63–68 deg

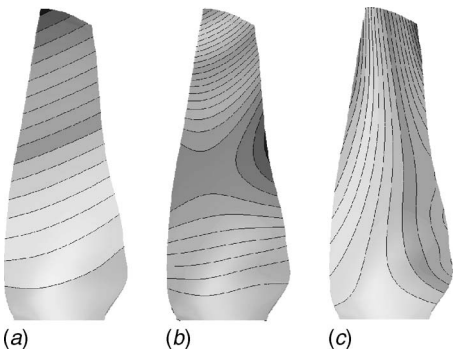

Fig. 3 Dominant low-frequency mode shapes: (*a*) first flap, (*b*) second flap, and (*c*) first torsion

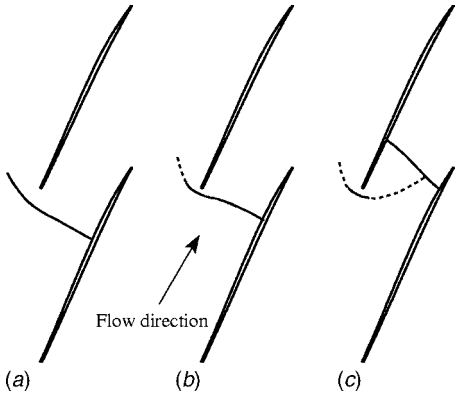

Fig. 4 Schematic diagram of shock location for nominal blade near the tip: (*a*) unstarted, (*b*) intermediate, and (*c*) started flow

metric variability will be greatest at this operating condition. As a result, all calculations are performed under sea-level conditions.

To ascertain the density of the aerodynamic mesh required to produce acceptably accurate untwist results, a mesh sensitivity study was carried out using two mesh densities. It was found that increasing mesh size by a factor of two only marginally influenced the predicted untwist and aerodynamic performance, as shown in Figs. 5 and 6. The isentropic efficiency of the fan was also relatively insensitive to the mesh used, the largest discrepancy of 0.36% occuring at peak efficiency, the mean discreapancy being 0.19%. As a result of this study, the coarser meshes containing approximately 200,000 and 320,000 points per blade passage for the inviscid and viscous end-wall models, respectively, were adopted for the analysis.

4 Nominal Assembly Results

Before a discussion of the effects of stagger variability is given, it is useful to investigate the untwist behavior of a nominal assembly at the desired operating points. To analyze a misstaggered assembly, all blades in the assembly must be included in the model. However, if all blades are identical, only a single passage is required with appropriately defined periodic boundaries. As such the model size and, hence, computational effort required is greatly reduced, allowing a wider range of conditions to be analyzed. Exploiting this, the analyses at the three speeds giving rise to unstarted, started, and the intermediate flow regimes was extended to generate constant speed characteristics. In reality, a characteristic is generated by changing the size of the exit nozzle of the fan. Computationally, this is achieved by modifying the static pressure profile prescribed at the exit boundary. The shaft speeds producing unstarted and started flow on the working line are denoted "low" and "high," respectively.

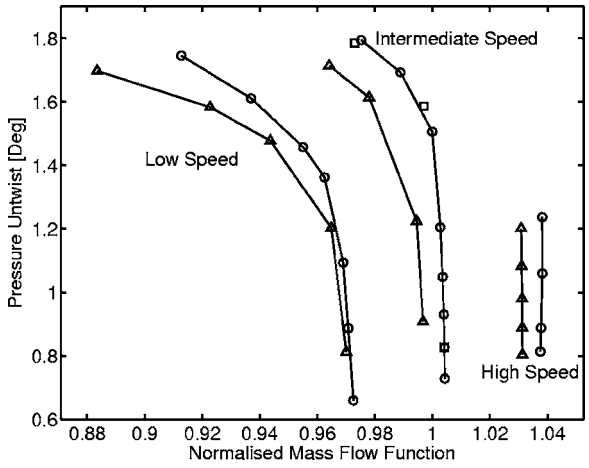

Fig. 6 Fan untwist: △: CF+gas with tip gap, ○: CF+gas without tip gap, and □: fine mesh CF+gas without tip gap

The fan characteristics are shown in Fig. 5 for blades displaced by the centrifugal forces only (denoted as "CF only") and for blades displaced by both centrifugal and aerodynamic loads (denoted as "CF + gas"). Results for models including and excluding the tip gap are shown. The corresponding pressure untwist for each case is shown in Fig. 6, and the CF-only and CF+gas tip static pressure distributions for the working line points are shown in Figs. 7 and 8, respectively.

One main difference between the CF-only and the CF+gas characteristics is in the mass-flow rate passing through the fan. As the fan untwists in response to the aerodynamic loads, the stagger reduces and the blades turn toward the axial direction. This increases the throat area of the fan and, hence, the mass-flow rate increases, shifting the characteristic to the right.

As the characteristic is traversed from high to low pressure ratio (i.e., from the "stall side" to the "choke side" of the characteristic), the pressure untwist reduces. For the extent of the generated characteristics, the pressure untwist reduces by ~1.2 deg at the low and intermediate speeds for the analyzed geometry. The partial characteristic at high speed displays a correspondingly small

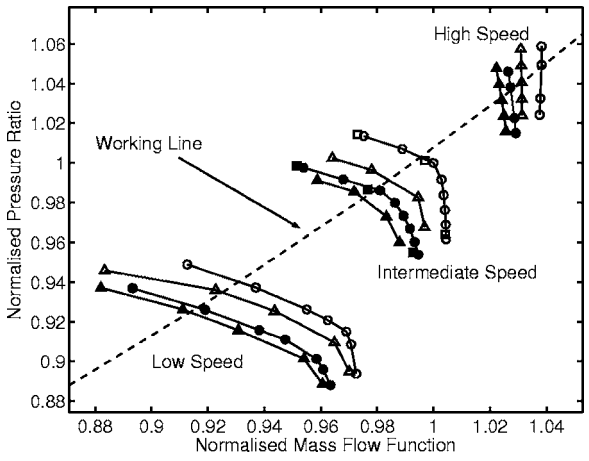

Fig. 5 Fan characteristics: ▲: CF-only with tip gap, △: CF+gas with tip gap, ●: CF-only without tip gap, ○: CF+gas without tip gap, ■: fine mesh CF-only without tip gap, and □: fine mesh CF+gas without tip gap

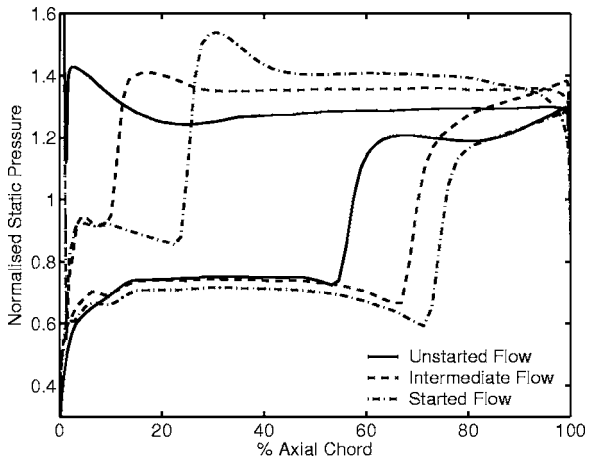

Fig. 7 Fan-blade static pressure distributions on working line, CF-only without tip-gap, 91% height

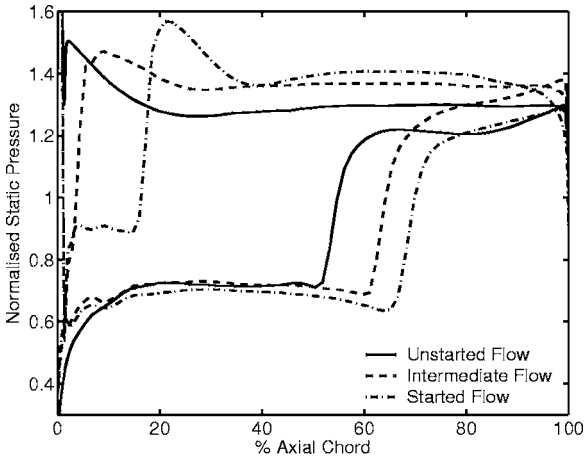

Fig. 8 Fan-blade static pressure distributions on working line, CF+gas without tip-gap, 91% height

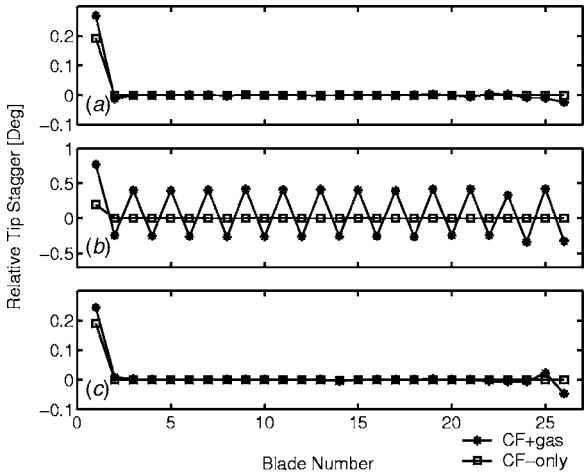

Fig. 9 Tip stagger relative to nominal blade, blade 1 misstaggered (+0.2 deg): (*a*) unstarted, (*b*) intermediate, and (*c*) started

pressure untwist variation, namely, 0.4 deg. Increasing the nozzle size at constant speed has a similar effect on the flow structure as increasing the speed at constant nozzle size; the shock moves rearward, toward the trailing edge of the blade, as can be seen in Figs. 7 and 8. As the shock moves rearward, the distribution of lift changes, thereby reducing the pitching moment about an axis in the direction of the span of the blade. This results in the reduced pressure untwist displayed in Fig. 6.

The reduction in pressure untwist as the pressure ratio of the fan is lowered has an effect on the shape of the predicted characteristic. The CF+gas characteristic is steeper on the choke side than the CF-only case, where the blade geometry held fixed for all operating points. This is because the reduction in untwist results in a reduction in flow area, thereby lowering the mass-flow capacity of the fan. At high speed, the characteristic has "fallen over," that is, the mass flow reduces with reducing pressure ratio. At the intermediate speed, a study was performed where the fan geometry was fixed at the CF+gas working line point and a characteristic generated. The fixed geometry blade passes 0.8% more flow than the dynamic untwist case. This highlights the importance of including the correct fan geometry when the pressure untwist is significant.

As can be immediately seen, including the tip gap in the model only marginally influences the dynamic untwist behavior of the nominal fan. The change in shape and location of the characteristics is comparable with the inviscid end-wall cases, as is the range of pressure untwist at each speed.

5 Misstaggered Assembly Results

There are numerous geometric features of a fan blade that vary from one blade to another. The shape of the leading edge, thickness distribution, camber lines, stagger distribution, and blade chord represent only a selection of parameters that can vary as a result of manufacturing limitations. Variation can also arise during assembly when blades are located at subtly different axial locations. Small variations in root location are magnified at the tip of the high aspect ratio blades. The tip stagger of a blade is intimately related to untwist, and is also a powerful aerodynamic parameter. For this reason, tip stagger was chosen as the variable feature between otherwise identical blades.

The stagger variation was achieved by modifying the stagger profile of individual blades in a linear fashion and applying zero displacement at the root and maximum stagger change at the tip. The deformations of blades rotating in a vacuum serve to reduce the stagger variation of an assembly relative to static conditions; a ±0.35 deg static misstagger translates to a ±0.26 deg misstagger at the intermediate shaft speed. However, the stagger variation changes by only 0.003 deg from the low- and high-speed cases studied here, for this level of static misstagger. As such, all stagger variations were applied to the centrifugally displaced blades, acknowledging that this translates to a slightly larger static stagger variation. All mechanical properties of the blades were held fixed, ensuring that all observed effects originate from aerodynamic effects caused by the imposed geometric variability.

5.1 Unstarted and Started Flow. Untwist calculations for assemblies containing a solitary misstaggered blade (±0.2 deg tip stagger) were performed at both low and high shaft speeds corresponding to unstarted and started flow conditions, respectively. The range of imposed misstagger is well within typical manufacturing tolerances. The results presented in this section are derived from calculations with inviscid end walls, that is omitting the tip gap. The CF-only and predicted CF+gas tip stagger patterns are shown in Figs. 9(*a*), 9(*c*), 10(*a*), and 10(*c*). The blades are numbered consecutively in the direction of rotation of the fan.

For both unstarted and started flow conditions, the presence of a solitary misstaggered aerofoil in the assembly predominantly influences the untwist of the misstaggered blade itself. The misstagger changes the passage geometries either side of the rogue blade, thereby changing the shock location on the pressure and suction surfaces of the blade. The misstaggered blade is therefore subject to a lift distribution that is distinct from the nominal, and,

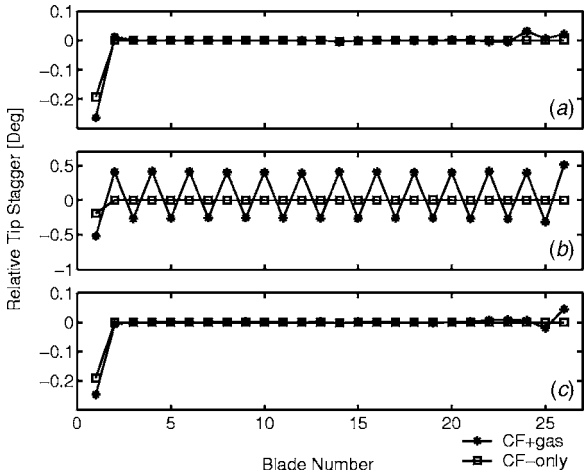

Fig. 10 Tip stagger relative to nominal blade, blade 1 misstaggered (–0.2 deg): (*a*) unstarted, (*b*) intermediate, and (*c*) started

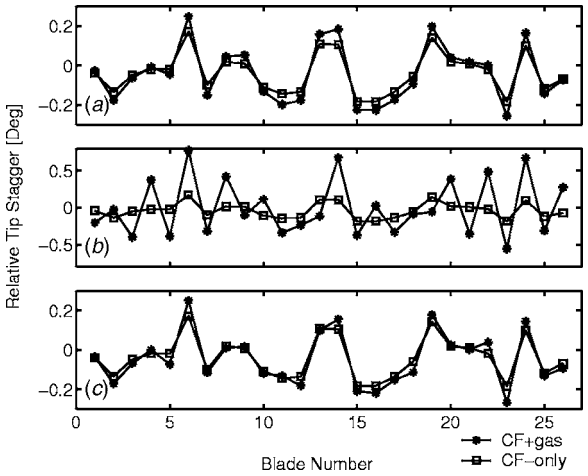

Fig. 11 Tip stagger relative to nominal blade, random misstagger: (*a*) unstarted, (*b*) intermediate, and (*c*) started

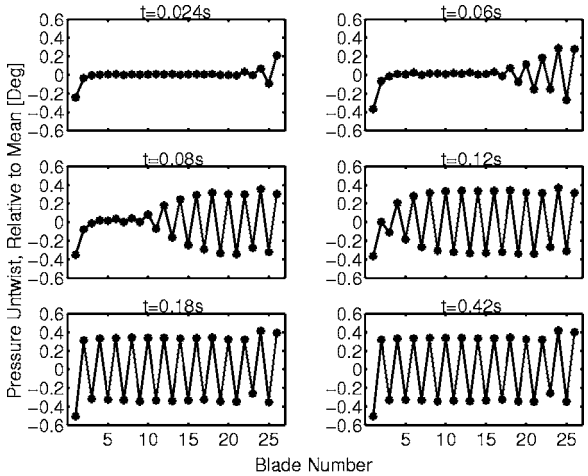

Fig. 12 Intermediate speed pressure untwist snapshots, blade 1 misstaggered (+0.2 deg)

hence, untwists differently. The aerofoils adjacent to the misstaggered blade are also subjected to a different lift due to the passage geometry changes, and untwist accordingly. The first upstream blade, that is the blade adjacent to the misstaggered blade in the direction of rotation, is only marginally influenced by the misstaggered blade. The domain of influence extends further downstream to the second or third blade, depending on the operating condition. This suggests that geometry discrepancies in the passage adjacent to the suction surface of the blade are most influential in terms of untwist. The change in untwist on all blades other than the misstaggered blade is very subtle (±0.04 deg) and considerably lower than the imposed stagger variation of ±0.2 deg. The resultant stagger patterns for the two cases studied display symmetry; that is, the predicted pattern for the +0.2 deg case is approximately the same, up to a sign, as the predicted pattern for the –0.2 deg configuration.

Similar untwist calculations were performed for an assembly containing blades misstaggered randomly in the range [–0.2, 0.2]. The CF-only and predicted CF+gas patterns are shown in Figs. 11(*a*) and 11(*c*). For both operating conditions, the CF+gas pattern closely resembles the CF-only configuration. In general, the most severely misstaggered blades deviate from the CF-only pattern by the greatest margin. The CF-only stagger range increases by 42% and 45% after the aerodynamic loads have been accounted for, for unstarted and started flow, respectively. The results show that the CF-only pattern can be used as a good approximation of the CF+gas configuration, provided that the nominal untwist is accounted for.

5.2 Intermediate Flow Condition. Untwist calculations for the stagger patterns discussed in Sec. 5.1 have been carried out at the intermediate shaft speed, near the transition between unstarted and started flow regimes. As above, the results here are derived from a model excluding the gap between the tip of the blade and the casing. At this operating point, the shock wave forms near the leading edge of a nominal blade in a uniformly staggered assembly.

The CF-only and CF+gas stagger patterns for assemblies containing a solitary misstaggered blade and a random assembly are shown in Figs. 9(*b*), 10(*b*), and 11(*b*). The contrast between the intermediate flow condition and the started and unstarted flow regimes discussed in Sec. 5.1 is clear. Whereas for unstarted or started flow, the domain of influence of a solitary misstaggered blade is limited to its close neighbors, at the intermediate condition the untwist of every blade in the assembly is influenced by the misstaggered blade. The CF+gas patterns shown in Figs. 9(*b*) and 10(*b*) overwhelm the prescribed CF-only misstagger, with a 0.2 deg misstagger, resulting in a blade-to-blade pressure untwist variation of ±0.54 deg, as opposed to ±0.074 deg for unstarted flow.

The generation of the "saw-tooth" pattern at the intermediate condition can be explained as follows. Consider the configuration comprising a single misstaggered blade (denoted blade 1) that is closed by 0.2 deg, that is the stagger is increased by +0.2 deg relative to a nominal blade. As before, the blades are numbered consecutively from 1 to 26 in the direction of rotation of the fan. The presence of the misstaggered blade changes the geometry of both adjacent passages in the CF-only assembly. The shock wave in the passage adjacent to the pressure surface of the misstaggered blade; that is, the passage between blades 1 and 2 moves rearward toward the trailing edge as a result. Analogously, the shock wave in the passage between blades 26 and 1 moves forward toward the leading edge. The change in lift distribution affects the untwist of the misstaggered blade and also its immediate neighbors. The lift distribution of blade 2 is only marginally changed, due to a small movement of the shock on the suction surface, and so the untwist is only subtly affected. Blade 26, on the other hand, is subject to a larger change in lift relative to nominal, caused by the relatively large shock movement on the pressure surface, increasing the overall torque exerted by the gas about the span of the blade. The greater pitching moment increases the pressure untwist of blade 26 relative to a nominal assembly. This, in turn, affects the geometry of the passage between blades 25 and 26, causing the shock to move rearward. The untwist of blade 25 is duly affected by the change in pressure surface shock position. At this operating condition, the shock is very sensitive to misstagger. Indeed, it has been shown that the nominal equilibrium is unstable relative to misstagger [17]. The instability results in the unattenuated propagation of the pattern, in contrast to the localized disturbance from nominal for the started and unstarted flow conditions.

Figure 12 shows the unsteady process resulting in the saw-tooth pattern at the intermediate flow condition. After 0.024 s, the stagger pattern is reminiscent of the CF+gas pattern for started flow, although the variation from the mean is larger. The amplitude of the pressure untwist grows further, up to ±0.35 deg, thereby extending the region of influence of the solitary misstaggered blade. The saw-tooth pattern propagates around the entire annulus, in the direction opposite to the rotation of the fan, until the signal reaches the misstaggered blade once more. The time evolution of the mass-flow rate, total pressure ratio, and isentropic efficiency of the fan during the unsteady process is shown in Fig. 13. Up to ~0.02 s, the aerodynamic forces displace all blades away from the CF-only equilibrium. During this phase, the total pressure ra-

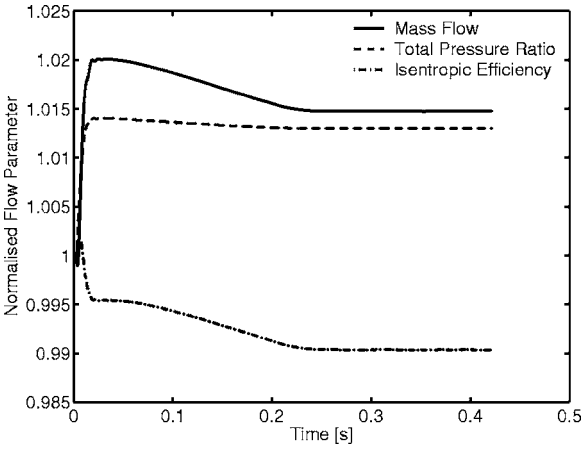

Fig. 13 Time evolution of flow parameters, normalized to CF-only steady-state, intermediate speed, blade 1 misstaggered (+0.2 deg)

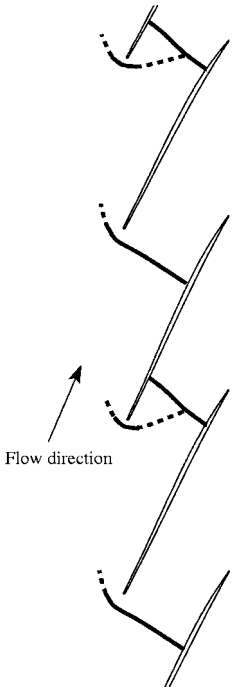

Fig. 14 Schematic diagram of shock structure on casing for equilibrium running geometry, no tip-gap, one blade misstaggered (+0.2 deg)

tio and mass-flow rate increase while the isentropic efficiency decreases, in agreement with the results presented in Sec. 4. Between approximately 0.02 s and 0.25 s, the saw-tooth pattern propagates around the annulus, causing the mass-flow rate and isentropic efficiency of the fan to steadily reduce. The total pressure ratio of the fan also reduces slightly during this phase of the unsteady process.

A significant difference between the unstarted and started flow regimes and the intermediate flow condition is the correlation between the CF+gas and CF-only patterns for the random stagger pattern, shown in Fig. 11. As noted above, for unstarted and started flow the CF-only and CF+gas patterns are similar, differing only in variance. The correlation coefficient between the CF+gas and CF-only patterns for unstarted and started flows is high, at 0.99 and 0.98, respectively. At the intermediate flow condition, however, the CF-only and CF+gas stagger correlation drops substantially to 0.62, showing the significant change in the stagger pattern at this condition. This suggests that the CF-only stagger pattern cannot be directly used to infer a CF+gas stagger pattern at this operating condition.

The resultant saw-tooth pattern for an assembly containing a single misstaggered blade strongly resembles the behavior noted by Carstens and Belz [18], who observed a similar pattern emerging prior to a transonic cascade running into flutter. Carstens and Belz did not model any blade-to-blade variability, the pattern was produced as a result of the unsteady aerofoil vibration forcing the blades from the nominal unstable equilibrium.

5.3 Two Misstaggered Blades. Figure 12 shows that when the saw-tooth pattern extends around the entire annulus and approaches the misstaggered blade, it is in phase with itself. The even number of blades in the assembly ensure this is the case. This raises the question as to what would happen if the pattern was not in phase when it interacts with itself or another similar pattern. This is the case when two misstaggered blades are introduced in an otherwise nominal assembly. One such configuration in the 26 blade assembly used in this study is where diametrically opposite blades are misstaggered by +0.2 deg. Let the misstaggered blades be denoted by A and B. Allowing this configuration to untwist in response to the aerodynamic loads initially generates saw-tooth patterns emanating from both A and B. The pattern produced by A propagates until it reaches blade B. At this instant the pattern emanating from blade B is out of phase with that produced by A. As such, destructive interference occurs due to the changing pressure distribution on the pressure surface of blade B. This increases the pressure untwist of blade B toward the unstable nominal equilibrium, allowing the pattern generated by A to propagate past B. Because of the symmetry of the situation, the same process occurs at blade A in response to the pattern emanating from B. Therefore, when the pattern initially produced by blade A reaches blade A once more, it is out of phase. This once more initiates a destructive interference process, and the saw-tooth pattern propagation continues. The aeroelastic calculation proceeds until it eventually fails due to an accumulation of numerical errors generated by the mesh movement routine. As a result, no equilibrium between the fluid and the structure is found for this configuration.

The case with two misstaggered blades that does not allow an equilibrium between the fluid and the structure may be idealized, but it introduces an interesting phenomenon. If, for example, the assembly analyzed contained an odd number of blades, the cases containing a solitary misstaggered blade would not have produced an equilibrium configuration. The randomly misstaggered assembly analysed does have a running equilibrium. However, it is feasible, although not yet demonstrated, that an assembly where all blades are misstaggered could be built that exhibits perpetual propagation of saw-tooth patterns at the intermediate shaft speed.

5.4 Misstaggered Fan Performance. This section presents a comparison of the aerodynamic performance of misstaggered and nominal fan assemblies. The total loss in the flow around transonic blades can be considered in two parts, the loss created by the shock and the blade profile loss [19]. The strong shock forming ahead of the blade passage in unstarted flow dominates the total loss. For started flow, the complex series of shock waves forming in the blade passage reduce the shock loss relative to the unstarted case, and the blade profile loss dominates. The intermediate speed, where the shock forms near the leading edge, balances the shock and profile losses, and as such, the fan is most efficient at this condition. This discussion is relevant to the case of a misstaggered fan due to the untwist mechanism at the intermediate condition described above. The configurations containing a single misstaggered blade form a saw-tooth pattern at the intermediate flow condition. The equilibrium flow comprises alternate started and unstarted passages, as shown in Fig. 14. Both started

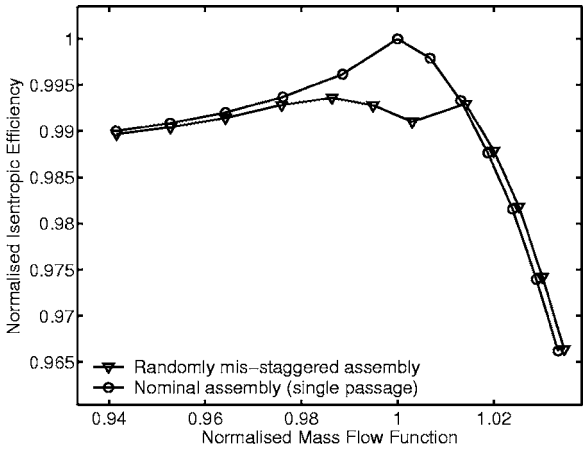

Fig. 15 Nominal versus randomly misstaggered fan isentropic efficiency along working line; Mass flow and efficiency normalized relative to intermediate operating point

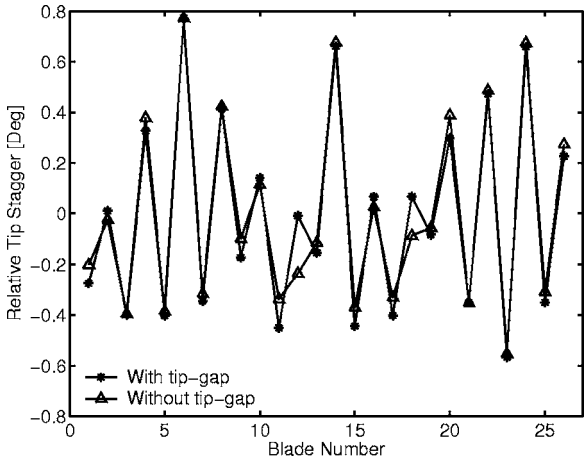

Fig. 16 Tip stagger relative to nominal blade, random misstagger, with and without tip gap

and unstarted passages generate a greater loss than nominal due to increased profile and shock losses, respectively. The increased loss reduces the efficiency of the misstaggered assembly by 0.7% of that of the nominal assembly.

Figure 15 shows the predicted isentropic efficiency of a nominal and a randomly misstaggered assembly at a range of speeds between the unstarted and started flow conditions. The mass flow and efficiency are normalized relative to the intermediate flow condition. The same centrifugally displaced blade and the same mode shapes are used at each of the speeds in this case. As such the change in blade shape due to the differing centrifugal loads is ignored, as are CF-stiffening effects. The results show that for unstarted and started flow conditions, occurring at low and high mass flow, respectively, the efficiency of the misstaggered assembly matches that of the nominal. However, for a small speed range in the vicinity of the intermediate flow condition, the efficiency of the randomly misstaggered assembly is reduced by a significant margin relative to the nominal assembly. The loss in efficiency of 0.72% of nominal is comparable to that observed for the configuration containing a solitary misstaggered blade.

5.5 Tip-Gap Effects. Including a representation of the tip gap in the untwist prediction model was shown in Sec. 4 not to alter the untwist behavior of a nominal fan. However, it remains to be shown that the tip-gap effects in a misstaggered fan assembly are significant or otherwise.

The position of the shock near the tip of the blade is influenced by the overtip flow. It does not immediately follow, therefore, that the shock position at the intermediate flow condition will display the same properties as the inviscid end-wall case. To investigate the effect of including the tip gap in the model, a tip gap was added to the randomly misstaggered assembly used in Sec. 5.2. The same gap between each centrifugally displaced blade and the casing was imposed, that is each blade has the same tip gap before it is allowed to deform in response to the pressure loads. In reality, the gap between each blade and the casing will vary, but the investigation into this form of variability is beyond the scope of this paper. However, as each blade in a misstaggered assembly untwists differently, the tip-gap at the final equilibrium position will vary from blade to blade.

The final equilibrium stagger of the misstaggered assembly is shown for both cases with and without a tip gap in Fig. 16. The two resultant patterns are very similar, differing only in subtle detail. As it is difficult to obtain precisely equivalent operating conditions for the two cases, it is not surprising that they differ slightly. The result shows that the sensitivity of the shock position with respect to small levels of misstagger is not reduced by the influence of the tip gap. This does not mean that the shock position is unaffected by the tip gap, rather the change in blade loading with respect to misstagger is insensitive to the presence of the tip gap. It is therefore concluded that a model excluding the tip gap, which is computationally more efficient, is adequate for the purpose of untwist prediction. In the authors' opinion, this is a general result and not specific to the this case.

6 Conclusions

An integrated, nonlinear aeroelastic code has been used to predict the effect of stagger variability in gas turbine fan assemblies at sea level. An analysis of a nominal assembly has also been given. The main conclusions of the study are as follows:

1. As both a constant speed characteristic and a working line is traversed at sea level, the change in blade shape due to the varying aerodynamic loads is significant. The common practice of using a constant blade shape to analyze a characteristic is shown to produce significantly different results relative to the dynamic untwist calculations.
2. The equilibrium stagger pattern at both unstarted and started flow conditions closely resembles the prescribed CF-only pattern. The pressure untwist of the most heavily misstaggered blades deviate from nominal by the greatest margin.
3. At the intermediate flow condition, the presence of a single misstaggered blade can influence the pressure untwist of every blade in the assembly. For certain configurations, this can produce an unstable condition with no equilibrium between the structure and the fluid. The CF+gas equilibrium stagger pattern for a randomly misstaggered assembly correlates poorly with the CF-only pattern, in contrast to the unstarted and started flow conditions.
4. The isentropic efficiency of a misstaggered fan is substantially reduced in the vicinity of the intermediate operating condition, relative to a nominal assembly.
5. The inclusion of a tip gap in the aeroelastic model does not significantly change the predicted untwist behavior.

Acknowledgment

The authors would like to thank Rolls-Royce plc for both sponsoring this work and allowing its publication. The support of the DTI (Project No. TP/2/ET/6/I/10073) is also gratefully acknowledged.

Nomenclature

CF = centrifugal
U = total untwist
U_{CF} = untwist due to centrifugal loads

U_p = untwist due to aerodynamic loads
ϕ_r = running tip stagger
ϕ_s = static tip stagger

References

[1] Fleeter, S., and Hoyniak, D., 1986, "Forced Response Analysis of an Aerodynamically Detuned Supersonic Turbomachine Rotor," ASME J. Vib., Acoust., Stress, Reliab. Des., **108**(2), pp. 117–124.

[2] Fleeter, S., and Hoyniak, D., 1986, "Aerodynamic Detuning Analysis of an Unstalled Supersonic Turbofan Cascade," ASME J. Eng. Gas Turbines Power, **108**(1), pp. 60–67.

[3] Stratford, B. S., and Newby, D. R., 1977, "A New Look at the Generation of Buzz-Saw Noise," AIAA Paper No. AIAA-1977-1343.

[4] Roberts, W. B., Armin, A., Kassaseya, G., Suder, K. L., Thorp, S. A., and Strazisar, A. J., 2002, "The Effect of Variable Chord Length on Transonic Axial Rotor Performance," ASME J. Turbomach., **124**(3), pp. 351–357.

[5] Roehle, I., Le Guevel, A., and Fradin, C., 1999, "3D-Shock Visualisation in a Transonic Compressor Rotor," Opt. Laser Technol., **31**(1), pp. 67–73.

[6] Kamakoti, R., and Shyy, W., 2004, "Fluid-Structure Interaction for Aeroelastic Applications," Prog. Aerosp. Sci., **40**, pp. 535–558.

[7] Yamamoto, O., and August, R., 1992, "Structural and Aerodynamic Analysis of a Large-Scale Advanced Propeller Blade," J. Propul. Power, **8**(2), pp. 367–373.

[8] Srivastava, R., Sankar, L. N., Reddy, T. S. R., and Huff, D. L., 1991, "Application of an Efficient Hybrid Scheme for Aeroelastic Analysis of Advanced Propellers," J. Propul. Power, **7**(5), pp. 767–775.

[9] Guruswamy, G. P., 1989, "Integrated Approach for Active Coupling of Fluids and Structures," AIAA J., **27**(6), pp. 788–793.

[10] Marshall, J. G., 1996, "Prediction of Turbomachinery Aeroelasticity Effects Using a 3D Nonlinear Integrated Method," Ph.D. thesis, Imperial College of Science, Technology and Medicine, University of London.

[11] Sayma, A. I., Vahdati, M., and Imregun, M., 2000, "An Integrated Non-Linear Approach for Turbomachinery Forced Response Prediction—Part 1: Formulation," J. Fluids Struct., **14**(1), pp. 87–101.

[12] Sayma, A. I., Vahdati, M., Sbardella, L., and Imregun, M., 2000, "Modelling of 3D Viscous Compressible Turbomachinery Flows Using Unstructured Hybrid Grids," AIAA J., **38**(6), pp. 945–954.

[13] Sbardella, L., Sayma, A. I., and Imregun, M., 2000, "Semi-Unstructured Meshes for Axial Turbomachine Blades," Int. J. Numer. Methods Fluids, **32**(5), pp. 569–584.

[14] Spalart, P. R., and Allmaras, S. R., 1992, "A One-Equation Turbulence Model for Aerodynamic Flows," AIAA Paper No. AIAA-1992-0439.

[15] Batina, J. T., 1991, "Unsteady Euler Algorithm With Unstructured Dynamic Mesh for Complex-Aircraft Aerodynamic Analysis," AIAA J., **29**(3), pp. 327–333.

[16] Robinson, B. A., Batina, J. T., and Yang, H. T. Y., 1991, "Aeroelastic Analysis of Wings Using the Euler Equations With a Deforming Mesh," J. Aircr., **28**(11), pp. 781–788.

[17] Wilson, M. J., Imregun, M., and Sayma, A. I., 2005, "The Effect of Stagger Variability in Gas Turbine Fan Assemblies," International Conference on Compressors and Their Systems, Sept. 4–7, Institution of Mechanical Engineers, pp. 507–515.

[18] Carstens, V., and Belz, J., 2001, "Numerical Investigation of Nonlinear Fluid-Structure Interaction in Vibrating Compressor Blades," ASME J. Turbomach., **123**(2), pp. 402–408.

[19] Cumpsty, N. A., 1989, *Compressor Aerodynamics*, Longman Scientific & Technical, UK.

Multibladerow Forced Response Modeling in Axial-Flow Core Compressors

M. Vahdati

A. I. Sayma

M. Imregun
e-mail: m.imregun@imperial.ac.uk

Imperial College,
MED,
Exhibition Road,
London SW7 2BX, UK

G. Simpson
Rolls-Royce plc,
P.O. Box 31,
DE24 8BJ, UK

This paper describes the formulation and application of an advanced numerical model for the simulation of blade-passing and low-engine order forced response in turbomachinery core compressors. The Reynolds averaged Navier–Stokes equations are used to represent the flow in a nonlinear time-accurate fashion on unstructured meshes of mixed elements. The structural model is based on a standard finite-element representation. The fluid mesh is moved at each time step according to the structural motion so that changes in blade aerodynamic damping and flow unsteadiness can be accommodated automatically. A whole-annulus 5-bladerow forced response calculation, where three upstream and one downstream bladerows were considered in addition to the rotor bladerow of interest, was undertaken using over 20 million grid points. The results showed not only some potential shortcomings of equivalent 2-bladerow computations for the determination of the main blade-passing forced response, but also revealed the potential importance of low engine-order harmonics. Such harmonics, due to stator blade number differences, or arising from common symmetric sectors, can only be taken into account by including all stator bladerows of interest. The low engine-order excitation that could arise from a blocked passage was investigated next. It was shown that high vibration response could arise in such cases. [DOI: 10.1115/1.2436892]

1 Introduction

Unsteady turbulent high-speed compressible flows often give rise to complex aeroelasticity phenomena by influencing the dynamic behavior of structures on which they act. The problem is particularly severe for aero gas turbines where virtually all bladerows are susceptible to aeroelasticity effects either by inherent self-induced motion (flutter) or by response to aerodynamic flow distortions and blade wakes (forced response). The most complex and the least understood aeroelasticity phenomena occur in multistage core compressors, the subject of this paper, because of their wide operating envelope. During engine development programs, very costly structural failures are known to occur because of a mixture of aeroelastic instabilities such as acoustic resonances, rotating stall, surge, flutter, blade passing, and low engine-order forced response, buffeting, etc. The numerical modeling of core-compressor aeroelasticity is a formidable challenge as the analysis must be able to represent accurately not only the aerodynamic and structural properties of a large number of bladerows but also the interactions through these. Two fundamental difficulties can be identified from the outset. First, the close spacing of the bladerows compromises the accuracy of single-bladerow analyses, but multibladerow studies yield very large models and may require prohibitively large amounts of CPU time for time-accurate viscous unsteady flow representations [1]. Second, the model must be able to deal with a vast range of time and length scales of the flow. For instance, the time scale can be determined by the axial propagation of the low-frequency acoustic waves, or by the blade vibratory motion at several times the blade-passing frequency. Similarly, the length scale can be the circumference/axial length of the machine, or the blade boundary layer thickness.

Here we will focus on rotor/stator interaction problems as the forced response vibration of core compressors remains a major design problem. From the outset, it is appropriate to distinguish between two types of forced response. The first type, or blade-passing forced response, is due to the excitation forces generated by the rotation of the bladed system past a nonuniform flow field, the strength of which varies periodically with angular position around the circumference. Such flow variations are mainly caused by the stator blades which act as upstream obstructions, and the rotor blades experience their wakes as time-varying forces with a frequency, or periodicity, based on the rotation speed. The spatial distribution of the forcing function will be primarily determined by the number of upstream stator blades and by its aliases with respect to the rotor blades, though the effects of downstream stages can also be significant. A Fourier transform of this forcing function will reveal the harmonics that will excite the assembly modes. Typically, such harmonics will excite high nodal diameter modes as their actual order is related to the blade numbers in the rotor/stator row of interest. Although it is difficult to predict the corresponding rotor blade vibration levels accurately, turbomachinery designers rely on Campbell diagrams, or their variants, which indicate the likelihood of encountering forced response resonances of the first type within the operating range. In principle, it is then possible to design the rotor wheels away from the primary resonances, subject to being able to predict the assembly's dynamic behavior to a required degree of accuracy.

The second type of forced response, a much less researched variant, arises when the unsteady aerodynamic forcing function contains low-order harmonics, hence the term LEO forced response. Such harmonics are due to some loss of symmetry in the flow which may be due to a general unsteadiness that persists throughout the engine. Similarly, blade-to-blade variations due to manufacturing tolerances, errors in controlling the variable stator vane angles, and "blocked" stator passages are known to generate low harmonics. A different LEO mechanism is due to multibladerow interactions: wakes from upstream bladerows and reflections from downstream bladerows give rise to engine-order (EO) harmonics of the type

$$\mathrm{EO} = nS_i - mS_j \tag{1}$$

where S_i and S_j are the stator blade numbers, n and m being two arbitrary integers. It should be noted that, for $n=1$ and $m=0$, Eq. (1) will give the main blade-passing harmonic. Similarly, the case

Contributed by the Turbomachinery Division of ASME for publication in the JOURNAL OF TURBOMACHINERY. Manuscript received February 11, 2004; final manuscript received June 3, 2005. Review conducted by Marc P. Mignolet.

$n=0$ and $m=-1$ corresponds to the excitation from the downstream stator bladerow. Generally speaking, the amplitude of the aerodynamic excitation will diminish as the values of n and m increase. Similarly, if S_i and S_j form a symmetric sector of α^0, they will create an EO harmonic of order $p=360/\alpha$ if p is an integer. Equation (1) will also apply even if both S_i and S_j are upstream of a given rotor bladerow and, as will be shown in the case study, such cases can be significant.

Given the multiple interactions, it may be argued that single bladerow models are, in the main, unrepresentative of turbomachinery unsteady flows. Indeed, the spacing between the bladerows is no more than a fraction of the blade's chord and the neighboring bladerows are aerodynamically coupled via the pressure, vorticity, and entropy waves. However, the modeling of such interactions is not straightforward. The difficulties arise not only because of a lack of typical sector due to arbitrary blade numbers, but also because of the complex propagation pattern of the elementary acoustic, entropy, and vorticity waves obtained by decomposing the stator outflow, as they travel through the bladerows. Indeed, such single-frequency waves will give rise to multiharmonics (scattering) and multifrequencies (shifting) because of its reflected and transmitted components. Also, it is not that uncommon for a wake pattern to travel through the immediate downstream bladerow without exciting it, but causing vibration response further downstream.

Given the very significant computational resources required for time-accurate forced response simulations, a great deal of research effort has been devoted to the time-linearized methods where the flow unsteadiness is considered to be a fixed-frequency small perturbation about a nonlinear, steady-state flowfield. In other words, the flow is considered to be periodic in time, a feature which allows its decomposition into a time-independent steady part and a periodic unsteady part. Such an assumption allows the calculation to be performed in the frequency domain by considering one excitation frequency at a time, though it is possible to study the effects of multifrequency disturbances by superimposing single harmonic results. The linearization of the Euler equations was performed by Lindquist and Giles [2], and Ning and He [3] while work by Clark and Hall [4] included the linearization of the viscous terms, including that of the turbulence model. The standard time-linearized formulation was extended by Chen et al. [5] who used a nonlinear harmonic approach to improve the accuracy of the unsteady flow calculations. A general methodology was developed by Sbardella and Imregun [6] who linearized the Navier–Stokes equations for three-dimensional (3D) unstructured grids of mixed elements. A potential shortcoming of standard time-linearized analyses is their inability to deal with downstream and multibladerow interactions. Similarly, multibladerow effects cannot be incorporated because of the fixed frequency assumption, though a 2D analysis by Silkowski and Hall [7] has demonstrated the feasibility extending the standard formulation to such situations. The multibladerow problem was also considered by Chen et al. [8] who combined full nonlinear time-marching and linearized methods.

The long-term objectives favor the development of virtual test models in order to shorten the development cycles by minimizing rig and flight tests. Such a task can only be achieved by time-accurate whole-annulus multibladerow models, not only from a forced response perspective, but also from a performance viewpoint. Erdos et al. [9] were among the pioneers for tackling nonlinear unsteady flows by time-marching methods. They predicted the 2D unsteady flow in a fan stage, including the use of an algorithm to treat unequal pitches. Such methods were soon extended to 3D and viscous effects were also included [10,11]. With currently available computing power, it is possible to undertake unsteady viscous flow predictions for very large models, such as the 13-bladerow turbine computation reported by Barakos et al. [12] who used an unstructured mixed-element mesh of 47 million points. Running their code in parallel mode on 32 R12000 CPUs, they quoted a computing time of about 5 min/time step, which is expensive but not unattainable for say, 10,000 time steps.

The aim of this paper is threefold: (i) to describe briefly an integrated fluid–structure interaction methodology based on combining unsteady viscous time-accurate flow modeling on unstructured meshes of mixed elements and standard finite-element representation for the structural properties of the bladerows; (ii) to apply the methodology to the blade-passing and low-engine-order multiblade forced response of core compressors with emphasis on modeling requirements; and (iii) to study the additional excitation that will arise from a blocked stator blade.

2 Overview of the Forced Response Methodology

2.1 Flow Model. The unsteady, compressible Reynolds–averaged Navier-Stokes equations for a 3D bladerow can be cast in terms of absolute velocity $\mathbf{u}$ but solved in a relative non-Newtonian reference frame rotating at angular velocity $\boldsymbol{\omega}$. This system of equations, written in an arbitrary Eulerian–Lagrangian (ALE) conservative form for a smoothly bounded control volume Ω with boundary Γ, take the form

$$\frac{d}{dt}\int_{\Omega}\mathbf{U}d\Omega+\oint_{\partial\Omega}\left(\mathbf{F}_i-\frac{1}{\mathrm{Re}}\mathbf{G}_i\right)\cdot n_i d\Gamma=\int_{\Omega}\mathbf{S}d\Omega \tag{2}$$

where i is the coordinate direction index; and n_i represents the ith direction component of the outward unit vector of the control volume boundary Γ. The viscous term $\mathbf{G}_i$ on the left hand side of Eq. (2) has been scaled by the reference Reynolds number for nondimensionalization purposes. The solution vector $\mathbf{U}_i$ of conservative variables is given by

$$\mathbf{U}_i=\begin{bmatrix}\rho\\ \rho u_1\\ \rho u_2\\ \rho u_3\\ \rho\varepsilon\end{bmatrix} \tag{3}$$

The inviscid flux vector $\mathbf{F}_i$ can be written as

$$\mathbf{F}_i=\begin{bmatrix}\rho(u_i-w_i)\\ \rho u_1(u_i-w_i)+p\delta_{i1}\\ \rho u_2(u_i-w_i)+p\delta_{i2}\\ \rho u_3(u_i-w_i)+p\delta_{i3}\\ \rho E(u_i-w_i)+pu_i\end{bmatrix} \tag{4}$$

where δ_{ij} is the Kronecker delta function; and u_i and w_i are the absolute and the grid velocities, respectively. The pressure p and the total enthalpy h are related to density ρ by two perfect gas equations

$$p=(\gamma-1)\rho\left(\varepsilon-\frac{|\mathbf{u}^2|}{2}\right);\quad h=\varepsilon+\frac{p}{\rho} \tag{5}$$

where γ is the constant specific heat ratio. The viscous flux vector $\mathbf{G}$ can be written as

$$G_i=\begin{bmatrix}0\\ \sigma_{i1}\\ \sigma_{i2}\\ \sigma_{i3}\\ u_k\sigma_{ik}+\dfrac{\gamma}{\gamma+1}\left(\dfrac{\mu_l}{\mathrm{Pr}_l}+\dfrac{\mu_t}{\mathrm{Pr}_t}\right)\partial T/\partial x_k\end{bmatrix} \tag{6}$$

where μ_l represents the molecular viscosity given by the Sutherland's formula; and μ_t denotes the turbulent eddy viscosity, which must be determined using a suitable turbulence representation, here via the one-equation turbulence model of Baldwin and Barth [13]. The laminar Prandtl number Pr_l is taken as 0.7 for air while

the turbulent Prandtl number Pr_t is taken as 0.9. The viscous stress tensor $\boldsymbol{\sigma}_{kj}$ is expressed using the eddy viscosity concept which assumes that, in analogy with viscous stresses in laminar flows, the turbulent stresses are proportional to mean velocity gradients

$$\boldsymbol{\sigma}_{ij} = (\mu_l + \mu_t)\left(\frac{\partial u_i}{\partial x_j} + \frac{\partial u_j}{\partial x_i}\right) + \lambda \delta_{ij}(\nabla \cdot \mathbf{u}) \tag{7}$$

The value of λ is given by the Stokes relationship $\lambda = -2/3(\mu_l + \mu_t)$. Vector $\mathbf{S}$, which contains the terms due to the rotation of the coordinate system, can explicitly be written as

$$\mathbf{S} = \begin{bmatrix} 0 \\ 0 \\ \rho\omega u_2 \\ \rho\omega u_3 \\ 0 \end{bmatrix} \tag{8}$$

Equation (2) is discretized on unstructured mixed-element grids via a finite volume, the details of which are given by Sayma et al. [14]. As described by Sbardella et al. [15], the blades are discretized using a semi-structured mesh which consists of brick elements in the boundary layer and triangular prisms further away in the blade passage. To achieve further computational efficiency, the mesh is characterized via an edge-based data structure, i.e., the grid is presented to the solver as a set of node pairs connected by edges, a feature that allows the solver to have a unified data structure. Furthermore, the edge-based formulation has the advantage of computing and storing the edge weights prior to the main unsteady flow calculation, hence reducing the CPU effort. The central differencing scheme is stabilized using a mixture of second- and fourth-order matrix artificial dissipation. In addition, a pressure switch, which guarantees that the scheme is total variation diminishing (TVD) and reverts to a first-order Roe scheme in the vicinity of discontinuities, is used for numerical robustness. The resulting semi-discrete system of equations is advanced in time using a point-implicit scheme with Jacobi iterations and dual time stepping. Such an approach allows relatively large time steps for the external Newton iteration. For steady-state calculations, solution acceleration techniques such as residual smoothing and local time stepping are employed. For unsteady computations, an outer Newton iteration procedure is used where the time steps are dictated by the physical restraints and fixed through the solution domain. Within the Newton iteration, the solution is advanced to convergence using the traditional acceleration techniques described previously.

For the sliding planes that occur at bladerow boundaries, the solution is updated at the interface by interpolating the variables in the stator computational domain to obtain rotor fluxes, and in the rotor computational domain to obtain the stator fluxes [16,1]. The fluxes are computed using a characteristic technique, which allows the correct propagation of the information. In other words, flow data are exchanged between the two grids via specially formulated boundary conditions at the interface.

2.2 Structural Model and Calculation of the Aeroelastic Response. It is implicitly assumed that the vibration amplitude remains within the bounds of linear behavior. The global aeroelasticity equations of a structural motion can be written as

$$\mathbf{M}\ddot{x} + \mathbf{C}\dot{x} + \mathbf{K}x = \mathbf{p}(\mathbf{t})A\mathbf{n} \tag{9}$$

where $\mathbf{M}$, $\mathbf{K}$, and $\mathbf{C}$ are the mass, stiffness, and damping matrices; $\mathbf{x}$ is the displacement vector; $\mathbf{p}(\mathbf{t})$ is a vector of pressures; A is the application area; and $\mathbf{n}$ the normal unit vector on the blade's surface. A standard structural finite-element formulation is used to obtain the left-hand side while the flow model above is used to obtain the unsteady forcing of the right-hand side. The free vibration problem can be solved to yield the natural frequencies ω_r and mode shapes $\boldsymbol{\phi}_\mathbf{r}$ of the bladed disk assembly in vacuum, r being the mode index.

The forced response analysis can be conducted in two different ways; the so-called fully coupled and the uncoupled analyses. In the fully coupled method, the structural mode shapes are interpolated onto the aerodynamic mesh as the two discretization levels between structural and aerodynamics meshes are unlikely to be wholly coincident. To accommodate the structural motion, the fluid mesh is moved at each time step using a network of springs whose compression/extension is prescribed by the mode shape at the blade surface and becomes zero at the far field. The frequency of the motion is dictated by the natural frequency of the corresponding mode. An exchange of boundary conditions takes place at the fluid–structure interface at each time step. The main advantage of the fully coupled method is the automatic inclusion of the aerodynamic damping while the main drawback is the computational overhead arising from the need to compute much longer time histories to reach periodic convergence. The unsteady pressure distribution, especially its phasing, is known to be affected by the blade vibration and hence more accurate results will be obtained by using a fully coupled method. However, the inclusion of blade motion affects the aerodynamic forcing less than it affects the unsteady pressure since the latter is an integrated quantity. A comparative study has been reported by Vahdati et al. [17] who investigated the forced response of a fan blade. In any case, unless the change in aerodynamic damping is likely to be important, say in the case of a large blade vibrating in a resonant condition, the forced response analysis can be simplified by considering the unsteady flow and the blade motion separately. Such an uncoupled analysis consists of computing the blade unsteady pressures without any blade movement. The validity of this simplification will depend on both the blade size and the actual amplitude of vibration. Extensive numerical and experimental evidence indicates that the forced response of core-compressor blades can be treated in this fashion while a coupled analysis might be required for fan assemblies for which the unsteadiness arising from the blade motion can be significant.

In the case of an uncoupled analysis, the aerodynamic damping may still be obtained from an aeroelastic transient (or flutter) analysis and these values can be used when calculating the blade's response. A case study comparing the relative accuracy of both approaches is reported by Vahdati et al. [17].

Whichever method is chosen, the excitation can be monitored by calculating the modal force $\boldsymbol{\Theta}\mathbf{r}$ corresponding to the rth mode

$$\boldsymbol{\Theta}_r(t) = \sum_{j=1}^{\text{nodes}} \phi_{rj}(\Delta A_j n_j)\mathbf{p_j}(\mathbf{t}) \tag{10}$$

where r is the mode index; j is the node index; and ΔAj is the blade surface element area associated with node j.

The modal force, which represents the strength of unsteady forcing in a particular mode of vibration, can best be visualized by considering a rigid body motion where the blade is plunging only. In this case, the modal force can be considered to be the unsteady lift on the blade. For a given mode, the strength of the modal force depends on the pressure perturbation, as well as the correlation between the pressure perturbation shape and the structural mode shape. The maximum resonant amplitude of mode r can be computed from

$$X_{\max} = \frac{\boldsymbol{\Theta} Q \boldsymbol{\Phi}_{\max}}{\omega_r^2} \tag{11}$$

where $\boldsymbol{\Theta}$ is the amplitude of the modal force after a periodic solution is obtained; $\boldsymbol{\Phi}_{\max}$ is the value of the largest modeshape element; and Q is the Q factor representing the sum of aerodynamic and structural damping. The structural part Q, consisting of inherent hysteretic damping, is determined from laboratory vibration tests while the aerodynamic part is determined from a separate flutter analysis of each bladerow. Damping due to friction at the blade root is usually ignored, though, if available, a represen-

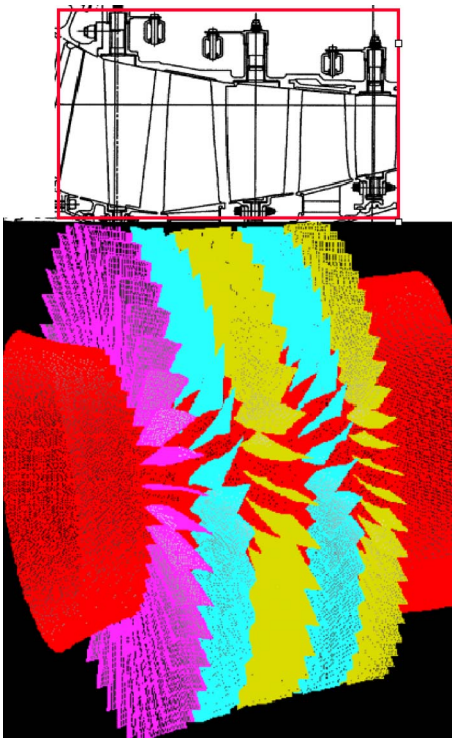

Fig. 1 The core-compressor geometry and the 5-bladerow mesh. Starting from first bladerow, the blade numbers are 40, 31, 32, 38, and 50.

tative value can be added to the inherent structural damping value. If the forced response analysis is conducted in a coupled fashion, only the structural part of Q is used as input data since the aerodynamic part is computed inherently during the computation by virtue of taking the blade motion into account.

A coupled forced response analysis must be conducted at the resonant speed and hence a new run is needed for each resonance of interest. Such an approach is not only computationally expensive, but it also requires a new set of aerodynamic boundary conditions at each new analysis speed. On the other hand, a major advantage of the uncoupled method is its ability to rank all modes within a relatively narrow frequency range by assuming they are all excited at the same speed.

3 Case Study

3.1 Preliminaries. As shown in Fig. 1, the case study is conducted for the first five bladerows of an aero-engine core compressor, hereafter labeled as S1 (40), R1 (31), S2 (32), R2 (38), and S3 (50), where S refers to variable-angle stator bladerows, R refers to rotor bladerows, and the number within brackets indicates the number of blades. Interest is confined to the forced response of the R2-bladerow. Because of the nonmatching blade numbers, there is no periodic sector to reduce the size of the computational domain. Therefore, the analysis can only be conducted by considering all five whole annuli, leading to a large mesh with over 25,000,000 points.

As can be seen from an inspection of a standard Campbell plot, resonance will occur each time an EO excitation matches, both in frequency and shape, an assembly mode. Such assembly vibration modes arise from individual blade modes and are labeled in terms of nodal diameters (NDs) because of the possible disk vibration patterns. Here, the analysis is focused on R2 and the main blade-passing excitation, 32EO, which arises from the S2 wakes, as well as the potential effects. As will be discussed in the next section, a 32EO excitation will affect the 6ND mode on a 38-bladed rotor. In addition, as indicated by Eq. (1), there are low-engine-order harmonics due to blade number differences in the upstream and downstream stator bladerows. Once the unsteady aerodynamic forcing is determined at the speed(s) of interest, the blade response can be determined by computing the corresponding modal force.

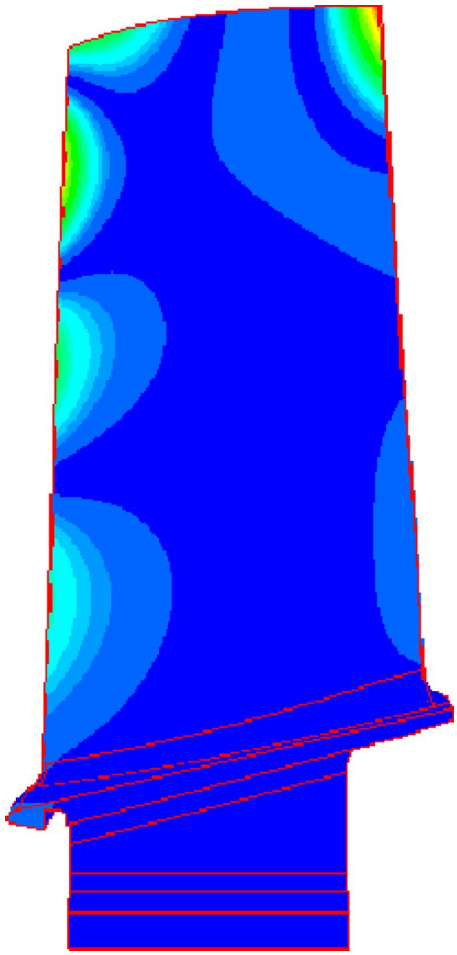

Fig. 2 Vibration mode shape displacement contours for Blade Mode 11

3.2 Structural Model. The vibration mode families of the R2 assembly, consisting of the so-called nodal diameter modes because of their actual vibration shapes, were obtained from a standard finite-element formulation. Each family corresponds to a specific blade mode, such as first flap (1F), first torsion (1T), nth blade mode (BMn), etc. In the interest of brevity, assembly modes will be labeled using "blade mode/ND number" format. For instance, an eight nodal diameter assembly mode arising from the 1T blade mode will be called 1T/8ND. Here of particular interest is Blade Mode 11/6ND because of its susceptibility to 32EO excitation arising from the main blade passing harmonic. The blade vibration mode shape is shown in Fig. 2. It is well known that an nth EO excitation will excite the corresponding nth nodal diameter mode. However, if there is periodicity R, orders n and R-n will be coupled because of spatial aliasing. In this particular case, the response will occur in BM11/6ND because of the aliasing between $n=32$EO excitation and $R=38$ Rotor 2 blades. The inherent structural mechanical damping was represented using a Q factor value of 200 for all modes included in the calculations.

3.3 Blade-Passing Forced Response Computations. Using the 5-bladerow mesh of Fig. 1, the first set of forced response calculations were conducted at the shaft speed of 12,000 rpm. The

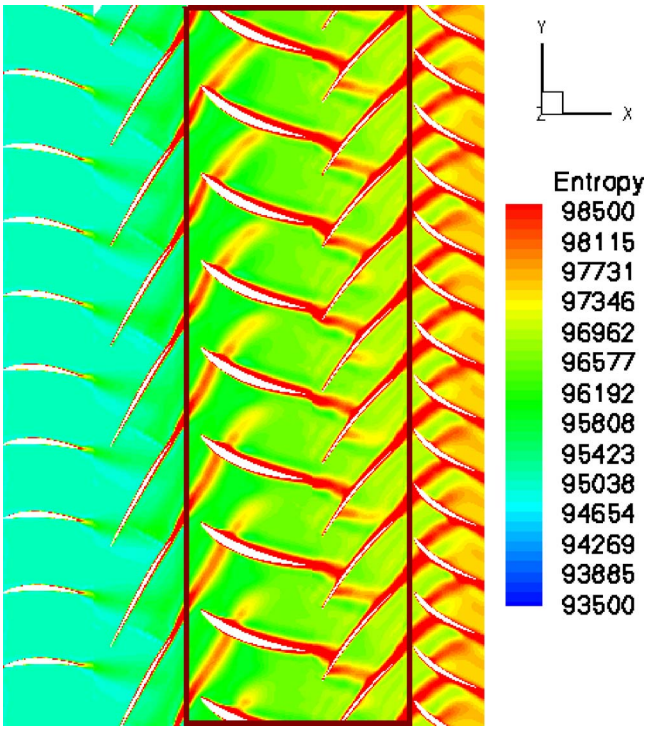

Fig. 3 Instantaneous entropy contours at 90% blade height (5-bladerow computation)

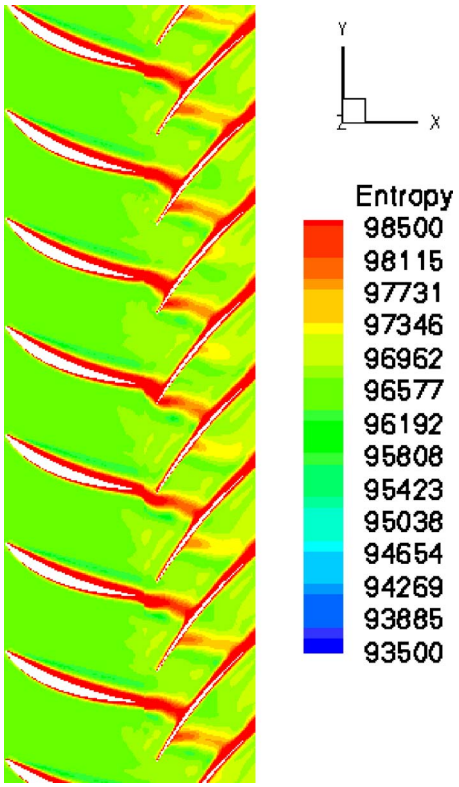

Fig. 4 Instantaneous entropy contours at 90% blade height (2-bladerow computation)

procedure consists of determining a whole-annulus steady-state flow first by using individual single-blade solutions as initial guesses. The upstream and downstream boundary conditions are specified using data obtained from a simplified throughflow model which is calibrated using available experimental data. As will be discussed later, the specification of *correct* boundary conditions is a major problem in core compressors since imposed fixed boundary conditions do not always allow the flow to develop naturally, especially at off-design conditions. Together with multistage interactions and low-engine-order harmonics, such a shortcoming is one of the main reasons to include further upstream and downstream bladerows in addition to the main stage of interest. In any case, once a steady-state flow is determined for the whole-annulus multibladerow model, the forced response calculations were conducted using a time-accurate viscous flow representation.

The instantaneous entropy contours, showing the wake rotor interaction through the five bladerows at 90% height, are plotted in Fig. 3. For comparison purposes, the same calculation was repeated using two bladerows only, namely S2 and R2. Here, because of a common factor between the blade numbers, it was possible to reduce the computational effort by using a typical periodic sector of 16 S2 and 19 R2 blades. As before, the instantaneous entropy contours at 90% height are plotted in Fig. 4. A comparison of Figs. 3 and 4 reveals that, although the main blade-passing excitation is similar additional interactions, arising from the added upstream and downstream bladerows, are present in the 5-bladerow computation. It should be noted that the rotor/stator blade meshes must be both well matched and of sufficient resolution to avoid numerical discontinuities at the sliding planes.

Using Eq. (10), the BM11/6ND modal force was computed for both the 2- and 5-bladerow calculations. The resulting time histories, shown in Fig. 5, indicate that the amplitude of the modal force is predicted to be much higher by the 2-bladerow calculation, a feature that can partly be explained by the presence of the additional harmonics in the 5-bladerow analysis. Interactions between these, governed by their relative phasing, can indeed affect the magnitude of the main blade passing harmonic but it is unlikely they can account for such a large difference in the modal force magnitude. Some of the discrepancies are undoubtedly due to boundary condition differences between 2- and 5-bladerow calculations. As the R1 flow develops and the exit flow becomes different from the imposed experimentally derived boundary conditions, the modal force time histories begin to deviate from each other.

Two further possible causes for modal force time history differences should also be mentioned: clocking effects (i.e., the relative positioning of the bladerows) and boundary condition differences between the 2- and 5-bladerow calculations. The former was checked by considering a different clocking between Bladerows S1 and S2, both upstream of the bladerow of interest R2. The calculations were conducted using a 3-bladerow mesh, consisting

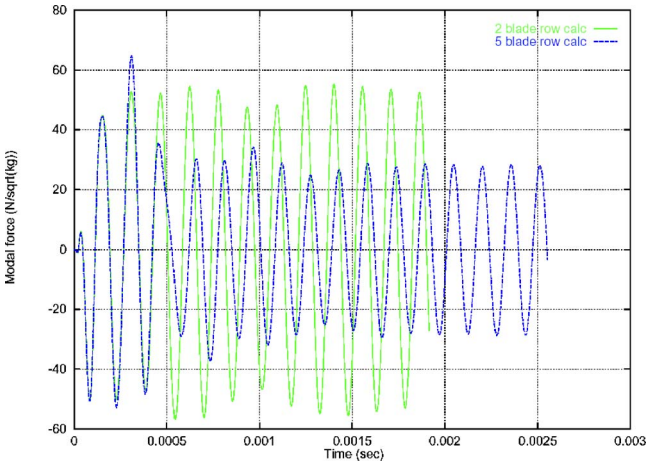

Fig. 5 Blade Mode 11/6ND modal force

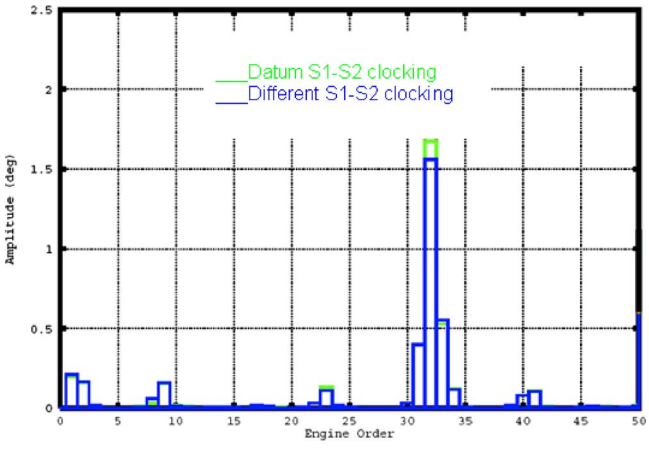

Fig. 6 Clocking effects on EO excitation harmonics

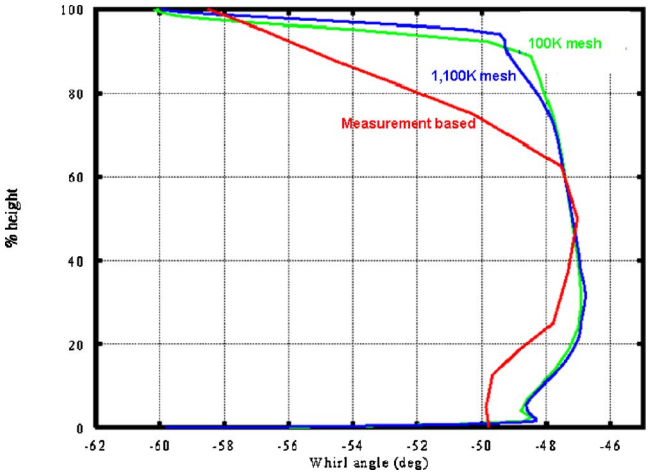

Fig. 7 Whirl angle at R1 exit—measurement based versus fine mesh versus coarse mesh

of the S1, R1, and S2 domains. The magnitude of the harmonics was evaluated by taking the Fourier transform of the whirl angle at the S2 exit. The results, plotted in Fig. 6, indicate some effect on the strength of the 32EO excitation, though it is difficult to generalize on the strength of a single clocking configuration.

In multibladerow core-compressor modeling, there are, in the main, two types of uncertainties. The first type is related to uncertainties in upstream and downstream boundary conditions that must be imposed on either side of the bladerows of interest. As more bladerows are included in the model, the boundary condition error will, in principle, decrease as, in the limit, atmospheric boundary conditions can be used at both the inflows and the outflows. The second type arises from modeling errors such as geometric simplifications, discretization inaccuracies, and turbulence modeling. If such errors cause a relatively poor flow simulation in a given bladerow, the neighboring bladerows will become adversely affected since their boundary flow is no longer correct. In such cases, where the modelling of a given bladerow is particularly problematic, it may be a better strategy to remove the bladerow from the model and use measurement-based boundary conditions instead, provided such boundary conditions have good resolution, accuracy, and can be obtained in the first place. Such a scenario will now be investigated by comparing 2- and 5-bladerow calculations.

The measurement-based boundary conditions were imposed at the S1 inlet in the 5-bladerow computations, and at the S2 inlet in the 2-bladerow calculations. An examination of the whirl angle at the R1 exit revealed some discrepancies between the 2- and 5-bladerow calculations and the differences were traced back to the R1 flow which was predicted directly in the 5-bladerow calculations and imposed as an exit boundary condition in the 2-blade calculations. A comparison of the whirl angle at R1 exit is given in Fig. 7 for both sets of calculations. It is seen that the measurement-based whirl angle is significantly different from the whirl angle that is obtained by explicitly modeling the S1 and R1 bladerows. It is also seen that this is not a meshing issue since both standard and very fine meshes yield, in the main, the same solution. After some investigation, it was found that R1 flow was sensitive to S1 exit flow, especially near the tip and the hub, which in turn depended on accurate geometric modeling of the "pennies" and of the end walls. Furthermore, the flow was found to be very sensitive to the actual S1 angle, the value of which was known with a finite accuracy.

Given such uncertainties, it was not possible to reach a conclusion on the relative accuracy of the 2- and 5-bladerow calculations in terms of predicting the magnitude of the 32EO excitation harmonic on R2. However, provided that all geometric features can be captured correctly at the expense of increasing the computational effort very significantly, the inclusion of more bladerows will improve the quality of forced response predictions, because not only will the flow develop better, but also aerodynamic boundary condition uncertainties will be eliminated. Conversely, if the measurement-based boundary conditions are more representative of interbladerow flows than a full calculation because of modeling limitations associated with a particular bladerow, the removal of that particular bladerow may be more appropriate.

As indicated by Eq. (1), the inclusion of more bladerows will enable the prediction of low-engine-order harmonics arising from blade number differences. Of particular interest here is the 1T/8ND mode of the R2 assembly which is susceptible to 8EO excitation. The 8EO excitation cannot be predicted by the 2-bladerow calculation since it is due to the blade number differences between stator bladerows S1 and S2, i.e., it can only be predicted if S2 is included in the model. Also, further work, not reported here, revealed that the amplitude of the 8EO was sensitive to the actual clocking configuration, a finding that highlights the difficulties of forced response analyses for multistage core compressors.

Finally, the predicted blade vibration levels were compared to test rig measurements. The results are listed in Table 1 for a best estimate of the Q factor for each mode. As explained earlier, the structural part of Q was obtained from actual vibration measurements while the aerodynamic part was obtained from a separate flutter analysis of the corresponding bladerow. Therefore, the choice of Q is not arbitrary. The agreement is good for the main blade passing response, though there is a significant discrepancy for the 1T/8EO mode. However, further calculations showed that the 8EO aerodynamic excitation was sensitive to S1/S2 clocking. Also, the presence of structural mistuning and uncertainties about the amount of inherent mechanical damping are expected to be further adverse factors on the accuracy of the calculation.

3.4 Low Engine-Order Forced Response Computations. As discussed earlier, any loss of symmetry is likely to give rise to low-engine-order excitation harmonics. A typical case is the blade throat width variation due to manufacturing tolerances. Also, in the case of variable inlet guide vanes, it may not be possible to control all stator blades to the same level of accuracy, thus creat-

Table 1 Predicted and measured response for Rotor 2

R2 assembly mode	Excitation	Measured pk–pk displacement (mm)	Predicted pk–pk displacement (mm)
BM11/6ND	32EO	0.22	0.27
1T/8EO	8EO	0.75	0.32

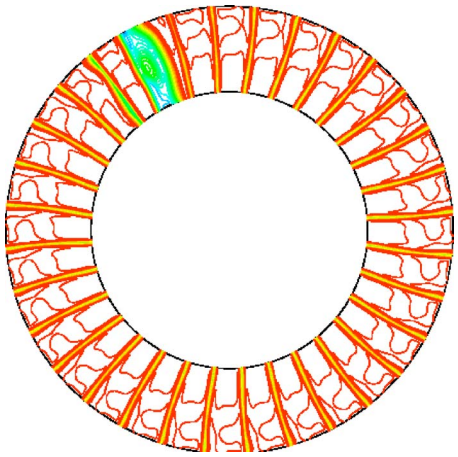

Fig. 8 Steady-state Mach number contours at S2 exit

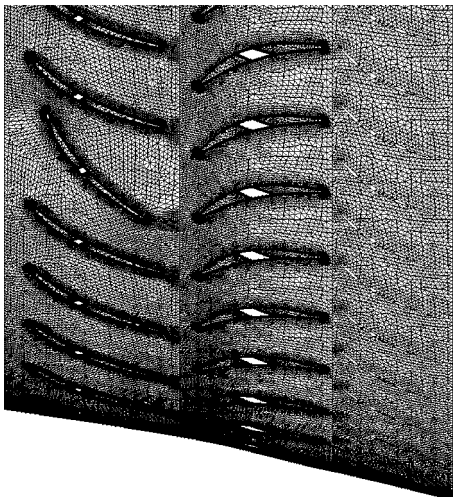

Fig. 10 3-bladerow mesh for blocked passage studies

ing an angle variation along the circumference. Still worse, under extreme circumstances, e.g., due to a malfunction of the control mechanism, a blade might block a stator vane passage, thus creating significant excitation for both upstream and downstream bladerows. Using the same geometry and focusing on bladerow R2, we will attempt to assess the additional excitation due to such a situation.

The analysis was conducted for a gradual blockage by rotating one of the S2 blades by 10 deg, 20 deg, and 25 deg, an approach that allows us to obtain the R2 response levels as a function of the blockage angle. The steady-state Mach number contours at S2 exit for the 25° blockage case are plotted in Fig. 8. It is seen that the effects of the blockage on the flow are confined to the blocked passage and to its immediate neighbors. The whirl angle variations arising from such a flow will cause low-engine-order harmonics which will excite the vibration modes of bladerow R2. The Fourier transform of the whirl angle at the S2 exit is plotted in Fig. 9 for all three blockage cases. Although the blockage has a relatively small effect on the main 32EO harmonic, the amplitude of the low-engine-order harmonics increases sharply as the amount of blockage increases.

Preliminary studies indicated strong unsteady interaction between the S3 and R2 bladerows and the forced response study was conducted using a 3-bladerow model, consisting of S2, R2, and S3. The resulting mesh, with about 7 million grid points, is shown in Fig. 10 while the instantaneous entropy contours are shown in Fig. 11. It is difficult to follow the details without an animation of the unsteady pressures to which the following discussion relates. The solution is highly nonlinear with shocks forming and disappearing in R2 and S3 passages. Moreover, there is significant flow separation and the effects of the blocked passage can be seen as far downstream as the S3 bladerow. The flow accelerates on the

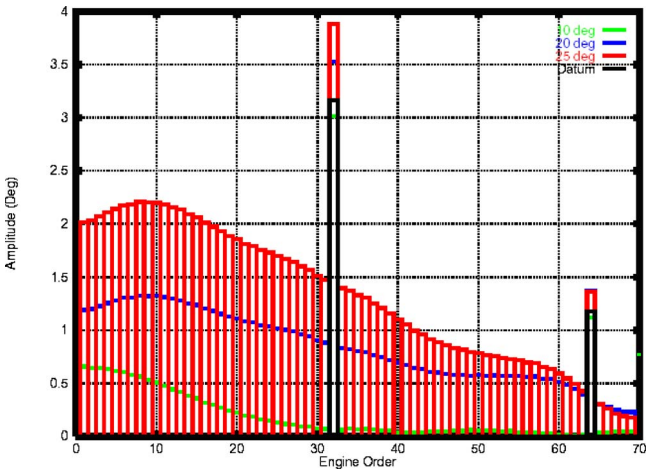

Fig. 9 The Fourier transform of the whirl angle at S2 exit for all three blockage cases

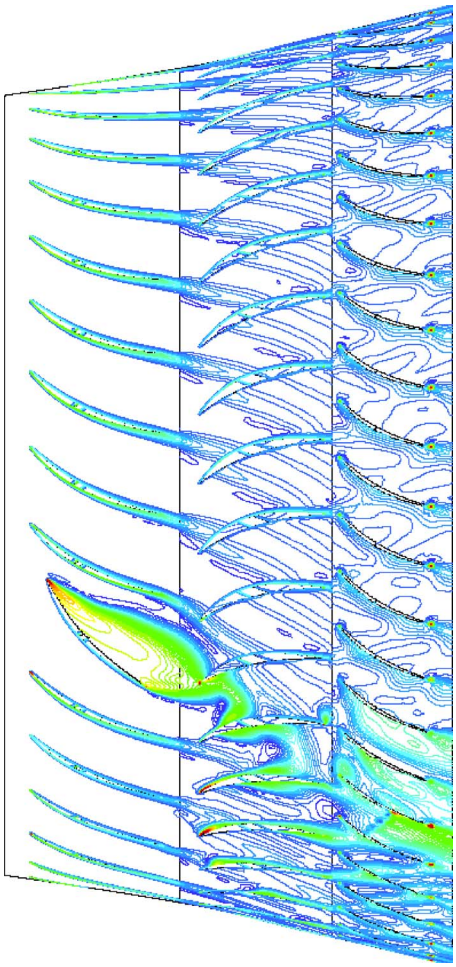

Fig. 11 Instantaneous entropy contours for 25 deg blocked passage

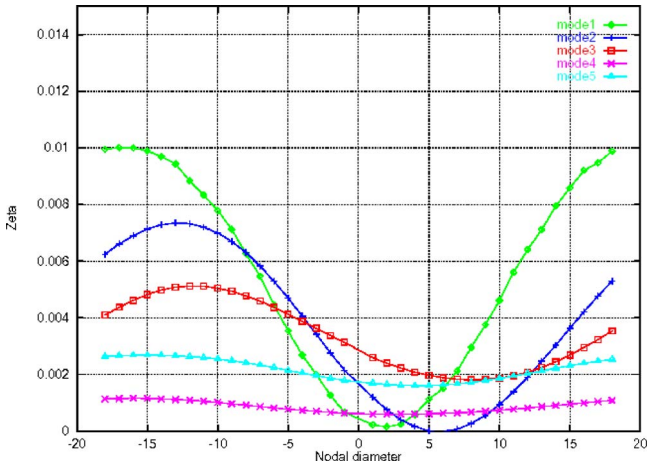

Fig. 12 Aerodynamic damping values as obtained from a transient flutter analysis Mode 1=1 F, Mode 2=1 T

pressure side of the blocked S2 passage, resulting in an increased angle of attack on two R2 passages which are not directly downstream of the blocked passage because of the R2 rotation. The increased angle of attack causes an upstream interaction toward S2, which is reflected downstream, causing shocks in further R2 passages. Similar interactions cause fluctuating shocks in the S3 passages. The distortion pattern is repeated in a similar fashion around the annulus, though the flow is quick to recover away from the blocked passage.

The aerodynamic damping was determined via a single bladerow flutter analysis which was initiated by giving an initial velocity to all blades in the assembly and monitoring the displacement time histories. The R2 assembly modes were included in the analysis by interpolating the structural mode shapes onto the fluid mesh which was then moved at each time step according to the structural motion. A damping value was obtained by monitoring the decay of successive vibration cycles. The results are plotted in Fig. 12 for the first blade mode families. As expected, the low-order forward traveling nodal diameter modes have the lowest damping. The modal forces were then obtained using Eq. (10), a typical modal force time history and its Fourier transform being shown in Fig. 13 for the 1T/6ND mode. The modal force time history is highly nonlinear, with many harmonics being present in the time history. As mentioned earlier, the 6ND mode and the 32ND mode are spatially aliased. In any case, what is of primary interest to the designer is the actual maximum displacement values for each mode so that fatigue life assessments can be made. The maximum displacement in each mode was determined using Eq. (11) together with the damping values of Fig. 12. Structural Q factors of 50 and 200 were used, respectively, for the bending and torsional blade modes. The results are plotted in Fig. 14 for the assembly modes of interest as a function of blockage angle. It is seen that the response for Mode 1 is very high at 25 deg blockage, a feature that must be considered duly in the design process.

4 Concluding Remarks

1. An integrated aeroelasticity methodology, based on large-scale numerical modeling, has been described for whole-annulus multibladerow forced analysis of core compressors. The model, which uses nonlinear aerodynamics and 3D structural finite-element representation, can deal with both blade-passing and low-engine-order excitation.
2. The blade motion, which can change the aerodynamic damping and flow unsteadiness, is automatically incorporated into the model. For computational efficiency, this feature can be switched off and the maximum response can be determined from knowledge of the maximum modal force amplitude and the amount of aerodynamic and structural damping. If necessary, the aerodynamic damping can be calculated from a transient aeroelasticity (or flutter) analysis.
3. It is shown that partially blocked stator passages can cause large vibratory response. Although extremely unlikely, such eventualities are addressed at the design stage. Stator angle variations, due to the difficulties of controlling all variable inlet guide vanes to the same level of accuracy, may also

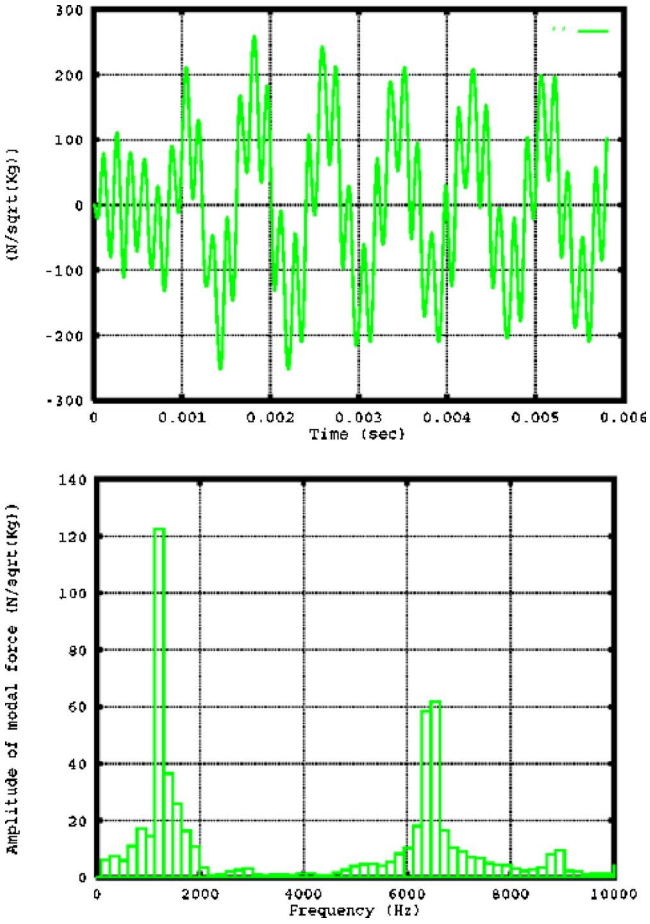

Fig. 13 1T/6ND modal force time history and its Fourier transform

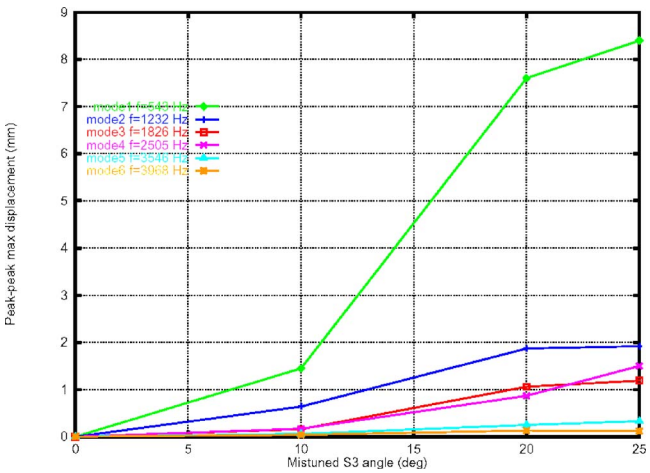

Fig. 14 Maximum blade response for assembly modes of interest as a function of blockage

cause unexpected low-engine-order excitation, though further research, not reported here, showed that the excitation levels are much lower than those in the blocked stator passage case.

4. Clocking between the stator bladerows affects the strength of both the main blade passing and the LEO harmonics. Although it is difficult to generalize on the strength of having studied only one configuration, the LEO harmonics seem to be affected much more, though their magnitude is smaller.
5. The inclusion of a *suitable* number of bladerows is crucial when dealing with core-compressor forced response. At one end of the spectrum, the study of isolated rotor bladerows under some imposed stator excitation may not be adequate. On the other hand, in spite of the large CPU effort required, large multibladerow calculations are not necessarily more accurate because of possible modeling deficiencies in simulating the flow in a particular bladerow. Such modeling deficiencies may arise from a lack of mesh resolution to describe a certain geometric feature, which in turn may cause a large error in the predicted flow. In such cases, the use of experimentally derived aerodynamic conditions may be preferable. On the other hand, when dealing with unexpected instabilities such as rotating stall, acoustic resonance, and surge deflection, all bladerows should be included.
6. From a design perspective, the key issue is the identification of the *minimum* number of bladerows that must be included in a compressor forced response analysis. For identifiable engine-order excitations, a small computational domain may well be sufficient for determining the response amplitude within engineering accuracy, especially bearing in mind the uncertainties associated with the structural damping values. However, it should be remembered that unsteady bladerow interactions are not confined to a single stage, especially at off-design conditions. Furthermore, the existence of low-engine-order harmonics, arising from blade number differences, may necessitate the consideration of several bladerows. Experience shows that stator/rotor/stator configurations are usually preferable to single stage ones.
7. Code parallelization on distributed memory machines has been a key enabling feature for undertaking large whole-annulus multibladerow analyses with several million grid points. Whole-compressor aeroelasticity models, as described above, are beginning to be contemplated. The next challenge will be the formulation of fast solution techniques to overcome the run time difficulties arising from diverse time and length scales.

Acknowledgment

The authors would like to thank Rolls-Royce plc for both sponsoring the work and allowing its publication. They also thank UK Engineering and Physical Sciences Research Council (EPSRC) for a JREI grant towards the procurement of computing equipment. They also thank Dr. Simon Gallimore for many useful discussions.

References

[1] Sayma, A. I., Vahdati, M., and Imregun, M., 2000, "Multi-Bladerow Fan Forced Response Predictions Using an Integrated 3D Time-Domain Aeroelasticity Model," J. Mech. Eng. Sci., **214**(12), pp. 1467–1483.
[2] Lindquist, D. R., and Giles, M. B., 1991, "On the Validity of Linearized Unsteady Euler Equations with Shock Capturing," AIAA Paper No. 91-1598-CP.
[3] Ning, W., and He, L., 1998, "Computations of Unsteady Flows around Oscillating Blades using Linear and Nonlinear Harmonic Euler Methods," ASME J. Turbomach., **120**, pp. 714–722.
[4] Clark, W. S., and Hall, K. C., 2000, "A Time-linearized Navier–Stokes Analysis of Stall Flutter," ASME J. Turbomach., **122**, pp. 467–476.
[5] Chen, T., Vasanthakumar, P., and He, L., 2001 "Analysis of Unsteady Bladerow Interaction using Nonlinear Harmonic Approach," J. Propul. Power, **7**(3), pp. 651–658.
[6] Sbardella, L., and Imregun, M., 2001, "Linearized Unsteady Viscous Turbomachinery Flows on Hybrid Grids," ASME J. Turbomach., **123**(3), pp. 568–582.
[7] Silkowski, P. D., and Hall, K. C., 1998, "A Coupled Mode Analysis of Unsteady Multistage Flows in Turbomachinery," ASME J. Turbomach., **120**(3), pp. 410–421.
[8] Chen, J. P., Celestina, M., and Adamczyk, J. J., 1994, "A New Procedure for Simulating Unsteady Flows Through Turbomachinery Blade Passage," ASME Paper No. 94-GT-151.
[9] Erdos, J. I., Alzner, E., and McNally, W., 1977, "Numerical Solution of Periodic Transonic Flow through a Fan Stage," AIAA J., **15**, pp. 1559–1568.
[10] Rai, M. M., 1987, "Navier–Stokes Simulations of Rotor/Stator Interaction Using Patched and Overlaid Grids," J. Propul. Power, **3**(5), pp. 387–396.
[11] He, L., and Denton, J. D., 1993, "Inviscid-Viscous Coupled Solution for Unsteady Flows through Vibrating Blades: Part 1," ASME J. Turbomach., **115**, pp. 94–100.
[12] Barakos, G., Vahdati, M., Sayma, A. I., Bréard, C., and Imregun, M., 2001, "A Fully-Distributed Unstructured Navier–Stokes Solver for Large-Scale Aeroelasticity Computations," Aeronaut. J., **105**(1050), pp. 419–426.
[13] Baldwin, B. S., and Barth, T. J., 1991, "One-Equation Turbulence Transport Model for High Reynolds Number Wall-Bounded Flows," AIAA Paper No. 91-0610.
[14] Sayma, A. I., Vahdati, M., Sbardella, L., and Imregun, M., 2000, "Modelling of 3D Viscous Compressible Turbomachinery Flows using Unstructured Hybrid Grids," AIAA J., **38**(6), pp. 945–954.
[15] Sbardella, L., Sayma, A. I., and Imregun, M., 2000, "Semi-Structured Meshes for Axial Turbomachinery Blades," Int. J. Numer. Methods Fluids, **32**(5), pp. 569–584.
[16] Rai, M. M., 1986, "Implicit Conservative Zonal Boundary Scheme for Euler Equation Calculations," Comput. Fluids, **14**, pp. 295–319.
[17] Vahdati, M., Bréard, C., Sayma, A., and Imregun, M., 2002, "An Integrated Time-Domain Aeroelasticity Model for the Prediction of Fan Forced Response due to Inlet Distortion," ASME J. Eng. Gas Turbines Power, **124**(1), pp. 196–208.

Numerical Investigation of the Effect of Different Back Sweep Angle and Exducer Width on the Impeller Outlet Flow Pattern of a Centrifugal Compressor With Vaneless Diffuser

A. Hildebrandt
e-mail: andre.hildebrandt@de.manturbo.com

M. Genrup

LTH,
Lund Institute of Technology,
Department of Energy Sciences,
P.O. Box 118,
22100 Lund, Sweden

This paper presents a numerical investigation of the effect of different back sweep angles and exducer widths on the steady-state impeller outlet flow pattern of a centrifugal compressor with a vaneless diffuser. The investigations have been performed with commercial computational fluid dynamics (CFD) and in-house programmed one-dimensional (1D) codes. CFD calculations aim to investigate how flow pattern from the impeller is quantitatively influenced by compressor geometry parameters; thereby, the location of wake and its magnitude (flow angle and relative velocity magnitude) are analyzed. Results show that the increased back sweep impeller provides a more uniform flow pattern in terms of velocity and flow deviation angle distribution, and offers better potential for the diffusion process inside a vaneless (or vaned) diffuser. Secondary flux fraction and flow deviation angle from CFD simulation are implemented into the 1D two-zone program to improve 1D prediction results. [DOI: 10.1115/1.2447873]

Introduction

Background. Centrifugal compressors are favored for application with high pressure ratio and small mass flow, as demanded by turbo chargers, microturbines, or future small-scale power generation systems based on turbomachinery and fuel cells. In systems such as the latter one, one requirement for the turbomachinery refers to extended operation range because of the sensitivity of transient operation on the compressor surge margin. Besides the option of using variable inlet guide vane (VIGV), a rotated vaned (low solidity) diffuser or casing treatment (shroud bleed or ported shroud), the impeller design itself can also support the extension of the operational range. Extension of operation range and continuous improvement of stage performance have been achieved by: (a) using modern tools and methods such as inverse direct design based on computational fluid dynamics (CFD) [1] or optical measurements [2]; and (b) better understanding of the flow physics such as the secondary flow field development [3].

Although the impeller efficiency of a centrifugal impeller reaches up to 92–94%, modern centrifugal compressor stages (with vaned diffuser) end up at 87% (moderate loading) lacking up to 4%, when compared with axial compressors. The reason for the poor stage efficiency is the low diffuser performance in off-design operation with either a choked or highly stalled condition at the diffuser throat. Rotor stator interaction in the very small vaneless space [4] and nonuniform impeller outlet flow conditions significantly influence the diffuser inlet flow, causing severe flow separation inside the diffuser. Therefore, in order to improve the diffuser performance, one should aim at an impeller outlet flow relatively uniform in tangential and axial direction. However, the primary flow is influenced by secondary flow effects resulting from the curvature of channel and acceleration/deceleration of flow (coriolis and centrifugal forces). Tip clearance flow further distorts the flow pattern, which finally results in the well-known jet-wake pattern of the impeller flow that was experimentally confirmed in several research studies as early as in the 1960s (see Eckardt [5]).

In the open literature, qualitative and quantitative one-dimensional 1D results on the influence of impeller performance by different back sweep blade angles are often found [6–8]. However, detailed 3D flow field results of the comparison between different impeller back sweep and exducer width are very seldom. In the past, most reliable flow field analysis could be only performed by applying experimental methods such as laser Doppler anemometer (LDA) or laser 2 focus (L2F) [2], which limit the range of investigation on only one impeller geometry because of extreme time consumption for these methods. In contrast to hardware experiments, numerical experiments provide the advantage of relatively short calculation time, but this is at the expense of relatively unreliable results in the past. Special care still has to be taken in applying CFD for analysis of centrifugal turbomachinery because of the strong curved geometry and implied sensitivity on secondary flow effects.

The goal of this paper is to quantify the effect of different back sweep angles and exducer widths on the magnitude of slip factor, exducer swirl angle, efficiency, and performance by means of CFD and 1D calculations. The base case impeller (MTU) of the numerical analysis is a design with both transonic impeller ($Ma_{w1}=0.95$) and diffuser inlet ($Ma_{c2}=0.94$) conditions, specific speed equal to 0.69, maximum pressure ratio equal to 4.07, and maximum reduced mass flow equal to 2.5 kg/s. Detailed information on the geometry and experimental results are available on request (open CFD test case "Radiver") from the Institute of Jet Propulsion and Turbomachinery, RWTH Aachen.

Contributed by the International Gas Turbine Institute of ASME for publication in the JOURNAL OF TURBOMACHINERY. Manuscript received June 17, 2006; final manuscript received August 9, 2006. Review conducted by David Wisler. Paper presented at the ASME Turbo Expo 2006: Land, Sea and Air (GT2006), Barcelona, Spain, May 8–11, 2006. Paper No. GT2006-90622.

Effect of Back Sweep Angle on the Impeller Performance. Variation of the back sweep angle will effect the impeller performance in two ways: first in changing the Euler work according to Eq. (1), and second by also varying the slip factor (being a measure for the deviation of flow angle from blade angle as a result of a relative eddy inside the blade channel). Optimum blade angles for maximum efficiency have been confirmed by both experiments [7] and loss-oriented 1D considerations (see Eckert and Schnell [9]).

$$w = u_2(\sigma u_2 - c_{m2} \tan \beta_{2b}) \tag{1}$$

The slip factor is defined according to Eq. (3), being valid for design and off-design conditions. For design calculation, several correlations of slip factor exist such as the one by Buseman, Stanitz or by Wiesner, Eq. (2). Slip velocities c_S, Eq. (4), required for the calculation of the off-design slip factor might come from 1D two-zone calculations (see the Appendix for a short introduction into the two-zone model) or from 3D CFD viscous calculations providing a mass averaged value for c_S

$$\sigma = 1 - z^{-0.7}\sqrt{\cos \beta_{2b}} \tag{2}$$

$$\sigma = 1 - \frac{\bar{c}_S}{u_2} \tag{3}$$

$$\bar{c}_S = u_2 + \bar{c}_{m2m} \tan \beta_{2b} - \bar{c}_{\Theta 2m} \tag{4}$$

By utilizing the impeller two-zone approach, tangential outlet velocities and the slip factor are mainly dependent on the magnitude of the diffusion ratio and the predefined deviation angle of the primary and secondary flow (see Japikse and Osborne [10]).

Although the magnitude of secondary flow area and wake mass flux can be determined from 1D prediction programs by applying empirical relationships for secondary flux-area correlation, the jet and wake at impeller exit cannot be predicted spatially. However, for an advanced vaned diffuser design, knowledge of the spatial axial and tangential distribution of flow angle and flux magnitude is necessary. Furthermore, primary flow deviation angle and secondary flow (to be understood as a term of the two zone model and not vorticity based) are very specific for each impeller design and cannot be generalized. CFD may form a database for such information as shown in this paper.

A combined impeller/vaned diffuser stage was not computed here. However, conclusions can be drawn that the impeller with more uniform outlet flow pattern calculated with a vaneless diffuser might also perform better with a vaned diffuser. It should be noted that the interaction between a vaned diffuser (wedge or airfoil) and impeller causes further distortion on the impeller outlet flow field, which can be properly predicted only by means of unsteady-state moving grid simulation. In the case of a vaned diffuser, it is important to minimize the steady-state diffuser incidence loss. For that reason, knowledge about the distribution of the impeller swirl angle (or swirl factor λ_{2m}) at design point is of high importance.

Effect of b_2 on Operation Range and Performance. Besides the back sweep angle, another parameter that influences the operating range of the compressor is the exducer width. The selection of exducer width effects the swirl angle or swirl parameter directly by manipulation of the velocity triangle.

Wide operation range and maximum efficiency are reported for $\lambda_{2m}=2.00–2.25$ and increased vaneless diffuser loss will occur at conditions below or beyond this optimum value [6].

The swirl angle α_2 in off-design condition will change according to the velocity triangle at impeller outlet. At low-flow coefficient, a large swirl angle (measured from the radial direction) will lead to a mild and abrupt rotating stall with high amplitude up- and downstream of the impeller (see Frigne et al. [11]).

Of high importance is the determination of diffuser critical inlet flow angle at which separates the range of steady flow and unsteady flow ($\alpha_2 < \alpha_{2c}$). The critical inlet flow angle can be set as a function of the ratio of exducer width to tip radius b_2/r_2 according to a comparison between experimental results and numerical prediction [11]. Reducing the parameter b_2/r_2 causes the critical flow angle to extend up to 86 deg. However, for low b_2/r_2, especially in the case of a vaneless diffuser, very high frictional loss may occur which limits the usual application of the vaneless diffuser to a pressure range up to just 3.5 [6].

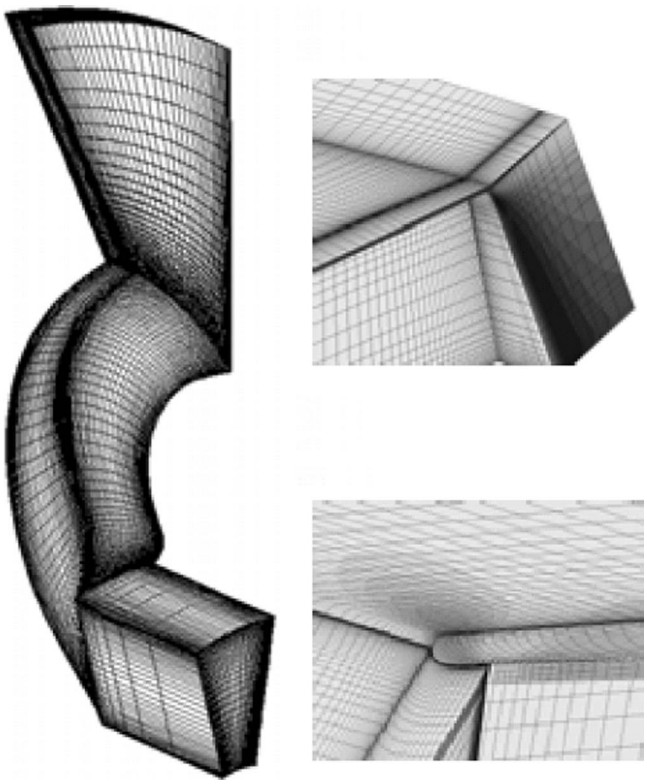

Fig. 1 Structured multi-block mesh of impeller, trailing, and leading edge details (complete vaneless diffuser not shown here)

Effect of b_2 on the Secondary Flow Field of Impeller. Nonuniformity because of the secondary flow within centrifugal compressors can be explained with the streamwise vorticity equation of a rotating system. In Brun [3], a secondary flow model was derived applying known meridional velocities to the streamwise vorticity equations to determine the vorticity. Since different values of exducer width b_2 will alternate the meridional velocity (to satisfy the continuity equation), b_2 will indirectly effect the streamwise vorticity coming from the nonuniform flow in the hub to shroud direction during rotation of the impeller shaft [3].

CFD Methodology

Boundary Conditions and Validation. Viscous calculations were performed with commercial software StarCd, V 3.150A [12]. The computational block and mesh structure of the impeller is shown in Fig. 1. The model comprises an *H*-type multi-block grid, utilizing cyclic boundaries for tip clearance, inducer, exducer, and vaneless diffuser flow. The computational mesh in one impeller blade comprises up to $125 \times 50 \times 40$ cells streamwise, pitchwise, and spanwise, respectively. For reasonable y^+ values at the wall boundaries, appropriate cell stretching was utilized. To minimize the computational effort, only one blade channel was computed in steady state using the SIMPLE algorithm. The high Re number k-ε model with standard coefficients and a closure by the ideal gas

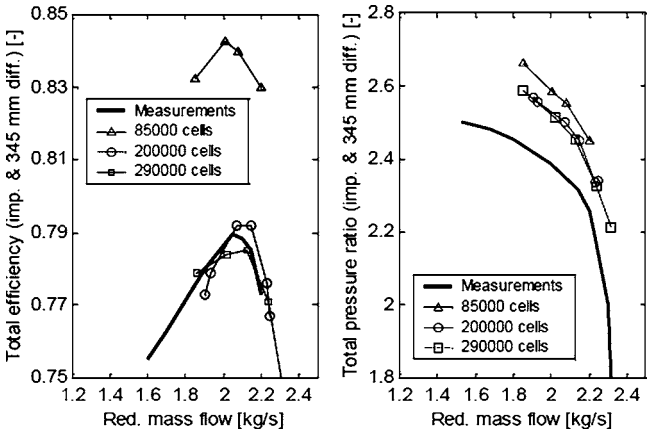

Fig. 2 Validation of total efficiency and total pressure ratio (impeller and 345 mm diffuser), measurements reproduced from Ziegler [4]

law were applied. Boundary conditions are total pressure, total temperature, flow angle, turbulence intensity, and turbulent length scale at inlet and static pressure at outlet.

As a constant tip clearance gap (2.5% of exit height), up to ten cells in spanwise direction above the shroud surface were implemented (see Fig. 1). As stated in Weiss et al. [13], a three cell layer in the clearance gap is sufficient for accurate prediction of clearance flow, which is mainly driven by pressure potential but not viscous effects. The grid upstream the impeller is extended to 30% of the axial impeller length. On solid wall boundaries, the turbulence wall function approach was chosen since even in the case of high grid density (600,000 cells in one impeller channel), the boundary layer on the suction side (SS) and pressure side (PS) near impeller exit had not been resolved with the low Re number k-ε model (y^+ values up to 10–15). Notice that the CFD model has the opposite shaft turning direction from the real impeller.

CFD Base Case Validation and Grid Independence Study. Validation of CFD results were performed only for the case of 80% speed; for 100% speed, no detailed flow field measurement data had been available. A grid independence study with three different grids was performed, whereas the results of the medium-dense grid showed satisfactory agreement with measurements from RWTH Aachen regarding the compressor stage (impeller and vaneless diff.) total efficiency and total pressure ratio (see Fig. 2).

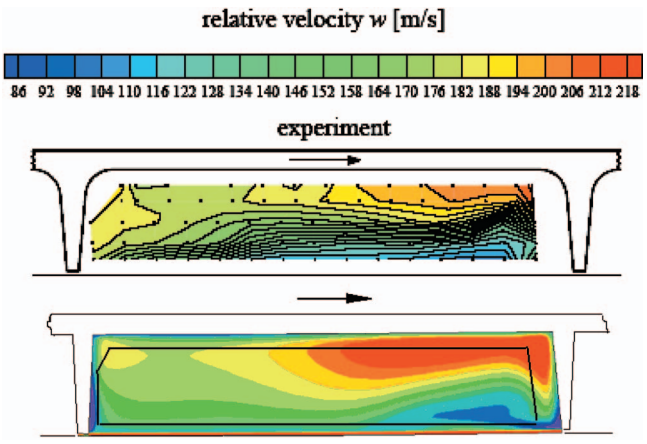

Fig. 3 Relative velocity at impeller outlet: (top) Aachen measurements by Ziegler [4]; (bottom) LTH calculations at N =0.8 N_{des}, m=1.8 kg/s, numerical results mirrored

Table 1 Results of second grid sensitivity study, diffuser length (200 mm)

Cell number	m (kg/s)	$\eta_{tot,imp}$ (-)	$p_{tot,imp}$ (bar)	$T_{tot,imp}$ (K)	σ (-)	λ_{2m} (-)
250,000	1.76	0.922	2.974	401.38	0.9128	2.69
375,000	1.77	0.926	2.974	400.78	0.9124	2.68
250,000	2.14	0.921	2.775	393.22	0.9190	1.95
375,000	2.14	0.922	2.776	393.15	0.9177	1.98

In comparison with measurements (RWTH Aachen) of the relative flow field near impeller outlet, the flow field structure in the calculations was quite well captured (see Fig. 3).

The jet-wake flow pattern is qualitatively resolved by the calculations, however, differences exist in the velocity magnitude between the measurements and the calculations. The relative velocity of jet flow toward the PS is underpredicted, while the velocity of the jet toward the SS is overpredicted by approximately 15 m/s in the LTH calculations. In the measurement results, the wake flow near the shroud spans a region from SS to half the blade pitch, while in the calculations, the wake is more concentrated toward the SS. Results might be improved by application of a nonconstant height of tip clearance (0.7–0.48 mm, hot run conditions) [13]. However for the studies in this paper, the assumption of constant tip clearance is sufficiently precise. The correct prediction of flow field for centrifugal compressors is still more challenging than for axial compressors, see i.e., Galerkin et al. [14], where relatively significant differences in flow field have been predicted with different numerical (commercial) tools. Bearing this in mind, the calculation of flow field presented here is rather satisfactory.

Two grid independence studies were performed. The first study was performed with the original diffuser length (r_4=0.345 m) at three different grid sizes of 85,000, 200,000, and 290,000 cells, in order to analyze the overall performance at variation of grid density, and to validate the prediction against measurement results taken at diffuser length r_4=0.345 m. The spanwise tip clearance grid density was kept constant. In Fig. 2, the smallest grid shows significant difference in results from the medium and large grid size regarding total pressure rise and total efficiency. For prediction of total efficiency, there is still a slight difference between the medium size grid and large size grid (0.75%). For this reason, the grid density of the entire computation domain was increased by shortening the original diffuser length r_4=0.345 m to a diffuser length of r_4=0.200 m but keeping the number of cells constant. For the reduced computation domain, the grid independence study was repeated with a grid size of 250,000 cells and 375,000 cells. The grid independence of the shortened domain was confirmed for 1.77 kg/s and 2.14 kg/s (see Table 1). The dependence of grid density on the impeller flow field can also be seen in Fig. 4, where the relative flow field near impeller outlet is compared for two cases: (a) between the grid of 85,000 cells and 200,000 cells (r_4 =0.345 m) and (b) between the grid of 250,000 cells and 375,000 cells (r_4=0.200 m). In comparison to case: (a), maximum difference of relative velocity for case (b) is rather small (±1 m/s). As numerical scheme for these calculations, a second-order total variation diminishing (TVD) scheme, called (monotone advection and reconstruction scheme (MARS) [12]) was applied. Using a first-order upwind scheme for the momentum equations on the grid of 200,000 cells underpredicted the jet/wake flow separation due to numerical diffusion in similar magnitude as the calculation on the small grid size (85,000 cells) with a second-order scheme.

As a result of the grid independence study, it was decided to perform the further simulations with the medium grid size of approximately 250,000 cells with the second-order scheme for the momentum and energy equations.

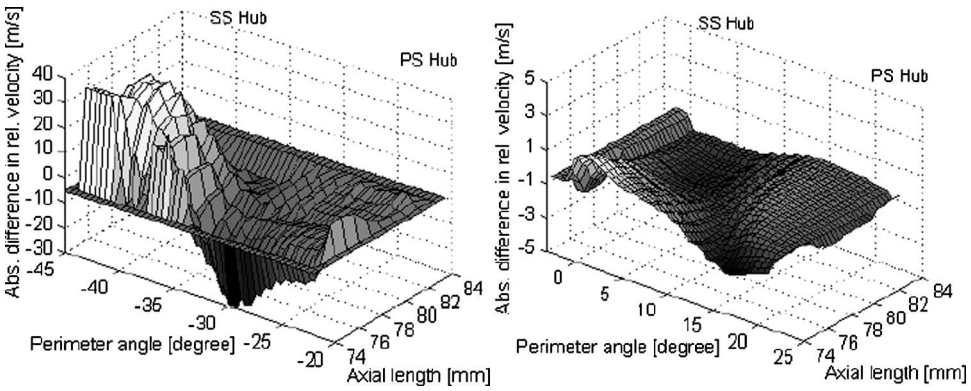

Fig. 4 (Left) Difference in relative velocity between the grid of 200,000 cells and 85,000 cells; (right) difference in relative velocity between the grid of 250,000 cells and 375,000 cells; $N = 0.8\ N_{des}$, $m = 1.8$ kg/s

Base Case Impeller Performance. The flow diffusion of the MTU impeller at 80% speed is relatively moderate over the meridional impeller length without any separation. The loading is rather constant at a low level having its minimum value toward the trailing edge. Maximum diffusion ratio of the mean relative velocity is below 0.65. Due to reduced rear loading, the secondary flow development is relatively small, resulting in high rotor efficiency of around 92% at design speed. The efficiency distribution at impeller outlet (see Fig. 5 for two different operation points) shows a typical pattern of high efficiency near the PS and very low efficiency near shroud SS as has been reported by Japikse [6]. Due to boundary layer flow from the shroud PS to the shroud SS, the flow region near the SS is highly dissipative, showing secondary flow and higher temperature, which can be derived from the calculated efficiency at impeller outlet. The secondary flow causes blockage of the flow near the shroud at the impeller outlet.

Base Case Vaneless Diffuser Performance. The flow field inside the vaneless diffuser of the MTU compressor shows a classical pattern with the passage wake smearing out over the radius (see Fig. 6). The wake of the trailing edge is mixed out relatively fast, while the wake of the secondary flow area remains almost constant in the diffuser downstream the impeller. Another observation is that the tangential part of the wake mixes out faster than the

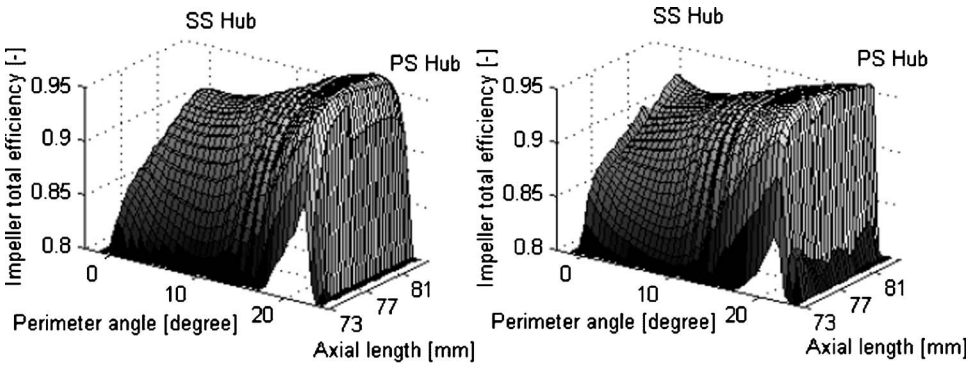

Fig. 5 Calculated total efficiency distribution at impeller outlet at $N = 0.8\ N_{des}$; (left) $m = 2.24$ kg/s; (right) $m = 1.549$ kg/s

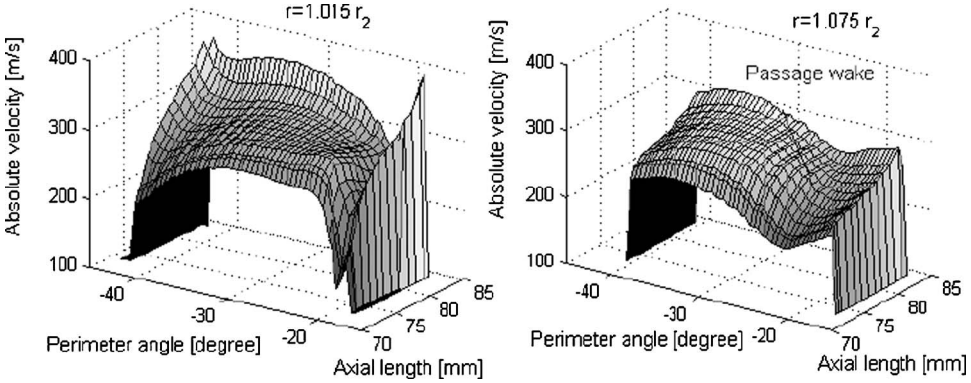

Fig. 6 Diffuser absolute velocity distribution at $N = 0.8\ N_{des}$, $m = 1.80$ kg/s: (left) radial position at $r/r_2 = 1.015$; (right) radial position at $r/r_2 = 1.075$

Table 2 Nomenclature for impeller derivatives

	β=38	β=45
$b_2=0.925b_{2,\text{orig}}$	38@0925	45@0925
$b_2=1.000b_{2,\text{orig}}$	38@1000	45@1000
$b_2=1.075b_{2,\text{orig}}$	38@1075	45@1075

axial part of wake flow. In the case of a vaned diffuser, the diffuser leading edge (LE) may experience a distortion of flow not only from SS to PS but also from impeller hub to shroud due to an unfinished secondary wake mixing process.

Setup of Numerical Experiment. The numerical experiment is set up according to the matrix shown in Table 2. The blade angles have been extended only to larger values, since increased stability of the impeller was the goal. The magnitude of b_2 variation has been defined with help of the 1D program, leading to a predicted variation of swirling parameter of $\Delta\lambda_{2m}=\pm 0.3$. Meridional distribution of the impeller blade angle for the hub and shroud geometry is shown in Fig. 21 in the Appendix. The blade is radially stacked. To account for different backsweep, the blade angle distribution is varied in the range from the last third of the original meridional path length up to the trailing edge. Other changes such as applied to the shroud, hub contour, or blade thickness have not been accounted for here. Additional blade stress due to increased back sweep angle must also be taken into account but is beyond the scope of this paper, where only the flow field characteristics are analyzed. Meridional curvature has been changed to apply for the different exducer width. The value of the vaneless diffuser width equals that of impeller exducer width.

Computations for all different impellers were performed with the same grid size (250,000 cells), same vaneless diffuser of shorten length (r_4=200 mm), same boundary conditions at inlet (T_{tot}=288.15 K and p_{tot}=1.0325 bar, turbulence intensity=0.09, turbulence length scale=$0.1d_{\text{hydr}}$), and same numerical scheme (SIMPLE algorithm, second-order discretization for the momentum and energy equation). Convergence was reached at a residual of 1.E-06.

Results

CFD Overall Performance Prediction. For determination of a complete speed line, the calculations were spanned over the mass flow range from the numerical stall to the choke point. At numerical stall, the continuity and energy equation did not sufficiently converge (residual just down to 1.E-03–1E-04), leading to unreliable results by means of a vertical slope for the static pressure, total pressure, and the remaining post-processed properties (not shown in the figures).

In general, all the impeller derivatives showed the same magnitude of the choke flow overprediction (+6%) in comparison with experimental results from Aachen. The impeller derivatives with the higher exducer width revealed only a minor absolute increase in choke flow equal to 0.1%. Obviously, the movement of the shroud contour caused an extension of the through flow area only in the impeller region downstream of the choke regime. The numerical stall mass flow of the original 38@1000 impeller was overpredicted by 7% in comparison with the measurement results. The impeller derivatives of reduced exducer width provided lower values of the numerical stall mass flow.

The overall performance of the impeller and diffuser is shown in Figs. 7 and 8.

Impeller Static and Total Pressure Rise. The static pressure slope is qualitatively correctly represented. The smaller pressure slope is given for 38 deg impellers. For both the 38@0925 and 45@0925 impeller, the static pressure is reduced by approximately 0.025 bar when compared to impellers of original width. In contrast to this, the pressure rise for the 45@1075 impeller is increased by approximately 0.05 bar over the entire operation range. The reason for increased pressure at increased width is explained by the higher diffusion. A steeper slope for higher back sweep impeller is preserved for the total pressure rise (Fig. 7). Total pressure of the 38@1000 and 38@0925 impeller differ less than for static pressure. Total pressure of the 45@1075 is less than for the original 38@1000 impeller as expected from 1D considerations (reduced Euler work at increased blade sweep).

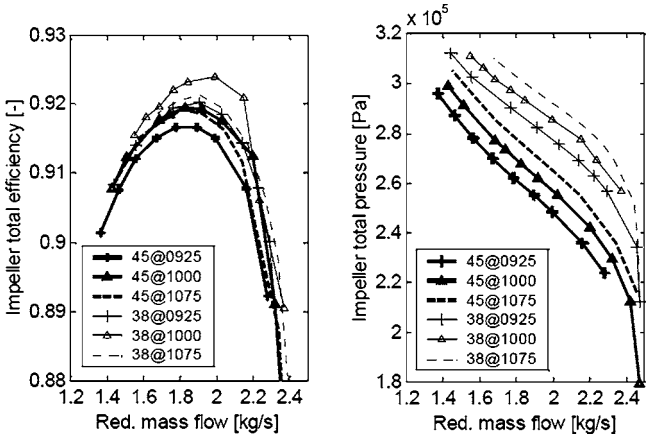

Fig. 7 Impeller total efficiency and total pressure

Impeller Total Efficiency. The original impeller shows the highest impeller total efficiency. Total efficiency curves for all impellers show a similar shape with a maximum peak inbetween the surge and choke operating regime. Toward higher mass flow, efficiency curves of the 45@1000 and 38@1000 impeller show more deviation among each other, probably because the higher friction loss of the 45@1000 impeller (increased meridional chord length due to increased blade wrap angle), becomes more dominant. The 45@1000 impeller shows 0.4% higher efficiency than its derivative of reduced exducer width. With increased back sweep and reduced exducer width, efficiency optima are slightly shifted toward smaller mass flow.

Impeller Slip Factor. The absolute variation of mass averaged slip factor over the operation range is small, only 2%. The slip factor shows a minimum at similar mass flow as for the maximum total efficiency. Dependency of the slip factor on alternated back sweep angle or impeller width is small. The 38@0925 impeller shows the highest slip factor among all impellers. The 45@1075

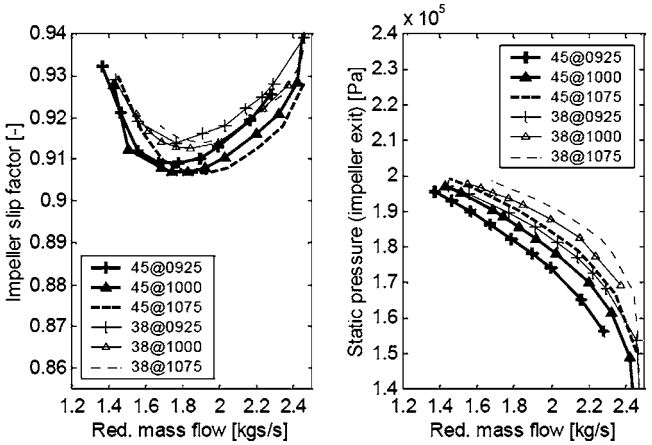

Fig. 8 Impeller static exit pressure and mass averaged slip factor

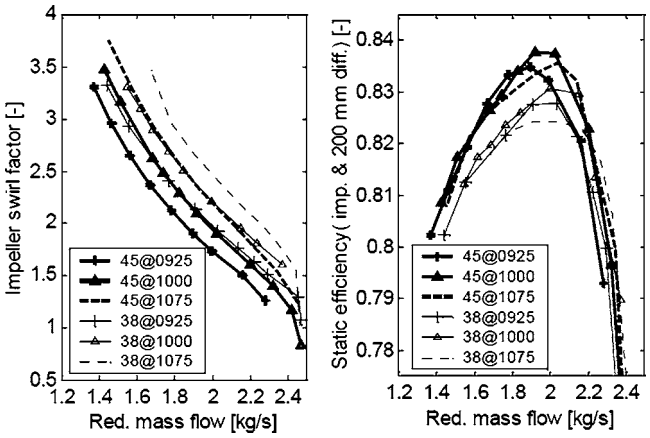

Fig. 9 Impeller swirl and static efficiency (impeller and 200 mm diffuser)

impeller has the lowest minimum of slip factor among all impellers. The slip factor for the 45 deg and 38 deg impellers is overestimated by approximately 4–5% than could be expected from the Wiesner slip factor ($\sigma_{45\ \mathrm{deg}}=0.873, \sigma_{38\ \mathrm{deg}}=0.867$) at design point.

Results of the impeller swirl factor, static efficiency (impeller and 200 mm diffuser), diffuser exit static pressure, and pressure recovery factor are presented in Figs. 9 and 10.

Impeller Swirl Factor. With variation of impeller width (±0.075), the swirl number is effected by ±0.35. The 45@1000 and 38@0925 impeller provide the same swirl factor over the operation range. Numerical stall seems to be excited at swirl equal to 3.5 for the 38@1000 and 45@1075 impeller. Operation range toward surge is alternated by ±0.1 kg/s at ±0.075 variation of the impeller width.

Diffuser Performance. For the diffuser exit static pressure, characteristics are calculated similar to those of the impeller static pressure rise. Figure 10 states an increase of pressure recovery for the impellers of reduced exducer width. Best off-design pressure recovery performance is presented for the 45@0925 impeller (almost 4% increase at high-mass flow in comparison with the 38@1000 impeller). The lowest pressure recovery is predicted for the 38@1075 impeller. Static efficiency maxima (at diffuser exit) show a realistic magnitude of approximately 82–84%. Due to the improved diffuser performance, the 45 deg impellers seem superior to the 38 deg impellers regarding the static efficiency at diffuser exit. For impellers of decreased exducer width, the shift of static efficiency maxima toward the surge line (Fig. 9) is more dominant than the shift of impeller total efficiency maxima shown in Fig. 7.

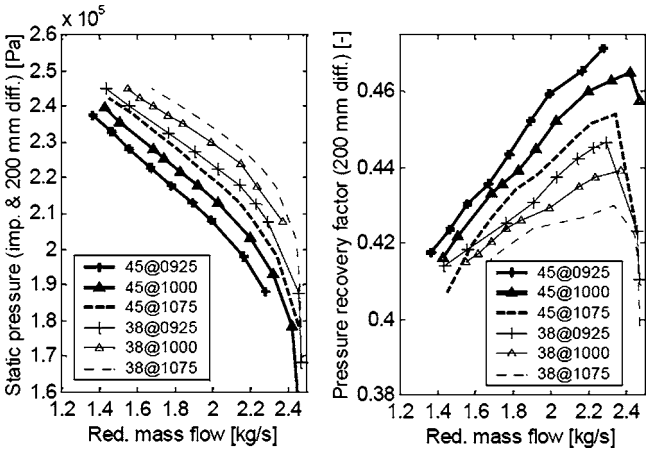

Fig. 10 Static pressure and static pressure recovery factor (200 mm diffuser)

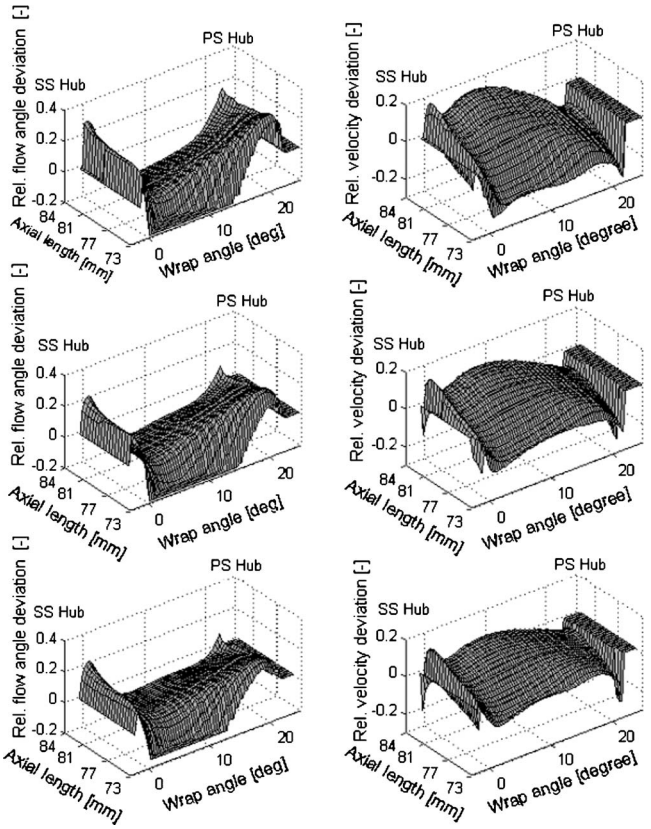

Fig. 11 Relative deviation of relative flow angle (left) and relative deviation of relative velocity (right). Top: 38@1000, *m*=1.767 kg/s, second from top: 45@1000, *m*=1.780 kg/s, bottom: 45@0925, *m*=1.782 kg/s.

The impellers of increased width show more flattened characteristics of the pressure recovery factor than the ones with original or reduced width.

CFD Impeller Flow Field Prediction

Impeller Flow Field Comparison. Because of the relatively large number of calculation points, the comparison of flow field of the different impellers is limited to only one operation point for the three impellers 38@1000, 45@1000, 45@0925. Results for relative deviation (see the Nomenclature for definition) from mass averaged relative velocity and mass averaged relative flow angle in the exit plane close to impeller outlet are shown in Fig. 11. Mass flow is approximately 1.76 kg/s with a deviation of ±1% mass flow for the different impellers. Since static pressure is set as a boundary condition, the mass flow is the result of a calculation that makes it difficult to predict.

Flow pattern of nonuniformity for all three different impellers is similar, however, at different magnitude. Flow field for the 38@1000 impeller is most distorted by the primary flow secondary wake pattern, when compared to the other two impellers. In comparison with the 38@1000 impeller, the magnitude of deviation is reduced by ±5% for the 45@1000 impeller. Further reduction of ±5% of flow deviation from average are achieved for the impeller of reduced exducer width. Due to the reduction of velocity wake, one expects better performance of the diffuser flow as it is approved by the higher pressure recovery factor for the impeller of higher back sweep angle. Noticeable is the strong deviation in

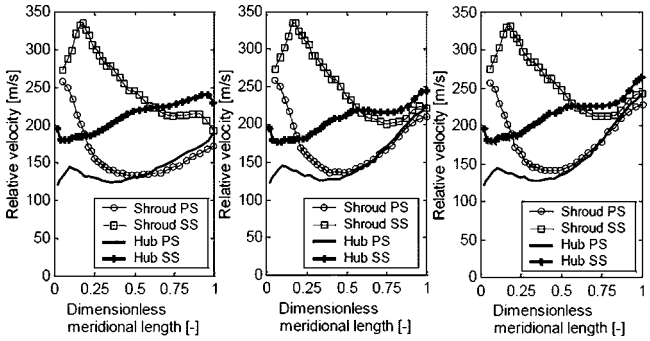

Fig. 12 Impeller relative flow diffusion: (left) 38@1000 (m=2.237 kg/s), (middle) 45@1000 (m=2.248 kg/s), and (right) 45@0925 (m=2.235 kg/s)

flow angle at the shroud close to SS. Here, the core flow interferes with the tip clearance flow and causes high swirl at an almost tangential direction.

Surprisingly, the result of the superiority of the 45 deg impellers regarding the flow field uniformity stays in contrast to the slip factor results (Fig. 8), where the 38 deg impellers showed approximately (0.75%) better values than the 45 deg impellers.

Comparison of Impeller Diffusion Characteristic. For further investigation of the flow field inside the impeller, the diffusion characteristics have been plotted for the impellers 38@1000, 45@1000, 45@0925 impeller at two different operation points (m=2.2 kg/s and m=1.7 kg/s), (see Figs. 12 and 13).

Since the variation of the through flow area and the blade angle only apply to the last third of the meridional length, all three different impellers show the same diffusion in the first two thirds of the meridional chord length. However, in the last third of the chord length, the 45 deg impellers experience a slightly higher flow acceleration on the SS and PS shroud than the 38@1000 impeller. This reduced diffusion on the shroud leads to a reduced shroud blade loading which is to be aimed for the reduction of flow nonuniformity at the impeller exit. The blade loading for the 45 deg impellers is also reduced on the hub. The reduction of gradients of relative velocity from hub to shroud and from PS to SS lead to minimized secondary flow development, which is approved by the velocity distribution at impeller outlet where the 45 deg impellers produce a less significant passage wake than the 38@1000 impeller. Comparing the 45@1000 and 45@0925 impellers to each other, almost no differences in blade loading can be found according to Figs. 12 and 13, which may misguide the designer to also assume similar flow uniformity at the impeller exit for both 45 deg impeller derivatives. However, according to the detailed flow distribution (Fig. 11), the 45@0925 impeller clearly shows its superiority to the 45@1000 impeller regarding

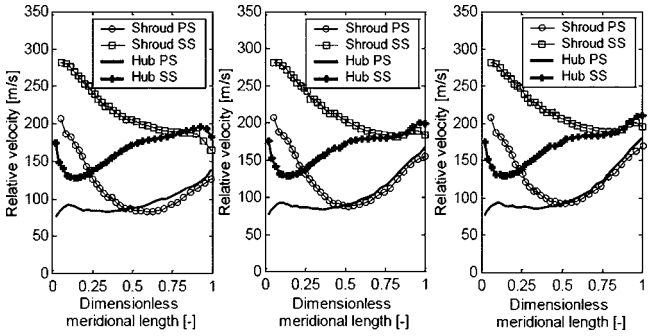

Fig. 13 Impeller relative flow diffusion: (left) 38@1000 (m=1.767 kg/s), (middle) 45@1000 (m=1.780 kg/s), and (right) 45@0925 (m=1.782 kg/s)

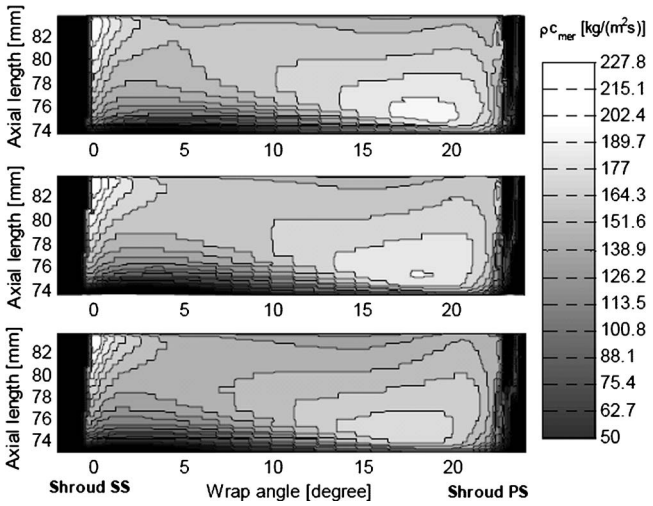

Fig. 14 Mass flow distribution at impeller exit: (top) 45@0925, m=1.559 kg/s; (middle) 38@0925, m=1.556 kg/s; (bottom) 38@1000, m=1.549 kg/s

flow field uniformity. Analyzing the diffusion characteristics of the 45@1000 and 45@0925 impeller, a slightly better diffusion (reduction of relative velocity of 20–25 m/s at the exit) can be observed for the 45@1000 impeller. This improved diffusion results in the higher static pressure and higher impeller total efficiency of the 45@1000 impeller when compared with the 45@0925 impeller.

Mass Flow Distribution at Impeller Outlet. In general, at high mass flow, the jet flow is confined by the PS to SS near hub. At reduced mass flow, the jet flow near the hub reduces, while one region near the shroud PS corner remains and develops to a high momentum region. Comparison of the mass flow distribution at the impeller outlet (0.5 mm downstream trailing edge (TE)) is presented in Fig. 14. The top, middle, and bottom subfigures in Fig. 14 show the 45@0925, 38@0925, and 38@1000 impeller, respectively. Distance from one iso contour line to another one is 12.7 kg/(m^{2}s).

All three impellers show the same qualitative characteristics of the jet/wake structure. The wake region of the 45@0925 impeller is extended toward the direction of the hub while the jet near the PS shroud has a higher magnitude than the one of the 38@0925, impeller. The wake flow magnitude of the 45@0925 impeller is, however, slightly reduced as shown in Fig. 14.

Distribution of Relative Rlow Angle Deviation at Impeller Outlet. At same mass flow rate as for the comparison of mass flow distribution, in Fig. 15, the relative flow angle distribution is shown for the 38@1000, 38@0925, and 45@0925 impeller. Highly positive deviation of the relative flow angle (for a definition see the Nomenclature) exists in the vicinity of the passage wake. Highly negative deviation of the relative flow angle can be found in the corner of shroud PS and very close to SS.

Deviation angles ranged from −6 deg to 20 deg. In the region where the mass flux reaches the maximum value, its deviation is close to zero. Following the trend of velocity distribution, with reduced impeller width and increased back sweep angle, the 38@1000 impeller shows a less uniform plateau of deviation angle than the 38@0925 and 45@0925 impeller. The result of highly positive deviation of the relative flow angle (equal to low absolute flow angle) is typical for a centrifugal compressor and has also been confirmed, i.e., for the original MTU impeller [4], or reported from L2F measurements of a transonic centrifugal compressor at DLR, Germany [2]. Knowledge about the flow angle distribution over the impeller depth might support 3D design of advanced vaned diffuser devices [2]. Close to stall operation, the

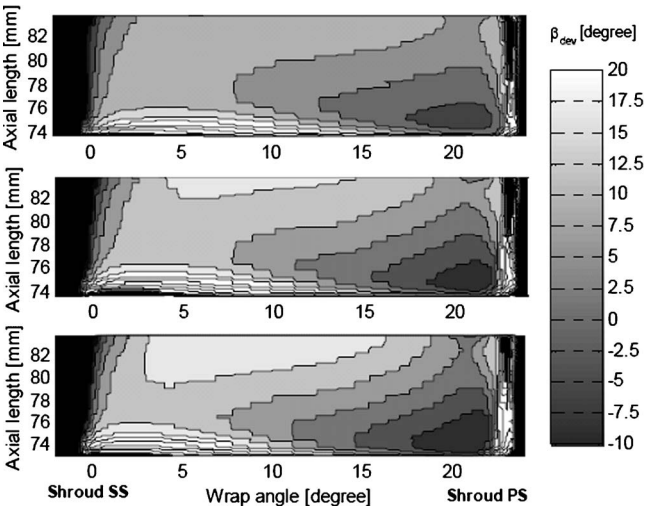

Fig. 15 Absolute deviation of relative flow angle: (top) 45@0925, m=1.559 kg/s, (middle) 38@0925, m=1.556 kg/s, (bottom) 38@1000, m=1.549 kg/s

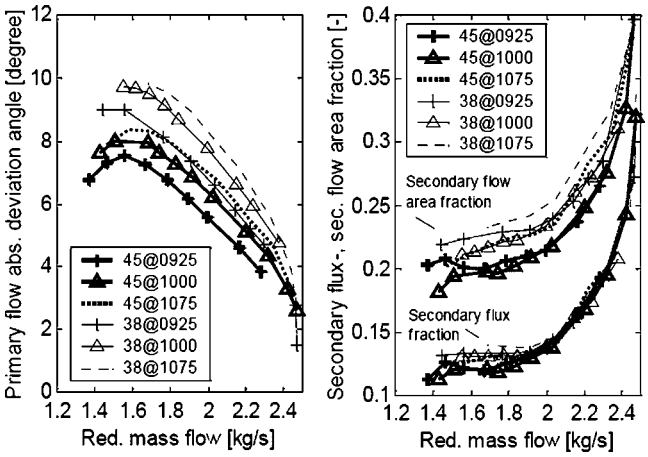

Fig. 16 CFD post-processed data: mass averaged primary flow deviation (left) and secondary mass flux- and -area fraction (right)

flow in the shroud region almost becomes tangential, which could also be counteracted by application of a so-called rib diffuser (see Sorokes et al. [15]). An important design issue for such a rib diffuser is the width of the rib that is occupied by the area of high swirl flow. Numerical or experimental optimization of such a rib diffuser could significantly improve diffuser off-design performance.

1D Impeller Performance Prediction

Determination of 1D Model Input Data. This section aims at comparison between the results of CFD and the results of the 1D two-zone impeller model [10]. Although the two zone-model is claimed to be less dependent on empirical data than other models, still it needs (at minimum) four important input data; namely the efficiency of inlet and passage diffusion, the deviation angle for primary flow, and the relationship between secondary mass flux and secondary flow area. Correlations of these four input data are specific for each design and dependent on the size of the compressor and the quality of its design. The appropriate data range of the diffusion efficiency can be found in Japikse and Osborne [10]. More difficult is the specification (or determination) of the flow deviation angle and the relationship between the secondary mass flux fraction and the secondary flow embedded area fraction. Information for these two important parameters are collected from the CFD calculation and serve as input into the two-zone model. Secondary mass flux and area fraction are calculated according to Eq. (5), where the spatially calculated efficiency η_i is compared to the mass averaged efficiency in the impeller exit plane. It should be noticed that the constant in Eq. (5) is chosen arbitrarily (k_{sec} =0.05), since according to the flow distribution there is a smooth transition between the jet and the wake flow. Other definitions of secondary flow fraction might be possible, i.e., not based on deviation to the mean value but based on deviation to an absolute value of efficiency.

$$\text{if } [\eta_i \leq (1 - k_s)\bar{\eta}] \quad \text{then } m = m_s \quad \text{endif} \tag{5}$$

The characteristic lines of secondary flux and area fraction versus flow range are similar for all impellers (see Fig. 16). Toward the surge flow, the characteristics of secondary flow flattens out. Reduced exducer width and increased back sweep lowers the fraction of secondary mass flux and secondary area. Near choke regime, the secondary flux curves of all impellers gather. Changes for flow area fraction are more significant than for the flux fraction. The flow deviation angle shows a similar dependency on the back sweep angle and exducer width. With reduced back sweep angle and increased exducer width, the flow deviation angle rises.

General Comments on 1D Performance Prediction. The nonideal diffusion characteristics is a function of the inlet diffusion and passage diffusion. While the inlet diffusion can be expected to be constant for all six impeller derivatives, the passage diffusion geometry factor C_{pb} is effected by the exit width and exit back sweep angle. Both increased width and reduced back sweep angle cause an increase of C_{pb}. The complete diffusion characteristics $\text{MR}_2/\text{MR}_{2i}$, however, are degraded with increased width, resulting in lower diffusion at a given swirl factor (see Fig. 17). Besides the lower diffusion potential, efficiency and the slip factor are also degraded and the secondary mass flow ratio increased. With reduced width and increased back sweep, the swirl parameter reduces because of increased meridional velocity. The static and total pressure increase with increased exducer width. The qualitative behavior of the secondary flow fraction, impeller exit pressure, and swirl number remains constant for different diffusion efficiencies.

Nontuned 1D Performance Prediction. The correlation between secondary mass flux fraction χ and secondary flow area fraction ε according to Eq. (A3) (Appendix) was used. The inlet diffusion efficiency was chosen equal to 0.7, while the passage diffusion efficiency was selected to 0.4 and 0.5 for the 45 deg and 38 deg impellers, respectively. Comparison of the 1D diffusion characteristics with the CFD post-processed diffusion characteristics gave reasonable agreement. The deviation angles of secondary flow and primary flow for all impeller derivatives over the entire mass flow range were set to 5 deg and 6 deg, respectively. Straight dashed lines in the top left subfigure of Fig 17 show a diffusion reference band as indication of the diffusion quality [10].

Maximum diffusion is around 1.65, a reasonable value for a well-designed impeller of medium size such as the MTU base impeller. Secondary mass flux is below 15%, which is in the similar order of magnitude as predicted by the CFD calculations. However, the secondary mass flux fraction increases toward the surge flow, which is in contrast to the post-processed CFD data. Furthermore, at constant back sweep angle and mass flow, the variation of secondary mass flux with alternated exducer width is ±2.5%, which is more significant than in the CFD results. The derivatives of the 38 deg impeller and the 45 deg impeller have efficiency maxima at different mass flows. With reduced width and increased back sweep, efficiency curves are slightly shifted toward the surge line. The efficiency slope is steeper than predicted from CFD. Surprisingly, the slip factor seems relatively

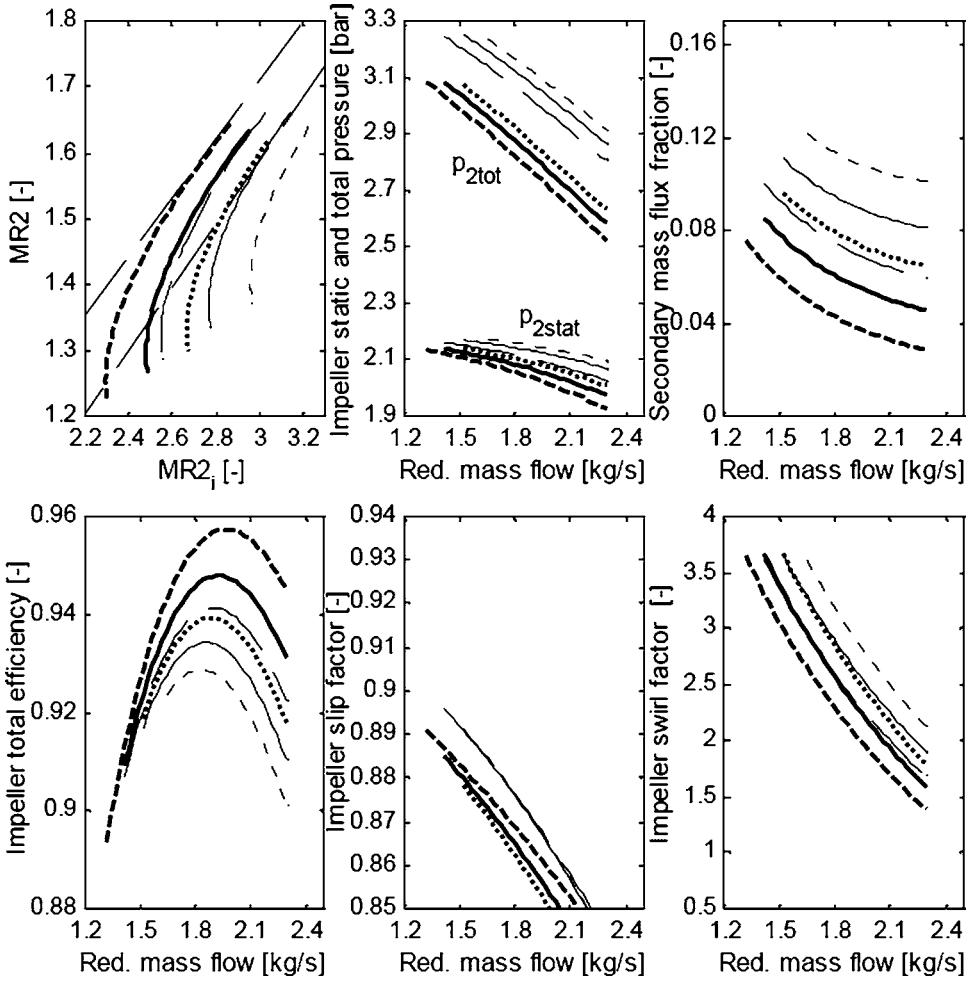

Fig. 17 1D impeller performance prediction without "tuning": (thick lines) 45 deg impeller, (thin lines) 38 deg impeller, (solid line) 1.00 width, (dashed line) 0.925 width, (dotted line) 1.075 width

independent of the variation of exducer width. At constant mass flow, slip factors of all impellers differ only by 1–2%. The absolute value of slip factor at design mass flow (m=2.3 kg/s) is around 2–6% points less than predicted from the 3D program but in a similar range as to be expected from the Wiesner slip factor ($\sigma_{45\ \mathrm{deg}}$=0.873, $\sigma_{38\ \mathrm{deg}}$=0.867). In general, the 1D swirl factor shows relatively good agreement with CFD data, only having slightly higher values than CFD results toward the higher mass flow range.

1D Performance Prediction With Tuned Secondary Mass Flux. The next step was the performance prediction with implemented information about secondary flux fraction χ coming from CFD calculations. The flow deviation angle was kept constant equal to 5 deg. Figure 18 shows a significant change in both the slip factor and the efficiency prediction. These slip factors show the right curvature and more reasonable absolute values closer to the CFD prediction and Wiesner slip factor as well. Still, the minimum of slip is not shown as in the CFD prediction. The magnitude of efficiency maxima is reduced to values similar to the CFD prediction. Swirl factor and the diffusion characteristics are not effected by the implementation of CFD- secondary mass flux distribution.

While total pressure is satisfactorily predicted in the vicinity of surge, it is overestimated close to choke flow. With alternative geometry, the total efficiency does not follow a trend similar to the CFD results. With increasing mass flow, total efficiency drops down too early. However, the quantitatively lowest efficiency maximum is given for 45@0925 as predicted from CFD.

In order to further improve the 1D prediction, there was an attempt to implement data for both the secondary flux fraction χ and secondary flow area fraction ε from CFD (Fig. 16). In Fig. 19 the ε-χ values are correlated to each other and compared to the correlation from the 1D program. The left part of Fig. 19 also shows the standard correlation $\chi=\varepsilon^2$ in comparison with CFD processed data. CFD data follow the same trend as the standard correlation, though shifted toward smaller ε. The ε-χ correlation from the 1D program looks different, showing a discontinuity. For operation away from surge and increasing exducer width, the ε-χ lines for 38 deg and 45 deg impellers move toward both higher flux and area fraction. It should be noted that for 1D prediction calculation of the flux area fraction ε is based on conservation of continuity. Attempts to implement the combined CFD ε-χ correlation into the 1D program failed since results gave unreasonably high secondary flux and very low total impeller efficiency (not shown here). Selecting a different constant k_{sec} in Eq. (5) for the calculation of secondary mass flow from CFD data resulted in a similar slope for the characteristic trend as given in Fig. 19, but shifted toward higher χ values. Unfortunately, the authors cannot explain the reason for the relatively small embedded area of secondary flow, compared to common relationships from the literature such as (Eq. (A3)) in the Appendix.

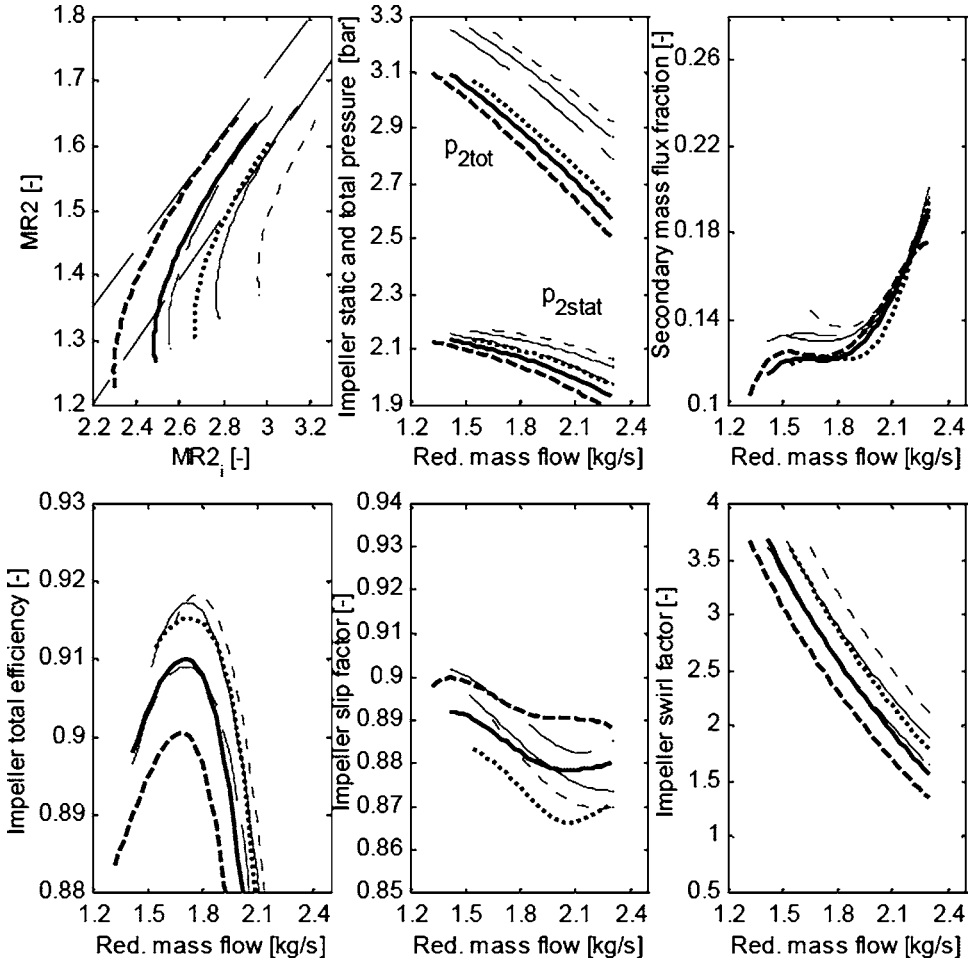

Fig. 18 1D impeller performance prediction with "matched secondary flux": (thick lines) 45 deg impeller, (thin lines) 38 deg impeller, (solid line) 1.00 width, (dashed line) 0.925 width, (dotted line) 1.075 width

1D Performance Prediction With Tuned Secondary Mass Flux and Deviation Flow Angle Distribution. The 1D model is tuned by implementing the secondary mass and flow angle distribution from Fig. 16. The most important change occurs in the slip factor prediction (see Fig. 20). The slip factor better follows the characteristic from CFD, also showing a minimum over the operation range. Still, the difference of slip factor in between the several impellers is overpredicted in comparison to CFD. By implementing secondary flux information, the total pressure rise is only slightly effected showing a smooth dent over the operational range. The diffuser pressure recovery predicted from the 1D program (Eqs. (A6)–(A8), see Appendix) features the same trend as the one from CFD results, with a maximum pressure recovery for the 45@0925 impeller (see Fig. 20). However, there is no dependency of back sweep angle and exducer width on the slope of pressure recovery in the 1D results as shown from CFD.

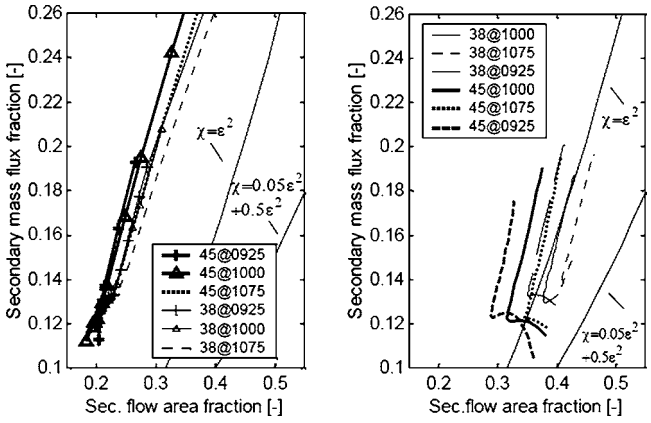

Fig. 19 (Left) ε-χ correlation from CFD: (right) ε-χ correlation from 1D program

Conclusions

A CFD model was validated against measurements showing satisfactory agreement with experimental data regarding the prediction of impeller flow field and impeller performance.

The effect of two different back sweep angles and three different exducer widths on the flow field and performance was analyzed. Extended operation toward the surge line, improved impeller exit flow uniformity, and increased pressure recovery were shown for the 45 deg impeller with reduced width (45@0925 impeller). The more uniform flow field of 45@0925 impeller showed higher performance potential for vaned diffuser arrangement, which was not investigated here. According to CFD, the effect of different back sweep and exducer width on total impeller efficiency was around a 1% difference among all different impellers at efficiency maximum, in contrast to the 1D prediction where total efficiency varied over 2%.

CFD flow field data were post-processed for the implementation of characteristics of flow deviation angle and secondary mass

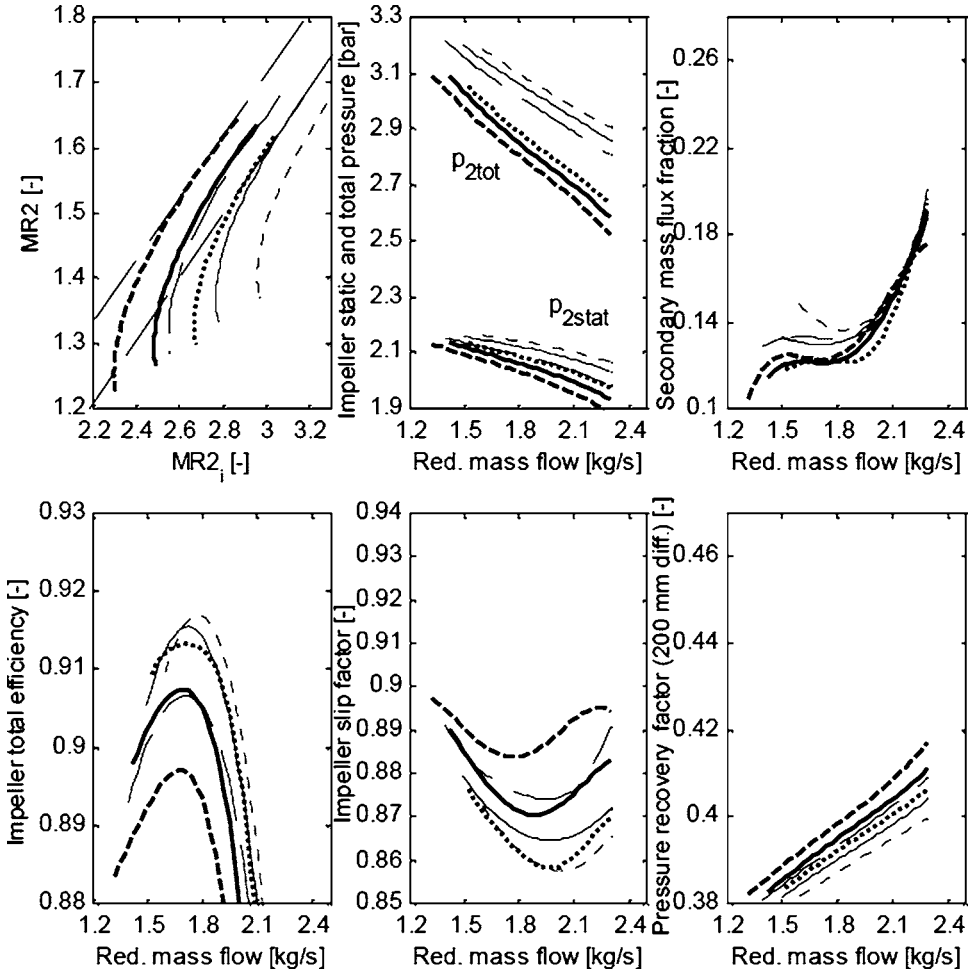

Fig. 20 1D impeller performance prediction tuned with ε and deviation flow angle distribution: (thick lines) 45 deg impeller, (thin lines) 38 deg impeller, (solid line) 1.00 width, (dashed line) 0.925 width, (dotted line) 1.075 width

flux distribution into the 1D program. Thereby, the 1D prediction of the slip factor over the operation range was set in better agreement with the CFD data. Except for the total efficiency, the overall 1D performance prediction was relatively satisfactory without tuning. By utilizing CFD data, the dependency of back sweep and impeller width on total efficiency could be quantitatively improved.

Relatively high sensitivity of the impeller efficiency prediction for the two-zone model input data was shown by comparison of the case with standard data (Eq. (A3)) for "flow deviation angle and secondary flux" and the CFD post-processed data. In the future, implementation of post-processed CFD data (for impellers of geometry different than the ones utilized in this work) might serve as a platform for generating a database of two-zone model relevant input data.

Acknowledgment

Professor Dr.-Ing. R. Niehuis and Dr.-Ing. H. Hönen (RWTH Aachen, Institute of Jet Propulsion and Turbomachinery) are gratefully acknowledged for provision of the "Radiver" test-case data and additional information on the MTU compressor. The authors are also thankful to Prof. T. Torisson, Associate Prof. M. Assadi (LTH, Dep. of Energy Sciences) and especially to MSc M. Ising (Volvo Aero VAC Sweden) for support and discussion.

Nomenclature

A_{Geo} = geometric area (m^2)
A_S = secondary flow embedded area (m^2)
b_2 = exducer width (m)
c_m, c_{2m} = meridional velocity, absolute velocity component at, impeller exit, mixed condition (m/s)
$\bar{c}_{m2m}, c_{m2p}, c_{m2s}$ = meridional absolute velocity component at impeller exit. Mixed, primary and secondary flow, respectively (m/s)
$\bar{c}_S$ = mass averaged slip velocity (m/s)
$c_\Theta, \bar{c}_{\Theta 2m}$ = tangential absolute velocity component at impeller exit, mixed condition (m/s)
C_f = friction factor
C_{pb} = passage diffusion factor
d_{hydr} = hydraulic diameter (m)
m, m_s = mass flow, secondary mass flux (kg/s)
$M_{1t,\mathrm{rel}}$ = relative Mach number, inducer tip
$M_{2p,\mathrm{rel}}$ = relative Mach number of primary flow, impeller exit
$\mathrm{MR}_2 = M_{1t,\mathrm{rel}}/M_{2p,\mathrm{rel}}$ = diffusion ratio based on relative Mach number

$MR_{2i}=M_{1t,rel}/M_{2p,rel,i}$ = ideal diffusion ratio based on relative Mach number
N, N_{des} = shaft speed, design shaft speed (rpm)
p, p_{2stat}, p_{2tot} = pressure, static-, total impeller exit pressure (bar, Pa)
r, r_2, r_4 = radius, impeller exit-, diffuser exit radius (m)
t_{2b} = blade thickness, trailing edge (m)
u_2 = exducer tip speed (m/s)
w_{2p} = relative velocity (primary flow), exit (m/s)
$w_{dev,rel}=(w-\bar{w})/\bar{w}$ = relative deviation of relative velocity
Z = blade number
$\alpha, \alpha_2, \alpha_{2c}$ = absolute flow angle, swirl angle, and critical swirl angle (deg)
β_2, β_{2b} = relative flow angle and relative impeller blade angle, from meridional direction (deg)
β_{2p}, β_{2s} = relative angle of primary- and secondary flow (deg)
$\beta_{dev=}\beta_2-\beta_{2b}$ = absolute deviation of relative flow angle (deg)
$\beta_{dev,rel}=(\beta-\bar{\beta})/\bar{\beta}$ = relative deviation of relative flow angle
ε = secondary flow area fraction
$\lambda_{2m}=c_{\Theta 2m}/c_{m2m}$ = swirl factor
η_i = spatially resolved efficiency
$\rho, \rho_{2p}, \rho_{2s}$ = density, density of primary and secondary flow (kg/m^3)
$\sigma, \sigma_{38\ deg}, \sigma_{45\ deg}$ = impeller slip factor, Wiesner slip factor for the 38 deg and 45 deg impeller
ϕ = diffuser inclination angle (deg)
χ = secondary mass flux fraction

Appendix

A1. Short Introduction to the Impeller Two-Zone Model. The area occupied by the secondary flow is defined by Eq. (A1), whereas ε, Z, t_{2b}, b_2, r_2, and β_{2b} refer to the ratio of secondary flow area to the geometric area A_{geo}, the number of blades, the blade thickness, the exducer width, the exit tip radius and the relative blade outlet angle, respectively,

$$A_s = \varepsilon A_{geo} = \varepsilon\left(2\pi r_2 b_2 - \frac{Z b_2 t_{2b}}{\cos\beta_{2b}}\right) \tag{A1}$$

$$m(1-\chi) = (1-\varepsilon)\rho_{2p} W_{2p} A_{geo} \cos\beta_{2p} \tag{A2}$$

$$\chi = 0.05\varepsilon + 0.5\varepsilon^2 \tag{A3}$$

The fraction of secondary mass flow can be calculated by applying the continuity equation on the outlet sectional area with χ as the fraction of secondary mass flow; ρ_{2p} as the primary density; w_{2p} as relative velocity; and β_{2p} as the relative flow angle of primary flow. To close the system of equations, the relative flow angle of primary flow or the deviation from the blade angle has to be defined as an input parameter. The flow angle deviation is in the range from −5 deg to +15 deg, dependent on parameters such as specific speed. The static pressure is assumed to be equal for the primary and secondary flow before mixing. The process of mixing of the primary and secondary flow at the impeller outlet is accomplished by applying the momentum and continuity equation.

The derivation of sensitivity coefficients (i.e., to be used for an uncertainty study of the two-zone model) reveals that the sensitivity coefficient $\partial p_{2tot}/\partial\beta_{2p}$ is a function of mass flow and geometry (b_2, r_2), see Eq. (A4). The sensitivity coefficient $\partial p_{2tot}/\partial\varepsilon$ (Eq. (A5)) is dependent on the velocity triangle of secondary flow and primary flow (being a function of the geometry, shaft speed, the mass flow and the secondary flow angle β_{2s})

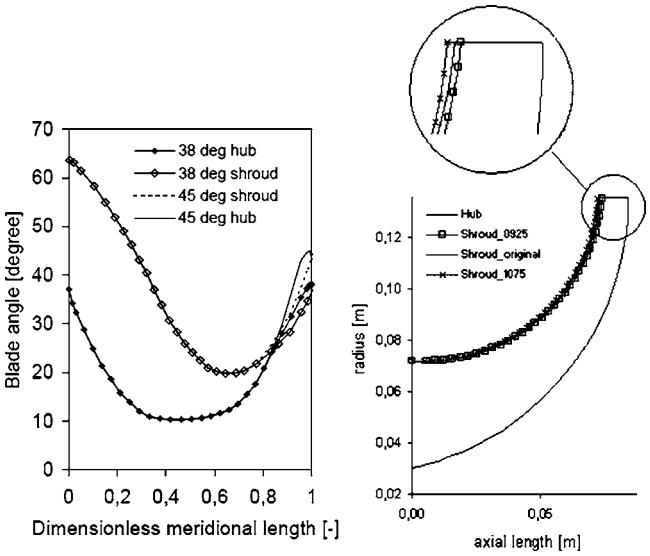

Fig. 21 Hub- and shroud angle distribution and meridional contour

$$\frac{\partial p_{2tot}}{\partial\beta_{2p}} = \frac{\partial p_{2tot}}{\partial c_{m2p}}\frac{\partial c_{m2p}}{\partial\beta_2} = \frac{m}{2\pi r_2 b_2} w_{2p}\sin\beta_{2b} \tag{A4}$$

$$\frac{\partial p_{2tot}}{\partial\varepsilon} = f\left(c_{2s}, c_{m2s}, \frac{\partial c_{2s}}{\partial c_{m2s}}, \frac{\partial c_{m2s}}{\partial\varepsilon}, \beta_{2s}\right)$$

$$\frac{\partial c_{m2s}}{\partial\varepsilon} = f(m, \rho_{2p}, \rho_{2s}, \varepsilon, r_2, b_2, \beta_{2b}, z) \tag{A5}$$

$$\frac{\partial c_{2s}}{\partial c_{m2s}} = f(u_2, c_{m2s}, \beta_{2s})$$

A2. Impeller Blade Geometry Variation

A3. 1D Vaneless Diffuser Model Equations

$$c_m\frac{dc_m}{dr} - \frac{c_\Theta^2}{r} + C_f\frac{c^2\cos\alpha}{b\sin\phi} + \frac{1}{\rho}\frac{dp}{dr} = 0 \tag{A6}$$

$$c_m\frac{dc_\Theta}{dr} + \frac{c_\Theta c_m}{r} + C_f\frac{c^2\sin\alpha}{b\sin\phi} = 0 \tag{A7}$$

$$\frac{1}{\rho}\frac{d\rho}{dr} + \frac{1}{c_m}\frac{dc_m}{dr} + \frac{1}{b}\frac{db}{dr} + \frac{1}{r} = 0 \tag{A8}$$

References

[1] Zangeneh, M., Schleer, M., Ploger, F., Hong, S.S., Roduner, C., and Ribi, B., 2004, "Investigation of an Inversely Designed Centrifugal Compressor Stage—Part 1: Design and Numerical Verification," ASME J. Turbomach., **126**, pp. 73–81.
[2] Krain, H., 2002, "Unsteady-Diffuser Flow in a Transonic Centrifugal Compressor," Int. J. Rotating Mach., **8**(3), pp. 223-231.
[3] Brun, K., 2003, *Analysis of Secondary Flows in Centrifugal Impellers*, Southwest Research Institute, San Antonio, TX, Solar Turbines Inc.
[4] Ziegler, K.U., 2003, "Experimentelle Untersuchung der Laufrad-Diffuser-Interaktion in einem Radialverdichter variabler Geometrie," (Dissertation RWTH Aachen), Shaker Verlag, Germany, Aachen, D82.
[5] Eckardt, D., 1975, "Instantaneous Measurements in the Jet-Wake Discharge Flow of a Centrifugal Compressor Impeller," ASME J. Eng. Power, **97**, pp. 337–345.

[6] Japikse, D., 1996, *Centrifugal Compressor Design and Performance*, Concepts ETI, Inc.
[7] Rodgers, C., 1979, "Specific Speed and Efficiency of Centrifugal Impeller," *Performance Prediction of Centrifugal Pumps and Compressors*, S. Gopalakrishnan, P. Cooper, C. Grennan, and J. Switzer, eds., ASME, New York, 191–200.
[8] Cumpsty, N.A., 1989, *Compressor Aerodynamics*, Wiley, New York.
[9] Eckert, B., and Schnell, E., 1961, *Axial- und Radial-Kompressoren, Anwendung, Theorie und Berechnung*, Auflage, Springer, Berlin, Vol. 2.
[10] Japikse, D., and Osborne, C., 1986, Optimization of Industrial Centrifugal Compressors, Part 6a and b: Studies in Component Performance- Eight Design Cases from 1972 to 1982, *Proceedings of the International Gas Turbine Conference and Exhibit Düsseldorf*, West Germany, June 8–12.
[11] Frigne, P., and Van den Braembussche, R., 1985, "A Theoretical Model for Rotating Stall in the Vaneless Diffuser of a Centrifugal Compressor," Trans. ASME: J. Eng. Gas Turbines Power, **107**(2), 507–513.
[12] StarCd V 3.150A, 1998–2002 *Methodology Manual*, CD-Adapco Group.
[13] Weiss, C., Grates, D.R., Thermann, H., and Niehhuis, R., 2003, "Numerical Investigation of the Influence of the Tip Clearance on Wake Formation Inside a Radial Impeller," *Proceedings of ASME Turbo Expo 2003*, Atlanta, GA, June 16–19, ASME Paper No. GT2003-38279.
[14] Galerkin, Y. B., Mitrofanov, V. P., and Prokofiev, A. Y., 2003, "The Experience of CFD Calculations for Flow Analysis in Centrifugal Compressor Stages," *Proceedings of the International Gas Turbine Congress*, Tokyo, November 2–7, IGTC2003 Tokyo OS-020.
[15] Sorokes, J. M., and Kopko, J. A., 2001, "Analytical and Test Experiences Using a Rib Diffuser In a High Flow Centrifugal Compressor Stage," *Proceeding ASME Turbo Expo 2001-GT-0320*, New Orleans, LA, June 4–7.